Investigation of CoCrFeNiMn high entropy alloy depositions during cold spray additive manufacturing

Cletus John Akisin

A thesis submitted for the degree of

Doctor of Philosophy

University of Nottingham

UK | CHINA | MALAYSIA

United Kingdom

January 2024

Abstract

Cold spray is steadily becoming a popular solid-state additive manufacturing (AM) and repair technique, referred to as cold spray additive manufacturing (CSAM). It is a material deposition technique that utilises the kinetic energy of microparticles to form dense deposits layer-by-layer on a target surface. Because of the solid-nature of the CSAM process, various components manufactured with CSAM have found applications in aero-engines as those components can withstand the extreme operating conditions of aero-engines. Since the CSAM process retains the initial microstructure of feedstock materials, being also an eco-friendly process, makes it a viable option for the deposition of several metals and alloys. Hence, substantially reducing environmental footprint and manufacturing cost.

The recent advancements in new materials development characterise the cutting-edge high performance of high entropy alloys (HEAs), attracting industrial attention for their end-use in critical parts of aero-engines. These alloys are composed of multi-principal elements with near or equal atomic proportions and striking mechanical properties that surpass those of conventional superalloys. The CoCrFeNiMn HEA has been found to possess properties like or that surpass alloys employed in manufacturing aero-engine components. The HEA's good strength-ductility combination, resistance to hydrogen embrittlement, and high fatigue resistance make it an alternative alloy for manufacturing components such as the integral parts of liquid hydrogen fuel turbopumps. However, very little has been done to explore the CSAM of the CoCrFeNiMn HEA. Therefore, this research project aims to develop and investigate deposits of the CoCrFeNiMn HEA using the CSAM technique, that can find applications for the repair and manufacture of aerospace

components, such as restoring the structural integrity of integrally bladed rotors or turbine blisks, jet engine fan shaft, thrust chamber, impellers and nozzle guide vanes. This study focused on the deposition mechanism of the HEA during the CSAM process, the effect of subsequent post-deposition annealing on the microstructure and mechanical properties of the deposits, and the residual stress formed in the deposits.

To demonstrate the repair and manufacturing of components made of several materials with CSAM of the HEA, the deposition mechanisms of the HEA on austenitic stainless steel, titanium alloy, and aluminium and its alloy materials were investigated using experimental and numerical techniques. It was found that metallurgical bonding and mechanical interlocking mechanisms were responsible for the deposition of CoCrFeNiMn HEA particles on the substrates depending on the substrate material properties. When particles are sprayed with the CSAM process, they travel at supersonic speed, and the particles stick to the targeted surface at a particle impact velocity above a certain threshold called critical velocity. At the critical velocity, the sprayed particles severely deform at the impact interfaces and bond to the substrate and previously deposited particles. The particle bonding mechanism is attributed to adiabatic shear instability (ASI). With the concept of ASI, the critical velocities of the HEA on the substrates were determined. Consequently, the optimum process conditions for the repair and manufacturing of components with CSAM of the HEA can be obtained.

With the determined process conditions, the possible manufacture and or repair of aerospace components made of stainless steel with the HEA using the CSAM process was demonstrated by spraying thick deposits on the substrate. The

deposition mechanism of the HEA during deposit build-up on the stainless steel substrate was investigated. The investigation involved the use of advanced materials characterisation techniques and numerical analysis. It was found that during the deposition of the HEA on the substrate, dynamic recrystallisation (DRX) produced by subgrain rotation and ASI are the dominant deposition mechanisms at the particle interfaces. These thermomechanical phenomena result in particle interfaces characterised by highly misoriented equiaxed ultrafine grains, whereas the particle interiors consist of coarse grains with limited deformation. The heterogeneous microstructure formed in the CSAM deposit can contribute to a good strength-ductility combination of the HEA. Nevertheless, porous microstructures were obtained in the deposits, hence post-deposition annealing treatments were performed to improve the microstructure of the deposits. The post-deposition annealing treatment resulted in the consolidation of the deposit and increased metallurgically bonded areas, leading to enhanced mechanical properties. Also, the annealing treatment thus changed the failure behaviour of the as-sprayed deposit from mostly particle-particle interface failure to ductile failure. Interestingly, it was found that the deposit annealed at 600 °C exhibited partially recrystallised microstructure with a small volume fraction of the Cr-rich phase formed at grain boundaries of the sprayed particles. It was argued that this distinct microstructure can contribute to improved strength without loss of ductility of the deposited HEA.

For the repaired or manufactured parts, it is important to measure and understand the residual stress formed in the part during the CSAM of the HEA. The residual stress of the deposited HEA on the stainless steel 304 substrate sample was studied using the contour method of stress measurements and numerical analysis. Tensile

and compressive residual stresses were formed in the HEA deposit and substrate sample. The formation of these residual stresses was based on two dominant mechanisms: temperature gradient and thermal mismatch after the cool-down stage. These mechanisms were dominant over the compressive peening effects typical of the CSAM process. Because of the thermal impacts that arose from the spraying parameters that were employed for the CSAM deposition of the HEA, tensile residual stress was formed in the sample. Consequently, the tensile stress formed in the deposit would compromise the structural integrity of the manufactured or repaired parts, which can result in early components failing in service. Hence there is a need for optimisation of the CSAM of the HEA process conditions for restoring the structural integrity of repaired parts and obtaining required structural properties of the manufactured parts. The results obtained in this study shed light on the effect of process conditions on the residual stress formation mechanisms during CSAM.

Acknowledgements

“By the grace of God, I am what I am, and His grace toward me was not in vain… 1 Corinthians 15:10”

I would like to first express my sincere gratitude to my primary supervisor, Professor Tanvir Hussain, and my co-supervisors Professor Chris Bennett and Dr Federico Venturi. Professor Tanvir Hussain was not only concerned with the research project but also with my mental and financial well-being. Thanks to Professor Chris Bennett for his thoroughness of the research work, and Dr Federico for his support and guidance. I learnt to be thorough also, critical of ideas and analytical in my investigations. I would also like to thank Mr John Kirk for his support in running the cold spray lab. My gratitude extends to the technicians at the Wolfson building and the nano-and microscale research centre (nmRC) for their support. Also, thank you to all team members at the Centre of Excellence for Coatings and Surface Engineering who made my research study at the university a memorable one.

A special thank you to my lovely wife, Godswill Akisin, who withers the storm with me and was here through tough times. Thank you, Godswill (my Emerald) for your understanding, love, and prayers. We have been blessed with two beautiful daughters: Tinaya and Adriel, during this research. Thank you, Tinaya, for your hugs when I arrived home stressed, and that always changed everything. Adriel, thank you for always touching my head and kissing me while writing. My gratitude extends also to my friends and family, and the RHN (Rehoboth House, Nottingham) community for your prayers and support.

I gratefully acknowledge financial support from the University of Nottingham through the Faculty of Engineering award scheme for international research students for this PhD. I also acknowledge the financial sponsorship of the Petroleum Technology Development Fund (PTDF), Nigeria, for this PhD.

Journal Publications

- Akisin, C.J., Bennett, C.J., Venturi, F., Assadi, H. and Hussain, T., 2022. Numerical and experimental analysis of the deformation behaviour of CoCrFeNiMn high entropy alloy particles onto various substrates during cold spraying. Journal of Thermal Spray Technology, 31(4), pp.1085-1111.

- Akisin, C.J., Dovgyy, B., Bennett, C.J., Pham, M.S., Venturi, F. and Hussain, T., 2023. Microstructural Study of Cold-Sprayed CoCrFeNiMn High Entropy Alloy. Journal of Thermal Spray Technology, pp.1-24.

- Akisin, C.J., Bennett, C.J., Venturi, F. and Hussain, T., Influence of annealing treatment on the microstructure and mechanical properties of cold-sprayed CoCrFeNiMn high entropy alloy. Journal of Thermal Spray Technology, (*Under review)*

- Akisin, C.J., Bennett, C.J., and Hussain, T., Measurement, and numerical modelling of residual stress build-up in CoCrFeNiMn high entropy alloy deposit during cold spray additive manufacturing. (*In preparation*)

Journal publication on the research area but not included in this thesis:

- Akisin, C.J., Venturi, F., Bai, M., Bennett, C.J. and Hussain, T., 2021. Microstructure, mechanical and wear resistance properties of low-pressure cold-sprayed Al-7Mg/Al_2O_3 and Al-10Mg/Al_2O_3 composite coatings. Emergent Materials, pp.1-13.

Conference

- Cletus J. Akisin, Chris J. Bennett, Federico Venturi, & Tanvir Hussain; May 22–25, 2023. "Effect of Heat-Treatment on the Microstructure and Mechanical Properties of CoCrFeNiMn High Entropy Alloy Additively Manufactured via Cold Spray." Proceedings from the International Thermal Spray Conference (ITSC), 2023. Québec City, Canada. (pp. 400-407). ASM International.

Table of Contents

List of Figures

List of Tables

1 Introduction

1.1 Additive manufacturing for aerospace & space

The aerospace & space sector, being one of the largest industries in the world, consists of the commercial aircraft and defence (military aircraft, missiles, and so on) sector, space launch, and in-space systems. The sector supports $3.5 trillion in world economic activities at 4.1 % of GDP [1]. Moreover, the global space exploration market size was valued at $486 billion and is expected to reach $1.9 trillion by 2032, at a compound annual growth rate (CAGR) of 16.21 % [2]. Although, in late 2022, the sector dealmaking activity has hit the lowest point since the 2019 COVID-19 pandemic, deals in commercial and military aircraft and spacecraft components manufacturing, repair, and maintenance have continued steadily [3]. This demand and growth are mainly due to the long-term demand for new aircraft, increased military expenditure as security threats continue intensely, increased space launch and exploration leading to high market activity, and substantial ongoing research and development [4].

Thus, there is a need for sustainable manufacturing in the aerospace sector. One of the most effective methods to reach the target of a 50% reduction in aviation emissions by 2050 is to increase the energy efficiency of aircraft through mass reduction techniques [4]. Additive manufacturing (AM) techniques have been demonstrated to help reduce the mass of components aboard aircraft and spacecraft while reducing cost and lead times. AM describes numerous techniques that allow for the automatic manufacturing of components by introducing a layer-by-

layer material addition approach rather than subtractive methods or forming materials in moulds [4,5]. AM offers unparalleled design freedom and complexity within the time and cost constraints [4]. AM has emerged as a game-changer and transformative technology in aerospace component manufacturing [4,6] and in-space manufacturing, where components or tools are manufactured in outer space [7].

According to Richard et al. [8], the AM market has grown significantly, valued at $7.85 billion in 2020, $9.12 in 2021 (CAGR of 16.2 %) with predicted growth to $21.06 billion by 2026 (CAGR of 18.2 %). The aerospace and defence sector is a prime moving sector, as shown in Figure 1.1. The AM market in that sector is predicted to increase to $3.2 billion by 2025 (CAGR of 20.4 %) [4,9]. These reports reveal substantial investment and key developments in AM technology in the aerospace sector and are expected to grow exponentially in the coming years.

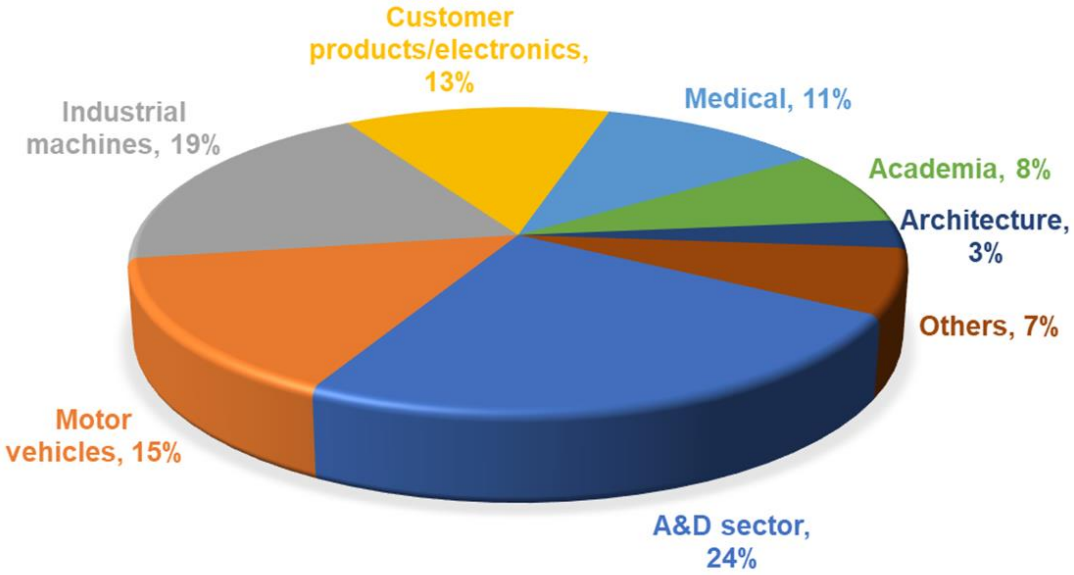

Figure 1.1: 2017 Global AM market share by sector or industry [10]. A&D annotate the aerospace and defence sector.

AM has been demonstrated to produce components by consolidating several parts without requiring an assembly. The most referenced component manufactured using the AM technique is the General Electric LEAP engine fuel nozzle, as shown in Figure 1.2a. Moreover, NASA has demonstrated the application of AM to manufacture combustion chambers and rocket nozzles for space launch vehicles using various alloys, such as GRCop-42, Inconel 718, and other superalloys [4]. In addition, SpaceX successfully developed and launched an AM-built main oxidiser valve aboard the Falcon 9 rocket and the SuperDraco engine series used in the Dragon V2 spacecraft, as shown in Figure 1.2b and c [4]. AM has also been extended to repair damaged aerospace components [11,12]. Most of these components are manufactured and repaired using metal AM processes, with the most established techniques in the sector being powder bed fusion (PBF) and direct energy deposition (DED) [13]. Despite the maturity and advantages of these metal AM techniques, achieving high-quality parts without detrimental process effects,

such as component distortion owing to undesirable thermal residual stresses, elemental segregation, and chemical compositional changes that can result from the high temperature of the processes [14–17], can limit their widespread application in component manufacturing and repair. In addition, AM uses more electricity per unit output than similar traditional methods which can contribute to CO_2 emission [18]. Hence, there is a need to explore solid-state AM methods with an even more beneficial process economy, such as a high deposition rate, shorter lead times, eco-friendliness, and ease of use for manufacturing and on-field repair.

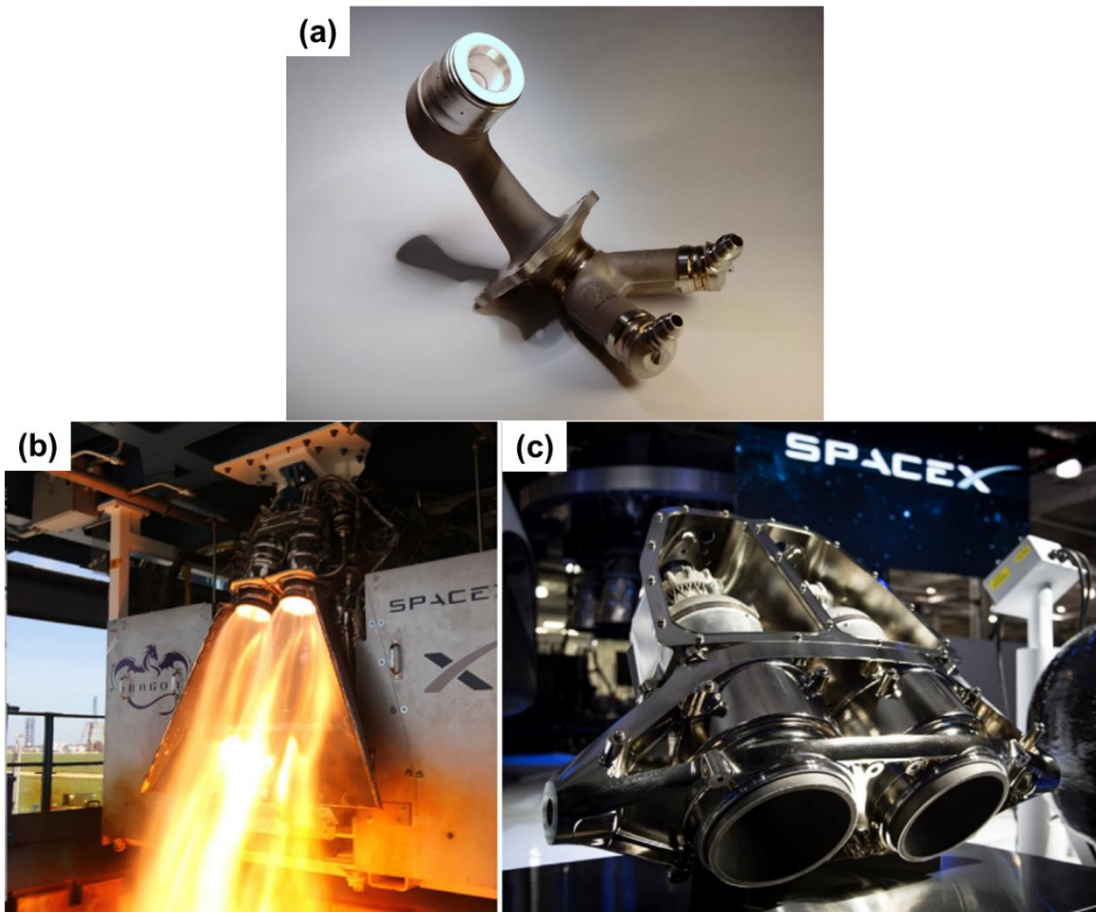

Figure 1.2: AM-built component for the aerospace sector: (a) General Electric LEAP fuel nozzle (b) Test fire of AM-built SuperDraco by SpaceX and (c) SuperDraco by SpaceX [4].

Cold spray or cold spray additive manufacturing (CSAM) has been successfully developed as a metal AM solid-state material deposition technique that meets the requirements for sustainable manufacturing and repair in the aerospace sector. The status report of AM techniques for repair applications shown in Figure 1.3 suggests that CSAM represents 10% deployment in the sector but falls behind laser direct energy deposition and arc wire direct energy deposition (i.e. DED techniques) [12]. A report by Research and Markets [19] anticipated the global CSAM market size to reach $1.6 billion by 2030 at a CAGR of 6.5 % from 2023. Moreover, the market size surpassed $900 million in 2022. The aerospace and defence sector dominates the market, accounting for 28 % of the global market share in 2022 [19], which is attributed to the adoption of CSAM for the on-field repair of many aircraft parts. Furthermore, a strong drive is seen in manufacturers undertaking acquisitions and product launches to strengthen their presence in the aerospace and defence sector, including key companies such as ASB industries, Impact Innovations GmbH, SPEED3D, and Titomic [19]. Furthermore, the US market generates significant benefits and savings from CSAM repair, which is evaluated at $22.5 million [20]. Moreover, North America dominates the CSAM market and accounts for 41 % of the global market share in 2022 [19]. Australia is also viewed as a moving prime continent in the market. This suggests the need for the UK market to take up CSAM for manufacturing and repair of components used in many sectors to strengthen their geographical presence, as few institutes in the UK share in the market size, such as the welding institute (TWI) Ltd.

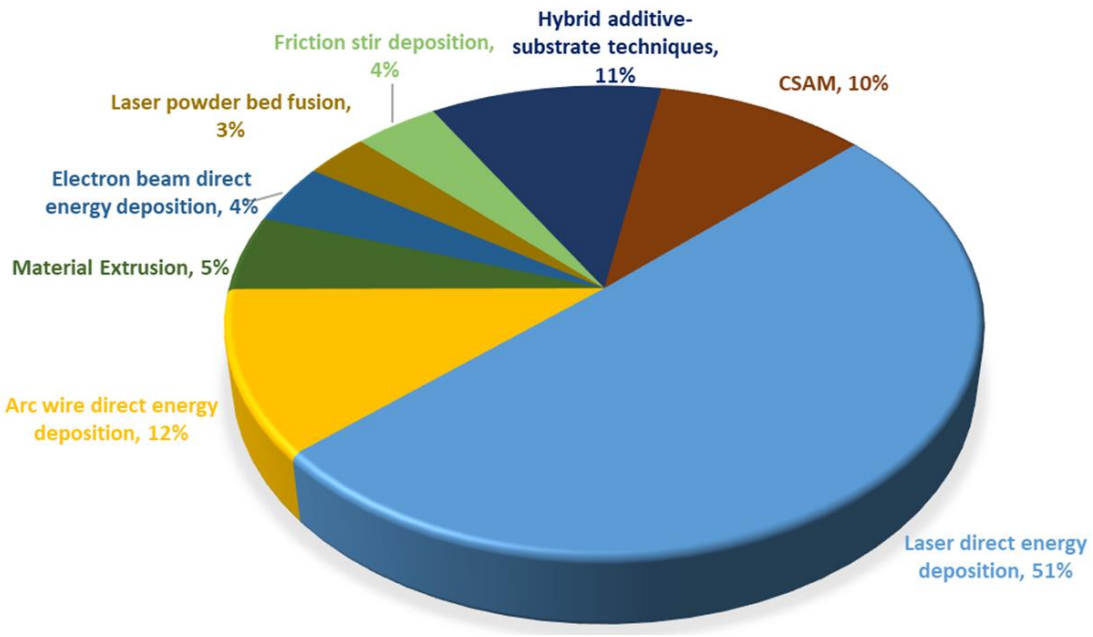

Figure 1.3: Deployment of various AM technologies for repair and manufacturing in the aerospace sector [12].

Growth drivers of the CSAM market include advancement in its capability to deposit a wide range of materials, with the aluminium (and its alloys) segment accounting for 30.6 % of the global market share in 2022, followed by titanium and its alloys estimated to have a CAGR of 7.5 % [19]. Other materials used include copper- and nickel-based superalloys. In addition, CSAM uses the kinetic energy of microparticles rather than the thermal energy of other metal AM techniques to develop deposits through a layer-by-layer material addition approach [21–23]. This solid-state nature of CSAM avoids the melting of feedstock materials and the associated effects such as phase transformation, elemental segregation, and oxidation. In addition, CSAM is eco-friendly because it uses inert gases, less electricity and has a high deposition rate. These features make CSAM suitable for manufacturing and repairing aerospace components.

1.2 Applications of CSAM in the aerospace sector

Robot-assisted and toolpath programming of CSAM is an emergent field that provides new opportunities for manufacturing complex 3D near-net components [24]. CSAM has been applied to manufacture and repair parts used in the aerospace sector. For example, Impact Innovation demonstrated a cold spray additively manufactured turbojet aircraft engine fan shaft using Ti6Al4V, as shown in Figure 1.4a [25]. The manufacturing process was completed in approximately two hours at a deposition rate of 2.7 kg/h. Additionally, NASA recently partnered with Aerojet Rocketdyne to manufacture a 3D-printed bimetallic lightweight thrust chamber assembly using CSAM and other metal-AM techniques, as shown in Figure 1.4b [26]. These manufacturing outcomes highlight the importance of CSAM in near-future manufacturing technologies and process economies. Further examples include the CSAM copper flange shown in Figure 1.4c. Other applications include the deposition of bond coats in thermal barrier coatings on turbine blades [27], aluminium heat sinks [28], and copper deposits for nuclear fuel storage [29].

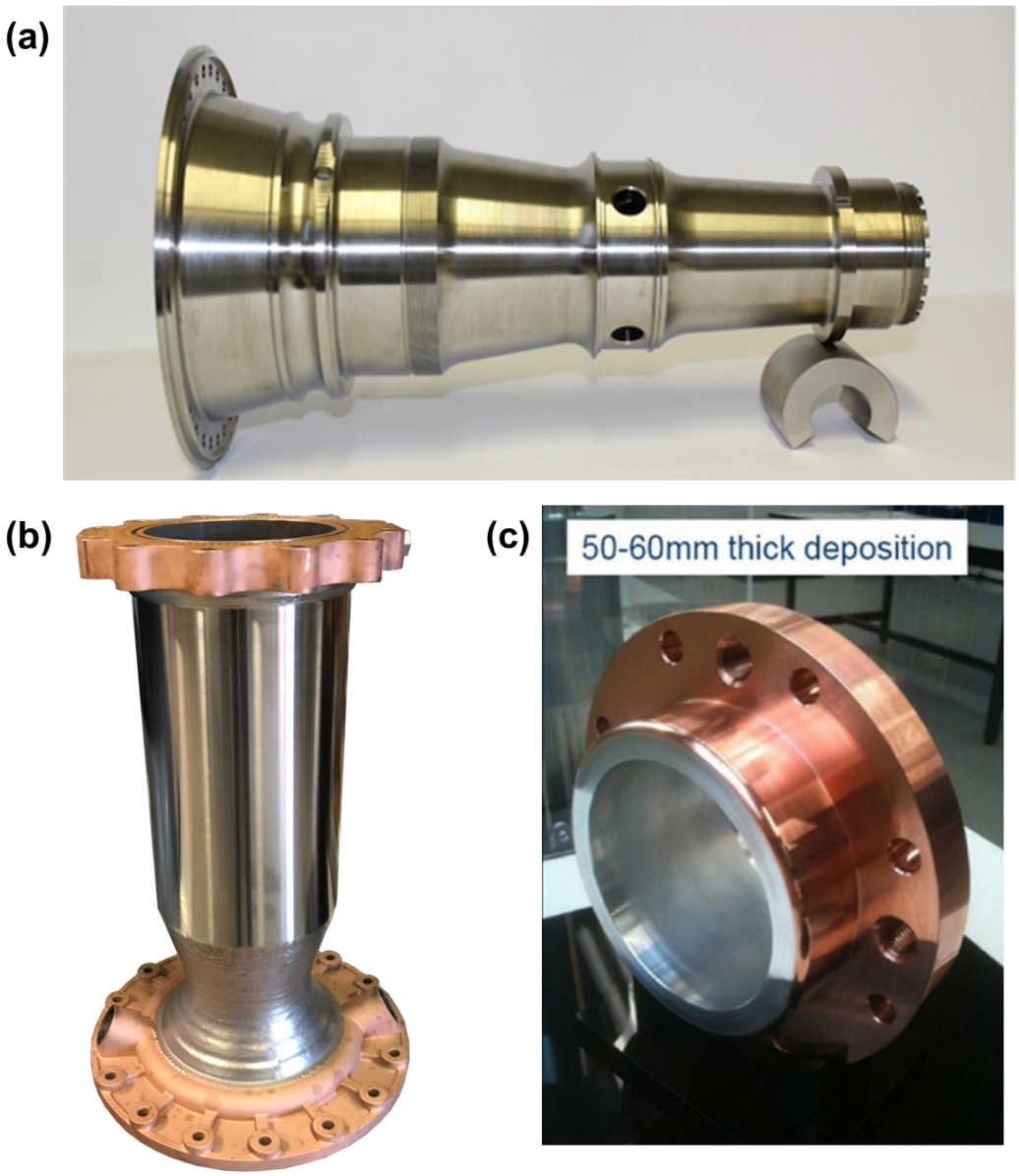

Figure 1.4: Digital photographs of CSAM: (a) turbojet aircraft engine fan shaft made of Ti6Al4V (Impact Innovation, Germany) [25], (b) bimetallic lightweight thrust chamber (NASA, USA) [26], and (c) copper flange [30,31].

CSAM can also be employed as a surfacing technique for the on-field repair of aerospace components [31]. Surface engineering involves the application of surface layers or coatings to modify the surface of a component (bulk material) to improve surface properties such as wear resistance, corrosion resistance, oxidation resistance, and thermal insulation. Surface coating deposition techniques include

thermal spraying and cold spraying (CSAM). These techniques have had a profound impact on reducing sustainment costs in the aerospace and defence sectors. CSAM has been employed to improve corrosion resistance and reduce the amount of maintenance required by the sector, owing to the significant cost of corrosion and wear prevention and mitigation experienced by the sector. The most severe corrosion of certain aerospace components is associated with gearbox housings for rotorcraft made with magnesium alloys, and CSAM repair applications have become an accepted practice for providing corrosion protection layers [32,33]. Figure 1.5 displays several repairs and restorations of damaged parts for various applications using CSAM. Several of these components are returned to service. In addition, CSAM can be used to add additional features to a machine component, as shown in Figure 1.5. The repair of these damaged components with CSAM in the aerospace sector, as well as in several other industries, is an attractive cost- and time-saving practice. Thus, CSAM requires consistent and further development to adapt to changes in the requirements of these industries.

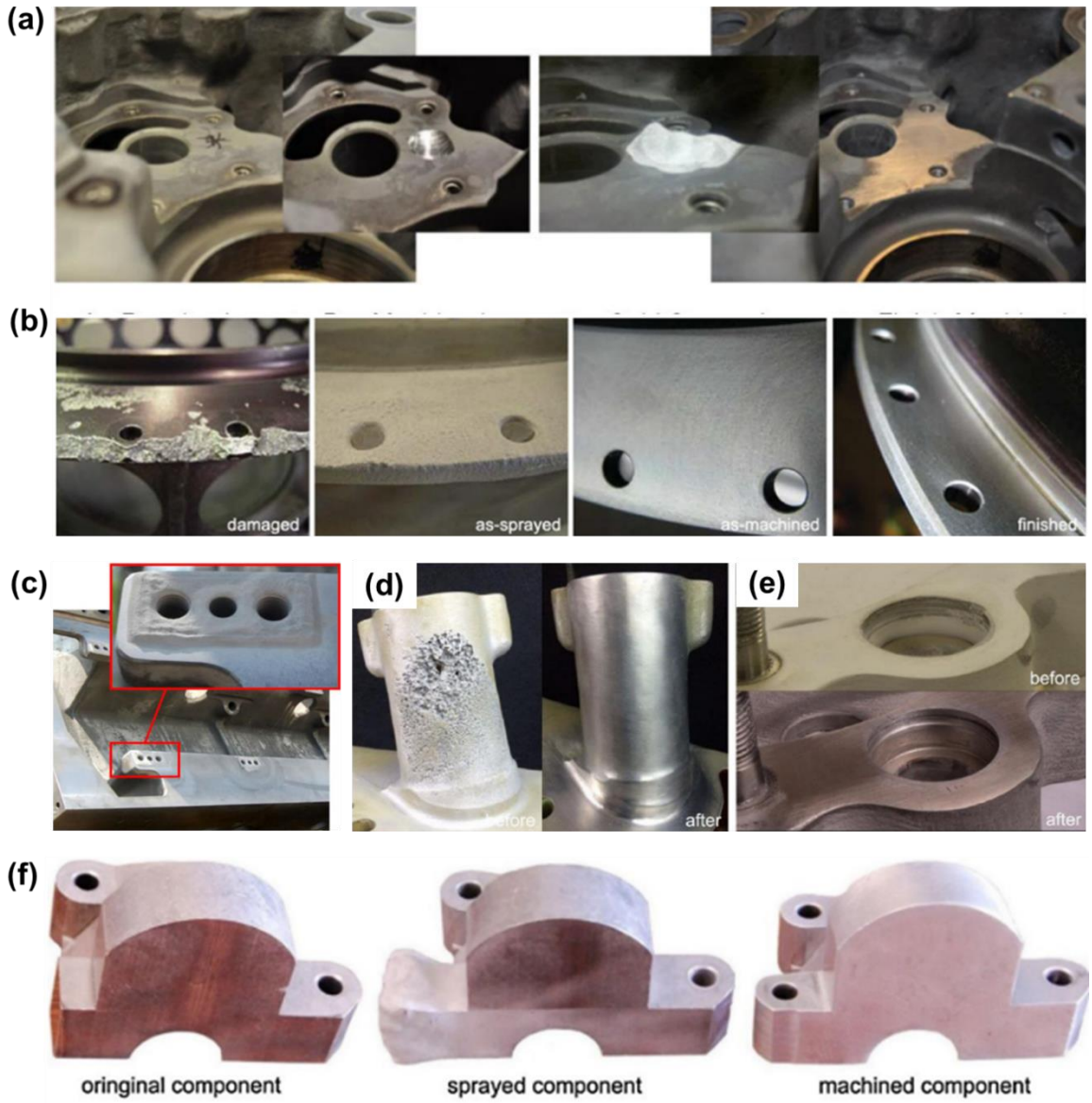

Figure 1.5: CSAM for repair and restoration of damaged components: (a) Z341 magnesium alloy gearbox housing repair [32], (b) steps involved in the restoration of damaged parts [31],(c) dimensional restoration of an iron engine block [32], (d) repair of an S-92 helicopter gearbox sump, (e) repair of an oil tube bore in CH47 helicopter accessory cover, and (f) addition of features to a component [31].

1.3 High entropy alloys for aerospace

Material selection for end use in the aerospace sector is critical for components and mission success. Metals and metal alloys are most commonly used for the manufacturing and repair of aerospace components, which often come from copper,

aluminium-, stainless steel, titanium-, nickel-, and iron-based superalloys and refractory alloys [6]. These materials must meet a long list of technical requirements for the aerospace sector, including high strength-weight ratios, the ability to withstand cryogenic and elevated temperatures, the capacity to operate under cyclic and dynamic loading conditions, oxidation, and hydrogen embrittlement resistance [6]. Because the aerospace sector tends to be more risk-sensitive, manufacturing and repair of components may lead to the use of common alloys. As many AM processes, and even CSAM, have become widely accepted and adopted for manufacturing and repair in the aerospace sector, the adoption of new alloys can readily occur to increase end-use performance and eliminate issues arising during traditional manufacturing. Moreover, NASA and GE identified the need for new alloy development for the aerospace sector [6,34].

New metallic alloys, high entropy alloys (HEAs), first introduced in 2004 [35,36], offer excellent mechanical properties [37] that meet the requirements of the aerospace and space sector. In a recently published article by Paul et al. [6], it was mentioned that NASA is developing custom refractory HEAs for the AM of components in space propulsion systems. Nevertheless, research on the AM of HEAs has seen a tremendous increase in publications over the last few decades, as presented in Figure 1.6. More than 2000 articles have been published each year for the last three years, with nearly 12500 articles published since it was first introduced in 2004. This suggests that the outlook on the AM of HEAs is promising, particularly for aerospace component manufacturing. In addition to technological advancement and the adoption of AM of HEAs for the aerospace sector, several issues are limiting its applications to niche areas. These issues include less control

over the elemental distribution within the bulk parts after solidification when exposed to laser irradiation, susceptibility to cracking, and nonequilibrium solidification features [38]. This is where CSAM occurs and provides unique advantages owing to its minimal thermal input. The feedstock microstructure in CSAM is retained after deposition, as in the solid-state AM method.

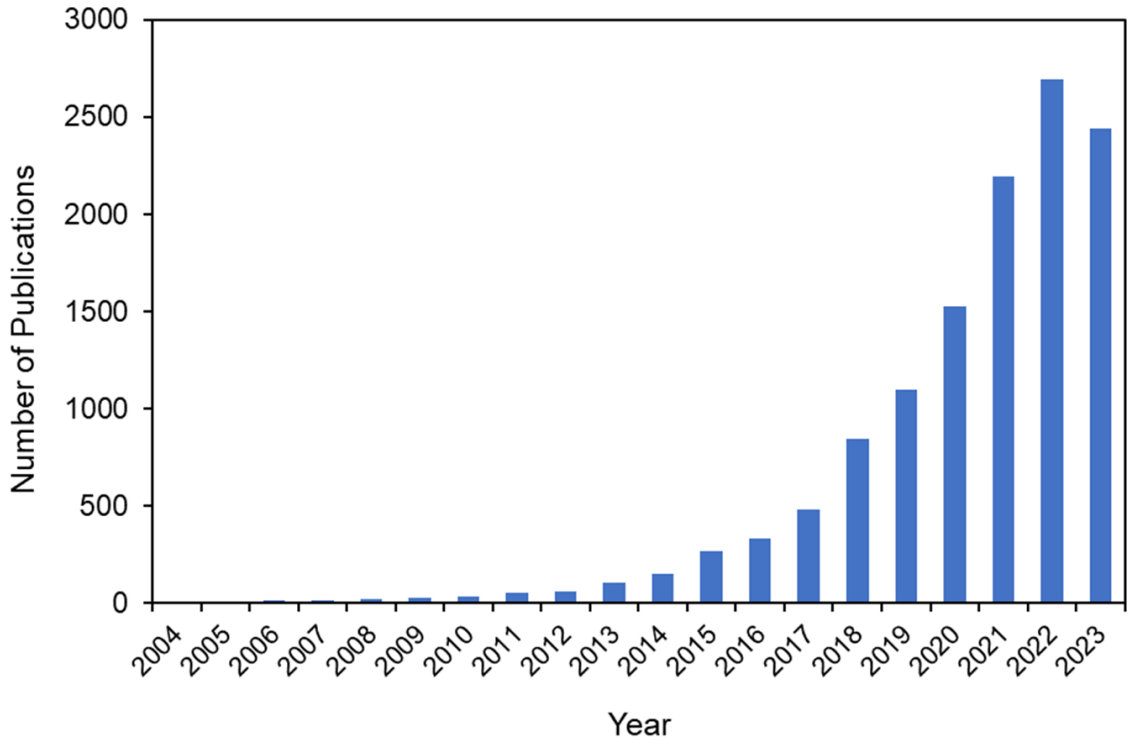

Figure 1.6: Number of publications on AM of HEAs year-wise over the last two decades. Note that the data was obtained from Web of Science using the keywords: “additive manufacturing” and “high entropy alloys”. In addition, other variants or keywords of high entropy alloys, such as high-entropy alloys, were included.

CSAM of HEAs has also seen a significant increase in publications, with a total of 42 articles published since 2019, when CSAM was first demonstrated to deposit HEA [39,40]. The CoCrFeNiMn HEA, commonly known as the Cantor alloy, is the first and most widely studied HEA. The HEA forms a solid solution with a single-phase FCC crystal structure, with attractive mechanical properties. It has been

reported that the HEA displays exceptional damage tolerance with tensile strength of 730 to 1280 MPa, and fracture toughness properties exceeding 200 MPa.$m^{1/2}$ at cryogenic temperatures down to 77 K [41]. Also, the HEA shows excellent low-temperature ductility up to ~71% at room temperature to ~90% at cryogenic temperature (77 K) [42]. These properties of the HEA have been reported to be comparable to austenitic stainless steels and high-nickel steels, but with its fracture toughness exceeding those of all pure metals and metallic alloys [41]. Moreover, the excellent tensile strength of the HEA was reported after repeated rolling at 77 K and 293 K, reaching 1.5 and 1.2 GPa, respectively [43]. Also, the HEA exhibits Vickers microhardness (HV) in the range of 222-418 HV0.3 after cold rolling [44]. Other properties reported for the HEA are its resistance to hydrogen embrittlement [45], wear, corrosion [46], and oxidation [47] resistances. These properties have motivated the advancement and adoption of HEA for the repair and manufacturing of components in the aerospace and defence sector using CSAM.

1.4 Aim and objectives of the research

The overall aim of this study was to develop and investigate CoCrFeNiMn HEA deposits using CSAM, with a focus on understanding deposit formation and improving the deposit microstructure through post-deposition heat treatment.

To achieve this, the objectives of this study were set as follows:

- To investigate the deformation behaviour of HEA particles and evaluate the critical velocity of the HEA during CSAM using experimental and numerical

techniques. To overcome the challenge of limited material model data that exists for the HEA to capture the plastic deformation of the material during the ultra-high strain rate CSAM deposition.

- To provide a better and more detailed understanding of the dynamic recrystallisation (DRX) mechanism and microstructure evolution occurring during the CSAM of HEA using advanced material characterisation and numerical analysis.

- To evaluate the effect of post-deposition annealing treatment on the microstructure and mechanical properties of HEA deposits using materials characterisation and mechanical testing techniques.

- To measure, analyse and predict the residual stress formed in the HEA deposits during the CSAM process using both experimental techniques and numerical analysis.

1.5 Thesis structure

This section provides an overview of the organisation of this thesis and a brief description of the content of each chapter.

Chapter 2 presents a comprehensive and critical literature review. This chapter is divided into seven sections: Sections 1 & 2 provide the fundamentals of CSAM. Section 3 discusses gas and particle dynamics through a converging-diverging nozzle, governing equations for analytical estimation, and computational fluid

dynamics modelling to predict gas flow features. Section 4 summarises the deposition mechanism in the CSAM of metallic materials, this includes the bonding mechanism, critical velocity and window of deposition. Section 5 focuses on the DRX mechanism in the CSAM deposition of metals. Section 6 provides current studies on the numerical modelling of particle deposition during CSAM. Finally, Section 7 discusses the current studies on residual stresses in CSAM deposits. Section 8 provides a summary of HEAs and specifically discusses the CoCrFeNiMn HEA. Current studies on the CSAM of HEA are discussed in Section 9.

Chapter 3 describes the experimental methods and details of the various techniques employed in this research work. The CSAM rig, material characterisation techniques and residual stress measurements are included in this chapter.

Chapter 4 provides detailed information on the numerical modelling methods employed in this research work. The numerical methods for particle impact deposition modelling and residual stress modelling are included in this chapter.

Chapter 5 provides a comprehensive and detailed study of the particle impact phenomena and critical velocity of the CoCrFeNiMn HEA. A single-particle impact test was performed using the swipe test. The impact morphology of the particles on various substrates was observed through scanning electron microscopy (SEM). The flattening ratio (FR) as a mechanistic “diagnostic tool” was employed to assess and select the appropriate material model data that best predicted the particle deformation behaviour during CSAM. Numerical analysis using the Abaqus/Explicit code was employed to determine the critical velocity and explain the bonding mechanism of the HEA on various substrates.

Chapter 6 presents a study of the deposition mechanism during deposit build-up using advanced material characterisation techniques and numerical simulations. The DRX mechanism during CSAM deposition of HEA was examined using electron backscattered diffraction (EBSD) imaging. A multiparticle impact simulation was performed using the Abaqus/Explicit code to explain the deposition mechanism of the HEA.

Chapter 7 presents a detailed investigation of the influence of post-deposition annealing treatment on the CSAM HEA deposits. A post-deposition annealing treatment was used to improve the microstructure of the deposit, and the effects on the microstructure and mechanical properties were studied. The resulting microstructures were characterised using SEM, EBSD, and energy-dispersive X-ray spectroscopy (EDX). The hardness and tensile properties of the as-sprayed and annealed deposits were also measured. Thermodynamic modelling was performed using the CALculated PHAse Diagram (CALPHAD) approach using the Thermocalc software.

Chapter 8 presents a study on the measurement and modelling of the residual stress formed in a thick HEA deposit. The X-ray diffraction (XRD) $\sin^2\boldsymbol{\psi}$ technique and contour method were used to measure the residual stress in the deposit. The XRD technique provides near-surface stress, whereas the contour method was employed to obtain a through-thickness stress profile. A numerical analysis using an explicit (element birth) finite element scheme was employed to predict and explain the residual stress development during the CSAM of the HEA.

Chapters 9 and 10 provide the general conclusions and contributions to the knowledge of the thesis and describe future work that can be performed based on the knowledge developed during this research.

2 Literature review

In the mid-1980s, the cold spraying (also known as cold gas dynamic spraying) technique was accidentally discovered by scientists at the Institute of Theoretical and Applied Mechanics of the Russian Academy of Science (Siberia Division, Novosibirsk) [48,49] while studying the interactions of smaller tracer particles in fluid flow using a supersonic wind tunnel test. Since then, the cold spraying technique has been further developed in several patents [50]. Research groups from different parts of the world are actively involved in maturing this technique, its use in surfacing techniques, and the repair of structural components. Beyond these applications, the cold spraying technique is also being developed for additive manufacturing (AM) of 3D components [25]. This chapter provides an overview of the principles and published work in relevant areas related to the cold spray additive manufacturing (CSAM) process of materials deposition. This chapter explains how the CSAM technique works and discusses current theories of bonding mechanisms based on experimental and numerical modelling of particle impact. An overview of high entropy alloys (HEAs), CSAM of HEAs, deposition mechanisms and microstructures, and deposit properties is also included. This chapter constitutes a critical systematic literature review that provides context for the study presented in this thesis, as well as gaps in the literature that need to be addressed.

2.1 Introduction to metal additive manufacturing

In contrast to conventional subtractive manufacturing processes, AM of metal utilises layer-by-layer addition of feedstock materials, usually powder or wire, that

is melted by a focused heat source, which can be a laser or electron beam, and solidifies to produce a near-net shape directly from 3D model data created to define the heat source trajectory [4,5]. The design freedom and complexity afforded by the AM process are significant advantages of the technology, especially for aerospace components, as it enables the manufacture of complex geometries, lightweighting, consolidation of multiple components, and enhanced mechanical performances within the timeline and cost constraints [4]. According to the international standard ISO/ASTM 52900 [51], AM consists of seven process categories with two main metal AM categories: powder bed fusion (PBF) and direct energy deposition (DED). These two techniques are closely related to the CSAM process. A detailed review of metal AM can be found in [13]. The PBF and DED techniques have been the most adopted AM processes in the medical, aerospace, oil, and gas industries. On the one hand, PBF utilises high-power laser(s) or electron beams (in a vacuum) to selectively melt and solidify thin layers of metal powder spreading on a build platform layer by layer. On the other hand, in DED techniques, the feedstock material, typically a feeding wire or powder, is deposited locally through a nozzle, directly into the melt pool created by an energy source, for example, electrical arc, lasers, or electron beams [4,13].

Despite the advantages of AM techniques, the large multitude of process parameters associated with the complexity of AM techniques can affect the quality of the components produced. For instance, alloying elements can vaporise during AM of important engineering alloys [52,53]. This is due to the high molten-pool temperatures, which ultimately lead to changes in the overall composition of the alloy in the produced components. In addition, AM parts are associated with

microstructural inhomogeneity and often exhibit elemental segregation, which affects their mechanical properties [54]. Other defects include porosity and lack-of-fusion voids produced in AM parts that need to be minimised [55]. In addition, cracking and delamination are commonly observed in additively manufactured parts, which are attributed to residual stresses resulting from steep temperature gradients [14–17]. These limitations can be overcome by following an alternative concept that works without a high-energy source, the CSAM process. Being a solid-state material deposition technique, it provides an additive manufacturing route for the deposition of a wide range of materials. The technique is discussed in detail in the following sections.

2.2 Cold spray additive manufacturing

This section describes the working principles of the cold spray or cold spray additive manufacturing (CSAM) technique. Its advantages and limitations are provided as well as the main spraying parameters involved in materials deposition in the CSAM process.

2.2.1 The CSAM process

CSAM is a high-strain-rate material deposition technique that utilises the kinetic energy of microsized powder particles to form dense deposits on a target substrate or component. During deposition, feedstock powders (typically 5-50 μm in size) are injected into a convergent-divergent (De Laval) nozzle by a carrier gas and then accelerated supersonically by a pressurised and/or heated gas (300-1100 ºC), which can either be nitrogen (N_2), helium (He), or air [21–23]. The particles are accelerated to high impact velocities (300-1400 m/s) towards a substrate at temperatures below the melting point of the feedstock material. At a material- and size-dependent critical velocity [56,57], the particles plastically deform as they impact the substrate, bond to the substrate, and previously deposited particles. Deposits are then formed through layer-by-layer addition of the material. The advantage of this technique compared to other AM processes is that the heat input to the powder material and substrate is relatively small; hence, the microstructure, as well as the mechanical and chemical properties of the feedstock material, are retained. Consequently, the CSAM process is recognised as a solid-state additive manufacturing method, which allows for the deposition of temperature-sensitive

materials, such as amorphous materials, as well as oxygen-sensitive materials, such as Cu, Ti, and Al [58,59]. The major advantage of laser-based AM techniques over the CSAM process is their high resolution and geometrical accuracy, resulting in high-quality part production capabilities with fine features [4], compared to the low-resolution (hundreds of μm vs. few mm) of the CSAM process [60]. The CSAM technique is mainly used for large-scale deposits or 3D components with near-net shape accuracy at higher deposition rates and lower costs, which are not feasible using PBF AM techniques [4,13,60].

CSAM, which is an ultrahigh strain-rate plastic deformation process, usually requires ductile materials to achieve beneficial deposition efficiency (DE); however, this limits the range of materials that can be deposited. Nonetheless, this technique has proven successful in the deposition of a wide range of materials apart from metals, such as bulk metallic glasses [61,62], HEAs [40,63,64], ceramics [65], cermet and composites [66], and polymers [67] onto a range of substrate materials. For the deposition of these materials, different CSAM techniques or systems have been developed considering the cost, process economy, and flexibility of usage. Generally, there are two types of CSAM systems: high-pressure cold spray (HPCS) and low-pressure cold spray (LPCS). These two techniques differ mainly in terms of the gas pressure and temperature, powder injection point, and nozzle design. Thus, these differences affect the particle velocities obtained using both techniques. The schematics shown in Figure 2.1 explain the differences between the techniques. In the HPCS system, He or N_2 under pressure, typically 2.0-6.0 MPa, is employed to accelerate the powder particles to high velocities. The gas can be heated to a temperature of 1100 °C using a gas preheater, increasing the gas

velocity and facilitating particle deformation through thermal softening of the powder particles. Powder feeders are often used to introduce feedstock powder into the gas flow. The two-phase flow; gas and particles are then propelled onto a target substrate. An important component of a CSAM system is the nozzle, which expands and accelerates the gas supersonically to generate a high-velocity gas-particle flow to the required particle velocity for deposition. The nozzle, usually the convergent-divergent nozzle (or de-Laval nozzle), consists of two sections: convergent and divergent. The area between these sections is termed the throat. As shown in Figure 2.1, the powder is introduced at the converging section of the nozzle in the HPCS, whereas it is introduced at the diverging section (downstream injection) of the nozzle in the LPCS. In this case, it is not required to pressurise the powder feeding line, as powder injection is achieved through the venturi effect caused by the expanding gas.

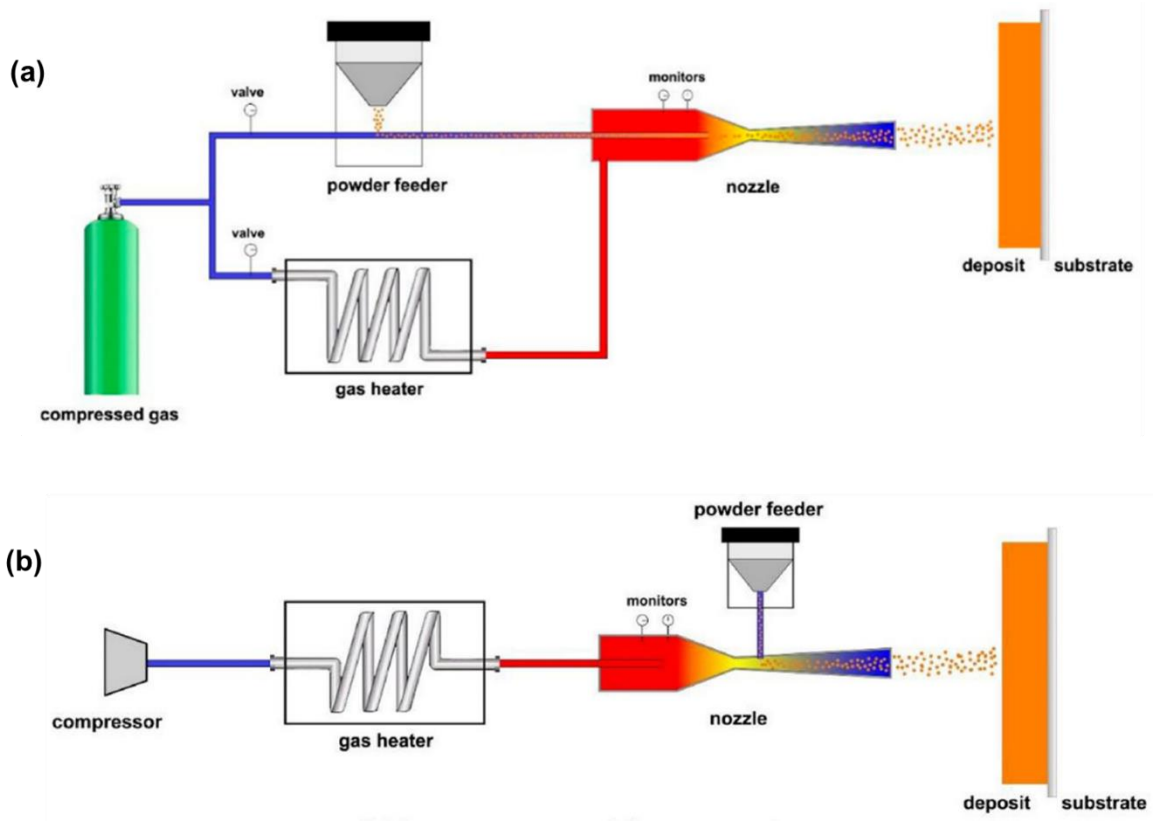

Figure 2.1: Schematics of (a) high-pressure cold spray (HPCS) system and (b) low-pressure cold spray (LPCS) system [31].

Thus, HPCS provides the possibility of depositing a wide range of materials because high particle velocities can be obtained with the system. In contrast, in the LPCS, gas pressures not exceeding 1.0 MPa and under 600 °C for equipment such as Dymet 423 are often employed for spraying. At this low pressure, the critical velocities required for bonding to occur may not always be reached, limiting the range of materials that can be deposited. Most metallic materials deposited using LPCS are materials with lower critical velocities, such as Cu. However, the DE of LPCS can be improved by adding hard reinforcement particles, such as ceramics (usually Al_2O_3, B_4C, and SiC), to the ductile metallic matrix, resulting in composite deposits [66,68,69]. The hard-phase particles improve the DE by eroding the substrate surface—surface activation, thereby enhancing deposition. Additionally,

deposition is improved by the compaction and accumulative shot-peening effect of hard particles on the ductile matrix during deposition. These characteristics make LPCS particularly suitable for depositing wear-resistant coatings [70,71]. In addition, because of the portability of simpler LPCS systems, they are suitable for the on-field repair and restoration of damaged components. LPCS is much cheaper than HPCS because LPCS equipment is affordable and has lower operating costs.

Other variants of CSAM systems have been developed in recent decades. This includes vacuum cold spraying (VCS), also known as aerosol deposition (AD), which works under partial vacuum [72,73]. Laser-assisted cold spraying (LACS) is also a variant of the CSAM system, where a laser is mounted on the system and used in parallel during spraying to provide additional heat input for particle deformation and deposition on the substrate surface [74,75]. These systems and techniques have been developed to overcome the limitations of conventional CSAM systems, such as the deposition of ceramics (i.e., VCS), and to improve the deposition of “difficult-to-spray” materials such as Ni-based superalloys (i.e., LACS).

2.2.2 Advantages and limitations of CSAM

Advantages

The main advantage of CSAM is its solid-state deposition process. In comparison with fusion-based metal AM techniques such as PBF and DED, CSAM, as a member of the AM family, has unique advantages. Because of the absence of melting during deposition, the elemental composition of the feedstock powder and substrate materials remains unaltered throughout the process, avoiding unwanted

phase formation, which often occurs during the conventional AM process. Moreover, high-reflectivity metals such as Cu and Al, which are challenging to manufacture using laser-based AM techniques, are the most commonly deposited materials using CSAM. Furthermore, the low-temperature deposition process of the CSAM technique allows for the deposition of materials that easily oxidise, such as Cu and Ti, and it minimises the detrimental effects of high oxygen content in the deposits [76]. Other important benefits of CSAM over other AM techniques are shorter production times owing to its high deposition rate, manufacturing of larger components, high flexibility, lower cost of running, and suitability for repair of damaged components [77].

A high particle impact velocity is essential in the deposition of materials in CSAM to produce dense deposits with minimal porosity. Dense deposits are produced by the kinetic energy of the incident particles, which results in plastic deformation of the particles, which in turn aids in the shot-peening and compaction of previously deposited layers. The low porosity and oxygen content in the deposits can further improve the thermal and electrical conductivities of the deposits, particularly Cu and Al [59]. Another advantage of the CSAM process is that there is no grain growth due to the absence of melting. On the other hand, the CSAM technique can be employed to produce nanocrystallites resulting from the high degree of plastic deformation of the particles [78]. Consequently, the high strength and hardness of deposited materials are often obtained compared with those of bulk materials.

The residual stress formed in the deposits plays an important role in the formation and mechanical performance of the deposit, especially under in-service conditions. Residual stresses in additively manufactured components are formed because of

the temperature gradient (quenching and cooling) of the layers and differential thermal contraction during the cooling stage of the deposit layers and substrates. Tensile residual stresses are usually formed in deposits produced using other metal AM techniques [16,79]; however, compressive residual stresses are often observed in CSAM deposits induced by severe plastic deformation and shot-peening effects of the particles. Such compressive residual stresses allow for the deposition of thick deposits before adhesion failure, which can also lead to an increased fatigue life of the components [80–82]. However, recent studies have observed tensile and compressive residual stresses formed in CSAM deposits depending on the spraying process parameters and material combinations employed [83–85].

Limitations

As with other AM techniques, CSAM has limitations. Because CSAM is a solid-state deposition process, feedstock powder materials with a low ductility that need to melt for deformation and deposition to occur are challenging to deposit. Recently, more methods have been found to deposit these hard materials, such as ceramics using AD (a CSAM variant), but there are still limitations in obtaining dense deposits even with metallic materials of high strength and hardness [59]. Moreover, because the CSAM process is based mainly on plastic deformation, the particles experience a loss of ductility owing to work hardening. Consequently, brittle deposits that are prone to cracking are formed. However, this outcome can be solved using an appropriate feedstock powder and optimised spraying parameters [86]. Moreover, post-deposition heat treatment has been found to improve the ductility and strength of CSAM deposits, which has been attributed to increased metallurgical bonding and the “sintering effect” of splats [59,87,88].

Components manufactured using the CSAM process usually require post-machining, because it is challenging to obtain products with the final geometry or roughness [77,89]. However, the recent development of complex robot manipulations and micronozzles (as they have smaller spot sizes) [90] can significantly reduce the need for extensive post-machining of CSAM deposits. Another limitation of CSAM is its high gas consumption and high cost. Because CSAM deposits materials with a high impact force and kinetic energy, high gas flow is usually required. Air, He, and N_2 are frequently used in the process. Although the use of He allows the manufacturing of dense deposits with a wide range of feedstock materials, the shortage of He makes it the most expensive. On the other hand, N_2 can also provide reasonable particle velocities while being cheaper, but a gas heater may be required to reach the desired particle velocities for deposition to occur and to form dense deposits. Air, as is often used in LPCS, is mainly used for processes that require lower particle impact velocities and materials that are not easily oxidised.

2.2.3 Spraying parameters for CSAM

For deposition to occur in CSAM, many factors must work in unison and under careful control and optimisation to produce dense deposits. These factors are generally categorised into three groups: (1) characteristics of the feedstock powder (size and shape, microstructure, and surface oxide layer), (2) nozzle design and spraying kinematics (standoff distance, transverse speed, and incidence angle), and (3) process parameters (gas type, temperature and pressure, substrate materials and surface roughness, and powder feed rate). In this section, some of

these spraying parameters are discussed, along with other factors. These factors determine the particle velocity and temperature, thereby influencing the DE and, thus the quality of the deposits. A typical CSAM spraying parameter is shown in Figure 2.2.

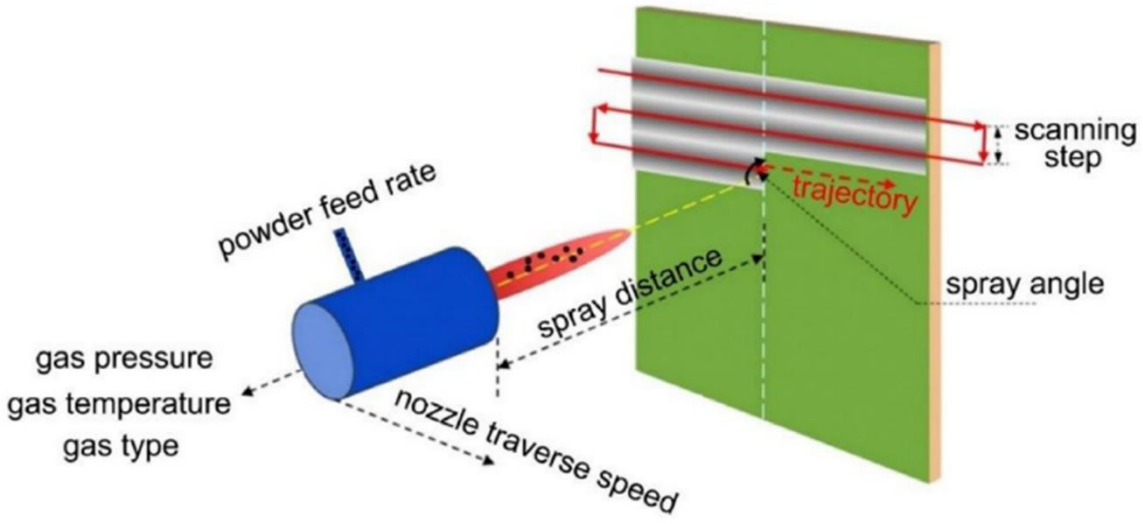

Figure 2.2: Schematic layout of CSAM spraying parameters [31].

2.2.3.1 Feedstock powder characteristics

Because CSAM relies on the kinetic energy of incident particles, parameters such as particle size, microstructure, shape, hardness, and formability influence the deposition. The particle size determines the critical velocity and, hence, the deposition in the CSAM [57,91]. Schmidt et al. [57] revealed the important role of the rate at which powder particles dissipate heat during CSAM deposition. In addition to the heat capacity and thermal conductivity, the cooling rate of the powder material is affected by the particle size. The cooling rate decreases with increasing particle size; consequently, the shear instability required for bonding (Section 2.4) can be hindered in smaller particles owing to their high thermal gradients [57].

Moreover, shock waves formed at the nozzle exit (Section 2.3) have been reported to influence mostly smaller particles, decelerating them owing to their lower mass [92]. In addition, after the production of feedstock powder, smaller particles tend to exhibit greater levels of impurities owing to their greater surface-to-volume ratios [57]. Another factor that can affect particle deformation is the hardness of powder particles. According to the Hall-Petch relationship, smaller particles usually exhibit greater hardness during deposition because of their higher quenching rates.

The powder particle microstructure and shape, for example, spherical or irregular, can strongly affect the particle deformation behaviour during CSAM [93]. Different manufacturing methods have been employed to produce feedstock powder for CSAM, for example, mechanical milling or gas atomisation, which would strongly influence the physical characteristics of the powder [94,95]. Generally, mechanically milled powders result in harder and irregular-shaped powder particles, while gas-atomisation, on the other hand, usually produces spherical particles. Another important characteristic of feedstock powder that influences particle deformation is the oxide film on the powder surface. The oxide content and layer thickness influence the critical velocity of particles in CSAM [96–99]. After deposition, remnants of the cracked oxide layers can be present in the deposit, which can affect the resultant mechanical properties.

2.2.3.2 Effect of powder feed rate and nozzle transverse speed

In CSAM, a powder feeder is used to control the powder feed rate, and the quantity of powder per unit of time is introduced into the gas stream in a nozzle. The powder feed rate can influence the particle velocity during CSAM because it affects the

powder loading in the flow stream through a nozzle [100,101]. The effect of powder feed rate on particle impact velocity is shown in Figure 2.3. A higher powder feed rate decreases the particle velocity, which is due to strong gas-particle interactions at high powder loading. The particle velocities decreased by over 14 % when the powder feed rate was increased from 30 to 120 g/min [102]. In addition, the powder feed rate can affect the deposit thickness and the track profile. Higher powder feed rates resulted in thicker deposits. This outcome can also be achieved with a slower nozzle transverse speed [103,104]. Moreover, the nozzle transverse speed determines the CSAM duration and particle impact flux onto the substrate surface per unit time. This can determine the thickness of the deposited layer. The effect of the nozzle transverse speed on the microstructure and thickness of a CSAM Stellite 21 deposit is shown in Figure 2.4. The spray kinematics also influence the porosity and microhardness of the deposit. Hence, these two factors must be considered simultaneously during CSAM to achieve better control of deposit quality. However, there are no frameworks or principles on how to select the nozzle transverse speed and powder feed rate, as these would depend on the other spraying parameters and feedstock material selected.

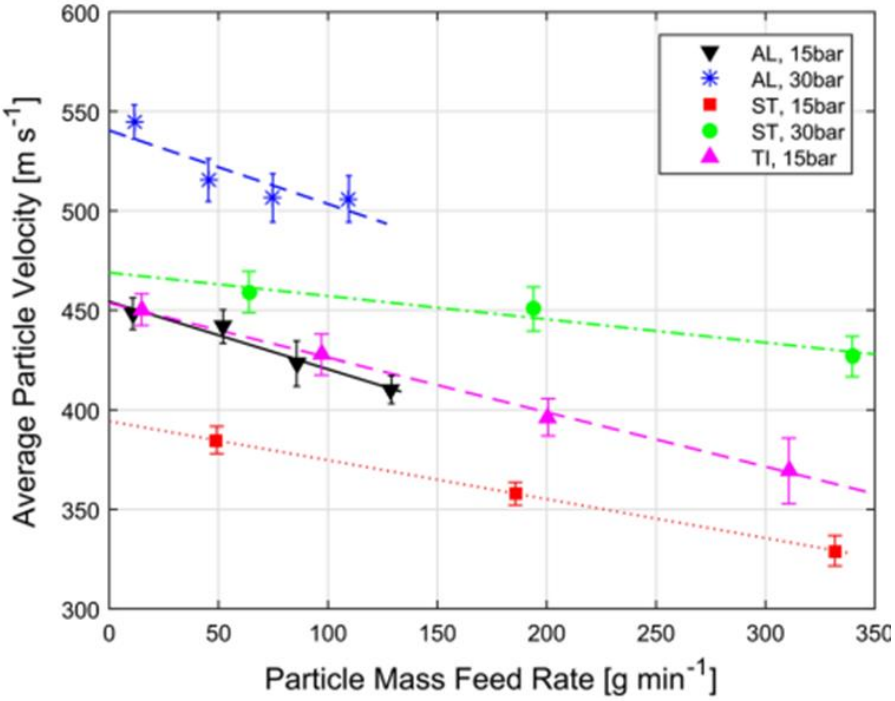

Figure 2.3: Effect of powder feed rates of different materials on average particle impact velocity during CSAM [102].

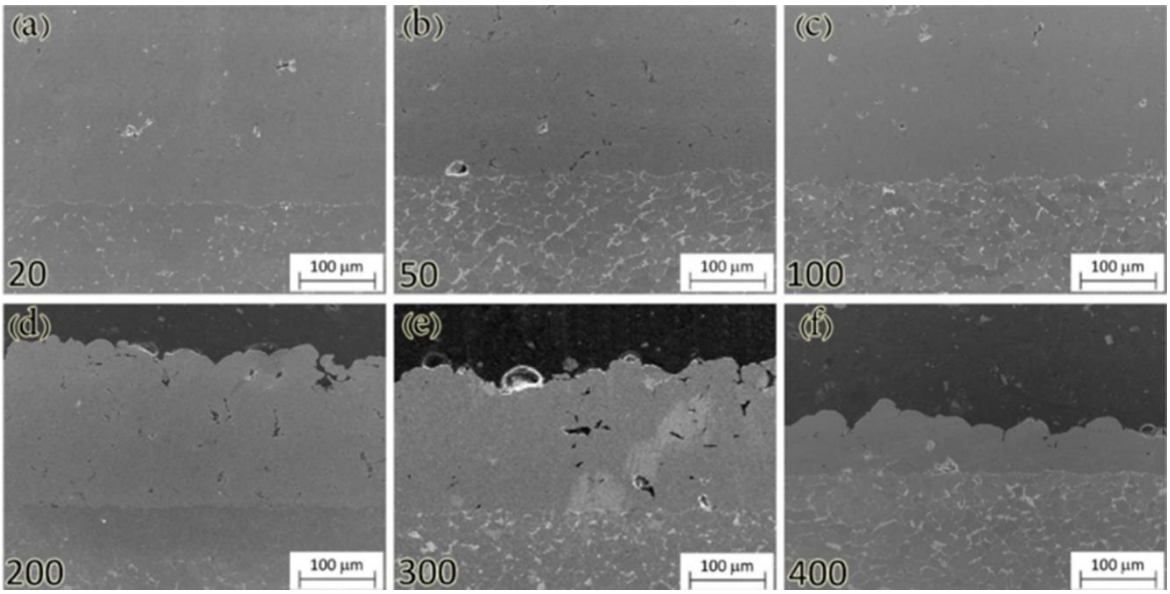

Figure 2.4: Effect of nozzle transverse on CSAM Stellite 21 deposit microstructure and thickness [103].

2.3 Gas and particle dynamics in CSAM

In CSAM, feedstock powder particles are accelerated to high-impact velocities by supersonic gas flow, and nozzle design plays a key role in achieving successful deposition. The convergent-divergent or de Laval nozzle is a key component in the CSAM system, such that its design determines the particle velocity and temperature upon impact on a substrate. Therefore, it is important to understand the dynamics of the gas and particle flow through the nozzle. Figure 2.5a shows a schematic of a convergent-divergent nozzle. The gas is fed at high pressure into the back of the nozzle, after which it expands as it passes through the constriction or throat. The convergent section accelerates the flow to subsonic conditions, wherein at the throat, the Mach number M = 1. In the divergent section, the flow accelerates to supersonic conditions, where M > 1 (Figure 2.5b). The flow continues to accelerate as it reaches its maximum velocity, while the gas cools below room temperature [105]. The acceleration of the particles results from the drag force exerted on them by the supersonic gas stream, which accelerates them to the required velocity for the formation of deposits [21]. Even though the particles cool downstream of the nozzle exit, they usually retain a higher temperature than the gas.

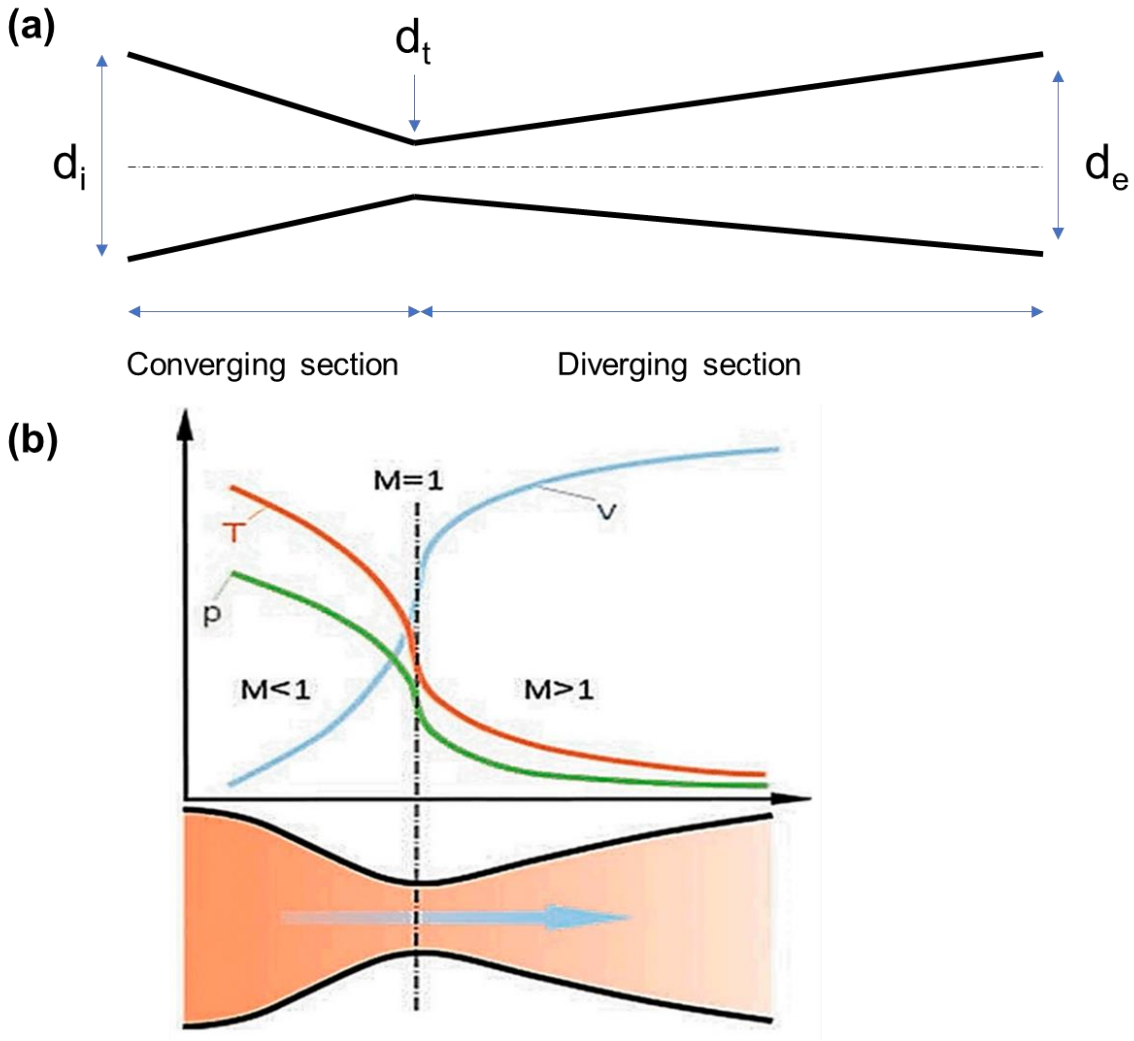

Figure 2.5: Schematics of converging-diverging nozzles (a) and (b) shows a diagram illustrating the changes in gas pressure (***P***), temperature (***T***), and velocity (***V***) corresponding to the Mach number, ***M*** [105,106]. The nozzle inlet d_i, throat d_t, and exit diameter are shown in the schematic diagram.

At the exit of the nozzle, shockwaves can occur because of the alteration of the supersonic flow conditions to downstream flow perturbations at the substrate surface. Figure 2.6 shows a schematic diagram of the gas-substrate impingement zone. Because of the dynamics and interactions of the gas with the substrate surface, the shockwave can be curved and detached, resulting in bow shock [92], as shown in Figure 2.6. This compressed layer (bow shock) encloses a region of high-density, low-velocity recirculating fluid characterised by strong gradients and

sudden changes in flow properties [92]. This compressed layer has a significant effect on particle velocity, and its effect is greater for smaller particles [23,107]. Therefore, it is important to consider the nozzle geometry that provides optimal conditions, particularly for the successful deposition of new metallic materials such as high entropy alloys (HEAs) whose deformation dynamics and behaviour have not been fully elucidated during CSAM.

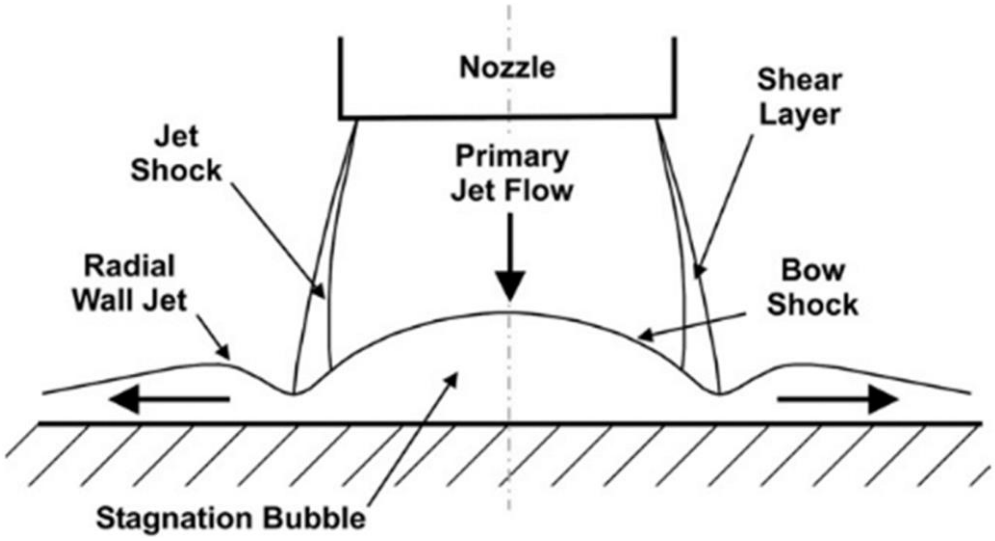

Figure 2.6: Illustration of supersonic impingement zone at substrate surface during CSAM, showing bow shock [92].

Efforts have been made over the years to investigate two-phase flow inside and outside the nozzle. The most direct way to capture and investigate the physical phenomena involved in CSAM is through experimental investigations; however, its relatively high cost and time limit its widespread application. For this reason, analytical and computational modelling has been developed and employed in many studies to understand the gas-particle flow properties and predict the velocity and temperature during CSAM. Analytical models were first employed in the early years [21]; however, with the advent of high-performance computing, computational fluid

dynamics (CFD) has become a popular approach for predicting gas-particle flow variables. Although analytical models were first developed and employed for such problems, the assumptions and simplifications introduced in these models for real physical problems limit their applications [108]. This can be due to some physical phenomena not included in the models, such as the effect of ambient pressure, bow shock effect, and supersonic flow outside the nozzle. These features can be captured using a well-designed CFD model and are less expensive than experimental approaches. Moreover, studies have shown good agreement between CFD models and experimental results. For example, Figure 2.7a and b show the impinging jet zone outside the nozzle captured using the CFD model and an experimental Schlieren photograph [109]. In addition, the study by Bray et al. [74] revealed that the measured average particle velocity and CFD results were in good agreement, although with slight overestimation, as shown in Figure 2.7c. However, for simple and approximate calculations, analytical models have still been employed because they save both computational and experimental costs. The following sections present the analytical models used to predict the gas-particle flow and some studies showing the application of the CFD technique for gas-particle flow modelling.

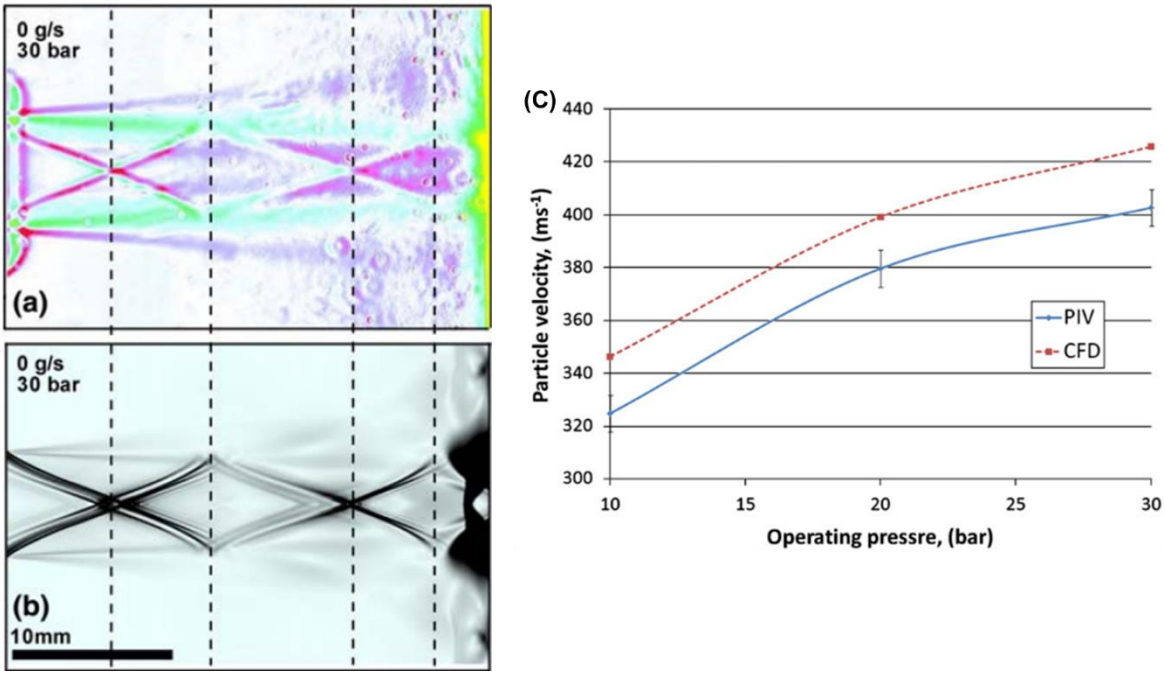

Figure 2.7: (a) and (b) show the comparison between the experimental Schlieren photograph and CFD results used to capture the impinging jet outside the nozzle during CSAM [109]. A comparison of the average particle velocity at the nozzle exit measured experimentally and calculated using the CFD model is shown in (c) [74].

2.3.1 Governing equations for the analytical models

One-dimensional (1D) isentropic equations for ideal gas flow were used to estimate the flow features [21,110,111]. For a specific nozzle with a known exit area, the Mach number ***M*** at the nozzle exit has the following relationship with the throat area ***A****. Where ***A*** is the nozzle cross-sectional area, and γ is the ratio of gas-specific heat capacities.

$$\frac{\boldsymbol{A}}{\boldsymbol{A^*}} = \frac{\mathbf{1}}{\boldsymbol{M}}\left[\left(\frac{\mathbf{2}}{(\boldsymbol{\gamma}+\mathbf{1})}\right)\left(\mathbf{1}+\frac{\boldsymbol{\gamma}-\mathbf{1}}{\mathbf{2}}\boldsymbol{M^2}\right)\right]^{\frac{\boldsymbol{\gamma}+\mathbf{1}}{\mathbf{2}(\boldsymbol{\gamma}-\mathbf{1})}} \quad (2.1)$$

Once the exit $\boldsymbol{M}$ is determined, the corresponding gas variables of the flow inside the nozzle can be derived using the isentropic Equations (2.2)-(2.5). Where $\boldsymbol{P_0}$, $\boldsymbol{P}$, $\boldsymbol{T_0}, \boldsymbol{T}, \boldsymbol{\rho_0}, \boldsymbol{\rho}, \boldsymbol{R}$, and $\boldsymbol{V_g}$ are the gas stagnation pressure, gas pressure, gas stagnation temperature, gas temperature, gas stagnation density, gas density, gas constant and gas velocity, respectively. Thus, Equation (2.5) can be used to obtain the gas velocity.

$$\frac{\boldsymbol{P_0}}{\boldsymbol{P}} = \left[\left(\mathbf{1}+\frac{\boldsymbol{\gamma}-\mathbf{1}}{\mathbf{2}}\boldsymbol{M^2}\right)\right]^{\frac{\boldsymbol{\gamma}}{(\boldsymbol{\gamma}-\mathbf{1})}} \quad (2.2)$$

$$\frac{\boldsymbol{T_0}}{\boldsymbol{T}} = \mathbf{1}+\frac{\boldsymbol{\gamma}-\mathbf{1}}{\mathbf{2}}\boldsymbol{M^2} \quad (2.3)$$

$$\frac{\boldsymbol{\rho_0}}{\boldsymbol{\rho}} = \left[\left(\mathbf{1}+\frac{\boldsymbol{\gamma}-\mathbf{1}}{\mathbf{2}}\boldsymbol{M^2}\right)\right]^{\frac{\mathbf{1}}{(\boldsymbol{\gamma}-\mathbf{1})}} \quad (2.4)$$

$$\boldsymbol{V_g} = \boldsymbol{M}\sqrt{\boldsymbol{\gamma RT}} \quad (2.5)$$

The deposition of materials in CSAM is determined by the particle velocity rather than by the gas stream. Assuming the particulate phase in the gas stream is sufficiently dilute and moves along the nozzle axis, the particle velocity can be calculated by solving the differential equation [110],

$$m_p \frac{dV_p}{dt} = C_D \rho (V_g - V_p)|V_g - V_p| \frac{A_p}{2} + F_B \quad (2.6)$$

where m_p is the mass of the particle, V_p refers to the particle velocity, t is time, C_D is the drag coefficient, V_g is the gas velocity, A_p is the particle cross-sectional area, and F_B is the body force. The drag coefficient accounts for the effects of Mach number on particle acceleration. If the gas velocity, gas density, and drag coefficient are held constant, a rough estimate of the particle velocity can be obtained using Equation (2.7), where x is the axial distance travelled by the particle (measured from the nozzle throat) [21,110]. When the particle velocity is small compared to the gas velocity, Equation (2.7) is simplified to yield Equation (2.8). Examination of the equations indicates that the incident particle velocity is proportional to the square root of the distance travelled over the particle diameter. It also shows that the particle velocity increases with gas velocity and gas density but decreases with an increase in particle size. However, the smaller particle sizes even though of higher particle velocities do not always contribute to deposition in CSAM due to bow shocks and flow outside the nozzle [23,92].

$$\log\left(\frac{V_g - V_p}{V_g}\right) + \frac{V_g}{V_g - V_p} - 1 = \frac{C_D A_p \rho x}{2 m_p} \quad (2.7)$$

$$V_p = V_g \sqrt{\frac{C_D A_p \rho x}{m_p}} \quad (2.8)$$

Because the particle velocity exit of the nozzle would not be the same upon impact on the substrate owing to particles passing through a series of bow shocks in front

of the substrate, the above equations may not accurately predict the particle impact velocity. To deal with the effect of the flow outside the nozzle, Grujicic et al. [110] proposed an empirical model based on experimental and computational validations, as presented in the following equations:

$$V_p^{impact} = V_p^{exit} e^{\frac{-3\rho^{st} L^{st}}{4\rho_p d_p}} \tag{2.9}$$

$$\rho^{st} = Re(-1.44 + 2.77M - 0.21M^2) \tag{2.10}$$

$$L^{st} = Re(0.97 - 0.02M), 1 \leq M \leq 5 \tag{2.11}$$

Where ρ^{st}, L^{st}, d_p, ρ_p, and Re are average gas density in the stagnant region, thickness of stagnant region, particle diameter, particle density and gas Reynolds number.

2.3.2 Computational modelling

In the CFD model, the Navier-Stokes (NS) equations are solved for the gas flow. The equations given in the following consist of the conservation of mass, momentum, and energy.

$$\frac{\partial \rho}{\partial t} + \frac{\partial}{\partial x_j}(\rho u_j) = 0 \tag{2.12}$$

$$\frac{\partial}{\partial t}(\rho u_i) + \frac{\partial}{\partial x_j}(\rho u_i u_j) = \frac{\partial}{\partial x_i}\left[-p\delta_{ij} + \mu\left(\frac{\partial u_i}{\partial x_j} + \frac{\partial u_j}{\partial x_i}\right)\right] + S_M \tag{2.13}$$

$$\frac{\partial}{\partial t}(\rho C_P T) + \frac{\partial}{\partial x_j}(\rho u_j C_P T) = \frac{\partial}{\partial x_i}\left[\lambda\left(\frac{\partial T}{\partial x_j}\right)\right] + S_T \tag{2.14}$$

where t, ρ, μ, λ, C_P, p, T, u_i, S_M, *and* S_T, and denote the time, gas density, dynamic viscosity, thermal conductivity, specific heat at constant pressure, gas static pressure, gas temperature, gas velocity components, and additional source terms in momentum and energy, respectively [112]. The flow inside and outside the nozzle during CSAM is typically assumed to be in a steady state. Because of the supersonic gas speed, the equation of state for compressible flow is required to close the NS equations, which is usually considered an ideal gas law. The additional source terms are usually neglected; however, they become important when considering high powder loading. In this case, the momentum and energy transfer between the gas and particles are thus accounted for by the respective phase coupling through additional terms [108,109].

CFD models can be divided or meshed using structured or unstructured methods. The former method is usually more efficient and accurate than the latter. However, when dealing with complex geometries, such as in 3D models, an unstructured mesh can be more suitable [108,113]. Sufficient and appropriate boundary conditions were applied to the domain to accurately model the impingement jet. One such proper boundary condition is to arrange the surrounding atmosphere

sufficiently far from the region of the impinging jet to eliminate its influence on the computational results [108]. Furthermore, the discretisation scheme is very important for accurately predicting supersonic compressible flow and capturing shockwave structures. For such flows, there can be variations in viscosity with temperature, which can be accounted for using Sutherland law [92,114]. Other thermophysical parameters, if insensitive to temperature, can be assumed constant in the models.

As mentioned earlier, deposition during CSAM is largely dependent on the particle velocity. The injected particles in the gas flow occupied a small volume fraction of the flow field. As a result, one-way Lagrangian discrete phase modelling (DPM) is predominantly used to capture particle velocity and temperature. In this method, the gas flow is solved first, and then the particle parameters, such as velocity and temperature, are solved based on the resultant gas flow. This method neglects the effect of the particles on the gas phase. Some studies, however, employed a two-way Lagrangian approach to account for the effect of particles on the gas phase [101,109,115]. Nevertheless, this method is more suitable for high-particle-loading flows. The particle velocity is predicted by solving for the drag force balance equation given in Equation (2.6) in section 2.3.1. In addition to Lagrangian approaches, Eulerian DPM has also been employed in a few studies, where the particle velocity is calculated by solving additional discrete equations [108,116].

The drag coefficient is the most influential factor in predicting particle velocity and trajectory. Several equations were employed to calculate the drag coefficients during CSAM. A review article by Yin et al. [108] provides more information on this topic. Some of the drag coefficient equations have been integrated into the

commercial software package Ansys/Fluent and, thus, are widely used for CSAM modelling. Most importantly, owing to the supersonic gas flow at the divergent section of the nozzle and the shock patterns that can be experienced by the particles, it is better to use drag coefficients with Mach numbers that account for these effects. The drag coefficients developed by Crowe [117] and Henderson [118] are such coefficients, as they were developed for compressible flow around spheres.

The particle temperature, T_p, can be calculated using the heat transfer Equation (2.18). This equation assumes that the particle temperature during CSAM is homogeneous within individual particles. The reason for this is based on the Biot number ***Bi*** <0.1. It represents the ratio of internal conduction and external convective resistance to heat transfer [111,115]. This is given by $Bi = {h_p d_p}/{\lambda_p}$, where h_p is the convective heat transfer coefficient, d_p is the particle diameter, and λ_p is the thermal conductivity of the powder material. In Equation (2.15), C_p is the particle specific heat capacity, h_p is the convective heat transfer coefficient and T_r is the recovery temperature dependent on the particle Mach number, M_p. T_r was calculated using the relation, $T_r = T_g(1 + r\frac{\gamma-1}{2}{M_P}^2)$, where r is the recovery coefficient close to 1 in gases, and T_g is the gas temperature [108]. The heat transfer coefficient, h_p (Equation (2.16)) was evaluated from the Nusselt number using the Ranz-Marshall correlation [119] given by Equation (2.17), which is suitable for flow past a sphere. The thermal conductivity of the gas is given as k_g, μ_g is the dynamic viscosity of the gas, ***Pr*** is the Prantl number of the gas (Equation (2.18)), and ***Re*** is the Reynolds number of the particle.

$$m_p C_p \frac{dT_p}{dt} = A_p h_p (T_r - T_p) \quad (2.15)$$

$$h_p = \frac{k_g Nu}{d_p} \quad (2.16)$$

$$Nu = 2 + 0.6 Re^{0.33} Pr^{0.33} \quad (2.17)$$

$$Pr = \frac{C_p \mu_g}{k_g} \quad (2.18)$$

One of the most important factors influencing the accuracy of computational results in CFD models is the turbulence model employed. Various turbulence models have been used to model the gas flow in a CSAM. Most of the turbulence models are based on solving the closure of the Reynolds Averaged Navier-Stokes (RANS) equations. Most turbulence models used for gas flow modelling in CSAM are the 1-equation Spalart-Allmaras, 2-equations standard *k-ε*, RNG *k-ε*, realisable *k-ε*, and 7-equations advanced Reynolds stress model (RSM). Other turbulence models such as SST *k-ω*, modified *k-ε* models, and the large eddy simulation (LENS) have also been employed. Yin et al. [108] provide a detailed summary of the turbulence models used in CSAM modelling. The turbulence model can indeed have significant effects on the prediction accuracy of the flow field in CSAM modelling.

2.3.3 Effect of spraying conditions on particle velocity and temperature

Besides the nozzle geometry, the gas velocity can also be determined by the main gas conditions that determine the particle velocity. The main gas conditions include gas stagnation pressure, stagnation temperature, and gas type. An increase in stagnation pressure may result in a higher gas velocity. Studies have shown that stagnation pressure affects the flow inside and outside the nozzle because of ambient pressure [120]. This effect becomes negligible when the stagnation pressure is sufficiently high such that the ambient pressure does not affect the flow inside the nozzle. In this case, the nozzle expansion ratio augments the Mach number and gas velocity at the nozzle exit. Moreover, a study by Yin et al. [121] indicated that a high gas velocity was obtained with a large expansion ratio nozzle but required sufficiently high stagnation pressure at the same time. The nozzle divergent length was also found to influence the gas velocity; a longer divergent length resulted in a decreased Mach number because of higher energy dissipation. However, a shorter divergent length can also result in a thicker bow shock or compressed layer at the substrate front. This suggests the need for a nozzle design for optimal spraying conditions.

The use of helium (He) as a propellant gas can increase the particle velocity significantly because of the smaller molecular weight, $\boldsymbol{M_w}$ of He (4.002) than that of air (28.966) or N_2 (28.014). Moreover, from the expression, $\boldsymbol{V_g} = \sqrt{\boldsymbol{\gamma RT}/\boldsymbol{M_w}}$, there is a positive correlation between gas velocity and $\sqrt{\boldsymbol{\gamma}/\boldsymbol{M_w}}$, which is higher for He

than N_2 (γ=1.66 for He and 1.4 for N_2). Figure 2.8 displays the results from several studies on the effect of carrier gas on the resulting particle velocity.

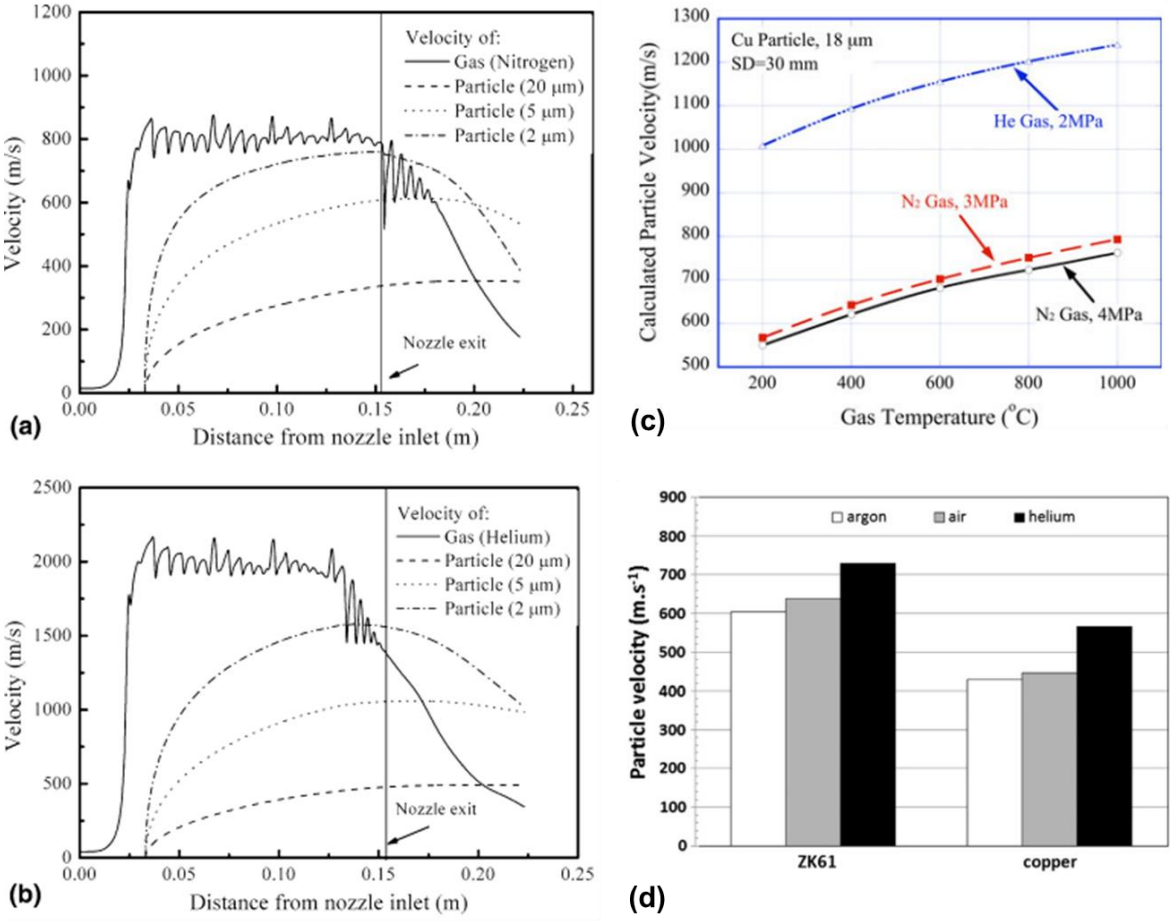

Figure 2.8: CFD modelling results of gas velocity and in-flight particle velocity with different particle sizes: (a) N_2 gas and (b) He gas [122]. (c) shows the modelling result of particle velocity as a function of gas type, gas stagnation pressure, and temperature [123], and (d) shows the particle velocities as a function of gas type for different powder materials [124].

The particle velocity primarily depends on the gas flow features. In general, a higher gas velocity results in a higher particle velocity. Therefore, the particle velocity increases with the gas stagnation pressure, stagnation temperature, and use of He as propellant gas [123]. As previously mentioned, increasing the stagnation temperature can increase the gas velocity inside the nozzle. Furthermore, it has

been reported that a higher stagnation temperature facilitates particle heating owing to the higher gas heat input. A higher particle temperature was found to decrease the critical velocity required for deposition to occur [57,91,125]. Because of the energy conservation of the gas flow, one cannot simultaneously increase particle velocity and temperature without an additional device attached to the CSAM nozzle [108]. To achieve this, a preheating chamber or gas heater can be attached before the nozzle, and several results have proven that this increases the particle velocity and temperature [108]. However, it is noteworthy that increasing the gas stagnation temperature may result in thermally induced defects in the deposit, such as thermal residual stresses. Other spraying conditions that can affect the particle velocity are the powder feed rate, nozzle transverse speed, and particle properties (or feedstock characteristics), as discussed in Section 2.2.3.

Another important parameter that affects particle velocity and, consequently DE is the standoff distance (SOD), which is the distance between the nozzle exit and the substrate surface during CSAM. Some studies have proposed that the pressure in the bow shock region changes with an increase in SOD. The studies indicated that the pressure determined the particle deceleration, and as such, the substrate should be in the region of lowest pressure to achieve deposition. Pattison et al. [92], however, proposed that particle velocity is determined by the combination of outside supersonic jet core length and bow shock. They reported that, based on these gas dynamics and experimental validation, there exists an optimal SOD to reach the maximum particle velocity and DE. Another study by Li et al. [126] showed that the DE, and thus particle velocity upon impact, decreased as SOD increased. Typical SOD employed in CSAM range between 5-60 mm [92,126], with lower SOD (5-10

mm) often employed in LPCS [68,69,127]. For HPCS, the optimal SOD often lies within 15-50 mm [126,128]. These results indicate a wide range of SOD for optimal deposition, which can depend on particle size and powder material density. However, few studies have explored these spraying parameters to determine the optimal window of deposition for the CSAM of HEAs [63,75,128,129].

2.4 Deposition mechanisms in CSAM

Particles impacting a substrate surface during CSAM can be reflected off the surface, stick to the surface, or penetrate a solid body. The outcome of the impact depends on several spraying parameters (particle characteristics, spraying conditions, and substrate characteristics), but is largely determined by the particle velocity and temperature. Often, the impact of a particle on a substrate surface causes plastic deformation, which is an intrinsic aspect of CSAM deposition as it affects both particle and substrate bonding and metallurgical processes, such as work hardening and dynamic recrystallisation (DRX). As CSAM relies on the kinetic energy of the incident particles to form deposits, it is imperative to understand the particle-substrate bonding mechanisms and the criteria required to form dense deposits. The microstructure of the deposit can have adverse or beneficial effects on the mechanical properties of the additively manufactured components. Thus, the following sections aim to discuss the bonding mechanisms in CSAM and the evaluation of critical velocity and window of deposition.

2.4.1 Bonding mechanisms

Bonding in CSAM deposition can be classified into two distinct types: particle-substrate bonding and particle-particle bonding. The former is necessary for the first-layer deposition of particles on the substrate, hence determining the adhesion strength of the deposit on the substrate surface. The latter concerns deposit build-up and hence determines the cohesive strength and performance of the deposit [130]. Despite the numerical and experimental investigations on the impact

phenomena during CSAM, the actual bonding mechanism in CSAM is still a matter of debate. A major part of the published work on particle deposition focuses on the basic understanding of similar particle-substrate material bonding. For example, Cu particle on Cu substrate [56]. However, there is equal interest in understanding the bonding between dissimilar materials during deposition [131,132].

Generally, bonding between materials in CSAM is primarily related to the high strain rate deformation during impact and the localised heating of the impacting interfaces. The plastic deformation of a material under high-impact velocity is generally accepted to occur through adiabatic shear instability (ASI) [56,57,133]. As a particle hits a surface at or above a threshold velocity, the impact creates a pressure wave which propagates spherically into the material, as illustrated in Figure 2.9a and b. The pressure wave generates a shear load, which accelerates the material, resulting in the formation of a localised shearing strain. An ASI is formed under optimal conditions and impact pressure. At this point, a transition occurs in the deformation process: the work hardening induced by the plastic deformation is overtaken by the thermal softening induced by the impact, which leads to abrupt changes or a jump in the strain and temperature and a drop in the flow stresses [56,133]. Thermal softening of the materials is induced by the dissipation of the plastic strain energy as heat, resulting in a temperature rise (localised heating at the interacting interfaces). Thus, the metal behaves as a viscous material flowing in the outwards direction of the interface. This appears as a ring of jet-type morphology around the particle, as shown in Figure 2.9c and is usually referred to as a “metal jet”. Metal jets have been reported to be helpful in the disruption and cleaning of thin oxide layers on metal surfaces and to enable intimate contact between freshly

exposed clean metal surfaces [99,134,135]. Figure 2.10 summarises the deposition process, involving oxide film breakup and cleaning during CSAM.

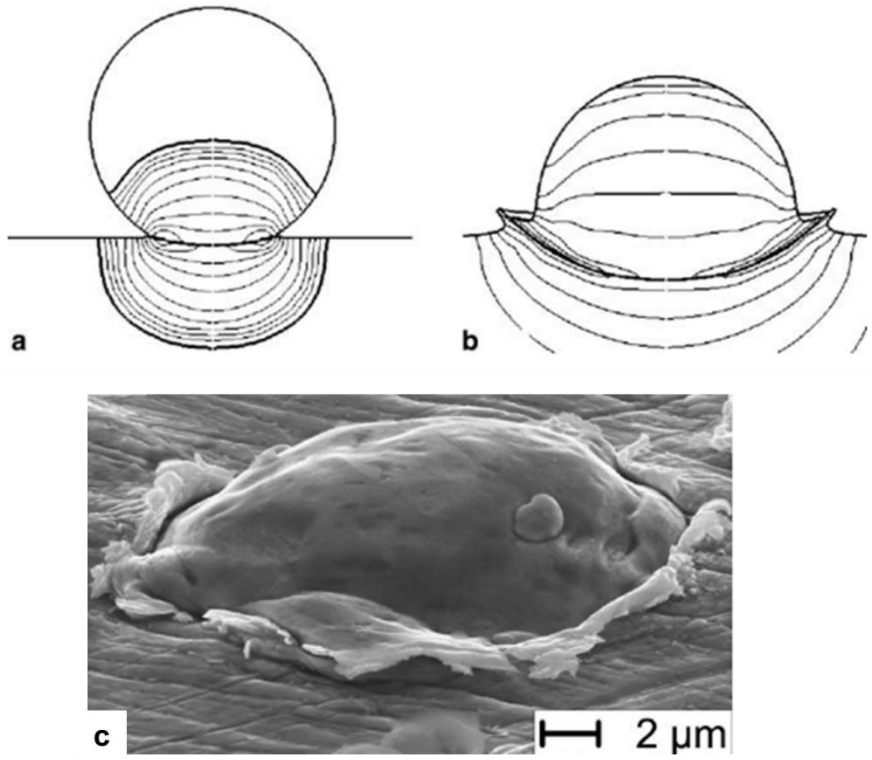

Figure 2.9: Pressure generated during particle impact in (a) CSAM deposition and (b) metal jetting formed [57]. An SEM micrograph showing the metal jet morphology of a Cu particle on a Cu substrate [56].

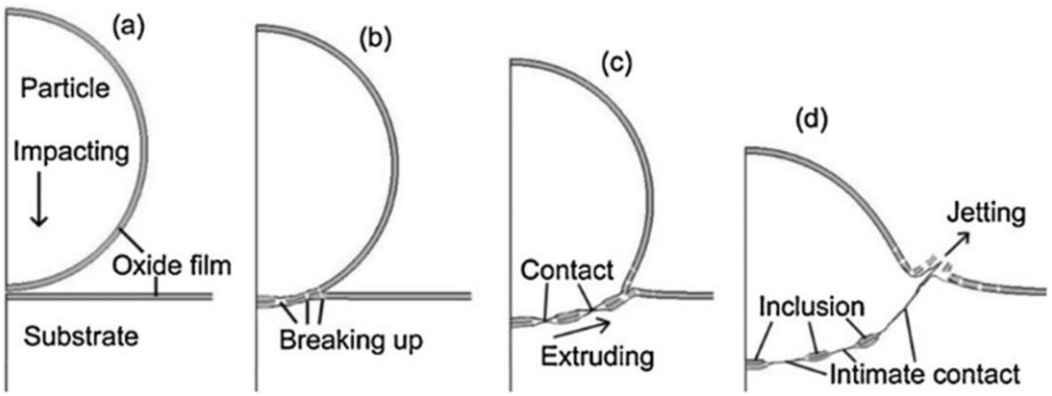

Figure 2.10: Schematic illustration of the deposition process during CSAM: breaking and extrusion of surface oxide films and metal jet formation [135].

Hassani-Gangaraj et al. [136] reported that ASI is, however, not necessary for bonding to occur in CSAM deposition. The authors argued that the large interfacial strain required for bonding does not require an ASI to be triggered. This implies that jetting can occur without any heat or thermal softening. Instead of thermal softening, they proposed that jetting during particle deformation is caused by hydrodynamic plasticity, which affects the bonding. This hydrodynamic jetting mechanism is due to the strong pressure waves interacting with the free surfaces of the materials during impact. The pressure wave mechanism relates the critical velocity linearly to the bulk speed of sound of pure metals such as Cu, which may not be true for all materials. Moreover, certain thermomechanical processes, such as sub-grain rotations and dynamic recrystallisation (DRX), are often affected by the ASI phenomena [137,138].

Impact-induced bonding mechanisms can be broadly classified as metallurgical bonding, mechanical interlocking, and material intermixing. Metallurgical bonding is associated with metal jetting induced by ASI [56,133] or the pressure-wave release mechanism [136]. In contrast, mechanical interlocking occurs when sprayed

particles penetrate the substrate (or are trapped, embedded, or anchored in the substrate) [139]. This occurred when the particles were harder and heavier than the substrate. The condition for material intermixing is similar to that of mechanical interlocking but at a low DE. At this DE, most of the sprayed particles rebound, causing severe accumulative plastic deformation of the first deposited layer of the particle and substrate material; consequently, a vortex-like intermixing interface is formed [140].

2.4.2 Critical velocity

It is important to optimise the spraying parameters in CSAM to obtain high-quality deposits of new metallic materials such as HEAs. There is an impact velocity that particles need to reach for them to plastically deform and bond with themselves and with a target substrate. This impact velocity is known to initiate ASI and is referred to as the critical velocity, which is material-, particle size-, and temperature-dependent [56,57,91].

Numerical and experimental methods have been employed to determine the critical velocities of several metallic materials. The outcome of some studies resulted in the expression of the critical velocity as a function of the material properties [56,57]. Equation (2.19) was first proposed by Assadi et al. [56] using a Cu model and was validated experimentally. Where $\boldsymbol{V_{cr}}$ = critical velocity, $\boldsymbol{\rho}$ = material density, $\boldsymbol{T_m}$ = material melting temperature, $\boldsymbol{T_R}$ = reference or room temperature, $\boldsymbol{T_P}$ = particle impact temperature and $\boldsymbol{\sigma_u}$ = temperature-dependent ultimate tensile strength, all

in SI units. However, the use of this equation is restricted to materials with properties that are comparable to those of Cu.

$$V_{cr} = 667 - 0.014\rho + 0.08(T_m - T_R) + 10^{-7}\sigma_u - 0.4(T_P - T_R) \quad (2.19)$$

Following the study by Assadi et al. [56], Schmidt et al. [57] developed Equation (2.20) to predict the critical velocity of a wide range of materials in CSAM more accurately. Where ***A*** and ***B*** are fitting parameters and C_p is the material heat capacity. The particle and substrate were assumed to be similar materials at the same temperature. The analysis of both equations for several materials was compared with the experimental results, as shown in Figure 2.11.

$$V_{cr} = \sqrt{\frac{A\sigma_u}{\rho} + BC_p(T_m - T_P)} \quad (2.20)$$

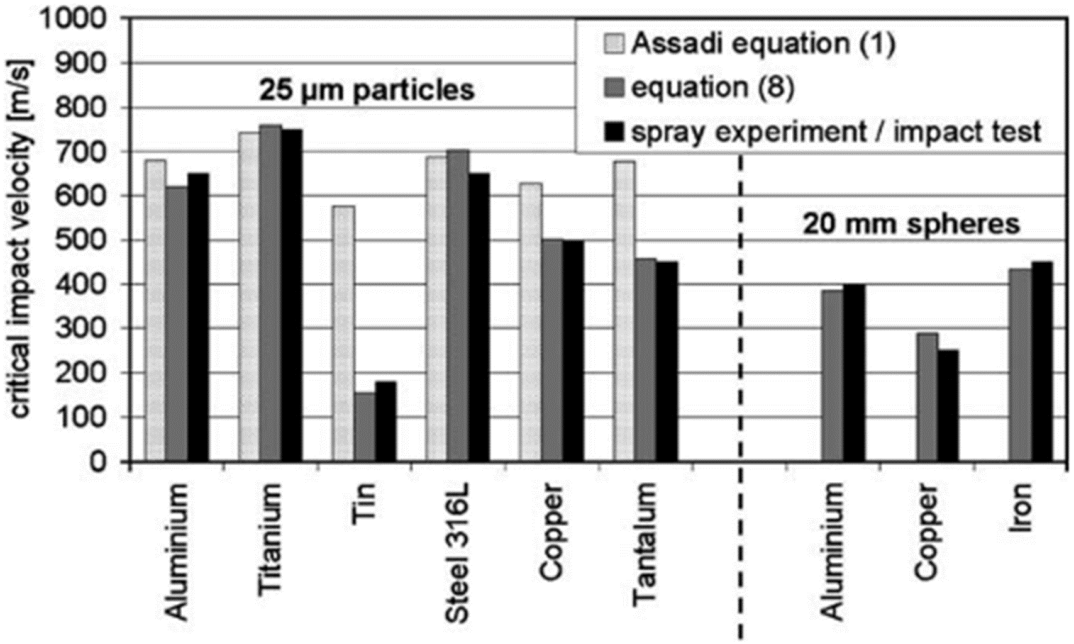

Figure 2.11: Comparison of the critical velocities of several materials using Equations (2.19) and (2.20) and experimental impact tests [57].

The authors further proposed a model that can determine the critical particle size, $\boldsymbol{d_{cr}}$ for bonding to occur, as given in Equation (2.21). Where $\boldsymbol{k}$ = particle material thermal conductivity and $\boldsymbol{V_p}$ = particle velocity. Figure 2.12 shows the minimum particle size for bonding to occur for different materials based on Equation (2.21). These values indicate that thermal diffusion can limit the bonding of small particles; however, this depends on the powder material. By calculating the particle velocity and critical velocity as a function of the particle size, the optimum particle size distribution can be determined, as demonstrated by Schmidt et al. [57] in Figure 2.13. Although the critical velocity of many materials has been determined, the critical velocity of HEAs and their deposition mechanism during CSAM have yet to be widely investigated [40,63,141].

$$\boldsymbol{d_{cr} = 36\left(\frac{k}{C_p.\rho.V_p}\right)} \tag{2.21}$$

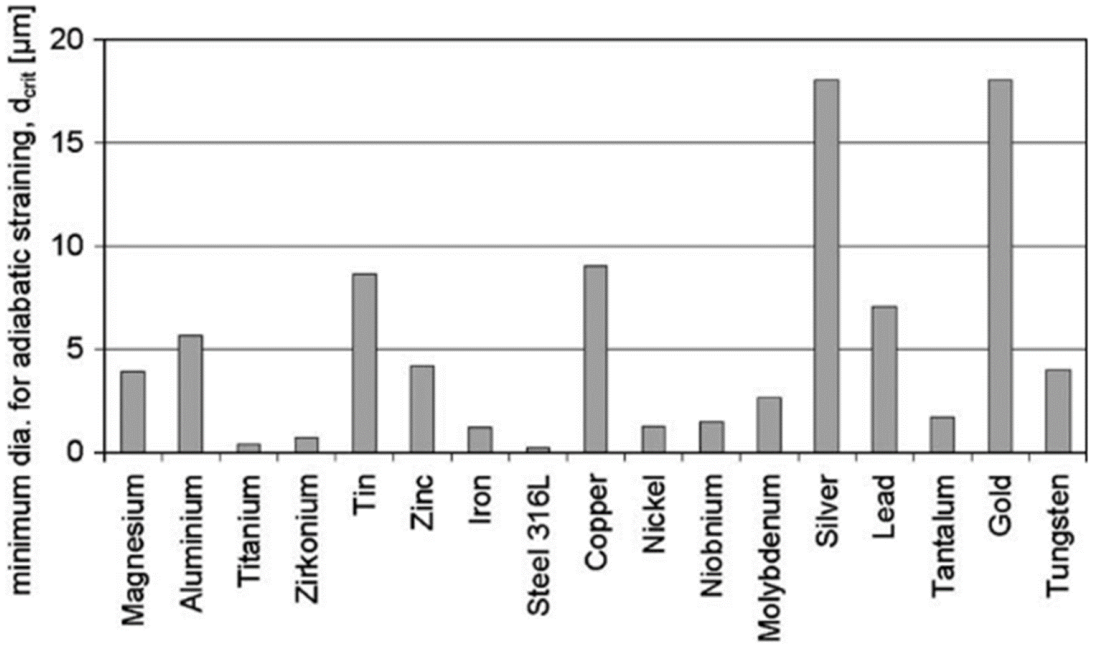

Figure 2.12: Minimum particle size required for ASI or bonding of several materials during CSAM using the empirical Equation (2.21) [57].

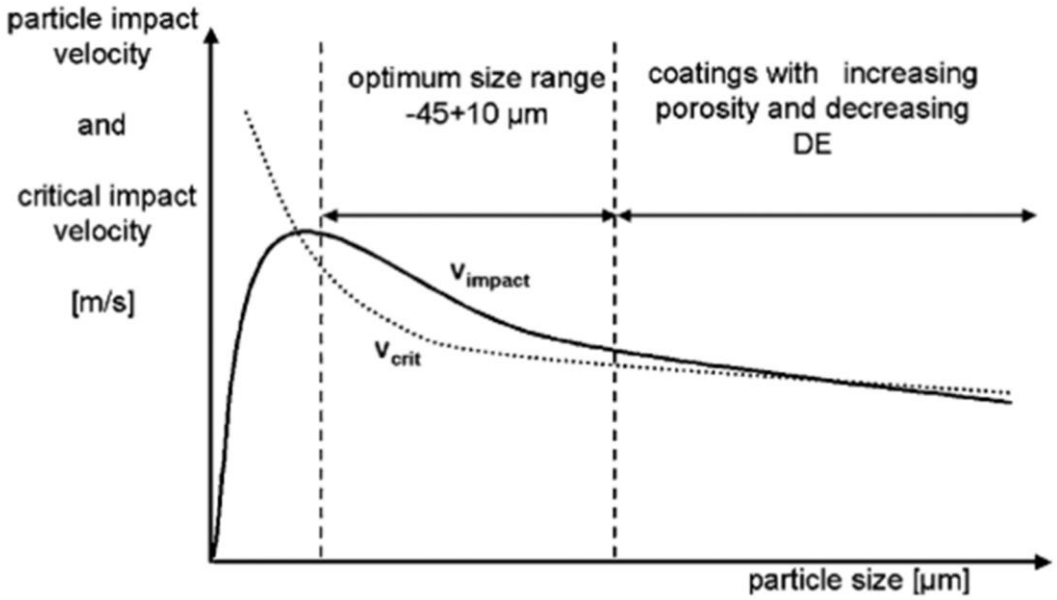

Figure 2.13: Optimised particle size distribution using particle velocity and critical velocity over particle size [57].

The above equations were established based on the similar material properties of the particles and substrates. In the case of dissimilar materials, particularly mechanical interlocking and material intermixing, there are limited studies that estimate the critical velocity for such cases [131,141,142]. Several researchers have observed nanoscale–microscale interfacial material mixing interlocking mechanisms [140,142,143]. This interfacial material intermixing was attributed to the Kelvin-Helmholtz instability mechanism, which resulted in the formation of roll-ups and vortices at the particle-substrate interface. Champagne et al. [142] also proved the interfacial material intermixing mechanism when high-velocity Cu particles impact on Al substrate, creating a viscous mixing between Cu and Al. In their study, they proposed the empirical model given in Equation (2.22) to estimate the critical velocity required for interfacial material mixing. Where $\boldsymbol{H_B}$ = Brinell hardness of the substrate and $\boldsymbol{\rho_p}$ = particle density. Furthermore, Yin et al. [140] in their study identified the conditions necessary to trigger the formation of material-intermixing interfaces. Two factors were identified to trigger this mechanism: low DE and material properties (particles should be denser than the substrate material). The material intermixing mechanism occurs under accumulative plastic deformation caused by rebounding particles. Nevertheless, the expression of the critical velocity for a hard particle to be anchored within a soft substrate (as in the case of particle penetration—mechanical interlocking) is yet to be determined. This is particularly important for first-layer deposition, without accumulative plastic deformation.

$$V_p = \sqrt{75000\left(\frac{H_B}{\rho_p}\right)} \quad (2.22)$$

2.4.3 Window of deposition

During CSAM, the particles bond to the substrate if the impact velocity is within a defined range of velocities. The critical velocity is considered the minimum velocity required to deform the particle and bond it to the substrate. The erosion velocity, on the other hand, is considered the maximum velocity required to reach beneficial DE [57,91]. When the impact velocity is below the critical velocity, the particles rebound, and their impact is reflected by shallow craters formed on the substrate surface. On the other hand, above the erosion velocity, the incident particles erode the substrate, resulting in material loss [91]. Under rebound and erosion conditions, lower values of the bonding ratio are often obtained. The bond ratio is defined as the fraction of bonded particles to the total impacted particles (craters + bonds) per unit impact surface area [144]. A graphical representation of the conditions that lead to particle bonding and beneficial DE is referred to as the window of deposition. The window of deposition is the area between the critical and erosion velocities, as represented in Figure 2.14 [91].

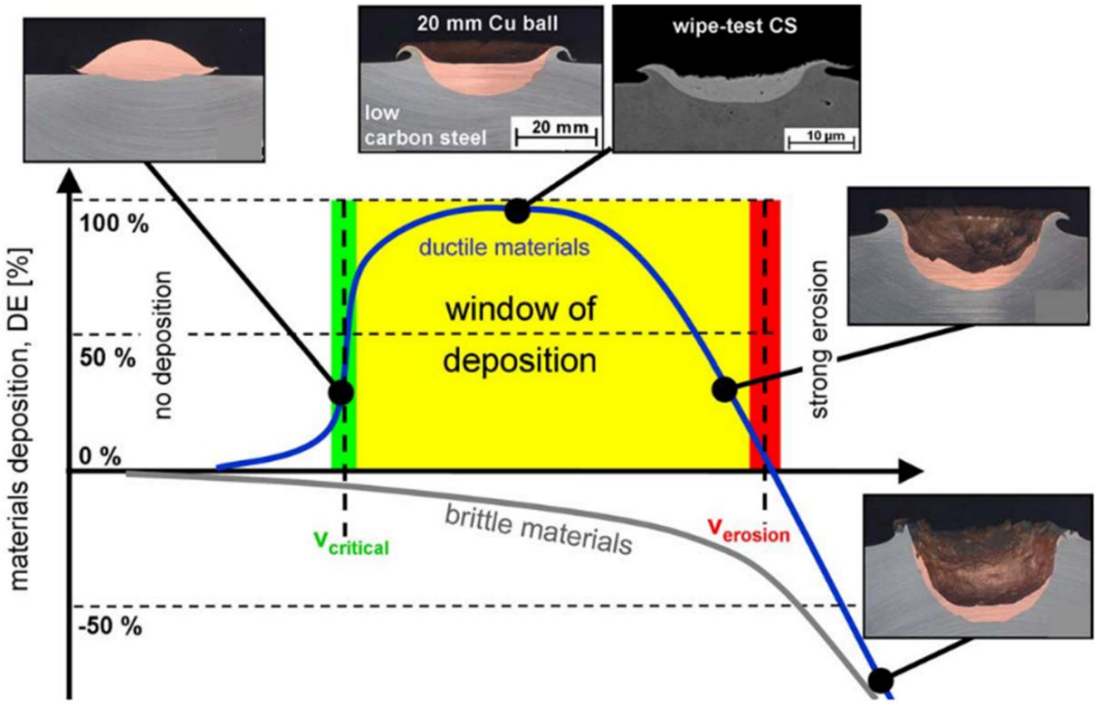

Figure 2.14: Window of deposition showing deposition efficiency and impact effects at a specific impact temperature for CSAM [91].

Assadi et al. [125] in their study found that deposit characteristics can be determined by examining the ratio of particle impact velocity and critical velocity, referred to as η. This dimensionless parameter allows for the prediction of the DE and deposit bond strength as a function of the main process parameters, gas pressure and temperature, and material parameters for the examined materials. It is well established that higher gas pressures and temperatures result in higher particle velocities, and consequently, higher DE. DE is also a unique function of the dimensionless parameter η. The schematic in Figure 2.14 clearly explains the window of deposition, as it relates to the DE and particle impact velocity. The critical velocity for ductile materials was defined as 50% DE. A further increase in the particle velocity reaches the threshold DE at 100%. Above this value, DE decreases owing to erosion. Brittle materials are considered to have negative DE values owing to their lack of ductility for solid-state deformation upon impact; however, studies

have proven the cold-sprayability of brittle materials, achieving thin films of deposits on several substrates [73].

2.5 Dynamic recrystallisation

During the deposition of materials in CSAM, particles interact with themselves and the substrate, leading to the formation of distinct microstructures because of the impact or deposition mechanism. In this section, the deposition mechanism resulting in the microstructure formed in CSAM deposits is discussed and its effect on the nano-mechanical properties of the various regions of the microstructure formed in the deposits is also included.

2.5.1 Deposit build-up during CSAM deposition

CSAM utilises the kinetic energy of sprayed particles to form dense deposits of materials layer by layer. Van Steenkiste et al. [18] proposed a model that explains the layer-by-layer powder consolidation process to explain deposit formation during CSAM [22]. The powder consolidation and, hence, deposit formation proceeds via four stages: (1) substrate surface activation by substrate cratering and first particle layer build-up, (2) deposit particle deformation and realignment resulting from successive particle impacts, (3) inter-particle metallic bonds forming in increasing numbers at higher impact velocities as deposit build-up, and (4) constant particle bombardment and peening during deposit build-up, resulting in dense and work-hardened deposits. The deposit formation process is schematically illustrated in Figure 2.15.

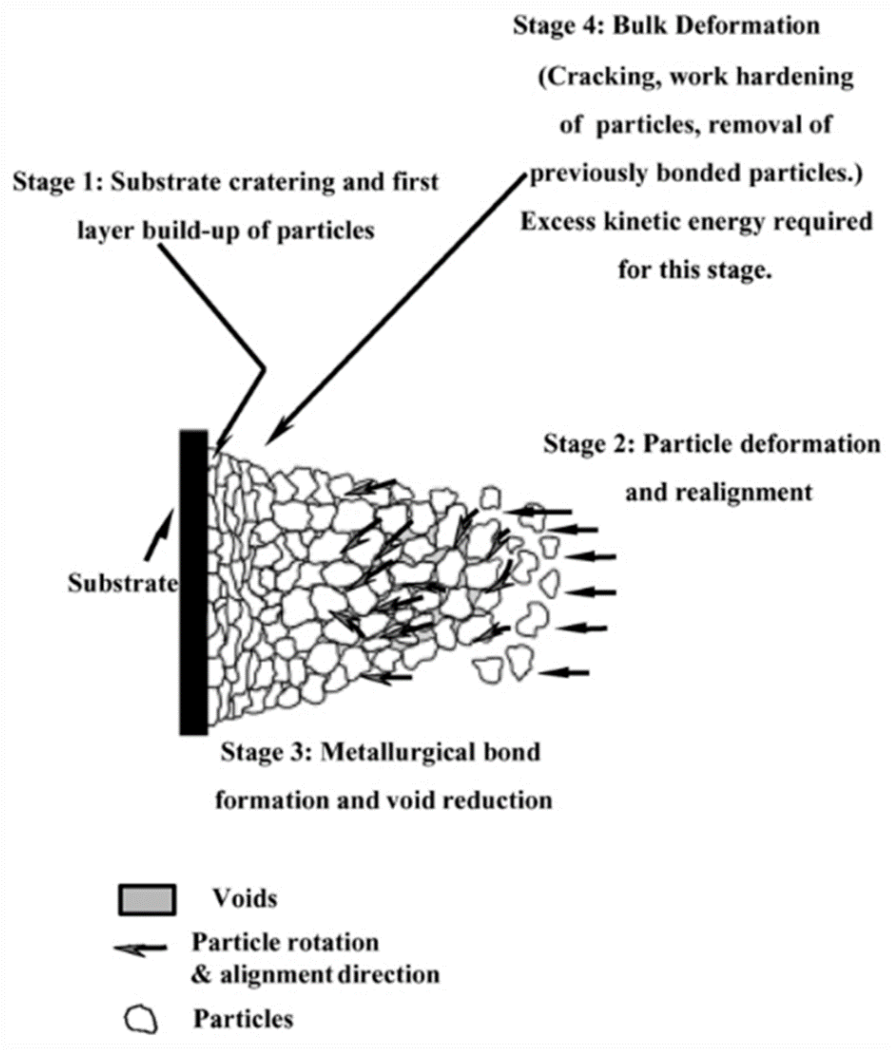

Figure 2.15: Stages of powder consolidation and or deposit build-up during the CSAM process [22].

2.5.2 Dynamic recrystallisation in CSAM

The absence of melting in CSAM-deposited material suggests that the feedstock microstructures are retained; however, the work hardening experienced by the material upon impact leads to the formation of specific microstructures, distinct from those produced by non-solid-state AM methods. The change in the feedstock microstructure was associated with the impact phenomena in CSAM deposition. As discussed earlier, ASI is the generally accepted bonding mechanism responsible

for particle deposition in CSAM [56,133]. This bonding mechanism is linked to another thermomechanical phenomenon that occurs during CSAM, dynamic recrystallisation (DRX) [137,145].

Detailed microstructural characterisation of CSAM deposits is usually performed using transmission electron microscopy (TEM), scanning electron microscopy (SEM), and electron back-scattered diffraction (EBSD) [59]. Studies have revealed that the deposits exhibit heterogeneous microstructures [59,146,147]. In-situ grain refinement has often been observed at interparticle and particle-substrate interfaces [138,148,149]. For instance, Figure 2.16 depicts the formation of ultrafine grains in the bonding region of a particle as it impacts the substrate. Particle deformation is composed of an extensively deformed interface and a metal jet region, and the interior to the top surface of the particle exhibits limited deformation.

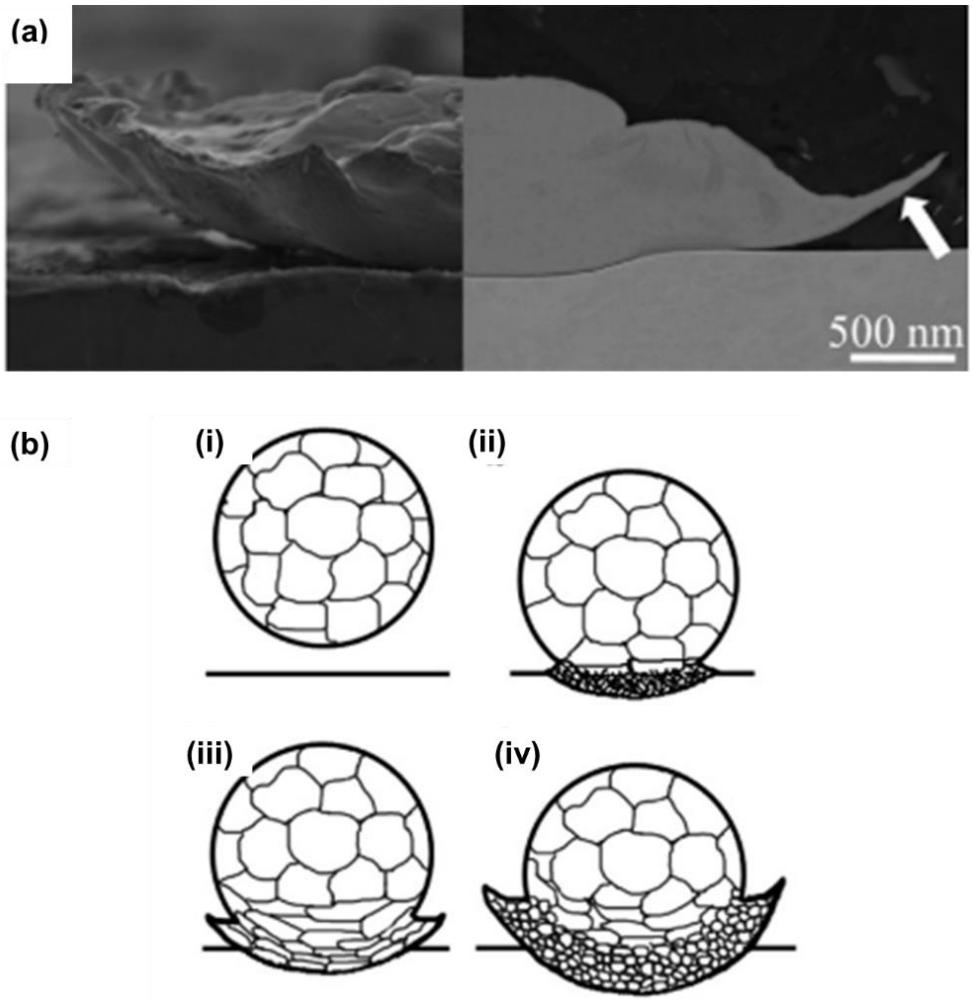

Figure 2.16: (a) Side view and corresponding cross-sectional view of SEM micrograph of a single titanium splat on a substrate. The metal jet is indicated by the white arrow. (b) shows the schematic evolution of grain refinement via DRX: (i) particle is sprayed onto a substrate, (ii) dislocation entanglement, (iii) formation of cell structures and subgrains, and re-elongation, and (iv) breaking-up, rotation, and recrystallisation of subgrains by thermal softening effects, which can be sufficient to trigger viscous flow and hence metal jetting [138].

The occurrence of DRX is largely dependent on deformation and temperature. This thermomechanical process occurs via two main mechanisms: discontinuous DRX (DDRX) and continuous DRX (CDRX). Zou et al. [137] inferred that in-situ grain refinement during CSAM deposit build-up occurs through CDRX, which occurs through subgrain rotation and high-angle grain boundary (HAGB) migration. The authors performed microstructural characterisation of CSAM Ni deposits using the

EBSD technique, as shown in Figure 2.17. The deformation of the Ni particles was heterogeneous, consisting of a mixture of equiaxed ultrafine grains and elongated coarse grains. The CDRX mechanism is schematically illustrated in Figure 2.18. Using misorientation profiles along the CSAM Ni deposit, a progressive misorientation gradient was observed from the central region of the particle to the particle-particle interface. A low misorientation gradient was observed in the central region because of the low lattice strain and dislocation density during the deposition. As particle deformation progresses, many dislocations, accumulations and alignments occur in a short time, and strain increases, resulting in some elongated "pancaked grains" formed towards the particle-particle interface. The flattened, elongated subgrains (see Figure 2.17 and Figure 2.18) reflect extensive deformation in the shear or compression direction. Further deformation and dislocation accumulation led to subdivision of the elongated subgrains into equiaxed ultrafine grains with HAGBs. Similar microstructural features were reported by Rokni et al. [173–175] for different CSAM-deposited Al alloys[150–152]. In addition, Liu et al. [147] reported a similar distinct microstructure in CSAM-deposited Cu, with an additional feature observed, deformation twinning. Recrystallised grains, shear bands, deformation twinning, and nanosized grains were also observed in the Cu samples prepared at different gas temperatures. The microstructure formed was attributed to dynamic and static recrystallisation, which were dependent on the spraying conditions.

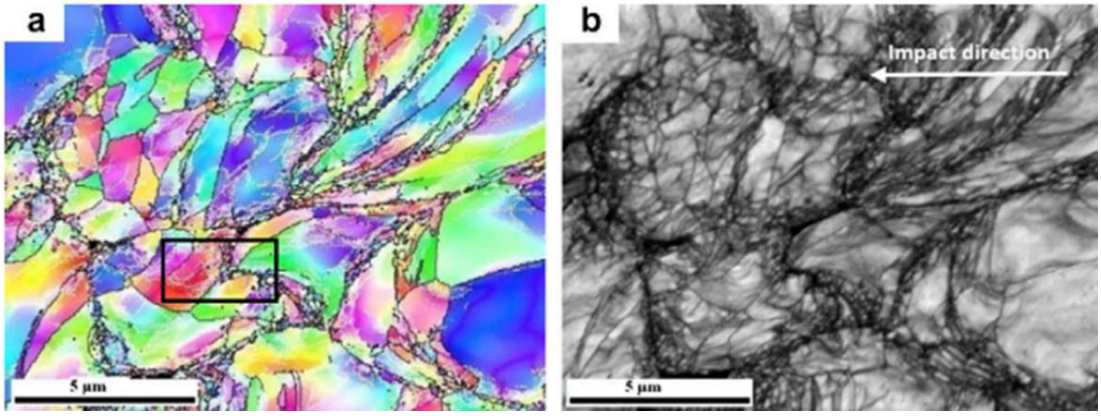

Figure 2.17: EBSD characterisation of cross-sectioned CSAM-deposited Ni particles: (a) Euler angle map and (b) image pattern quality map of the same area as in (a) [137].

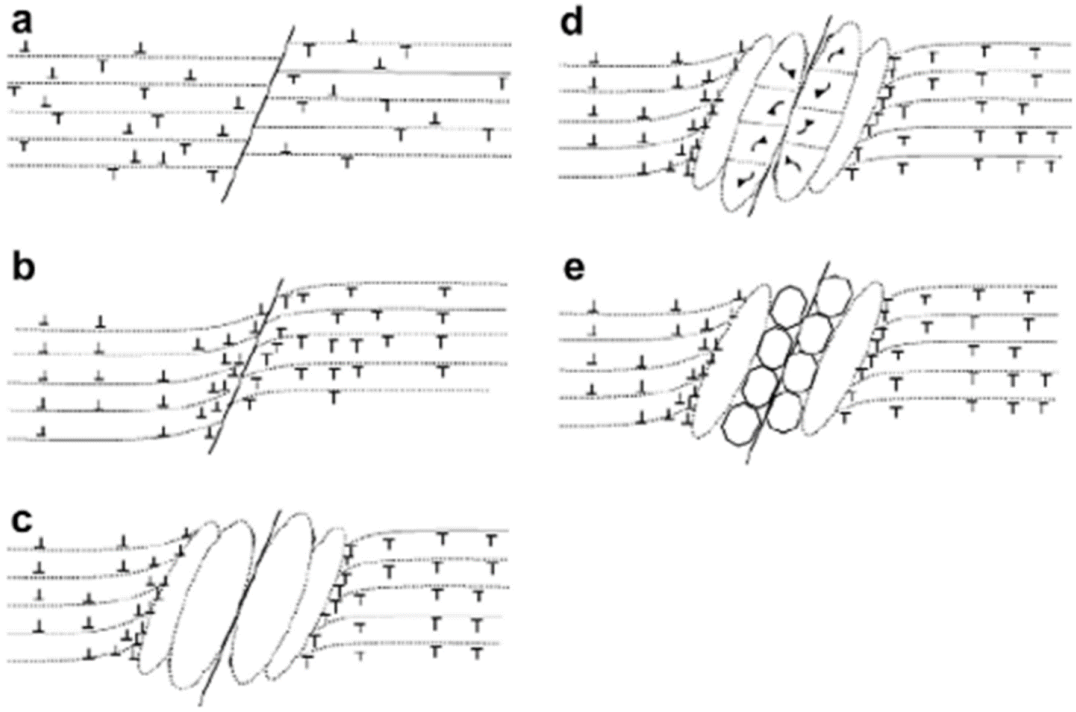

Figure 2.18: Schematic illustration of the proposed mechanism of dynamic recrystallisation in Ni particles during CSAM: (a) uniform microstructure with low dislocation density before deposition; (b) dislocation propagation and progressive lattice rotation upon impact; (c) dislocation accumulation and formation of elongated subgrains to accommodate deformation; (d) elongated subgrains subdivided into equiaxed subgrains and rotated to accommodate further deformation; (e) formation of highly misoriented and equiaxed grains [137].

The degree of recrystallisation and the extent and distribution of ultrafine grains depend on the properties of feedstock materials [59]. Differences in material properties such as stacking fault energy (SFE), activation energy for recrystallisation, and thermal conductivities can also influence the extent of recrystallisation [59]. For instance, Zou et al. [153] reported a more homogeneous microstructure in Cu deposits than that in Ni. This was attributed to the low activation energy of Cu for recrystallisation, and, hence, the static recrystallisation of the microstructure. Similarly, Bae et al. [154] observed extensive static recovery and static recrystallisation in Ti deposits owing to their poor thermal conductivity and local retention of transient thermal energy. These studies suggest that the extent of deformation and the material properties can affect the resulting microstructure formed. Therefore, new materials such as CoCrFeNiMn HEAs, their deposition mechanism, and microstructure evolution require extensive investigation.

2.5.3 Influence of microstructure formed in CSAM on the local nanohardness of the deposits

The deformation mechanism of materials in CSAM creates different regions in the microstructure, that is, a heterogeneous microstructure: coarse grains and ultrafine grains, with varying degrees of deformation. Consequently, these different regions affected the local mechanical properties, such as the nanohardness of the deposit. Because of the grain size differences in distinct microstructural regions, non-uniform hardness distributions are often reported. Rokni et al. [150,151] and Zou et al. [153] employed EBSD together with nanoindentation to measure local variations of nanohardness, as shown in Figure 2.19 and Figure 2.20. They reported a higher

hardness at the interfacial regions in Al alloys, Cu and Ni deposits. The greater hardness at the interfacial regions was attributed to the increased density of the grain boundaries and dislocations. Grain boundary strengthening and strain hardening induced by CSAM were the main mechanisms responsible for the increased nanohardness at the interfacial regions in the deposits.

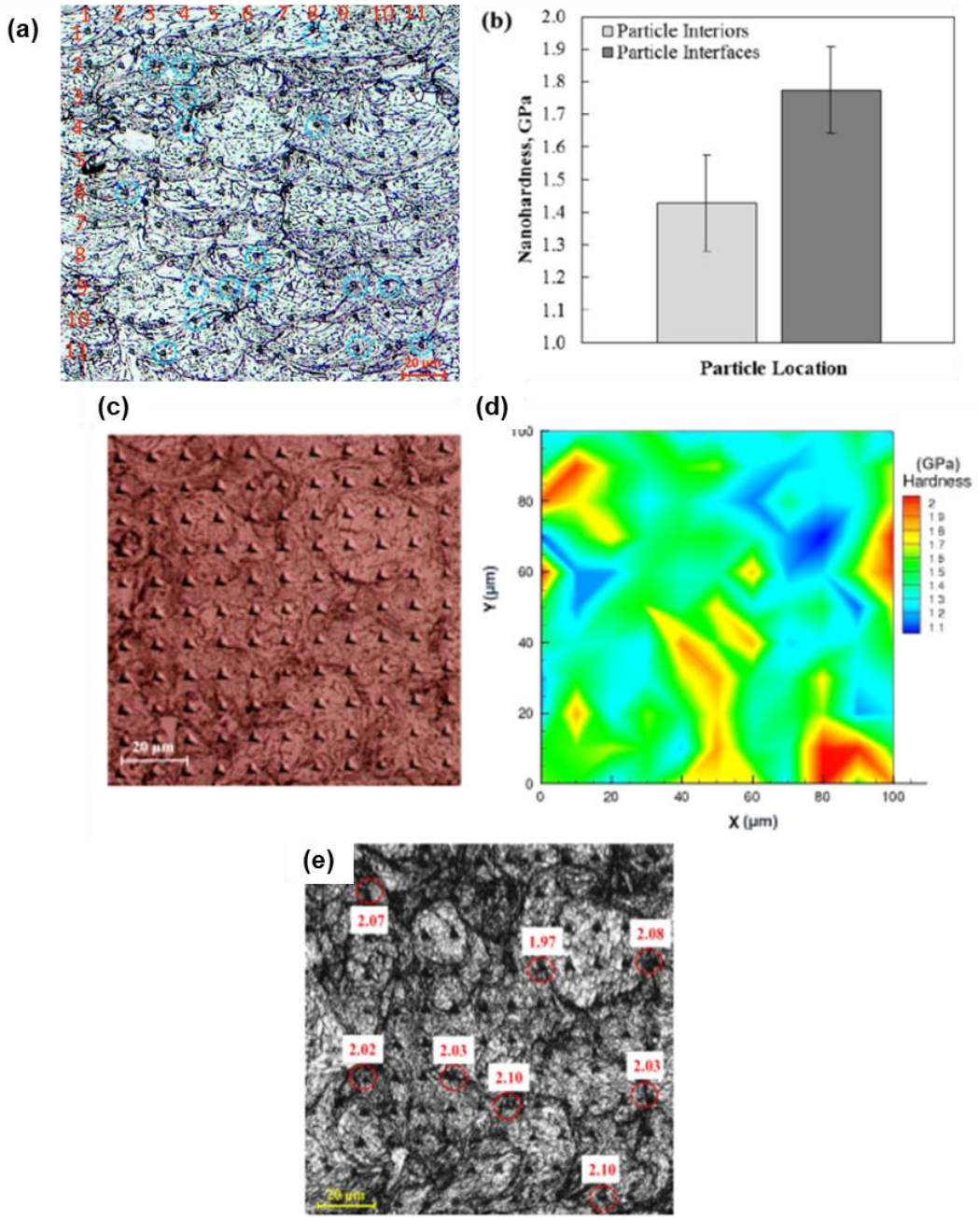

Figure 2.19: Effect of the microstructure formed in CSAM-deposited Al alloy on nanohardness variations: (a) optical micrograph showing a square array of nanoindentations on CSAM-deposited Al 6061; (b) nanohardness obtained from the CSAM-deposited Al 6061 from the particle interior and interface regions [150]; (c) optical micrograph showing a square array of nanoindentations on the CSAM-deposited Al 7075, with the corresponding contour map of the nanohardness value vs. position within the deposit (d). The image quality map with circles indicates regions of high local hardness (in GPa), mainly in the interfacial regions [151].

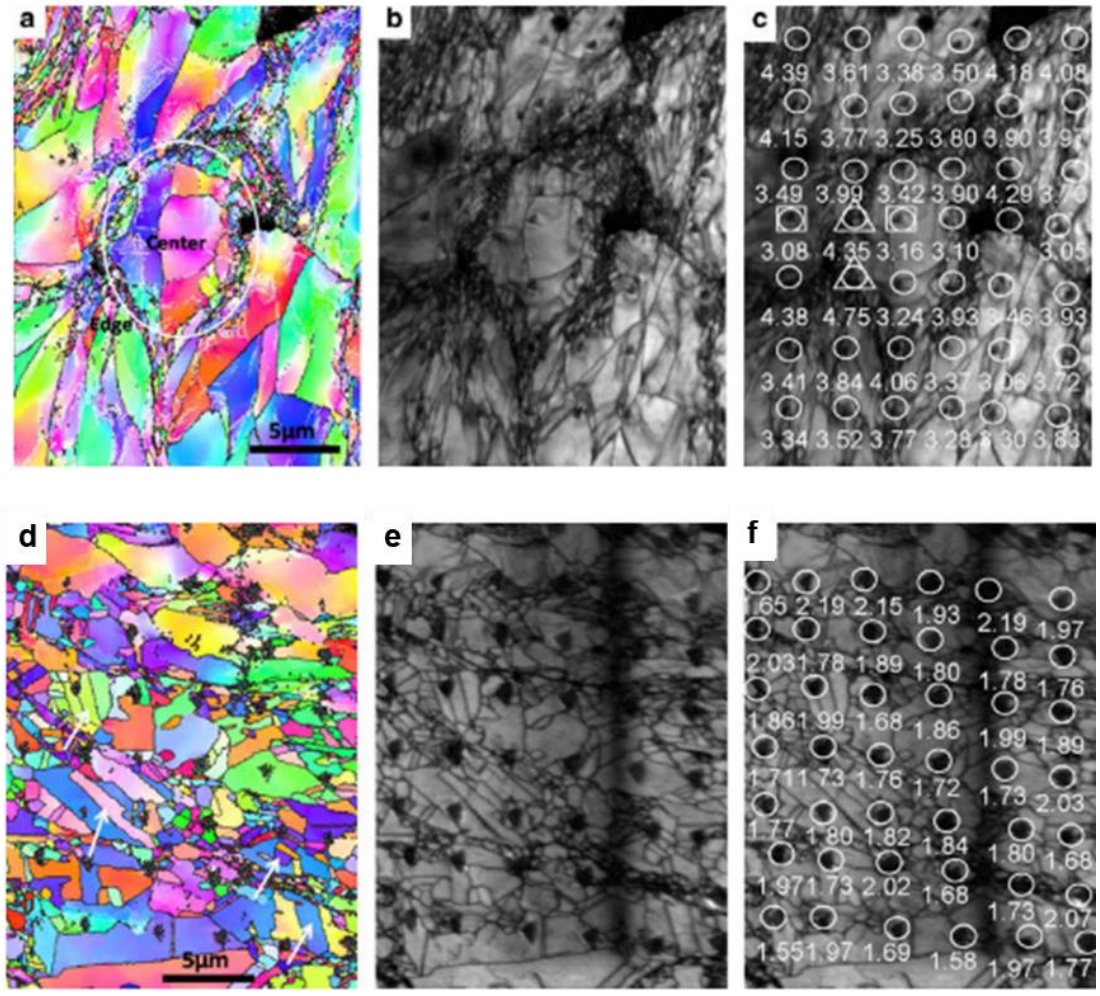

Figure 2.20: EBSD characterisation of cross-sectioned CSAM deposits after nanoindentation: (a)–(c) Ni, and (d)–(f) Cu. The circles indicate local nanohardness in GPa [153].

2.6 Numerical modelling of particle depositions in CSAM

Because of the small time and length scales, and the nature of contact in CSAM deposition, experimental investigations with sufficient resolution of particle interactions with themselves and the substrate and related phenomena can be very challenging. Recent experimental developments have been made to monitor high-velocity particle impacts within microscale and nanosecond-level resolutions [155]. However, the associated phenomena responsible for bonding are still examined post-deposition using microstructural and microanalytical techniques. Therefore, numerical simulations using different tools and methods have been used to predict the critical velocity and provide insight into the bonding mechanism associated with the CSAM process [56,57,133]. The main objective of the numerical simulations was to evaluate the temporal evolution of the deformation morphology and the respective field variables, namely, stress, temperature, and strain. This can be evaluated with various combinations of materials and spraying conditions. The results of the numerical simulations were then used to interpret particle bonding and deposit formation. Comparisons are often made between numerical simulations and experimental post-deposition analysis to ascertain the accuracy of the simulations, such as single-particle impact performed using the so-called swipe test [156]. Figure 2.21 shows an example of the comparison between a numerical simulation of a single particle impact and the experimental result.

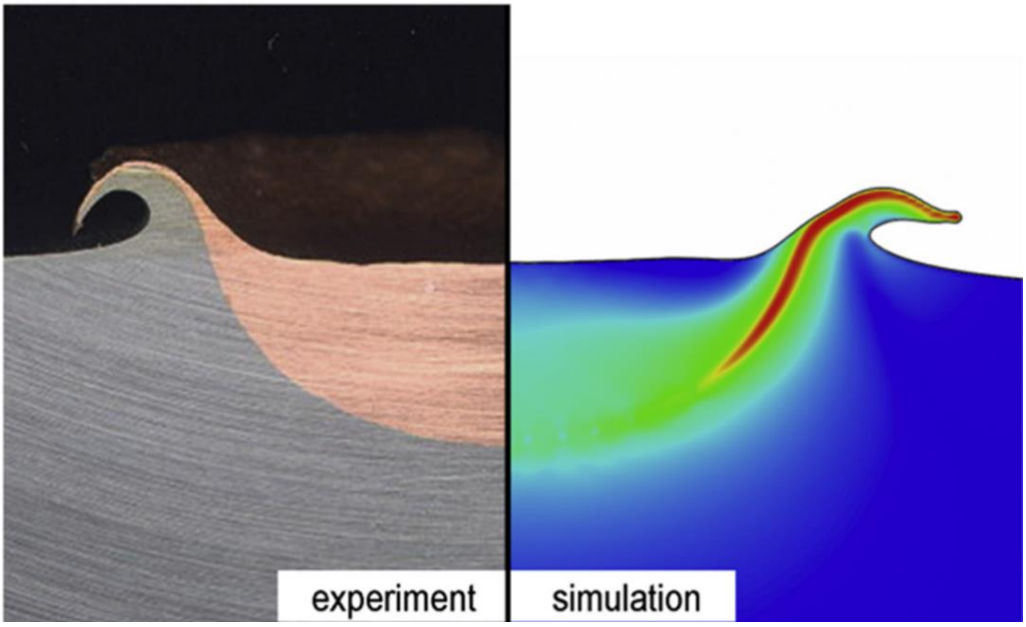

Figure 2.21: Comparison between impact experiment and numerical simulation of a 20-mm copper ball on a steel substrate [57,130].

Over time, researchers have employed various numerical techniques and tools to simulate single- and multi-particle impacts on a substrate during CSAM. These numerical methods include mesh-based Lagrangian and Eulerian finite element models (FEMs) and meshless Smoothed Particle Hydrodynamics (SPH) methods. Other methods that have been employed fall within the categories of mesh-based methods, such as Arbitrary Lagrangian Eulerian (ALE) and Coupled Eulerian-Lagrangian (CEL) methods. These numerical techniques are implemented in various computer codes or commercial software packages, with the most commonly used being the Abaqus/Explicit finite element (FE) code. More recently, Molecular Dynamics (MD) has also been used to simulate particle impact in CSAM [157,158], but the particles are of sizes in the nanometre range, which is challenging to relate to the deposition process. Each mesh- and meshless-based FEM has its advantages and disadvantages owing to the limitations of the techniques to resolve the effect of large deformations and high strain rates on the severe element

distortion of the mesh. This computational challenge is considered to usually occurs in the Lagrangian-based FEM. Nevertheless, this method has been the first and most widely used FEM for the simulation of particle impacts and deformation in CSAM [56]. The review articles by Fardan et al. [159] and Li et al. [160] provided more information on these different modelling methods.

2.6.1 Overview of modelling methods

Lagrangian-based FEM has been widely used to model particle impact in CSAM deposition [56,57,133]. In the numerical approach, the computational mesh element is fixed within the material coordinates. During deformation, the mesh element moves together with the material; as the material deforms, the element deforms. This is ideal in cases of small deformation and possibly large displacements; however, at large deformations and high strain rates, there is an issue of severe element distortions that can lead to early termination of the computation. Nonetheless, with an appropriate mesh size, the Lagrangian FEM is computationally efficient, and it facilitates the treatment of complex material models such as history-dependent material constitutive relations. This method has mainly been used in solid structural mechanics. Moreover, some studies have employed the ALE method to resolve the issues associated with the pure Lagrangian method [161,162]; however, there is an issue of early termination of the simulation with this method, and ASI may not be observed in the simulation. The Lagrangian approach can be implemented using 2D and 3D models in Abaqus/Explicit software. In addition, the use of the axisymmetric model with heat transfer significantly reduces the computational expense of the Lagrangian method.

On the other hand, Eulerian-based FEM is mainly used in fluid dynamics but has been useful in modelling particle depositions during CSAM [163]. In this method, the computational mesh elements are fixed in space, and the material continuum moves through the mesh elements. Because the mesh elements are fixed in space in Eulerian-based FEM, severe element distortion is not encountered during the computation; however, this approach does not provide precise mesh element and material interface definitions and the resolution of the flow details [130,164]. This is attributed to the void material that can be formed at a certain point in the simulation and the contact properties, such as the coefficient of friction and conductance, which cannot be varied as default values are set in the Abaqus/Explicit solver. However, this numerical limitation can be resolved using the CEL technique; herein, the particle is Eulerian-based, and the substrate is Lagrangian-based. Moreover, Xie et al. [161] reported that the CEL method is the most robust FEM for particle deposition simulations in CSAM. However, Eulerian-based FEM can only be implemented using 3D models in the Abaqus/Explicit code, which thus increases the computational cost of the method.

2.6.2 Material models

Material models are required to model and predict particle deposition and deformation during CSAM. In the deposition process, several physical phenomena are crucial to the deposition of deformable material particles. Viscoplastic deformation under a dynamic shearing load is the most important physical phenomenon [130,165]. Several material models (and their modifications that fit experimental data) have been employed in CSAM material deformation modelling.

The models are often described through constitutive equations that link the flow stress $\boldsymbol{\sigma}$, to strain $\boldsymbol{\varepsilon}$, strain rate $\dot{\boldsymbol{\varepsilon}}$, and temperature $\boldsymbol{T}$. Rahmati and Ghaeli [166] in their study performed deformation modelling of material in CSAM using six different materials models; Johnson-Cook (J-C) [167], Modified Zerilli-Armstrong (MZA) [168], Voyiadjis-Abed (VA) [169], Preston-Tonk-Wallace (PTW) [170], Modified Khan-Huang-Liang (MKHL) [171], and Gao-Zhang (GZ) [172] models. Of these models, J-C is the most widely used and can be implemented directly in the Abaqus/Explicit solver. Other models are complex and rarely employed for particle deposition modelling in CSAM. Although the study of Rahmati and Ghaeli [166] showed that the PTW model proved to be more accurate than the J-C model when compared with experimental observations, the use of J-C has proven sufficient in predicting the critical velocity of particles and the behaviour of materials under high impact [56,173] during CSAM. The J-C material model is given by Equation (2.23), where $\boldsymbol{A}$, $\boldsymbol{B}$ and $\boldsymbol{C}$ are material constants, $\dot{\boldsymbol{\varepsilon}}^{*}$ is the equivalent plastic strain rate, and $\boldsymbol{\theta} = {(\boldsymbol{T} - \boldsymbol{T_R})}/{(\boldsymbol{T_m} - \boldsymbol{T_R})}$ is the normalised temperature.

$$\boldsymbol{\sigma} = (\boldsymbol{A} + \boldsymbol{B\varepsilon^n})(\mathbf{1} + \boldsymbol{Cln\dot{\varepsilon}^{*}})(\mathbf{1} - \boldsymbol{\theta^m}) \tag{2.23}$$

The capability of a material model to predict the high-strain-rate deformation of materials in CSAM influences the accuracy of the numerical simulation. Despite a range of material models that have been investigated for CSAM particle depositions, and some models appear to be more appropriate than others, there is the challenge of selecting the “best” material model for CSAM. This is because CSAM lies in the region of ultrahigh strain rate deformation of up to 10^9 s^{-1} [56]. Material data for this

high strain rate hardly exist. This is also the case for even low-strain-rate regimes, as limited data exist for microsized particles under dynamic loading or deformations. To solve this problem, Assadi et al. [174] used a single-particle compression method to develop material data for Cu and MCrAlY under a low-strain-rate regime (10^3 s^{-1}). However, this method has not been widely employed because of the challenge of implementing the experimental techniques for microsized particles. Although the J-C model has been widely used for a range of materials in CSAM particle deformation modelling, there is limited J-C material model data available for HEAs even in a low-strain-rate regime [175,176]. Therefore, there is a need to assess and select the J-C material model data that best predicts the deformation morphology of HEAs in CSAM deposition. Consequently, this allows the accurate prediction of the critical velocity of the HEA particles.

2.6.3 Critical discussion on the modelling of particle depositions in CSAM

Numerical simulations have been employed over the past few decades to predict the critical velocity and other process parameters, preceded by experimental observations. This has helped develop windows of deposition for several materials, which serves as a process requirement for the optimisation of the CSAM process. Most studies in the open literature have focused on single-particle impact and not on complete deposit formation, which requires a large number of particles. Nevertheless, the advent of high-performance computing has allowed for numerical simulations of multi-particle impacts but at the expense of computational cost. The key findings on the modelling of impact deformation in CSAM relevant to this thesis

are discussed here, with a focus on single-particle impact. A brief discussion of the key findings of multi-particle impact modelling is also included.

2.6.3.1 Single particle impact modelling

Prediction of critical velocity

The critical velocity of a material is an important process requirement in CSAM deposition. Numerical simulations and experimental investigations have been beneficial for estimating the critical velocity in early research on CSAM. A significant outcome of numerical simulations is the prediction of ASI preceding experimental observations [130]. ASI can occur at the particle-substrate interface during impact, which is signified by an abrupt increase in the plastic strain and temperature at the impacting interfaces, as shown in Figure 2.22. A velocity range from below the critical velocity to higher velocities was evaluated to clarify the effect of particle impact on the bonding phenomena. The abrupt changes in the strain and temperature of a critical element (defined as the element with the highest value of these field variables) at the contact interface show a transition in the deformation mechanism from plastic flow to viscous flow within a narrow range of particle velocities between 550 and 580 m/s for Cu. The particle velocity that initiates these deformation changes (ASI) is referred to as the critical velocity.

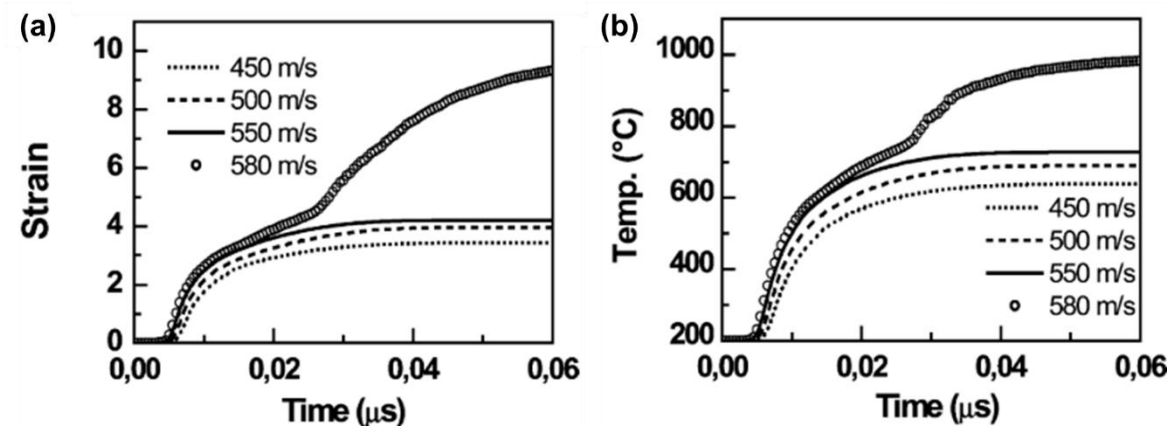

Figure 2.22: Calculated temporal evolution of (a) plastic strain and (b) temperature at the critical node of a sprayed Cu particle on a Cu substrate at different impact velocities [56].

In a similar study, Grujicic et al. [133] performed Lagrangian-based FEM for the deformation of several metallic materials with similar and dissimilar particle and substrate material combinations. The numerical simulations were performed by the authors following the study by Assadi et al. [56]. The typical time evolution of the particle and substrate deformation shape during the impact is shown in Figure 2.23. The figure shows the formation of a crater as the particle penetrates the substrate. The diameter and width of the crater increased with the contact time. However, the height-to-width aspect ratio of the particles decreased with time. An interfacial metal jet concentrated in a narrow region at the contact interface was formed, which was composed of a highly deformed material. Furthermore, the study reveals the tendency of the development of ASI at the particle-substrate interface, as shown by the temporal evolution of the plastic strain rate, plastic strain, temperature, and flow stress in several elements at the contact interface of a 25 μm Cu particle on a Cu substrate. This is shown in Figure 2.24. The results revealed that at lower impact velocities (400-500 m/s), there was a monotonic change in strain, temperature, and stress with time. At a higher impact velocity (600 m/s), there was an abrupt increase

in the strain and temperature past the contact time, while the stress decreased to a value near zero. Therefore, these studies suggest that ASI plays a key role in the bonding of materials in CSAM. However, there are several factors that affect the critical velocity, including the particle size and its surface oxidation state, particle temperature, and material properties such as hardness.

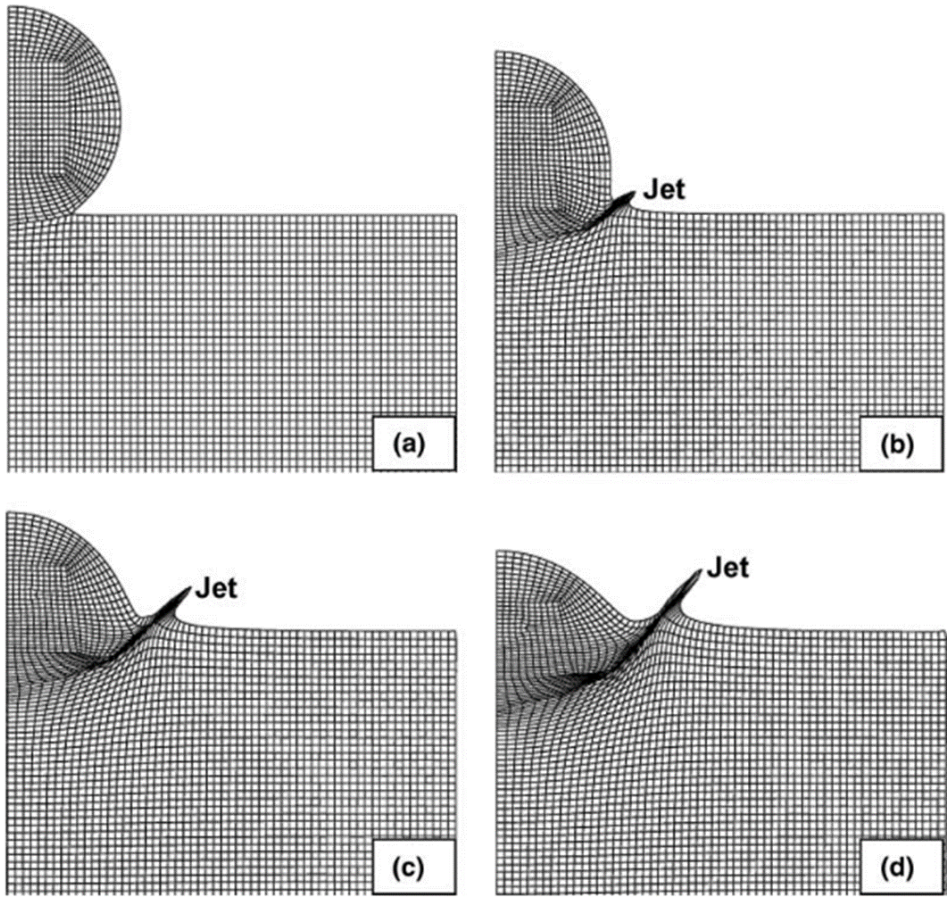

Figure 2.23: FE simulations of particle impacts in CSAM, showing the temporal evolution as materials deform: (a) 4.4 ns; (b) 13.2 ns; (c) 22.0 ns and (d) 30.8 ns [133].

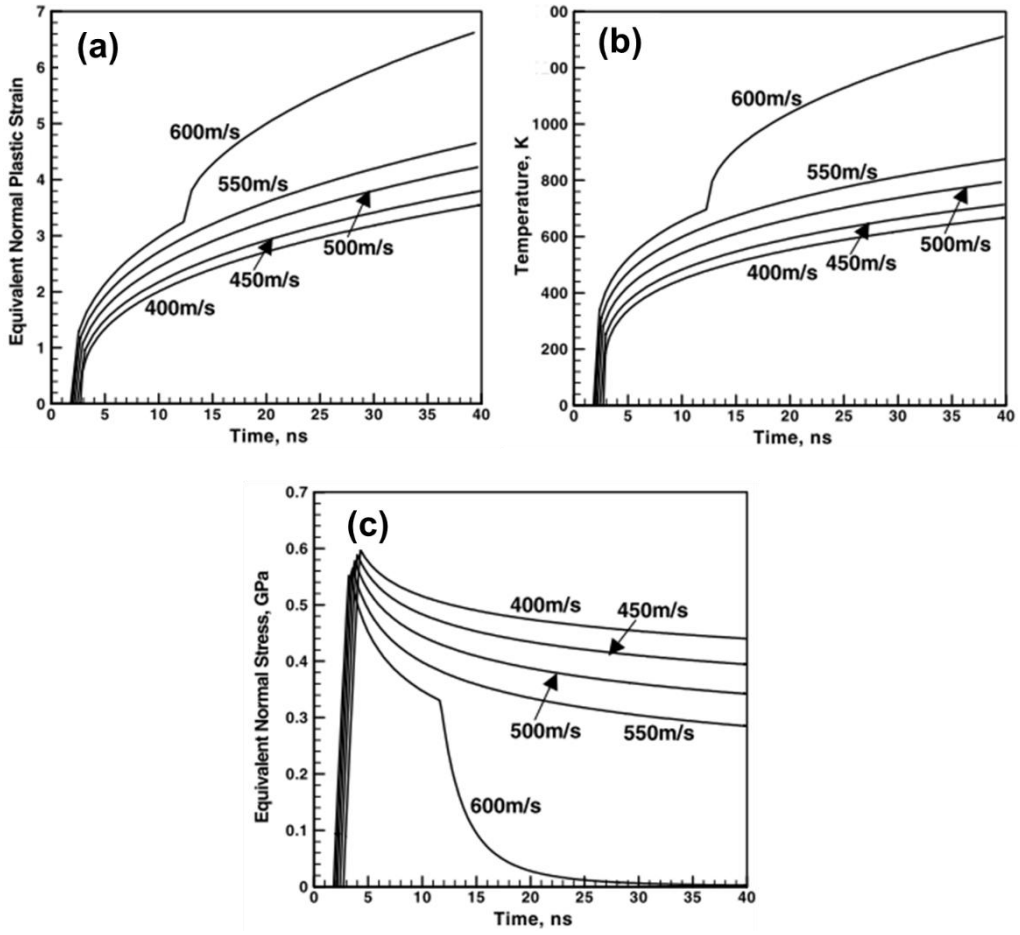

Figure 2.24: Temporal evolution of (a) plastic strain, (b) temperature, and (c) flow stress in a key element at the Cu particle interface during impact with a Cu substrate at different velocities [133].

Effect of particle size

Schmidt et al. [57,91] investigated the effect of particle size on the critical velocity of several materials. The results clearly show that the critical velocities decreased with an increase in particle size. This is believed to be due to heat conduction and strain-rate hardening. The temporal evolution of the temperature at the shear interface of Cu particles of different sizes and impact velocities is shown in Figure 2.25. The ASI was detected by the occurrence of a jump in temperature. For small particles (~ 5 μm), no shear instability was observed. This was attributed to the fast rate of heat transfer over the small particle volume, which hindered ASI. In another

study, Gnanasekaran et al. [177] observed that an increase in particle size resulted in changes in plastic strain, deformation shape, and temperature. This was attributed to an increase in the kinetic energy of the particle as its mass increased with respect to its size. The temperature also increases with particle size because higher kinetic energy is achieved by larger particles, which are converted to heat and plastic strain energy. Hence, it was concluded that larger particles led to effective bonding and successful deposit formation. However, the CSAM process does not employ a fixed particle size, but rather a particle size distribution with varying particle impact velocities. This brings complexities in developing a window of deposition for the process, especially in the deposition of new metallic materials such as HEAs. Hence, there is a need to explore the window of deposition for these new materials through numerical and experimental analyses.

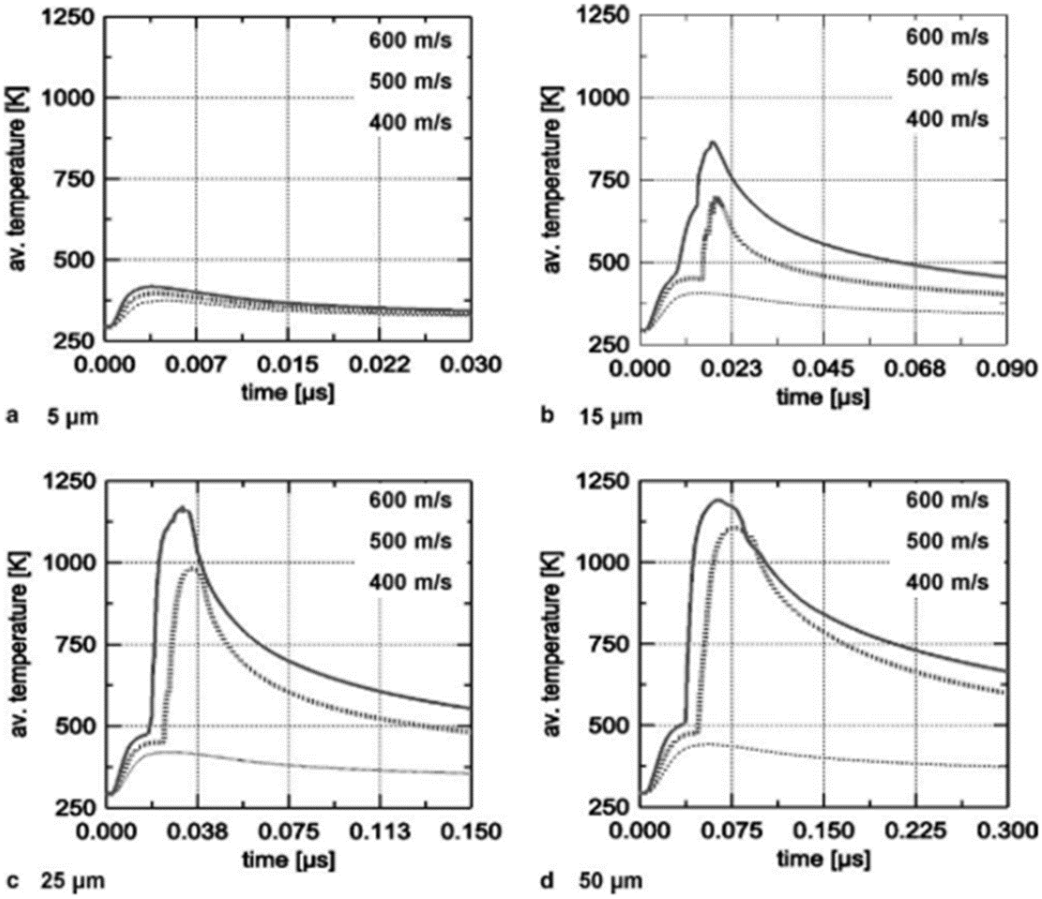

Figure 2.25: Temporal evolution of Cu particles of different sizes at different particle impact velocities [57].

Effect of temperature

The initial temperature of the particle and substrate during CSAM deposition can also help in effective bonding, and hence, improved DE. An increase in material temperature can facilitate deformation, particularly for difficult-to-spray materials such as Ni-based superalloys [178–180] and stainless steels [74,181,182]. This is because the increase in temperature causes thermal softening of the material before particle impact, and this provides a more uniform deformation [183]. Moreover, studies [59] have shown that an increase in particle and substrate temperatures increases the plastic strain, particle deformation, crater depth, and metal jet width. The critical velocity required for the deposition of a material can also

be reduced by increasing the material temperature, as shown in Figure 2.26. However, residual stresses in the CSAM (refer to Section 2.7) can be influenced by the particle and substrate temperatures, changing it from compressive to tensile stresses depending on the material temperatures and particle-substrate material combinations.

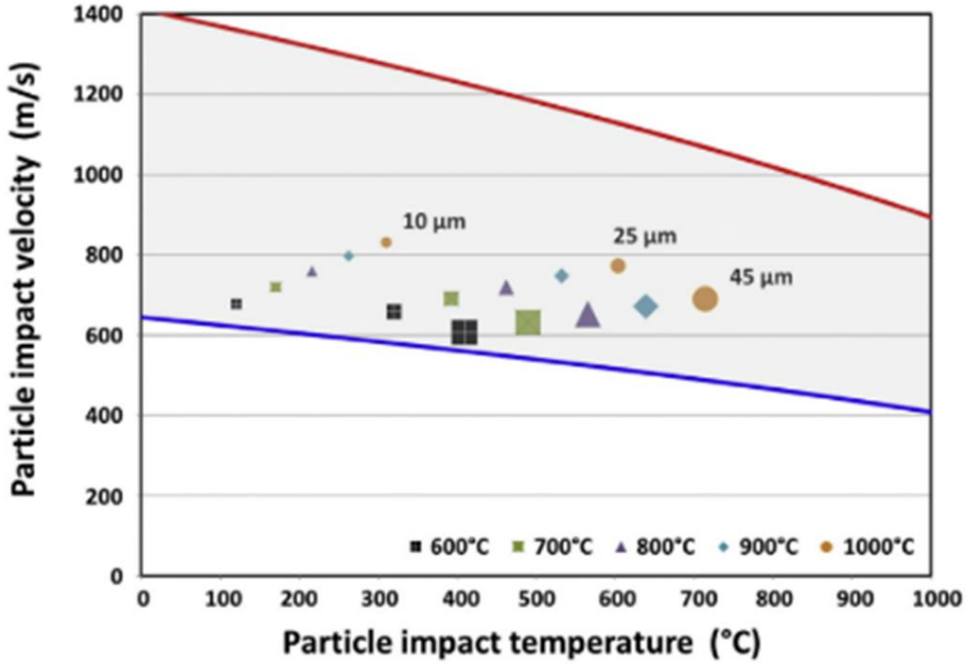

Figure 2.26: Window of deposition for CSAM of Ti with N_2 at 4.0 MPa and at different gas stagnation temperatures. The critical velocity which initiates ASI is reduced at higher gas temperatures; hence, the region of deposition in the figure [130,184].

Particle-substrate material interactions

Most of the investigations of particle deposition in CSAM involve bonding between the particles and substrates of similar materials. This problem complicates further in the case of dissimilar materials. In this case, the bonding between the materials largely depends on differences in their properties, such as density and hardness. If the substrate is softer than the incident particles, mechanical interlocking can occur

when the particles penetrate the substrate. The kinetic energy of the incident particles was used to deform the substrate. Because the particles were rarely deformed in this case, ASI was suppressed on the particle side [131]. However, deposition can be achieved even with better adhesion on the substrate, possibly because of the ASI on the substrate side and the mechanical interlocking mechanism [130]. Bae et al. [131] provided information on bonding phenomena between different materials. Numerical simulations of 22 different materials with different particle-substrate combinations were performed. They proposed the existence of a thermal boost-up zone (TBZ) induced by ASI. This thermomechanical phenomenon has been reported to be the dominant mechanism responsible for bonding in CSAM. The TBZ is formed after an incubation time during impact when the materials are undergoing ASI. Equation (2.24) defines the TBZ, where $\boldsymbol{T_{max}}$ = maximum impact temperature, $\boldsymbol{t_c}$ = contact time and $\boldsymbol{t_c}$ = incubation time. The formation of TBZ after the transition point is illustrated in Figure 2.27.

$$\boldsymbol{TBZ} = \left[\left((\boldsymbol{T_{max}} - \boldsymbol{T_R})/\boldsymbol{T_m}\right)\right].\left[(\boldsymbol{t_c} - \boldsymbol{t_i})/\boldsymbol{t_c}\right] \quad (2.24)$$

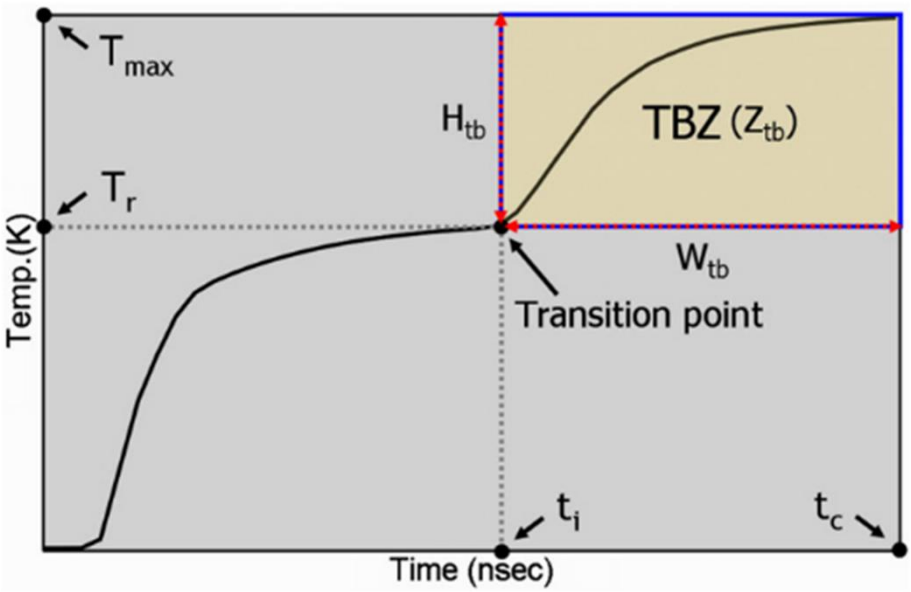

Figure 2.27: Schematic illustration of the thermal boost-up zone (TBZ) during CSAM bonding [131].

Differences in the material properties were reported to determine the size of TBZ. Cu/Cu had a larger TBZ, whereas Al/Al or Ti/Ti had a smaller TBZ. A transition point was observed for similar materials before TBZ, similar to the formation of the ASI. However, for dissimilar materials such as Ti/Al, no “transition point” was observed before the TBZ. Bae et al. [131] reported a high heating rate and collapse in the flow stresses for dissimilar materials. Although the deposition of dissimilar materials has been reported in recent studies [132,185], the prediction of the critical velocity for dissimilar materials requires further investigation.

The deformation pattern of the four categories of particle-substrate combinations, as reported by Bae et al. [131], is shown in Figure 2.28. The figure shows the differences in the interactions in the various particle-substrate combinations. The particle and substrate can have similar hardness and ductility (soft/soft and hard/hard); the particle can be softer and more ductile than the substrate, or the opposite (soft/hard). In the case of similar materials such as soft/soft (Al/Al) and

hard/hard (Ti/Ti), large deformation (wider metal jet) and high penetration in the substrate were observed for the former, owing to the extensive formability of Al. In the case of dissimilar materials, extensive deformation occurs on the softer side. In the Al/Ti case, the incident particle underwent plastic deformation, whereas in the case of Ti/Al, a large penetration of the incident Ti particles in the soft Al substrate was observed owing to a large difference in hardness. In both cases, the interface temperatures reached the melting point of the softer side. Additional factors can affect the deformation behaviours, such as work hardening, strain, and strain-rate hardening of the materials, which also determines the delay in the onset of TBZ. Relatively low critical velocities of 365 m/s and 665 m/s were numerically estimated for Al/Ti and Ti/Al [131], respectively, whereas critical velocities of 775 m/s and 865 m/s were estimated for Al/Al and Ti/Ti, respectively, as presented in Figure 2.29. These values are higher than those for Cu/Cu (550 m/s), which is attributed to the low density and high heat capacities of Al and Ti.

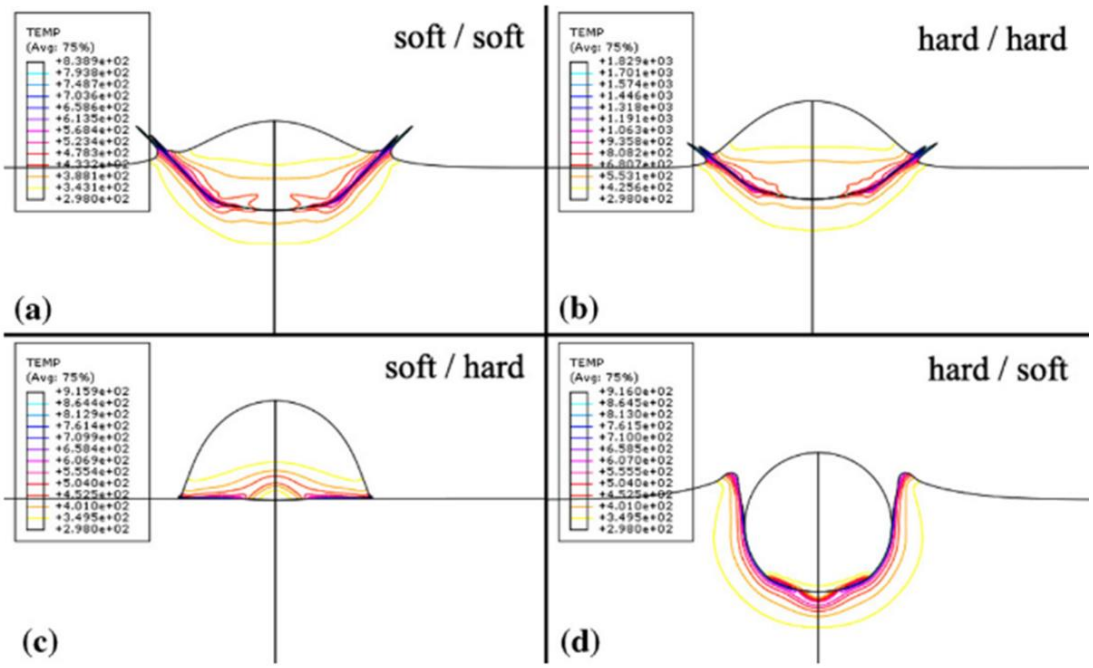

Figure 2.28: Deformation patterns of four different cases of particle impact on substrates: (a) soft/soft (Al/Al at 775 m/s), (b) hard/hard (Ti/Ti at 865 m/s), (c) soft/hard (Al/mild steel at 365 m/s), and (d) hard/soft (Ti/Al at 655 m/s) [131].

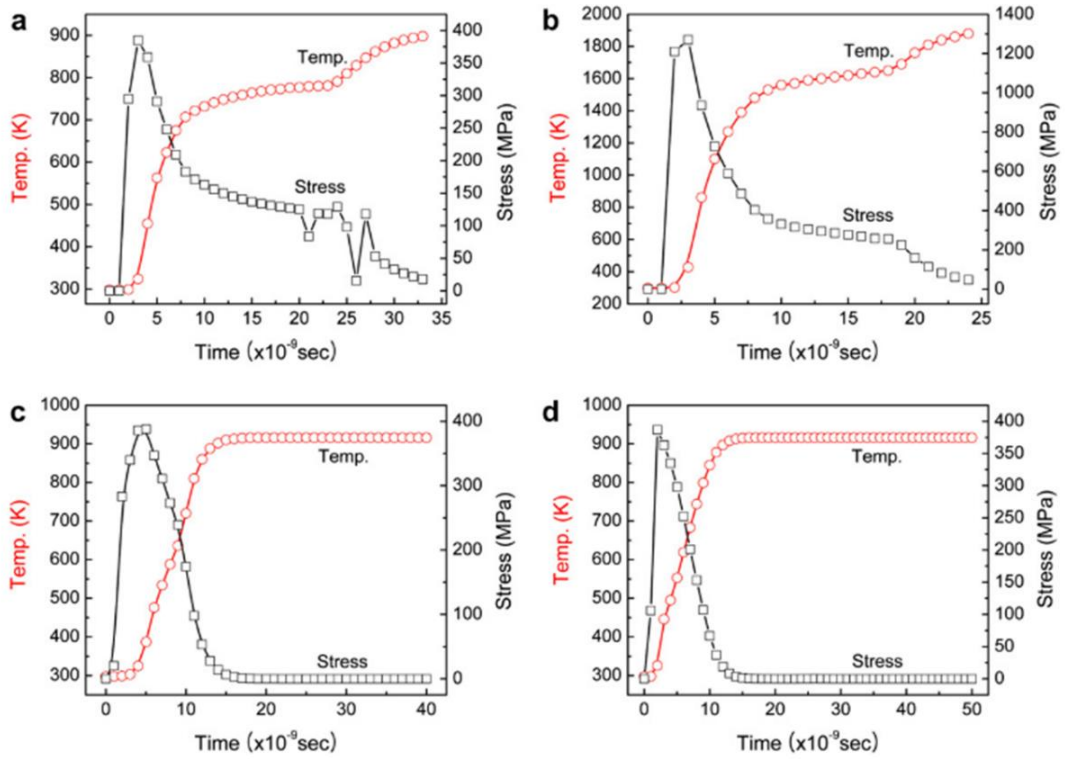

Figure 2.29: Temporal evolution of the interface temperature and flow stress of (a) Al/Al, (b) Ti/Ti, (c) Al/mild steel, and (d) Ti/Al at critical velocities of 775, 865, 365, and 665 m/s, respectively [131].

Flattening ratio

The flattening ratio (FR) can be used as an indicator to describe quantitatively, the extent of particle deformation in CSAM. FR is defined as the ratio of the splat width W to the original particle diameter, d_p (W/d_p). Another definition is given as $1 - h_p/d_p$, where h_p is the splat height as presented in Figure 2.30a. Following the work of Assadi et al. [56], Schmidt et al. [57], and Assadi et al. [125] investigated the effect of particle velocity on FR through Lagrangian-based FEM using Abaqus/Explicit FE code. Simulations were performed for the adiabatic deformation of large particles of approximately 20 mm to alleviate the issues of excessive mesh distortion and the effect of particle size on the results. As shown in Figure 2.30b, the FR increased with increasing particle velocity. The figure shows the results of the modelling for different impact conditions corresponding to Cu and Al particles. This agrees well with the results of several other studies and is comparable to the experimental results. For example, Figure 2.30c shows a comparison of the FR evaluated from numerical simulations and experimentally measured values for Cu [186].

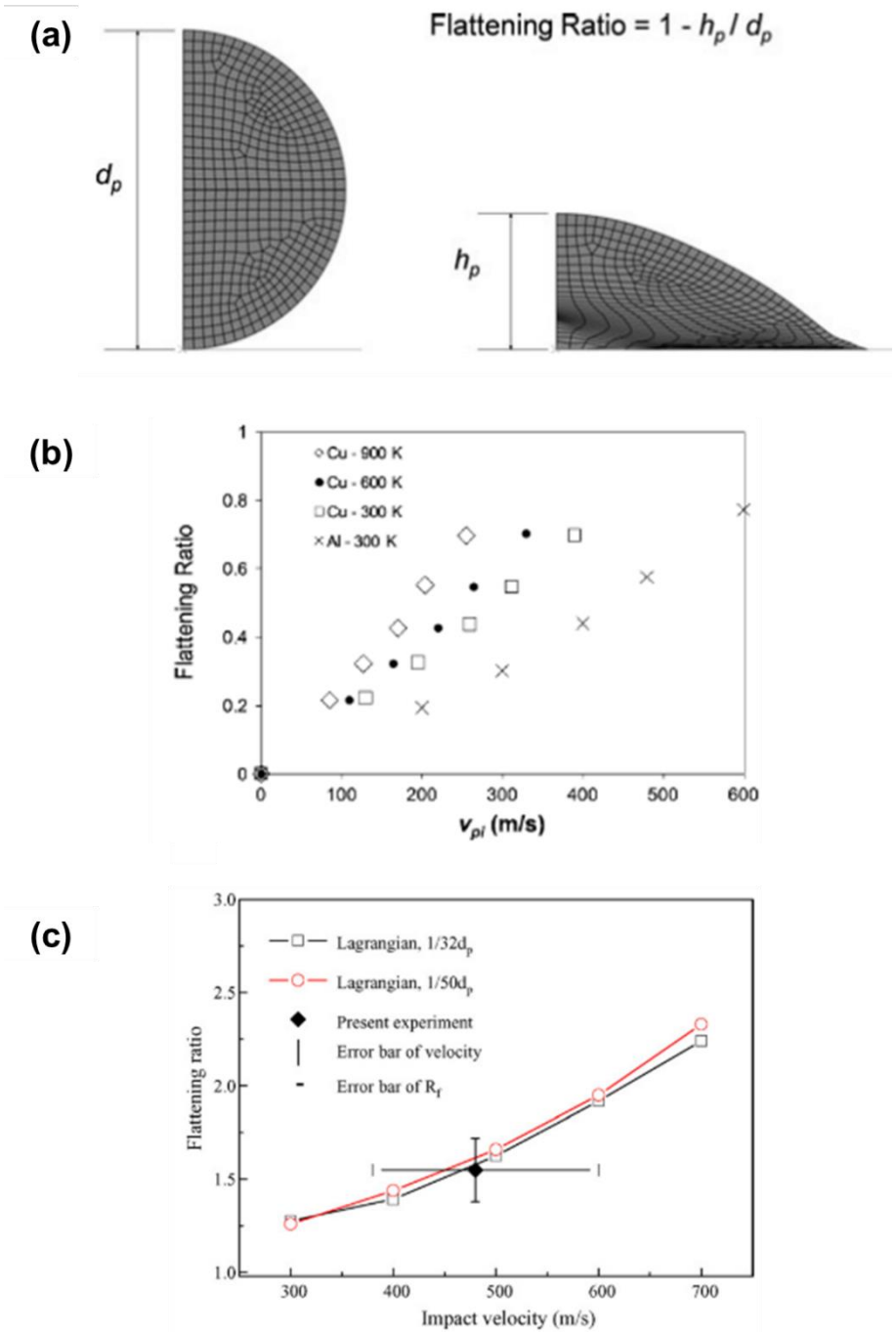

Figure 2.30: Flattening ratio of particle impacts during CSAM: (a) evaluation of the flattening ratio of a particle impact on a rigid surface, obtained using FEM [125]; (b) calculated flattening ratios of 20 mm Cu and Al particles as a function of particle velocity [125], and (c) effect of particle impact velocity on flattening ratio of deformed Cu particles modelled using the Lagrangian approach and compared with experimentally measured values [186].

King and Jahedi [187] provided an expression for analysing FR. Because the original diameter of the particle cannot be known *a priori*, the authors employed an

ellipsoidal function to describe the flattening of the particles depending on the extent of the particle deformation [187]. The accuracy of the approximations was verified by particle dissections performed using a focused ion beam/scanning electron microscope (FIB/SEM) [187,188]. When the particle deformation is minimal, the original particle diameter can be given as $\boldsymbol{d_p} = \sqrt[3]{(\boldsymbol{W^2 h_p})}$, whereas for particles that deform extensively, $\boldsymbol{d_p} = \sqrt[3]{\boldsymbol{0.75(W^2 h_p)}}$. Flattening data can also be extracted from SEM images of mechanically cut and polished samples of the sprayed particles; however, this is always associated with measurement errors, as the sectioning is likely not to pass through the centre of the splats. Nonetheless, this technique is cost- and time-effective, allowing for quick measurements and analysis of particle deformations. FR of sprayed particles have been considered a “diagnostic” tool for assessing the extent of particle deformation and hence deposit quality [189] but not widely employed for assessing the appropriate J-C material model [189] for predicting critical velocities in CSAM.

2.6.3.2 Multi-particle impact modelling

Several numerical simulations of multi-particle impact behaviour in CSAM have been reported in the literature [159]. Early studies involved a few particle impacts (>2) [190–192], whereas the advent of high-performance computing allowed for more particle impacts (≥100) [193–195]. However, this occurs at the expense of the computational cost. Bae et al. [192] performed multi-particle simulations of Ti on mild steel using Lagrangian-based FEM. Twelve 25 µm particles with their corresponding particle impact conditions were employed for the simulations. Figure

2.31 shows the deformation patterns and temperature profiles of the simulation for the different spraying conditions employed. The local interfacial thermomechanical responses of the particles upon subsequent impacts on the substrate were revealed by the FE simulation. The extent of particle deformation differs under different impact conditions, with severe deformation occurring at higher particle velocities and/or impact temperatures. The temporal evolution of the field variables in the regions marked in Figure 2.31 is shown in Figure 2.32. The subsequent impact of particles on previously deposited particles increases the strain and temperature at the particle-substrate interface.

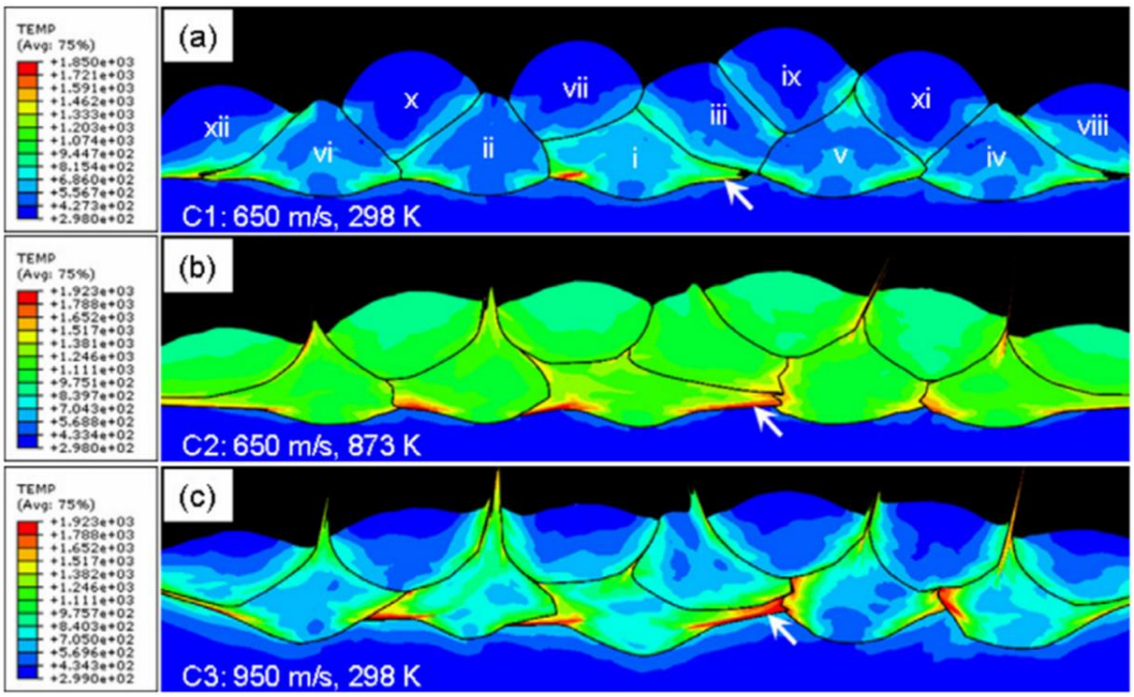

Figure 2.31: Lagrangian-based FE simulation of Ti particles on mild steel substrates showing deformation patterns and temperature profiles under different process conditions: (a) C1—650 m/s and 298 K, (b) C2—650 m/s and 873 K, and (c) C3—950 m/s and 298 K [192].

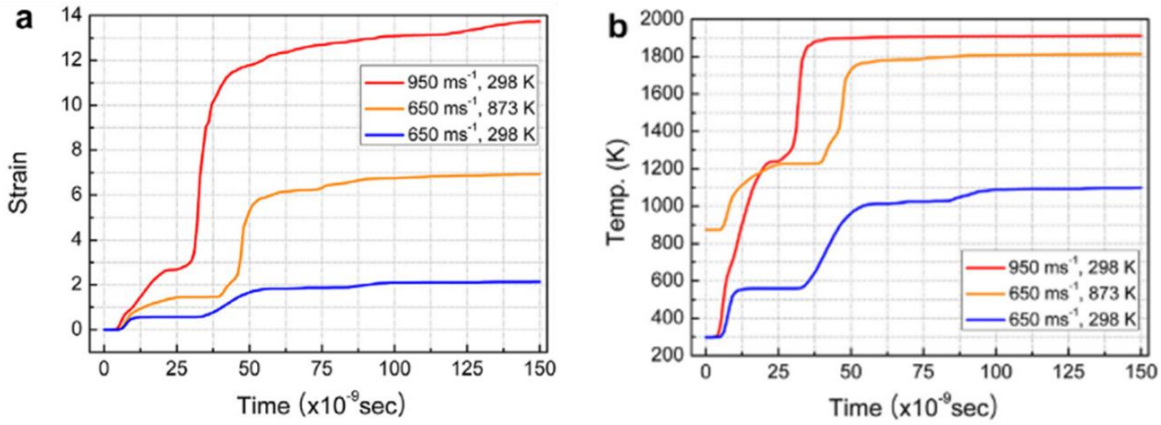

Figure 2.32: Temporal development of (a) plastic strain and (b) temperature of severely deformed Ti particles on mild steel substrates under different impact conditions. The field variables were selected from the marked region in Figure 2.31 [192].

Yin et al. [190] in another study performed a multi-particle impact of 20 μm Cu particles on a Cu substrate using the Lagrangian-based FEM. They concluded that interactions between the particles determine particle deformation and, hence, the porosity of the deposit. The simulation with Lagrangian-based FEM provided an understanding of localised deformation and the field variables (stress, strain, and temperature) between particles and the particle-substrate. This method, however, was not beneficial for evaluating porosity due to severe element distortion. Another study by Yin et al. [196] revealed that multi-particle impact modelling using Eulerian-based FEM provided results that was comparable to experimental observations than other FEMs. Similar observations were reported by Yin et al. [197] using Eulerian-based FEM. The effect of substrate hardness on the extent of particle deformation during deposit build-up was reported in their study. Other studies have revealed that the subsequent impact of particles on previously deposited particles affects the degree of deformation, with an increase in deformation attributed to tamping, interlocking, and extruding effects during deposit build-up [139,140,197,198].

More recent studies [193–195] on multi-particle impact modelling have employed CEL for porosity evaluation and the effect of spraying conditions on porosity. This method has been reported to be the most appropriate and robust FEM for such simulations [161]. For example, Song et al. [193] employed the CEL multi-particle model to assess the effect of impact conditions, such as temperature and velocity, on Ti6Al4V deposit porosity. The average FEM macroscopic porosity agreed well with the experimental results. A typical deposit modelled using the CEL method is shown in Figure 2.33a. The model was further employed to understand the effect of

the spraying conditions on the deposit porosity. It was reported that the substrate temperature had no significant effect on the deposit porosity, whereas the particle temperature and velocity contributed significantly to the deposit porosity change, as shown in Figure 2.33b and c. In another study, Terrone et al. [194] employed the CEL multiparticle impact model to design and develop porous structures through multimaterial CSAM deposition. The model employed a blended material feedstock of Ti, Al, and Cu, with varying volumetric fractions. The obtained results agreed with the experimental results. The study revealed that Ti-Cu can yield deposits with higher Ti particle deformation than the Ti-Al blend, and hence better inter-particle bonding. Another study employed the CEL multiparticle model to investigate the effect of Al particle characteristics on deposit porosity [199]. In addition, Sebastien et al. [195] investigated the mechanism of pore formation in CSAM deposition using the CEL multiparticle model of 500 particles. Their study revealed that porosity is mainly caused by two intricate mechanisms: interfacial porosity created by geometrical effects at particle-particle interfaces and stack porosity caused by particle density variations in the gas flow. However, there is a wide gap in knowledge on the CEL multi-particle impact modelling of HEAs during CSAM.

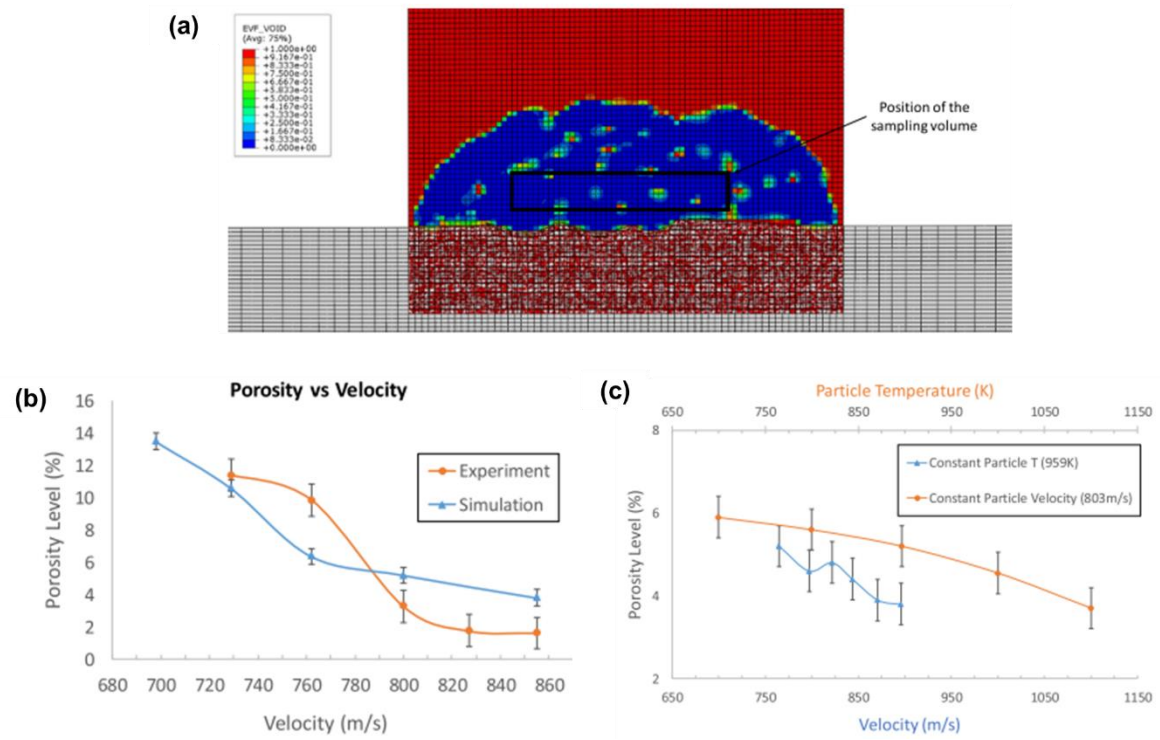

Figure 2.33: CEL method for evaluating porosity under different impact conditions: (a) cross-sectional view of the deposit modelled using the CEL method; (b) comparisons of the experimental and numerical results of deposit porosity vs. particle velocity, and (c) plot of the independent effect of particle velocity and temperature on deposit porosity [193].

Another important aspect of multi-particle impact modelling that can be beneficial for CSAM process optimisation is the effect of particle size distributions on deposit porosity. Although the effects of different particle size distributions have been investigated experimentally [200,201], there has been very limited work on numerical simulations, which can eliminate the need for costly and time-consuming experimental tests. This is particularly important for the optimisation of the CSAM process for new materials such as HEAs. Moreover, because critical velocity depends on particle sizes, the use of numerical models validated with experimental observations to obtain the optimal particle size distribution would be beneficial for the CSAM deposition of HEAs with high deposit quality.

2.7 Residual stresses in CSAM deposits

Residual stress plays a key role in the formation and mechanical performance of additively manufactured deposits. Residual stresses often remain in the deposit after the removal of external loads. Depending on their nature and magnitude, they can be either beneficial or harmful. Compressive residual stresses can be more beneficial than tensile residual stresses because they tend to extend the fatigue life of the components under service conditions. Residual stresses evolve during and after deposition; hence, their prediction can be overly complex. They strongly depend on the type of materials involved and spraying conditions or process history. The stresses formed during deposition and post-deposition affect the final residual stress state of the deposit.

Deposition stresses in CSAM, occurring at the micro- and mesoscale, can result from (1) the peening action of high-velocity sprayed particles (peening stress), (2) contraction of severely deformed particles restricted by the underlying cooler deposit or substrate (quenching stress), and (3) high thermal gradients between deposit layers. Post-deposition stresses, occurring at the macroscale, can develop after the deposit cools down to room temperature, due to the difference in thermal expansion coefficients between the deposit and substrate materials (thermal stress). Figure 2.34 shows the schematic representation of residual stress distribution that can occur in the CSAM of materials. Residual stresses formed in CSAM-deposited metallic materials have been reported to be mostly compressive due to the solid-state nature of the process: solid-state deformation and the peening effect of sprayed particles [81,202,203]. However, other studies have reported

tensile residual stress in CSAM deposits [83,85]. Therefore, the nature and magnitude of the residual stress depend on the materials involved and the spraying conditions employed. These have been investigated for several CSAM-deposited metals; however, studies on the residual stress of CSAM of CoCrFeNiMn HEA are limited [204,205]. Therefore, the following paragraphs discuss previous reports on residual stress in other CSAM metallic deposits. The experimentally measured and numerically predicted results are included. Thus, this discussion provides a fundamental understanding of the development of stresses and the final residual stress state in metals during CSAM relevant to the work in this thesis. This insight can be employed in the investigation of residual stress development in CoCrFeNiMn HEA during CSAM.

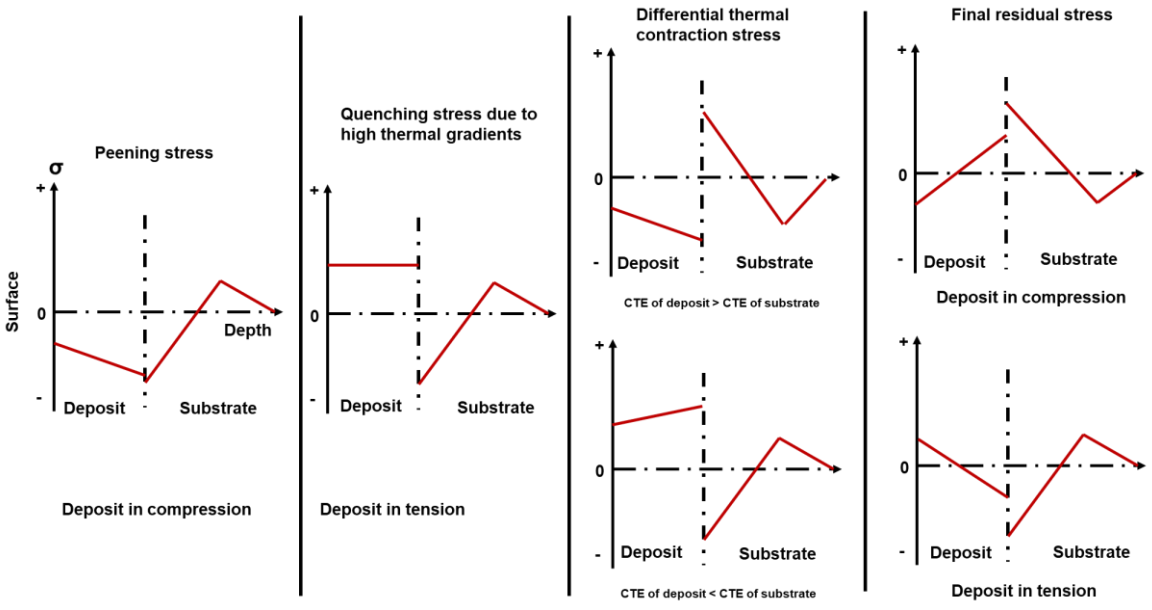

Figure 2.34: Schematic representation of residual stress distribution with the deposit-substrate system for CSAM [206].

2.7.1 Experimental measurement techniques

Two common experimental techniques, destructive and non-destructive, have been employed to measure residual stress in CSAM deposits. Nondestructive techniques measure residual stress without damaging the deposit, except in some cases where thin material is removed for through-thickness measurements [81,207]. The common techniques employed for CSAM deposits include diffraction methods such as X-ray diffraction (XRD) [207–210], neutron diffraction methods [83,84,211], and curvature measurements [202,212].

Destructive techniques, on the other hand, measure residual stress by strain relaxation through the removal of materials from the deposit. The removal of materials from the deposit alters the displacement field and shape of the deposit, which is measured using strain gauges or a coordinate measurement machine (CMM). The resultant stress can then be evaluated by the change in strain and using constitutive material laws. This technique includes common methods such as hole drilling [213,214], layer removal [215], and contour methods [85,216–218]. These methods are suitable for thick deposits, such as those obtained using CSAM. The advantage of these methods is the simplicity of their approach, and the results are independent of the microstructure of the deposit. A major disadvantage of these methods is the permanent damage caused to deposited samples.

2.7.2 Critical discussion on residual stress of CSAM deposits

In a study by Luzin et al. [219], compressive residual stresses were measured in Al and Cu deposits using the neutron diffraction technique, as shown in Figure 2.35. Cu deposits show more significant compressive residual stress (~50-80 MPa) than Al deposits (<10 MPa). The greater compressive stress in the Cu deposits is attributed to the dominant accumulative peening stress over the thermal stress as the Cu particles deformed more severely than the Al particles, regardless of the substrate material. Thermal contraction stresses had little effect on the overall stress profile owing to the small temperature accumulation of ~100 °C during the CSAM process. In another study, Suhonen et al. [202] used the curvature-based approach to determine the residual stress formation during CSAM deposition of Al, Cu and Ti deposits on carbon steel, stainless steel and Al substrates. Compressive stress was mainly formed owing to the nature of the CSAM process, but neutral and tensile residual stresses were also formed in the studied deposits. The authors reported that the evolution of the stresses in the deposits can be either compressive or tensile depending on (1) the density of the particles and their deformation behaviour upon impact and (2) the difference in the coefficient of thermal expansion (CTE) of the sprayed material and the substrate. Owing to the low density and high CTE of Al compared to the stainless-steel substrate, tensile residual stress was observed in the Al deposits. They also reported that thermal stresses were dominant in the Ti deposits owing to the quenching stress formed during the spraying of Ti particles on the substrates at a gas temperature of 700 °C. To form dense microstructure of deposits using difficult-to-spray powder metals, high gas temperatures are often employed to thermally soften the sprayed particles. Under

these conditions, thermal stress may become dominant, even larger than the peening stress; hence, the nature and magnitude of the residual stress may vary significantly depending on the spraying conditions employed and the CTEs of the particle-substrate materials.

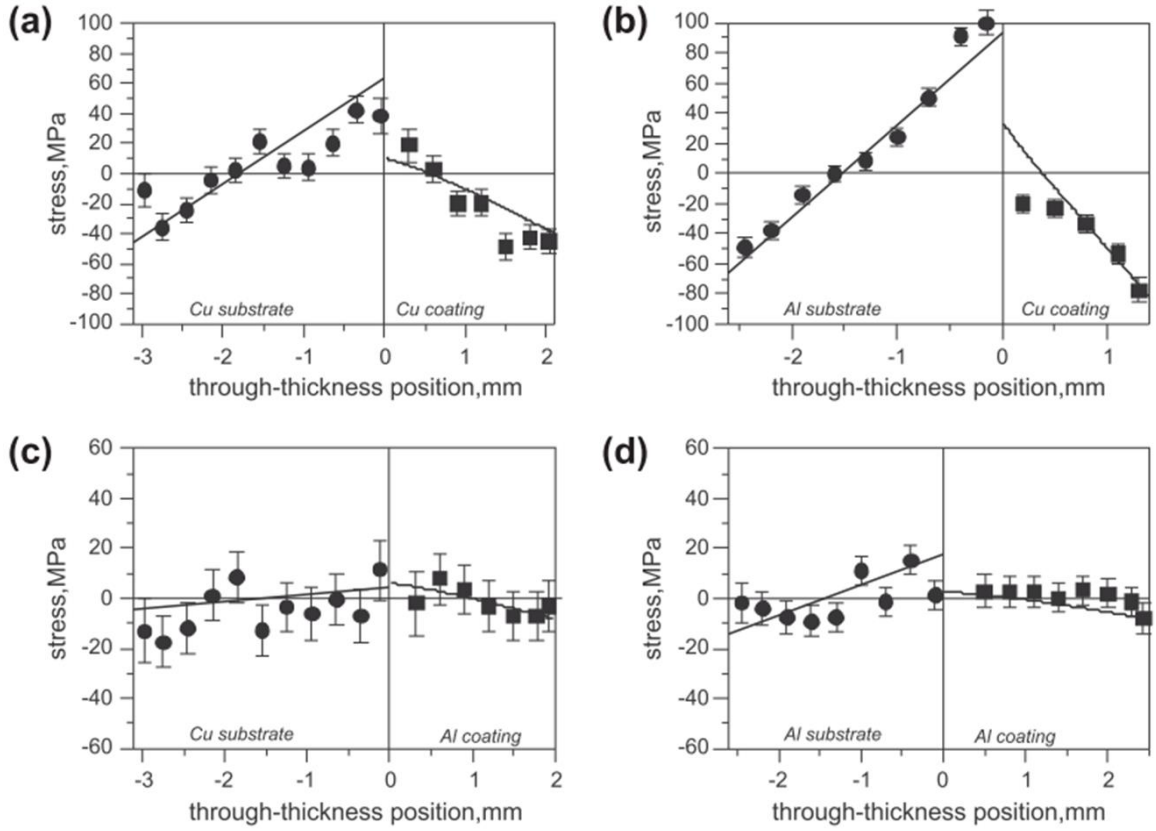

Figure 2.35: Measured residual stress (symbols) and fitted (lines) of through-thickness stress profiles of (a) Cu/Cu, (b) Cu/Al, (c) Al/Cu, and (d) Al/Al samples [219].

In contrast to the commonly observed compressive residual stress in CSAM deposits, Luzin et al. [84] demonstrated that the residual stresses in CSAM Ti deposits on Fe and Al substrates mainly formed through a thermal mismatch mechanism because of the difference in the CTEs of the materials. This thermal effect was ten times larger than the compressive deposition (peening) stress, resulting in tensile residual stress. Similarly, Spencer et al. [220] reported a thermal

mismatch dominant mechanism in sprayed pure Al particles on Mg alloy substrate using N_2 at 550 ºC and 3.85 MPa. Moreover, tensile residual stresses (quenching stress and thermal mismatch dominant mechanisms) in CSAM deposits have been reported by several other researchers [83,85,202], which were attributed mainly to the gas temperatures and material combinations employed.

Apart from the aforementioned spraying conditions, the nozzle transverse speed and powder feed rate have been reported to significantly influence the nature and magnitude of the residual stresses in CSAM deposits. For instance, Vargas-Uscategui et al. [211] reported the formation of tensile residual stress in a CSAM hollow Ti cylinder. The tensile residual stress formed was attributed to the slow nozzle transverse speed and high powder feed rate employed. Furthermore, Brown et al. [212] reported the compressive residual stress in a CSAM CuNi deposit when using a higher nozzle transverse speed. These studies suggest that slow transverse speed and high powder feed rate during CSAM can contribute to an increase in the accumulation of heat, resulting in high thermal gradients and hence the formation of tensile residual stresses. Moreover, Ghelichi et al. [207] in their study found that the accumulated temperature during CSAM had an adverse annealing effect on the compressive residual stress and promoted residual stress relaxation.

Another factor that can influence residual stress in CSAM deposits is the thickness of the deposit [178,208], particularly for 3D thick components, where alternating changes in the sign and magnitude of the stresses for each layer can, in some cases, result in the delamination of the deposit [85]. A study by Boruah et al. [85] showed the residual stress formed in a thick deposit of Ti6Al4V on a Ti6Al4V substrate using neutron diffraction and contour methods for stress measurement.

Tensile residual stress was measured on the deposit near the surfaces and then became compressive closer to the interface and the substrate as shown in Figure 2.36. The tensile residual formed in their study was attributed to a high thermal gradient and quenching dominant process as the feedstock was sprayed using N_2 at 5 MPa and 1100 ºC.

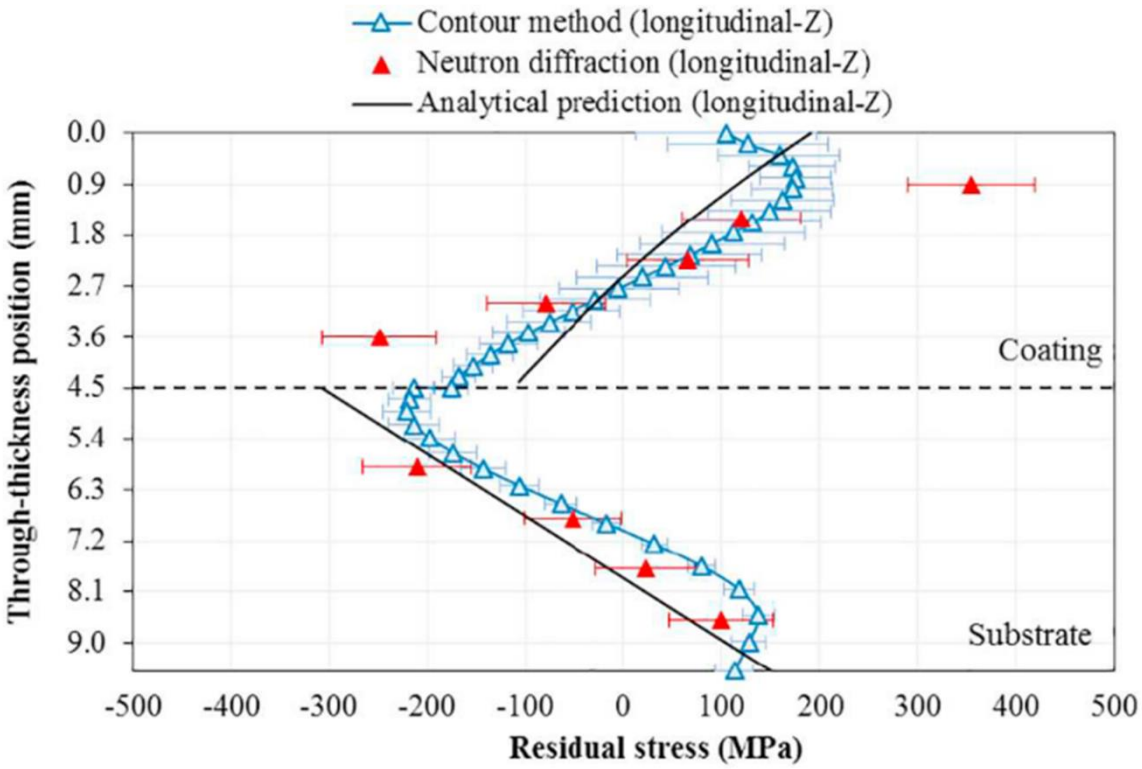

Figure 2.36: Measured residual stress using the neutron diffraction and contour method and analytically predicted through-thickness stress profile of CSAM Ti6Al4V deposit on Ti6Al4V substrate [85].

Many published articles on the residual stress of CSAM deposits employ mainly diffraction techniques for stress measurement; however, the use of the contour method for CSAM deposits is limited in the literature [83,85,211,216,217]. This technique is advantageous for large components fabricated using the CSAM technique. In general, residual stresses formed in CSAM deposits will thus influence the fatigue and fracture performance of a repaired part or component [80–82], and,

hence, the mechanical integrity of the components. It is therefore important to evaluate and understand residual stress formation during CSAM, which can be beneficial in optimising the process for repair and manufacturing in the aerospace sector.

2.7.3 Critical discussion on numerical modelling of residual stress in CSAM deposits

Due to the limitations of experimental measurements of residual stress in CSAM deposits, numerical models have become more popular in predicting residual stresses in deposits. Experiments require a long time to perform, and at high cost, which makes it challenging to optimise the CSAM process. With recent advances in computational resources and methods, finite elements (FE) methods are now widely used to predict residual stresses within a shorter period, making it easier to optimise the deposition process. The common FE methods employed in the numerical modelling of residual stresses in CSAM are the numerical methods discussed in section 2.6.1: coupled temperature-displacement Lagrangian-based FEM methods, Eulerian, and CEL methods. A recent review by Fardan et al. [159] provided information on the numerical modelling of residual stress in CSAM. Both single-[221] and multi-particle impacts have been employed to predict the evolution of residual stress in CSAM deposits [207,222].

Ghelichi et al. [207] studied the annealing effect of process temperature on the residual stress relaxation of Al alloys. Numerical simulations of the CSAM process were performed, and the results were verified using XRD in-depth stress

measurements. In their study, multi-particle impact analysis (explicit dynamic analysis) was performed to predict and evaluate the residual stress formation in the CSAM process. In another study, Lin et al. [223] performed a multi-particle impact analysis to investigate the influence of interface bonding of sprayed particles on the residual stress of CSAM Al6061. Moreover, Saleh et al. [224] and Wang et al. [217] also employed multi-particle impact analysis to predict and understand the formation of residual stress during CSAM. Although explicit dynamic analysis of particle depositions is more effective for modelling peening stresses in CSAM because of the nonlinearity associated with the impacts, the residual stresses predicted using explicit multi-particle dynamic impacts can be highly oscillating, reaching the local yield point of the material owing to complex interactions of temperature and time-dependent localised plasticity between and within splats [207,222,224]. Moreover, convective and radiative heat transfer sources that can be present during CSAM were not included in those explicit dynamic models, which can result in poor quantitative agreement between the experimental and numerical results.

Recently, modified FE schemes, such as the explicit-implicit and or element birth-death techniques, have been used to model residual stress development in CSAM deposits. For instance, Bansal et al. [225,226] and Oviedo et al. [227] employed the explicit-implicit FE technique to model residual stress formation in high-velocity impact depositions. The explicit scheme was used to model particle impact, that is, peening stress, whereas the layer-by-layer addition of the deposit was modelled using the implicit scheme. In their study, the explicit scheme employs single-particle impacts; however, it omits the contributions of multi-particle impacts of random

distributions of particle diameters. The implicit scheme, on the other hand, employs the element birth-death technique, where elements in the layers of material are activated and deactivated based on the deposition time, nozzle location, nozzle transverse speed, and deposit thickness. This scheme allows the capture and inclusion of the heat source from the nozzle [228–230] into the FEM. In addition, the heat loss by convection and radiation can be inputted in the FEM.

Using these modified FE schemes, Arabgol et al. [231] analysed the thermal history and residual stress in CSAM Cu deposits on Cu and steel substrates. The measured thermal history of the materials during spraying is shown in Figure 2.37. They reported that the heat input and associated thermal history play a significant role in the final residual stress in the deposits, which can change the in-plane stress from compressive to tensile. Similar investigations have been performed by several other researchers using these modified FE implicit schemes [232–235]. However, the FE method in most of these studies did not include the deposition peening stress, which can be obtained using explicit dynamic particle impacts. Therefore, a better result can be obtained using the multi-particle explicit scheme, with random distributions of particles representing the spraying process, to model the peening stress. This peening stress can then be employed as the initial stress in the element birth-death technique for the thermo-mechanical analysis of residual stress in CSAM deposits. This FE technique has not been employed for CSAM residual stress predictions in the open literature. Furthermore, the deposit element can be activated block-by-block [232] instead of layer-by-layer in the implicit scheme, to correctly track the evolution of stresses as the deposit layers are formed.

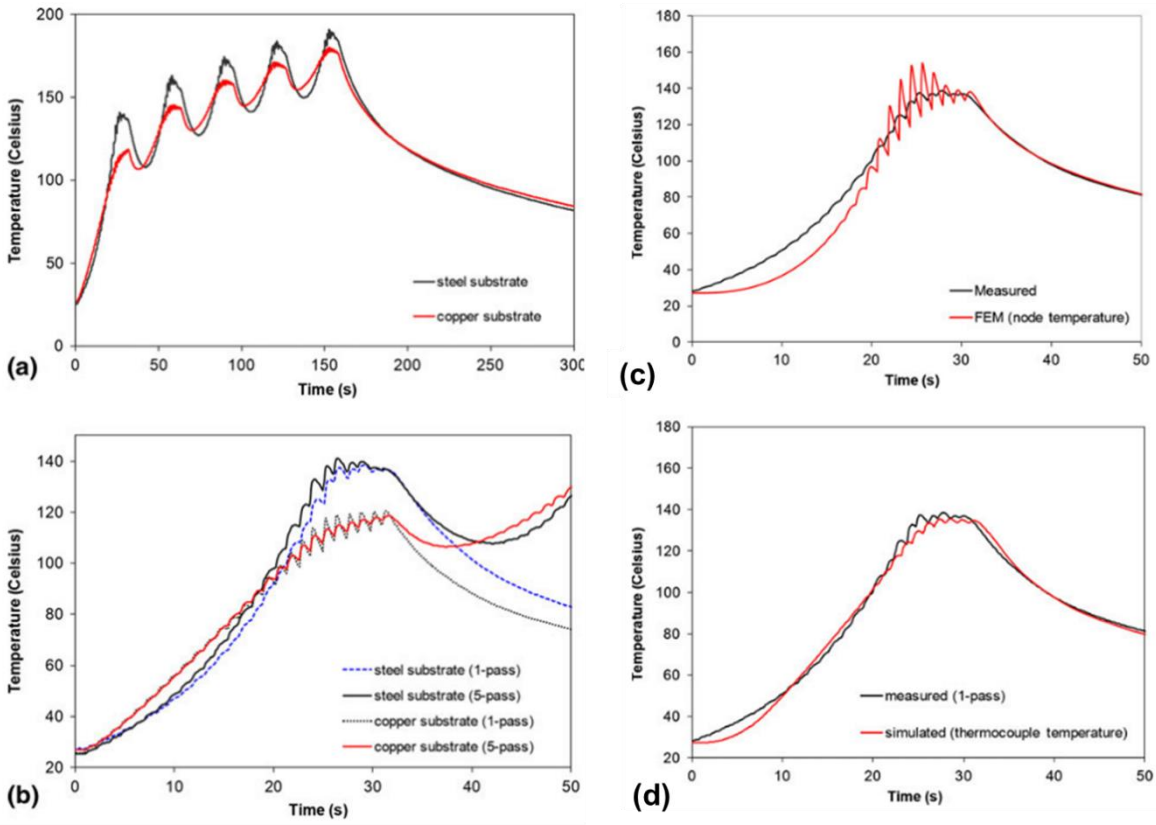

Figure 2.37: Measured and FE temperature history during cold spraying of Cu, Cu, and steel. For the measured thermal histories, (a) shows an overview of the deposition of five layers and (b) a close-up view of the first-layer deposition. (c) and (d) shows a comparison of the measured and FEA thermal histories of steel substrates before and after CSAM [231].

2.8 CoCrFeNiMn high entropy alloy

2.8.1 Introduction to high entropy alloy

In the conventional strategy of developing alloy materials, testing begins with a single element, and thereafter, certain proportions of alloying elements are gradually added or removed until the desired properties for certain uses are found. This implies that the final alloy material is composed of one or two principal elements, with numerous other elements in minute quantities. For example, steel is principally based on Fe, and Mg alloys are based on Mg. In 2004, Yeh et al. [35] and Cantor et al. [36] independently published articles on high entropy alloys (HEAs), which are composed of multiple principal elements in equiatomic or near-equiatomic proportions. These materials are known to form single-phase crystalline structures; for example, CoCrFeNiMn, commonly known as the Cantor alloy [36].

The widely accepted definition of a HEA is an alloy of at least five metallic elements (i.e., N ≥ 5), each with a concentration ranging from 5-35 at.% [236]. The hypothesis behind this definition is that the presence of multiple elements near equiatomic proportions would increase the configurational entropy of mixing **(**$\Delta \boldsymbol{S_{mix}}$) to enough able to overcome the enthalpy of mixing ($\Delta \boldsymbol{H_{mix}}$), thereby hindering the formation of brittle intermetallics [35]. Based on phase diagrams, it is generally believed that there is a higher probability that intermetallics will form when elements react near the centre of the phase diagram as opposed to the corners where solid solutions can be easily formed. However, Yeh et al. [35] reasoned that as the element in alloy increases, the contribution of $\Delta \boldsymbol{S_{mix}}$ in the total free energy (***G***) would overcome that

of $\Delta \boldsymbol{H_{mix}}$, as provided in Equation (2.25), and hence stabilises the formation of solid solutions.

$$\boldsymbol{G} = \Delta \boldsymbol{H_{mix}} - \boldsymbol{T}\Delta \boldsymbol{S_{mix}} \quad (2.25)$$

The entropy of ideal solid solutions can be estimated with the Boltzmann equation, which requires atoms to occupy random lattice positions. The value of the estimated entropy provides the basis for distinguishing low ($\Delta \boldsymbol{S_{mix}}$< 0.69R); where $\boldsymbol{R}$ is the ideal gas constant, medium (0.69R <$\Delta \boldsymbol{S_{mix}}$< 1.61R), and HEAs ($\Delta \boldsymbol{S_{mix}}$< 1.61R) [237]. This is illustrated in Figure 2.38.

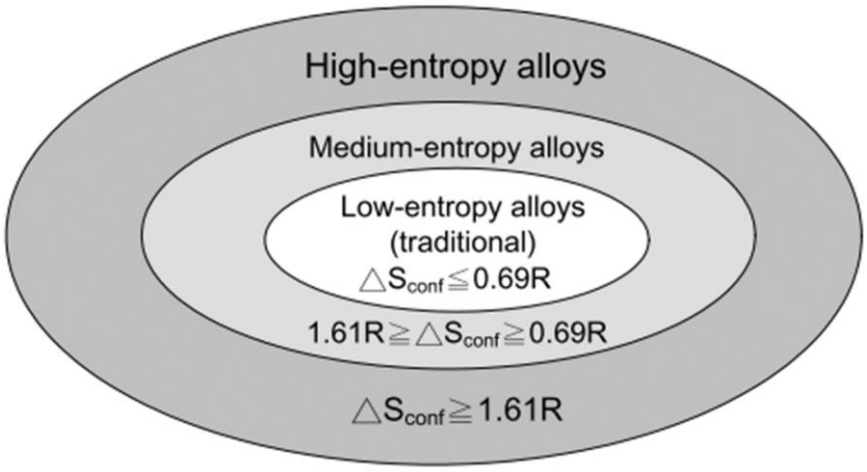

Figure 2.38: Random solid-solution alloys divided by their entropy of mixing [238].

Equation (2.26) shows the relationship between $\Delta \boldsymbol{S_{mix}}$, $\boldsymbol{R}$, and the mole fraction $\boldsymbol{x_i}$ of the element $\boldsymbol{i^{th}}$. The $\Delta \boldsymbol{S_{mix}}$ in Equation (2.26) has four contributions: configurational, thermal (or vibration), magnetic dipole and electronic randomness; however, $\Delta \boldsymbol{S_{mix}}$ is approximately the configurational contribution being the more dominant among the contributions, and that simplifies the calculations. Increasing

the number of elements in Equation (2.26) would increase the ΔS_{mix} and it is maximised when the molar fraction x_i of each constituent element are equal [35]. From Figure 2.39, a maximum of 13 elements is suggested as the upper limit for the HEAs composition. This is because increasing the number of elements from 13 to 14 produces a negligible increase (2.7%) in the ΔS_{mix} [238]. Thus, increasing the number of elements is likely to increase the complexity and cost of the HEA system, and this becomes less beneficial.

$$\Delta S_{mix} = -R\sum_{i=1}^{N} x_i(lnx_i) = RlnN \tag{2.26}$$

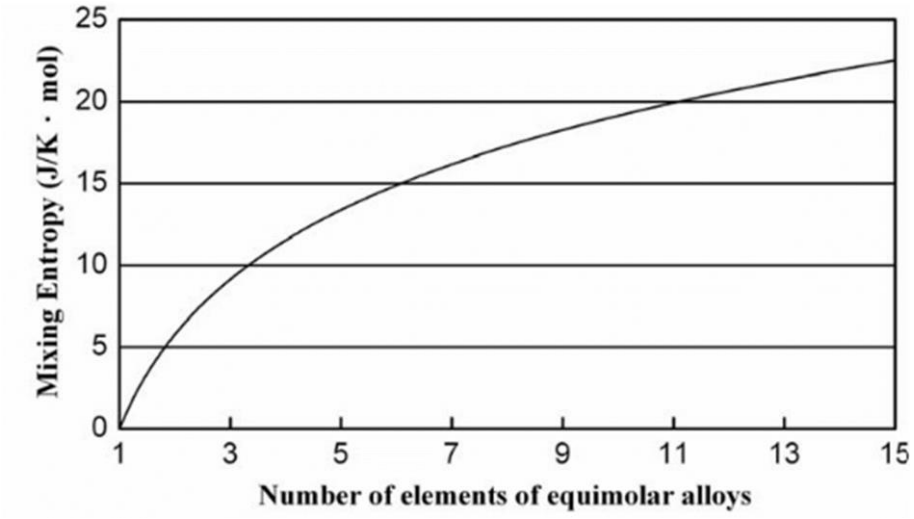

Figure 2.39: Number of elements as the entropy of mixing increases in solid solution equimolar alloys [238].

As HEAs are composed of multi-principal elements that form solid solutions with simple crystalline structures, their properties have been reported to surpass those of conventional alloys. This makes HEAs attractive in many fields, both in academia and industry, owing to their promising structural applications and functional properties compared to common structural materials, as shown in the Ashby plot in

Figure 2.40. Notwithstanding these advantages, most HEAs cover a limited range of material systems, typically on transition metals such as Cr, Co, Fe, Ni, Mn, and Cu, or on refractory metals such as V, Ta, Ti, Mo, Cr, Nb, W, Zr, and Hf [237].

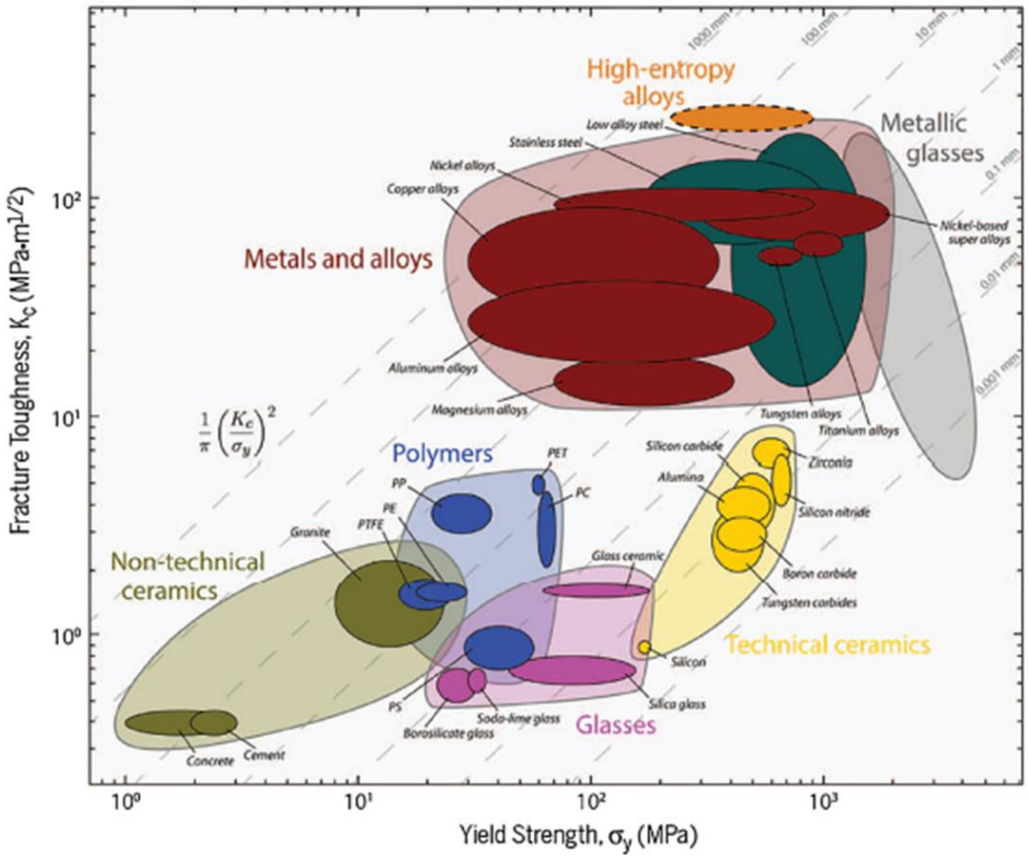

Figure 2.40: Ashby plot of fracture toughness versus yield strength of common structural materials. HEAs exhibit an outstanding combination of damage-tolerant mechanical properties compared with other materials [41].

These HEAs do not always form simple crystal structures (FCC and BCC), but also complex phases (e.g. laves) and intermetallics. For instance, equiatomic CoCrFeNiMn, first studied by Cantor et al. [36] upheld as a stable solid solution phase, has been shown to decompose into a multiphase component when exposed to temperatures below 800 °C [239,240]. This suggests that the formation of solid

solutions with simple crystal structures and other phases in HEAs is largely dependent on the competition between $\Delta \boldsymbol{S_{mix}}$ and $\Delta \boldsymbol{H_{mix}}$.

2.8.2 The core effects

Many factors have been reported to contribute to the formation of solid solutions in HEAs, but only four have been widely accepted as the main ones: (1) high entropy, (2) lattice distortion, (3) sluggish diffusion and (4) “cocktail” effects. Collectively, these four factors were grouped as core effects.

The core effects of HEAs have been thoroughly discussed in several studies [238,241–244]. A brief discussion is provided in this section.

- For the high entropy effect, the high configurational entropy of HEA interferes with the formation of complex phases. The high entropy in solid solution HEAs has a dominant effect on the phase Gibbs energy, which can result in the stability of solid solutions relative to intermetallic phases.

- Because of the atomic size mismatch of the different alloying elements in HEAs, their lattices are severely strained, as illustrated in Figure 2.41. This can affect the physical and mechanical properties of HEAs.

- Sluggish diffusion kinetics are generally observed in HEAs, which in turn can slow the phase transformation. This is because atomic diffusion is more difficult through solid solutions with many elements having high

concentrations, mainly because of variations in the bonding environment through their lattices.

- The so-called “cocktail effect” results from the complexity of HEAs compositions, in which interactions between elements give rise to unusual behaviours, as well as average composite properties (rule of mixtures) [242].

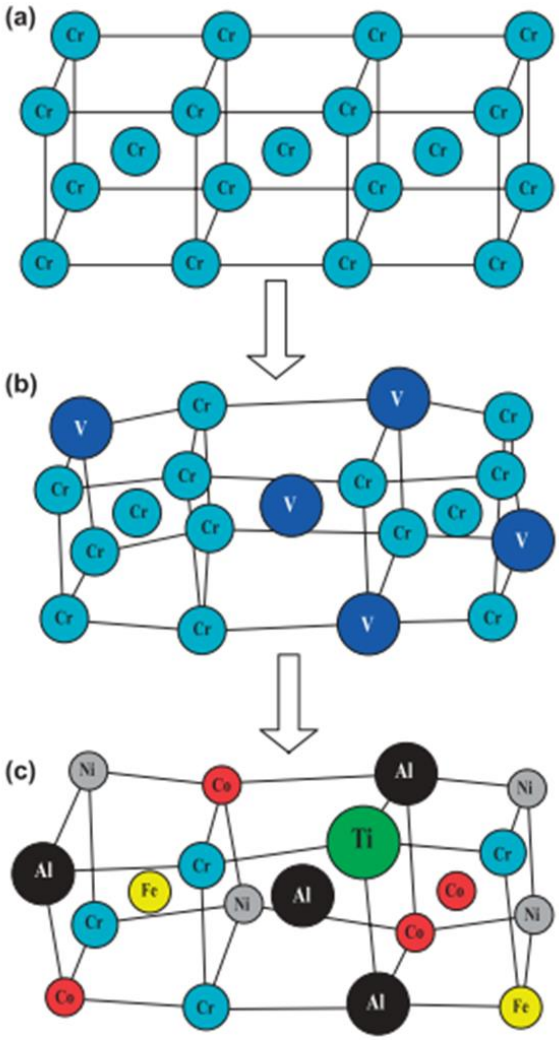

Figure 2.41: Schematic illustration of lattice distortion in a bcc crystal structure, as atoms of different sizes are randomly distributed in the crystal lattice [245].

2.8.3 CoCrFeNiMn HEA

The CoCrFeNiMn HEA, known as the Cantor alloy, is the most studied HEA owing to its single-phase, simple crystal structure, and exceptional mechanical properties. The HEA exhibit excellent strain hardening capability and ductility at room and cryogenic temperatures [42], and excellent fracture toughness at cryogenic temperatures [41], making them a promising structural material for space applications and other cryogenic or room temperature applications. However, many efforts are being made to improve the mechanical properties of HEA for practical applications, as the HEA show a relatively low yield strength (YS ~ 300 MPa) and ultimate tensile strength (UTS ~ 500 MPa) at room temperature [246].

Several essential parameters were employed to predict the solid solutions and other phases of the HEA. These parameters include the atomic size mismatch ($\boldsymbol{\delta}$), $\Delta \boldsymbol{S_{mix}}$, $\Delta \boldsymbol{H_{mix}}$, electronegativity ($\Delta \boldsymbol{\chi}$) and valence electron concentration (VEC). These parameters are defined by Equations (2.27)-(2.30) [245,247,248]. Where $\Delta \boldsymbol{\chi_i}$ = Pauling electronegativity's for each element, $\boldsymbol{r_i}$, $\boldsymbol{r_j}$ = atomic radii of ith and jth element, $\boldsymbol{4\Delta H_{AB}^{mix}}$ is related to the $\Delta \boldsymbol{H_{mix}}$ of pairs of elements A and B. The calculations performed for the CoCrFeNiMn HEA revealed values provided in Table 2.1. The calculated $\Delta \boldsymbol{\chi_i}$ = 13.84% predicted the formation of the sigma phase in the HEAs [249], which were confirmed experimentally by several other studies after annealing at <800 ºC [239,240].

$$\boldsymbol{\delta} = \sqrt{\sum_{i=1}^{N} \boldsymbol{x_i}\left(\mathbf{1} - \frac{\boldsymbol{r_i}}{\sum_{j=1}^{N} \boldsymbol{x_i r_j}}\right)^2} \tag{2.27}$$

$$\Delta\boldsymbol{\chi} = \sqrt{\sum_{i=1}^{N} \boldsymbol{x_i}\left(\boldsymbol{\chi_i} - \sum_{j=1}^{N} \boldsymbol{x_j \chi_j}\right)^2} \tag{2.28}$$

$$\Delta\boldsymbol{H_{mix}} = \sum_{i=1, j>1}^{N} \mathbf{4}\boldsymbol{\Delta H_{AB}^{mix} x_i x_j} \tag{2.29}$$

$$\boldsymbol{VEC} = \sum_{i=1}^{N} \boldsymbol{x_i}(\boldsymbol{VEC_i}) \tag{2.30}$$

Table 2.1: Calculated values of prediction parameters for CoCrFeNiMn HEA [245,248,249].

Parameters	Values
$\Delta\boldsymbol{H_{mix}}$	-3.36 kJ/mol
$\Delta\boldsymbol{S_{mix}}$	13.38 J/K/mol
$\boldsymbol{\delta}$	≤ 4.3 or 3.27 %
VEC	≥ 8

Phase diagrams can also be used to design and predict the HEA phases. Phase diagrams are guidelines or roadmaps that provide key information on a given alloy composition and temperature. This includes the phases present and their compositions, volume fractions, and transformation temperatures. CALPHAD (CALculated PHAse diagram) has been employed as a modelling technique integrated with essential experiments to effectively determine HEA phase diagrams [250–252]. In this approach, thermodynamic functions which empirically fit the experimental data from binary and ternary phase diagrams were developed and subsequently combined and extrapolated to multicomponent alloys [253].

2.8.4 Plastic deformation of CoCrFeNiMn HEA

Four fundamental methods can be employed to improve the plastic deformation resistance of a metal: (1) solid solution strengthening associated with atomic-size mismatch and local chemical bonding between constituent elements, (2) strain hardening, (3) grain refinement induced by severe plastic deformation, and (4) precipitation hardening by ageing or appropriate thermomechanical processes. Thermomechanical processing of the CoCrFeNiMn HEA has been performed by several researchers to overcome the strength-ductility trade-off associated with the HEA [246]. This process involves imposing plastic deformation and subsequent ageing to relieve the stress and improve the ductility of the deposit. Techniques such as high-pressure torsion and equal-channel angular pressing are often used to induce severe plastic deformation in HEA [246,254,255]. However, the ductility of these deposits is limited. In addition, laser- and electron-based AM techniques have been employed to manufacture parts made with HEA [79,256–258]; however,

non-equilibrium solidification structures and elemental segregation resulting from the high thermal input and rapid cooling are often observed in the microstructure. Nonetheless, observations of the microstructure of HEA processed with these techniques revealed intensive deformation twinning and significant grain refinement as the two main microstructural features. Thus, these microstructures affected the mechanical properties of the deposits. A typical microstructure obtained using high-pressure torsion is shown in Figure 2.42. Table 2.2 provides a summary of the mechanical properties of HEA manufactured using various techniques.

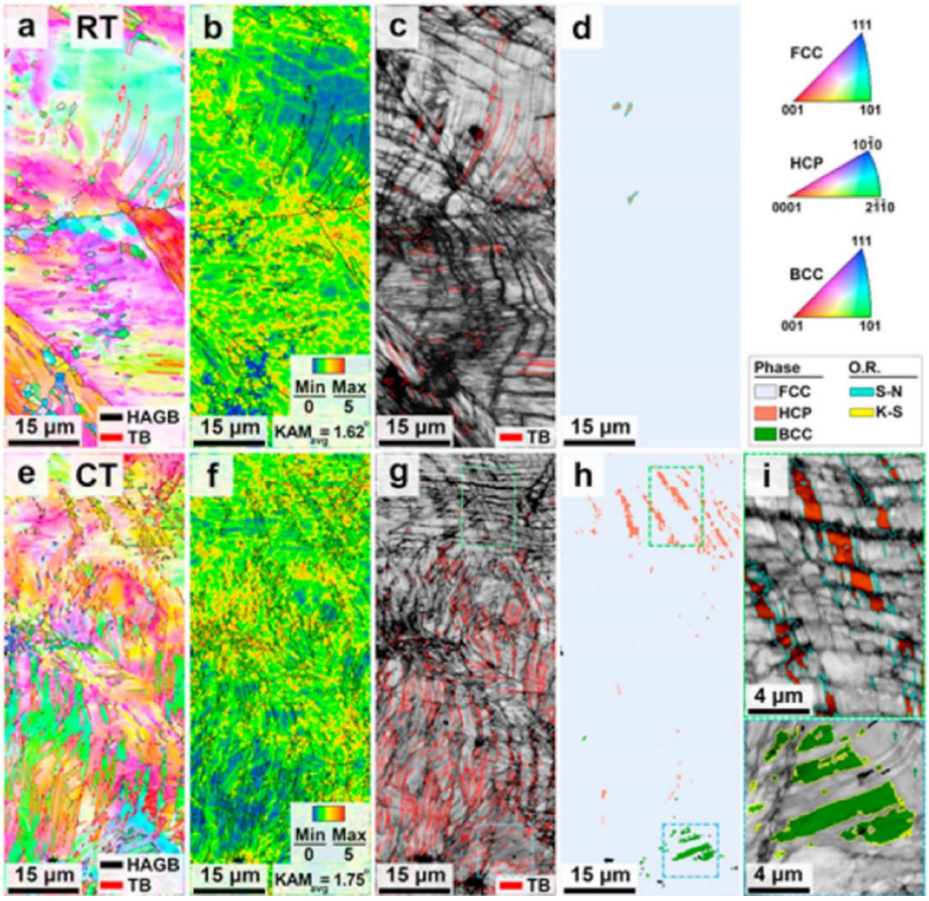

Figure 2.42: EBSD inverse pole figure (IPF) map (a,e), kernel average misorientation (KAM) map (b,f), image quality (IQ) (c,g), and phase distribution (d,h, i) maps of the high-pressure torsion processed CoCrFeNiMn HEA at room temperature (a-d) and cryogenic temperature (e-i). High-angle grain and twin boundaries are shown in the maps [259].

Table 2.2: Summary of the mechanical properties of the CoCrFeNiMn HEA manufactured using various techniques. Where HV is Vickers hardness.

Paper	Processing	Grain size	HV	YS (MPa)	UTS (MPa)	Elongation (%)
Shahmir et al. [254]	As-cast homogenised	-	~135	240	500	90
Shahmir et al. [254]	High-pressure torsion (strain > 40)	<50 nm	~455	1400	1740	4
Li et al. [260]	Cold-rolled (>90 %)	130 nm	-	1199	1335	5
Shahmir et al.[255]	Equal-angular channel pressing: after the 4th pass	100 nm	~315	980	990	35
Otto et al.[44]	Cold-rolled (96 %)	4.3 µm	418	-	-	-
Schuh et al. [240]	High-pressure torsion (strain >50)	~50 nm	520	~1750	~2000	<2
Dovgyy et al. [256]	Powder bed fusion	0.3-1 µm	~215	~530	~783	~23
Tong et al. [79]	Powder bed fusion	~2 µm	~200	346	566	~30

2.8.5 Phase decomposition of the CoCrFeNiMn HEA

Annealing treatment is usually applied after severe plastic deformation to improve the ductility of the CoCrFeNiMn HEA; however, annealing of the HEA at intermediate temperatures has been reported to result in significant phase decomposition, which reduces the ductility. Although the HEA was upheld as stable, several studies have revealed the decomposition and formation of precipitates of the HEA when exposed to temperatures below 800 °C. For example, Otto et al. [239] studied the decomposition behaviour of the HEA under prolonged annealing (500 days) at intermediate temperatures of 500 and 700 °C. As shown in Figure 2.43, Cr-rich bcc and sigma (σ), FeCo (B2), and NiMn (L10) phases with complex morphologies were distributed at the grain boundaries of the homogenised coarse-grained HEA. These phases were dissolved at 700 °C. Pickering et al. [261] also reported Cr-rich precipitates in coarse-grained HEA following prolonged annealing at 700 °C.

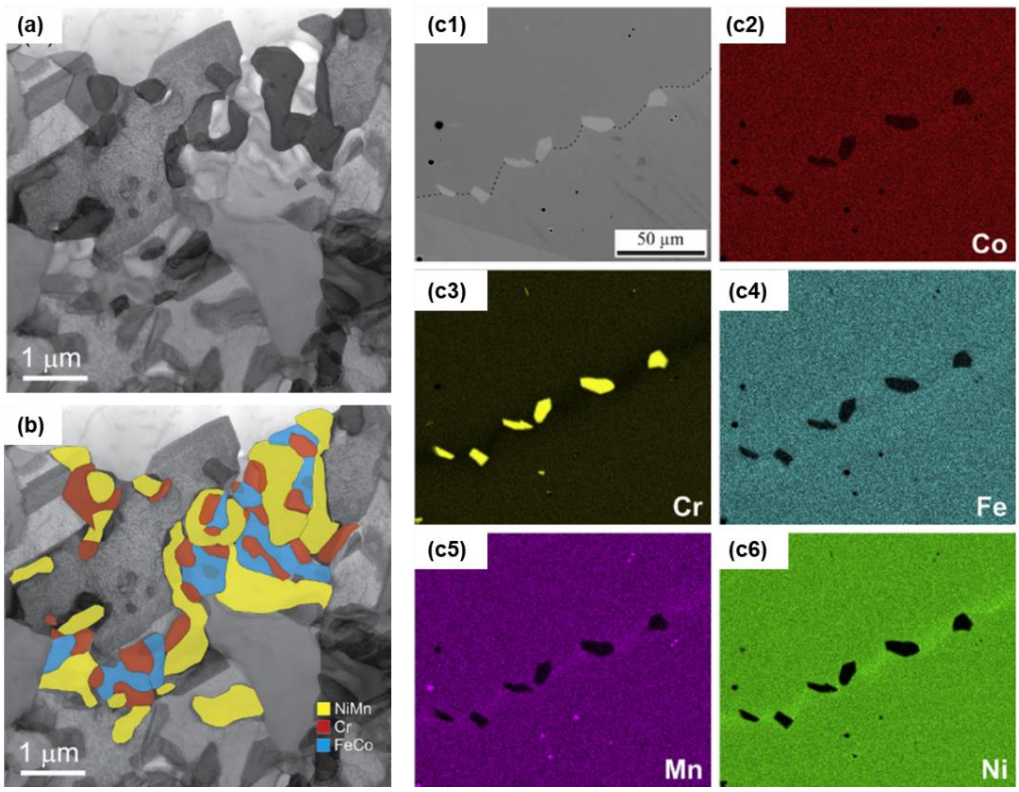

Figure 2.43: STEM and EDX analyses of an FIB lamella extracted from the CoCrFeNiMn HEA after annealing at 500 °C for 500 days. (a) TEM contrast image reveals the presence of several precipitates at the grain boundaries of the HEA matrix. (b) EDX maps superimposed on the image in (a) show the distinct compositions of the phases. (c) Microstructure of the HEA after 500-day anneal at 700 °C showing enrichment of Cr-rich precipitates, depletion of other elements, and slight enrichment of Ni and Mn along the grain boundary [239].

While these phases were observed in the coarse-grained HEA under prolonged annealing, they were also observed in the severely deformed HEA after short-term annealing. For example, Schuh et al. [240] subjected a homogenised coarse-grained CoCrFeNiMn HEA to severe plastic deformation using high-pressure torsion. After the severe plastic deformation, the HEA remained a single-phase solid solution; however, after annealing the deformed sample for a short time of 5 min, NiMn and Cr-rich phases were observed. With increasing the annealing time, the volume fraction of the phases increased, and a FeCo phase was formed. The phase

decomposition of the severely deformed HEA occurred relatively quickly, which was attributed to the nanocrystalline grain size of the severely deformed HEA.

The large number of grain boundaries and defect density appear to facilitate the phase transformations in the severely deformed HEA, as the grain boundaries and dislocations serve as fast diffusion pathways and preferential nucleation sites for the formation of the precipitates [240,261,262]. Tensile and microhardness tests revealed excellent strength levels but low ductility. In contrast, Bae et al. [263] reported a strength-ductility combination of the HEA after severe plastic deformation by cold rolling and subsequent annealing at 650 °C for 1 hr. The strengthening effect of partial recrystallisation, with a remaining small volume fraction of the Cr-rich phase, led to improved strength at minimised ductility loss. Similarly, Gu et al. [264] reported the heterogeneous structure of cold-rolled CoCrFeNiMn HEA samples subjected to annealing treatment between 550-700 ºC. Partial recrystallisation occurred together with the formation of Cr-rich σ and bcc phases, which improved the strength-ductility combination of the HEA. These studies show that partial recrystallisation at intermediate temperatures of the HEA after SPD can be utilised to improve the mechanical properties of the HEA components; however, there are very limited detailed investigations on the influence of annealing treatment on the microstructure of the HEA after CSAM and the resulting mechanical properties.

2.9 CSAM of CoCrFeNiMn HEA

In this section, the impact phenomena, deposition mechanism, microstructure, and properties of the CoCrFeNiMn HEA deposits manufactured using CSAM are reported. Despite many published articles on the processing of HEA using several techniques, published articles on the CSAM of HEA remain limited.

2.9.1 Deposition mechanism and deposit microstructure

Shuo et al. [40] deposited the CoCrFeNiMn HEA on Al6082 substrate using He as a carrier gas at a pressure of 3 MPa, and preheating temperature of 300 ºC. SEM and EBSD were used to characterise the microstructure and observe the deformation behaviour of the HEA particles on the substrate. Figure 2.44a and b show a single-particle impact, while Figure 2.44c presents the dense structure of the cold-sprayed HEA deposit. Mechanical interlocking phenomena were observed for the single-particle impact, which was also observed in the deposit-substrate interface. This impact was due to the SPD of the soft Al alloy substrate upon impact with the hard HEA particles. EBSD characterisation of the cold-sprayed HEA was performed to reveal its grain structure, as shown in Figure 2.44d and e. Characterisation revealed that the grains in the HEA deposit experienced significant refinement compared to those in the as-received powder. This was due to dynamic recrystallisation (DRX) in the severely deformed interfacial regions of the HEA particles. The increased dislocation density and grain boundaries in the CSAM deposit contributed to the higher microhardness measured compared to the as-received powder.

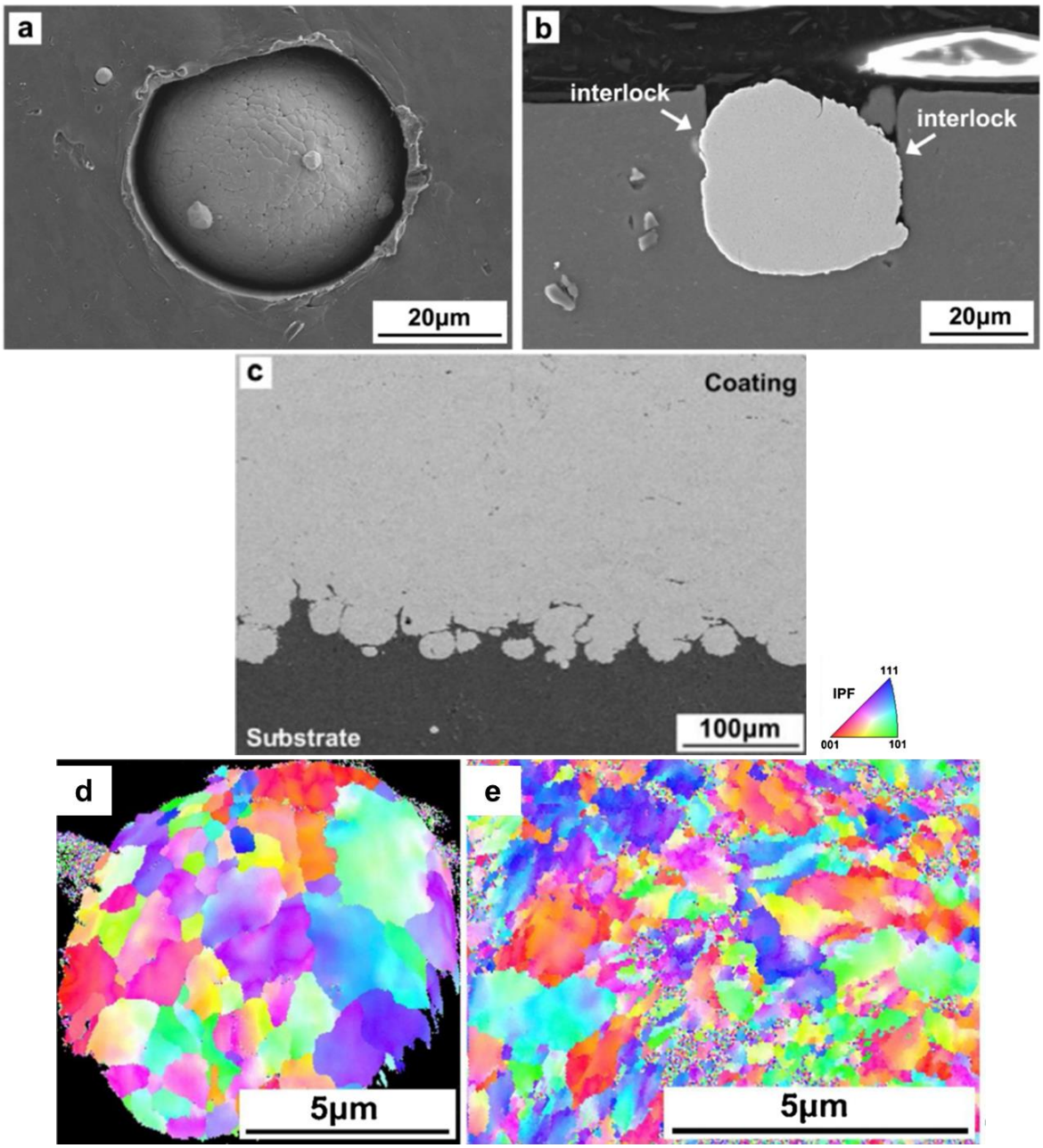

Figure 2.44: CSAM CoCrFeNiMn HEA deposit: (a) top surface micrograph, (b) cross-sectional view of a hard HEA particle embedded into a soft Al alloy substrate, and (c) cross-sectional image of the deposit microstructure. The EBSD inverse pole figure (IPF) maps of (e) a single HEA particle impact and (d) CSAM HEA deposit [40].

Severe plastic deformation of materials during CSAM deposition can significantly affect the grain structure of the deposits. Feng et al. [129], through EBSD, reported heterogeneous grain structure in the CoCrFeNiMn HEA deposit attributed to the ASI and DRX localised in the interfacial regions of the deposited particles. Elongated

grains were observed in the particle interiors, and ultrafine grains were observed in the particle-particle interfacial regions. Nanohardness was reported to be non-uniform in the deposit, which was attributed to the grain structure of the deposit, and greater values were measured in the interfacial regions. This was correlated with ultrafine grains through the Hall-Petch strengthening effect. However, these studies did not reveal the type of deformation mechanisms that occur in the HEA during CSAM, such as CDRX.

The solid-state nature of the CSAM process prevents the formation of defects associated with elevated temperatures, as is typical with other AM processes. The CSAM process not only retains the initial feedstock elemental compositions and structures of the HEA but also increases the hardness of the deposit through the induced severe plastic deformation. The high strain hardening and resistance to strain localisation of the CoCrFeNiMn HEA, however, limited the extensive particle deformation and hence inter-particle boundaries and porosity in the deposit. These microstructural defects reduce the oxidation resistance of the HEA compared to its bulk counterparts [39,265]. Hence, optimisation of the CSAM process for the deposition of HEA is important for achieving a desirable deposit quality. In that case, the work by Nikbakht et al. [63] on the bonding characteristics of HEA on various substrates provides information on the impact phenomena of the alloy during CSAM deposition. The study revealed the severe plastic deformation of the grains in the lower half of the deposited particles, as shown in Figure 2.45, leading to ultrafine grains in those regions and pancake (elongated) grains in the particle interior. In their work, single-particle deposition of the HEA on various substrates (Ni, In625, and stainless steel 304) showed an impact morphology that is strain-rate- and

microstructure-dependent. Larger particles deformed more intensely with the metal jets, whereas smaller particles penetrated the substrates more with limited deformation, as shown in Figure 2.46. Deformation-induced nano twins and FCC to HCP phase transformation features were also observed in the deposited HEA particles [63,75], which were attributed to the strain hardening rate of the HEA. The high critical shear strain of HEA can impede bonding, which requires a high critical velocity. However, numerical modelling, which can reveal the onset of ASI and hence the critical velocity of the HEA, has not been investigated.

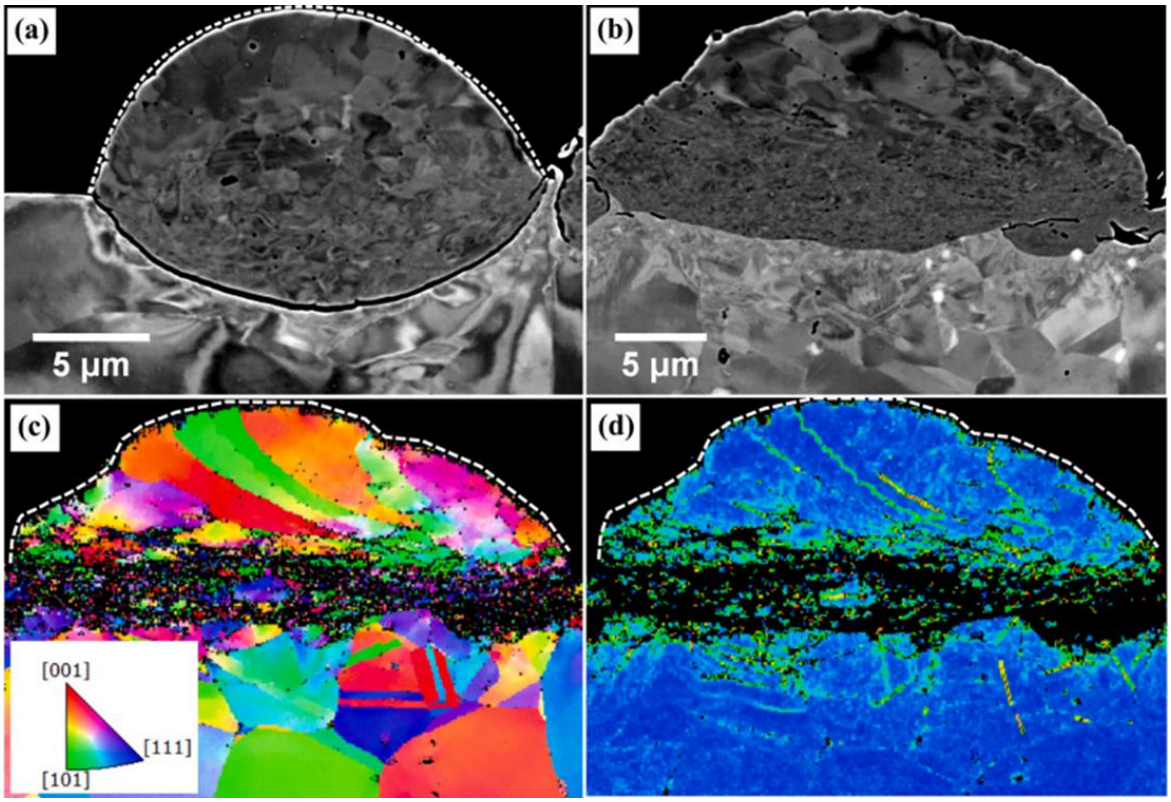

Figure 2.45: The powder particle microstructure affects the impact morphology of CoCrFeNiMn HEA particles upon impact on Ni substrates (a) and (b) and In625 substrates (c) and (d). The figure shows the electron channelling contrast imaging (ECCI) and EBSD maps [63].

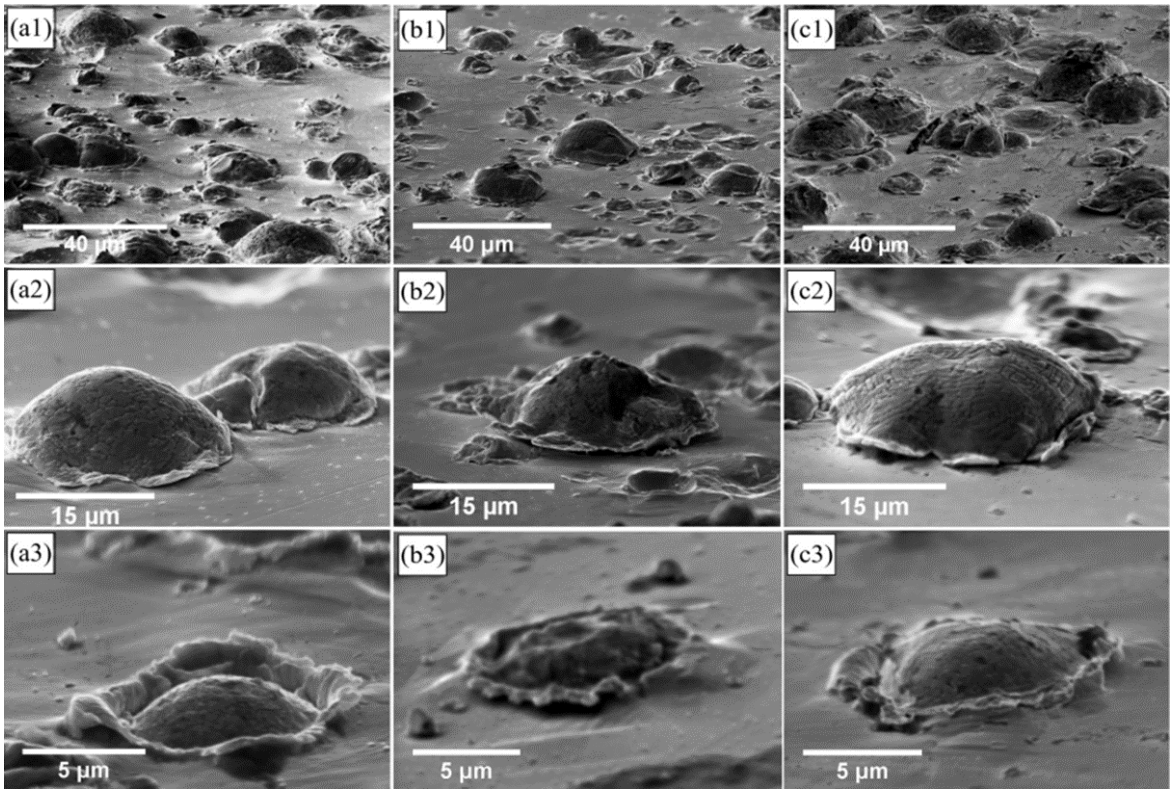

Figure 2.46: Deformation morphology of single-particle impacts of CoCrFeNiMn HEA on different substrates: (a1-a3) Ni, (b1-b3) stainless steel 304, and (c1-c3) In625. Smaller particles (a3-c3) were observed to penetrate the substrates more than larger particles [63].

In another study, Yu et al. [266] investigated the microstructure and composition evolution of CoCrFeNiMn HEA during extreme deformation at a strain rate of 10^8-10^9 /s induced by the CSAM process. The deformation mechanism of the HEA during deposition, as explained by the authors, is shown in Figure 2.47. The interfacial regions experienced large strain and high strain rate deformations and thus exhibited ultrafine nanograins with an average grain size smaller than 100 nm. This was attributed to the ASI and DRX. Interestingly, the authors reported a rapid redistribution of segregated Mn and Ni in extremely deformed regions. This phenomenon occurred because of the increased grain boundary area and dislocation density caused by the severe plastic deformation. It is noteworthy that the micro-segregation of Mn and Ni in the as-received powder results from the rapid

solidification process of the gas-atomisation technique, which is the preferred process for HEA powder manufacturing for AM. Moreover, the microsegregation of these elements during the solidification of the as-cast HEA was reported by Laurent-Brocq et al. [215][267].

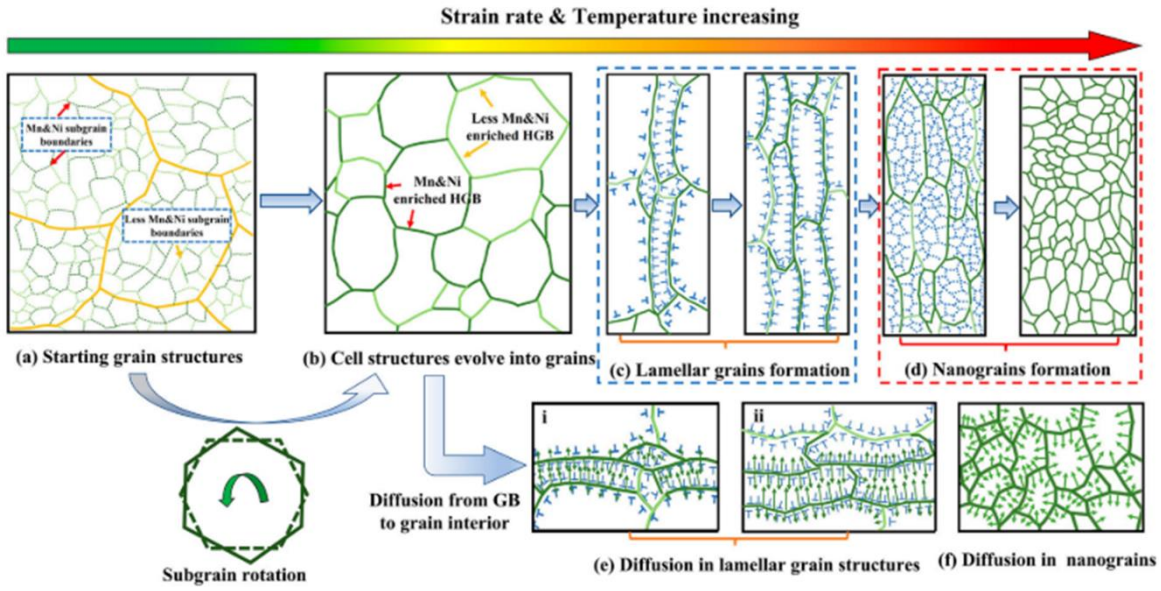

Figure 2.47: Schematic illustration of the deformation mechanism and redistribution process of Ni and Mn during CSAM. (a) Ni and Mn segregated in interdendritic regions in the as-received powder; (b) as particles deformed, LAGBs became HAGBs, (c) lamellar grains subsequently formed, and (d) equiaxed nanograins were formed under extreme deformation. Meanwhile, Ni and Mn diffused along the grain boundaries which then uniformly diffused into nanograins (e) and (f).

2.9.2 Deposit properties

The severe plastic deformation of the CoCrFeNiMn HEA induced by the CSAM process increased the hardness of the deposit by three orders of magnitude. However, this property is also influenced by porosity and interparticle boundaries in the deposit. The extent of these deposit microstructure defects was determined by the extent of splat deformation. A dense microstructure requires optimised spraying parameters to induce extensive splat deformation, leading to the desired deposit

quality. Table 2.3 summarises the data collected on the properties of the CSAM HEA deposits under different spraying conditions. The porosity of the HEA deposits ranges between 0.3-3.0%, and the microhardness is between 350-450 HV; depending on the load applied and the degree of porosity and interparticle boundaries. There is very limited work that reports other properties of the CSAM HEA deposit, such as tensile properties.

Table 2.3: Properties of CSAM CoCrFeNiMn HEA deposit.

Paper	Type of gas	Gas pressure and temperature	Porosity (%)	Microhardness (HV)		Thickness (mm)
				As-received powder	Deposit	
Yin et al. [40]	He	3.0 MPa and 300 ºC	~0.5±0.2	~124±39 (HV0.1)	~333±35 (HV0.1)	1.5
Ahn et al. [268]	He	3.0 MPa and 300 ºC (powder was also preheated to 600 ºC)	~0.32	-	~433 (HV0.5)	1.0
Nikbakht et al. [63,75]	He N_2	3.2 MPa and 400 ºC 4.9 MPa and 950 ºC	-	176 (HV0.025)	361±50 (HV0.1); 478±38 (HV0.01)	~0.25
Silvello et al. [128]	N_2	7.0 MPa and 1100 ºC	<1.0	~136	386±6 (HV0.1)	~0.6
Feng et al.[129]	He	3.0 MPa and 700 ºC	~0.7	-	-	-
Mahaffey et al. [269]	N_2	5.0 MPa and 900 ºC	~3.0	~163±19 (HV0.025)	~351±32 (HV0.3)	3.1

2.9.3 Post-deposition annealing treatment

Post-deposition heat treatment or annealing is usually employed to improve the microstructure of CSAM deposits and hence, enhance their mechanical properties. Annealing of various materials such as Cu, stainless steels, and Ni-based alloys has resulted in improved mechanical properties such as ductility. However, few studies have reported the use of post-deposition annealing treatment to reduce the porosity and internal defects in CSAM CoCrFeNiMn HEA deposits [129,265,268,270]. Ahn et al. [268] performed CSAM deposition of the HEA and heat treatments to control the microstructure and nanoindentation properties of the deposit. A heterogeneous microstructure was formed in the as-sprayed deposit with ultrafine grains at the particle interfaces, whereas coarse grains were formed in the particle interiors. In addition, deformation-induced nano twins were observed inside the deformed particles. After heat treatment at 550 °C for 2 hrs, fine Cr-rich precipitates formed at the grain and particle boundaries. Increasing the annealing temperature to 850 °C increased the size and volume fraction of the precipitate. At this annealing temperature, the deposit was fully recrystallised. The microhardness of the as-sprayed deposit was higher than that of the annealed sample as expected. This was attributed to the recovered and recrystallised grains in the annealed deposit.

In another study, Feng et al. [129] investigated the as-sprayed HEA deposit after subsequent annealing treatments at 650 and 1150 °C. Ultrafine and coarse grains were also observed in the as-sprayed deposit, leading to a heterogeneous microstructure. After annealing at 650 °C, the localised strain was relieved, and

ultrafine grains nucleated at the grain boundaries owing to static recovery and recrystallisation. After annealing at 1150 °C, large, dislocation-free equiaxed grains with annealing twins were formed. The microstructural evolution of this study is shown in Figure 2.48. However, this study did not reveal any precipitates formed during the annealing treatment at intermediate temperatures. There is thus a limited study on the effect of annealing treatment and formation of precipitates on the microstructure of CSAM-deposited CoCrFeNiMn HEA deposits. Furthermore, there are very limited reports on the tensile properties of the HEA [88,270]. Moreover, there exists a gap in knowledge on the effect of the annealing treatment of the deposit on the tensile properties of the HEA.

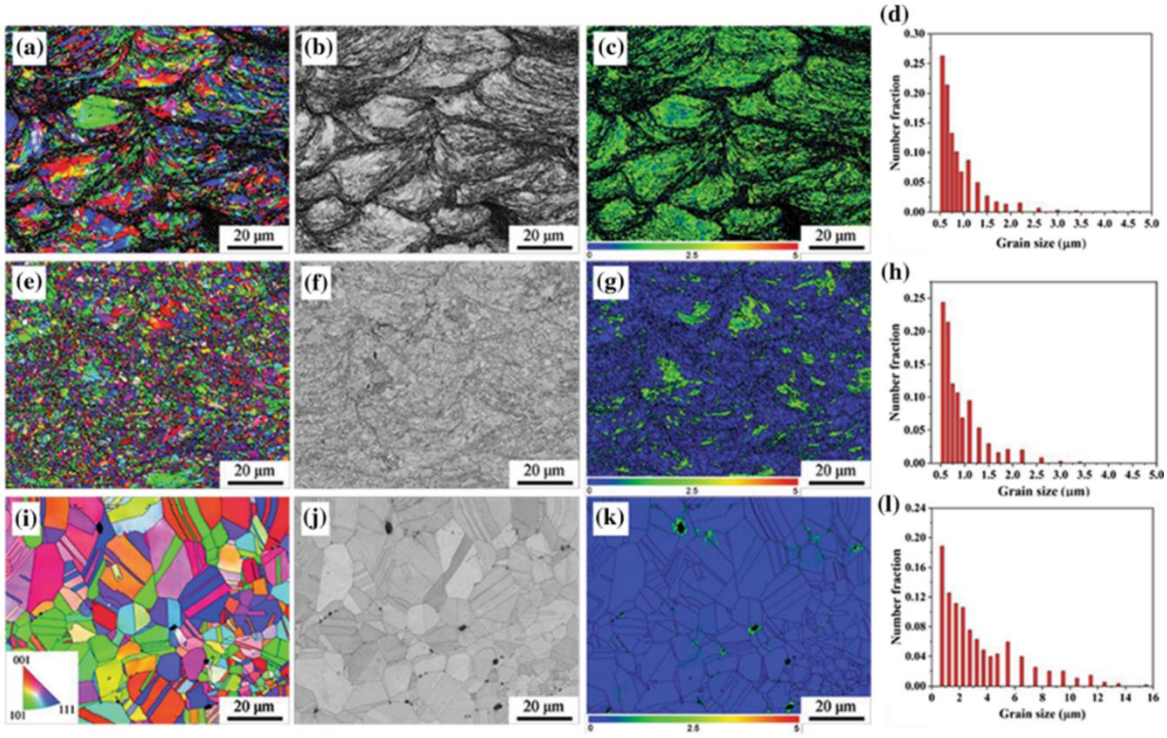

Figure 2.48: EBSD maps of CSAM CoCrFeNiMn deposits before and after annealing: (a)–(d) as-deposited, (e)–(h) annealed at 650 °C, and (i)–(l) annealed at 1150 °C The inverse pole figure (IPF), image quality (IQ), kernel average misorientation (KAM) maps, and grain-size distributions are shown in Figure [129].

Apart from the recrystallisation and precipitate formation that can occur during the annealing treatment of the cold-sprayed HEA, the atomic diffusion and improved metallurgical bonding of deformed splats to have a dense deposit are beneficial for improved mechanical properties. This was observed for CoCrFeNi HEA deposited using cold spray; for example, Fan et al. [88] fabricated bulk CoCrFeNi HEA by cold spray and performed post-deposition annealing at the temperature range of 500-1000 ºC for 2 hrs. In the as-sprayed condition, the deposit exhibited a high compressive strength but fractured within the elastic deformation regime. Annealing at higher temperatures resulted in an excellent combination of strength and ductility of the deposit because of partial and full recrystallisation, as well as the enhanced particle-particle interface diffusion and the resultant metallurgical bonding. A detailed investigation is thus required for the CSAM CoCrFeNiMn HEA deposit. The investigation could involve the optimisation of the annealing treatment for enhanced metallurgical bonding, and considering the strengthening effect of Cr-rich precipitates for improved mechanical properties.

2.10 Summary and gaps in the literature

2.10.1 Summary

The overall main points in the summary of the literature review in this chapter are as follows:

- Cold spray is an emerging solid-state AM technique that allows for the layer-by-layer deposition of a wide range of materials using the kinetic energy of sprayed particles, forming dense deposits. The technique has been employed for several applications, ranging from the repair and restoration of damaged components to the AM of large components. Several metallic materials have been employed for these applications, including Cu, Al, Ti, Ni, and their alloys; however, HEAs have yet to be explored for these applications.

- The deposit microstructure in CSAM is dependent on the spraying parameters employed, mainly the gas pressure, gas temperature, powder type, and spraying kinematics. Numerical and experimental analyses have been conducted to investigate the influence of these factors on the deposition mechanism during particle depositions.

- The bonding mechanisms in CSAM, though still under debate, have been understood through numerical and post-mortem analyses. The generally accepted phenomenon responsible for the bonding mechanism in CSAM is adiabatic shear instability. The two main bonding mechanisms include

metallurgical bonding and mechanical interlocking. These bonding mechanisms depend on several factors, including the material combination.

- The understanding of the deposition mechanisms in CSAM helps to develop the optimum window of depositions for the CSAM processing of a wide range of materials. Furthermore, for the deposition of particles on substrates, the particle impact velocity needs to reach a critical velocity, which is affected by the powder state, size, temperature, and the process condition itself. The critical velocity of a wide range of metallic materials has been determined using numerical and experimental techniques. The values of the critical velocities and particle velocities obtained can then be employed for the optimisation of the CSAM process.

- During CSAM deposition and hence powder consolidation, dynamic recrystallisation (via continuous dynamic recrystallisation) and adiabatic shear instability have been reported to contribute to the microstructure formed in deposits: a heterogeneous microstructure composed of severely deformed and highly oriented ultrafine grains at the impacting interfaces and lightly deformed coarse grains at the particle interiors. It was established that the degree of dynamic recrystallisation depends on the material properties.

- The deposition mechanism and spraying conditions employed during CSAM also influence the final residual stress state of the deposits. Compressive residual stress has mostly been observed in CSAM deposits; however, studies have shown that tensile residual stresses are also formed. Thus, the nature and magnitude of residual stresses in CSAM are dependent on the

spraying parameters and materials involved, owing to differences in the thermal expansion coefficients.

- Both numerical and experimental analyses have been performed to predict and measure residual stress in CSAM; however, there are limited studies on the prediction of residual stress using the explicit-implicit finite element scheme. In this FE method, the explicit scheme involves multi-particle impacts with random configurations of particle diameters and positions representative of the CSAM process, whereas the implicit scheme constitutes an element birth-death technique with block-by-block (instead of layer-by-layer) activation of deposit elements.

2.10.2 Gaps in the Literature

The following are gaps in knowledge in the literature to be addressed in this thesis:

- A major factor in the CSAM deposition of metals is the critical velocity, which corresponds to the minimum required impact velocity for the deposition of particles on substrates. Determination of the critical velocity of a metal is important for the optimisation of the CSAM process. There is a gap in knowledge on the critical velocity of CoCrFeNiMn HEA, and hence the optimisation of the CSAM process for obtaining high-quality deposits of the HEA.

- The literature shows that the degree of dynamic recrystallisation is affected by material properties, such as stacking fault energies and activation energy

for recrystallisation. While this has been observed between Ni and Cu, there is yet a detailed investigation of this deposition mechanism in the CoCrFeNiMn HEA during CSAM. Furthermore, numerical analysis can be combined with experimental investigation to explain the deposition mechanism of materials during CSAM; however, there is a wide knowledge gap in the numerical analysis of multi-particle impacts of the HEA.

- Post-deposition annealing treatment is often employed to improve the microstructure and mechanical properties of CSAM deposits. There is however a wide gap in knowledge on the effect of annealing treatments on the CSAM CoCrFeNiMn HEA deposits. Moreover, it is unclear the effect of the presence of precipitates such as the Cr-rich phase on the mechanical performance, particularly the tensile properties, of the CSAM HEA deposits.

- There is a knowledge gap on the residual stress of the CSAM CoCrFeNiMn HEA deposits. Moreover, there is a gap in the literature on explicit-implicit finite element schemes for residual stress prediction in deposits manufactured using CSAM.

3 Experimental Methods

This chapter provides an overview of the various experimental techniques employed in this thesis. The CSAM apparatus used for the deposition of materials onto various substrate materials, the various characterisation equipment and a summary of their principles are described. Additional information on the methods employed is also included in each chapter's methodology sections.

3.1 Materials

The feedstock powder used for this thesis was a gas-atomised, pre-alloyed CoCrFeNiMn HEA provided by HC Starck Surface Technology & Ceramic Powders GmbH (Goslar, Germany). Four substrates were used for the spray depositions: stainless steel (SS304), Ti6Al4V (Ti64), commercially pure aluminium (CPAl), and Al alloy 6082 (Al6082). As provided by the manufacturers, the nominal composition (wt.%) of the feedstock powder was 20 wt.% of each element in the material. The nominal compositions (wt.%) of the soft substrates—CP Al was provided as 0.09 Fe, 0.32 Si, 0.02 Zn and the balance being Al, and Al6082 was provided as 0.36 Mg, 0.27 Si, 0.04 Ti, 0.12 Mn, 0.02 Fe, Cr and Zn, 0.03 Cu, the remainder being Al. For the hard substrates nominal composition (wt.%) of Ti64 was provided as 6.54 Al, 4.13 V, 0.02 Si, 0.01 Mn, 0.03 Mo, 0.05 Fe, 0.04 Nb and Ti to balance, and SS304 was provided as 19.0 Cr, 9.3 Ni, 0.05 C and Fe to balance.

3.2 CSAM deposition

The deposition of the HEA feedstock powder was performed using a high-pressure CSAM system at the University of Nottingham. The CSAM system is an in-house built rig that uses helium and nitrogen gases. A schematic illustration of the rig is provided in Figure 3.1. The system runs using a 15-kW gas heater (Infinity Fluid, USA) attached to the rig, providing a maximum gas temperature of 537 ºC. The CSAM rig is designed to operate to a maximum accelerating gas pressure of 3.5 MPa, while the powder carrier gas was usually set approximately 0.1 MPa higher than the accelerating gas pressure to ensure powder feeding into the accelerating gas. A commercial high-pressure powder feeder (Praxair 1264 HP, Indianapolis, IN, USA) was used with a 12-slot feeding wheel. The powder feeding wheel was set to 0.5 rpm for the single particle impact test, (i.e., swipe test) and 2 rpm for deposit fabrication. The swipe test is a deposition process where the substrate is moved past the nozzle rapidly to allow for single-particle deposition from the powder-impacting flux. In this study, a mirror-polished substrate was moved rapidly through the spray jet, at a low powder feed rate and a high nozzle transverse speed to achieve the lowest impacting particle flux onto the substrates. The powder feeder set at 0.5 rpm corresponds to a powder feeding rate of ~9 g/min, while that set at 2 rpm corresponds to ~40 g/min of the HEA feedstock powder. It is noteworthy that the powder feeding rate can also be influenced by the powder particle size distribution and flowability of the feedstock powder.

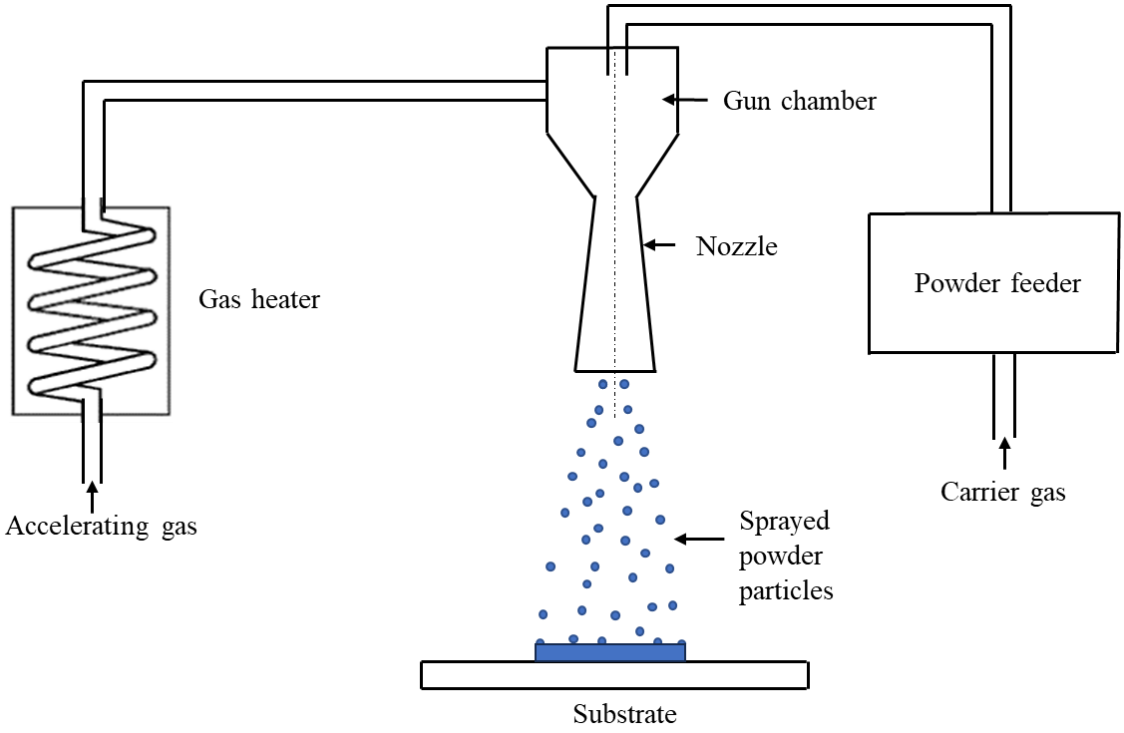

Figure 3.1: Schematic illustration of the set-up of the CSAM rig used in this thesis.

In this thesis, the nozzle was fixed to a frame while the substrate samples were transversed on two different configurations or set-ups: a programmable x-y table and a robotic arm (ABB Robot, UK). In the x-y table, the nozzle was held vertically, and the substrate moved below the nozzle, whereas the robotic arm allowed for the movement of the substrate horizontally to the nozzle. Nevertheless, these configurations did not affect the spraying performed as the configurations allowed a controllable scan pattern and velocity. The convergent-divergent nozzle was made of hardened stainless steel 316, designed with an area expansion ratio of ~8.9 and a divergent length of 150 mm. Figure 3.2 shows the schematic of the nozzle used in this thesis with its dimensions. The nozzle-substrate stand-off distance for all spray runs was fixed at 20 mm. The transverse speed, the relative motion between the nozzle and substrate, for the swipe tests was set to 1000 mm/s. For deposit

formation, 60 mm/s and 100 mm/s were set for the transverse speed. Figure 3.3 shows images of the CSAM rig set up at the spraying booth used in this thesis.

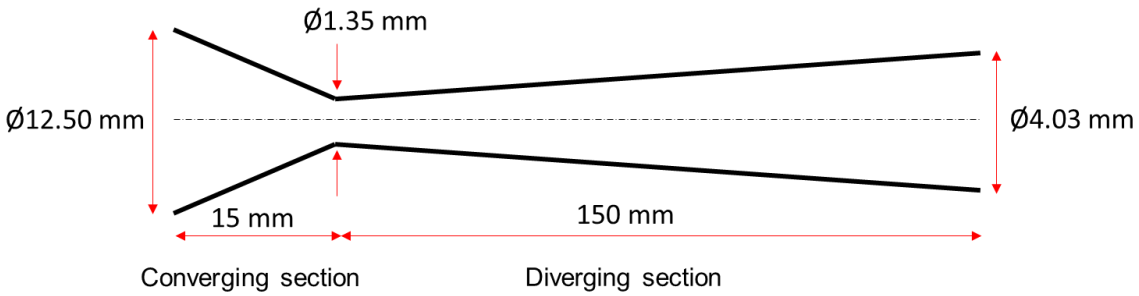

Figure 3.2: Schematic of the nozzle and its dimensions (not sketched to scale) used in this thesis. The symbol Ø denote diameter.

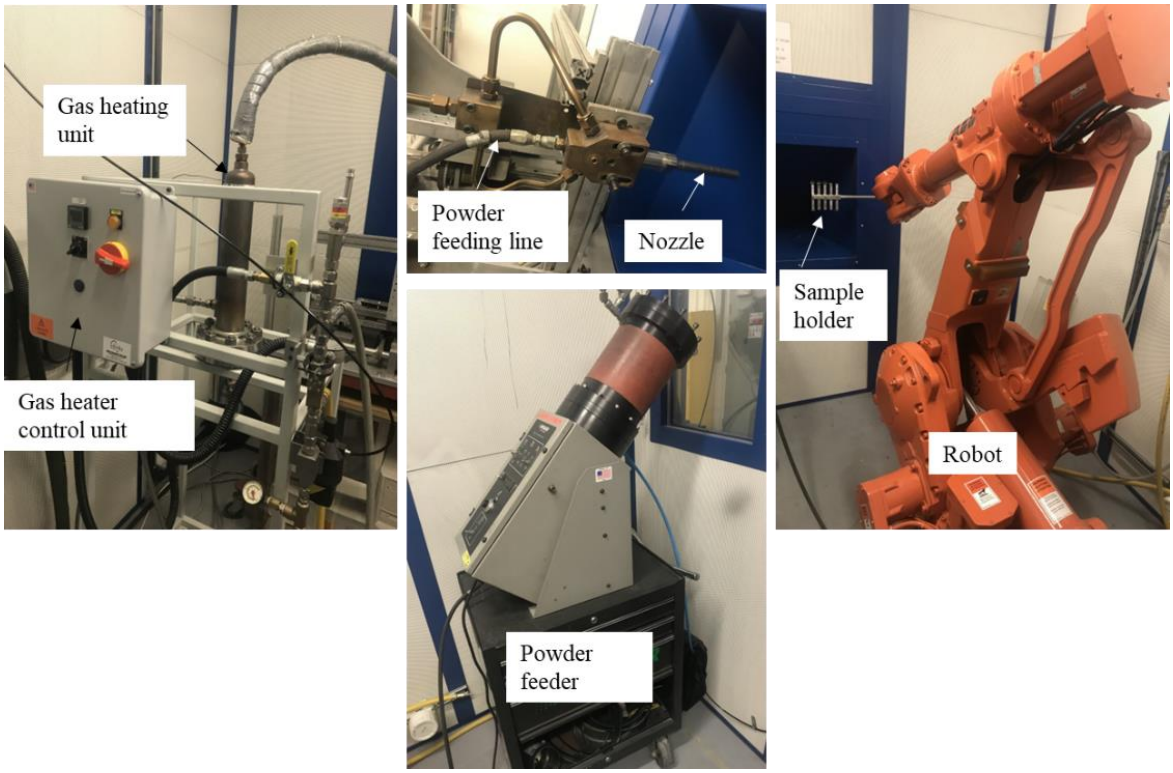

Figure 3.3: Photographs of the CSAM booth at the University of Nottingham, showing the different components or set-up.

3.3 Sample preparation

For the observation of the feedstock powder microstructures, powder samples were hot-mounted in a conductive mount of Bakelite using conducto-mount (Metprep, UK), put under pressure of 18 MPa and 150 ºC for 5 mins. The powder sample was subsequently ground using P800, P1200, and P4000 silicon carbide paper. The samples were subsequently polished to a 1 µm surface finish using diamond polishing pads, and final polishing was performed using a 0.04 µm colloidal silica suspension (Metprep, UK) for 20 mins. After polishing the samples, they were carefully rinsed and cleaned with either ethanol or industrial methylated spirit (IMS) and dried with compressed air.

For the swipe test, mirror-polished surfaces of the substrates were prepared following the metallographic procedure for the powder sample. On the other hand, to manufacture deposits of the feedstock powder, the substrate was ground with P240 silicon carbide paper. After grinding or polishing, the substrate samples were rinsed, cleaned with IMS or ethanol, and dried with compressed air.

Following the deposition of the feedstock powder on the substrates, deposit samples were cross-sectioned using a Qcut 200 precision cutting machine (Metprep, UK) and silicon carbide cutting disc (Metprep, UK). The sectioned samples were then hot-mounted in a conductive mount of Bakelite using conducto-mount (Metprep, UK), put under pressure of 18 MPa and 150 ºC for 8 mins. The samples were ground using P240, P400, P800, P1200, and P4000 silicon carbide

paper and thereafter prepared following the metallographic procedure for the powder samples.

3.4 Particle size measurement

The feedstock powder particle size distribution was obtained using the laser diffraction technique. The technique measures particle sizes with light, and the angle and intensity of the scattered light from the laser beam would depend on particle diameters. Larger particles would scatter light through smaller angles and high intensities, whereas smaller particles, higher angle scatter and small signals or low intensities [271]. The scattered light is captured with a series of detectors, and then the laser system software uses Mie light scattering theory to obtain the particles' energy distribution. Subsequently, the particle size distributions are produced based on an equivalent spherical diameter.

In this thesis, the feedstock powder particle size analysis was performed using a Horiba LA-960 (Horiba Scientific, Japan) laser diffractometer. Before measurement, ~20 g of the powder sample was dispersed in a wet medium via ultrasonication in the apparatus to prevent particle agglomeration.

3.5 Microstructural characterisation

3.5.1 Scanning electron microscopy

In a scanning electron microscope (SEM), a focused electron beam from a source is used to probe the surface of a sample. Electrons and X-rays are thus emitted from the sample, undergoing either elastic or inelastic collisions with the atom of the sample. The inelastic collision produces secondary electrons (SE) with energy less than the primary impinging electrons, providing surface topography information of the sample. The elastic collisions, on the other hand, produce backscattered electrons (BSE) with energy greater or equal to the primary impinging electrons depending on the atomic weight of the elements in the sample. Thus constitutes an important SEM imaging signal providing more detailed information on the sample microstructure and characteristics, such as the composition, topography and crystallography [272]. Furthermore, when electrons with greater energy above the BSE interact with core atoms, they can eject electrons from the atoms, causing excitation of the atoms. When the excited atoms decay to their ground states, they produce X-ray characteristics of the elements in the sample. The emission of such characteristic X-rays is stored as energy in a detector, energy dispersive X-ray (EDX) spectroscopy detector, which provides the possibility to identify the elements in the specimen through its atomic structure [272].

The powder and deposits microstructures in this thesis were characterised using an FEI XL30 SEM (Philips FEI, The Netherlands) operated in the SE and BSE modes at 20 kV accelerating voltage, a working distance of approximately 10 mm and a

spot size of 5 nm. Field-emission gun (FEG) SEM (7100F, JEOL, Ltd., Japan) was employed for high-resolution imaging, such as revealing precipitate phases and imaging of fractured surfaces. The FEG SEM was operated at 15 kV for all deposits and powder imaging at a working distance of 10 mm in SE and BSE imaging modes. BSE imaging can be used to visualise differences in elemental composition as high atomic weight elements more readily produce them. Also, because they have greater energy and can escape from deeper within the sample than SE, BSE images can provide a more accurate analysis for the porosity evaluation of the deposit than SE and optical microscope images.

Energy dispersive X-ray (EDX) (Oxford Instruments, UK) spectroscopy detectors mounted on the FEG SEM were employed to analyse the elemental composition and distribution in the powder particles and CSAM deposits. The EDX analysis was performed using the AZtecCrystal software (Oxford Instruments, UK).

3.5.2 Electron backscattered diffraction

The electron backscattered diffraction (EBSD) technique provided information on the local misorientations, grain size, boundary types, and crystallographic orientations of the powder and deposit microstructures. This technique uses the projection of BSE, produced most intensely downward and outward on a phosphor screen when an electron beam strikes a sample tilted at 70º. The BSE that travels along a crystallographic plane trace generates Kikuchi bands whose widths are dictated by Bragg's law and the distance between the specimen and the phosphor screen. A schematic representation of the EBSD system is provided in Figure 3.4. A charge-coupled device (CCD) or silicon-intensified target (SIT) detector or camera

detects these Kikuchi bands or patterns. A pattern matching algorithm or Hough transform compares the detected bands with those calculated from the crystal structure for the phase(s) of interest. These detected bands are solved or indexed to find the orientation of the crystal under the electron beam. The crystal structure of interest can be selected from a crystal structure database; for instance, the Inorganic Crystal Structure Database (ICSD). There were no specific databases for the CoCrFeNiMn HEA in this thesis, so the most closely matched database nickel or the *γ*-iron FCC database, was used. The EBSD analyses were performed on two FEG SEM: 7100F (JEOL Ltd., Japan) at the University of Nottingham, and Auriga Cross Beam (Zeiss, Germany) at Imperial College, UK. A CSAM deposit of the HEA on a stainless steel 304 substrate was sent to the latter for characterisation. All other ESBD work was performed using the former. While the former FEG SEM was operated at an accelerating voltage of 15 kV, with a scanning step size between 50 and 70 nm, a working distance of 16 mm and a detector insertion distance of 193 mm, the later FEG SEM was operated at an accelerating voltage of 20 kV, with a scanning step size of 50 nm, a working distance of 18 mm and a detector insertion distance of 10 mm. The obtained EBSD data at the University of Nottingham were analysed using the AZtecCrystal software (Oxford Instruments, UK), whereas analysis of the EBSD data obtained from Imperial College was performed using the MATLAB MTEX toolbox. The geometrically necessary dislocation (GND) density was estimated following Pantleon's methodology [273].

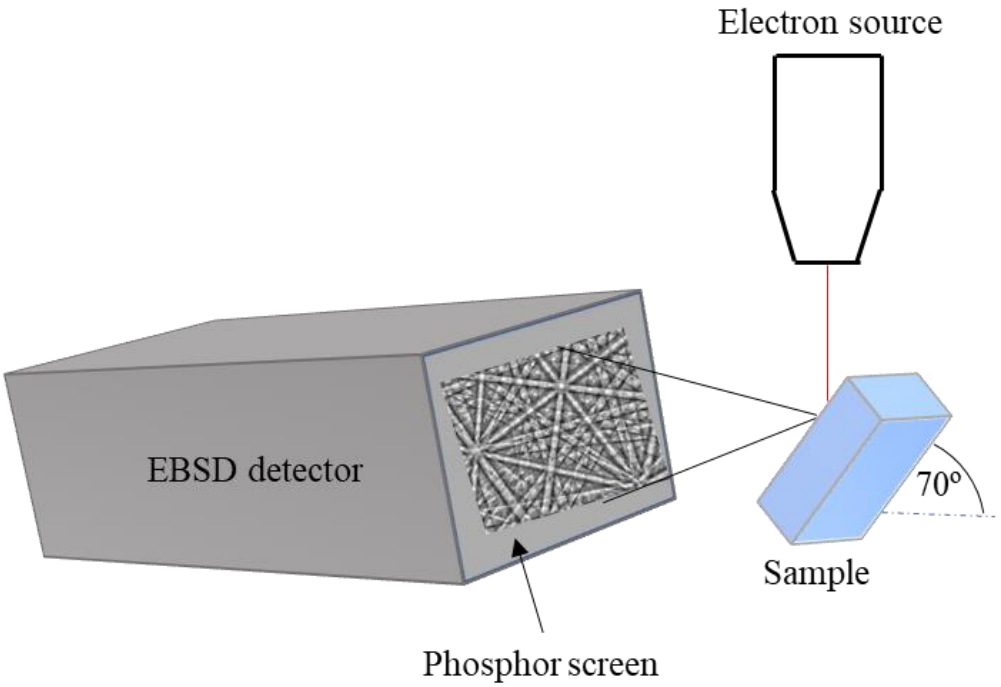

Figure 3.4: A schematic representation of an EBSD system layout.

Because of some surface blemishes resulting from sample preparation, or pores and cracks present in the sample analysed, there would be regions not indexed in the EBSD scan. This is usually because of the superposition of diffraction patterns on the sample. Also, some regions, specifically interfacial regions, in the analysed samples may have poor indexation quality due to severe deformation and ultrafine grains in those regions. A typical example of the EBSD micrograph is shown in Figure 3.5, showing the different information that can be provided by the EBSD scans. The figure also shows regions in the sample with poor indexation quality due to the severe plastic deformation experienced by the grains in those regions. Consequently, reliable EBSD data was obtained in this thesis by performing an automatic data clean-up procedure during the post-processing of the EBSD data. The automatic data cleaning process thus corresponds to a noise reduction of 3, where each non-indexed pixel with 6 indexed neighbours is examined. The

orientation of the non-indexed pixel is then replaced with the most common neighbouring orientations. High-angle (>15º) and low-angle grain boundaries (2-15º) were detected and represented on the inverse pole figure (IPF) maps with black and white lines, respectively. The IPF map is used to visualise the orientation of a grain by the colour of the crystal facing a specified direction of the sample. The local grain misorientations within the samples were represented with the kernel average misorientation (KAM) maps. The KAM represents the local lattice curvature. Here, the average misorientation of each pixel and its 8 neighbours are calculated, excluding grain boundaries higher than 5º, typically used to provide information on localised strain variations. A colour gradient was used on the KAM maps, where blue corresponds to the absence or very low misorientation, while green or yellow indicates a high misorientation.

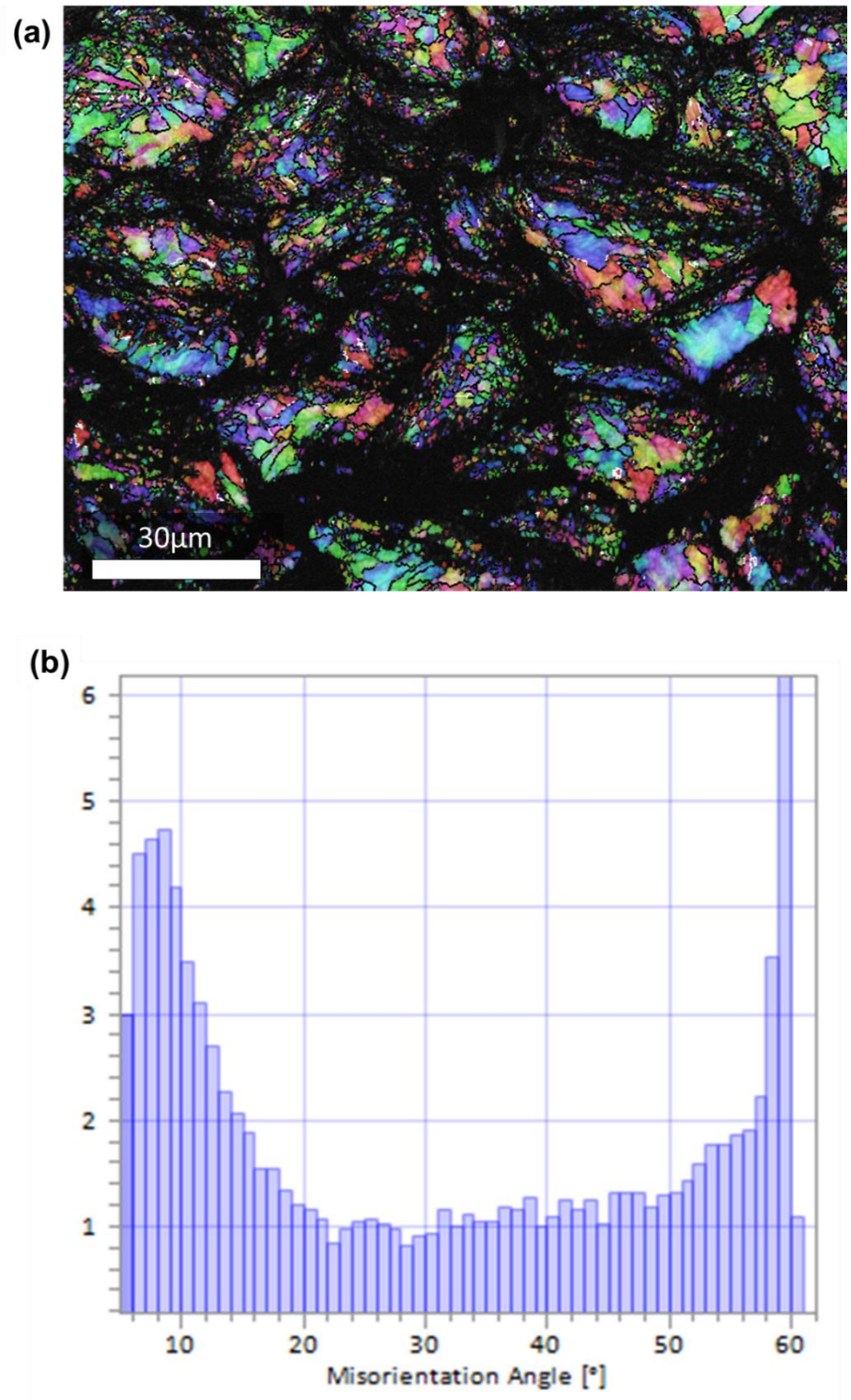

Figure 3.5: An example of an EBSD scan showing (a) an IPF micrograph and (b) the misorientation angle of the grains within the analysed region for a deposited HEA feedstock using the CSAM process.

3.5.3 X-ray diffraction

X-ray diffraction (XRD) analysis of the samples in this thesis was performed on a D8 advanced da Vinci x-ray diffractometer (Bruker, Germany) with a monochromatic Cu-Kα radiation (0.15406 nm) in Bragg Brentano $\boldsymbol{\theta}$-2$\boldsymbol{\theta}$ geometry. The basis of the XRD technique relies on the constructive diffraction from planes within grains that satisfy Bragg's law, as represented in Equation (3.1), when an X-ray beam strikes a crystalline material. From the Equation, $\boldsymbol{n}$ is an integer, $\boldsymbol{\lambda}$ is the wavelength of the incident X-ray, $\boldsymbol{d}$ is the interplanar spacing, and $\boldsymbol{\theta}$ is the angle between the incident X-ray and the scattering plane. The crystal structure of the material can be determined by analysing the angles and intensities of the diffracted X-ray beams.

$$\boldsymbol{n\lambda = 2d \sin \theta} \qquad (3.1)$$

XRD scans were performed on powder samples and deposits in the 2$\boldsymbol{\theta}$ range from 20-80º with a step size of 0.02º and a dwell time of 0.1 s. Phase identification in the samples was completed using EVA software (Bruker, UK), supported by PDF-2 database files (ICDD-PDF).

3.6 Porosity and thickness measurements

3.6.1 Porosity

The porosity of the CSAM HEA deposits was evaluated using a greyscale image analysis technique in ImageJ software (National Institute of Health, USA). BSE

images taken from the interface to the top of the deposit were used for the porosity evaluation. A typical example of a BSE image of a deposit microstructure showing porosity is displayed in Figure 3.6. The dark spots and lines in the image are pores and interparticle boundaries in the deposit. As mentioned earlier, BSE images were used for a more accurate evaluation of porosity as a better contrast between the particles and pores can be obtained by appropriately tuning the contrast and brightness knob of the SEM equipment. The porosity of the samples was evaluated using the image analysis technique, where the grayscale BSE micrographs with 255 levels were converted to binary black-and-white images such that pores appeared black and the sample microstructure appeared white, as shown in Figure 3.6b. These binary images are then analysed using the ImageJ software, which provides the surface area fraction (fraction of the black part of the binary images) of the pores. Five to ten BSE SEM images of area 0.5 × 0.5 mm^2 were captured at x500 magnification, with each image ranging from 100-500 μm in width and height, depending on the thickness of the deposit that was fabricated. The average value and standard error of the mean of the porosity measurement were calculated.

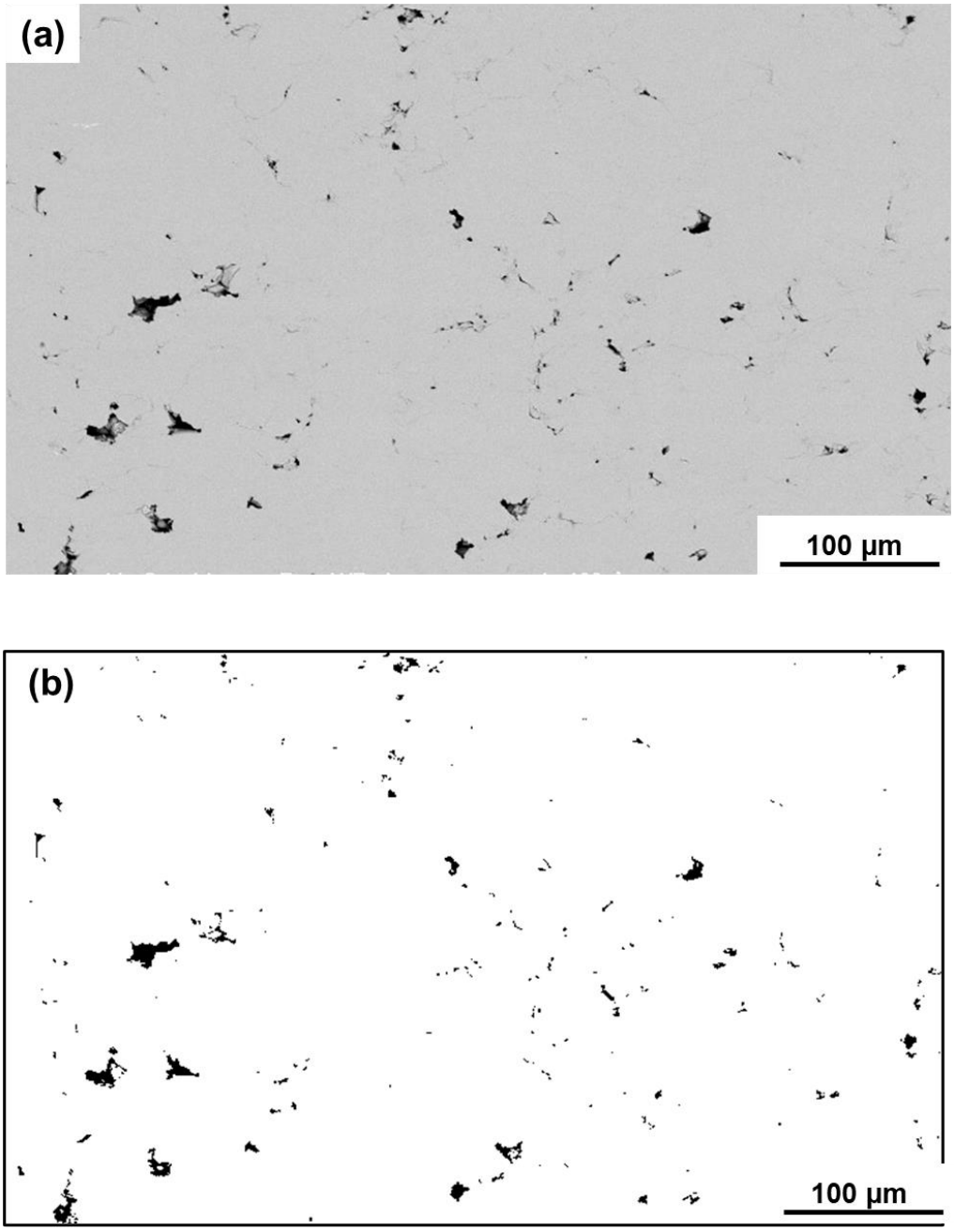

Figure 3.6: An example of a (a) BSE image and the (b) corresponding 255-pixel image showing the bright (deposited material) and dark phase (pores) using the ImageJ image analysis technique.

3.6.2 Thickness

The measurement function in the ImageJ software was employed to evaluate the thickness of the CSAM deposit. Five BSE images were captured at x250

magnification across the width of the deposits. The average value and standard error of the mean of the measurement were calculated.

3.7 Mechanical properties

3.7.1 Nanohardness testing

Nanohardness measurements were performed on polished cross-sections of powder, and CSAM deposit using a NanoTest P3 nano-indenter (MicroMaterials Ltd., UK). At least ten measurements were performed on the powder sample by indenting the centre of each powder particle. A 20 by 20 array (400 indents) was performed at the central region of the deposit samples as shown schematically in Figure 3.7.

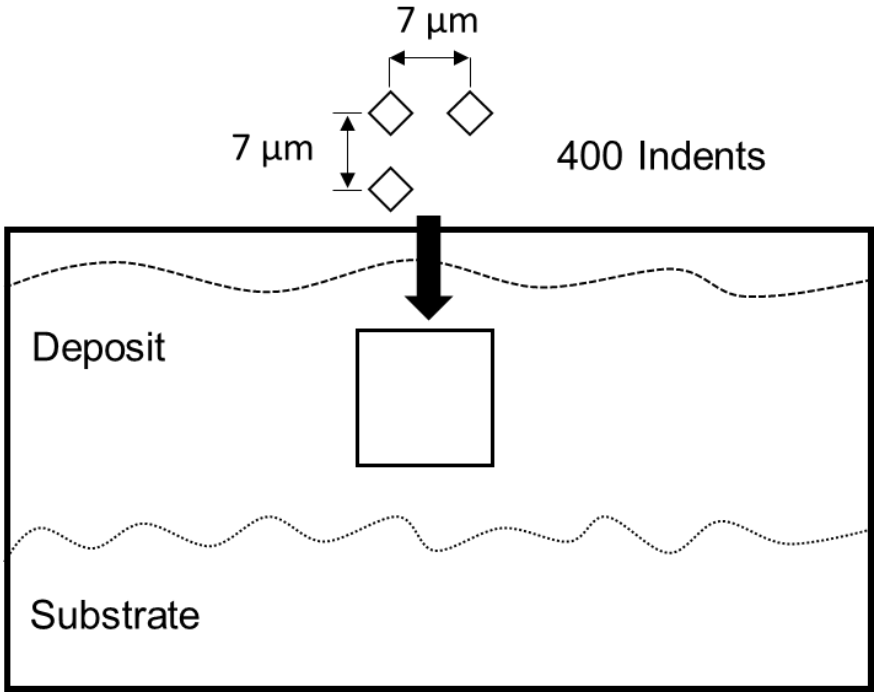

Figure 3.7: Schematic illustration showing the locations in the deposit for nanohardness measurements.

A diamond Berkovich indenter was used for the nanohardness testing, with a peak load of 3 mN, dwell time of 10 s, and 0.75 mN/s loading and unloading rate. The loading-unloading curves were examined to remove non-valid indents such as those on pores. The nanohardness apparatus provides the nanohardness and reduced modulus values following the Oliver and Pharr method [274], determined using Equations (3.2) and (3.3), where P_m is the maximum applied load (in mN), A is the projected contact area, and S is the contact stiffness (in µN/nm). Herein, the reduced modulus values were converted to the elastic modulus of the material considering the Poisson ratio (0.07) and elastic modulus (1140 GPa) of the Berkovich indenter diamond tip [275] using Equation (3.4). From the Equation, V_r, V_i, E_r, E_s and E_i are the Poisson ratios, reduced, and elastic modulus of the material and indenter, respectively. The final average values and standard error of the mean of the measurements were calculated.

$$H = {P_m}/{A} \tag{3.2}$$

$$E_r = {\sqrt{\pi}}/{2} \cdot {S}/{A} \tag{3.3}$$

$${1}/{E_r} = \left({(1 - {V_c}^2)}/{E_c}\right) + \left({(1 - {V_i}^2)}/{E_i}\right) \tag{3.4}$$

3.7.2 Microhardness testing

Microhardness of the substrates and CSAM deposit samples was measured using a Wilson VH3300 Vickers Microhardness instrument (Buehler, USA). While all microhardnesses were measured on polished cross-sectional surfaces of the deposit samples, measurements were performed on polished surfaces of the substrates. Ten measurements were performed on the substrates with a 500 gf load. The deposit samples underwent approximately 100 indents with a 300 gf load and a dwell time of 15 s. Figure 3.8 shows the schematic representation of the location in the deposit samples where micro-indentations were performed. The average values and standard error of the mean of the measurements were calculated.

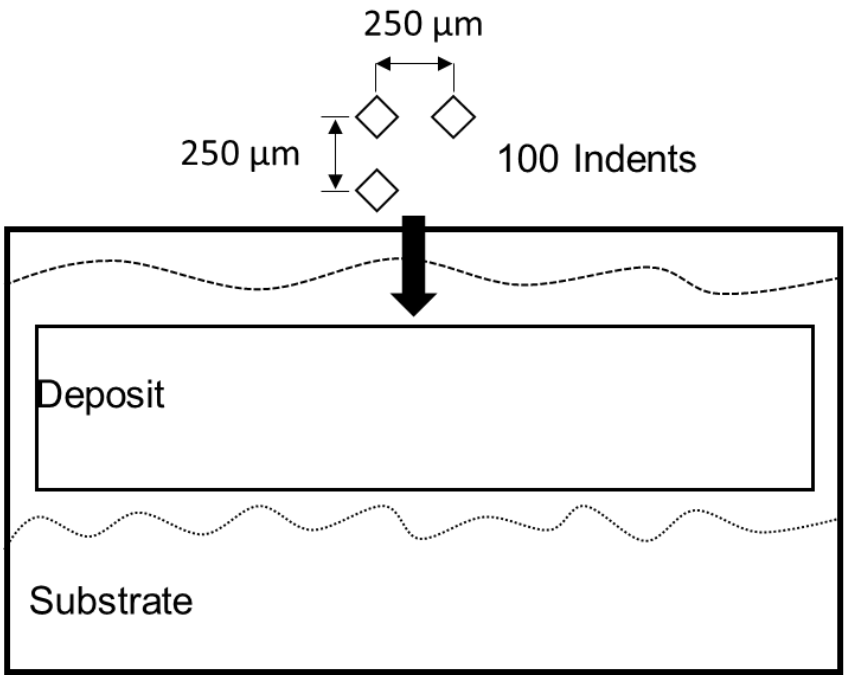

Figure 3.8: Schematic representation of the location in the deposit where microhardness measurement was performed.

3.7.3 Tensile testing

Tensile testing was performed to measure the tensile strength, and strain at failure, and to examine the fracture behaviour of the deposits and the subsequent effect of post-deposition annealing on the CSAM HEA deposits. Micro-flat samples with dogbone shapes were cut from the deposits following the ASTM E8 specification [276] and in [277]. The samples were cut from the deposits perpendicular to the spraying direction using wire-based electrical discharge machining (EDM). Figure 3.9 shows a schematic illustration of the tensile test sample orientation with respect to the build layers in the deposit. Other orientations of the samples were not explored such as machining the samples at an angle of 45º and or parallel to the spraying direction. The different orientations can influence the outcome of the tensile properties of the deposit [278]. These different orientations of the tensile test

samples with respect to the build layers can be explored in future investigations. The substrates were removed from the deposited sample using the EDM to obtain a free-standing deposit, thereafter micro-flat tensile test samples were sectioned out from the free-standing deposit. A limitation to the use of the EDM to remove the substrate is that the tensile test sample at the substrate-deposit interface may contain substrate materials, hence influencing the tensile test data. It is however recommended that a more robust protocol for extracting sub-size tensile specimens from CSAM deposits should be employed in future investigations.

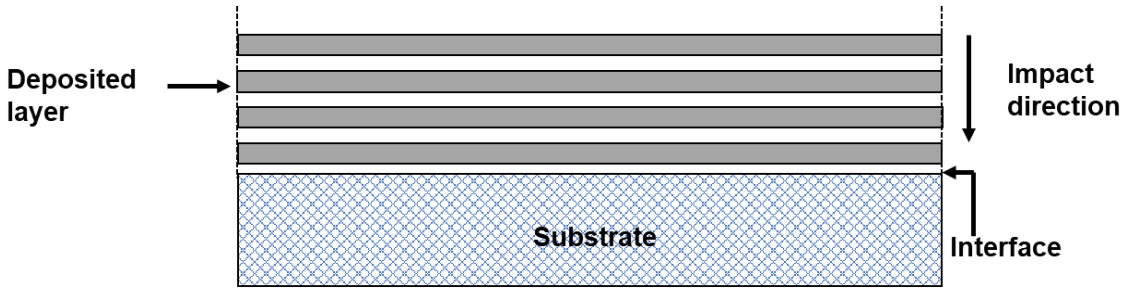

Figure 3.9: Schematic illustration of the deposited layers where tensile test samples were extracted from, showing the sample orientation with respect to the impact or build direction. The interface may contain materials from the substrate mixed with the layer for the tensile test sample.

The tensile test samples obtained for the analysis in this thesis had dimensions of ~10 mm gauge length, a width of ~5 mm and a thickness of ~0.5 mm, as shown schematically in Figure 3.10. These sample sizes are smaller than the standard specimen size as provided in the ASTM E8 specification. The study of Gartner et al. [277] reveals that microflat samples show slightly higher strength and elongation to failure than the standard specimen due to the slightly more non-uniform deformation of smaller geometries. Within the given tensile test data range, it is justifiable to use the microflat specimen sizes for the CSAM deposits as employed

in this thesis following the work of Gartner et al. [277]. In the industry, standard specimen sizes can be employed for larger deposited samples or components where tensile tests are required for larger parts; however, a more detailed investigation of the micro-deformation mechanisms of the sprayed particles can be readily studied using the microflat samples employed in this thesis. A universal testing system (Instron, 5969 dual column testing system, UK) was used to perform the tensile testing at a crosshead displacement of 1 mm/min and with a load cell of 5 kN. Elongation was measured using a video gauge. Before testing, the samples were sprayed with highly reflective speckled paint to supply sufficient contrast for the elongation measurement using the video gauge. It is noteworthy that due to the small size (and thickness) of the micro-flat tensile test specimens, it was challenging to section out samples from the free-standing deposit using EDM. Nevertheless, samples were sectioned out, 4 for each test condition. Tensile tests were then performed using these samples, however, average of two samples for each test conditions could provide more accurate results. The average and standard error of the mean of the measurement of the ultimate tensile strength and fracture (i.e., strain at failure) for each condition was analysed and reported. After the tensile tests, the deformation of the sprayed particles on the fractured surfaces of the tested specimens for each condition were examined under an SEM. The fracture morphologies of the fractured surfaces were supplied by the FEG SEM in the SE imaging mode. The examination of the fractured surfaces provides information on the behaviour of the metallurgically bonded interfaces of the sprayed particles under tensile loading and the subsequent effects of annealing on the interfaces.

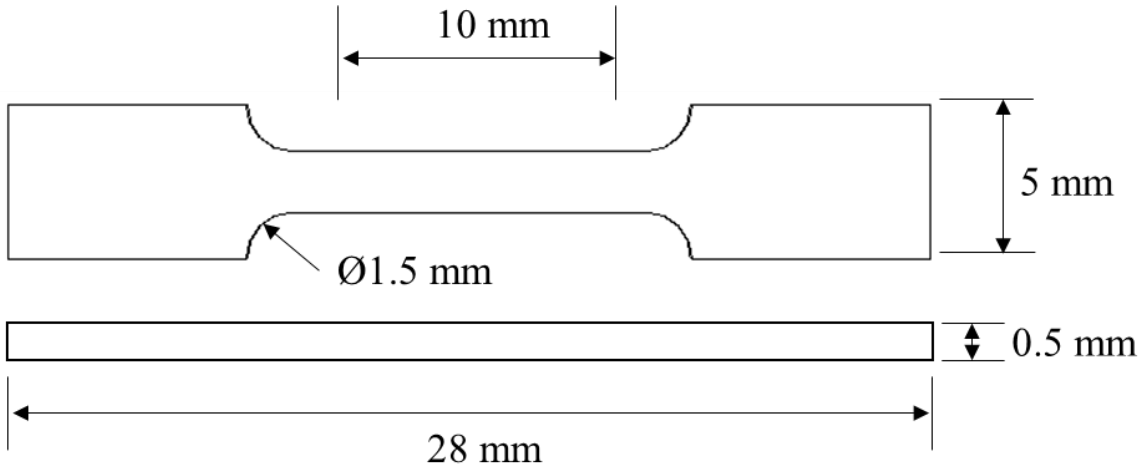

Figure 3.10: Schematic representation of the microflat dogbone-shaped samples used for the tensile testing.

3.8 Residual stress measurement

The residual stress of a thick deposit of the CSAM HEA on the austenitic stainless steel substrate was measured and analysed using the contour method. In this method, a sample is carefully cut into two halves using a micro wire-based electric discharge machining (EDM). The contour of the cut surface is measured using a surface profiling device, which gives the displacements due to the residual stress redistribution (or relaxation). By Bueckner's superposition principle, the cut surface is analytically forced back to its original flat state, which gives the residual stress that originally existed normal to the plane of the cut surface [218]. The superposition principle assumes elastic deformation of material during the relaxation of residual stress and that the material removal process does not introduce stresses enough to affect the measured displacements [279]. As part of the analysis, a finite element model (FEM) was developed, where the measured displacement data is imposed as boundary conditions on the FEM model. Also, the FEM account for the stiffness

of the material and the sample geometry. The output is a 2-dimensional map of residual stress normal to the measurement plane. It is important in the contour method that care is taken during the sample cutting, as this is the most critical step that can largely influence the outcome of the measurement. Data analysis or smoothing was performed to filter any "noise" or artefacts from the measured data, such as those resulting from the roughness of EDM cut and contour measuring, before analysing the FEM. Figure 3.11 shows a schematic illustration of the contour method explaining the different stages of evaluating the residual stress.

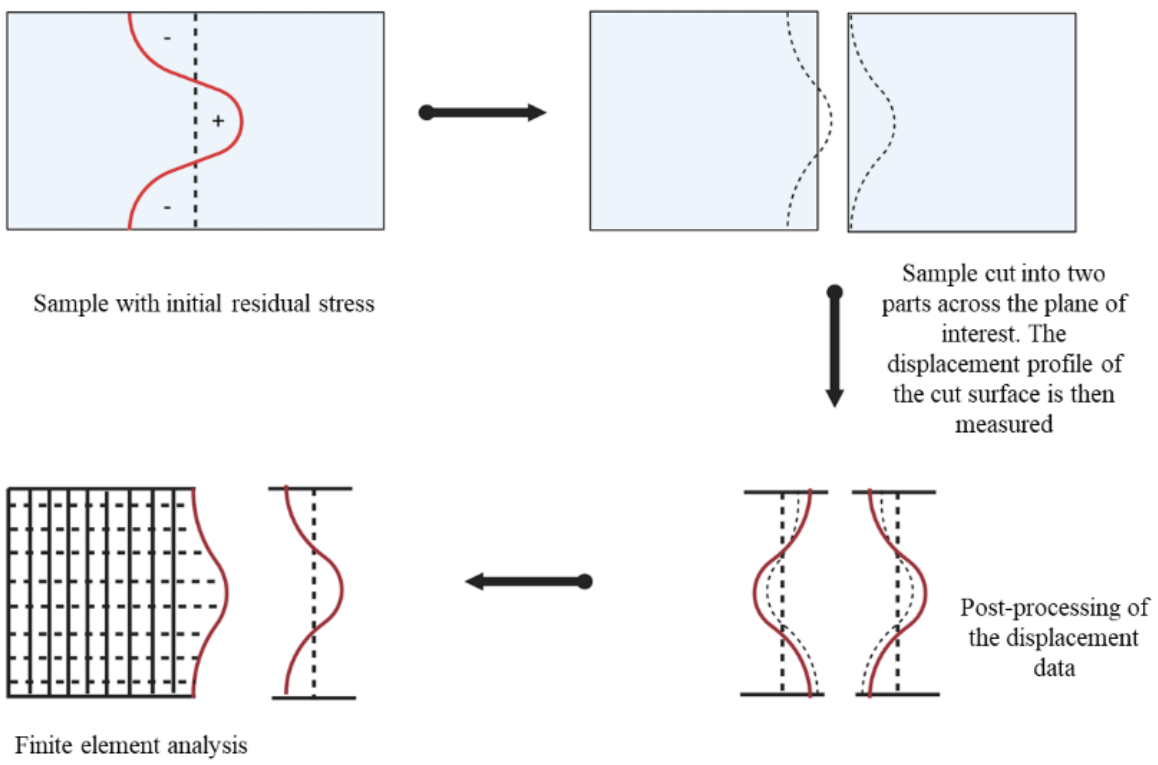

Figure 3.11: A schematic illustration of the contour method, providing the stages of measuring and analysing residual stress. The dotted straight lines indicate the cutting plane through the sample, while the dotted curve lines indicate residual stress relaxation after the cut.

Since the contour method was first presented by Prime et al. [218] in the year 2000, the method has been employed for residual stress measurement of additively manufactured parts. Figure 3.12 shows an example of the residual stress map of an additively manufactured titanium hollow cylinder manufactured using CSAM. The figure shows the residual stress of the wall of the cylinder. The figure also shows the microstructure of the wall, indicating no substantial deviation in the porosity of the microstructure across the thickness of the cylinder wall.

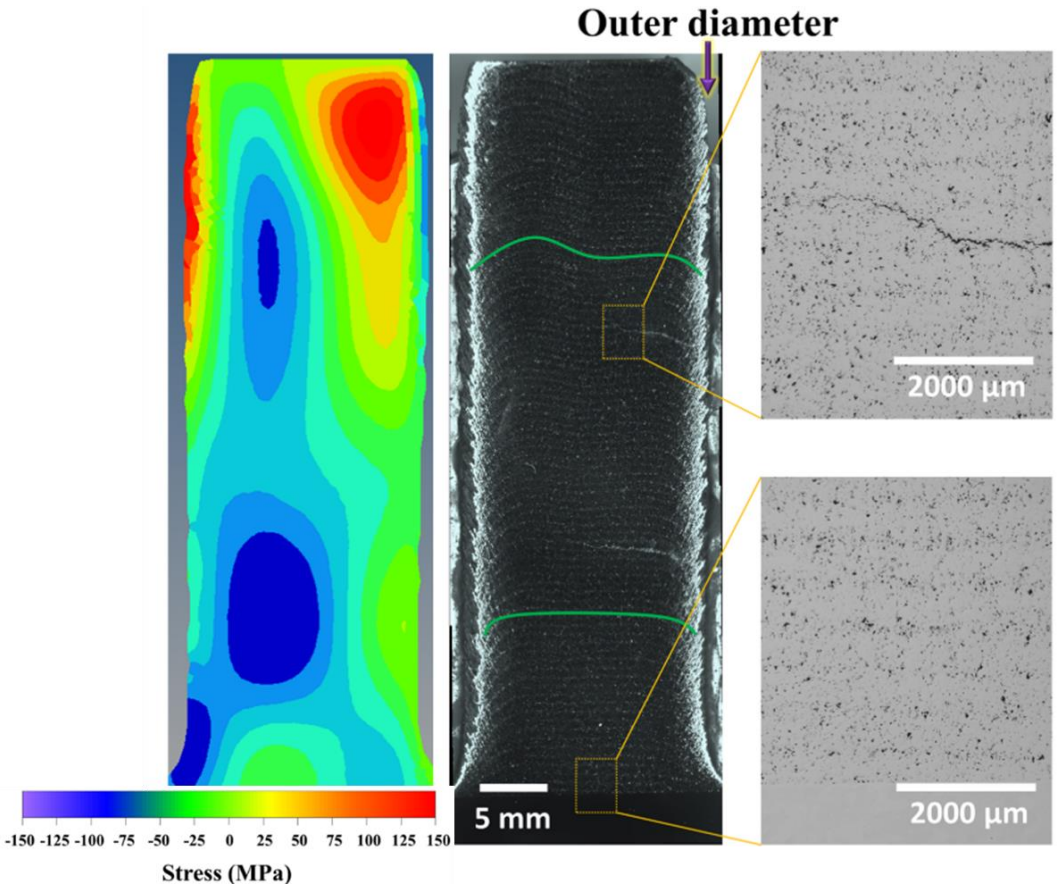

Figure 3.12: An example of a two-dimensional residual stress map obtained using the contour method for a titanium hollow cylinder wall. The cylinder was manufactured using the CSAM process. The figure shows stress distribution in the circumferential direction of the cylinder wall, along with optical micrographs of the cylinder wall microstructure [211].

The contour method was used in this thesis to measure the residual stress profile of a thick CSAM HEA deposit on a stainless steel 304 substrate, providing information on the residual stress distribution throughout the deposited thickness of the cut surface of the sample. The residual stress measurement with the contour method was performed in StressMap (The Open University, UK). The specific implementation process of the contour method is as follows:

- Firstly, the deposited sample was cut with slow-moving wire-based EDM equipment (Agie Charmilles Cut-1000) using a 0.1 mm diameter brass wire. The sample was rigidly clamped during cutting to avoid free movement. A careful clamping arrangement would avoid changes in the stress state caused by plastic deformation at the cut tip relative to the original stress as the cut progresses. The cutting speed of the sample was set at 1 mm/min with low-power cutting parameters to provide a better surface finish. The sample was submerged in temperature-controlled deionised water during cutting to minimise thermal effects. Since results from the contour method can likely be uncertain near edges, a sacrificial material was attached to the sample in all four cut-plane boundaries to improve the cut quality and measurement details [280,281]. Based on the stress-free cutting conditions, a stress-free reference cut was made to correct the displacement data.

- Secondly, the surfaces created by the cut were measured using a non-contact Zeiss Eclipse coordinate measuring machine (CMM) with a Micro-epsilon ILD2210 laser triangulation probe to provide the contour of the cut surfaces. The CMM was isolated from thermal fluctuations in a temperature-

controlled room. The CMM was programmed to acquire points over the entire surfaces with a point spacing of 0.025 mm and normal displacement resolution of 0.1 µm, sufficient to resolve the displacement field. The post-processing (screening, aligning, averaging, filtering, and smoothing) of the displacement data from the two cut surfaces was performed using a combination of manual cleaning of obvious outliers, a median filter and a local polynomial fitting algorithm proprietary from StressMap. The amount of smoothing was optimised based on the goodness of fit of the averaged displacement data.

- Finally, residual stress was determined from a linear elastic finite element analysis in Abaqus/Implicit code of one cut-half of the sample. An 8-node brick element (C3D8R) with reduced integration and hourglass control was selected. A uniform mesh size of 0.1 mm was set in the FEM. The smoothed displacement data with a reverse sign was imposed as the displacement boundary conditions normal to the nodes on the cut surface. Constraints (or point boundary conditions) were applied to the FEM to restrain rigid-body motion and ensure the calculated residual stress satisfies equilibrium. The elastic properties, elastic modulus of 202 GPa and Poisson's ratio of 0.265 of the HEA material [282] were used in the FEM.

The residual stress obtained using the contour method was employed to validate the numerical simulations performed in this thesis as presented in Chapter 4 Section 4.3 to predict the evolution of the residual stress during CSAM of the HEA.

4 Numerical modelling methods

This chapter presents the numerical methods employed in this thesis. The chapter consists of four sections:

- Computational fluid dynamics (CFD) procedure to predict the feedstock powder particle velocity and temperature before impact on the substrates during spraying.

- Particle deposition modelling methods to investigate the deformation behaviour of the particles during spraying on the substrates. This section is divided into three subsections: single-particle, multi-particle and the material model employed for the particle deformation modelling.

- Numerical methods to predict the thermal and mechanical fields of the CSAM process. This allows for the evaluation of the residual stress and the understanding of the evolution of the stresses during the CSAM process.

4.1 Computational fluid dynamics

In the computational fluid dynamics (CFD) model, the Navier-Stokes equations were solved using the finite-volume method to model any flow in the CFD domain. The Navier-Stokes equation consists of the mass, momentum, and energy conservation equations given by Equations (2.12), (2.13) and (2.14), respectively [108,112]. Here t, ρ, μ, λ, C_P, p, T, u_i, S_M, S_T and denote time, gas density, dynamic viscosity, thermal conductivity, specific heat at constant pressure, gas static pressure, gas temperature, gas velocity components and additional source terms in momentum and energy, respectively. The source terms in the momentum and energy equations account for the momentum and heat transfer between the gas and the particle. Compressible effects are encountered due to the supersonic gas speed during the CSAM process. In addition, the flow inside and outside the CSAM domain is usually regarded as a steady state; therefore, the Equation of state for the compressible flow is solved to close the Navier-Stokes equations [108]. This is taken as an ideal gas equation (Equation (4.4)), which is solved to account for the large variations within the fluid density experienced by compressible flows. In the ideal gas equation, R denotes the universal gas constant, M_w is the molecular weight of the gas and $\vec{p}$ refers to the operating pressure.

$$\frac{\partial \rho}{\partial t} + \frac{\partial}{\partial x_j}(\rho u_j) = 0 \tag{4.1}$$

$$\frac{\partial}{\partial t}(\rho u_i) + \frac{\partial}{\partial x_j}(\rho u_i u_j) = \frac{\partial}{\partial x_i}\left[-p\delta_{ij} + \mu\left(\frac{\partial u_i}{\partial x_j} + \frac{\partial u_j}{\partial x_i}\right)\right] + S_M \tag{4.2}$$

$$\frac{\partial}{\partial t}(\rho C_P T) + \frac{\partial}{\partial x_j}(\rho u_j C_P T) = \frac{\partial}{\partial x_i}\left[\lambda\left(\frac{\partial T}{\partial x_j}\right)\right] + S_T \tag{4.3}$$

$$\rho = \frac{(\vec{p} + p)}{\left(\frac{R}{M_w}\right)T} \tag{4.4}$$

In this thesis, the commercial CFD solver Ansys/Fluent V20.2 (Pennsylvania, USA) was employed to calculate the particle velocity and temperature before impact on the substrates during spraying. The CFD calculations were based on the nozzle dimensions and the experimental conditions used for the CSAM of the feedstock material in this thesis. A 2D axisymmetric model was developed, as shown schematically in Figure 4.1, with a single-particle trajectory. Table 4.1 provides the nozzle dimensions employed for the CFD calculations.

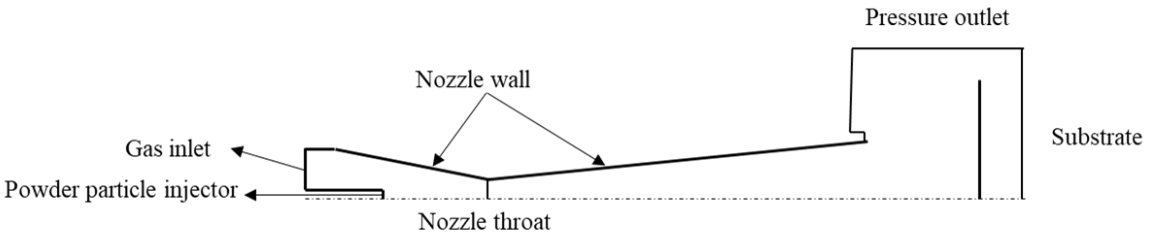

Figure 4.1: A schematic of the CFD computational domain.

Table 4.1: Nozzle dimensions employed for the CFD model.

Geometrical parameters	Length (mm)
Nozzle inlet diameter	12.50
Throat diameter	1.35
Nozzle exit diameter	4.03
Length of the converging section	15
Length of the diverging section	150

Table 4.2 summarises the boundary conditions employed for the CFD model. The surrounding atmospheric boundary was arranged sufficiently far from the impinging jet to eliminate its effect on the computational results. The nozzle inlet and outlet domains were modelled using pressure boundaries, and the nozzle wall was treated as adiabatic with a no-slip boundary condition. Figure 4.2 shows the CFD model meshed with a structured quadrilateral mesh, which is more computationally efficient and has a better convergence capability than an unstructured mesh [108,113]. The mesh was refined to capture steep variations in the flow properties, such as shock formation towards the nozzle exit as shown in Figure 4.2, owing to

the compressible nature of the flow. Adaptive remeshing was also considered to capture shockwave formation within the supersonic jet core.

Table 4.2: Boundary conditions for CFD modelling of the impinging gas jet in the cold spraying process.

	Pressure (MPa)	Velocity (m/s)	Temperature (K)
Nozzle inlet	N_2-3.5, He-3.5		N_2-798, He-673
Surrounding atmosphere	Ambient	$\frac{\partial v}{\partial n} = 0$	$\frac{\partial T}{\partial n} = 0$
Nozzle walls	$\frac{\partial p}{\partial n} = 0$	0	$\frac{\partial T}{\partial n} = 0$
Substrate	$\frac{\partial p}{\partial n} = 0$	0	$\frac{\partial T}{\partial n} = 0$
Symmetrical axis	$\frac{\partial p}{\partial r} = 0$	$\frac{\partial v}{\partial r} = 0$	$\frac{\partial T}{\partial r} = 0$

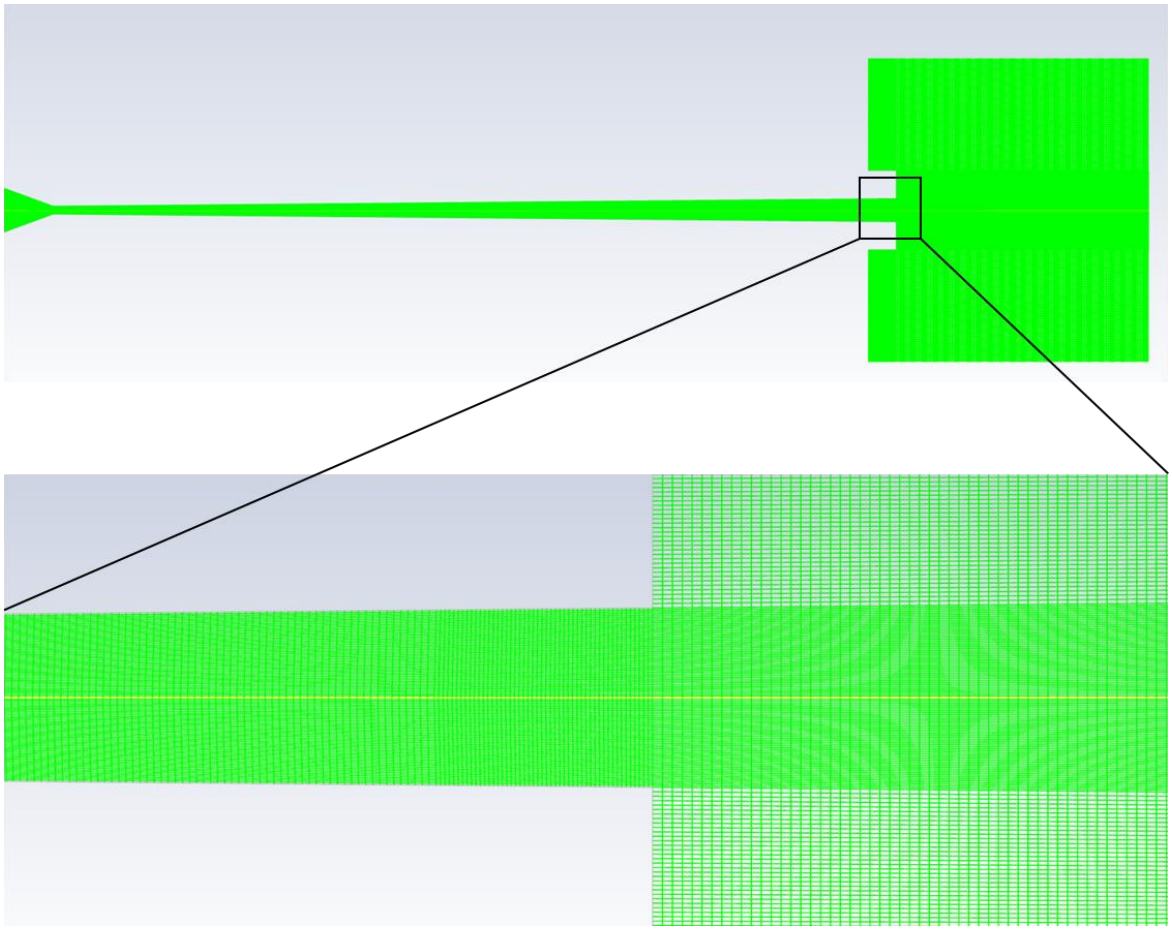

Figure 4.2: The figure shows the meshed CFD model and the refined mesh region, close to the nozzle exit to capture variations in the flow behaviour such as shock waves.

The CFD simulation applied the temperature-dependent Sutherland law for viscosity and a piecewise polynomial for the specific heat capacity of the N_2 gas thermophysical parameters. Other parameters, such as thermal conductivity, are assumed to be constant because they are insensitive to temperature and compressibility [108]. Temperature-dependent thermophysical parameters were also employed for He gas.

The turbulence in the CSAM flow field can be modelled using various formulations of the energy equations in Ansys/Fluent. The type of turbulence model used can influence the accuracy of the CFD results. As more turbulence flow is resolved, the

fidelity of the turbulence model can increase, but at the expense of computational cost. Most turbulence models used for CSAM simulations are based on solving the closure of the Reynolds Averaged Navier-Stokes equations (RANS) [108]. RANS decomposes the instantaneous variables in the Navier-Stokes equations [283]. In this thesis, the realisable $\boldsymbol{k–\varepsilon}$ model was employed to model turbulence in the CFD model. The energy model solves two transport equations that describe the turbulent kinetic energy per unit mass $\boldsymbol{k}$ and the dissipation rate $\boldsymbol{\varepsilon}$. Equations (4.5) and (4.6) provide the two transport equations, where $\boldsymbol{Y_M}$ denotes the dilatation in compressible turbulence, which accounts for the effect of compressibility on the overall dissipation rate, $\boldsymbol{G_K}$ denotes the production of turbulent kinetic energy due to the average velocity gradients, $\boldsymbol{\sigma_k}$ and $\boldsymbol{\sigma_\varepsilon}$ are the turbulent Prandtl numbers for $\boldsymbol{k}$ and $\boldsymbol{\varepsilon}$. $\boldsymbol{C_1}$ and $\boldsymbol{C_2}$ are constants of the realisable $\boldsymbol{k–\varepsilon}$ model. The model provides superior performance for flows under adverse pressure gradients and robust far-wall treatment with low computational cost wall functions. The standard wall function in the CFD model was employed for the near-wall treatment.

$$\frac{\partial \rho k}{\partial t} + \frac{\partial}{\partial x_j}(\rho u_j k) = \frac{\partial}{\partial x_j}\left[\left(\mu + \frac{\mu_t}{\sigma_k}\right)\frac{\partial k}{\partial x_j}\right] - \rho\varepsilon + G_K - Y_M \tag{4.5}$$

$$\frac{\partial \rho \varepsilon}{\partial t} + \frac{\partial}{\partial x_j}(\rho u_j \varepsilon) = \frac{\partial}{\partial x_j}\left[\left(\mu + \frac{\mu_t}{\sigma_\varepsilon}\right)\frac{\partial \varepsilon}{\partial x_j}\right] + \rho C_1 S\varepsilon - \frac{\rho C_2 \varepsilon^2}{k + \sqrt{v\varepsilon}} \tag{4.6}$$

The discrete phase modelling (DPM) approach was employed to simulate the injected particles into the nozzle to compute the particle velocity and temperature. The particles are modelled as discrete entities using mass and momentum conservation equations and are coupled to the gas phase. The gas phase is solved

first, and then the particle parameters are computed based on the resultant gas flow. The particle motion is predicted by the following drag force balance equation given by Newton's second law:

$$m_p \frac{dV_p}{dt} = C_D \rho (V_g - V_p)|V_g - V_p| \frac{A_p}{2} + F_B \quad (4.7)$$

where m_p is the mass of the particle, V_p refers to the particle velocity, t is time, C_D is the drag coefficient, V_g is the gas velocity, A_p is the particle cross-sectional area, and F_B is the body force. The drag coefficient accounts for the Mach number effects on the particle acceleration. The particle temperature T_p, was determined using Equation (4.16), where C_p is the particle specific heat capacity, h_p is the convective heat transfer coefficient and T_r is the recovery temperature dependent on the particle Mach number, M_p. T_r was calculated using the relation, $T_r = T_g(1 + r\frac{\gamma-1}{2}M_P{}^2)$, where r is the recovery coefficient close to 1 in gases, and T_g is the gas temperature. The heat transfer coefficient, h_p (Equation (2.16)) was evaluated from the Nusselt number using the Ranz-Marshall correlation [119] given by Equation (2.17), which is suitable for flow past a sphere. The particle diameter is given as d_p, k_g is the thermal conductivity of the gas, μ_g is the dynamic viscosity of the gas, Pr is the Prantl number of the gas (Equation (2.18)), and Re is the Reynolds number of the particle.

$$m_p C_p \frac{dT_p}{dt} = A_p h_p (T_r - T_p) \quad (4.8)$$

$$h_p = \frac{k_g Nu}{d_p} \quad (4.9)$$

$$Nu = 2 + 0.6 Re^{0.33} Pr^{0.33} \quad (4.10)$$

$$Pr = \frac{C_p \mu_g}{k_g} \quad (4.11)$$

The spatial discretisation scheme employed for solving the Navier-Stokes equation can affect the prediction accuracy of the shockwave structure. The low-order schemes can help with convergence and save computational costs but result in low accuracy in the results. The reverse is the outcome of the high-order schemes [108]. In this thesis, an initial solution was obtained using a first-order upwind scheme, and a final converged solution was obtained using the second-order upwind scheme. A density-based implicit solver was used for the calculations. To aid in the stability of the simulation, the CFD model was started with a Courant number of 1 and subsequently increased incrementally as the solution progressed. To ensure convergence, the residuals of the Navier-Stokes equations were monitored, and convergence was accepted when these values were < 10^{-4}.

An example of the CFD output is presented in Figure 4.3. The figure presents the centre contour map of the gas flow features during the cold spraying process. The flow profile shows shock waves due to the expansion of the gas at the nozzle exit. The particles injected into the gas stream are propelled by the gas flow. The output

of the particle velocity and temperature are extracted and employed as input data for further numerical analysis in this thesis.

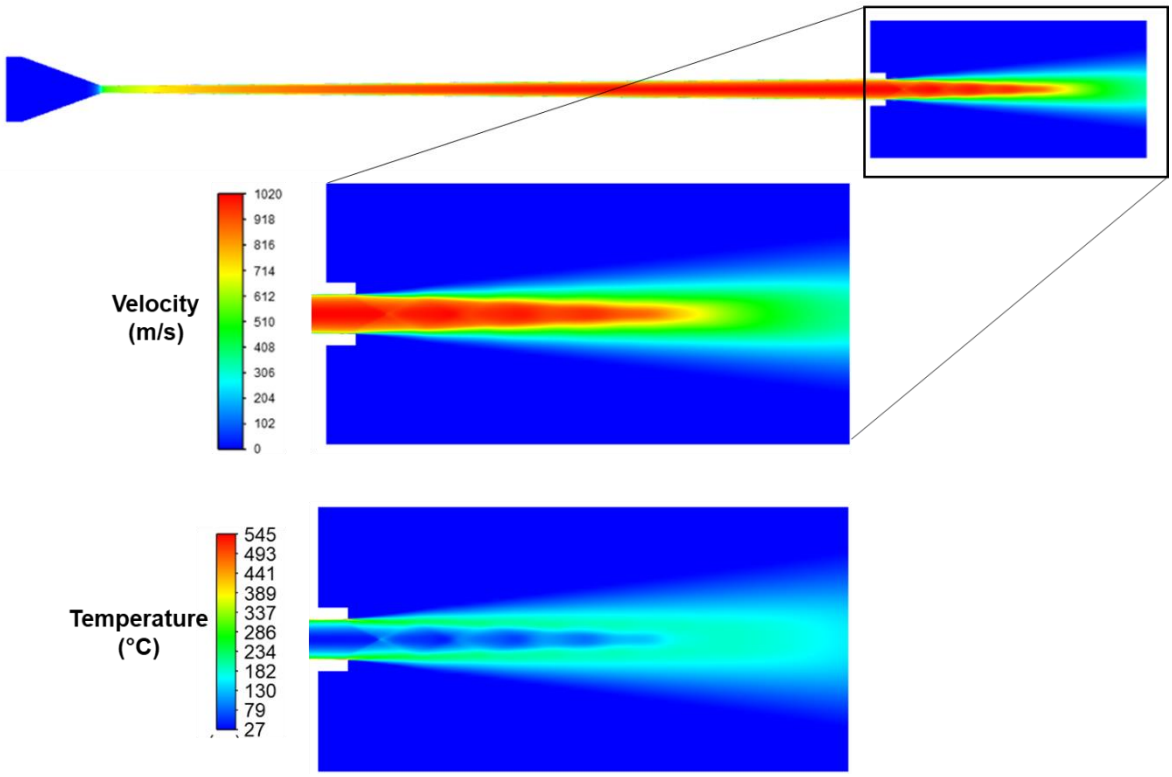

Figure 4.3: Centre contour map of the gas velocity magnitude and static temperature of N_2 gas flowing through the nozzle to the exit of the nozzle. The contour also shows the shock wave (or shock diamonds) at the nozzle exit.

4.2 Particle impact deformation modelling

4.2.1 Single-particle impact

Nonlinear, transient dynamic analysis was performed in Abaqus/Explicit involving the impact of micro-sized high-velocity particles on a substrate to predict the onset of deposition, that is the critical velocity and deformation behaviour of the HEA particles onto various substrates. Because of the geometrical and loading symmetries, a 2D axisymmetric model was employed for the single-particle impact analysis. The shape of the particle was assumed to be perfectly spherical and normal to the substrate during impact. Figure 4.4 shows a schematic representation of the single-particle impact model.

In the single-particle impact model, the substrate was modelled with a height and radius of 8 and 6 times the particle diameter, respectively. The diameter of the spherical particles was 25 µm, which corresponded to the mean particle diameter of the feedstock powder obtained by laser diffractometry. The substrate was modelled with the dimensions to ensure that the reflecting waves from the substrate bottom and far edges reached the impact region only after the particle rebound. The substrate bottom was fixed in all directions (X = Y = Z = 0), and a symmetry boundary condition (X = Y = Z_R = 0) was applied along the lateral edges (y-axis) of the substrate and particle.

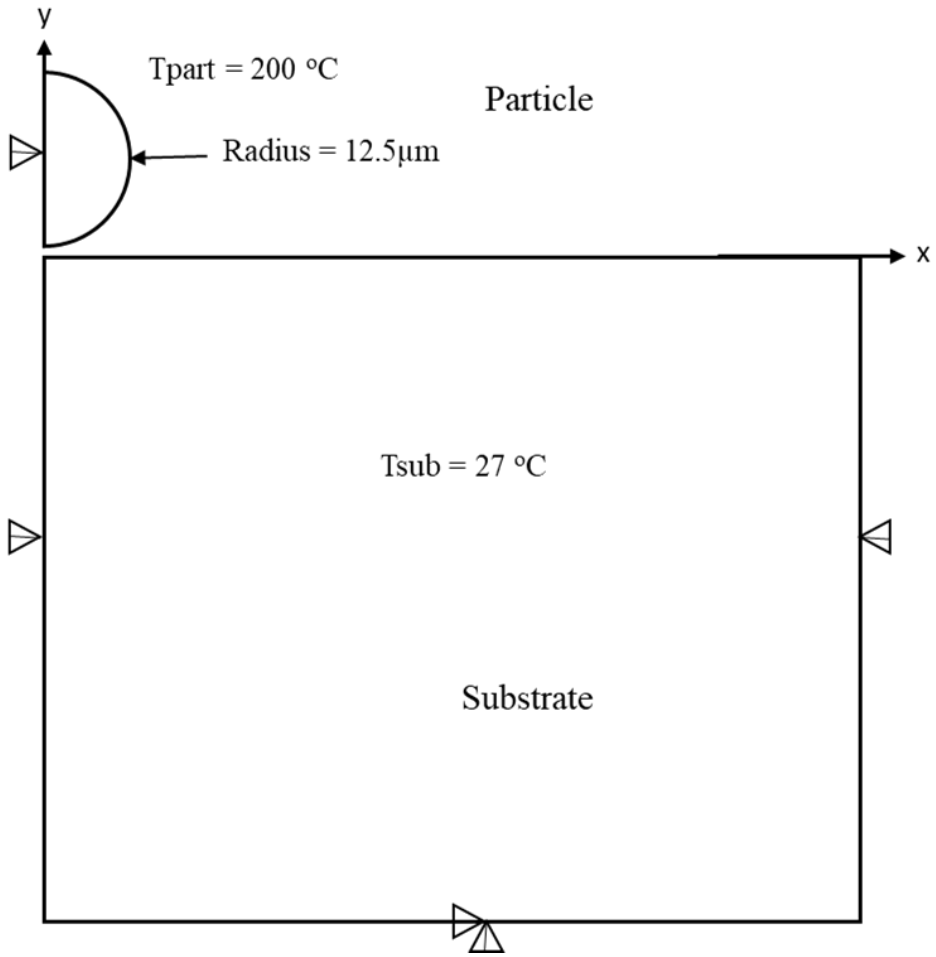

Figure 4.4: Schematic representation of Abaqus single-particle impact FE model.

The heating of the particle owing to the inelastic deformation of the material was assumed to be adiabatic for the single-particle impact model. Also, dynamic explicit with adiabatic heating and dynamic temperature displacement solution techniques were employed for the single-particle impact model. The single-particle impact model meshed with a 4-node bilinear axisymmetric quadrilateral element with reduced integration and hourglass control (CAX4R). Figure 4.5 shows the mesh of the impact region of the single-particle impact.

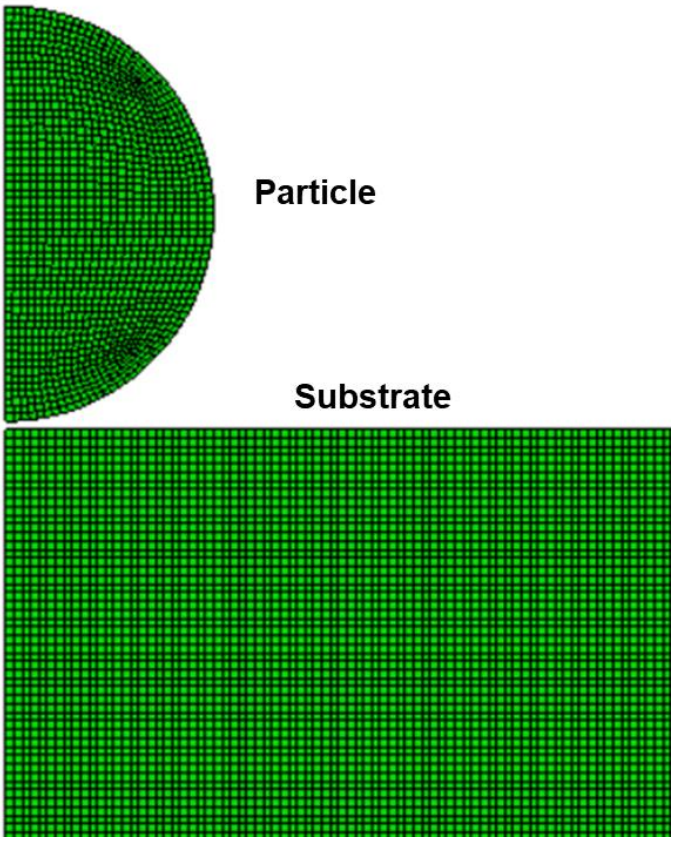

Figure 4.5: Meshed domain of the particle on the substrate. only the impact region of the substrate is presented.

To obtain accurate simulation results, a mesh convergence study was performed, where the mesh size at the HEA particle-stainless steel 304 substrate impact region was varied until there was a negligible difference in the maximum interface temperature with further refinement of the mesh. Figure 4.6 provides the mesh convergence study, with the acceptable difference in the maximum interface temperature between the mesh sizes 0.25 μm and 0.375 μm. Considering the computation time, a mesh size of 0.375 μm was used for further simulations and analysis. In addition, further refinement of the mesh resulted in the early termination of the simulation, which was due to the severity of element distortion at the impact interfaces. It is noteworthy that the mesh size in the substrate was decreased away from the impact region to reduce the overall computational time.

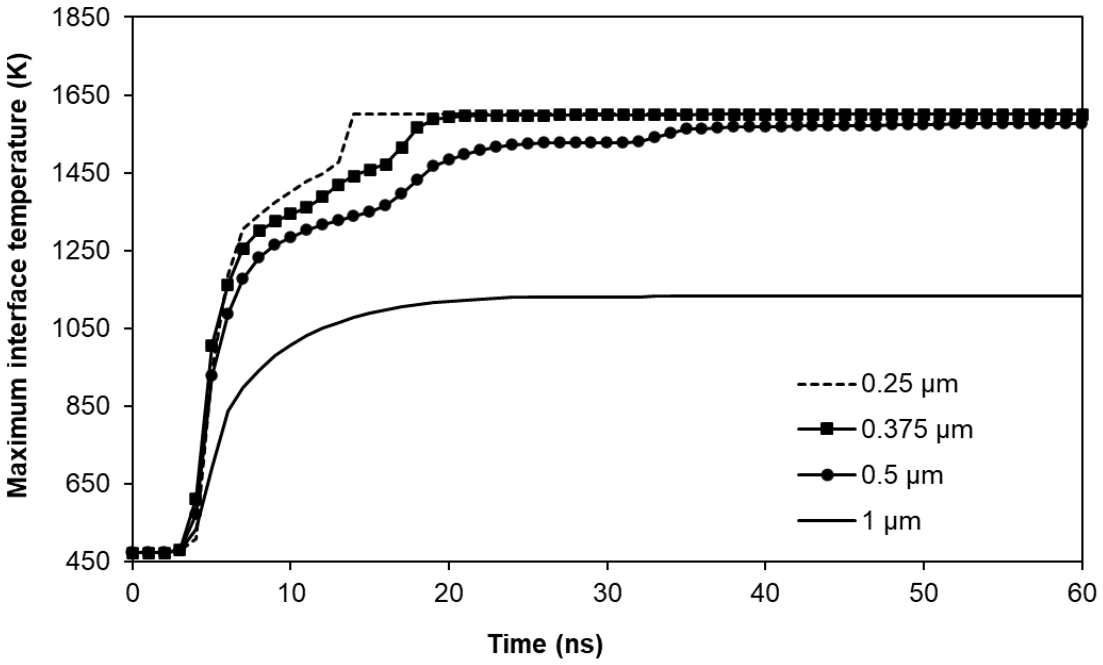

Figure 4.6: Mesh convergence study for a HEA particle on stainless steel 304 substrate at 700 m/s. A mesh size of 0.375 µm was selected for further simulation.

Abaqus/Explicit provides two contact methods for modelling contact interactions: general contact and contact-pair algorithms. The contact pair algorithm is more appropriate for the 2D contact model as it allows interaction behaviours not available in general contact. The general contact is, however, faster and particularly aimed at geometry with multi-elements and complex topologies, making it robust. A surface-to-surface contact pair algorithm was specified for all interface regions in the dynamic impact models. Penalty enforcement in the contact algorithm is specified for this study, where a small penetration between the nodes at the particle and substrate interface is allowed. Because of the nonlinear geometric effect of the particles, a finite sliding formulation was selected. This also allows for arbitrary motion of the surfaces. The balanced weighting contact algorithm was selected for surfaces in contact. A friction coefficient of 0.3 was employed to model the friction between the particles and substrates. It has been shown that a friction coefficient

between 0 and 0.5 has little effect on the output of the FEA [284]. Thus, the friction coefficient employed in this thesis was appropriate for the CSAM deposition modelling.

4.2.2 Multi-particle impact

A 2D plane strain multi-particle impact model, containing 50 randomly distributed particles between 10-45 µm was developed. The number of particles selected was deemed fit to account for both computational time and the limitations of the numerical approach employed. The chosen particle size range corresponds to the experimentally measured data of the feedstock powder. This was employed to investigate the deformation behaviour of the particles when interacting between themselves and with the substrate. The substrate was modelled with a height and width of 450 µm and 800 µm, respectively. A fixed boundary condition was applied to the substrate bottom, whereas the X-displacement constraint (X = 0) was applied to the substrate sidewalls. The model domain for the multi-particle impact simulation is illustrated in Figure 4.7. It should be emphasized that the number of particles depicted is purely for illustrative purposes and does not represent the actual number.

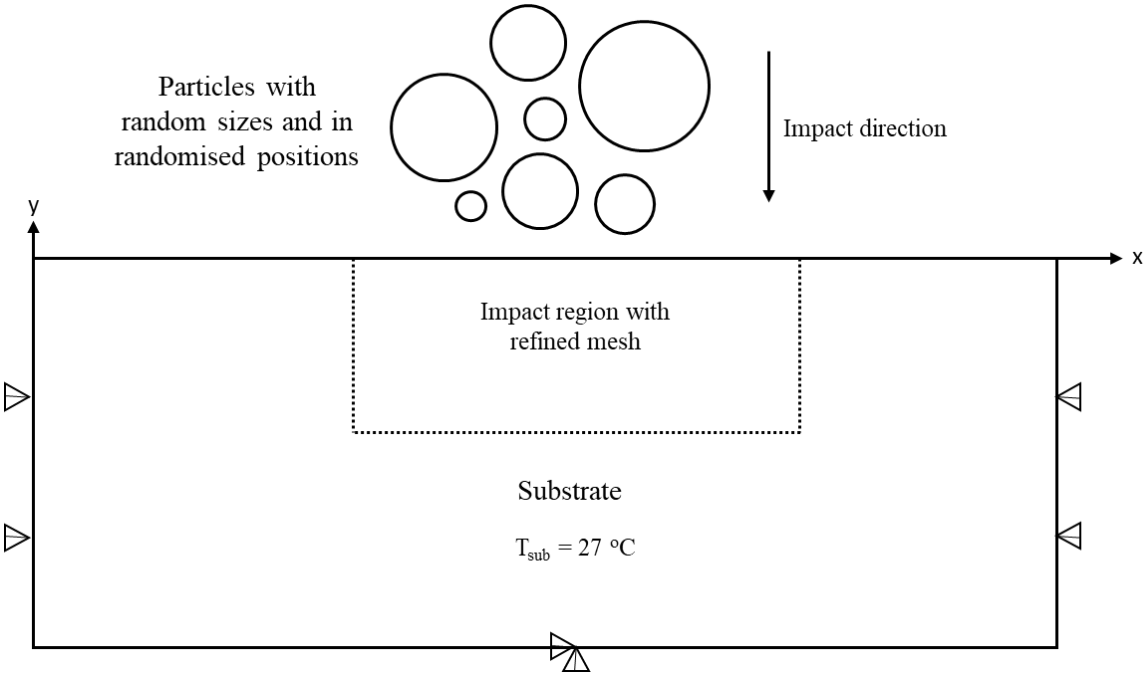

Figure 4.7: Schematic illustration of the multi-particle FEA model domain. The number of particles depicted is for illustrative purposes as it does not represent the actual number of particles employed.

A non-adiabatic condition was assumed for the multi-particle impact model. Nonetheless, 90% of the kinetic energy of the particle upon impact was assumed to be converted to heat, allowing for some heat transfer and stored energy. Dynamic explicit with adiabatic heating and dynamic temperature displacement solution techniques were also employed for the multi-particle impact model.

The multi-particle impact model was meshed with a 4-node plane strain thermally coupled quadrilateral, bilinear temperature-displacement element type, with reduced integration and hourglass control (CPE4RT). Figure 4.8 shows the meshed multi-particle model captured from the central region near the substrate surface.

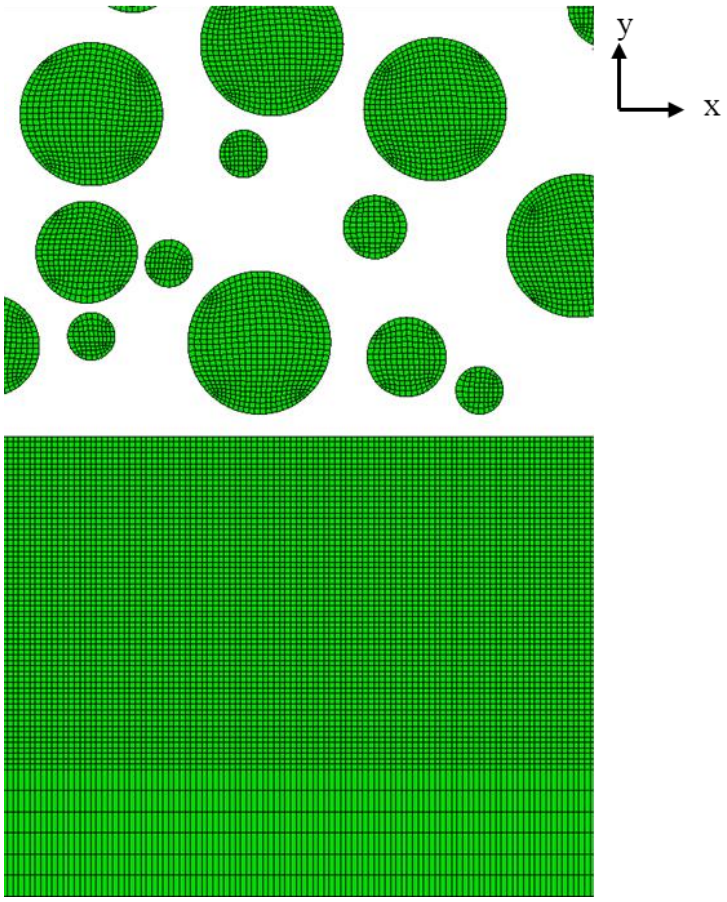

Figure 4.8: The multi-particle FEA model showing the meshed particle and the impact region in the substrate. Images were taken from the central region of the model domain.

The mesh size obtained from the mesh convergence study in the single-particle model was employed for the multi-particle impact model. Also, surface-to-surface contact was employed for the multi-particle model with all surfaces constrained to remain in contact during deposition. The contact conditions employed in the single-particle impact model were also employed for the multi-particle impact analysis.

4.2.3 Material model

The material model in FEA is a crucial part of the simulation as it defines the physics and behaviour of the material under investigation in the FE code. The accuracy of such models can influence the outcome of the FEA. In this thesis, the FEA

accounted for the strain hardening, strain-rate hardening, thermal softening, and heating due to friction, plastic, and viscous dissipation of the HEA and substrate materials during deformation. The behaviour of the materials was defined using constitutive equations or material models. The Johnson-Cook (J-C) material model was employed to capture the plastic deformation of the CoCrFeNiMn HEA and substrate materials in the transient nonlinear dynamic FEA. The J-C model assumes that the material is an isotropic linear-elastic, strain-rate-sensitive, strain-hardening, and thermally softening plastic material. The model utilises the J_2 yield function form of $F(\tau, \varepsilon) = \tau - Y(\varepsilon)$, where $Y(\varepsilon)$ is the von Mises stress and τ is the equivalent shear stress. This follows the von Mises yield criterion, which states that the material begins to yield or flow when the von Mises stress reaches the material yield strength. The von Mises stress for the J-C model is given by Equation (4.12), where $\varepsilon^* = \dot{\varepsilon}/\varepsilon_0$, $\dot{\varepsilon}$ is the equivalent plastic strain rate, ε_0 is the reference strain rate, and ε is the equivalent plastic strain. The other parameters were defined as follows: A is the yield strength (MPa) at zero plastic strain and room temperature, B is the strain hardening (MPa), n is the strain-hardening exponent, C is the strain rate constant, and m is the thermal softening exponent.

$$Y(\varepsilon) = [A + B\varepsilon^n][1 + CIn(\varepsilon^*)][1 - \theta^m] \quad (4.12)$$

The last part of the J-C constitutive equation given in Equation (4.12) accounts for the thermal softening of the material and θ is given in Equation (4.13). Where T is the homologous material temperature, T_{ref} is the reference temperature and T_{melt} is the melting temperature of the material. The adiabatic increase in temperature T is given by Equation (4.14), where ρ is the material density, β is the inelastic heat

fraction taken as 0.9, and C_P is the specific heat capacity of the material. The thermal response of the material in the Abaqus/Explicit model was described using the specific heat capacity, whereas the elastic response was assumed to be linearly elastic and described using the elastic modulus and Poisson's ratio of the HEA and substrate materials.

$$\theta = \frac{T - T_{ref}}{T_{melt} - T_{ref}} \tag{4.13}$$

$$T = T_{ref} + \frac{\beta}{\rho C_P} \int_0^{\varepsilon} Y(\varepsilon) d\varepsilon \tag{4.14}$$

4.3 Residual stress modelling

4.3.1 Introduction

A computational procedure for analysing the through-thickness residual stress of a thick CSAM HEA deposit on an SS304 substrate using finite elements model (FEM) with the Abaqus/Standard (or implicit procedure) is presented here. The thermal and mechanical effects of the CSAM process were simulated using a sequentially coupled thermo-mechanical numerical method. A 2D plane strain model was developed to simulate this process. Developing and simulating the process using a 2D model can reduce computational time and cost when compared with a 3D model. Although the temperature of the heat generated by the gas stream during CSAM is often lower than the melting temperature of the feedstock material, recent research has found that heat from the gas can have a significant impact on the associated

thermal field [84,228–230,285]. Additionally, increasing the nozzle dwell time during spraying can increase the heat transferred to the deposit. Consequently, a sequentially coupled thermo-mechanical model can be employed, where the heat generated during plastic deformation has little effect on the thermal field compared to the gas stream. In the thermal analysis, however, the FEM in this thesis considered the heat generated by plastic deformation and was applied as an initial temperature field in the thermal model. The FEM employed in this thesis is similar to the work of Bansal et al. [225] on the hybrid implicit-explicit FEM.

The FEA had three stages: explicit dynamic analysis, and thermal and stress analyses. The explicit dynamic analysis employs the output of the multi-particle impact model described in Section 4.2.2. Thermal analysis, on the other hand, was performed to determine the temperature distribution in the deposit-substrate system, following that was stress analysis performed to specify the stress and strain fields. Using the "Create Predefined Field" command in Abaqus, the temperature distribution from the thermal analysis was considered thermal loading in the stress analysis. The temperature and deposition stress of the deposit and substrate from the explicit dynamic analysis were applied as the initial conditions for the thermal and stress analyses. The residual stress analysis presented in Chapter 8 provides the values extracted from the explicit dynamic analysis. The residual stress analysis step types "heat transfer" and "static, general" were selected for the thermal and stress analyses, respectively. The mesh model for the thermal and stress analyses was the same for the models to be coupled.

4.3.2 Modelling layer-by-layer material deposition

To accurately simulate the CSAM process in the thermal and mechanical/stress FEM, a set of elements representing the deposit, layer by layer, must be created beforehand. Using the “Modal Change” module in the Abaqus finite element code, these elements can be activated or deactivated (“element death and birth” method) based on the physics of the problem being analysed. At the start of the analysis, all elements representing the deposit were deactivated using a single analysis step. This process involves resetting any previous loading conditions to zero, ultimately leading to a new equilibrium state and convergence that satisfies the initial boundary conditions. The FEM utilised here is computationally efficient as it reduces the material stiffness matrix at the beginning of the analysis, resulting in reduced computational time.

The FEM was established using the dimensions of the substrate (60 mm × 30 mm × 2 mm) and deposit (60 mm × 30 mm × 4.5 mm). Figure 4.10 shows the 2D meshed FEM: the deposit was divided into four layers as four passes were sprayed, following the spraying conditions provided in Chapter 8. Each layer was subdivided into an appropriate number of 2-mm wide and 1.125-mm thick ribbons corresponding to a line scan of the spray nozzle on the substrate. Each ribbon in each layer represents the set of elements to be activated. A new analysis step was defined for each activation, resulting in 120 calculation steps. Each layer was bonded to each other using a “tie constraint” in Abaqus. The tie constraint was used to bond the deposited layers together; however, this bonding constraint does not fully represent the actual bonding constraint between the deposited layers of the CSAM deposit. Also, the

layers interface in the FEM are of smooth surfaces, but in CSAM deposits, the deposited layer interface is usually wavy or rough. The tie constraint and interface shape employed in the FEM are simple representations of the actual deposited layers to allow for a computationally cost-effective model. The tie constraint likely over-constrains the deposited layers but is assumably within an acceptable range. To improve on the limitations of the FEM employed in this thesis, future investigations can employ the rough bonded interface of the deposited layers of the CSAM deposit in the FEM, which may provide a more accurate analysis of the residual stress.

As the nozzle moves over a position on the surface, the inactive material/ribbon is activated, and the thermal input or load is activated within that analysis step. The deposit was formed by rastering the nozzle from the top of the plate to the bottom, as illustrated in Figure 4.9. After depositing the first layer, the nozzle moves back to its original starting point, and the deposition of the second layer starts. An additional analysis step was set for the final cooling of the component after spraying.

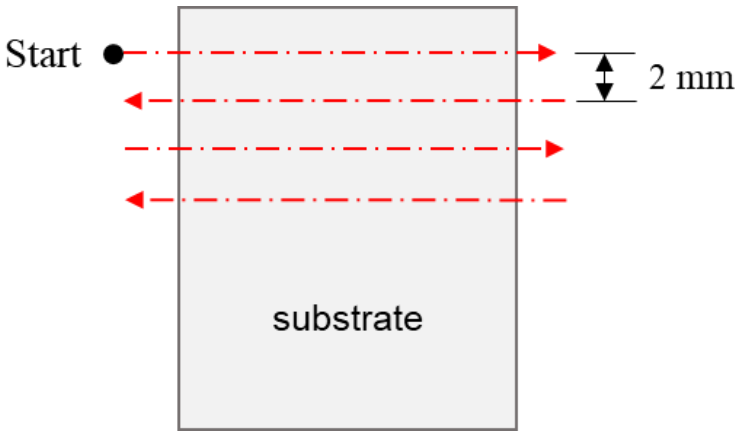

Figure 4.9: Schematic of nozzle movement for the deposition of a layer on the substrate during the CSAM of the deposit.

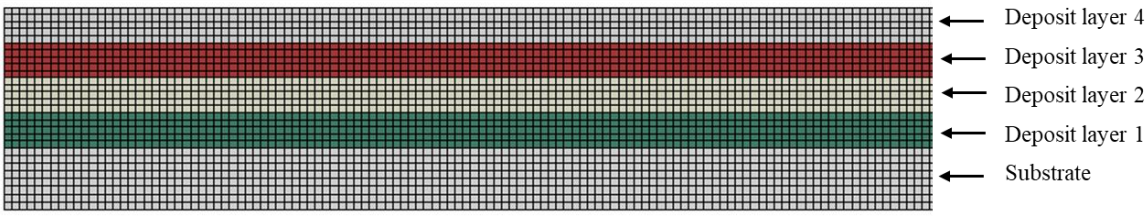

Figure 4.10: Meshed FEM for the sequentially coupled thermo-mechanical model, showing the substrate and deposit layers stack upon one another, using a "tie-constraint". Half the model dimension is shown here.

The FEA consists of a set of time steps, with each step representing the activation of a ribbon. To ensure accuracy, each step analysis was set to 4 s, the approximate time for the nozzle to move across the width of a layer during the CSAM process. The application of each ribbon includes a series of time increments, with a maximum allowable temperature change of 10 K set per increment. The cooling phase or step was set to 1800 seconds, which is the approximate time it takes for the sample to be removed from the sample holder or constraint, after spraying. The exact time was applied for the step analysis in the thermal and mechanical/stress models.

4.3.3 Thermal analysis

In the thermal analysis, the governing transient heat transfer Equation (4.15) (for a stationary medium) [286] is solved. Where $\boldsymbol{T}$ is the current temperature, $\boldsymbol{Q}$ is the rate of heat generation within the model and $\vec{\boldsymbol{q}}$ is the heat flux vector. The heat flux vector $\vec{\boldsymbol{q}}$ is solved using the Fourier's law of conduction expressed in Equation (4.16) [17,287], where $\boldsymbol{k}$ is the thermal conductivity of the materials in the model and $\boldsymbol{\nabla}$ represents the spatial gradient operator. The transient thermal analysis in time, $\boldsymbol{t}$, also requires the material properties of specific heat capacity at constant pressure, $\boldsymbol{C_p}$, and density, $\boldsymbol{\rho}$.

$$\boldsymbol{\rho C_p \frac{\partial T}{\partial t}}\ (\boldsymbol{x, y, z, t}) = \ -\boldsymbol{\nabla}.\vec{\boldsymbol{q}}\ (\boldsymbol{x, y, z, t}) + \boldsymbol{Q}\ (\boldsymbol{x, y, z, t}) \qquad (4.15)$$

$$\vec{\boldsymbol{q}} = \ -\boldsymbol{k\nabla T} \qquad (4.16)$$

Boundary conditions were applied to the above equations to solve them and obtain a closed solution to the thermal problem. The surfaces of the model underwent complex thermal energy exchange with their surroundings through convective and radiation heat fluxes, governed by Newton's (Equation (4.17)) and Stefan–Boltzmann's laws (Equation (4.18)), respectively:

$$\dot{q} = h\,(T_{\infty} - T) \tag{4.17}$$

$$\dot{q} = \sigma\epsilon[(T - T_{abs})^4 - (T_{\infty} - T)^4] \tag{4.18}$$

where, $\dot{q}$ is the surface heat flux, T is the temperature across the surface, ϵ is the emissivity of the material was taken as 0.8 for stainless steel and nickel-based superalloy [17,288], T_{abs} is the absolute zero temperature, T_{∞} is the ambient and sink temperature taken as 298 K, σ is the Stefan-Boltzmann constant given as 5.67 × 10^{-8} W/m^2K^4 and h is the surface convective heat transfer coefficient taken as 25 W/m^2K for air.

To accurately model the CSAM deposition, the heat flux from the gas jet impinging on the deposit's surface was accounted for. Moreover, the temperature increase in the model can be influenced by the hot gas impinging on the surface and the thermal energy from particle deformation. These deposition factors must be considered in the thermal analysis of the CSAM process. A uniform surface heat flux was assumed for the thermal flux produced by impinging gas. This was performed to simplify the model and make it more straightforward to implement. In this case, Equation (4.19) was employed to evaluate the thermal flux, $\dot{q}_g$ of the impinging gas, where h_g is the heat transfer coefficient of the gas, and T_g is the temperature of the impinging gas jet.

$$\dot{q}_g = h_g \left(T_g - T\right) \tag{4.19}$$

Various methods have been developed and employed to measure h_g and T_g during CSAM, using a thermal infrared camera and a low-conductivity substrate coupled with CFD models [228–230,285]. However, empirical equations were employed in this thesis to approximate the values of h_g and T_g. With the experimental spraying parameters, such as the gas pressure and temperature, a surface heat flux load of 1.3 W/mm^2 was evaluated and applied on the surface of the deposit.

An example of the thermal history of the CSAM process during the deposition of each ribbon and then a layer is displayed in Figure 4.11. The figure shows the temperature or thermal field of the deposited material and the substrate. As the nozzle moves past the surface of the substrate, heat is generated and conducted to the colder region and previously deposited ribbon. The analysis performed thus represents an approximate solution to the thermal field of the system during the CSAM process.

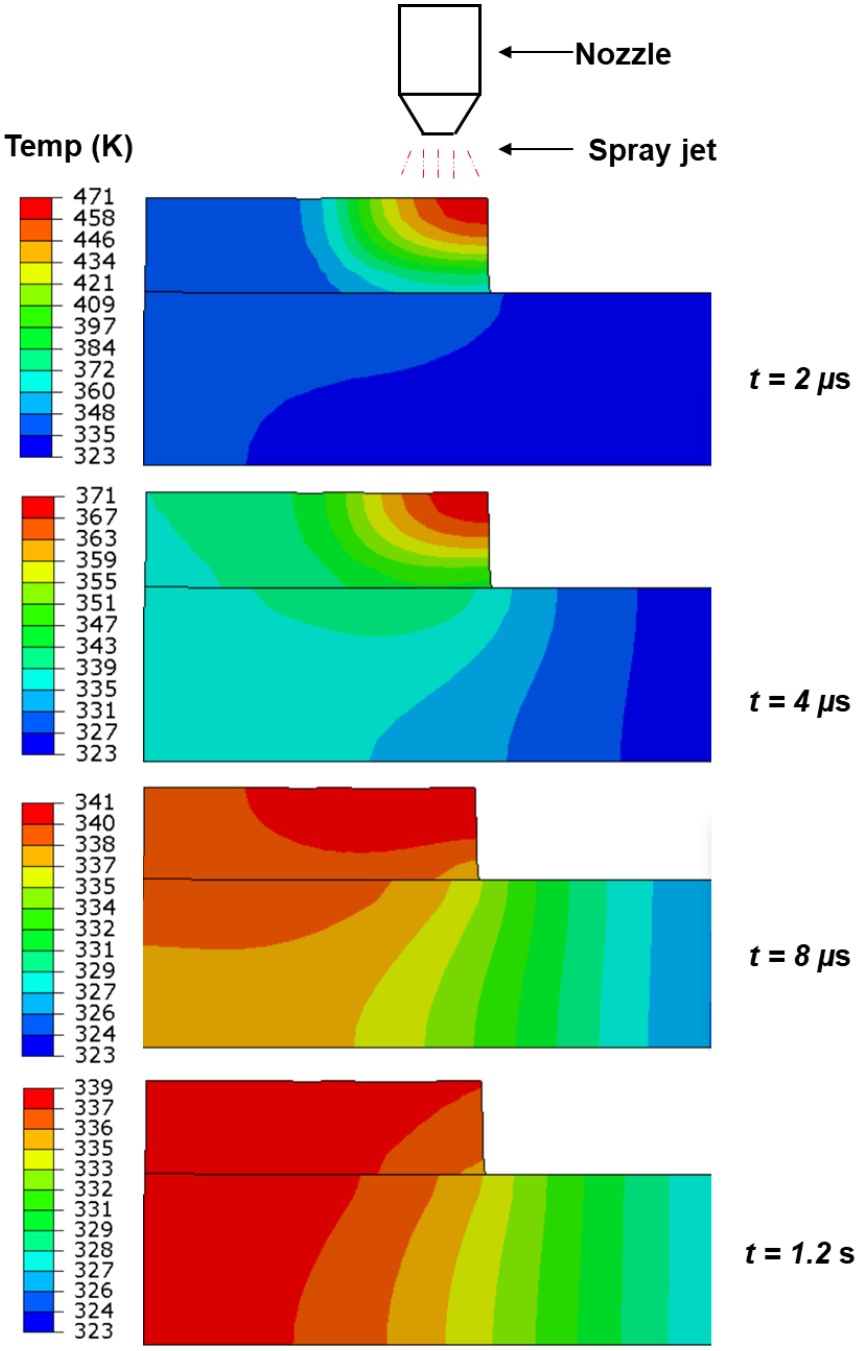

Figure 4.11: Example of the thermal history of a ribbon of a layer being deposited on the substrate. Heat is dissipated during the deposition process, the colder region becomes hotter as the nozzle moves past the substrate.

A mesh convergence study was conducted on the thermal model, as shown in Figure 4.12. The temperature history of a node at the substrate centre was plotted with different mesh sizes until convergence was reached, where the temperature history showed a negligible difference with the mesh size. A mesh size of 0.25 mm

was deemed sufficient for the numerical model considering computational cost and accuracy. The same mesh size was used for both the thermal and mechanical models.

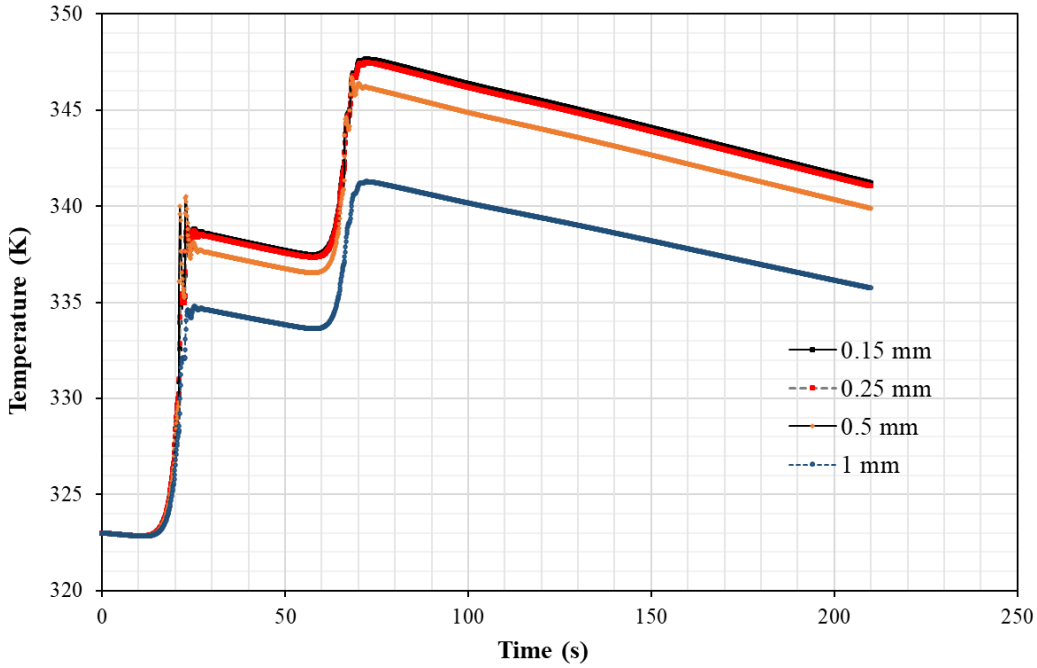

Figure 4.12: Mesh sensitivity study results showing the temperature history of a node at the centre of the substrate surface. The mesh size of 0.25 mm was employed for the thermo-mechanical FE model.

4.3.4 Stress (or mechanical) analysis

This stage of the analysis required the temperature histories of the thermal analysis to be applied as input data to the stress analysis model. The same thermal FEM was used except for the element type and boundary conditions. Based on the low-temperature CSAM process, the feedstock material is not expected to melt, meaning there is no phase transformation. As a result, the total strain, $\boldsymbol{\varepsilon_T}$ of the deposit-substrate system can be decomposed into three components given by Equation (2.1) [17,287]. Herein, the elastic strain component $\boldsymbol{\varepsilon^e}$, was modelled using

the isotropic Hooke's law with temperature-dependent elastic modulus and a constant Poisson's ratio. The thermal strain $\boldsymbol{\varepsilon^{th}}$, was computed using the temperature-dependent thermal expansion coefficient of the materials in the FEM in conjunction with the temperature history of the heating and cooling phases of the deposition process. The plastic strain $\boldsymbol{\varepsilon^{p}}$, on the other hand, was computed using a rate-independent plastic model following the von Mises yield criterion, temperature-dependent mechanical properties, and the isotropic hardening law. Because there is likely minimal thermal cyclic loading owing to the low-temperature deposition process, the isotropic hardening model was deemed sufficient to estimate the plastic strains in the FEM.

$$\boldsymbol{\varepsilon_T = \varepsilon^e + \varepsilon^p + \varepsilon^{th}} \tag{4.20}$$

The mechanical/stress analysis employed a thermo-elastic-plastic material model based on the von Mises yield criterion. The stress-strain relationship in Equations (4.21) and (4.22) [289] was computed for the stress values incrementally, using a full Newton-Raphson integration scheme. $\{\boldsymbol{D^e}\}$ is the elastic stiffness matrix, $\{\boldsymbol{D^p}\}$ is the plastic stiffness matrix, $\{\boldsymbol{C^{th}}\}$ is the thermal stiffness matrix, $\boldsymbol{d\sigma}$, $\boldsymbol{d\varepsilon}$, and $\boldsymbol{dT}$ are the stress, strain, and temperature increments, respectively.

$$\{\boldsymbol{d\sigma}\} = \{\boldsymbol{D^{ep}}\}\{\boldsymbol{d\varepsilon}\} - \{\boldsymbol{C^{th}}\}\boldsymbol{dT} \quad (4.21)$$

$$\{\boldsymbol{D^{ep}}\} = \{\boldsymbol{D^{e}}\} + \{\boldsymbol{D^{p}}\} \quad (4.22)$$

It is necessary to apply appropriate boundary conditions to find a solution for the systems of equations that represent the stress or mechanical formulation. The actual representation of the mechanical constraint provided by the support or sample holder during the CSAM deposition process is critical for accurately predicting deformations and stresses in the deposit-substrate system using the FEM. Moreover, the literature has scarce information on the clamping process and its implications on component distortion and residual stress during CSAM. This suggests the need for both numerical and experimental investigations on the influence of sample clamping on the residual stress of manufactured parts. For the case considered in this thesis, mechanical boundary conditions were applied on the nodes at the substrate bottom edges to prevent rigid-body motion because no fixed clamps were used. However, because of the constraint provided by the sample holder, as shown in Figure 4.13a, an additional displacement constraint in the Y-direction was applied to the bottom surface of the substrate in the FEM, as shown schematically in Figure 4.13b. This boundary constraint (applied on the substrate bottom) was deactivated after the cooling phase to determine the final residual stress state.

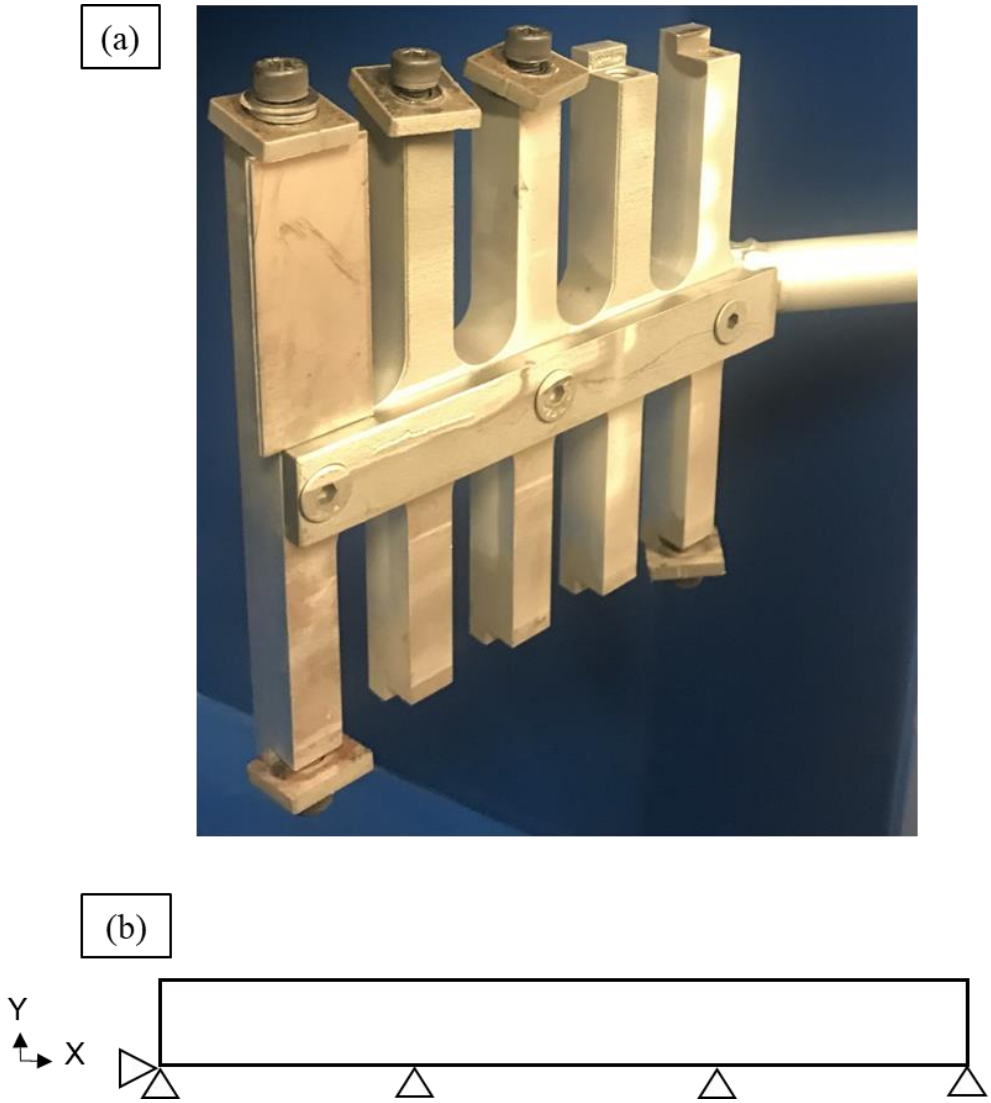

Figure 4.13: (a) shows the image of the CSAM sample holder, showing the mechanical constraint provided by the sample holder, and (b) shows a schematic illustration of the mechanical boundary conditions applied to the stress FEM.

An example of the stress analysis for each ribbon of a layer of the deposit on the substrate is presented in Figure 4.14. The figure shows tensile and compressive stresses formed in the sample during the CSAM process. The influence of the thermal loading of the sample presented in the example in Figure 4.11 can be seen in the stress evolutions of the sample in Figure 4.14. The unloading of the system and removal of the support would result in residual stress formed in the sample as presented in Chapter 8.

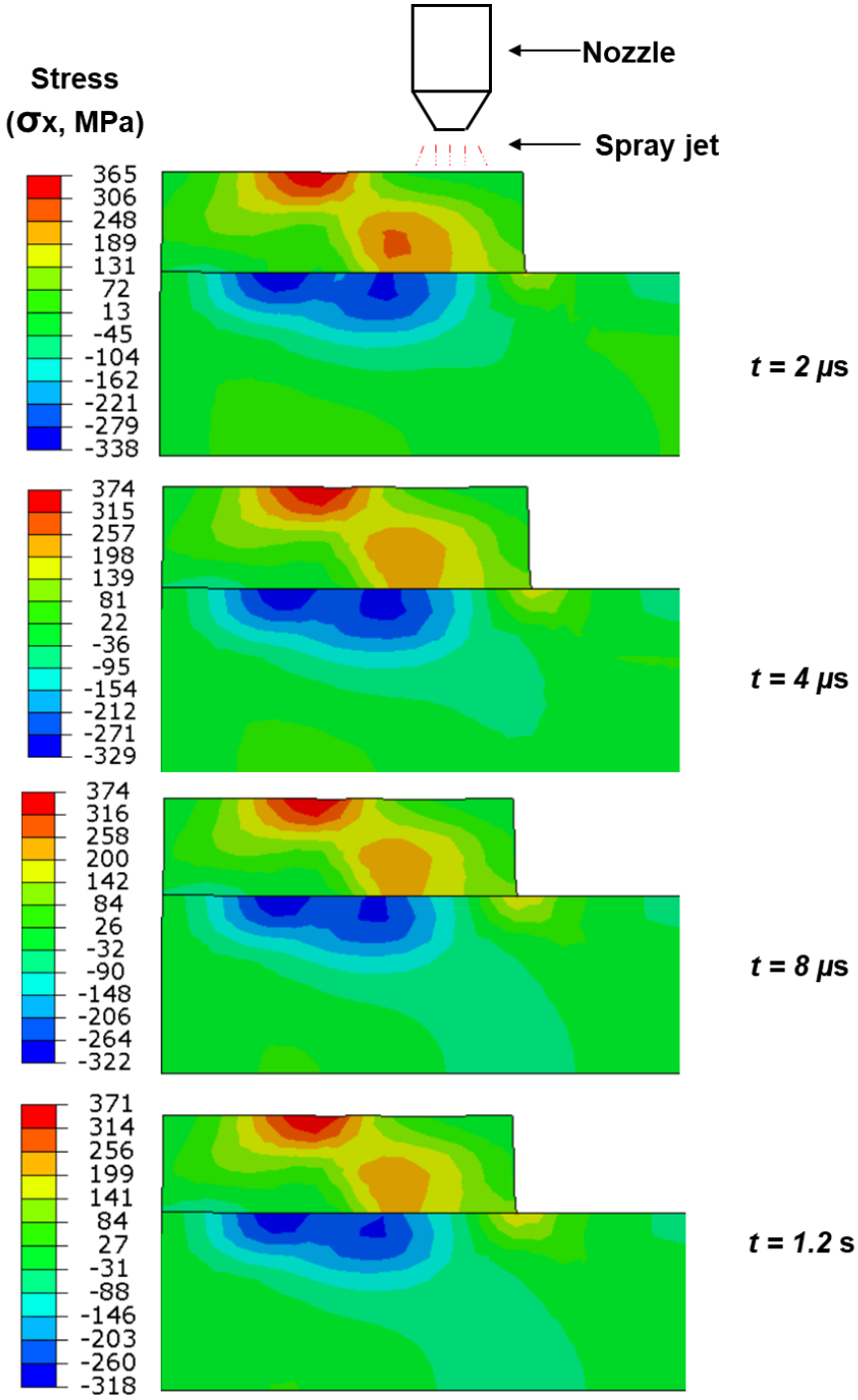

Figure 4.14: Shows an example of the stress evolutions during the CSAM process of a ribbon of the deposit on the substrate. Tensile stress was formed in the deposit whereas compressive in the substrate during the CSAM process. With time the area of maximum compressive and tensile zones changes.

4.3.5 Material properties

Temperature-dependent thermal and mechanical property data are needed for the CoCrFeNiMn HEA, and stainless steel 304 materials considered for the thermo-mechanical FEM. The material property data employed for the residual stress analysis—thermal and mechanical analysis, were obtained from experimental test data in the literature. Figure 4.15 [42,290,291] and Figure 4.16 [292,293] present the thermal-mechanical property data for the HEA and stainless steel 304 materials. The material property data were specified within Abaqus in tabular form, and the Abaqus FE code employs linear interpolation to determine material properties between the specified data. It is noteworthy that the irregular shape or anomaly observed for the specific heat capacity of the HEA presented in Figure 4.15a is indicative of the effect of phase transformation occurring within the material at the tested temperature (above 850 K). Phase transformation has been reported to be formed in this HEA during annealing at intermediate temperatures [239], which may have likely influenced the data of the plot presented here. Nevertheless, since the Abaqus FEA code employs linear extrapolation, data input in the FEM was extrapolated by the Abaqus FEA code for the specific heat capacity above 800 K.

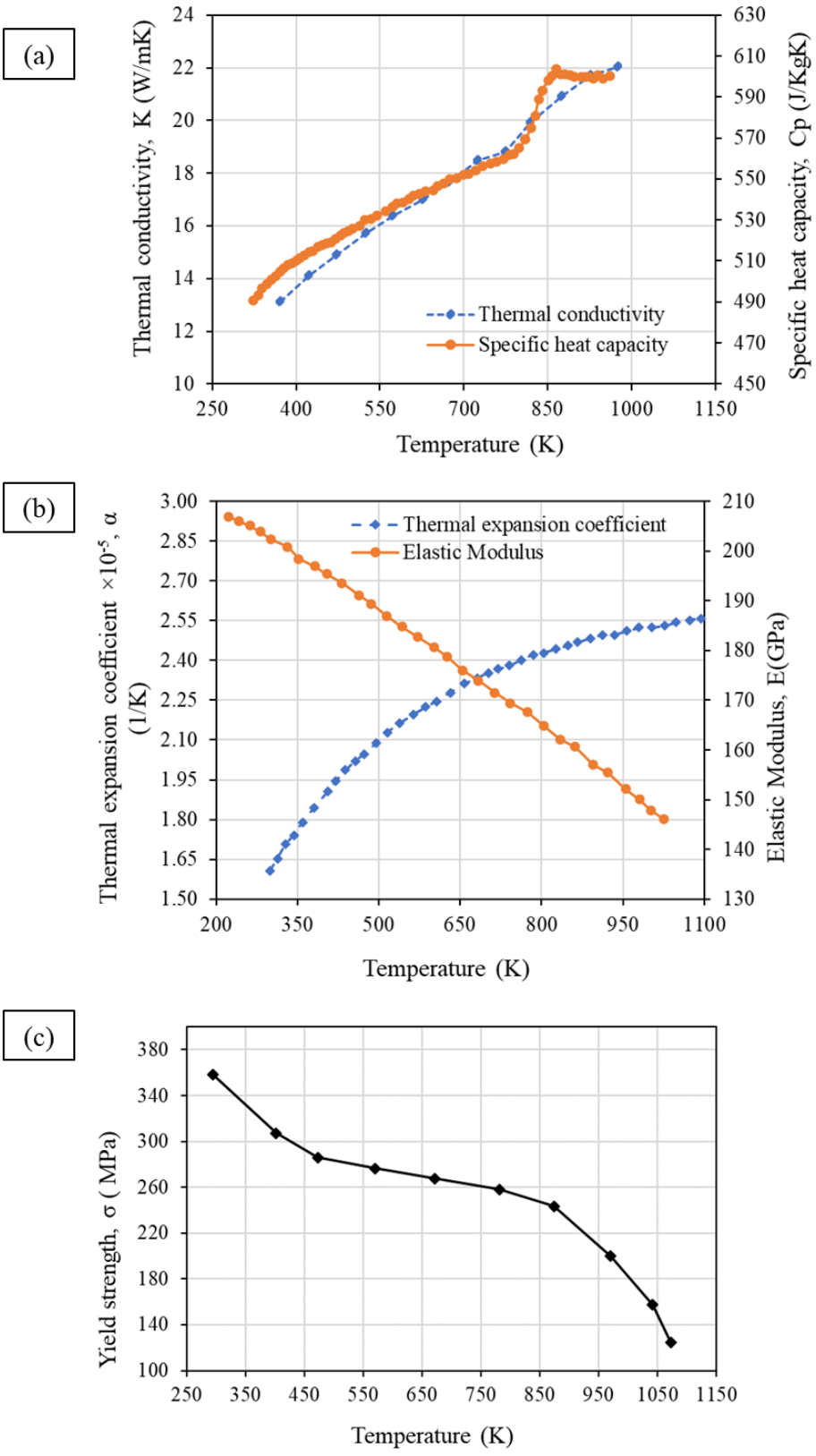

Figure 4.15: Temperature-dependent thermo-mechanical material properties for CoCrFeNiMn HEA (a) thermal conductivity, ***k*** and specific heat capacity, C_p, (b) Thermal expansion coefficient, ***α*** and Elastic modulus, ***E*** (c) Yield strength, ***σ*** [42,290,291].

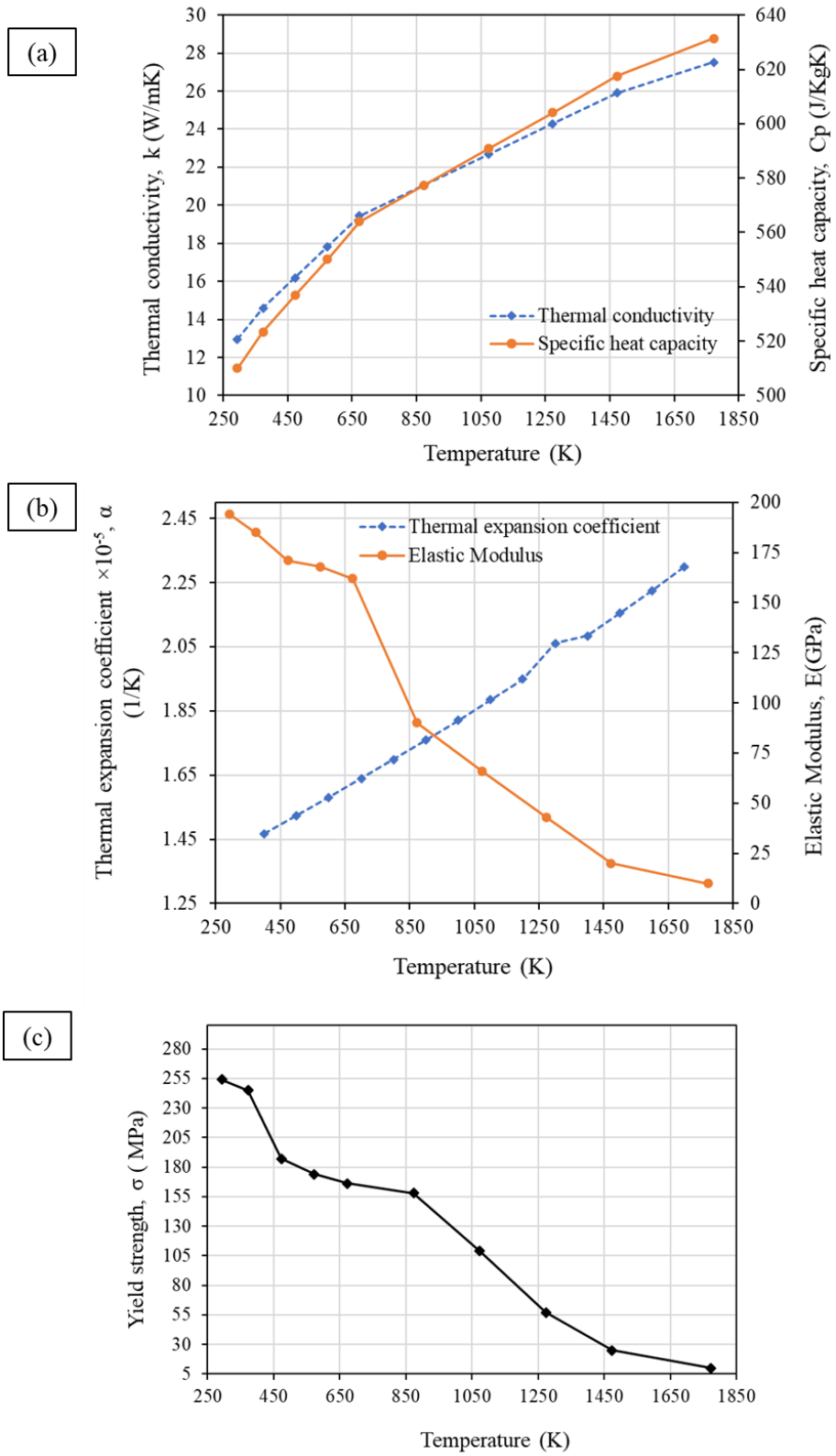

Figure 4.16:Temperature-dependent thermo-mechanical material properties for austenitic stainless steel 304L (a) thermal conductivity, ***k*** and specific heat capacity, C_p, (b) Thermal expansion coefficient, ***α*** and Elastic modulus, ***E*** (c) Yield strength, ***σ*** [292,293].

5 Experimental and numerical analysis of the deformation behaviour of CoCrFeNiMn HEA particles onto various substrates during CSAM

CSAM is a solid-state material deposition technique that relies largely on the kinetic energy of the powder particles to form dense deposits. During CSAM, solid powder particles (typically, 5-50 μm in diameter) are accelerated in a jet of compressed gas (N_2, He or Air) to supersonic velocities through a de-Laval nozzle [21,22]. The technique utilises the layer-by-layer approach to create deposits or components through the plastic deformation of the sprayed particles albeit below the melting point of the feedstock material [57]. Generally, there exists a critical velocity for a given material at a given particle temperature and size such that the transition from rebounding to deposition of the sprayed particles occurs [56,57]. This is especially important for new materials such as high-entropy alloys (HEAs), as it is desirable to know the window of deposition of the material for CSAM.

There have been several experimental investigations and numerical analyses published in the past decades on impact-induced bonding mechanisms in the CSAM of several metallic materials, which is still a matter of some debate. The impact-induced bonding mechanisms in the CSAM of materials can be broadly classified as metallurgical bonding [56,139], mechanical interlocking [40,139], and material intermixing [140,142]. Metallurgical bonding is attributed to the metal jetting of particles and substrates with similar material properties (such as density and hardness), associated with adiabatic shear instability (ASI) [56] or shockwave

release mechanisms [136]. A detailed discussion of these mechanisms has been provided in Section 2.4.1. These impact-induced bonding mechanisms have been observed in a wide range of deposited materials, such as Cu [56,91], Ni [131,153,178,294], Ti [173,192,295], and Al [86,139,156], on various substrates, with similar and dissimilar material combinations. However, the impact phenomena and bonding mechanisms of CoCrFeNiMn HEA have not been extensively explored [63].

The prevailing hypothesis for metallurgical bonding is ascribed to ASI which occurs when there is localised high-strain-rate plastic deformation at the particle-substrate interface due to the dynamic shearing load. At a high shearing strain, heat is generated due to stress and strain rate, causing thermal softening of the materials, which dominates the strain-hardening and reduces the flow stress. This deformation process can result in the formation of a jet-type outflow of materials at the impact interfaces, which can disrupt thin surface oxide films and thus enable intimate contact of fresh metal-metal interfaces, resulting in bonding [56,57,133]. As mentioned previously, the critical velocity is the particle impact velocity that necessitates bonding or initiates ASI [57]. Consequently, it is desirable to understand the deformation behaviour of the CoCrFeNiMn HEA and predict its critical velocity on various substrates.

The impact and deformation behaviour of CoCrFeNiMn HEA sprayed onto various substrates was investigated by Nikbakht et al. [63]. In their study, the deposition of CoCrFeNiMn HEA particles onto nickel, In625, and stainless steel 304 substrates showed impact morphology that was strain-rate, material-, and microstructure-dependent. Deformation twinning and FCC-HCP phase transformation features

were observed in the sprayed particles, which were attributed to the high strain-hardening rate of the HEA. It was reported that the CoCrFeNiMn HEA had the highest critical shear strain for strain localisation compared to the substrate materials. The excellent strain hardening and resistance to shear localisation of the HEA contributed to the high critical shear strain, which could postpone shear localisation. Consequently, a high critical velocity might be required for the complete bonding of the sprayed particles; however, the critical velocity of the HEA based on the concept of ASI was not investigated in their study.

Finite element analysis (FEA) is often employed to investigate the deformation behaviour of particles and particle-substrates in CSAM because of the time scale and contact nature of the process, which is very challenging to analyse experimentally. Although post-mortem microstructural and microanalytical examinations have been performed using several techniques, different numerical tools have been employed to investigate the impact behaviour of particles and substrates during CSAM, with several authors discussing how different spraying parameters influence the impact behaviour [159]. In addition, different numerical methods have been employed, such as the Lagrangian and Eulerian methods and the Smoothed Particle Hydrodynamics (SPH) method [159,160]. Among these methods, the Lagrangian method is computationally more efficient and facilitates the treatment of complex material models, such as history-dependent material constitutive relations [160]. Although the Lagrangian method is associated with extreme mesh distortion at impact interfaces, it was the first and has been the most used finite element (FE) method for CSAM modelling [56,159].

The constitutive relations employed in predicting the plastic deformation of materials using these numerical methods or tools are important. Several constitutive equations (and their modifications that fit experimental data [189]) have been employed to model the deformation behaviour of particles during CSAM. For instance, a range of constitutive equations or models, including the Johnson-Cook (J-C) model [165], was studied by Rahmati and Ghaeli [166], and they reported that the accuracy in predicting the impact morphology of CSAM deposited particles is largely influenced by the material model employed. However, there is very limited experimental data on the J-C material model data for the CoCrFeNiMn HEA and even for other HEAs, likely because the material space has not been widely explored.

Therefore, this chapter presents a fundamental study of the impact deformation behaviour of CoCrFeNiMn HEA on different substrates. Single-particle impacts were investigated, and the first part consisted of an experimental analysis of the deposited particles using advanced characterisation techniques, followed by numerical analysis using FE methods. The critical velocity of the mean experimental particle size was predicted for the HEA on the various substrates by assessing and selecting the best J-C model data that best predicted the impact morphology of the sprayed HEA particles.

It is noteworthy that this chapter has been published as a peer-reviewed article as presented in the “Publications” section.

5.1 Materials and experimental methods

5.1.1 Materials

The CoCrFeNiMn HEA powder was used as the feedstock powder material in this study. Table 5.1 presents the chemical composition of the powder material measured using an energy-dispersive X-ray spectroscopy (EDX) (Oxford Instruments, UK) detector mounted on a Philips FEI-XL30 scanning electron microscope (SEM). The morphology of the feedstock powder was observed by sprinkling a representative sample on a carbon stud and examining it using SEM equipped with secondary electron (SE) and back-scattered electron (BSE) detectors. The particle size distribution of the powder was measured using laser diffractometry (Horiba LA-960, Horiba Scientific, Japan). The phase structure of the powder material was determined using a D8 Advance da Vinci X-ray diffractometer (Bruker, Germany). The details of these characterisation techniques and procedures have been provided in Chapter 3 Section 3.5.

Table 5.1: Elemental composition of the CoCrFeNiMn HEA feedstock powder.

Element	wt.%	at.%
Co	22.3	21.3
Cr	19.3	20.8
Fe	20.0	20.1
Ni	20.7	19.8
Mn	17.6	18.0

The feedstock powder was deposited on four different substrates: commercially pure aluminium (CP Al), aluminium 6082-T6 alloy (Al6082), titanium alloy, Ti6Al4V (Ti64), and austenitic stainless steel 304 (SS304). The nominal composition of the substrates is provided in Chapter 3 Section 3.1.

5.1.2 CSAM deposition

Single-particle impacts were obtained by spraying the powder particles onto the four different substrates using the so-called swipe test as explained in Chapter 3 Section 3.2. The different substrates were exposed to the same spray run to ensure that the same impacting particle flux was sprayed onto the substrates. The swipe test experiments were performed using an in-house high-pressure CSAM system at the University of Nottingham. A schematic diagram and description of the CSAM rig are provided in Chapter 3, Section 3.2. The substrates were clamped side by side on an x-y table that allowed a controllable scan pattern and velocity (i.e., the relative motion between the nozzle and the substrates). Table 5.2 provides the spraying parameters employed for the deposition. Spraying was performed using nitrogen (N_2) and helium (He) as propellant gases. This was performed to obtain a wide

range of particle velocities owing to the differences in the gas dynamics. The powder carrier gas was set at a pressure 0.1 MPa higher than the accelerating gas pressure. The spraying parameters selected for the deposition of the HEA as presented in Table 5.2 were decided upon based on the window of deposition for difficult-to-spray materials such as stainless steel as found in the open literature. Thus, the spraying process conditions were then selected to lie below and above the window of deposition or bonding possible for the HEA material. With these range of spraying parameters one can determine the critical velocity for deposition of the HEA.

Table 5.2: CSAM spraying parameters employed for the single-particle impact test of the CoCrFeNiMn HEA feedstock powder on various substrates.

Spraying parameter		Value
Run 1	Gas (N_2) pressure (P; MPa)	2.8
	Gas (N_2) temperature (T; ºC)	525
Run 2	Gas (N_2) pressure (P; MPa)	3.3
	Gas (N_2) temperature (T; ºC)	525
Run 3	Gas (He) pressure (P; MPa)	3.3
	Gas (He) temperature (T; ºC)	400
Stand-off distance (mm)		20
Transverse speed (mm/s)		1500
Powder flow rate (0.5 rpm)		9 g/min

5.1.3 Sample preparation

Before spraying, the substrates were prepared following the procedure described in Chapter 3 Section 3.3. After spraying, the deposited samples were cut and prepared following the metallographic procedures as outlined in Chapter 3 Section 3.3. The single-particle impact morphology was examined using the XL30 SEM.

5.1.4 Hardness measurement

The nanohardness and microhardness of the cross-sectioned mirror-polished powder particles were measured following the procedure outlined in Chapter 3 Section 3.7. The section also provides information on the microhardness measurement of the substrate materials.

5.2 Numerical modelling methods

The computational fluid dynamics (CFD) model described in Chapter 4 Section 4.1 was employed to calculate the feedstock particle velocities and temperatures before impact on the substrates. The computation was based on the nozzle dimensions (described in Section 4.1), and the experimental conditions are listed in Table 5.2. A spherical CoCrFeNiMn HEA particle of 25 μm, corresponding to the experimental mean particle size and with an initial temperature of 25 °C, was injected at the nozzle inlet. The HEA density and specific heat capacity of 7958 kg/m^3 and 430 J/kgK were used as the material properties for the CFD model. The CFD analysis was conducted using a realisable k–ε model with a standard wall function for the

gas phase, whereas the particle was coupled with the gas phase flow using a discrete phase model. The model was meshed using a grid of quadrilateral elements. The output of the CFD calculations was employed as input parameters for the impact deformation modelling. The FEA of the impact deformation behaviour and the prediction of the onset of deposition of the 25 μm HEA particle onto the various substrates were investigated using the Abaqus/Explicit code with the Lagrangian approach. A detailed description of the single-particle impact deformation modelling is given in Chapter 4 Section 4.2.1.

The material model employed in this thesis to capture the deformation of the HEA material during the CSAM deposition has been provided in Chapter 4 Section 4.2.3. A detailed description of the Johnson-Cook (J-C) material model for the transient dynamic deformation simulations of the material is also provided in Chapter 4 Section 4.2.3.

5.3 Experimental results of the CoCrFeNiMn HEA particle impact on various substrates

Figure 5.1a and b shows the impact morphology of the CoCrFeNiMn HEA feedstock powder. Most of the powder particles exhibit a spherical morphology, with some small satellite particles attached to larger particles. The powder particle size distribution displayed in Figure 5.1c indicates that most of the particles were 15-38 μm in size. The Dv10, Dv50, and Dv90 values of the powder batch were 16.38, 25.53, and 41 μm, respectively. As the mean particle size, Dv50 = 25.53 μm, a particle size of 25 μm was employed for numerical modelling. In addition, the XRD

profile displayed in Figure 5.2 reveals that the HEA powder contains only a single-phase FCC structure.

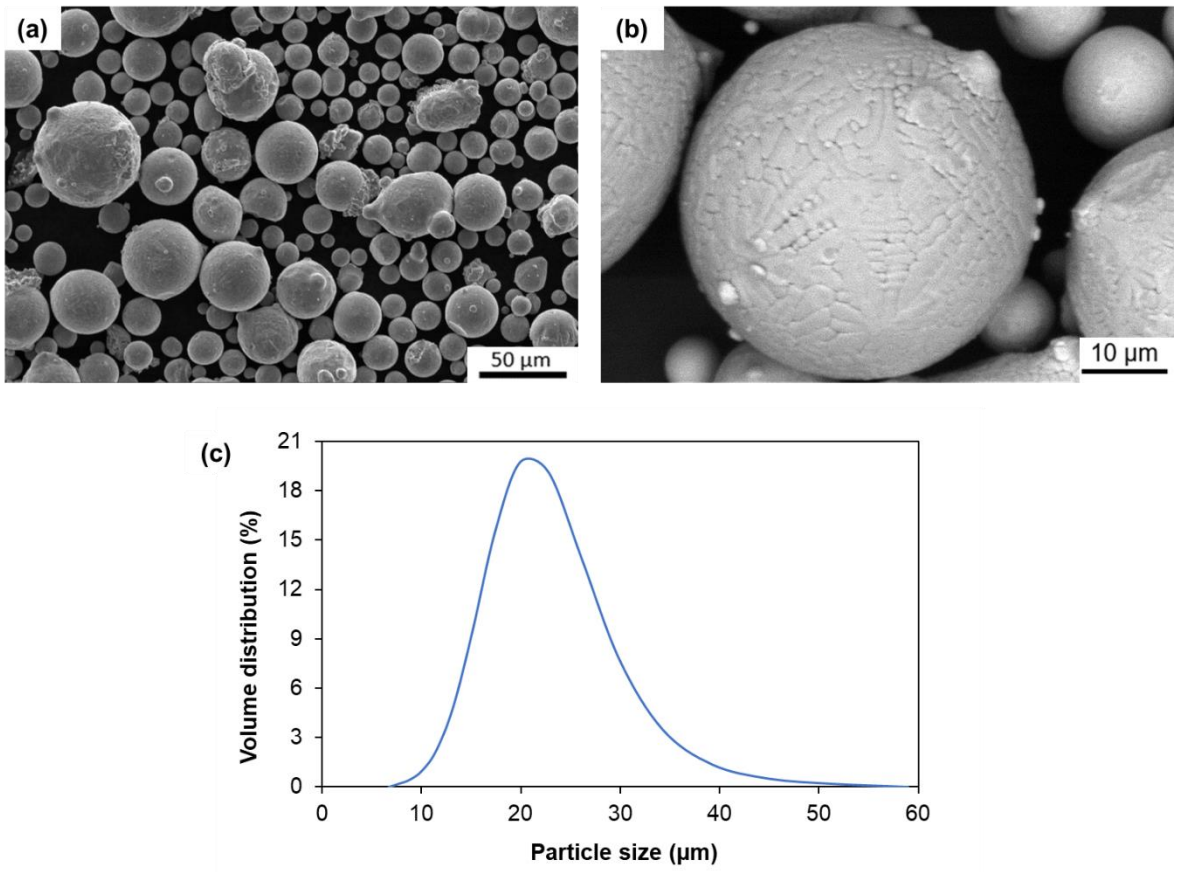

Figure 5.1: (a) SEM image of powder particles with mostly spherical morphology; (b) magnified BSE image of a single HEA particle showing dendritic structure; and (c) the particle size distribution measured by laser diffractometry.

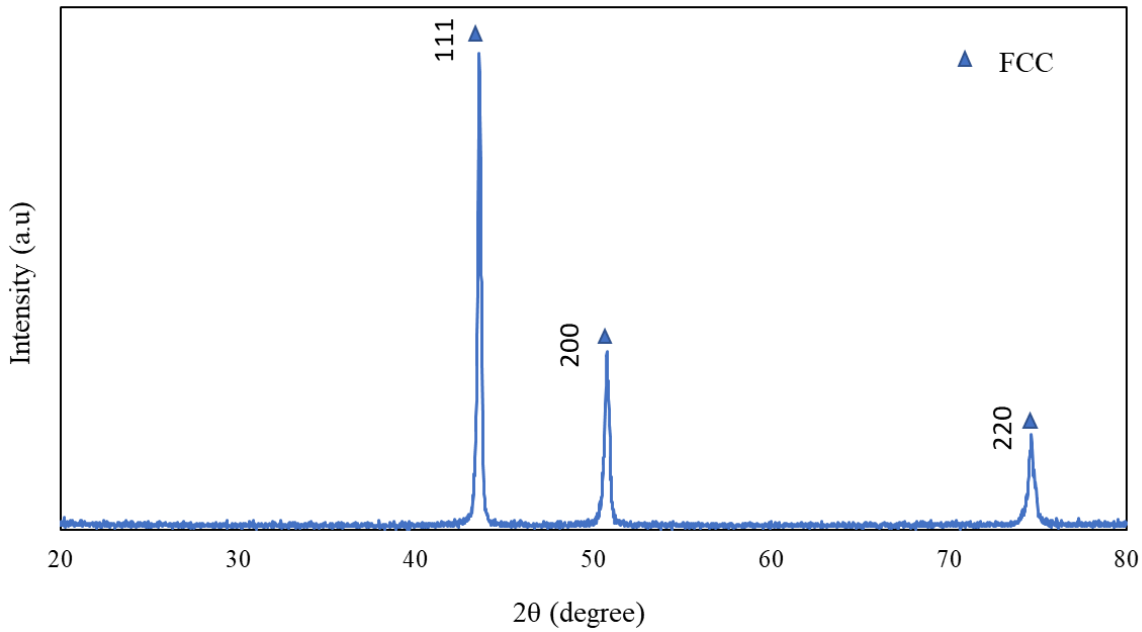

Figure 5.2: XRD profile of the CoCrFeNiMn HEA powder showing a single-phase FCC structure.

The HEA powder was sprayed onto the four different substrates. The substrates were grouped based on the microhardness values listed in Table 5.3. The SS304 and Ti64 substrates were grouped as hard substrates because of their greater microhardness, whereas CP Al and Al6082 were grouped as soft substrates because of their lower microhardness. The deviation of the microhardness value of the HEA powder material can be attributed to measurement errors, such as particle displacement in the resin during indentation or the indentation of both the powder and the resin, which would affect the accuracy of the microhardness measurement. Previous research has reported different values of the HEA powder microhardness; 124 HV [40], 139 HV [128] and 176 HV [63]. These values are close to the measured microhardness of the SS304 substrate (192 HV). Moreover, depending on the processing conditions and grain size, the microhardness of bulk HEA samples reported in the literature ranges from 140-350 HV [42,262]. The differences in the microhardness values can be attributed to the different applied loads, grain and

particle sizes, microstructures, and processing conditions. However, for this study, the HEA and SS304 materials are assumed to have little difference in their material properties (elastic modulus and crystal structure); that is, they are of similar combinations in the CSAM impact analysis. The substrate characteristics would influence the deformation behaviour of the HEA particles and hence, its impact morphology.

Table 5.3: Microhardness values measured for the HEA powder and the substrates.

Material	Hardness (HV)
CoCrFeNiMn powder	69.5 ± 1.5
Ti64	315.0 ± 4.5
SS304	192.1 ± 1.7
CP Al	35.4 ± 0.3
Al6082	42.6 ± 1.0

5.3.1 Impact morphology of the HEA particles on hard substrates

The top-surface SEM images of the HEA particles deposited on the SS304 and Ti64 substrates are shown in Figure 5.3. The figure shows images of the deposited particles at different spray runs—Run 1 (N_2; P_{gas} = 2.8 MPa and T_{gas} = 525 ºC), Run 2 (N_2; P_{gas} = 3.3 MPa and T_{gas} = 525 ºC) and Run 3 (He; P_{gas} = 3.3 MPa and T_{gas} = 400 ºC). An overview of the images demonstrates that less than 30% of the impacting HEA particles adhered to the surface of the substrates under the spray conditions of Run 1. A slight increase in the number of adhered particles was observed under the spray condition of Run 2. Under the spray conditions of Run 3,

shown in Figure 5.3c and d, more than 95 % of the substrate surfaces appear to be covered with adhered particles. In CSAM, a low bond ratio suggests that most of the particles were sprayed at impact velocities below their critical velocity; consequently, more craters that resulted from particle rebound were formed on the substrate surface. This suggests that the average particle impact velocities from Runs 1 and 2 were likely below the average critical velocity of the HEA particles. Furthermore, the influence of the substrates on the deposition of the HEA particles can be observed by comparing the number of adhered particles on the substrate surfaces (i.e., comparing Figure 5.3 (a, c and e) with (b, d, and f)). There is a higher number of adhered particles on Ti64 than on the SS304 substrate.

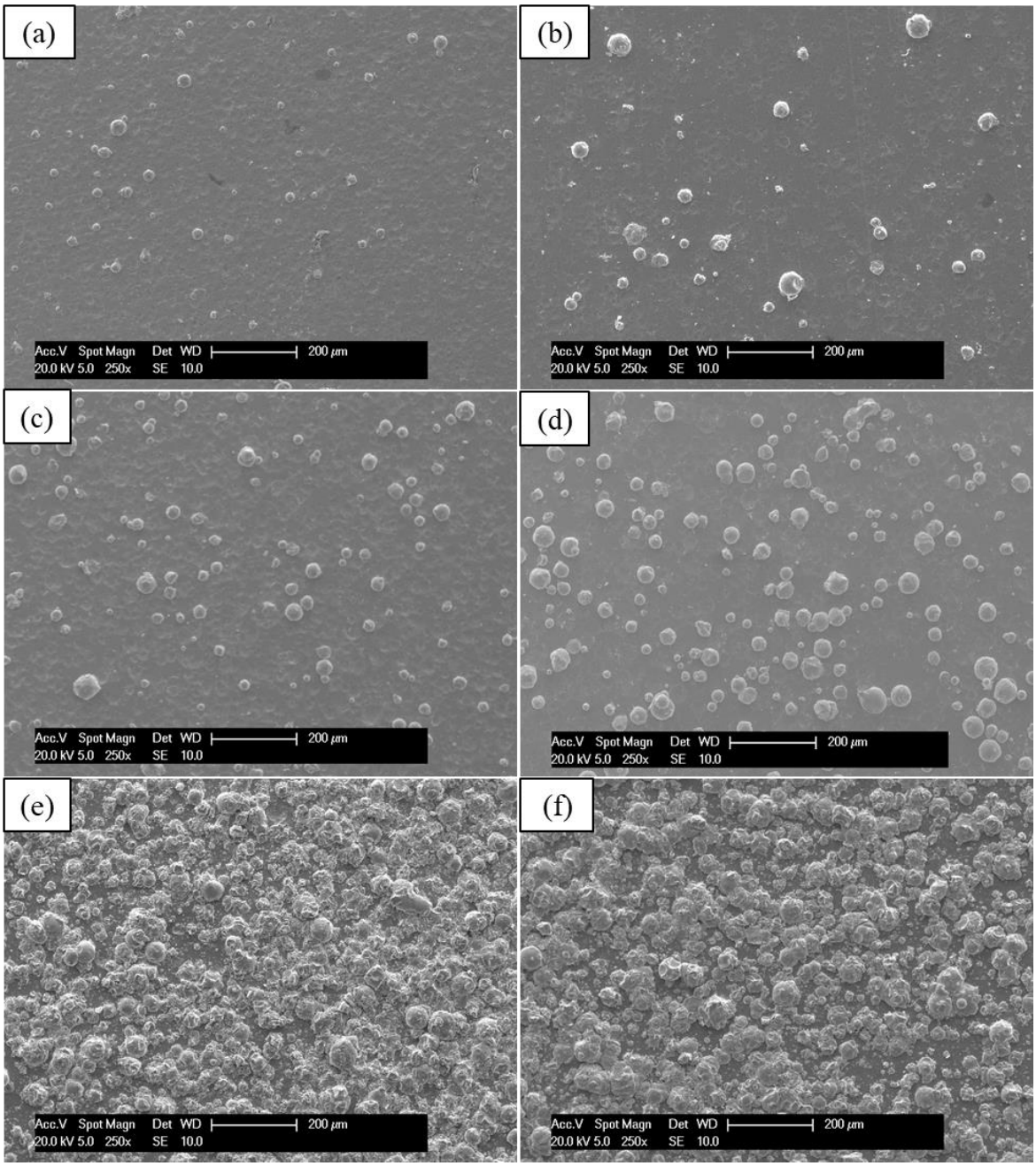

Figure 5.3: Low magnification top surface SEM images of the swipe test samples of deposited CoCrFeNiMn HEA particles on SS304 (a, c, e) and Ti64 (b, d, f) substrates at spray conditions Run 1 (a, b), Run 2 (c, d) and Run 3 (e, f).

Higher magnification images of bonded HEA particles at the different spray runs are shown in Figure 5.4. Extensive jetting of the sprayed particles is observed around the impact region on the substrates from spray Run 3 (as shown in Figure 5.4e and f). In contrast, spray Runs 1 and 2 exhibited less deformed HEA particles, as shown

in Figure 5.4 (a, b) and (c, d)). To further reveal the impact morphology of the HEA particles on the hard substrates, cross-sectional BSE images, as shown in Figure 5.5, were taken for samples with a higher number of adhered particles seen from Run 2 and 3. Figure 5.5a and b show the particle impact morphology from spray Run 2: half-flattened deformed HEA particles with slightly deformed substrates. In contrast, a different particle-substrate deformation pattern is observed from spray Run 3, as shown in Figure 5.5c and d. Metal jetting can be seen around the peripheral region of the particle-substrate interfaces. Also, an increase in the penetration depth of the particle into the substrates can be observed when compared with the deposits from the spray Run 2. The jet-type outflow of the material at the particle interface can be attributed to the higher impact velocity of the HEA particles using He gas for spray Run 3. It was also observed from the cross-sectional images that smaller particles significantly deformed the substrates, resulting in the jetting of the substrate material, as shown in Figure 5.5c and d, whereas larger particles deformed more than the substrate. In some cases, no jetting was observed on the substrate, as shown in Figure 5.5e (insert of Figure 5.5d).

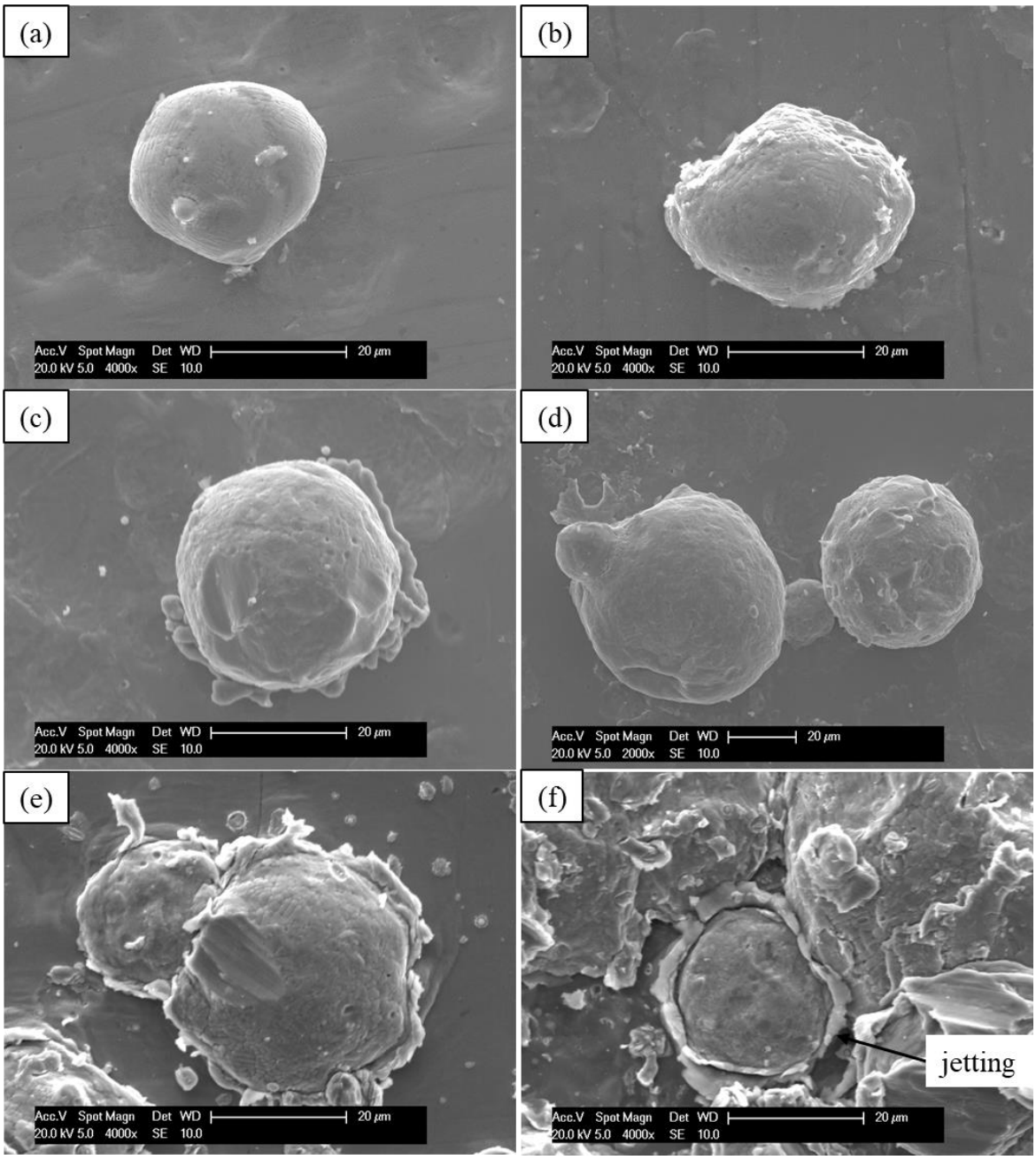

Figure 5.4: Close-up views of the top surface SE images of the CoCrFeNiMn HEA single-particle impact on SS304 (a, c, e) and Ti64 (b, d, f) substrates at spray conditions Run 1 (a, b), Run 2 (c, d) and Run 3 (e, f).

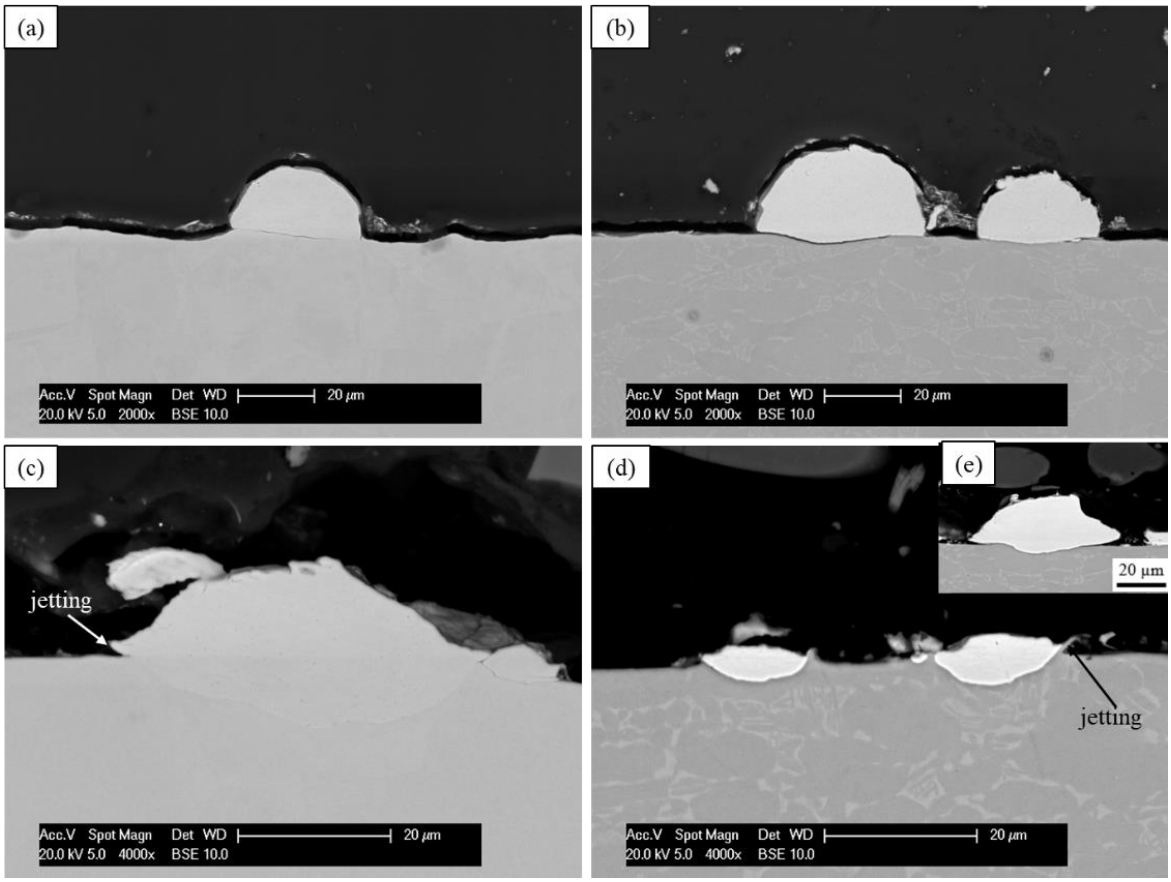

Figure 5.5: BSE cross-sectional images of the CoCrFeNiMn HEA impact morphology on SS304 (a, c) and Ti64 (b, d) substrates at spray conditions Run 2 (a, b) and Run 3 (c, d). Insert (e) shows a larger HEA particle that has deformed more than the Ti64 substrate, the same as observed on the SS304 substrate in (c).

The extent of particle deformation on the substrates and spray conditions can be quantified using the flattening ratio (FR). A detailed discussion on FR for cold spray deposits is provided in Chapter 2 Section 2.6.3. The FR is defined as the ratio of the splat width (***W***) to the original particle diameter (***D₀***). As the value of ***D₀*** is not typically known *a priori*, it was back-calculated through the conservation of volume between the initial sphere and final oblate spheroid shape of the deformed sprayed particles. This was evaluated according to King and Jahedi's analysis [187], given as $\boldsymbol{D_o = \sqrt[3]{(W^2 h)}}$ for the case where there is less particle deformation such as in Run 2 (as shown in Figure 5.5a and b). Meanwhile for Run 3, where particle spreads

over the substrate surface due to severe plastic deformation (Figure 5.5c and d), $\boldsymbol{D_o = \sqrt[3]{3/4}\,(W^2 h)}$, where $\boldsymbol{h}$ is the splat height. An increase in the value of the FR indicate increase in the particle deformation on the substrate under the spraying conditions. Also, FR is more akin to the average compressive strain in the deposition direction [296], suggesting that an increase in FR is an indication of an increase in compressive strain and particle deformation. A high FR value is desirable to achieve high deposit quality. As discussed in Chapter 2 Section 2.6.3, FR can be evaluated by examining the cross-sectioned morphology of the sprayed particles. Mechanical cutting and polishing of the samples were employed in this thesis for the FR evaluation and as such, the FR values can be associated with errors because mechanically polished cross-sections do not normally pass through the centre of splats. However, the connection of the FR value to the strain or extent of deformation is desirable from a fundamental mechanistic understanding and can be more suitable for comparison with FEA [296]. The average FR evaluated for about 10 particles with different sizes of the HEA on the hard substrates is presented in Table 5.4. There was an increase in the FR value as the spray conditions were changed from Run 2 to 3. Similarly, the value increased with an increase in the substrate hardness. Thus, the FR was observed to be influenced by the spraying conditions and substrate material.

Table 5.4: Flattening ratio (FR) evaluated for the HEA particle impact on hard substrates at spray conditions Run 2 and Run 3.

Particle-substrate combination	Flattening ratio (FR)	
	Spray condition Run 2	Spray condition Run 3
HEA/SS304	1.18 ± 0.06	1.43 ± 0.03
HEA/Ti64	1.28 ± 0.03	1.54 ± 0.02

5.3.2 Impact morphology of the HEA particles on soft substrates

SEM images of the top surfaces of the sprayed particles on the soft substrates are presented in Figure 5.6. The figure shows low-magnification images of the HEA particles on the CP Al and Al6082 substrates. The samples were sprayed with the spray runs, Run 1-Run3. For spray Runs 1 and 2, the CP Al substrate showed a higher number of adhered particles compared to the sprayed particles on the Al6082 substrate, as shown in Figures 5.6a, b, c and d. By changing the gas type, a greater number of adhered sprayed particles were observed on both substrates (see Figure 5.6e and f), showing no significant difference in the number of adhered particles. The spray Run 3 likely resulted in the transition from the rebounding of particles to the deposition of particles on the Al6082 substrate with the spray parameters employed. It is also observed that the substrate material properties thus influence the deposition of the HEA particles even for the case of the hard particle-soft substrate combinations.

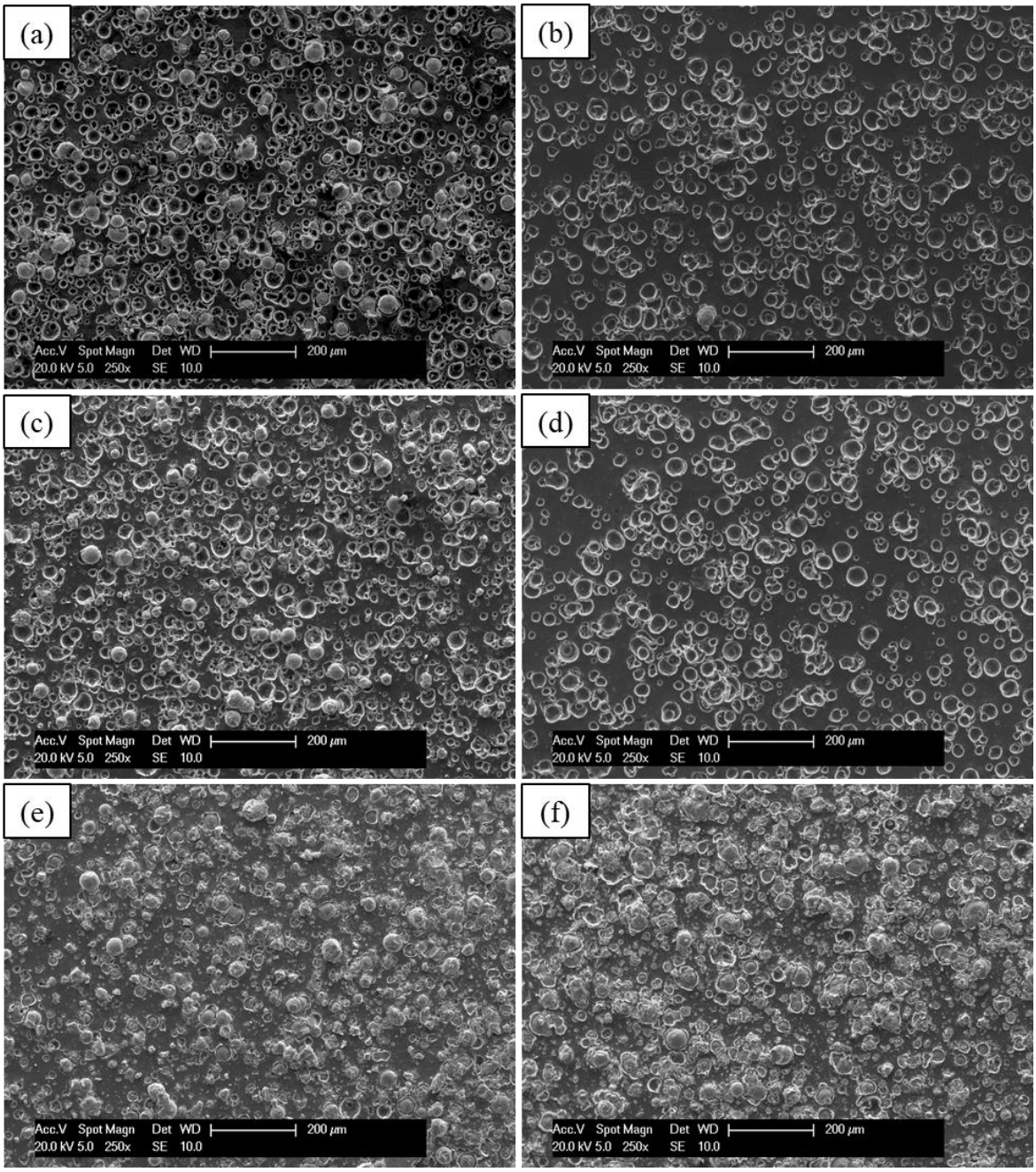

Figure 5.6: Low magnification top surface SEM images of the wipe test samples of sprayed CoCrFeNiMn HEA particles on CP Al (a, c, e) and Al6082 (b, d, f) substrates at spray conditions Run 1 (a, b), Run 2 (c, d) and Run 3 (e, f).

A high-magnification view of the top surface of the deposited particles on soft substrates is shown in Figure 5.7. In addition, BSE cross-sectional images of the particles are shown in Figure 5.8. The figures reveal that the HEA particles were trapped or embedded in the substrates. Moreover, the substrates appeared to be

extensively deformed, and the particles were less deformed. This type of deformation mechanism is called mechanical interlocking [40,139,142]. It was also observed that the HEA particle penetration depth into the substrate increased with a change in the spray runs from Run 1 to Run 3, as shown in Figure 5.8.

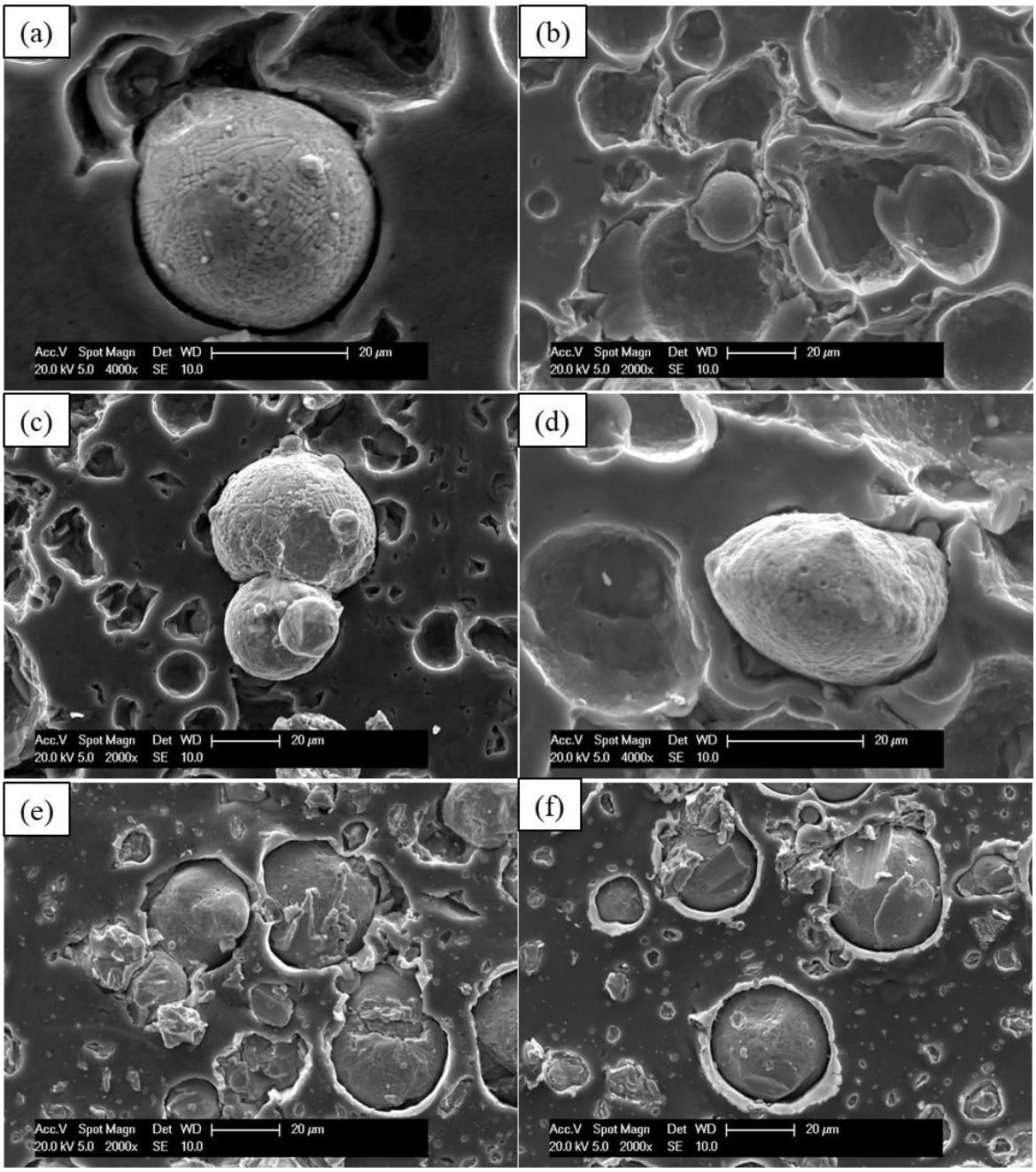

Figure 5.7: Close-up view of the top surface SEM images of sprayed CoCrFeNiMn HEA particles on CP Al (a, c, e) and Al6082 (b, d, f) substrates at spray conditions Run 1 (a, b), Run 2 (c, d) and Run 3 (e, f).

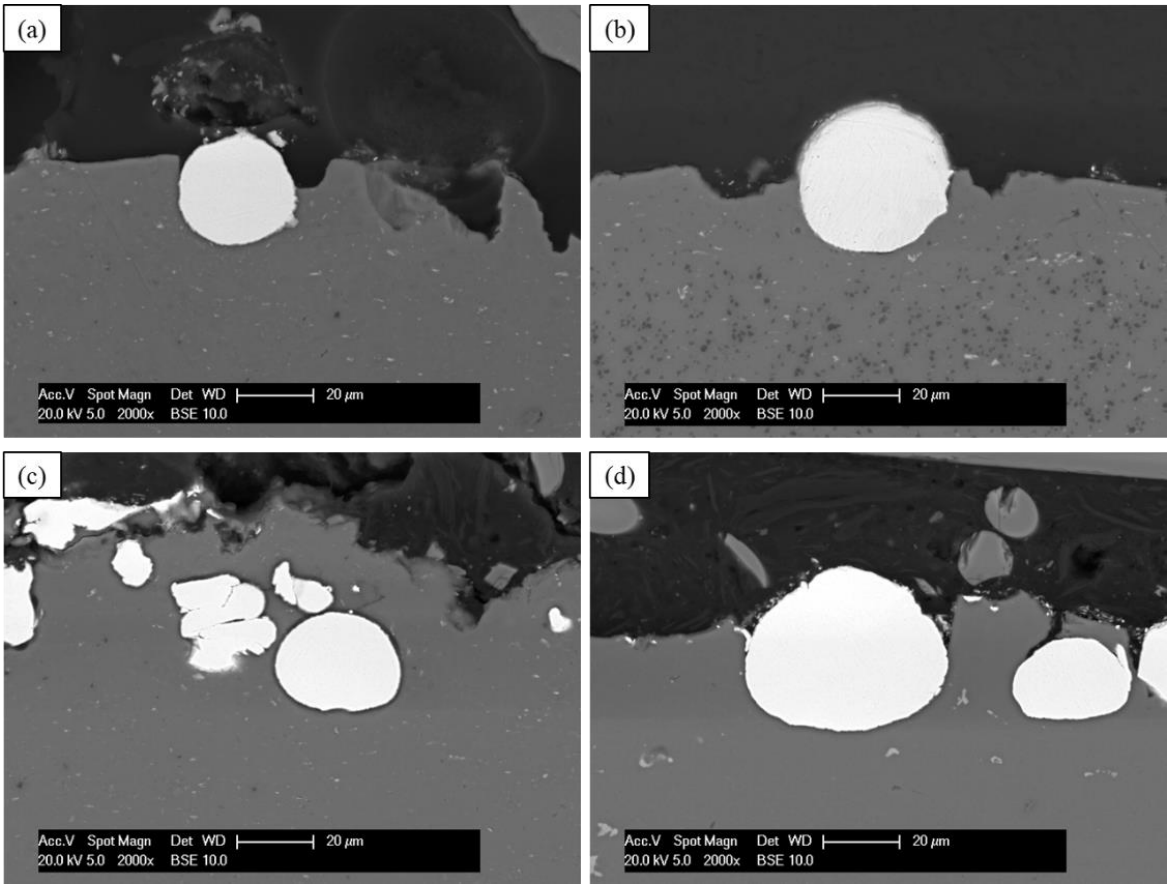

Figure 5.8: BSE cross-sectional images showing the impact morphology of CoCrFeNiMn HEA particles deposited on CP Al (a, b, c) and Al6082 (d) substrates at spray conditions Run 1 (a), Run 2 (b) and Run 3 (c, d)). The SEM images were taken on substrates with a higher percentage of adhered HEA particles. The arrow in (c) shows an embedded HEA particle.

5.4 Assessment and selection of CoCrFeNiMn HEA Johnson-Cook material model data

Limited data are available in the literature for the CoCrFeNiMn HEA Johnson-Cook (J-C) material model. This may be because the high-strain-rate plastic deformation of HEA has not been extensively explored. Even with the available J-C data for the HEA and other investigated materials for CSAM (such as Cu, Ni, Al, Ti, stainless steel, etc.), the choice of the J-C set of parameters and their values is very important for accurately predicting the deformation or impact morphology of particles during

CSAM. In this study, different sets of J-C model data for the CoCrFeNiMn HEA and materials with similar composition and or impact behaviour (for example, set_2 is for the CoCrFeNi HEA and the strain-hardening value ***B*** for set_3 and set_4 for Ti64) were collected from the literature, as listed in Table 5.5. All these sets were then compared, based on their impact morphology and FR, with the experimental results (presented in Section 5.3.1). The analysis was linked to the sets of J-C parameters, and the most suitable parameter for predicting the impact morphology was selected for further simulations. This approach ensures that the J-C parameters maintain the physical basis derived from experimental testing. A better fit could have been found using parameter optimisation, but this is not the focus of the study, as this would lose the link to the J-C experimental data which already exists for the HEA material.

The evolution of the stresses with strain for the different sets of the J-C parameters presented in Table 5.5, is plotted in Figure 5.9a. A temperature of 473 K and a strain rate of 10^7 s^{-1} were selected for the analysis plotted in the figure, which is assumed values of the initial particle temperature and strain rate during the deformation. There is a large deviation of the set_1 parameters from the other sets, which can be attributed to the high strain-hardening exponent, ***n***, and strain-rate sensitivity values (or strain-rate constant, ***C***) of the set_1 J-C parameters. From this analysis, it can be assumed that the strain-hardening exponent and strain-rate sensitivity values play a major role in predicting the deformation behaviour of materials in the CSAM process when using the J-C model. Furthermore, the variations in the evolution of stresses with strain plotted for sets 2-6 as shown in Figure 5.9b, can be attributed to the different values of parameters ***A*** and ***B***. There are very few studies

in the literature [189] that have shown the effect of different J-C parameters on material deformation during CSAM. The significant differences observed for the different J-C parameters in this study provided insight into the importance of the J-C material model parameters for predicting CSAM material deformation.

Table 5.5: Sets of parameters and their values for the Johnson-Cook model for CoCrFeNiMn HEA (the reference strain rate $\boldsymbol{\varepsilon_0}$, was assumed to be equal to 1 where data was not found in the literature).

Set	J-C model parameters for CoCrFeNiMn HEA					
	A (MPa)	***B*** (MPa)	C	n	m	$\boldsymbol{\varepsilon_0}$ (s^{-1})
1 [175]	590	2075	0.39	0.78	0.7	3000
2 [297]	340	412	0.021	0.3	1.1	1
3 [175,176,298]	590	762	0.028	0.18	0.7	1
4 [175,176,299]	590	1007	0.028	0.18	0.7	1
5 [175,176]	605	1365	0.028	0.18	0.7	2800
6 [175,176]	590	1365	0.028	0.18	0.7	1

The J-C model parameters from the sets provided in Table 5.5 were employed in the FE model, and the evaluated FR and impact morphology for each set were compared with the experimental results in Section 5.3.1. It is noteworthy that the assessment and selection of the J-C model parameters were performed for the impact on hard substrates as there is no significant deformation of the HEA particles on the soft substrates (presented in Section 0).

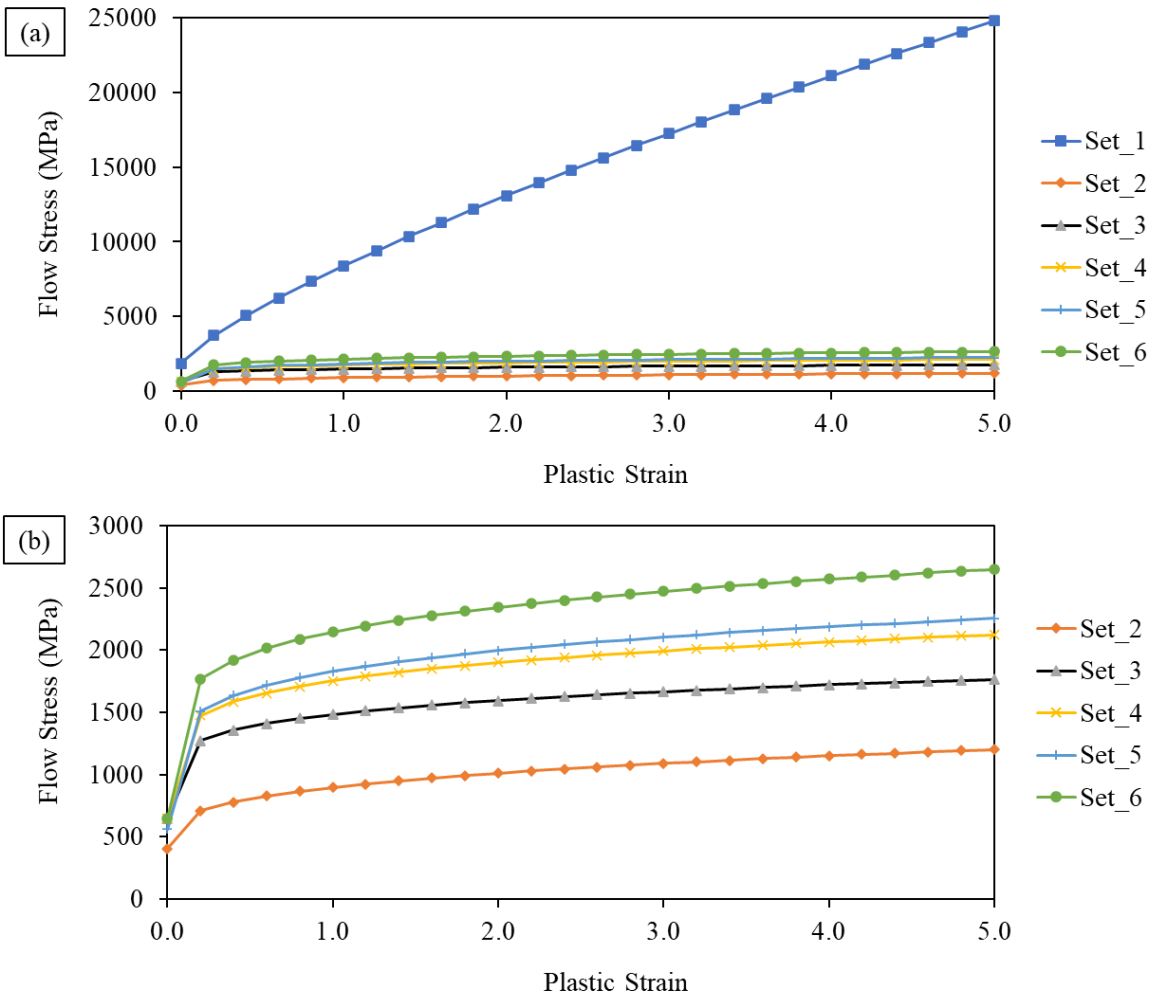

Figure 5.9: Stress-strain curves of the sets of J-C model parameters for the CoCrFeNiMn HEA at temperature, $\boldsymbol{T}$ = 473 K and strain rate, $\dot{\varepsilon}$ =10^7 s^{-1}. All the J-C sets are plotted (a) while (b) is without set_1.

For the FEA of the CoCrFeNiMn HEA particle deformation, input parameters such as the particle impact velocity and temperature are required, these were predicted using the CFD model described in Chapter 4 Section 4.1. The particle velocity and temperature of 25 µm of the CoCrFeNiMn HEA particle before impact on the substrates were computed based on the nozzle dimensions and spraying conditions listed in Table 5.2. Figure 5.10 shows the velocity of the particle for the different spray runs through the distance downstream of the nozzle inlet to the exit. The figure shows that a higher particle velocity was achieved with spray Run 3, where He was

used as the propellant gas. This is expected when compared with N_2 gas, as the use of He gas to achieve a higher particle velocity at the same process parameters has been well established in the literature [124]. The reason for this lies in the expression of the local gas velocity [110], $\boldsymbol{V_g} = \sqrt{\boldsymbol{(\gamma RT)/M_w}}$, where $\boldsymbol{\gamma}$ is the ratio of the constant-pressure to constant-volume specific heat, which is 1.66 for He and 1.4 for N_2; $\boldsymbol{R}$ is the gas constant; $\boldsymbol{T}$ is the gas temperature; and $\boldsymbol{M_w}$ is the molecular weight of the gas. The gas velocity correlates positively with $\sqrt{\boldsymbol{\gamma/M_w}}$, which is greater for He than N_2. The particle velocity and temperature, exit of the nozzle, from Figure 5.10 are about 598, 647 and 987 m/s for spray conditions Run 1, Run 2 and Run 3, respectively. In addition, the particle temperatures for the corresponding spray runs were predicted as 398, 398, and 367 °C as presented in Figure 5.10b. There was an overlap of the particle temperature for spray Runs 1 and 2. This is because the experimental values of the gas temperature for both spray runs were the same, as listed in Table 5.2. Because the CFD results are likely to deviate from the actual experimental values [74,108,300], particle velocities and temperatures of 600 m/s and 200 °C (473 K) were employed for the J-C material data assessment and selection. These values correlate with the spray conditions of Run 2. The initial temperature of the substrate was set at 27 °C (300 K).

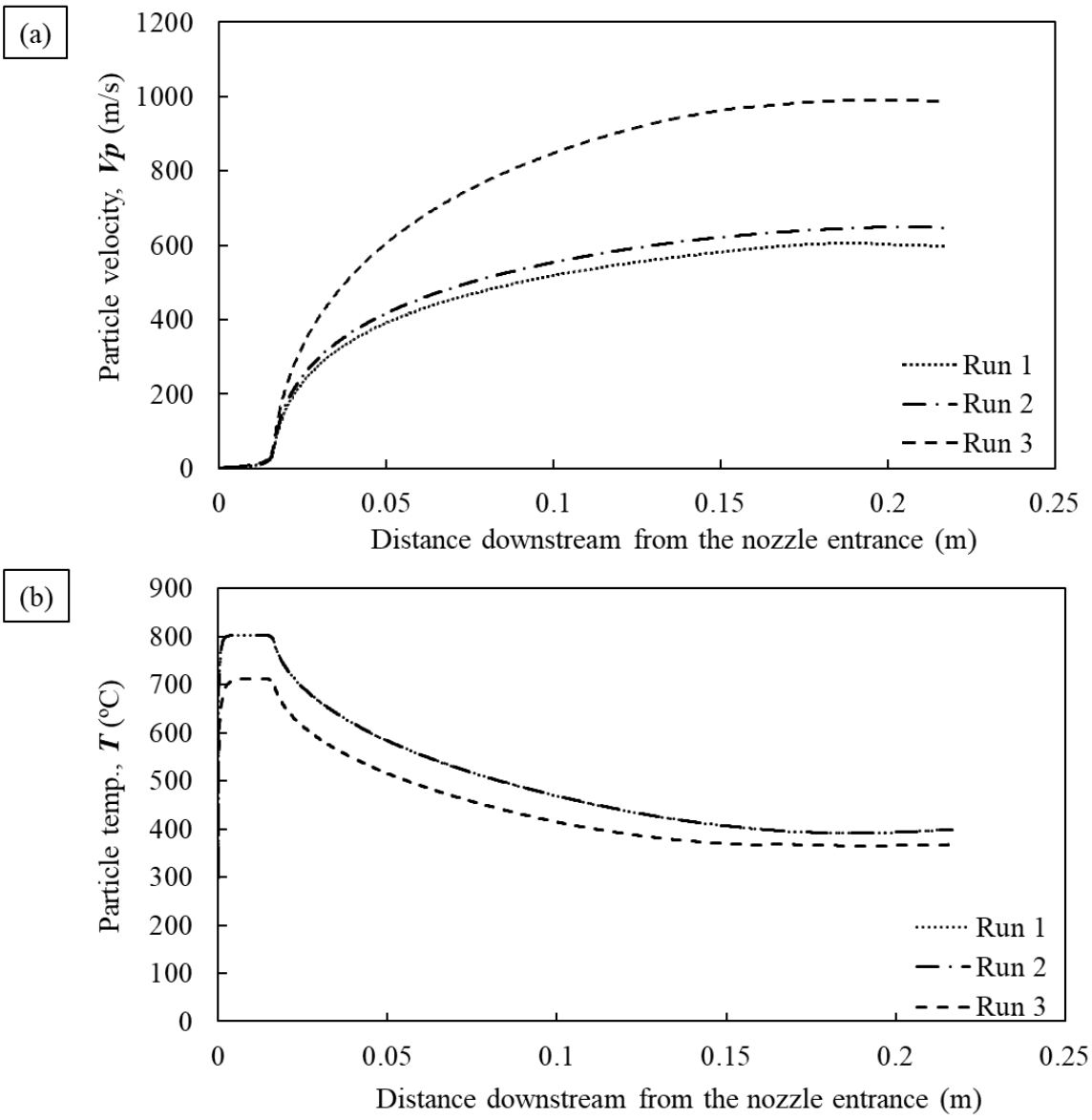

Figure 5.10: CFD results of a 25 µm CoCrFeNiMn HEA particle velocities (a) and temperatures (b) for the spray conditions Run 1- Run 3. The use of He as propellant gas (Run 3) has resulted in higher particle velocity compared to that of N_2 gas (Run 1 and Run 2).

The FEA impact morphology and the plots of their FR (herein splat width was used as it provides the particle flattening in the lateral direction or the major axes of the oblate spheroid) of the different sets of J-C model parameters are shown in Figure 5.11 and Figure 5.12. This was performed in the low-velocity regime (spray Run 2). Thereafter, the most suitable J-C model that best predicted the impact morphology

was employed to predict the deformation behaviour in the high-velocity impact regime where metal jetting was observed (spray Run 3). Figure 5.11 and Figure 5.12 were introduced to aid the FEA with the experimental reference. It can be seen that the set_1 J-C model data [175] shows the largest deviation in the impact morphology from the experiment, as shown in Figure 5.11. This suggests that the HEA particles for the set_1 data are much harder than the substrates, resulting in mechanical interlocking. As mentioned earlier, this can be attributed to the high strain-hardening exponent and strain rate sensitivity values of the set_1 J-C model data. In addition, the set_2 J-C model for the CoCrFeNi HEA deformed more extensively than the set_6 J-C model for the CoCrFeNiMn HEA. From the plots of the FR of the different sets of the J-C material model data and the experimental results presented in Figure 5.12, a link can therefore clearly be made between the set_6 J-C model and the experimental results. This set was selected for further simulations and evaluation of the critical velocity of the 25 µm CoCrFeNiMn HEA particle.

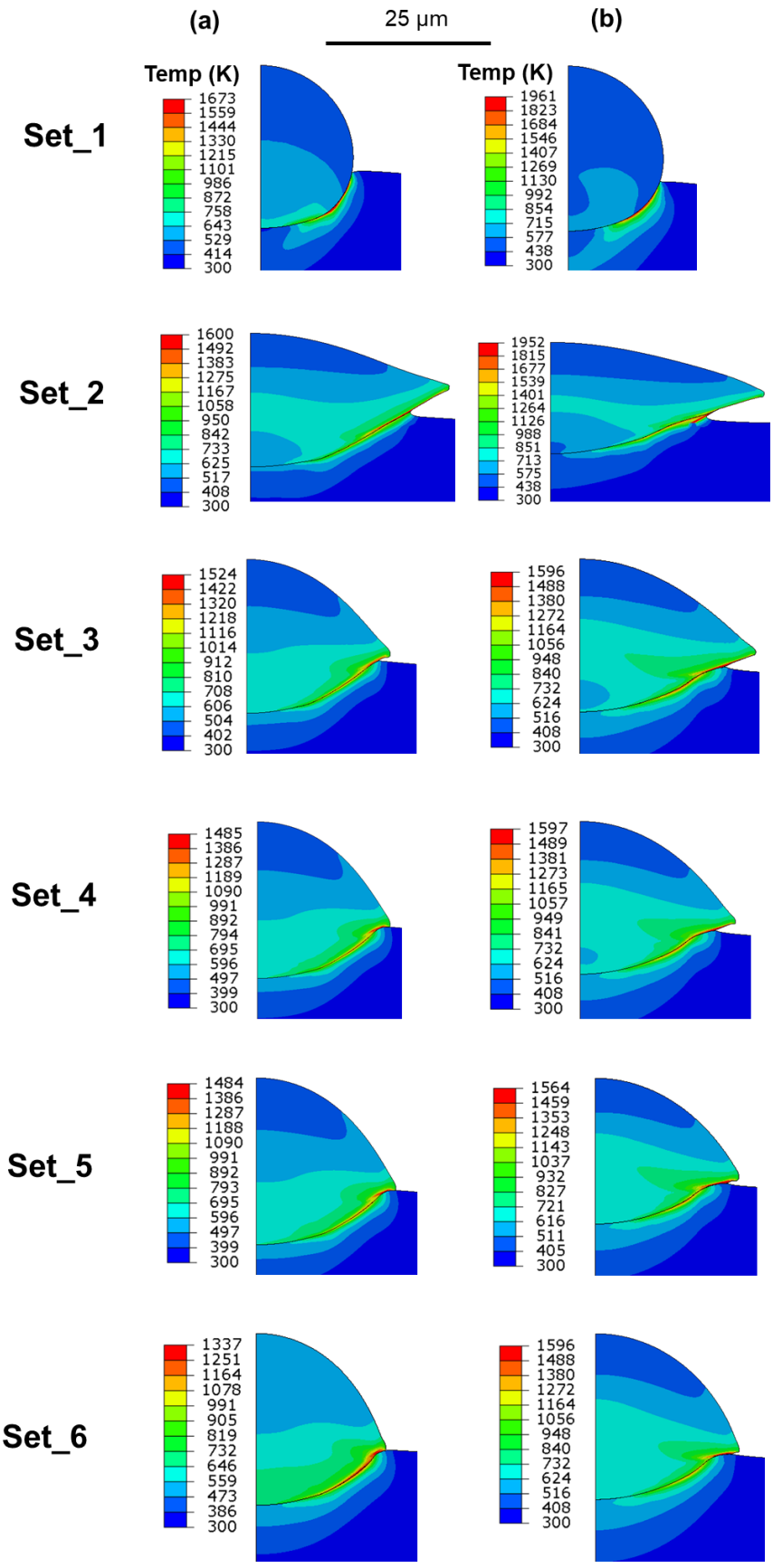

Figure 5.11: Impact morphology of the different sets of J-C model parameters for the CoCrFeNiMn HEA on SS304 (a) and Ti64 (b) substrates.

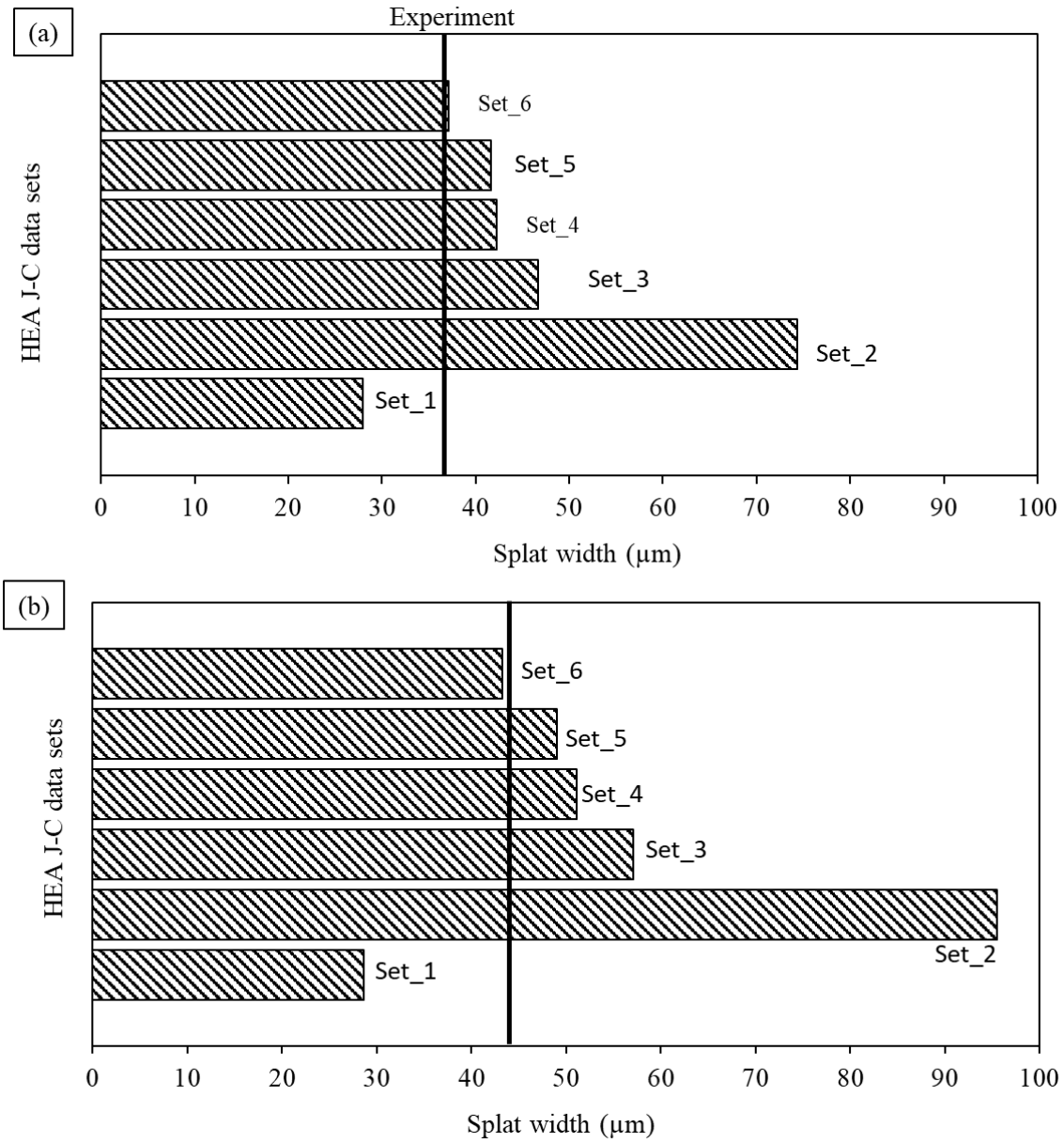

Figure 5.12: Experimental and FEA splat width of the different sets of J-C model parameters of the CoCrFeNiMn HEA on SS304 (a) and Ti64 (b) substrates. The experimental splat width is indicated by the vertical lines.

Table 5.6 provides the final J-C model data for the HEA particle, and the substrates used for further simulations in this study. It can be observed from the table that the HEA material has the highest strain-hardening value of 1365 MPa among the materials. Excellent strain hardenability and low thermal softening have been reported for the HEA [37,63,301]. Also, the critical shear strain for strain localisation

of the HEA (~ 7) has been reported to be greater than that of SS304 (~5) [63] and Ti64 (1-2) [37]. These characteristics of the HEA can influence its deformation behaviour during CSAM and, consequently, its critical velocity.

Table 5.6: The material properties and Johnson-Cook model data for the CoCrFeNiMn HEA particle and the substrates used in this study.

Material properties	CoCrFeNiMn [175,176,282,302]	SS304 [303]	Ti64 [304]	Al 6082 [305]	CP Al [131]
$\boldsymbol{\rho}$ (Kg/m^3)	7958	8000	4430	2710	2710
E (GPa)	202	207.8	113.8	70	70
v	0.265	0.3	0.33	0.3	0.3
A (MPa)	590	280	1098	428.5	148.4
B (MPa)	1365	802.5	1092	327.7	345.5
n	0.18	0.622	0.93	1.008	0.183
C	0.028	0.0799	0.014	0.00747	0.001
m	0.7	1.0	1.1	1.31	0.895
$\boldsymbol{\varepsilon_0}$ (s^{-1})	1	1	1	1	1
T_{melt} (K)	1600	1673	1961	855	916
T_{ref} (K)	300	298	298	293	293
$\boldsymbol{C_P}$ (J/KgK)	430	452	580	900	900

5.5 Numerical analysis of the HEA particle deformation behaviour on various substrates

The FEA of the CoCrFeNiMn HEA particle impact phenomena on hard and soft substrates is presented in this section. The analysis was performed using the J-C material model presented in Table 5.6, and with the computed particle impact velocities within the spray conditions, Runs 1-3.

5.5.1 Deformation behaviour of the HEA particle on hard substrates

Figure 5.13 shows the evolution of the impact morphology or deformation pattern of the HEA particle onto flat SS304 and Ti64 substrates, at velocities ranging from 550-900 m/s, which are within the spray conditions predicted for Run 1 to Run 3. The initial particle and substrate temperatures were set to 473 and 300 K, respectively. The FEA revealed localised heating (or high temperatures) at the particle-substrate interface for all impact velocities, although this was more severe for higher impact velocities. The figure also shows a change in the particle-substrate interaction from low-velocity (550 and 600 m/s) to high-velocity regimes (700-900 m/s), where a “nose-like” feature at the peripheral of the particle-substrate interface changed to a “lip-like” feature (metal jetting) at higher impact velocities. Similar impact morphologies were observed in the SEM micrographs (Section 5.3.1) under similar spraying conditions.

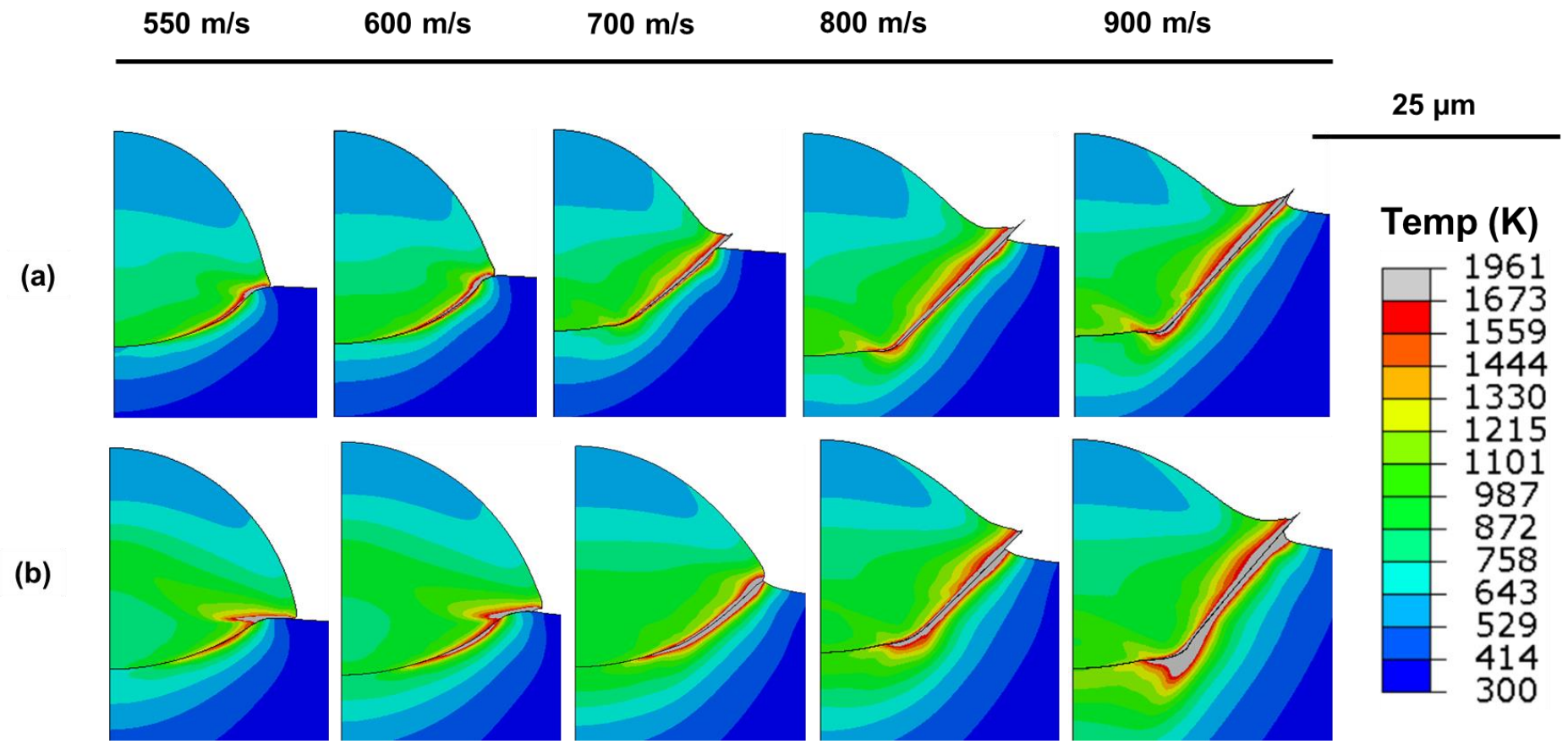

Figure 5.13: FEA impacts morphology of the HEA particle on SS304 (a) and Ti64 (b) substrates at impact velocity ranging from 550-900 m/s, which are within the computed spray conditions Run 1 to Run 3.

To obtain a better understanding of the change in the particle-substrate deformation behaviour, or localisation of plastic strain, the evolution of strain of a critical element that undergoes the highest amount of deformation at the HEA particle to hard substrate interface is plotted in Figure 5.14. There is an abrupt change in the strain evolution at particle velocities of 700 and 600 m/s on the SS304 and Ti64 substrates, as shown in Figure 5.14. The abrupt change in the strain is likely the result of the thermal softening of the HEA particle at the interface, dominating the strain hardening during the deformation, consequently resulting in a high strain value at those particle velocities. This impact phenomenon has been observed by several researchers in the simulation of CSAM deposition of metallic materials, for instance, Assadi et al. [56]. A similar trend was observed in the strain evolution of the critical element at the SS304 and Ti64 substrate interfaces, as shown in Figure 5.15. An abrupt change in the strain evolution at the SS304 and Ti64 substrate interfaces was observed at approximately 800 m/s and 700 m/s. Note that a higher particle velocity is required to cause an abrupt change in the strain evolution for the HEA/SS304 pair compared with the HEA/Ti64 pair. The FEA reveals, as also revealed by the impact experiment (presented in Section 5.3.1), the influence of the substrate material on the deposition of the HEA particles. The substrates deform less compared with the particles, which is revealed by the greater particle velocity at which the transition in the strain evolution is observed for the substrates. A similar observation was reported by Nikbakht et al. [63], where CoCrFeNiMn HEA particles deformed more intensely than the In625 substrate (with a microhardness value of 270 HV).

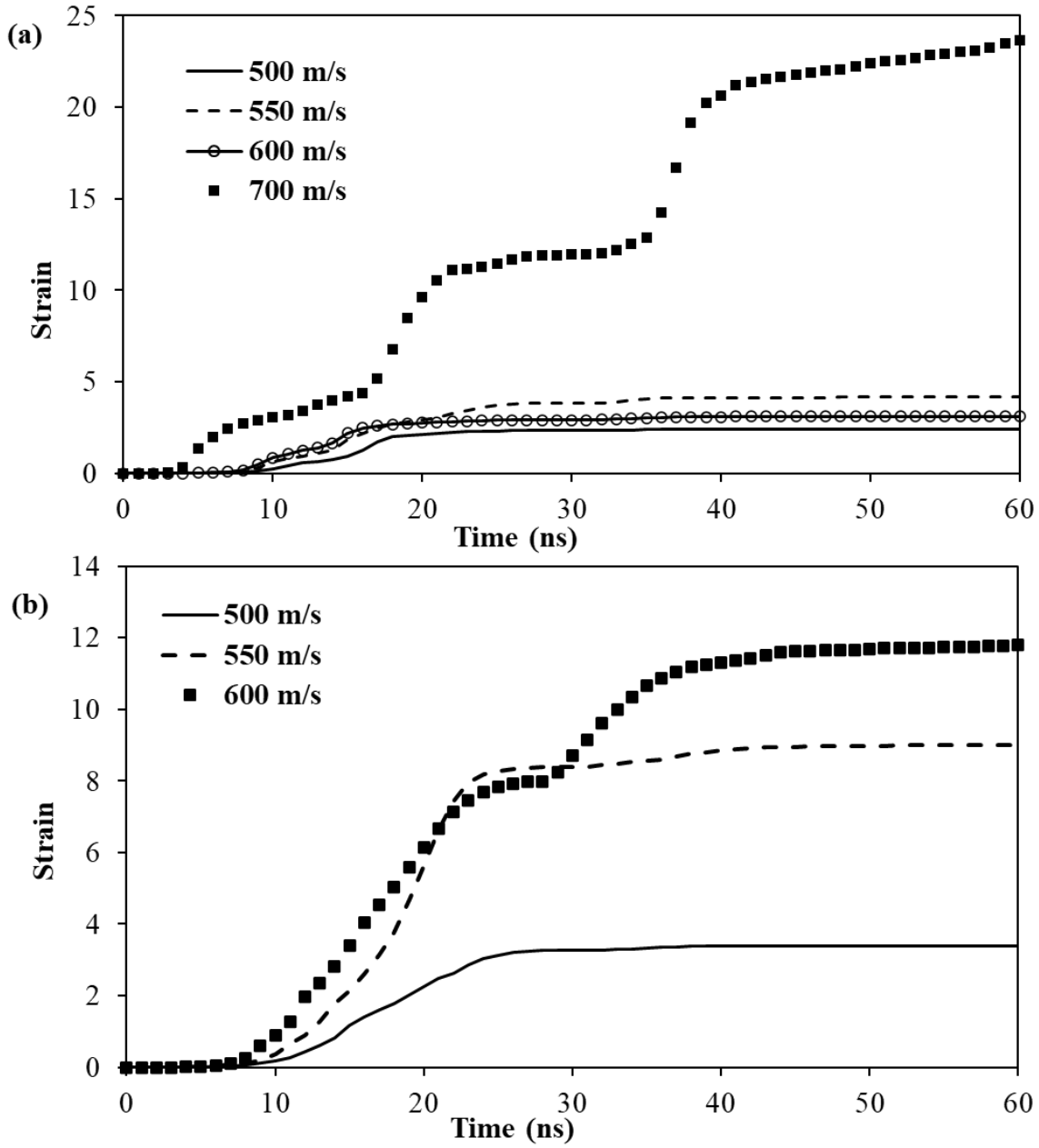

Figure 5.14: Plots of strain evolution of a critical element at the HEA particle interface, on SS304 (a) and Ti64 (b) substrates at various impact velocities. There is an abrupt change in the strain evolution indicating plastic strain instability at impact velocity 700 m/s and 600 m/s on the substrates.

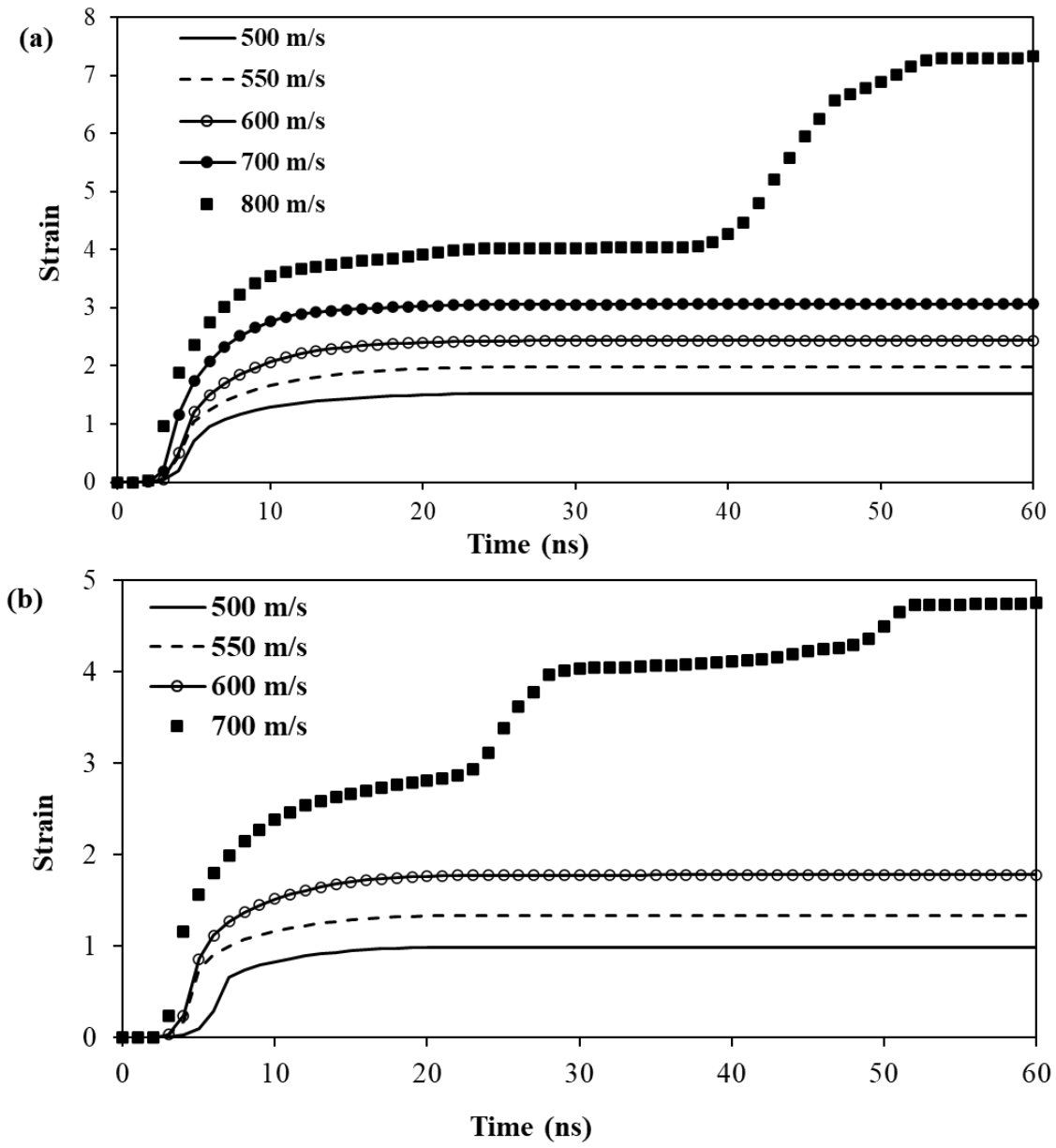

Figure 5.15: Plots of strain evolution of a critical element at the substrates interfaces; (a) on SS304, and (b) on Ti64 substrates. An abrupt change in strain evolution is observed at 800 and 700 m/s for the substrates.

5.5.2 Deformation behaviour of the HEA particle on soft substrates

The impact morphology of the HEA particles on soft substrates for impact velocities ranging from 400-700 m/s is shown in Figure 5.16. This range of particle velocities was chosen to obtain significant differences in the particle penetration depth within

the substrates. The FEA revealed deeply penetrated CP Al and Al6082 substrates, with the particles showing no significant deformation at all impact velocities. A similar impact morphology is observed in the SEM micrographs, as shown in Figure 5.8. Likely, the kinetic energy of the HEA particles is mostly dissipated into the plastic deformation of the soft substrates, and consequently, the particles are mechanically interlocked into the substrate. This contrasts with previous cases in which both the particles and substrates were deformed. Since the abrupt change in strain evolution of a critical element was not observed for the hard-soft material combination, the temperature profiles of a critical element at the substrates impact zone that experienced the highest temperature were plotted, as shown in Figure 5.17.

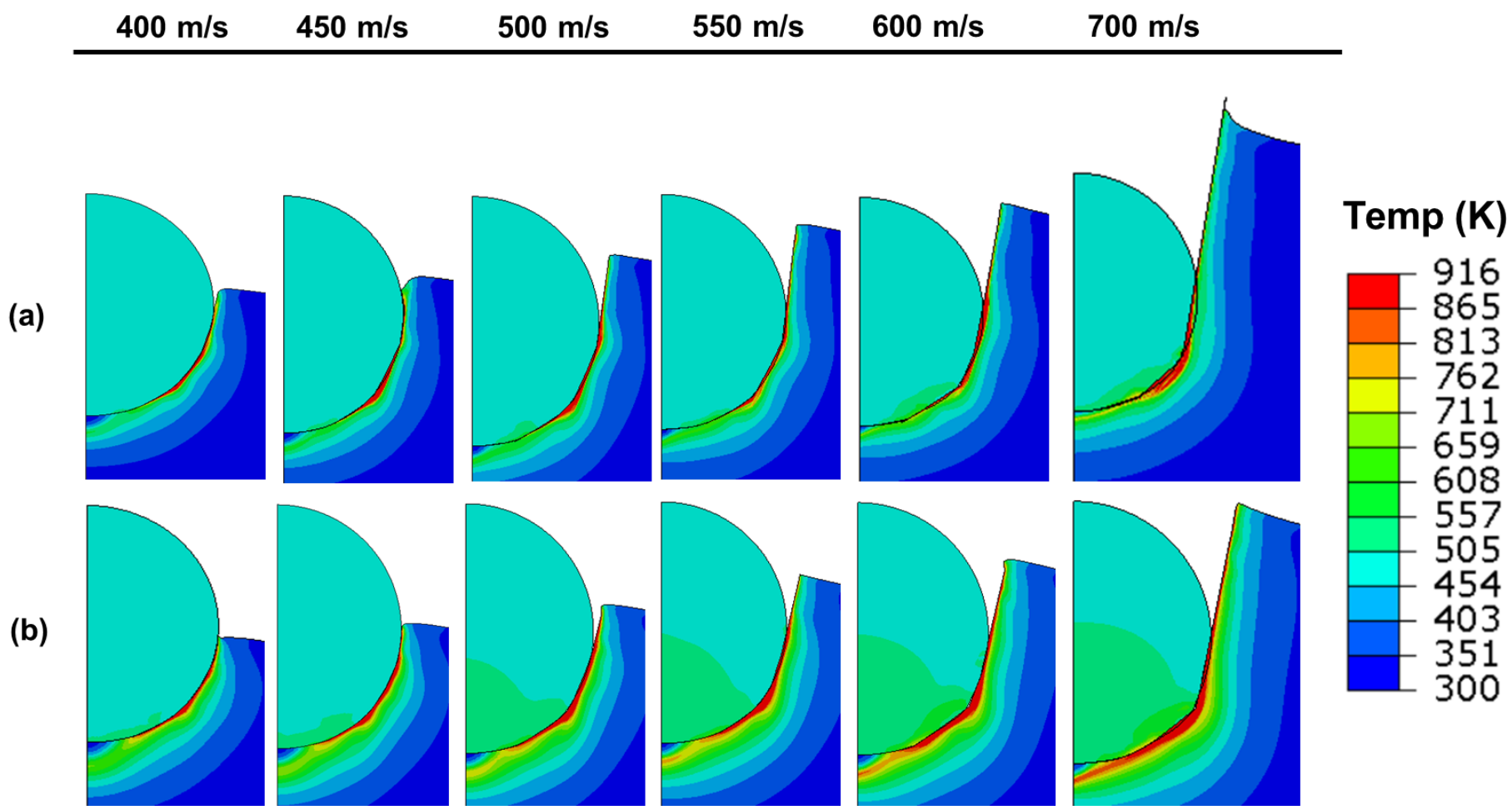

Figure 5.16: FEA impact morphology of the HEA particle on CP Al (a) and Al6082 (b) substrates at impact velocity ranging from 400-700 m/s. The particle penetration depth is observed to increase with the impact velocity as well as the substrate deformation.

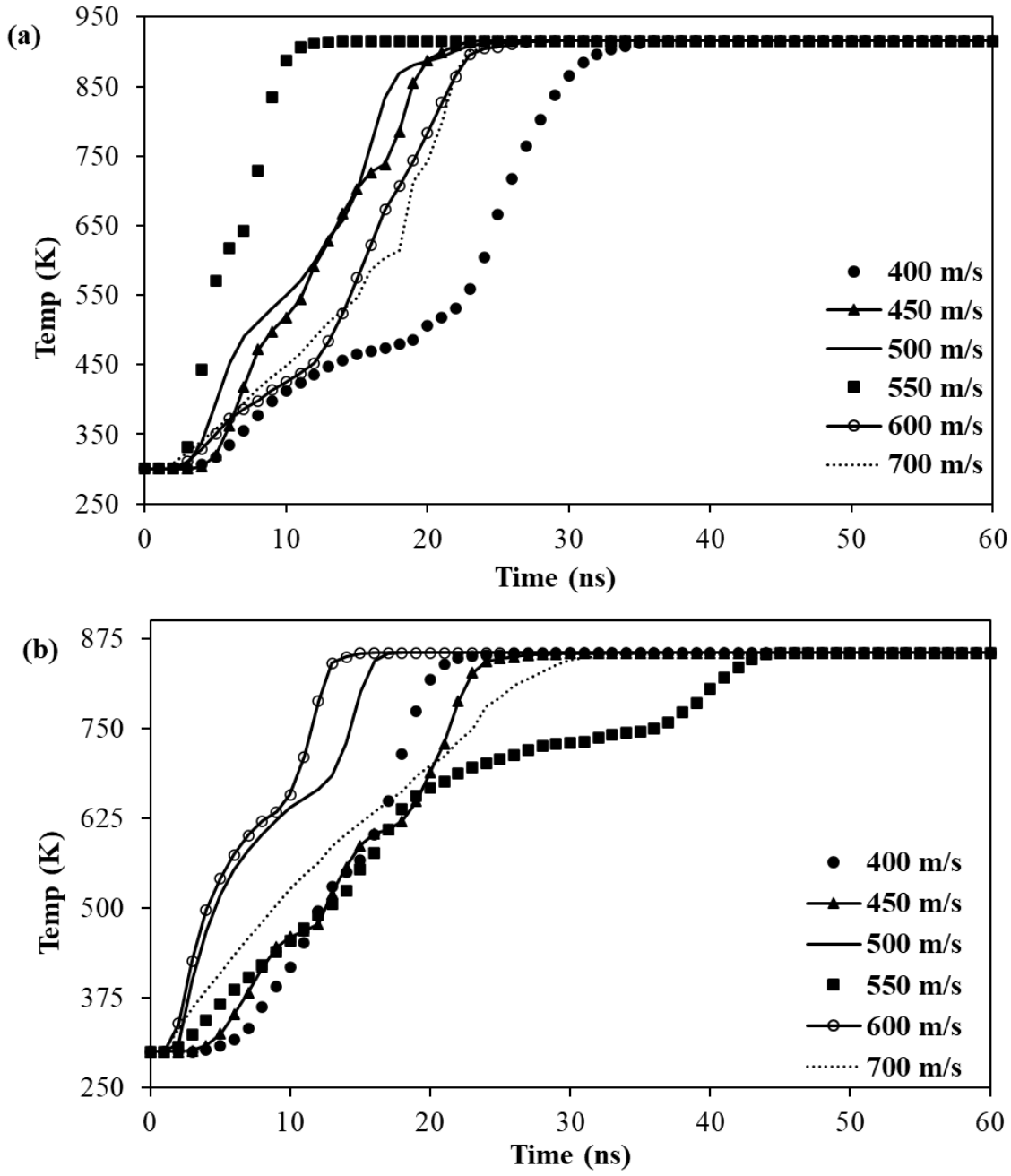

Figure 5.17: Plots of temperature evolution of a critical element on CP Al (a) and Al6082 (b) substrate impact interfaces at various impact velocities. There is a higher heat-up rate at 550 m/s and 600 m/s on the substrate interfaces during the deposition.

A previous FEA performed for Ti particles on Al substrates reported an abrupt change in the interface temperature at the soft Al substrate [131]. No abrupt change or “transition point” of the strain evolution was observed, which was due to the rapid temperature rise to the melting point of the Al substrate [131]. A similar trend was

observed for the FEA of the CoCrFeNiMn HEA particles on the CP Al and Al6082 substrates at all impact velocities, as shown in Figure 5.17. However, the temperature evolution of the CP Al substrate at 550 m/s shows a significant heating rate, which increases more rapidly than that of the other impact velocities. Although the heating rate at the interface of the CP Al substrate at all impact velocities was on the order of 10^9 K/s, the highest degree of heating to the substrate melting point (which can be determined by the slope of the temperature-time profile in the first 10 ns) was observed at 550 m/s. For example, the heating rates evaluated at 500, 550, and 700 m/s were 30 × 10^9, 65 × 10^9, and 16 × 10^9 K/s, respectively. The rapid temperature rise experienced by the CP Al substrate at 550 m/s suggests a threshold velocity for the deposition of HEA particles on the substrate. On the Al6082 substrate, on the other hand, the fastest temperature rise, or highest degree of heating was observed at 600 m/s with the heating rate of 40 × 10^9 K/s.

It is noteworthy that the interface temperature of the soft substrates reached the melting point over the range of impact velocities investigated, from 400 to 700 m/s. Using a 10 % deviation from the CFD results [108,300] presented in Figure 5.10 from the actual experimental particle velocity, the particle velocities for Run 1 and Run 2 would therefore be 538 and 583 m/s. This suggests that these impact velocities are below the threshold velocity required for the deposition of most of the HEA particles (i.e., the measured Dv50 particle size of 25 μm) on the Al6082 substrate. This is evidenced by the top-surface SEM images shown in Figure 5.6, where a few particles adhered on the Al6082 when compared with the CP Al substrate. Therefore, the degree of heating to the melting point of soft substrates

may be one of the factors contributing to the deposition or mechanical interlocking of the hard HEA particles in the soft substrates.

An additional criterion was observed for the mechanical interlocking of the hard HEA particle on the soft substrates, the particle penetration depth. Figure 5.18 shows the plot of the particle penetration depth on the soft substrates. This was evaluated as the vertical distance from the top surface of the substrate to the bottom of the particles within the substrate. There was a higher particle penetration depth on the CP Al substrate than on the Al6082 substrate for all impact velocities investigated. The particle penetration depth at 500 m/s on the CP Al was equivalent to that obtained at 600 m/s on the Al6082 substrate. Although the Al6082 substrate has a lower melting point than the CP Al substrate, as shown in Table 5.6, a higher particle velocity is required to achieve the equivalent particle penetration depth on the CP Al substrate. This suggests that the particle penetration depth likely plays a significant role in the bonding of hard particles on soft substrates (i.e., hard-soft material combinations) during cold spray deposition.

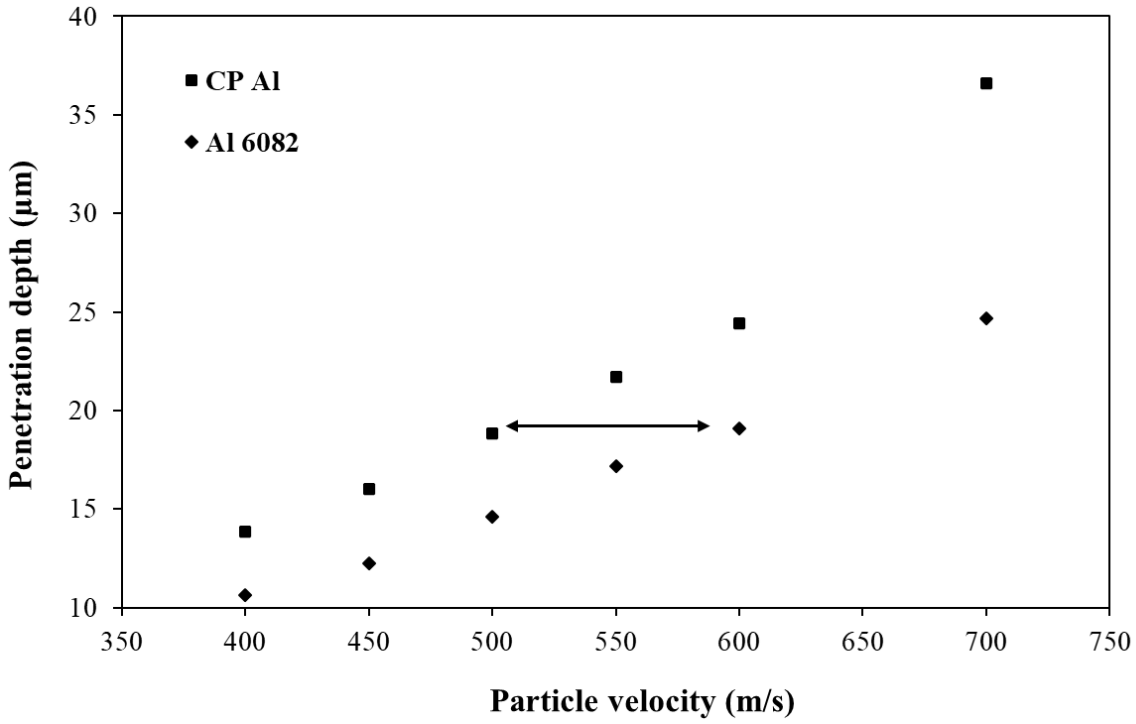

Figure 5.18: Evaluated particle penetration depth from the FEA of the CoCrFeNiMn HEA particle mechanically interlocked in the CP Al and Al6082 substrates. A particle penetration depth of ~ 19 µm on the CP Al substrate at 500 m/s is achieved on the Al6082 substrate at 600 m/s, as indicated by the arrow.

5.6 Discussion

In this section, the results from the experimental single-particle swipe test and FEA of HEA particles on various substrates are discussed. The impact of the HEA particles on the hard and soft substrates and their implications on the bonding and deposition of the HEA are discussed.

5.6.1 Impact phenomena of the HEA particles on hard substrates

It is clear from the results that the impact-induced bonding mechanisms of the CoCrFeNiMn HEA particles on hard and soft substrates can be grouped into

metallurgical bonding and mechanical interlocking. These bonding mechanisms can be influenced by various factors such as particle and substrate material properties, particle velocity, depth and width of the craters formed, and particle sizes. The metallurgical bonding mechanism observed for HEA particles on hard substrates can be attributed to adiabatic shear instability (ASI) at the impacting particle and substrate interfaces. ASI is a generally accepted thermomechanical deformation phenomenon that accounts for the metallurgical bonding of metallic materials during CSAM [56]. ASI is characteristically associated with high strain rate deformation, which results from an abrupt change in strain evolution [56,57,133]. The abrupt change in strain can lead to thermal softening (which dominates strain-hardening at a high strain rate) of metals; here, the mechanism of deformation changes from plastic flow to viscous flow, and consequently, a jet-type of material flow, as shown in Figure 5.4 and Figure 5.5 (e and f). The impact velocity which initiates the abrupt change in strain evolution is referred to as the material-dependent critical velocity for bonding during CSAM. As bonding in CSAM requires a combination of intimate contact and temperature, the transition to viscous flow at the critical velocity aids both of these.

The evaluation of the critical velocity of the CoCrFeNiMn HEA particles on hard substrates using the conventional concept of ASI has not yet been studied. In addition to ASI, pressure wave interactions have been proposed as another concept that involves the interactions of strong pressure waves with the expanding particle edge during deformation [136]. The pressure wave mechanism linearly relates the critical velocity to the bulk speed of sound of pure metals. While this can be true for some metals, such as Cu, Nikbakht et al. [63] suggested that the pressure-wave

concept cannot be relied on to predict the deformation mechanism and/or critical velocity of the HEA. Therefore, the concept of ASI can be employed to predict the deformation behaviour and critical velocity of the HEA particles on hard substrates during CSAM. However, the accuracy of this concept can be influenced by the approximations of the FE methods and material models used. Future work can include using different FE methods, such as the Eulerian method and other material models. Nevertheless, the fine-tuning of the J-C material data with the experimental particle flattening parameters or impact morphology performed in this study likely minimised the outcomes of any numerical inaccuracies.

The FEA of the HEA particle impact on hard substrates (SS304 and Ti64) revealed ASI at the particle and substrate interfaces. This occurred at lower velocities (600 and 700 m/s) at the particle interface when compared with those on the substrates (700 and 800 m/s), as presented in Figure 5.14 and Figure 5.15. This is because most of the kinetic energy is primarily dissipated in the plastic deformation of the HEA particles compared with the hard substrates both at lower impact velocity (where more craters were formed owing to particle rebounds, shown in Figure 5.3a, b, c and d), to high impact velocity where metal jetting was observed at the particle-substrate interfaces (as shown in Figure 5.4 and Figure 5.5 (c and d)). The substrate material properties and HEA particle sizes also influenced the impact morphology, with smaller particles resulting in pronounced jetting and penetration of the substrates, whereas larger particles deformed more intensely than the substrates (as seen in Figure 5.5d and e). The greater deformation of the substrates by the smaller particles can be attributed to the dynamic effects of small particles, such as the high viscous shear strength in the jetting region, high strain-hardening rate, and

higher strength following the Hall-Petch strengthening effect, which can hinder localised deformation, as stated by Schmidt et al. [57].

Despite the greater measured microhardness and strain-hardening ***B*** of Ti64 ((315.0 ± 4.5) HV0.5 and 1092 MPa) compared to the SS304 substrate ((192.1 ± 1.7 HV0.5) and 802.5 MPa), the critical velocity for bonding of the HEA on Ti64 (600-700 m/s) is lower than that on the SS304 substrate (700-800 m/s). If the plastic deformation of the substrate is considered for the determination of the critical velocity (as suggested by Ichikawa [306] and Ogawa, and Arabgol et al. [307]), this would therefore be 700 m/s and 800 m/s for a 25 µm particle size of the HEA on Ti64 and SS304 substrates. In addition, the evaluated particle FR (presented in Table 5.4) was found to increase with the increase in the substrate hardness (provided in Table 5.3), as well as an increase in the particle velocity (from spray Run 1 to Run 3). Therefore, as the substrate hardness and particle velocity increase, a higher proportion of kinetic energy is used to deform the impacting particles, particularly for larger particles, rather than the substrates.

It is speculated that the impact of the HEA particles on the harder Ti64 substrate would require a higher critical velocity for ASI to occur earlier than on SS304, but this is not the case. The underlying mechanism for this deformation behaviour can be explained as follows: the plastic deformation of materials at high strain rates can reduce their thermal diffusion distance, $\boldsymbol{D_{th}}$ [308]. Thus, the bonding of particles on substrates in the CSAM process can be determined by the degree of localised strain and thermal build-up during the deformation process. Quantifying the affected volume over which there is an adiabatic temperature rise, $\boldsymbol{V_{aff}}$ for the SS304 and

Ti64 substrates at an impact velocity of 600 m/s, by using $\boldsymbol{V_{aff} = D_{th} \times A_c}$ [309], where $\boldsymbol{A_c}$ is the maximum contact area extracted from the FEA. The maximum contact areas of HEA/SS304 and HEA/Ti64 at 600 m/s are 0.867 × 10^{-6} μm^2 and 0.827 × 10^{-6} μm^2. Thermal diffusion, $\boldsymbol{D_{th}}$ was evaluated using $\boldsymbol{D_{th} = \sqrt{\frac{K}{\rho C_P}} \times t_r}$, where $\boldsymbol{K}$ is the thermal conductivity, $\boldsymbol{\rho}$ is the material density, $\boldsymbol{C_P}$ is the specific heat capacity and, $\boldsymbol{t_r}$ is the contact time or residence time of the particle on the substrates given as the ratio of the particle diameters to the impact velocity, which is ~ 42 ns. The calculated $\boldsymbol{D_{th}}$ is 330 nm and 432 nm, and the corresponding $\boldsymbol{V_{aff}}$ is 27.3 nm^3 and 37.5 nm^3 for the Ti64 and SS304 substrates. Thus, a smaller thermal diffusion distance and volume affected by the high localised strain and thermal build-up were obtained on the Ti64 substrate. In addition, the FEA of the temperature profile shown in Figure 5.13, reveals a higher temperature rise at the Ti64 than on SS304 substrates interfaces. Therefore, these analyses indicate that the degree of localised interface shear straining, and thermal build-up is greater on the Ti64 substrate, which is likely contributing to the lower critical velocity for bonding of the HEA particle. This can be attributed to the lower density and thermal conductivity of Ti64 (4430 kg/m^3 and 6.7 W/mK). Moreover, this is evidenced by the fraction of adhered particles on the Ti64 substrate under the spray condition of Run 2 (approximately 600 m/s), which is higher than that on the SS304 substrate, as shown in Figure 5.3c and d.

The higher critical velocity for the deposition of HEA particles on the SS304 substrate, on the other hand, lies in the window of deposition for austenitic stainless steels 316L and 304—700 to 1500 m/s, as reported by Schmidt et al. [57] and Coddet et al. [310]. Since CoCrFeNiMn HEA and SS304 have similar material

properties (density and elastic modulus—Table 5.6, and crystal structure (FCC)), it is ideal for comparison of the HEA particle-particle and particle–substrate interactions during CSAM deposition. Schmidt et al. [57] calculated a critical velocity of approximately 700 m/s for a 25 μm SS316L particle on a similar substrate material, which correlates well with the calculated critical velocity for the 25 μm HEA particle on the SS304 substrate in this study as shown in Figure 5.19. However, the sluggish diffusion effect [35,36], higher critical shear strain, and yield strength of CoCrFeNiMn [63] are likely to result in a higher critical velocity for the deposition (and complete bonding of deformed particles) of the HEA/HEA pair compared to HEA/SS304. It is envisaged that the deposition of the HEA particle on the HEA substrate will provide a better representation of the HEA/HEA particle-substrate material interactions. Nevertheless, as stainless steel materials are currently used to manufacture aerospace components and structures, unlike the HEA material, the HEA material can therefore be employed to repair those components keeping the strength-to-weight ratio while improving the structural integrity of the components using the CSAM process. In general, CoCrFeNiMn HEA lies in the regime of difficult-to-spray materials for the CSAM process, such as austenitic stainless steel, titanium, and other engineering alloys, as the CoCrFeNiMn HEA material lies in the window of deposition and or critical velocity for CSAM of these materials as presented in Figure 5.19.

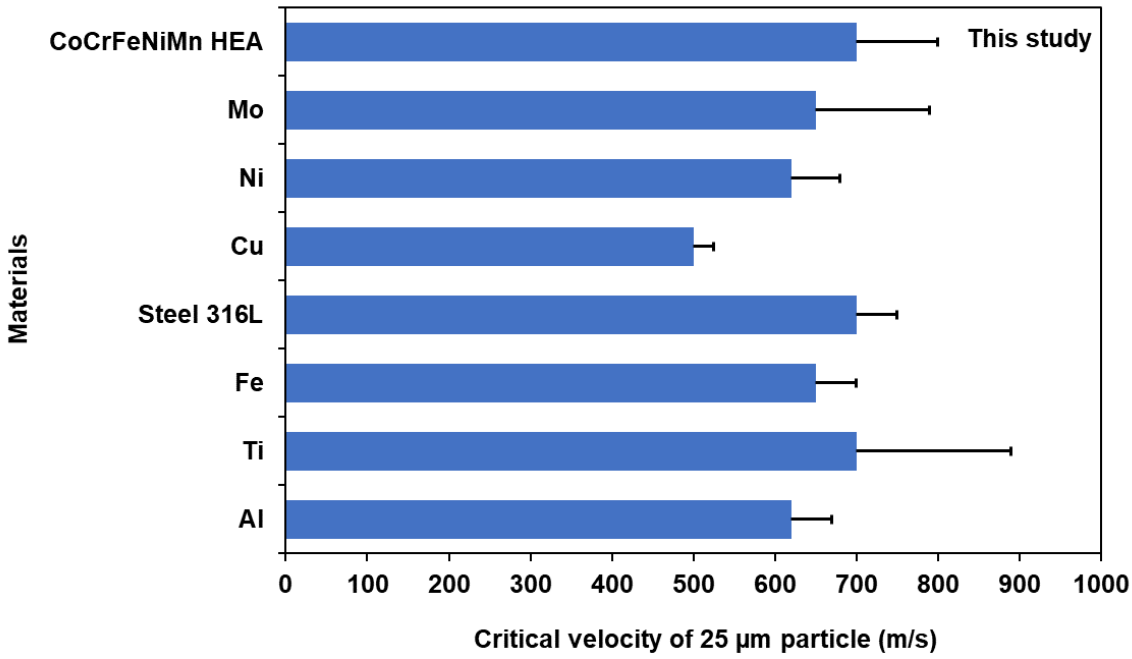

Figure 5.19: Critical velocity for a 25 µm particle for different materials from the literature [57] and that of the CoCrFeNiMn HEA determined in this study. The error bar indicates a range of values.

5.6.2 Impact phenomena of the HEA particles on soft substrates

The CSAM of the CoCrFeNiMn HEA on the Al6082 substrate resulted in a lower fraction of adhered particles and a higher number of craters formed on the surface compared to the CP Al substrate (as shown in Figure 5.6). Even though the deposited particles did not show any evidence of jetting due to limited deformation (Figure 5.8), a fraction of the sprayed particles were still deposited on the soft substrates. The particles were deposited because the substrates were significantly deformed, allowing mechanical interlocking of the particles.

The FEA revealed a special type of ASI occurring in the soft substrates, where no abrupt change in strain was observed but rather a high heat-up rate [131], as shown in Figure 5.17. As the impact velocity increased, the heating rate increased owing

to the increase in the deformation of the substrates at the impact interfaces, resulting from kinetic energy dissipation from the particle during deposition. A steep gradient in the temperature-time profile and calculated heating rates was observed at all impact velocities investigated; however, a higher heating rate was observed at impact velocities of 550 m/s and 600 m/s for the CP Al and Al6082 substrates. Below or above these velocities, the heating rate decreased (Figure 5.17). These observations can be associated with the findings of Hassani et al. [309,311], where an increase in the impact velocity above the threshold velocity for particle adhesion resulted in a decrease in the solidification/heating time; therefore, the deposition resulted in melt-driven erosion and, subsequently, rebounding of the sprayed particles. This effect is attributed to the short time scales for adhesion at impact velocities above the adhesion velocity, that is, the residence time for the HEA particle on the CP Al substrate at a velocity above 550 m/s is far lower than the solidification time (and/or heating time) of the heated volume material at the substrate interface. With a higher particle rebound energy at higher impact velocities [144] and insufficient bonding time, the particle is likely to rebound from the soft substrates with no mechanical resistance. Because there is likely an insufficient time for the solidification of the heated material needed for bonding, despite heating to the melting point of the substrate material, it is likely that there is an additional mechanism or factor responsible for the mechanical interlocking of the HEA particles.

In addition to the strain-induced melting at the soft substrate impact interfaces revealed by the FEA, there is likely a critical particle penetration depth that would allow for mechanical interlocking of the particle. Moreover, the particle penetration

depth increases monotonically as the particle velocity increases, as shown in Figure 5.18. This is due to the thermomechanical effects of the soft substrate during the particle deposition, which would increase the particle interlocking mechanism once embedded [156]. The FEA results agreed well with the single-particle impact experiments of the HEA particles on the soft substrates. The difference in the critical velocities of the soft substrates can be attributed to the behaviour of the precipitate-hardened aluminium alloy 6082 (Al6082) under the high strain-rate deformation during cold spraying. Although the microhardness values differ by 7 HV, which may affect their relative deformation behaviour, the strength differences at higher strain rates or temperatures most likely contributed to the difference in their deformation behaviour during the cold spray deposition. Moreover, the Al6082 substrate was characterised by a higher strain-hardening exponent ***n***, yield strength ***A***, and strain-rate sensitivity ***C***, values from the J-C model data presented in Table 5.6, which likely contributed to the shallower particle penetration depth, resistance to plastic deformation and hence higher critical velocity compared to that of CP Al substrate.

To relate the deep-impact particle penetration depth to the onset deposition velocity (i.e., critical velocity), the empirical projectile law by Eichelberger and Gehring [312] relates the crater volume (***V***, in m^3) produced by micrometeoroid impact on spacecraft to the material Brinell hardness (***B***) and, impact energy (***E***) of the micrometeoroid. This empirical law or equation has been employed by Victor et al. [142] to evaluate the interfacial mixing of Cu and Al during CSAM. The empirical equation is given by Equation (5.1).

$$V = \frac{(4 \times 10^{-5})E}{B} \tag{5.1}$$

The impact energy, $E = 0.5\left[4/(3\pi r^3 \rho)V_p\right]$, was substituted into Equation (5.1), where ρ is the particle density, r is the particle radius, and V_p is the particle velocity. In addition, it was assumed that the crater volume V equals the penetration depth D multiplied by the particle surface area (πr^2). Thus, Equation (5.1) becomes:

$$V = (\pi r^2)D = \frac{\left(4 \times 10^{-5}\right)0.5\left[4\rho/(3\pi r^3){V_p}^2\right]}{B} \tag{5.2}$$

The particle penetration depth D is then given as:

$$D = \left(4 \times 10^{-5}\right)\left(\frac{2\rho r}{3}\right)\left(\frac{{V_p}^2}{B}\right) \tag{5.3}$$

If the Brinell hardness B of the substrate is estimated from the HV values provided in Table 5.3, a 25 μm of the HEA particle on a CP Al substrate at 600 m/s would result in a particle penetration depth of approximately 27 μm, which agrees well with the experiment (26.4 μm) and FEA results (24.4 μm). If, again, it is assumed that the entire particle is embedded within the substrate (that is $D = 2r$) at the onset of the deposition, then the critical velocity for the deposition of the hard particle on the soft substrates is given as

$$V = \sqrt{75000 \times \left(\frac{B}{\rho}\right)} \quad (5.4)$$

Therefore, Equation (5.4) provides a simple, empirical equation for estimating the particle velocity required for the first monolayer deposition of the hard HEA particles on a soft substrate. For a 25 μm CoCrFeNiMn HEA particle impact on CP Al and Al6082 substrates, the critical velocities were approximately 563 m/s and 618 m/s, respectively. These values agreed well with the FEA results at 550 and 600 m/s.

The results obtained in this study suggest that the thermal effects, that is, the heating rate of the substrate material to its melting point and particle penetration depth should be evaluated to determine the critical velocity of hard particles on soft substrates. This depends on the hardness of the substrate and the particle density. Notably, this is true only for the first monolayer deposition. During deposit build-up, material intermixing of the particles on the soft substrates may occur under low deposition efficiency, which can be a future study; however, the repetitive impacts of rebounded particles must be allowed [140], which is not the case in this single-particle impact.

5.7 Conclusions

The impact morphology and deformation behaviour during CSAM of the CoCrFeNiMn HEA onto various substrates were investigated experimentally and numerically in this study. Different sets of Johnson-Cook material model parameters for the HEA were obtained from the literature. The numerical analysis of all sets was

then compared with the experimental impact morphology and particle-flattening ratio. The results and comparisons were linked to the sets of Johnson-Cook model parameters, and the most suitable one that best predicted the deformation behaviour of the HEA was selected and employed for further numerical analysis using the Abaqus/Explicit code with the Lagrangian approach. The following conclusions were drawn from the results of this study:

- CSAM of CoCrFeNiMn HEA onto SS304 and Ti64 (hard substrates) resulted in adiabatic shear instability at the particle and substrate interfaces—metallurgical bonding. On the other hand, the CSAM of the HEA onto CP Al and Al6082 (soft substrates) resulted in significant localised deformation and penetration of the substrates—mechanical interlocking. The hard substrate material properties, such as density and thermal conductivity, influenced the particle-substrate deformation behaviour and impact morphology, while the soft substrate hardness and particle density influenced the extent of mechanical interlocking and penetration depth of the HEA particles.

- An abrupt change in strain, which indicates the onset of ASI (and metal jetting), was observed in the HEA particles and SS304 substrate at particle velocities of 700 and 800 m/s, respectively. However, on the Ti64 substrate, ASI was observed at the particle and substrate interfaces at particle velocities of 600 and 700 m/s, respectively. The particle velocities for the onset of ASI in the substrates were chosen as the critical velocities for the deposition of the HEA particles, which were 800 m/s and 700 m/s on the SS304 and Ti64 substrates, respectively. Despite the higher hardness and

strain-hardening values of the Ti64 substrate, a lower critical velocity of the HEA on the Ti64 substrate was obtained, which was attributed to the lower density and thermal conductivity of Ti64.

- The FEA revealed an abrupt temperature rise of the CP Al and Al6082 substrates to the material melting point during CSAM deposition of the HEA. The fastest temperature rise was observed at 550 and 600 m/s on both substrates. The particles penetrated the soft substrates deeply because of the localised deformation of the substrates.

- In addition to the strain-induced melting of soft substrates at a high heat-up rate, the particle penetration depth has been reported as an additional criterion for the mechanical interlocking of CoCrFeNiMn HEA particles on soft substrates. An empirical equation relating the particle penetration depth to the particle velocity shows that mechanical interlocking is influenced by the hardness of the soft substrates and the particle density. Using the empirical equation, the critical velocities of the HEA on CP Al and Al6082 were found to be 563 and 618 m/s, respectively. The higher critical velocity of the HEA on Al6082 is attributed to its higher strain-hardening exponent and strain-rate sensitivity compared to CP Al.

The investigations in this chapter reveal that for the first layer deposition of the HEA using CSAM, CP Al would be more suitable because of the low critical velocity of the HEA on the substrate (550-563 m/s). For subsequent deposit build-up, it is however believed that spraying parameters within the window of deposition of the HEA (with the critical velocity of 700-800 m/s) would be required. This is because

during deposition the particle of the feedstock material interacts to bond and form a deposit, hence the critical velocity for similar material combinations. This is especially important for CSAM of aerospace components. Consequently, the interactions between the HEA particle and SS304 substrate closely represent the possible interactions of the HEA particles during deposit build-up. Therefore, the SS304 substrate was employed for the deposition of the HEA feedstock material in the studies presented in the following chapters. Also, as stated earlier, it is intended in this research project that aerospace components made of stainless steel could be repaired with the HEA feedstock using the CSAM technique.

6 Microstructural study of CoCrFeNiMn HEA deposit manufactured using CSAM

6.1 Introduction

The critical velocity for the deposition of the CoCrFeNiMn HEA on various substrates; grouped as hard and soft substrates, was determined in the study of the previous chapter. The window of deposition of the HEA was suggested to be within the range of difficult-to-spray materials such as stainless steel. The spraying parameters that resulted in the critical velocity of the HEA on the SS304 substrate were employed in this chapter to develop thick deposits of the HEA. The SS304 substrate material was selected for further study as it was intended that the HEA feedstock material could be employed for the cold spray repair of aerospace components made of stainless steel material. Another reason for selecting the substrate material, hence the material combinations, was to further study the deposition behaviour of the HEA/HEA pair without the effect of substrate material properties as the SS304 and HEA are of similar material properties.

Several studies have reported heterogeneous microstructure formed in metallic deposits after the CSAM process [137,147,313,314]. The heterogeneous microstructure contributed to excellent mechanical properties such as strength-ductility combination [313]; however, there are limited studies that have investigated the microstructure and its formation mechanism of the CoCrFeNiMn HEA during CSAM [40,63,129]. In addition, the use of finite element analysis (FEA) to

understand the splat formation during CSAM deposition of the HEA is limited [141,266]. There is also a wide gap in knowledge on multi-particle deformation modelling of the HEA, limiting our understanding of the microstructural evolution of the HEA during CSAM. This study provides insight into the interaction between the HEA particles and the substrate, when developing deposits layer by layer, enabling the repair of components using the HEA feedstock material to form dense heterogeneous microstructures via the CSAM technique.

Therefore, this chapter presents the microstructural study of the CSAM CoCrFeNiMn HEA deposit. The chapter involves advanced materials characterisation of the deposit using electron-backscattered diffraction (EBSD), scanning electron microscopy (SEM) and x-ray diffraction (XRD) to investigate the microstructure evolution of the HEA material under ultrahigh strain-rate deformation. The study combines experimental analysis with FEA to understand the bonding mechanisms and grain structure formation of the HEA resulting from the CSAM process. The influence of the microstructure on the nano- and micro-hardness properties of the deposit was analysed.

It is noteworthy that this chapter is published as a peer-reviewed article as presented in the “Publication” section of this thesis.

6.2 Experimental methods

6.2.1 Materials

The CoCrFeNiMn HEA feedstock powder was deposited on a 2-mm thick rectangular SS304 substrate plate with dimensions of 25 × 60 mm. Detailed analysis of the powder chemistry and particle size distribution has been provided in Chapter 5 Section 5.3. The substrate was ground with P240 SiC grit paper, cleaned with an industrial methylated spirit (IMS), and dried with compressed air before spraying to enhance the adhesion of the deposit during the CSAM.

6.2.2 CSAM deposition

A high-pressure CSAM system developed at the University of Nottingham, as described in Chapter 3 Section 3.2, was employed for the deposition of the HEA powder feedstock using Helium (He) as the accelerating gas. The pressure and temperature of the gas were maintained at 3.3 MPa and 400 ºC throughout the spraying process. The deposit was manufactured by spraying 4 passes at a nozzle transverse speed and powder feed rate of 100 mm/s and ~42 g/min. These spraying parameters employed were informed by the particle deformation dynamics and average critical velocity of the HEA particles, as revealed by the studies undertaken in Chapter 5. The powder carrier gas was set at 0.1 MPa higher than the accelerating gas pressure. The CSAM nozzle was held stationary while the substrates were mounted on a programmable x-y table that allowed a controllable scan pattern and velocity.

6.2.3 Materials characterisation

To examine the microstructure of the feedstock powder and the CSAM HEA deposits, samples were prepared following the metallographic procedures outlined in Chapter 3 Section 3.3.

The microstructure of the deposit was observed using the Philips XL30 SEM operated at 15 kV in the backscattered electron (BSE) mode. The porosity and thickness of the deposit were quantified by the image analysis described in Chapter 3 Section 3.6. Five BSE SEM images were used to measure the thickness of the deposit, while ten BSE SEM images were used to measure the porosity. The images were captured at × 500 magnification, resulting in a field of view with an area of 100 × 100 μm^2. The results are presented as average values with the standard error of the mean of the measurements.

The crystal structure of the powder and deposit was determined using the X-ray diffractometer (Bruker, Germany) described in Chapter 3 Section 3.5.3. The microstrain and crystallite size in the powder and deposit were estimated with the Williamson-Hall (W-H) method [315]. The W-H equation, which relates the actual peak broadening $\boldsymbol{\beta}$ to the microstrain $\boldsymbol{\varepsilon_p}$ and crystallite size $\boldsymbol{d}$, is given by Equation (6.1). Here $\boldsymbol{\theta_B}$ represents Bragg's angle of the peak, $\boldsymbol{\lambda}$ is the wavelength of the Cu Kα radiation source (0.1546 nm), and $\boldsymbol{\kappa}$ is a constant (0.89). The peaks' full width at half maximum (FWHM) values were evaluated after stripping the $K\alpha_2$ using the EVA software.

$$\beta cos\theta_B = \frac{\kappa\lambda}{d} + \varepsilon_p 4 sin\theta_B \quad (6.1)$$

To observe the morphology and measure the size of the grains in the powder, EBSD imaging was performed on a FEG SEM (7100F, JEOL Ltd., Japan). The EBSD scans of the powder sample and post-processing data were carried out using AZtecCrystal software (Oxford Instruments, UK). Detailed information on the EBSD analysis has been provided in Chapter 3 Section 3.5.2. The feedstock powder material's elemental distribution was studied using an energy dispersive x-ray spectroscopy (EDX) detector (Xmax 150 EDX detector, Oxford Instruments, UK) mounted on the FEG SEM. The EBSD imaging of the deposit was performed on a Zeiss™ Auriga Cross Beam SEM (Germany), a collaborative work with Imperial College, London. Details of the EBSD procedures have been provided in Chapter 3 Section 3.5.2.

The nanohardness of the feedstock powder and the CSAM deposit was measured using a NanoTest P3 nano-indenter (Micro Materials Ltd., UK). The nanohardness measurements performed in this study have been provided in Chapter 3 Section 3.7.1. The indentation load employed for the nanohardness was chosen after carefully selecting the indent size, the distance between the neighbouring indents (7 µm) to account for the plastic zone or indent impression, and the distance between indents and the splats boundaries to avoid pores when indenting the deposit. The nanohardness and reduced modulus from the nano-indentation were derived following the Oliver and Pharr method [274], as described in Chapter 3 Section 3.7.1. The microhardness of the deposit was also measured using a Wilson VH3300 Vickers Microhardness instrument (Buehler, USA). Detailed information on

the microhardness measurement has been provided in Chapter 3 Section 3.7.2. The deposit sample in this chapter however underwent an array of 280 micro-indents. The final value is presented as an average with the standard error of the mean of the measurements.

6.3 Numerical modelling

The impact behaviour of high-velocity, micro-sized HEA particles onto the SS304 substrate was modelled using the Lagrangian approach with the Abaqus/Explicit commercial code. A two-dimensional (2D) model was used to simulate the multi-particle deformation behaviour of the HEA material on the substrate, details of which are provided in Chapter 4 Section 4.2.2. The material model including the Johnson-Cook (J-C) material model assessed and selected in Chapter 5 Sections 5.4 was employed to model the deformation behaviour of the particles and substrate material in this chapter. The particles and substrate impact zone uses a mesh size of 0.4 µm, which follows the mesh convergence study as provided in Chapter 4 Section 4.1. The simulation was run for 1 µs to capture the whole deformation process.

The particle velocities and temperatures are required as input parameters for the Abaqus/Explicit impact model, which can be provided by the computational fluid dynamics (CFD) model described in Chapter 4 Section 4.1. The input parameters were predicted following the experimental spraying conditions employed for the deposition of the feedstock powder. Spherical CoCrFeNiMn particles from 5-60 µm, with an initial temperature of 25 ºC were used as powders injected at the nozzle

inlet. The result of the CFD analysis is provided in Figure 6.1, which reveals that the increase in particle size results in a decrease in velocity while temperature increases. Since the CFD results are likely to deviate from the actual experimental particle velocity and temperature [74,108,300], a 15% deviation from the CFD results is employed. With the spraying conditions employed, the estimated particle velocities for the particle size range from 10-45 μm would be from 1175-704 m/s. Thus, the average particle velocity (i.e., for a particle size of 25 μm) would be ~885 m/s, which is above the estimated average critical velocity of 800 m/s evaluated in Chapter 5.

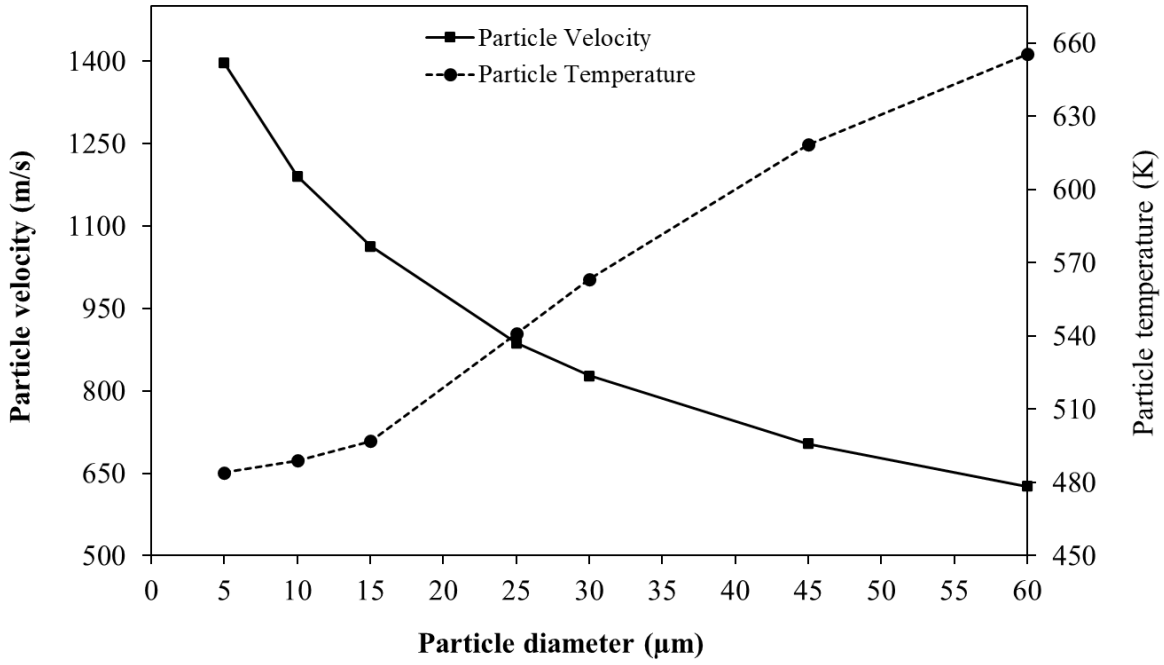

Figure 6.1: The results of the CFD analysis of the HEA particles' velocity and temperature as a function of particle sizes.

6.4 Results

6.4.1 Powder microstructures

A representative image of the microstructure and elemental distribution of the CoCrFeNiMn HEA feedstock powder particle obtained from the EBSD scan is presented in Figure 6.2 The figure also presents the grain size analysis of about 15 particles with different particle sizes. Figure 6.2a represents the EBSD Inverse Pole Figure (IPF) map of a HEA feedstock powder particle. The IPF map, with different colours representing the grain orientations, reveals several randomly oriented grains with different shapes and sizes within the HEA particle. The powder particle microstructure appears to consist of a mixture of columnar and equiaxed grains, likely growing outwards from the nucleation point, as indicated in Figure 6.2a. These features likely result from the undercooling and dendrite break-up during the gas-atomisation process [316]. Few poorly indexed grains at the particle edges can be seen, attributed to polishing artefacts. Figure 6.2b shows the size distribution of the grains in the HEA powder particles with an area-weighted average grain size of about 6-7 µm. EDX mapping of the elemental composition of the HEA powder particles is presented in Figure 6.2c, showing microsegregation of Co, Cr and Fe in the dendritic interiors, which has also been observed in a previous study [267]. The chemical composition of the powder is 22.3 wt.% Co, 19.3 wt.% Cr, 20.1 wt.% Fe, 20.7 wt.% Ni and 17.6 wt.% Mn.

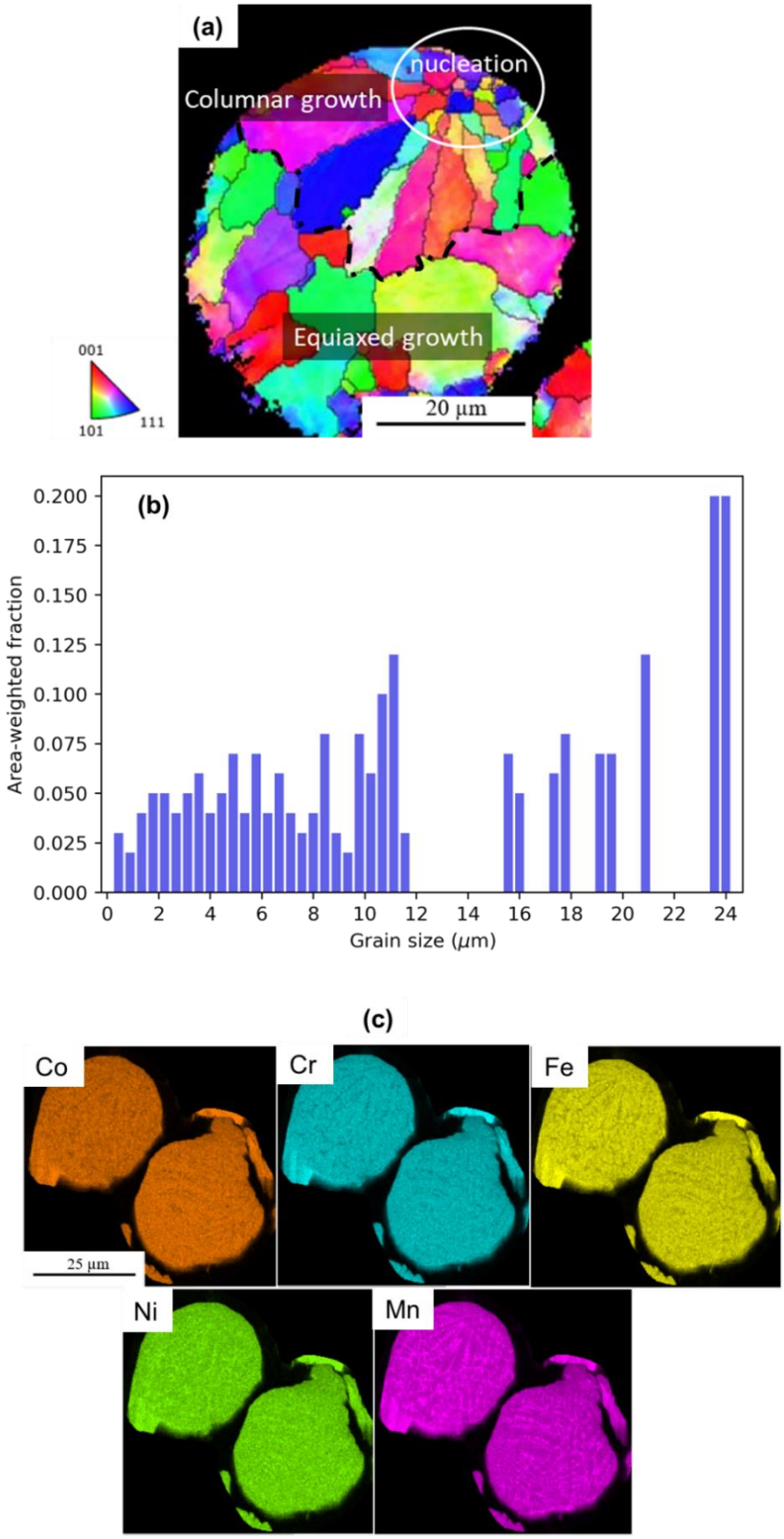

Figure 6.2: EBSD image showing the inverse pole figure (IPF) map of a powder particle (a); (b) grain size distribution of about 15 powder particles analysed. The short-dashed black lines in (a) were manually included to differentiate between the columnar and equiaxed grain growth in the powder particle. (c) shows the EDX mapping of the powder microstructure.

6.4.2 Porosity and inter-particle bonding

SEM micrographs of the CoCrFeNiMn HEA deposit cross-sections on the substrate at various magnifications are shown in Figure 6.3. The low magnification micrograph in Figure 6.3a presents a (1.67 $\pm$ 0.03) mm thick deposit showing no discontinuity or delamination at the deposit-substrate interface, indicating a good bonding between the deposit and the substrate during the CSAM. A porosity of (2.4 ± 0.3)% was measured in the deposit. Higher magnification micrographs of the deposit cross-sections in Figure 6.3b and c reveal a nearly homogenous distribution of pores.

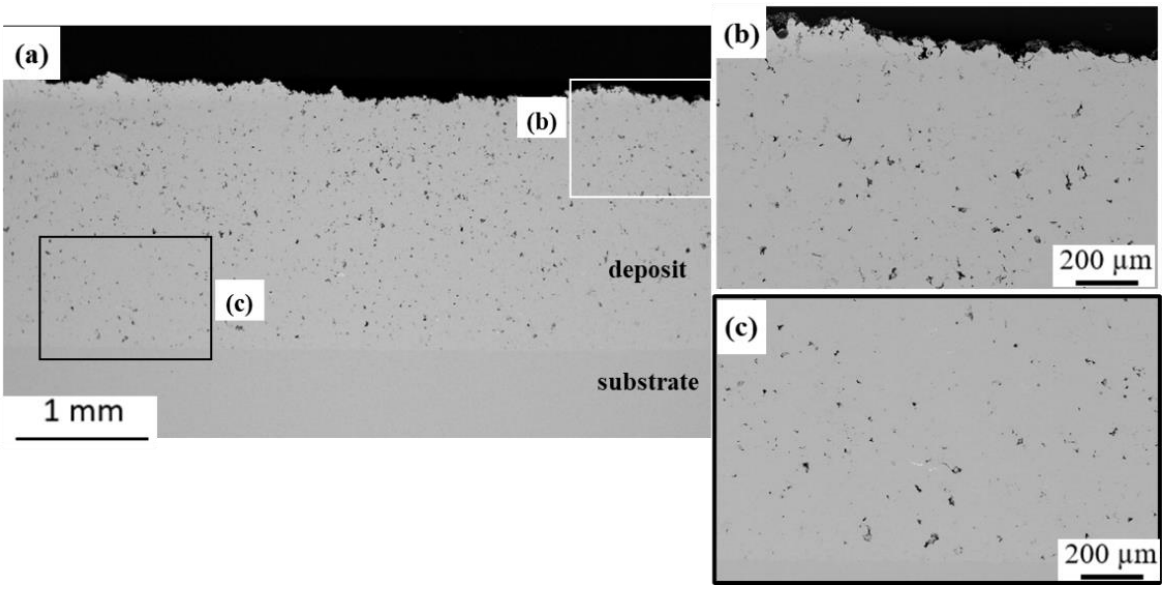

Figure 6.3: shows the microstructure of the CSAM HEA deposit; (a) low magnification BSE SEM image showing the deposit, interface and substrate, (b) and (c) showing high-magnification images of the deposit's top and bottom layers. The high-magnification SEM micrographs were taken from the region indicated with square boxes in (a).

As a representative of the deposit cross-section, the high-resolution SEM micrograph obtained using the FEG SEM at Imperial College and the FEA of the

multi-particle impact model of the HEA particles on the substrate is presented in Figure 6.4. The deposit microstructure shown in Figure 6.4a and b consists of splats with globular or oblate spheroid morphology, and similar deformation morphology is observed in the FE model. This suggests that the FE model employed thus represents the HEA particle deformation morphology well. Furthermore, a broad distribution of the splat size within the deposit microstructure was observed, correlating with the characteristic particle size distribution of the HEA powder, in addition to the effect of particle size-dependent impact energies on the deformation of the particles upon impact. The HEA splat flattening ratio (FR) in the SEM micrograph and FEA was evaluated. The splat width and height were evaluated as the major and minor axes of the oblate spheroid splat shape [317] within the deposit microstructure. Fifteen splats with clear splat boundaries and different sizes were evaluated within the SEM micrograph of the deposit cross-section and the FE model. The FRs (average with standard error of the mean) of (2.0 $\pm$ 0.2) and (1.9 $\pm$ 0.1) were obtained in the deposit microstructure and FE model. Again, these values indicate that the FEA predicts the HEA particle deformation behaviour during CSAM well. These values can be inevitably associated with errors as mechanically polished cross-sections do not usually pass through the centre of splats. In addition, actual CSAM spraying parameters such as particle impact and substrate temperature, actual mechanical properties of the powder material, and the limitations of the numerical approach would likely influence the FR calculations. Nevertheless, this approach has been employed in previous work [204,318], giving an approximation of the FR and, subsequently, the extent of plastic deformation of the particles.

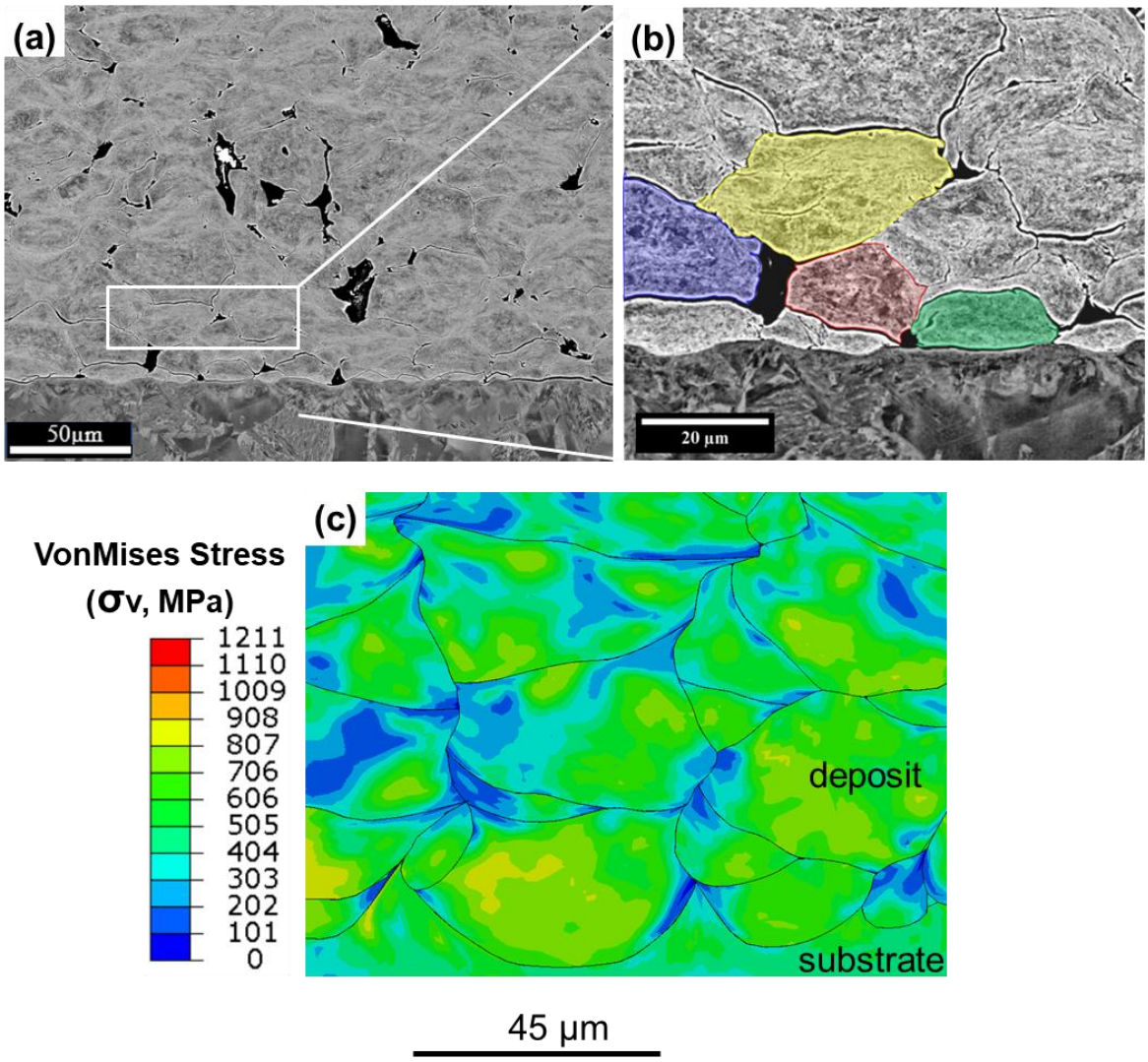

Figure 6.4: (a) shows a high-resolution BSE micrograph of the CSAM HEA deposit. A closer look at the interface and intersplat boundaries is seen in the magnified view in (b). Similar deformation morphology of the particles is observed in the SEM micrographs and the multi-particle FE deformation simulation (c).

As CSAM deposits are composed of many splats, their mechanical properties, such as elastic modulus and hardness, can be influenced by inter-splat bonding. The high-resolution BSE micrograph of the deposit closer to the deposit-substrate interface shown in Figure 6.4b (magnified view of Figure 6.4a) allowed a closer look at splat boundaries. The figure shows clear boundaries and gaps between splats (the colouring was done using the ImageJ software). The clear splat boundaries within the deposit likely suggest poor bonding between the HEA particles during

CSAM. Also, “textured” and “smooth” regions are generally observed at splat interiors and impact interface vicinity in the BSE micrograph. The smooth regions are likely the diffraction of high dislocation densities and the large number of grain boundaries at the impact regions, whereas the projection from the textured regions suggests lower dislocation densities and grain boundaries within splats.

6.4.3 Deposit microstructures

XRD analysis

The XRD profile for the HEA powder and CSAM deposit is provided in Figure 6.5a. The powder and deposit exhibited an FCC structure (PDF: 00-065-0528). As expected, the feedstock powder FCC structure was retained in the HEA deposit with no other phases detected by the used XRD analysis. The XRD profile of the deposit showed peak broadening, indicating the presence of subgrains and residual strain formed during the severe plastic deformation of the HEA. The subgrain size and residual strain were analysed using the W-H plot, as shown in Figure 6.5b. The figure shows the plot of the FWHM (in radians) against the peak positions (in radians). The intercept and slope of the fitted peaks to a linear plot determine the subgrain size and microstrain in the HEA deposit. A significant increase in the slope of the W-H plot (as shown in Figure 6.5b) indicates that the HEA material has undergone severe deformation during CSAM, with the strain increasing from 1 to 4 microstrain (~300 % increase). The subgrain size measured in the HEA deposit was ~ (188 ± 44) nm, significantly smaller than the crystallite size of the as-received HEA powder of ~ (492 ± 57) nm. The reduction in the subgrain size after CSAM deposition suggests grain refinement, which can be possible via dynamic

recrystallisation (DRX) [149]. It is noteworthy that the W-H plot from the XRD analysis can be associated with errors as it is preferred for nanoscale crystallite size. Also, notice that the linear plot did not fit well in the W-H plot for the HEA deposit compared to the powder, and there is a slight deviation or decrease in the FWHM values corresponding to the {200} and {220} reflections. Ungár et al. [319] reported that such a decrease in the FWHM values of these reflections could be associated with stacking faults and twins which may lead to deformation anisotropy in the deposit; however, these underlying deformation features or mechanisms require further investigation.

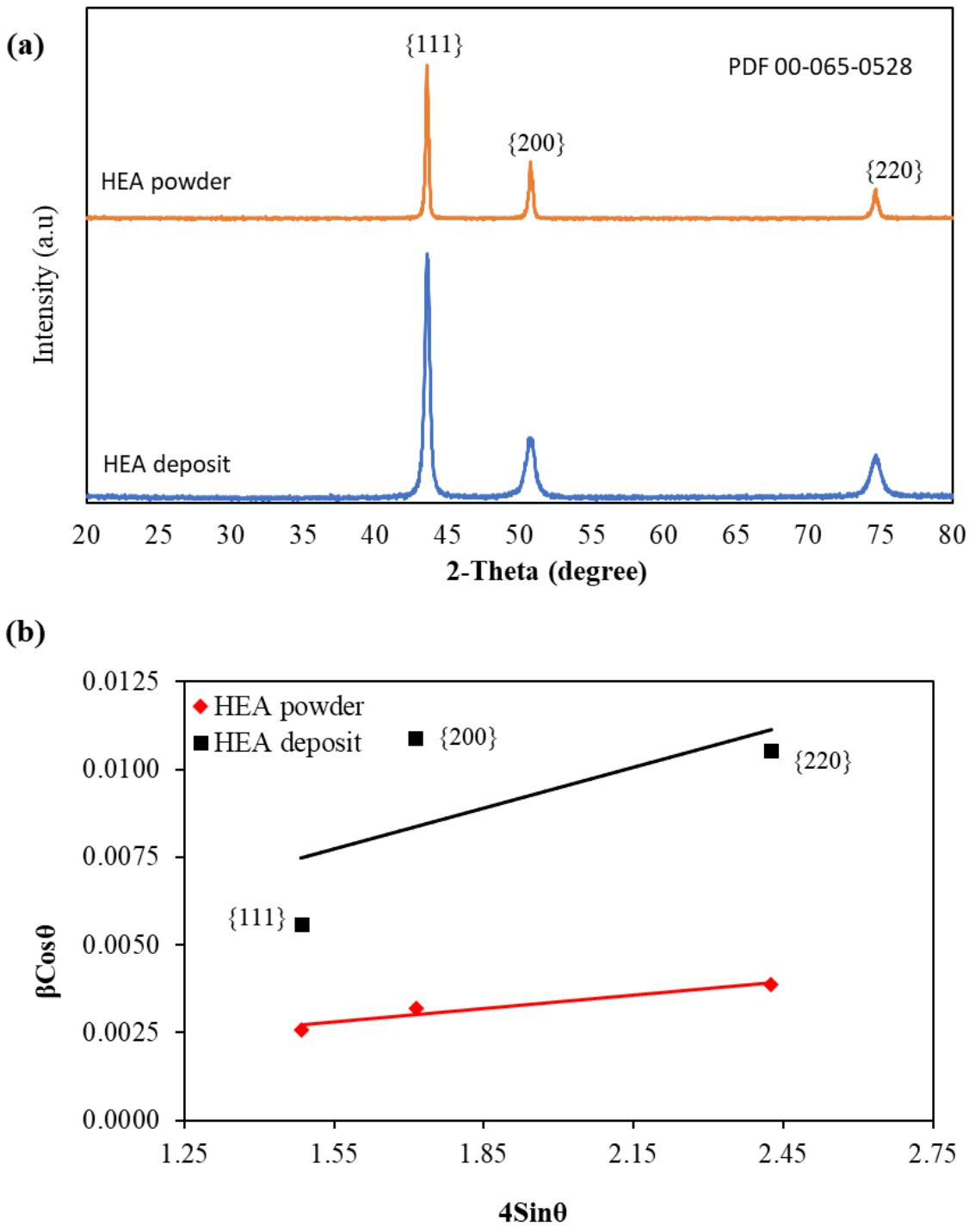

Figure 6.5: (a) shows the XRD profile of the powder feedstock material and sprayed deposit, showing that the CSAM process did not result in phase transformation of the sprayed powder. (b) shows the Williamson-Hall (W-H) plot of the powder and deposit, giving the subgrain size and lattice residual strain.

EBSD characterisation: close to the deposit-substrate interface

A high-magnification EBSD and high-resolution SEM micrograph of the deposit-substrate interface is presented in Figure 6.6. This was acquired to investigate the microstructural characteristics of the interface between the CSAM HEA particle-substrate that resulted from the impact-induced severe plastic deformation during CSAM. Figure 6.6a and b presents the SEM and band contrast images. The band contrast shows the quality of the backscattered signal, reflecting the degree of lattice distortion. In particular, regions of intense plastic deformation, such as grain boundaries containing lattice defects, correspond to the dark lines. Randomly oriented dark lines, usually corresponding to the presence of a network of dislocations, were seen in the vicinity of the deformed particle-substrate interface, suggesting severe plastic deformation mainly limited to the interface vicinity, which agrees with previous studies [40,137]. A closer view in the band contrast image reveals elongated, linear dark lines parallel to the impact direction present away from the splat vicinity towards the interior. These linear features also appear to be parallel to the impact direction, suggesting features similar to substructural deformation features such as twinning. Previous studies have reported similar deformation features. For instance, CSAM deposition of the CoCrFeNiMn HEA [63,75,268] and dynamic and static deformation of the bulk CoCrFeNiMn HEA [41,42,320]; however, these deformation features require further investigation as detailed characterisation of the feature may be difficult with the technique employed. Furthermore, Figure 6.6c and d show the IPF and kernel average misorientation (KAM) maps of the particle-substrate interface. The figures reveal coarse grains at regions away from the interface of the particle and substrate, and fine grains at the interface. The dark regions at the interface are a result of poor diffraction quality or

indexation. The regions likely contain refined grains with sizes below the resolution or step-size of the EBSD analysis (50 nm) and high density of dislocation as revealed by the band contrast in Figure 6.6b, hence the poor diffraction or indexation quality. Away from the interface, towards the centre of the particle, are elongated subgrains, likely deformed in the shear or compression direction. Using a colour gradient (threshold between 0-5), the KAM map illustrates localised strain variations within the microstructure. Blue corresponds to the absence of misorientation, while green or yellow indicates a high misorientation. Higher KAM reflects denser Geometrically Necessary Dislocations (GNDs). Higher local misorientations are concentrated at the interface, and away from the interface, the KAM value decreases to strain-free regions (showing mainly blue colours). The high misorientation indicates localised strain and a high density of dislocations. Figure 6.6d and e show the misorientation angle distribution of the region analysed, and the misorientation angle distribution for below 5º. The misorientation angle distribution suggests grains with low-angle grain boundaries (LAGBs < 15º) and high-angle grain boundaries (HAGBs > 15º). In addition to these grain boundaries, are boundaries with 60º misorientations. The KAM values reveal most misorientations are below 1.5º, suggesting DRX is dominant mainly at the particle-substrate interface.

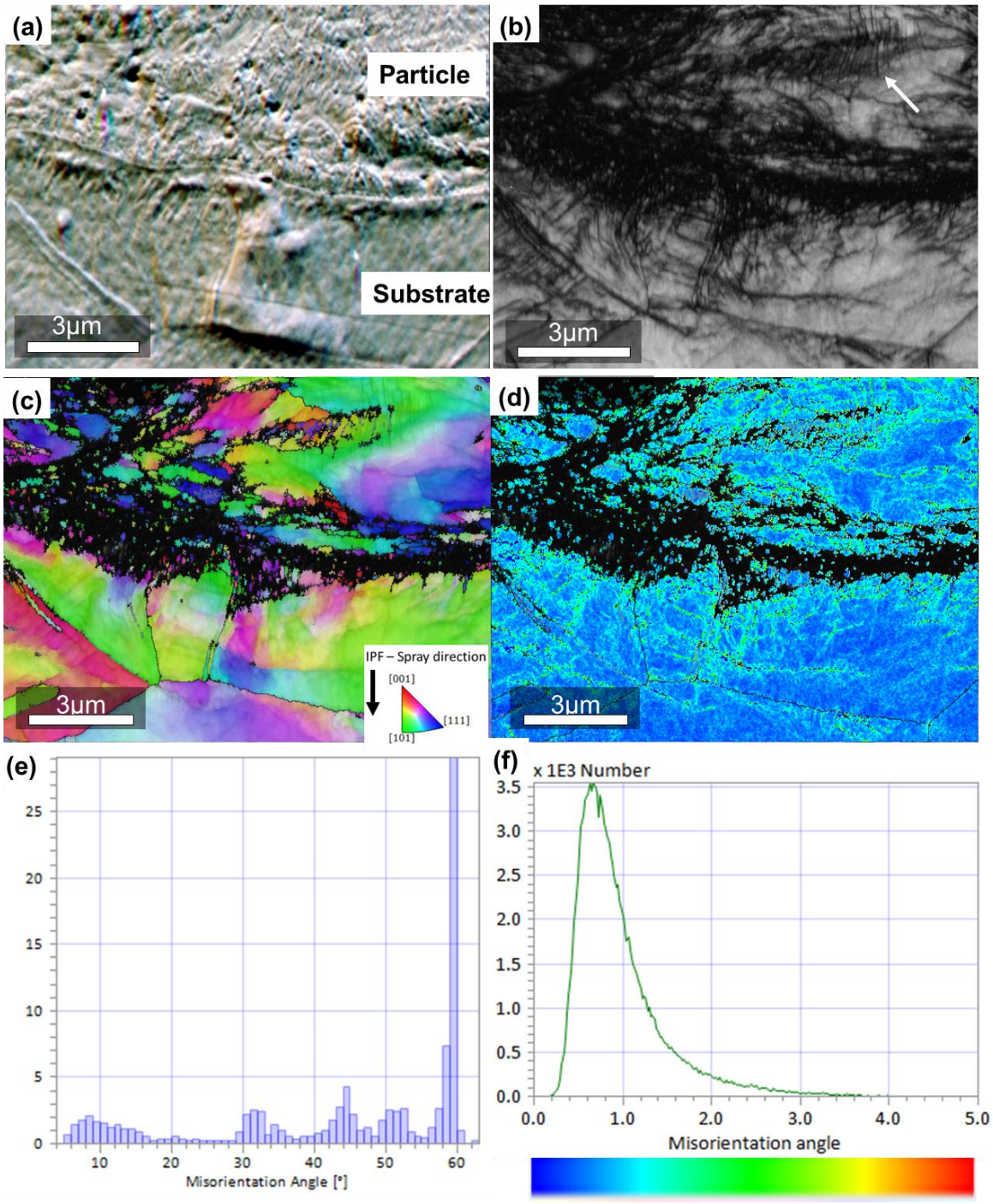

Figure 6.6: (a) shows a high magnification, high-contrast BSE image and (b) shows an EBSD band contrast image of a sprayed CoCrFeNiMn HEA particle at the deposit-substrate interface. A network of dislocations is observed at the interfaces, and likely substructure deformation features indicated by the white arrow close to the particle interior, likely deformation twins. (c) shows the IPF map of the region analysed and (d) shows the KAM map. The misorientation angle distribution and KAM distribution of the analysed region are presented in (e) and (f), respectively.

To further gain more insight into the particle-substrate and particle-particle interfaces at the deposit-substrate interface, the microstructure of a larger region at the deposit-substrate interface was characterised using the EBSD technique. Figure 6.7 presents the microstructure images of a region at the deposit-substrate interface with the indicated interface shown in Figure 6.7a. The micrographs reveal a similar microstructure observed for the particle-substrate in Figure 6.6. The IPF map in Figure 6.7b, shows a varied mix of colours indicating randomly oriented grains in the deformed particle without any preferential orientation. Grain boundaries were detected when the misorientation was above 5°, with a minimum of 2 pixels per grain and a kernel size of 3 × 3. The CSAM HEA deposit-substrate interface is characterised by a bimodal grain-sized microstructure with randomly oriented fined grains that are dominant at the impact boundaries and larger grains at the interior of the splat. Also, the interface between particles is characterised by ultrafine grains, as these regions are poorly indexed resulting from the high strain and likely the ultrafine grains are of sizes below the resolution or step-size of the EBSD technique employed (50 nm). Again, elongated subgrains are observed towards the interface, likely deformed in the direction of shear or compression. Furthermore, the KAM map shown in Figure 6.7c reveals a higher local misorientation at the impact boundaries. The dark areas at the impact boundaries result from the low indexation quality due to severe plastic deformation of the region, as explained earlier. Grains characterised with low strain (and a few strain-free areas mostly within grains) are observed in the interior of the splats (with blue colour indicative of low strain or dislocation density). Also, Figure 6.7d shows the plot of the KAM distribution of the deposit with most values below 1.5°, indicative of DRX mainly occurring at the impact interfaces. Referring to Figure 6.7e, the deposit microstructure likely consists

of a mixture of LAGBs (< 2° to 15°) and HAGBs (> 15°), and a fraction of grain boundaries that are Σ3 {111} 60° misorientation, which is characteristic of {111} ⟨112⟩ deformation twinning in FCC metals [321].

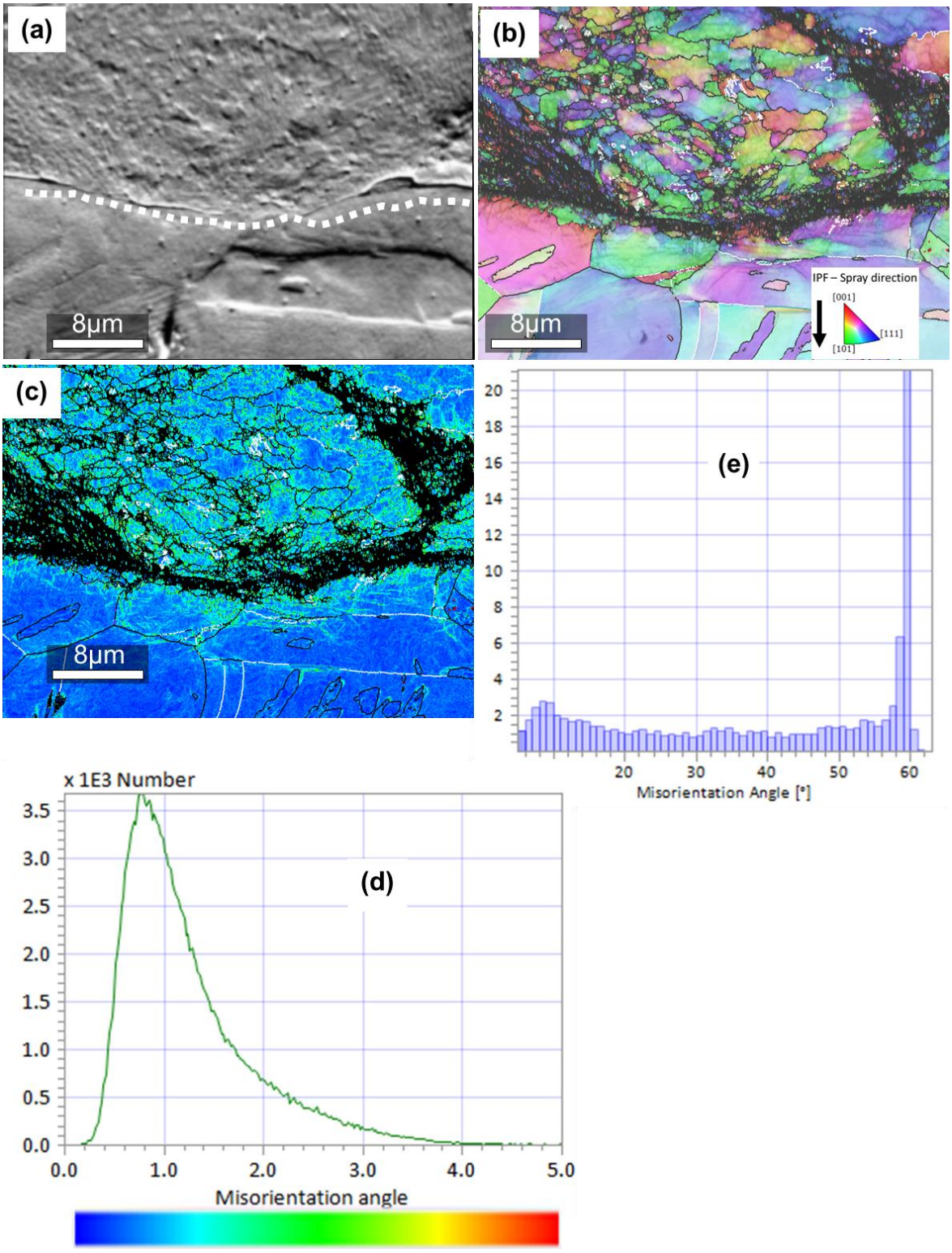

Figure 6.7: shows the (a) BSE image, (b) EBSD IPF map, (c) KAM map, (d) KAM distribution of (c) and misorientation angle distribution (e) of the sprayed CoCrFeNiMn HEA particle at the deposit-substrate interface.

To provide a more accurate picture of the LAGB and HAGB distribution across the impact interfaces and within a particle, point-to-point misorientation lines versus distance are plotted, as shown in Figure 6.8. The figure shows the IPF map from Figure 6.7b where the misorientations data were taken from. The misorientation profiles from each line, as labelled, are plotted in Figure 6.8. Three distinct regions were selected for the misorientation profiles: the central region of the particle (labelled (i)), the particle-substrate interface (labelled as (ii)), and the particle-particle interface (labelled as (iii)). In the central region of the particle, there are only a small number of LAGBs, mainly within the coarse grains. There are two peaks on the misorientation profile with high misorientation angles, which is likely the angle of the grain boundaries within the distance analysed, as seen in Figure 6.8. This suggests that subgrains were not well formed at the particle interior, indicating low local strain and dislocation density. Interestingly, in the impact regions, the particle-substrate and particle-particle interfaces, the ultrafine equiaxed grains appear to be highly misoriented, with misorientation angles reaching 40 and 60º. Although these regions are poorly indexed, HAGBs were likely formed at the bonding or impact regions.

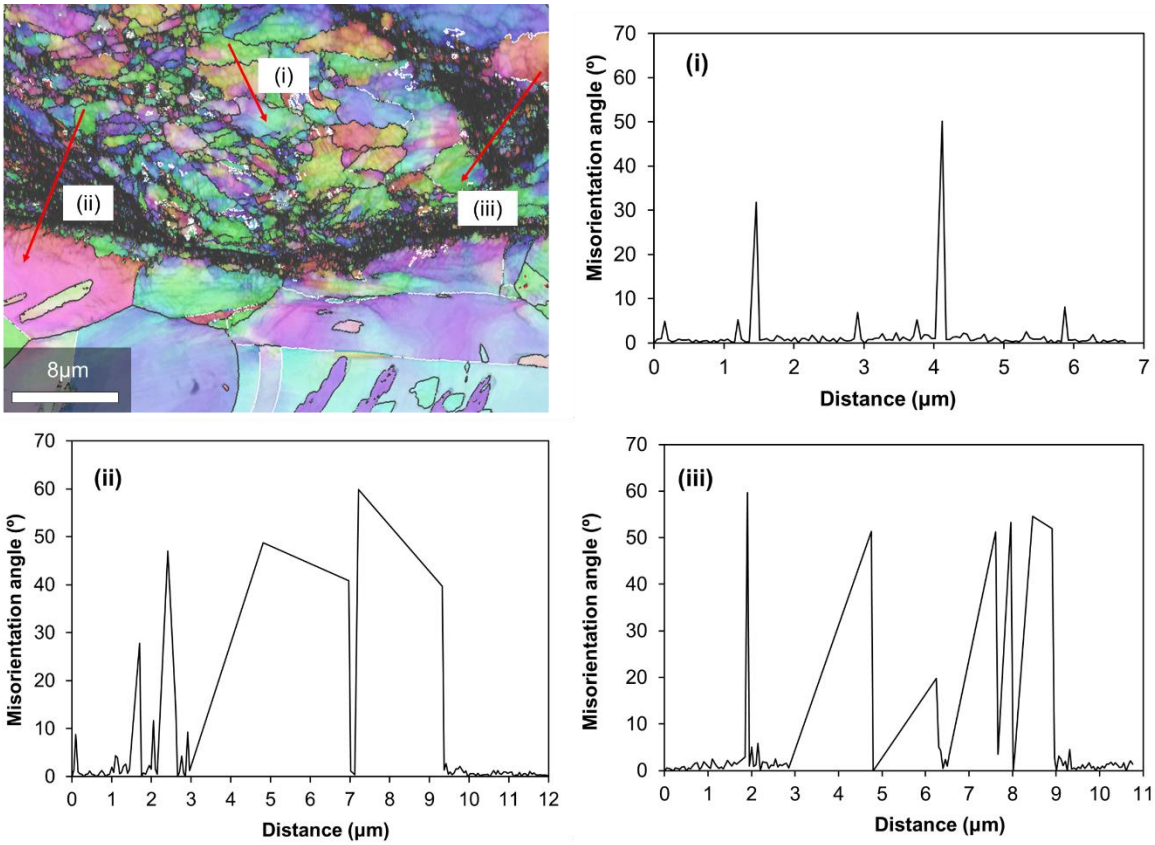

Figure 6.8: shows the IPF map in Figure 6.7, with marked red lines in different regions and their corresponding misorientation profiles. The profiles show point-to-point misorientations along the distance analysed.

From the EBSD results shown in Figure 6.6 to Figure 6.8, it is apparent that distinct regions or microstructures can be identified, namely, the central particle region (Figure 6.8 and (i)), with less deformed coarse grains (Figure 6.8), and ultrafine grain region (Figure 6.8, (ii) and (iii)) at the impact interfaces. Since the technique to extract strain and temperature profiles of these regions from the analysed EBSD scans is not yet available, the FE model of multi-particle impacts was employed to qualitatively estimate the temperature and strain profiles of the regions of interest. For the analysed regions, the central region of the deposited particle, impact interfaces between particle-substrate and particle-particle, and the strain and temperature profiles versus distance at the end of the deposition were estimated from the FE model, as presented in Figure 6.9. The distance of the region analysed

in the FE model was estimated from the Abaqus software. The unit of measurement in the Abaqus software is determined by the user, which in this case is in μm. It was ensured that the distance of the regions in the FE model is approximately equivalent to the distance in the analysed regions in the EBSD scans. Figure 6.9 shows an enlarged view of the multi-particle FE deposit-substrate interface and regions where the line profiles were taken from. The strain and temperature profile from each line is plotted as labelled in Figure 6.9. The central region of the deformed particle (labelled as (i)) reveals low strain and temperature value, with an average strain of 0.45 (45 %) and temperature of 650 K from the centre towards the south pole of the particle interior. At the particle-substrate interface region, there is a remarkable increase in strain and temperature, reaching approximately 4.5 (450%) and 1310 K, at the interface. Similarly, the strain and temperature profile at the particle-particle interface region reaches their highest values at the interface.

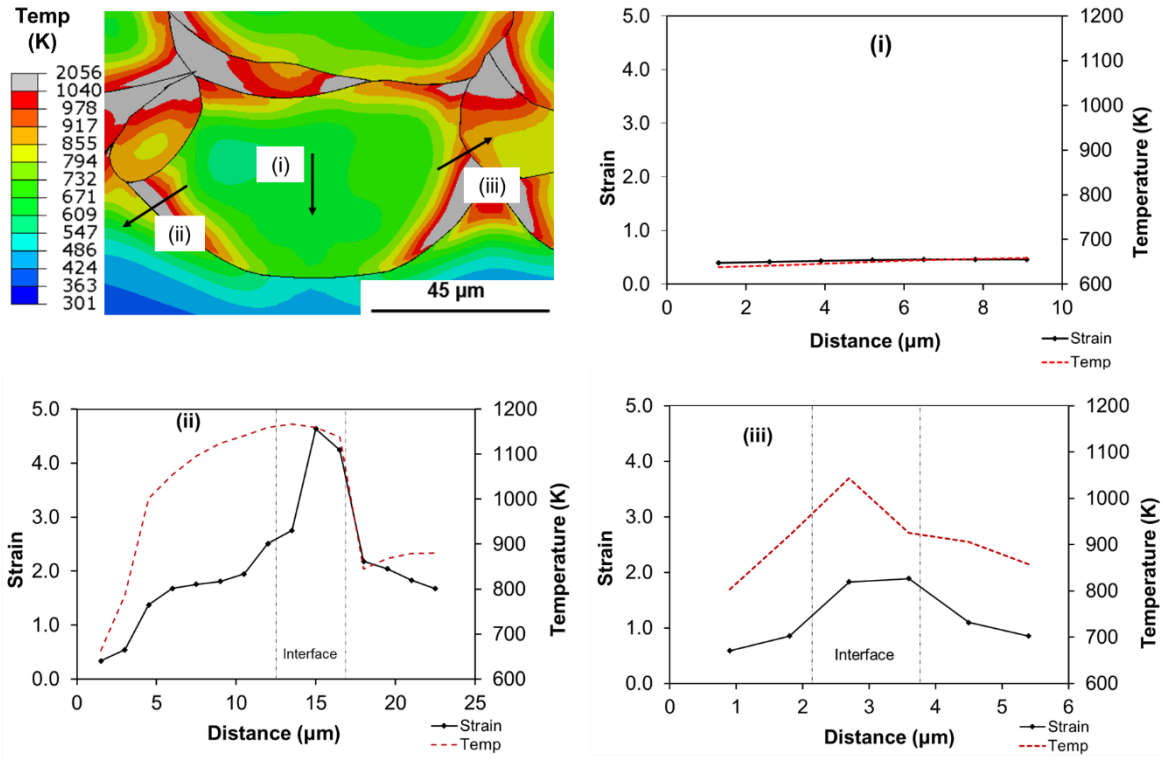

Figure 6.9: shows a close view of the temperature profile of a region in Figure 6.4c, of the FEA multi-particle impact model. The strain and temperature along the marked lines are presented in the corresponding temperature-strain vs distance plots.

The remarkable increase in the deformation field variables in the FEA at the interface suggests that these thermomechanical phenomena are responsible for the difference in the misorientation angles relative to the central region of the particle, as shown in Figure 6.8. Consequently, the formation of the ultrafine equiaxed grains that were observed at the impact interfaces in Figure 6.6 and Figure 6.7. The poorly EBSD-indexed regions at the interface may influence the misorientation profile plots; however, one can correlate qualitatively the deformation field variables to the microstructure formation mechanism during the CSAM of the HEA.

EBSD characterisation: within the deposit

The EBSD analysis of the deposit-substrate interface shown in Figure 6.6 and Figure 6.7, reveals a heterogeneous microstructure formed, with ultrafine grains at the impact interface while large grains are within the splats. To confirm the same within the central region of the CSAM HEA deposit, a lower magnification micrograph covering a wider area within the deposit was analysed using the EBSD technique. Figure 6.10a and b show high-contrast BSE and band-contrast images of a region within the deposit. The micrographs reveal that the HEA particles had undergone extensive plastic deformation, mainly at the particle interfaces. Also, in Figure 6.10a, a micro-crack is observed, likely a gap at the inter-particle boundaries resulting from incomplete bonding, similar to what was observed in Figure 6.4. Furthermore, Figure 6.10c shows grains coloured according to the IPF in the impact direction. Equiaxed ultrafine grains are dominant at the impact interfaces. Also, elongated subgrains can be seen close to the interface, likely deformed in the direction of shear or compression, first upon impact and then by subsequent particle impacts. The orientation of the elongated subgrains likely depends on the orientation of the particle during deformation. Within the particles or splats are coarse elongated, and equiaxed grains with sizes similar to the original feedstock powder shown in Figure 6.2a. Interestingly, the ultrafine grains surround the coarse grains within the splats, as the coarse grains have likely experienced less deformation, thus resulting in the HEA deposit with a heterogeneous grain-sized microstructure. Grain size analysis of the deposit (3500 grains, at least 5 pixels per grain) revealed an area-weighted average grain size of ~3.3 μm, with most grains below ~1 μm, as shown in Figure 6.10d, confirming grain refinement when compared to the original feedstock powder. Figure 6.10e, f and g present the KAM

map, dislocation density map and misorientation angle distribution. The KAM and dislocation density maps (shown in Figure 6.10e and f) reveal that the splat interfaces have experienced severe plastic deformation, leading to the high local strain and dislocation density—10^{16} m^{-2}. Naeem et al. [322] reported a similar value for the dislocation density of the HEA; a peak value of ~1 × 10^{16} m^{-2} was found at around 45 % of tensile plastic deformation. The dislocation density did not increase beyond the peak value attributed to dislocation annihilation due to dynamic recovery. The white areas in Figure 6.10e and f are poorly indexed locations due to severe plastic deformation of the regions. Again, as observed in the previous EBSD analysis (Figure 6.6 and Figure 6.7), the KAM value of the HEA deposit microstructure is below 1.5º, indicative of DRX during CSAM of the HEA particles. The misorientation angle distribution shown in Figure 6.10g reveals that a higher fraction of the grain boundaries is LAGBs, and Σ3 {111} 60° misorientation, characteristic of deformation twinning boundary, likely formed during the plastic deformation of the HEA material.

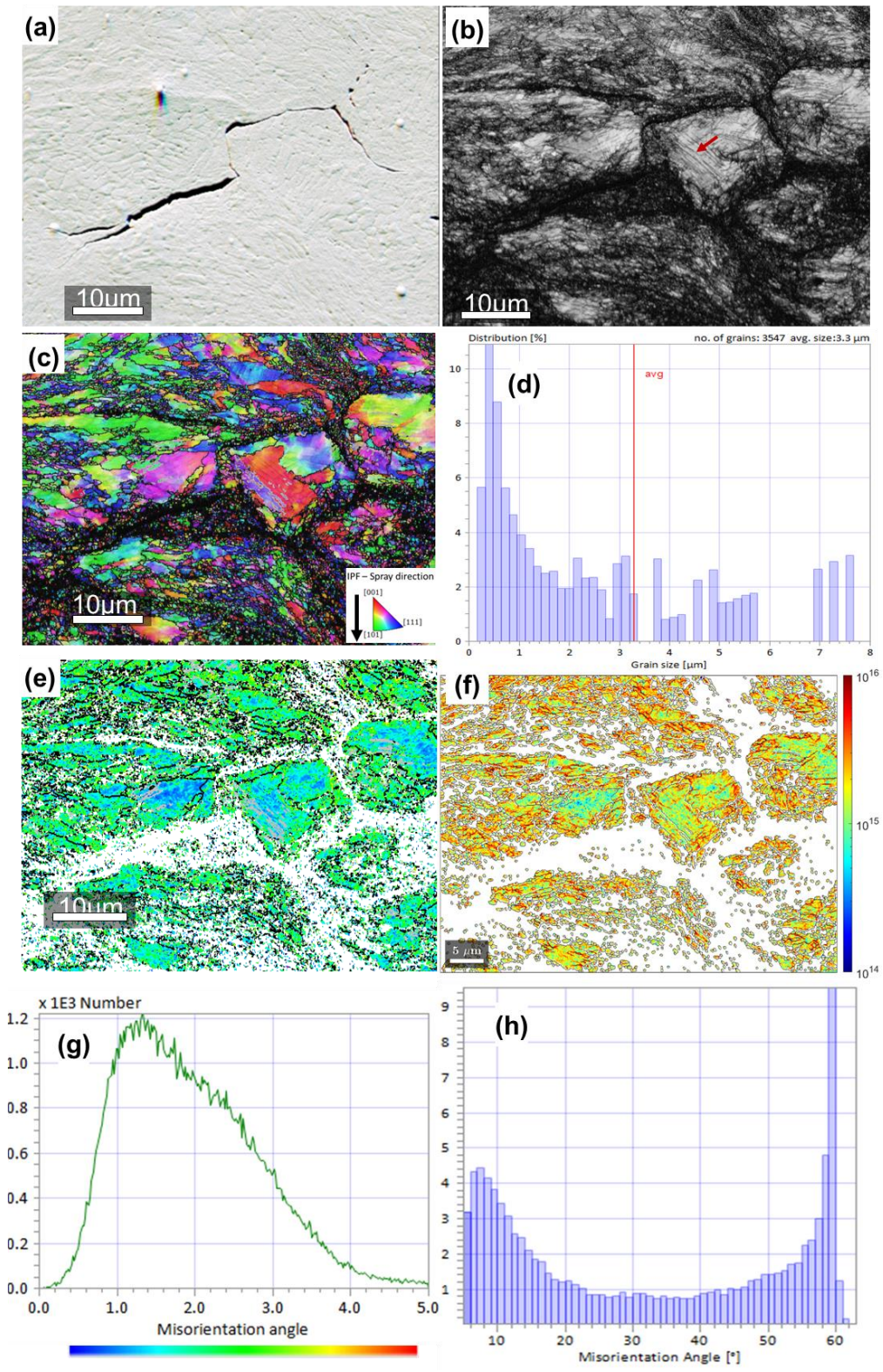

Figure 6.10: shows the high contrast BSE image (a), EBSD band contrast (b), EBSD IPF map (c) and grain size distribution (d) of the sprayed CoCrFeNiMn HEA deposit microstructure. The red arrow shows substructure deformation features that are likely twins. KAM map (e), dislocation density map (f), KAM distribution (g) and misorientation angle distribution (h) of the sprayed HEA deposit microstructure are also presented.

The multi-particle FEA was analysed to shed light on the particle DRX resulting from ASI, that is, strain localisation and strain-induced heating at the splats' periphery. Figure 6.11a and b show the results of the FEA of strain and temperature profiles of subsequently impacted HEA particles on the substrate. It is seen that highly localised strain (> 2.5) and temperature (> 0.95 of the HEA solidus temperature) near the impacting interface were prominent due to thermal softening dominating over strain hardening during severe plastic deformation. The higher strain and temperature at the impact interface would result in thermally-activated interfacial phenomena, ASI and DRX [56,137,323]. This is consistent with the indexing quality of the EBSD analysis; poorly indexed zones occur in regions with high plastic deformation, leading to significant lattice distortion and, hence, poor diffraction.

From the EBSD micrographs shown in Figure 6.10, smaller particles were observed to have interior grains with sizes close to those at the interface, whereas larger particles show a more heterogeneous microstructure with grains in the particle interiors larger than those at the interfaces. The possibility of this phenomenon during CSAM of the HEA was investigated using the FE model. Strain and temperature analyses were performed at the centre of the splats from the model. To evaluate the effect of particle size on the severity of deformation and grain refinement at the interior of the splats during deposition, five small and five large particles of sizes 10-25 μm (below the experimental mean particle size) and 30-45 μm (above the experimental mean particle size), respectively, were evaluated. The average temperature and strain evolution of the different particle size ranges are presented in Figure 6.11c and d. The average maximum temperature of 815 K obtained within smaller particles resulting from strain-induced heating could favour

the DRX of grains within the particles. This means that grains within smaller particles likely experienced more grain fragmentation when compared to those of larger particles (having an average maximum temperature of about 675 K). These analyses suggest that larger particle sizes would likely achieve a higher fraction of elongated coarse grains but with the smaller particles achieving a higher fraction of ultrafine grains. Both cases, nonetheless, contributed to the heterogeneous microstructure formed in the HEA deposit.

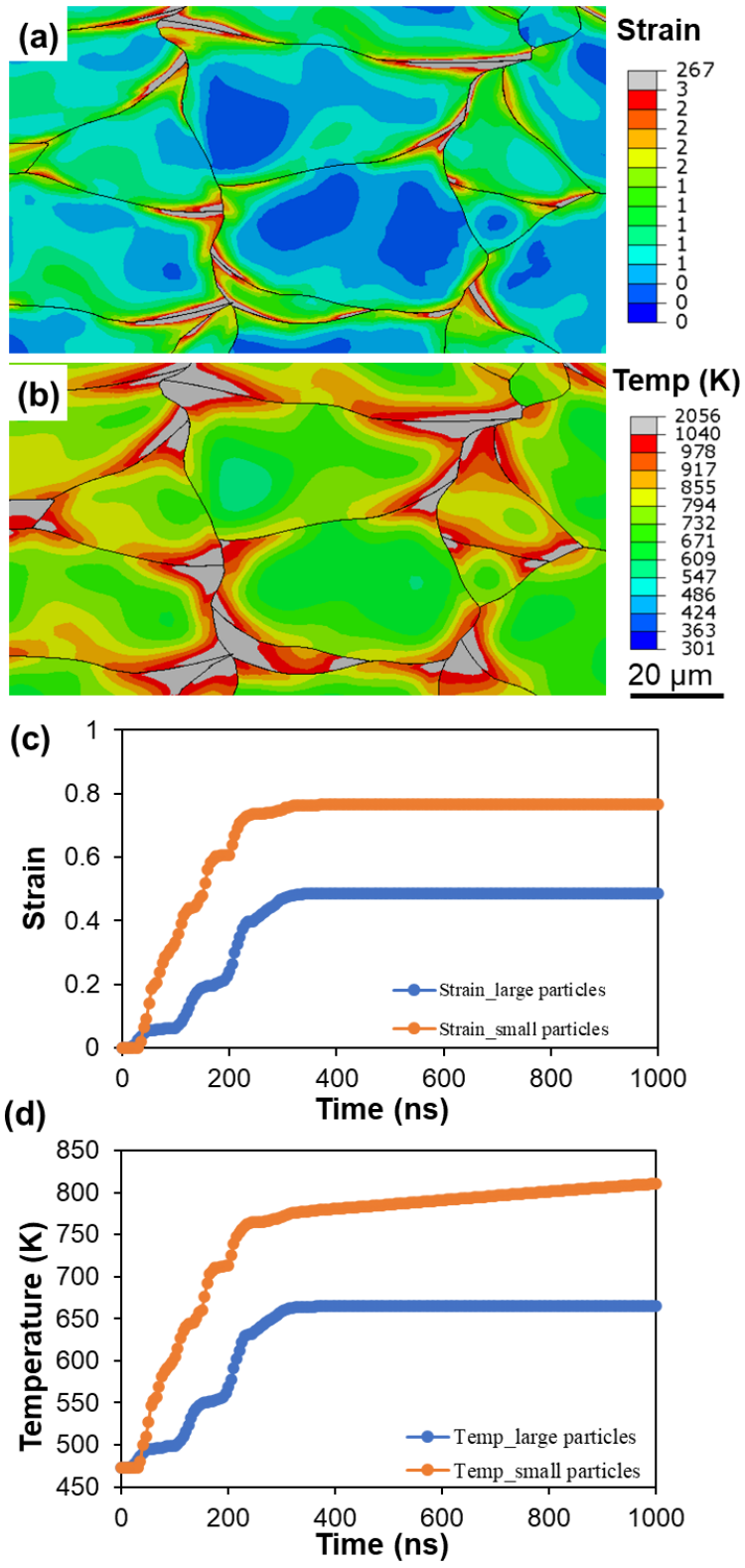

Figure 6.11: shows the FEA simulation contour plots of strain (a) and temperature (b) localisation of the multi-particle impact of the CoCrFeNiMn HEA. Higher strain (> 2.5) and temperature (> 0.65 Tmelt) are observed at the particle interfaces. Plots of average strain (c) and temperature (d) history of 10 particles with sizes ranging from 10-25 µm (small particles) and 30-45 µm (large particles). Data was extracted mainly from the centre of the FE particles.

6.4.4 Nanohardness evaluation

Nanohardness was measured on the mirror-polished HEA powder and deposit cross-sections. An average nanohardness value of 1.16 $\pm$ 0.49 GPa was measured on the powder particles. Figure 6.12a shows an SEM micrograph of the array of indents (the array shape displayed is due to avoiding regions of large pores during the nano-indentation testing) with the indents denoted at particle central regions and impact interfaces. The denoted indents were analysed to provide information on the effect of the CSAM HEA heterogeneous microstructure on the nanohardness variation. Figure 6.12b shows the nanohardness values of each indent, as denoted in the SEM image. Indents were taken from regions with clear interfaces from the SEM image. The corresponding nanohardness distribution histogram is provided in Figure 6.12c.

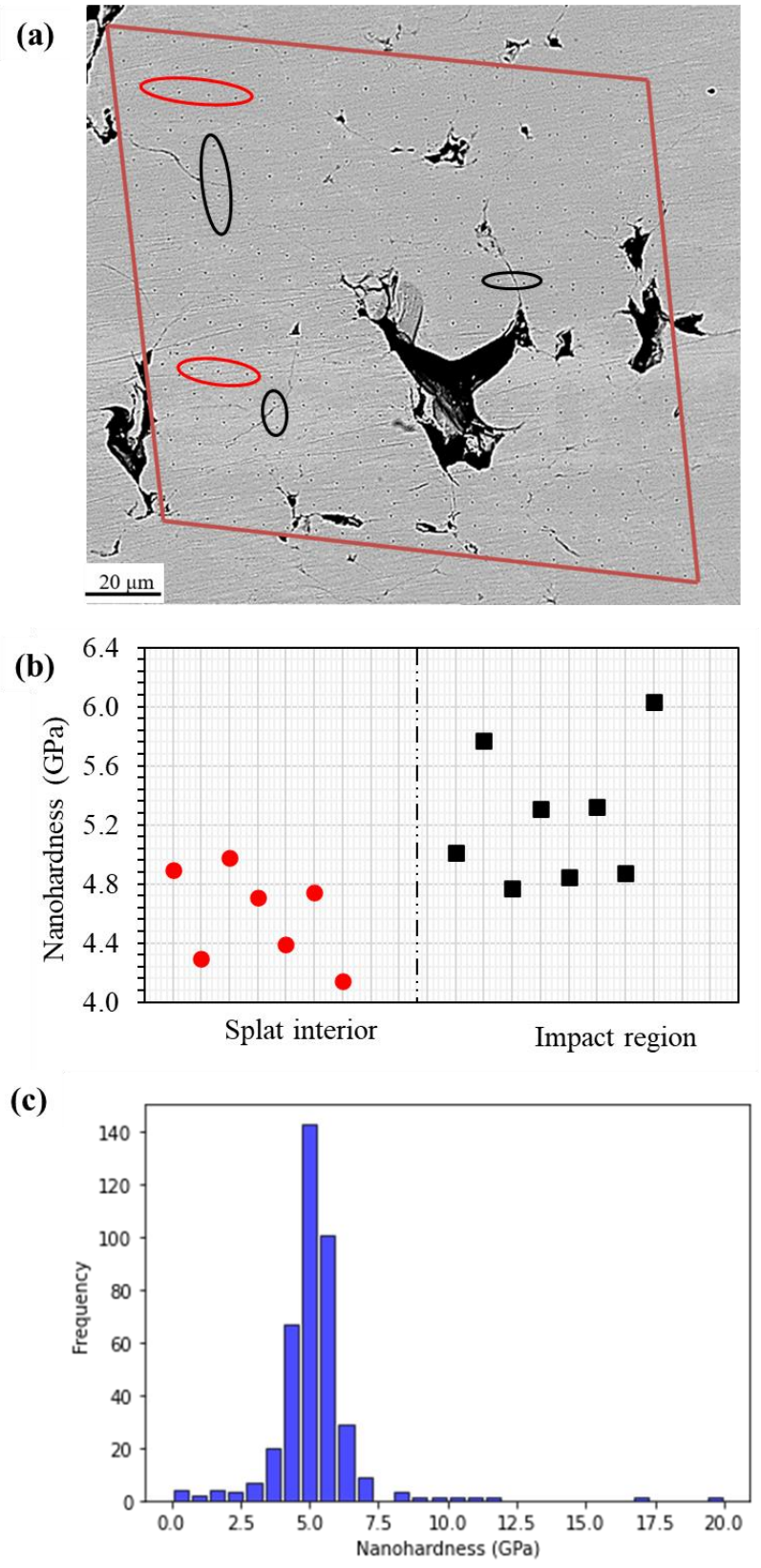

Figure 6.12: SEM micrograph showing an array of nano-indents (a), (b) shows the plot of the nanohardness values of each indent in the regions denoted with red (splat interior) and black (impact region) in (a), and (c) shows the corresponding nanohardness distribution of the CSAM HEA deposit.

It can be seen from the scatter plot in Figure 6.12b that the indents at the impact regions result in greater nanohardness measured when compared with those at the splat interior or central region. For the nanohardness analysed in those regions, it was found that the average nanohardness at the impact region is (0.65 ± 0.04) GPa greater than the average nanohardness at the central region of the particles. Moreso, the nanohardness values at the impact region analysed varied from 4.77 GPa to 6.30 GPa, meanwhile at the central region they varied from 4.29 GPa to 4.97 GPa. Moreover, the nanohardness distribution histogram presented in Figure 6.12c suggests heterogeneous variation in the nanohardness values measured within the CSAM HEA deposit.

An overall average nanohardness and Young's modulus values of (5.14 ± 0.08) GPa and (194 ± 1.64) GPa, respectively, were obtained for the deposit. A similar nanohardness value has been reported by Feng et al. [129] for the CSAM CoCrFeNiMn HEA deposit (5.64 GPa). The nanohardness value measured for the HEA deposit in this study is higher than the conventional as-cast HEA with a hardness value of 4.13 GPa, attributed to the high density of dislocations and grain boundaries resulting from the severe plastic deformation of the HEA particle during deposition, as mentioned in Section 6.4.3.

6.4.5 Microhardness evaluation

Microhardness was measured on the HEA deposit cross-section, with an average value of (280 ± 3.59) HV0.3. The distribution of the microhardness value measured for the HEA deposit is shown in Figure 6.13a, ranging from 118.97 to 490.21 HV0.3.

Figure 6.13b shows the average microhardness value measured from close to the top of the deposit to the substrate. There are negligible variations in the measured microhardness value within the deposit, indicating likely uniform plastic deformation throughout the deposition, layer by layer. The CSAM deposit in this study revealed a relatively higher measured microhardness value than conventional additively manufactured [256,324]—160 to 212 HV and as-cast CoCrFeNiMn HEA [268]—144 HV. The greater microhardness of the HEA deposit can be attributed to the severe work hardening and grain refinement during CSAM.

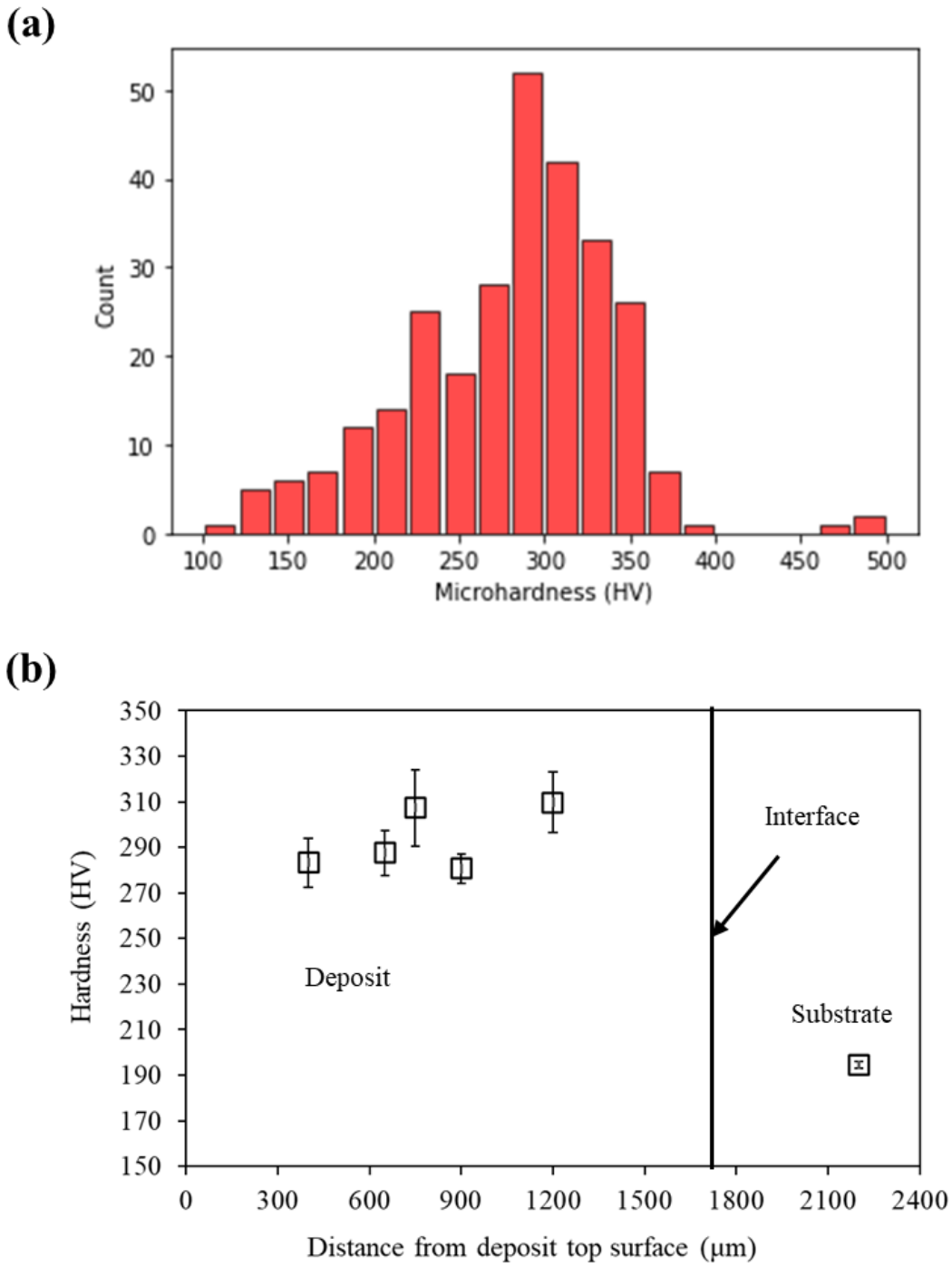

Figure 6.13: shows the distribution of the microhardness value measured for the CSAM HEA deposit (a), through-thickness hardness variations of the deposit from the deposit top (about 300 μm) to the substrate (b).

6.5 Discussion

6.5.1 Microstructure evolution

The moderate porosity (~2.4%) and inter-splat boundaries observed in the CSAM CoCrFeNiMn HEA deposit, shown in Figure 6.4b and Figure 6.10a, are consistent with the high strain hardenability and resistance to shear localisation of the HEA [301]. The poor inter-particle bonding suggests insufficient thermal softening and deformation for complete metallurgical bonding of the HEA particles during deposition. Higher particle velocities or gas temperature can reduce the microstructural defects in the HEA deposit but at the expense of cost. Since the CSAM equipment was operated at the upper limits of pressure and temperature, achieving a pore-free deposit may not be possible due to the HEA impact behaviour, which was also observed in a previous study by Nikbakht et al. [63]. Another plausible explanation for this deformation behaviour is likely a small, well-bonded area at the particle-particle interfaces and a high thermal gradient (as observed in Figure 6.11) within the particles. The outcome of these impact phenomena or deformation behaviour would likely result in the rupture of the splats' bond during the elastic unloading of the splats [144], hence the poor inter-particle boundaries.

Most notably, based on the evidence obtained from the EBSD analysis in Section 6.4.3, the overall deformation appears to result in heterogeneous microstructures formed in the cold-sprayed HEA deposit. The severe plastic deformation of the HEA particles resulted in elongated subgrains, formed close to the impact interfaces, and equiaxed ultrafine grains formed at the impact interfaces, whereas coarse grains

were observed at the central region of the particles (as shown in Figure 6.6, Figure 6.7 and Figure 6.10). The large deformation at extremely high strain and strain rates during the CSAM process can dramatically result in grain refinement via ASI and DRX, mainly at splat impact boundaries, and severe work hardening effects. Moreover, the dislocations formed and grain refinement during the impact-induced plastic deformation result in residual lattice microstrain, and peak broadening owing to grain refinement or formation of smaller subgrains as presented in Figure 6.5 of the XRD patterns and W-H plot.

The combined study of the EBSD characterisation and FEA shed light on the bonding mechanism and grain structure resulting from the thermomechanical phenomena; DRX and ASI. The misorientation profiles of the EBSD scans and the FEA strain and temperature profiles in Figure 6.8, Figure 6.9 and Figure 6.11a and b, reveal the mechanisms for bonding and formation of the heterogeneous microstructure of the cold-sprayed HEA. The deformation mechanism of the HEA feedstock material during CSAM can be explained as follows: the study reveals that during particle impact, the previously coarse grains likely experienced a dramatic increase in dislocation density. The dislocations accumulate and rearrange into LAGBs, forming subgrains. As deformation-induced strain and temperature increase during the deformation process, particularly the remarkable increase at the impact or bonding regions, the subgrains rotate, and their misorientation angle increases to accommodate the increasing strain, leading to the formation of HAGBs and randomly oriented ultrafine grains. The elongated grains formed close to the interface can be due to the accumulation and alignment of many dislocations in a short time. Similar deformation mechanisms and the resulting microstructural

features have been reported for CSAM deposition of Ni particles [137], the CoCrFeNiMn HEA [63,266] and high strain-rate deformation of bulk stainless steel [325]. This strain-induced increase of grain boundary misorientation via rotation of subgrains within the short time of deformation is representative of continuous dynamic recrystallisation (CDRX) [137], which is believed to be the dominant mechanism for grain refinement in the CSAM HEA deposit. The schematic illustration in Figure 6.14 explains the formation of the ultrafine grains at the impact interfaces by rotational DRX. Moreover, Assadi et al. [56] suggested that the bonding of particles during CSAM is attributed to ASI, due to localised strain and temperature at the bonding regions, as shown in Figure 6.9. Therefore, CDRX and ASI are likely the mechanisms of bonding and formation of highly misoriented ultrafine grains at the bonding regions between the HEA particles and particle-substrate interfaces.

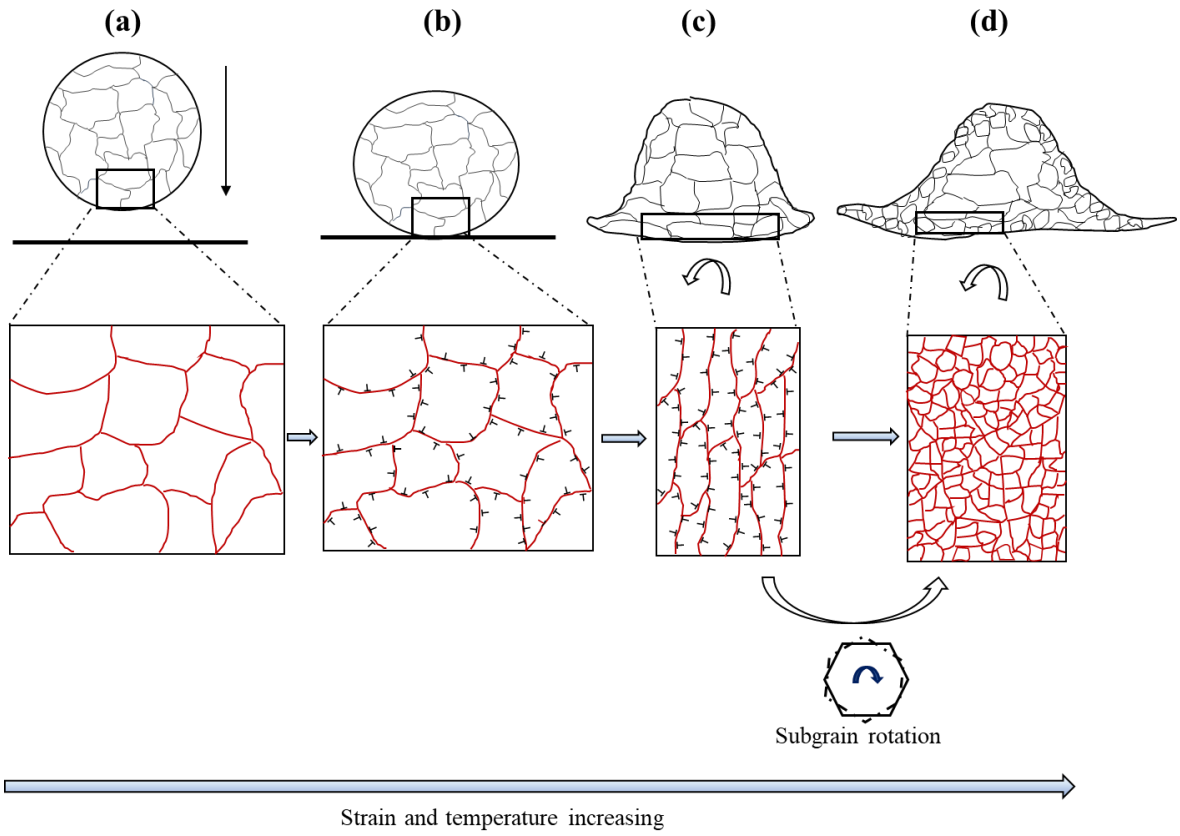

Figure 6.14: shows the schematic explaining the mechanism of grain refinement at the bonding regions by dynamic recrystallisation in the HEA particles during CSAM: (a) homogeneous strain-free grain structure of the original powder before deposition; (b) Upon impact, strain is induced due to deformation, and dislocations propagate; (c) with deformation going on, strain and dislocation density increases resulting in the formation of elongated subgrains due to the accumulation and rearrangement of dislocations; (d) due to the severe deformation and strain increase, the elongated subgrains rotate, increasing in their misorientation angles to accommodate the strain, resulting in the formation of highly misoriented equiaxed fine grains.

The microstructural features observed within the CSAM HEA deposit (as shown in the EBSD micrographs in Figure 6.10) provide evidence of the explained deposition mechanism in more detail. The figure reveals equiaxed ultrafine grains formed at the bonding or impact regions, whereas coarse grains were observed at the central regions of the particles. Moreover, one can see from the KAM map shown in Figure 6.10d that a high density of dislocations was accumulated at the impact interfaces, indicating localised high strain at the impact or bonding region. The higher

misorientation or local strain at the splat or impact boundaries can be due to the localised and intense deformation field variables, including temperature, strain, and strain rate, as explained earlier. Since measuring the plastic strain at the impact interfaces is not yet experimentally feasible, using FEA tools for the multi-particle impact deformation, as shown in Figure 6.9 and Figure 6.11, gave an idea of the strain and temperature experienced by the sprayed particles. From the FEA, a very high strain of more than 250% is found at the impact interfaces, with the temperature reaching over 90% of the alloy solidus temperature (Figure 6.8, Figure 6.11a and b). This induced high strain and temperature via severe plastic deformation result in thermal softening and grain refinement near the particle-particle and between the particle-substrate interface where ASI dominates. The deformation mechanism via DRX and ASI described for the particle-substrate and particle-particle interfaces at the deposit-substrate regions, as presented in Figure 6.8 and Figure 6.9, simply apply within the deposit. Also, elongated grains were observed to be formed close to the particle-particle interfaces, as shown in Figure 6.10c. This implies that the deposition of the HEA on the SS304 substrate likely shows similar deposition mechanisms between the HEA particles.

Additional microstructure features observed in Figure 6.6 are believed to possess boundaries with Σ3 {111} 60° misorientation (from misorientation angle distribution presented in Figure 6.10h) characteristic of deformation twinning. Moreover, The features appear parallel to the impact direction, confirming that these features were likely formed during the HEA particle deformation. Previous research has reported intensive deformation twinning and grain refinement to be the two main features of microstructure evolution in the HEA processed via the high-pressure torsion method

[254]. Similar features have been observed in previous studies of the CSAM HEA deposit [63,75]. However, future work can involve a detailed microstructural characterisation of the deformation twinning and its mechanism of formation in the HEA during CSAM.

6.5.2 Mechanical properties

The microstructure evolution—grain refinement and work hardening effects via the severe plastic deformation of the HEA during CSAM resulted in the greater deposit nanohardness when compared to the sprayed powder. The measured nanohardness value increased by over 300%, from 1.16 GPa in the powder to 5.14 GPa in the deposit. Also, the analysed average nanohardness near the particle-particle interfaces is greater than that of the central region by over (0.65 ± 0.04) GPa. The increased nanohardness near the impact interfaces can be attributed to a large number of grain boundaries and high dislocation densities induced by the CSAM process. Grain refinement and high density of dislocations or GNDs in the deposit can act as obstacles for dislocation motion during indentation, resulting in dislocation pileups at grain boundaries, leading to higher stress required to move dislocation through the pileups [326], therefore increasing the hardness value. Grain refinement contributes to the hardening of materials via the Hall-Petch strengthening effect [327], and the dislocation density contribution follows the Taylor hardening model [328].

Assuming a pore-free CSAM HEA deposit, one can estimate as a first approximation the yield strength of the deposit using Equation (6.2), following the contributions of grain refinement and dislocation hardening.

$$\sigma_d = \sigma_0 + {K_y}/{\sqrt{d}} + M\alpha G b \rho^{\frac{1}{2}} \quad (6.2)$$

Where σ_d is the yield stress, σ_0 represent the intrinsic yield stress of the HEA material (taken as 125 MPa [42]), and K_y is the Hall-Petch coefficient. K_y = 494 MPa.μm$^{-1/2}$ has been reported for the CoCrFeNiMn HEA [42]. Also, ***M*** is the Taylor factor (3.06 [329]), ***α*** is a constant taken as 0.4 [320], and ***G*** is the shear modulus (80 GPa for the HEA at room temperature [282]), ***b*** is the magnitude of the Burgers vector (0.255 × 10^{-3} μm at room temperature [262]), and ***ρ*** is the dislocation density taken from the EBSD analysis. Equation (6.2) gave an approximate yield stress σ_d of 647 MPa for an average grain size, ***d*** of ~3.3 μm (obtained from the EBSD analysis). The yield stress results from the grain refinement via dynamic recrystallisation and dislocation density, is comparable to bulk HEA produced by conventional additive manufacturing (601 MPa with 1 μm grain size) [330] but higher than as-cast (350 MPa with 4.4 μm grain size) [42]. To compare the yield stress estimated from the above model with the measured hardness, the yield stress from the measured Vickers hardness (HV) of the HEA cold-sprayed deposit was evaluated, using $\sigma_{HV} = \left({HV}/{3}\right) \times 0.1^n$, as proposed by Cahoon et al. [331]. The strain hardening exponent, ***n,*** of the HEA material is taken from J-C material model data provided in Chapter 5 Section 5.4, which is 0.18. Thus, the measured microhardness values of 280 HV0.3 of the CSAM HEA deposit correspond to an approximate hardness-derived yield stress of 605 MPa. There is slight difference in the estimated yield stress from the contributing mechanisms and the hardness-derived yield stress. The discrepancies can be attributed to the effect of porosity and poor inter-particle bonding of the deposit during the microhardness indentation

testing, and the approximation of the model employed. Future work can involve performing a standard tensile test to provide a more accurate representation of the tensile properties of the CSAM HEA deposit.

6.6 Conclusions

A CSAM process was employed to fabricate a ~2 mm thick deposit of CoCrFeNiMn HEA. The resulting microstructure from the ultra-high strain rate materials deposition process was characterised using SEM, XRD, EBSD and FEA, and the properties were measured using micro- and nano-indentation techniques. The main observations can be summarised as follows:

- The CSAM HEA deposit showed a heterogeneous microstructure consisting of ultrafine and coarse grains at the splat interfaces and interiors. Significant grain refinement was obtained mainly at the splat impact interfaces within the deposit. The formation mechanism of the heterogeneous microstructure is attributed to ASI and DRX produced by subgrain rotation dominating the impact areas. Large strain and temperature gradients within the deformed particles, as evidenced by the FEA, explain the heterogenous microstructure formed.

- The microstructural features in the CSAM HEA deposit contributed to the over 250% increase in the measured nanohardness value, from 1.16 GPa in the feedstock powder to 5.14 GPa in the HEA deposit. The increase in the hardness values was attributed to the grain refinement and high density of

dislocations in the CSAM HEA deposit. The high densities of grain boundaries and GNDs contributed to the greater nanohardness measured for the impact or bonding regions between particles when compared to that of the central regions of the particles.

- A Taylor-based strength model that includes the contributions from the grain size and dislocations measured using EBSD predicted yield stress of 647 MPa for the HEA deposit. A hardness-derived yield stress of 605 MPa was also estimated for the CSAM HEA deposit. These theoretical yield-stress values are comparable to the yield strength of bulk HEA produced by conventional AM methods; however, future work will involve tensile testing of a dense CSAM deposit of the HEA.

The CSAM of the HEA feedstock for the repair of stainless steel components is a promising cost-effective, solid-state AM repair technique; however, the deposit is characterised by porous microstructure which needs to be consolidated. The porous microstructure is due to the impact behaviour of the HEA and the nature of the CSAM process despite the use of heated helium gas. The next chapter aims to improve the microstructure of the deposited samples via annealing treatment.

7 Influence of annealing treatment on the microstructure and mechanical properties of CoCrFeNiMn deposits manufactured by CSAM

7.1 Introduction

As discussed in Chapter 2 of the literature review and conclusions of the investigation in Chapter 6, the CSAM process, being a solid-state materials deposition technique can, however, result in microstructural defects such as incomplete bonding of sprayed particles and pores formed in the deposit. The microstructural defects formed in the CSAM CoCrFeNiMn HEA, presented in the study in Chapter 6, are attributed to the high strain hardenability and resistance to shear localisation of the HEA [64,301]. The HEA particle deformation dynamics position the alloy in the window of difficult-to-spray materials [63,141], such as stainless steel and nickel-based superalloys [178,310,332,333]. As a consequence of the defects formed, premature failures are likely to occur under tensile loading conditions, primarily initiated from inter-particle boundaries [87,310,332]. The presence of these defects in the deposits limits their structural applications. As a consequence, post-deposition heat treatment would be required to improve the microstructure and the mechanical performance of the CSAM HEA deposit.

Therefore, this chapter presents the investigation of the influence of annealing treatment on the deposit characteristics and the role of the resulting microstructures on the mechanical properties of the deposit. The deposits were subjected to

annealing treatment at intermediate and high temperatures, and thereafter, the microstructures were characterised using a range of advanced materials characterisation techniques. The mechanical performance of the deposits was assessed by nano- and micro-hardness testing and tensile testing of sub-sized, micro-flat samples.

It is noteworthy that part of this chapter has been published in a conference proceeding and submitted as a full original article, which is under review in a refereed journal, as presented in the “Publication” section of this thesis.

7.2 Experimental methods

This section provides a summary of the experimental procedures that are specifically relevant to the work described in this chapter.

7.2.1 Materials and deposit heat treatment

The deposits developed in Chapter 6 were employed for further study in this chapter. To improve and consolidate the microstructure of these deposits, annealing heat treatment was conducted. In Chapter 6, approximately 2-mm thick deposits of the CoCrFeNiMn HEA were manufactured on the SS304 plates (25 mm wide × 60 mm long) using the CSAM process, as described in Chapter 3 Section 3.2 and Chapter 6. Subsequently, samples of dimensions 10 mm by 15 mm were sectioned from a deposit using a precision cutting machine (Qcut 200, Metprep, UK) with a SiC cutting disc (Metprep, UK). The samples were heat-treated at 600, 800 and

1000 ºC (annotated as HT600, HT800 and HT1000, respectively) for 5 hrs in a box furnace (Elite Thermal Systems, UK) in air, at a heating rate of 15 ºC/min, and then furnace-cooled to room temperature. These temperatures were selected based on the studies from the literature discussed in Chapter 2 Section 2.8.5. Since the studies show phase transformation or decomposition of the HEA at intermediate temperatures; 400-800 ºC and a solid solution of the HEA at higher temperatures; above 800 ºC, it was deemed fit to perform annealing heat treatment at temperatures that would likely result in phase transformation and solid solution, in turn, consolidate the deposits. The air-annealing was performed considering the industrial applications of the deposits as heat treatment in industrial settings would likely be subjected to air-annealing. This is likely because of the ease of heat treatment, time and cost-effectiveness.

7.2.2 Sample preparation and characterisation

The cross-sectioned HEA deposit and the heat-treated samples were prepared following the standard metallographic procedures described in Chapter 3 Section 3.3. The microstructure of the samples was obtained using the XL30 scanning electron microscope (SEM: Philips) operated at 15 kV in the backscattered electron (BSE) imaging mode. The microstructure of the samples captured was then employed for porosity following the procedure described in Chapter 3 Section 3.6.

For further microstructural characterisation of the as-sprayed and heat-treated samples, the cross-sectioned samples were hot-mounted in a conductive mount of Bakelite using conducto-mount (Metprep, UK) and the samples were prepared following the standard metallographic procedures and further polished using a 0.04

μm colloidal silica suspension for 20 mins on a polishing pad. All samples were washed and cleaned with ethanol or industrial methylated spirit (IMS) between each grinding and polishing step. Electron back-scattered diffraction (EBSD) imaging was performed on these samples on a FEG SEM (7100F, JOEL Ltd., Japan), with a step size of 70 nm. Grain boundaries: High-angle and low-angle grain boundaries (HAGBs and LAGBs), were detected when the misorientations were 2-15º and above 15º. The kernel average misorientation (KAM) map was plotted, indicating localised strain variations within the microstructure of the samples.

X-ray diffraction (XRD) of the phases and crystal structure of the as-sprayed and heat-treated samples was conducted using the XRD equipment described in Chapter 3 Section 3.5.3. The diffraction angle, $2\boldsymbol{\theta}$, selected for the as-sprayed sample ranges from 20-80º; meanwhile, a wider $2\boldsymbol{\theta}$ range, 20º-110º, was selected for the heat-treated samples to capture any second-phase diffraction peaks. The XRD analysis was completed using the EVA software (DIFFRAC.EVA, Bruker, Germany) with the ICDD database PDF 2.

High-resolution BSE imaging (with the detector mounted on the FEG SEM) was performed to reveal the precipitates formed in the heat-treated samples. For the high-resolution imaging, the samples were electrochemically etched using a 10 % oxalic acid dissolved in distilled water while applying a 6V direct current for 5 s. The elemental composition and mapping of precipitate and matrix phases were evaluated using an energy dispersive x-ray spectroscopy (EDX) detector (Xmax 150, Oxford Instruments, UK) mounted on the FEG SEM.

7.2.3 Equilibrium phase calculations

Making predictions of phases in HEAs is becoming increasingly crucial, especially for understanding phase transformation during experimental processes such as heat treatment. A commercially available software, Thermo-Calc, has proven to be a very useful tool, allowing for accurate prediction of phases as a function of temperature and composition. The Thermo-Calc^{TM} software version 2022a with the TCHEA5 database (HEA database version 5.1) was employed for thermodynamic equilibrium phase calculations following the CALPHAD approach. The calculation provides equilibrium phase diagrams, predicted phases, their volume fractions and compositions at the various heat treatment temperatures employed in this study. The phase calculations were performed to make a comparison with the phases that may be present in the annealed samples, providing insight into the possible mechanisms likely responsible for the phase transformations.

7.2.4 Mechanical properties evaluation

The nanohardness of the as-sprayed and heat-treated samples was measured following the procedures described in Chapter 3 Section 3.7. An array (20 × 20), resulting in 400 indents was performed on the samples. The indentation load of 3 mN was chosen after carefully selecting the indent size, the distance between the neighbouring indents (7 µm) to account for the plastic zone or indent impression, and the distance between indents and the splats boundaries to avoid pores when indenting the deposit. The nanohardness and reduced modulus from the nano-

indentation were derived following the Oliver and Pharr method [274], as described in Chapter 3 Section 3.7.1.

The microhardness of the samples was also measured using a Wilson VH3300 Vickers Microhardness instrument (Buehler, USA). Each sample underwent an array of approximately 100 micro-indents. A 300-gf load was applied to the deposit, using a dwell time of 15 s. The final values of the hardness measurements are presented as an average with the standard error of the mean of the measurements.

For the quantitative analysis of the tensile performance of the as-sprayed and heat-treated samples, micro-flat dogbone-shaped specimens were cut out from the CSAM deposit using wire-based electrical discharge machining (EDM), as described in detail in Chapter 3 Section 3.7.3. The specimens were heat-treated following the conditions outlined for the deposit. The tensile test was performed following the procedure described in Chapter 3 Section 3.7.3.

7.3 Results

7.3.1 Deposit consolidation and porosity

The SEM images of the as-sprayed and heat-treated deposit of the CoCrFeNiMn HEA are shown in Figure 7.1. The as-sprayed deposit was consolidated with the performed annealing heat treatment process at 1000 °C. The average porosity of the samples evaluated using the image analysis technique is presented in Figure 7.2. Porosity reduced from ~2.4% in the as-sprayed deposit to 0.6% after heat treatment at 1000 ºC (HT1000). Although porosity is reduced after heat treatment,

there is evidence that large pores remain in the heat-treated samples. Pores that were not completely closed in the as-sprayed deposit likely remained in the annealed samples after the annealing treatment. Nevertheless, in general, the annealing strategy thus consolidates the CSAM HEA deposit, closing tiny pores and inter-particle boundaries.

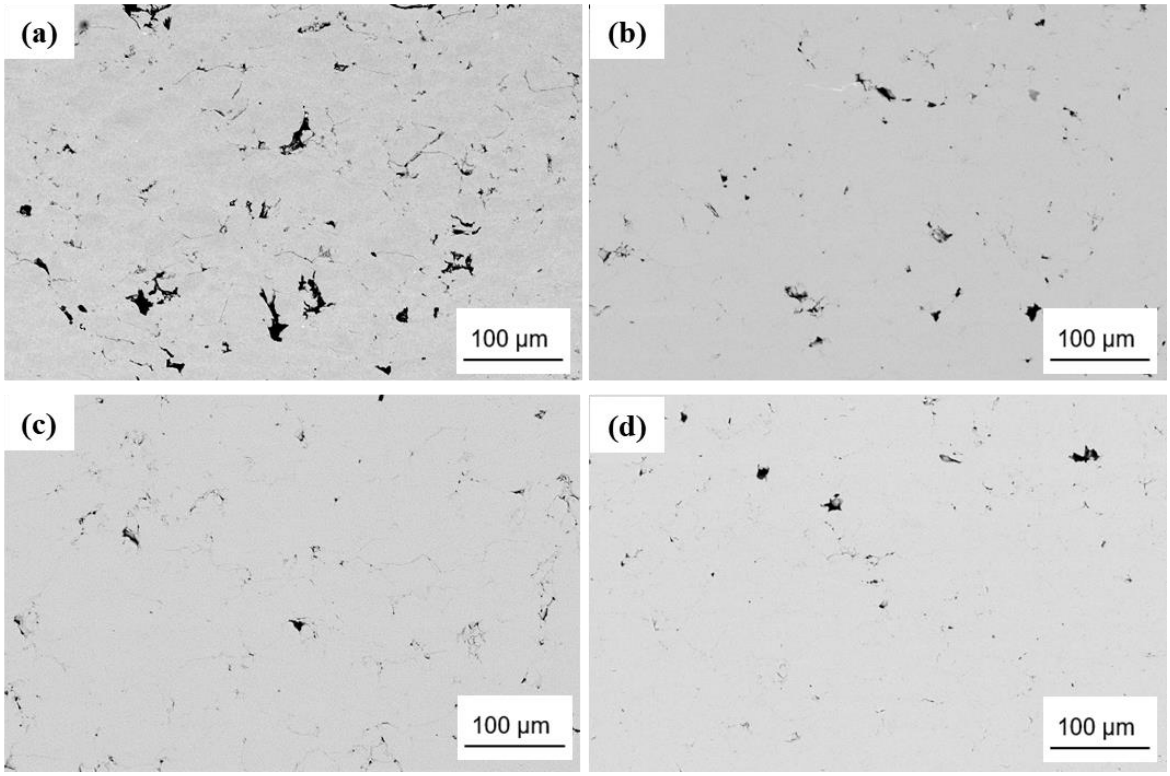

Figure 7.1: SEM images of the CSAM HEA deposit: (a) as-sprayed; (b) HT600; (c) HT800; and (c) HT1000 samples.

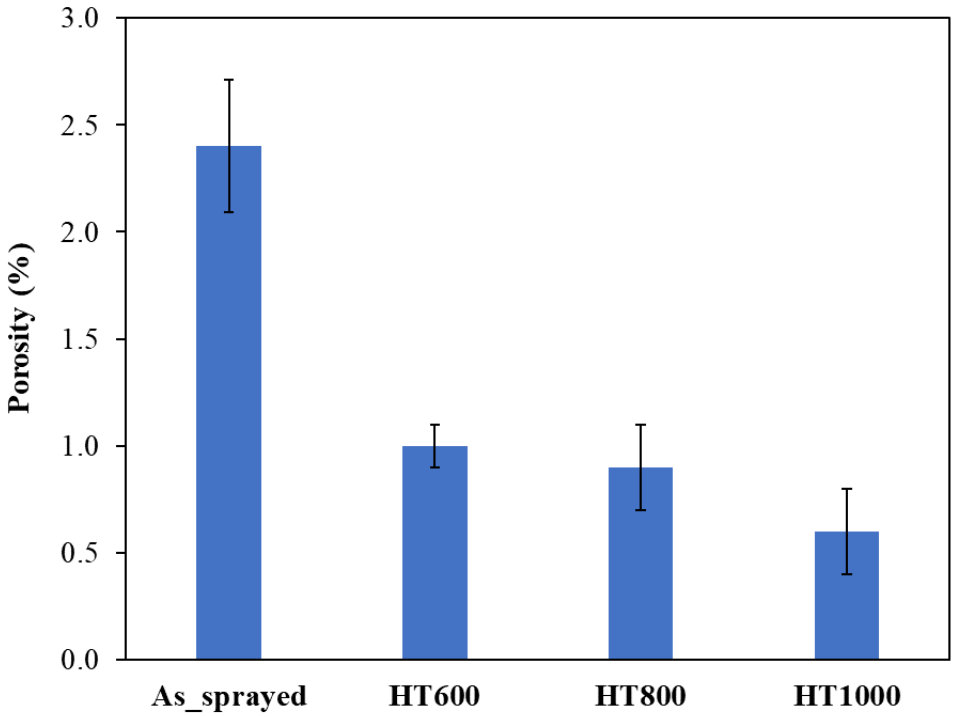

Figure 7.2: The plot of average porosity of the CSAM HEA deposit following annealing treatment at 600 ºC (HT600), 800 ºC (HT800) and 1000 ºC (HT1000).

7.3.2 Microstructure changes after annealing treatment

As reported in Chapter 6, the HEA powder retains its original structure after CSAM as no phase decomposition occurs due to the process, as expected. Annealing treatment performed at 600 ºC led to the precipitation of second-phase particles in the deposited sample. The presence of the second-phase particles is reflected by the additional diffraction peaks in the angular range between 35-55º 2$\boldsymbol{\theta}$, as shown in Figure 7.3a. The XRD analysis revealed these additional peaks as a Cr-rich phase, which is consistent with previous observations of a Cr-rich sigma phase ($P4_2/mnm$ tetragonal structure, with lattice constants a = 0.88 nm, c = 0.46 nm [239]) formed after the annealing of the HEA at intermediate temperatures (500-800 ºC) [239,240,261]. The BSE images shown in Figure 7.3b show the Cr-rich phase as bright particles, whereas the slightly darker phase is the FCC matrix. Note that the

tiny dark phases present in the SEM images are pores. The Cr-rich phase particles are observed to be generally formed along grain boundaries, and they exhibit irregular plate-like morphology. Moreover, the EDX mapping shown in Figure 7.4 certifies that the precipitate particles are enriched in Cr, but depleted in Ni, while other elements do not have significant concentration changes between the FCC matrix and the precipitate particles.

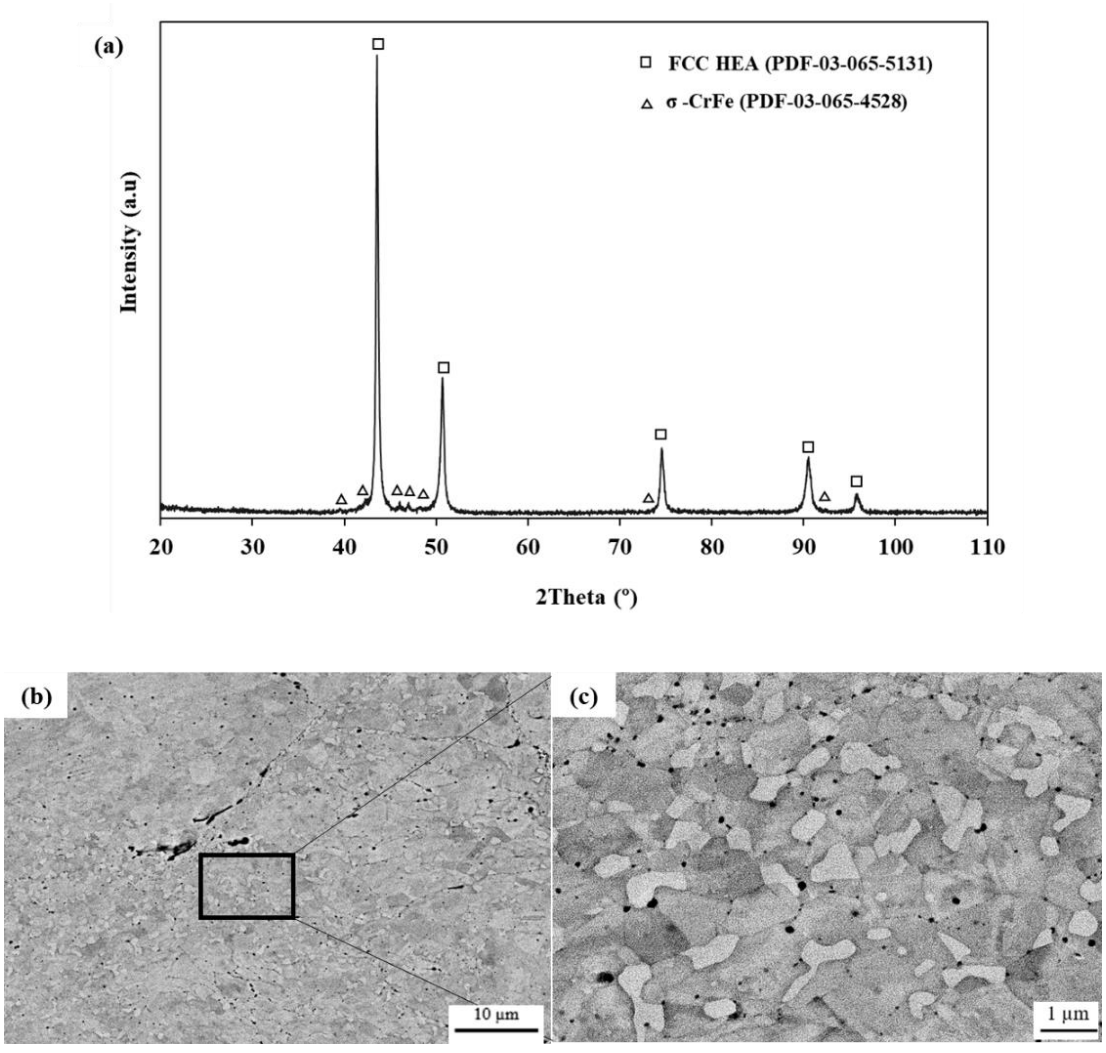

Figure 7.3: (a) shows the XRD profile and (b) BSE images of the CSAM CoCrFeNiMn HEA deposit heat-treated at 600 ºC (HT600). The Cr-rich precipitates are the brighter phase in the close-up view of the BSE image in (c), the slightly darker phase is the FCC matrix of the HEA, and the darker phases are pores.

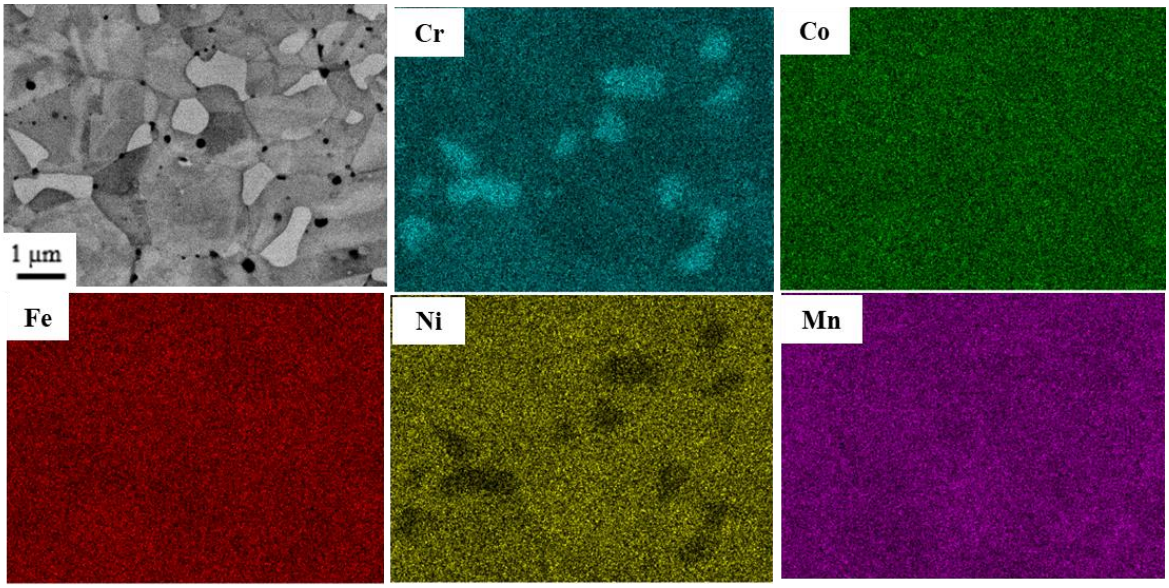

Figure 7.4: Shows the EDX mapping of the HT600 sample. The Cr-rich phase particles are confirmed to be enriched in Cr but depleted in Ni.

The constructed TCHEA version 5.1 thermodynamic database was used to perform stable phase equilibrium calculations using CALPHAD for the investigated alloy. Figure 7.5 shows the calculated phase fraction as a function of temperature. The computed solidus and liquidus temperatures are 1298 and 1340 ºC, which agrees well with the differential thermal analysis measurement (1290 and 1340 ºC) by Laurent-Brocq et al. [267]. The HEA composition is an FCC single-phase solid solution at high temperatures, but below 950 ºC, the FCC phase is predicted to precipitate phases that can co-exist within the HEA microstructure. A Cr-rich sigma phase is predicted below 950 ºC, while a Cr-BCC phase forms below 500 ºC. In addition, the calculated volume fraction of the Cr-rich sigma phases shows the peak volume fraction of the sigma phase at temperatures below 500 ºC. At 600 ºC, the calculated volume fraction of the Cr-rich sigma phase by CALPHAD is approximately 35%. For an approximate calculation of the volume fraction of the Cr-rich phase present in the HT600 sample, Rietveld refinement of the XRD profile was performed for the section of this study. The outcome of the Rietveld refinement and

the associated error related to the mathematical error of the fitting, the phase and sub-lattice composition errors [334] is presented in Figure 7.6. A surface area fraction of the phases could have been performed using the image analysis technique; however, due to the limitation of the technique in resolving the contrast and brightness of the sigma and the FCC matrix phases, Rietveld refinement was more suitable for the analysis. From the Rietveld refinement, a small volume fraction of about 7.5% of the Cr-rich phase was obtained in the HT600 sample. This significant difference can be associated with the composition of the sigma phase and the fidelity of the CAPHAD database in predicting accurately the formation of the sigma phase [335–337] during the annealing of the severely deformed HEA sample. Also, experiments are not always thermally stable, which may influence the formation and composition of the sigma phase, and consequently the volume fraction.

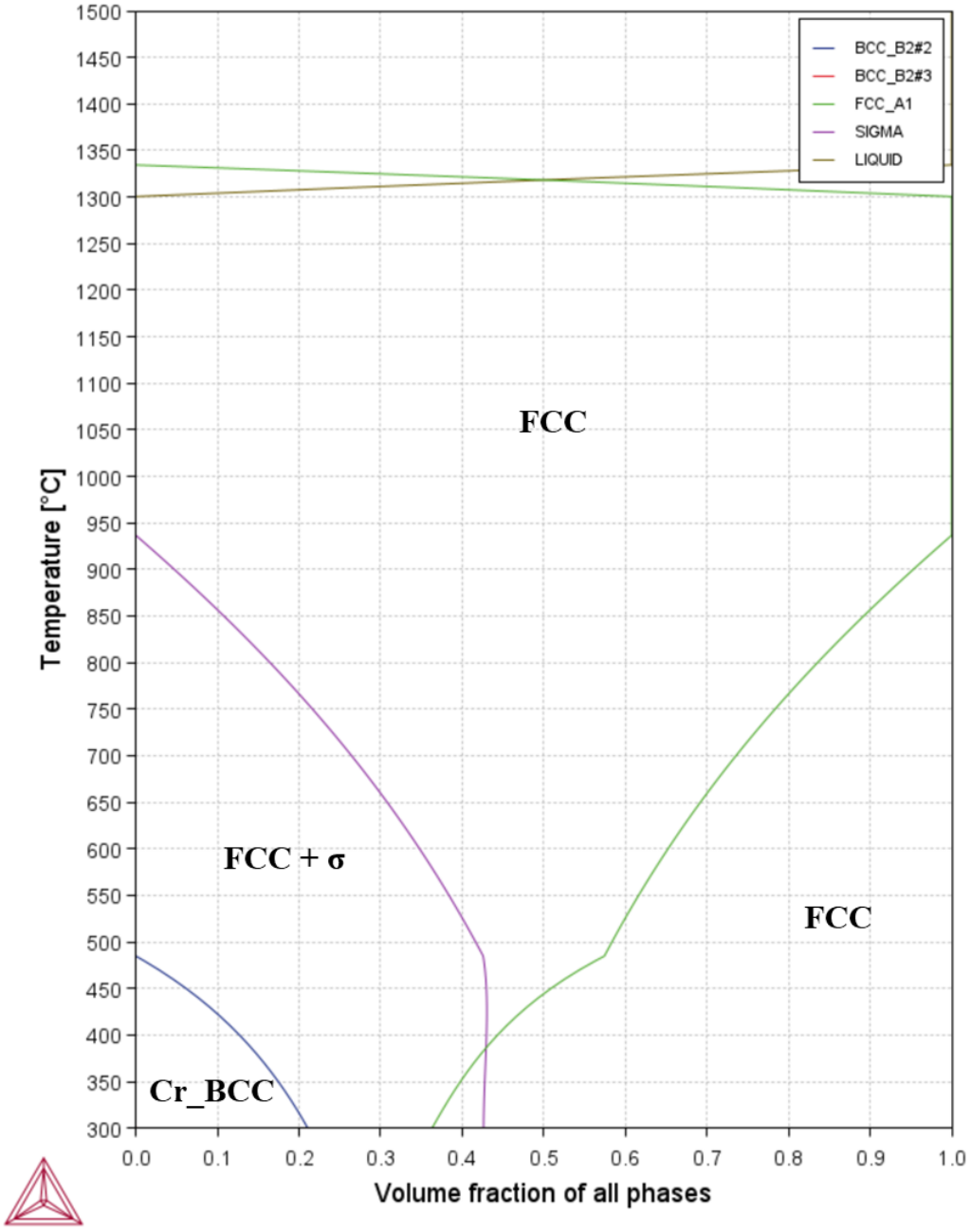

Figure 7.5: Calculated equilibrium phase diagram (phase fraction vs. temperature) of the equiatomic CoCrFeNiMn HEA from 300 to 1500 ºC using the CALPHAD approach in the ThermoCalc™ software.

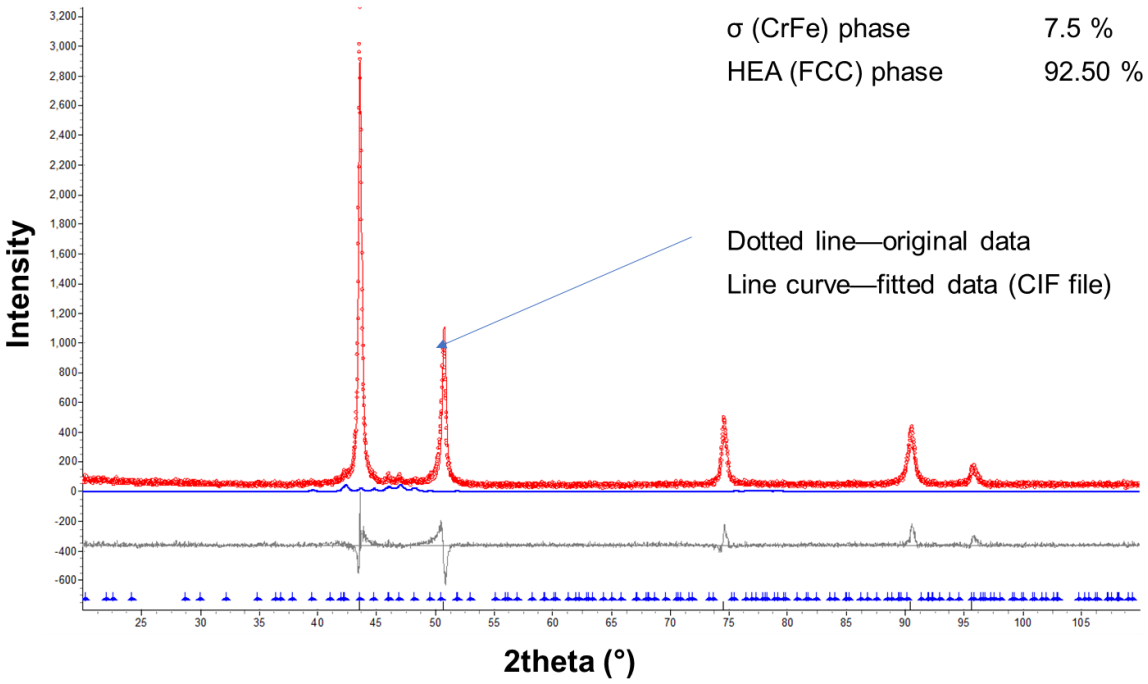

Figure 7.6: Rietveld refinement of the XRD profile analysis of the sample annealed at 600 °C. The sample microstructure contains the estimated volume fraction of 7.5% of the sigma phase (a CrFe-rich phase) with the CIF file for the refinement analysis.

The chemical composition of the Cr-rich phase particles from the experiment and CALPHAD was analysed. EDX point scans were performed on ten of the Cr-rich particles, and their average chemical composition (in wt.%) was found to be practically identical with a small standard error of the mean: Cr = 31.1 ± 1.15, Co = 19.6 ± 0.24, Fe = 19.5 ± 0.16, Ni = 13.3 ± 0.63, and Mn = 16.6 ± 0.39. Meanwhile, the elemental composition of the Cr-rich sigma phase calculated by CALPHAD at 600 ºC is given as: Cr = 31.0, Co = 14.6, Fe = 28.3, Ni = 4.5, and Mn = 21.7. When comparing the experimental and the CALPHAD calculated data, the wt.% Cr in the sigma phase shows negligible difference, but the wt.% of other elements differ significantly. These differences in the chemical composition of the Cr-rich phases likely suggest varying formation mechanisms, volume fraction (as mentioned earlier) and hardness. On the other hand, the elemental composition of the FCC

phases (in wt.%) for the EDX point scan measurement in the HT600 sample is given as: Cr = 17.74 ± 0.52, Co = 21.0 ± 0.25, Fe = 20.1 ± 0.39, Ni = 21.8 ± 0.34, and Mn = 19.3 ± 0.45, while that of the CALPHAD data at 600 ºC is computed as Cr = 14.0, Co = 25.8, Fe = 14.7, Ni = 30.0, and Mn = 15.5. These data, in general, show that the precipitate phase is a Cr-rich and Ni-lean phase, as observed in the EDX mapping in Figure 7.4.

Figure 7.7 shows the BSE image and EDX line scan across a bright phase formed in the HT800 sample. The EDX line scan reveals the bright phase to be enriched in Ni and Mn but depleted in other elements. This phase relates to the L10-NiMn phase reported in previous studies after subsequent annealing treatment at temperatures below or at 450 ºC of severely deformed samples of the HEA [240,254]. However, the NiMn phase was observed in this study at temperatures higher than previously reported [338], suggesting that the NiMn phase was likely stable up to 800 ºC for the CSAM deposit. Likely, the high strain energy and density of grain boundaries formed during the CSAM deposition of the HEA particles facilitate the stability of the NiMn phase up to 800 ºC [338]. The NiMn phase was not detectable within the sensitivity limit of the XRD analysis, likely due to the small amount within the microstructure of the sample. No attempt was made to check the formation of the NiMn phase in the stable thermal equilibrium calculations using CALPHAD for the same reasons given for the differences in the chemical composition and volume fraction of the Cr-rich phase. Moreover, there is limited research on the CALPHAD calculations of the NiMn phase formed at intermediate or high temperatures [324].

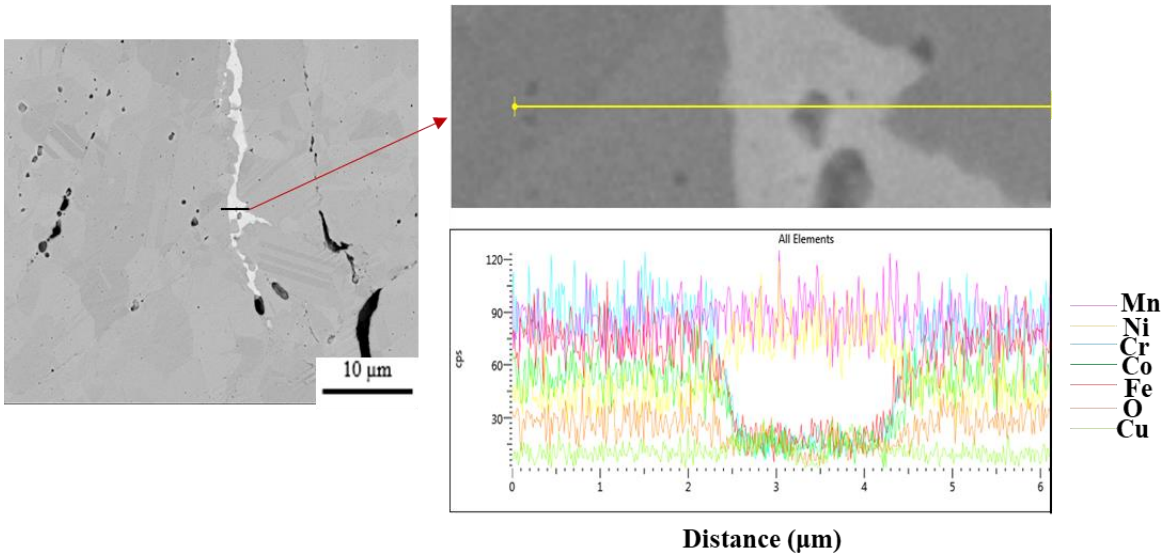

Figure 7.7: BSE image and EDX line scan across a bright phase observed in the HT800 sample. The EDX analysis reveals the precipitate phase to be enriched in Ni and Mn and depleted in other elements, hence a NiMn phase.

Due to the annealing treatment performed in the oxidising environment (air annealing), Oxides were observed in the samples heat-treated at higher temperatures (i.e., HT800 and HT1000 samples). The oxide particles are likely the darker particles in the BSE images shown in Figure 7.9. The particles were observed to be formed mainly at the inter-particle boundaries. Moreover, the presence of the particles, likely oxides, in the samples is evidenced by the XRD diffraction peaks shown in the figures. No other precipitate particles were observed in the HT1000 sample, likely due to the dissolution of the second-phase particles into the matrix. This is also evidenced by the CALPHAD calculations shown in Figure 7.5.

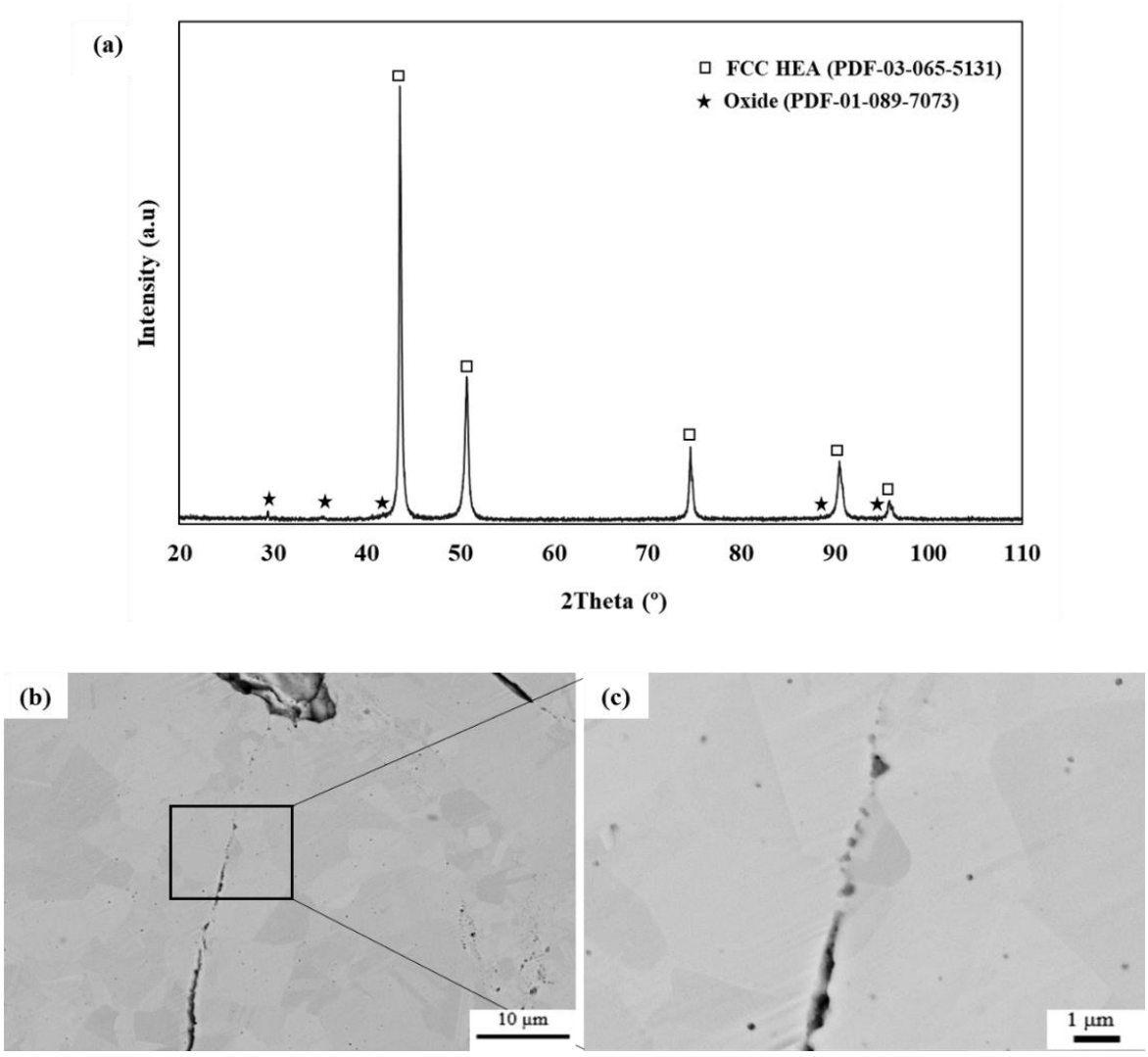

Figure 7.8: (a) shows the XRD profile and (b) BSE images of the HT800 sample. The high-magnification BSE image in (c) shows particles that are likely oxides, formed at the inter-particle boundary, while the other regions are pores.

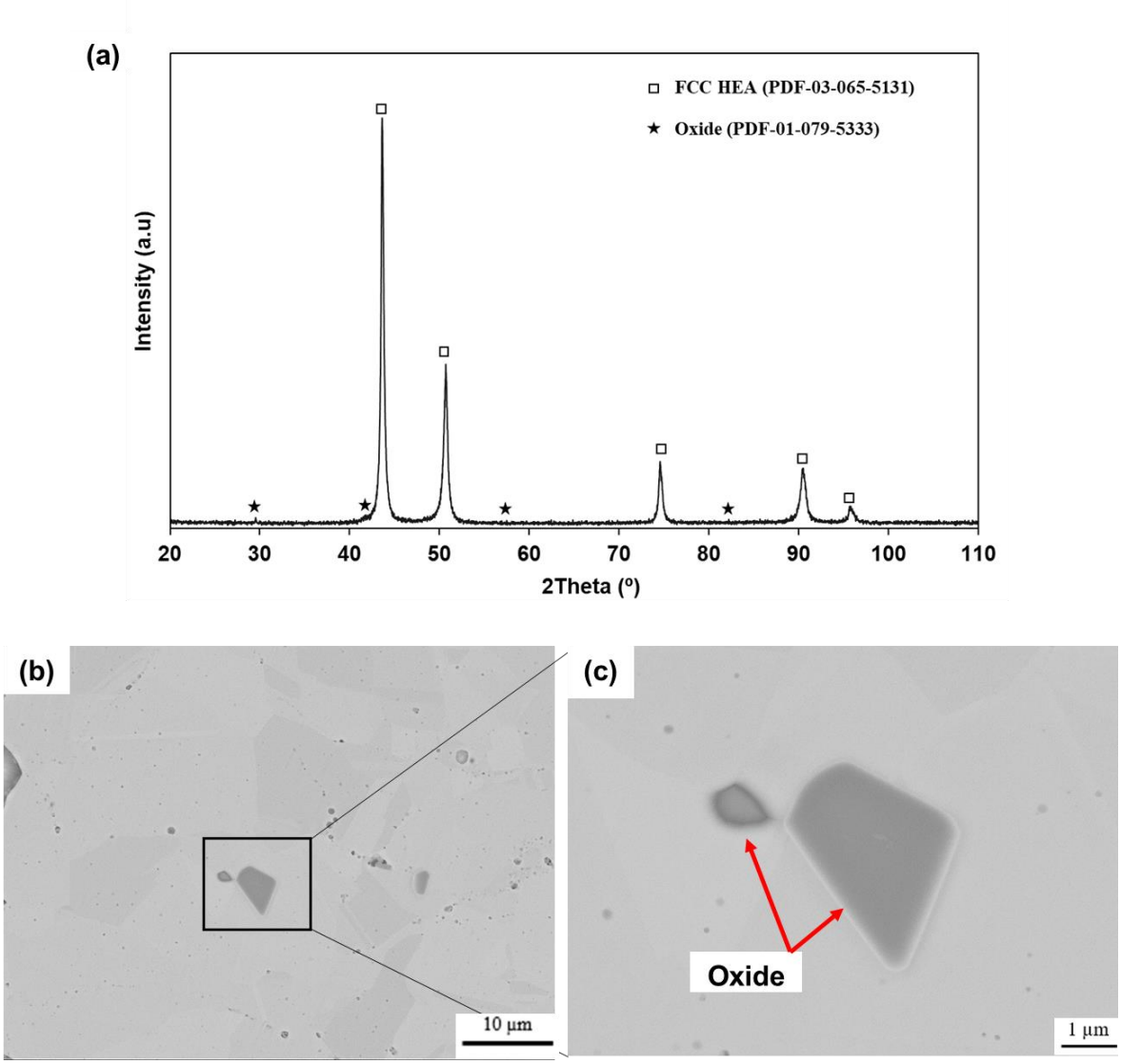

Figure 7.9: XRD profile (a) and BSE image (b) of the HT1000 sample. Oxide particles are observed as the darker particles shown in the BSE image in (c).

Further analysis was performed to clarify the chemical composition of the oxides present in the samples annealed at higher temperatures. Using the EDX mapping, the oxide particles were confirmed to be Cr-Mn oxides, presented in Figure 7.10. The oxide particles were likely formed from oxygen ingress into the deposit via incompletely metallurgical bonded areas and porosity in the samples. Since Cr and Mn are the elements in the HEA that are likely most reactive with oxygen, Cr-Mn oxide was, as a consequence formed in the samples.

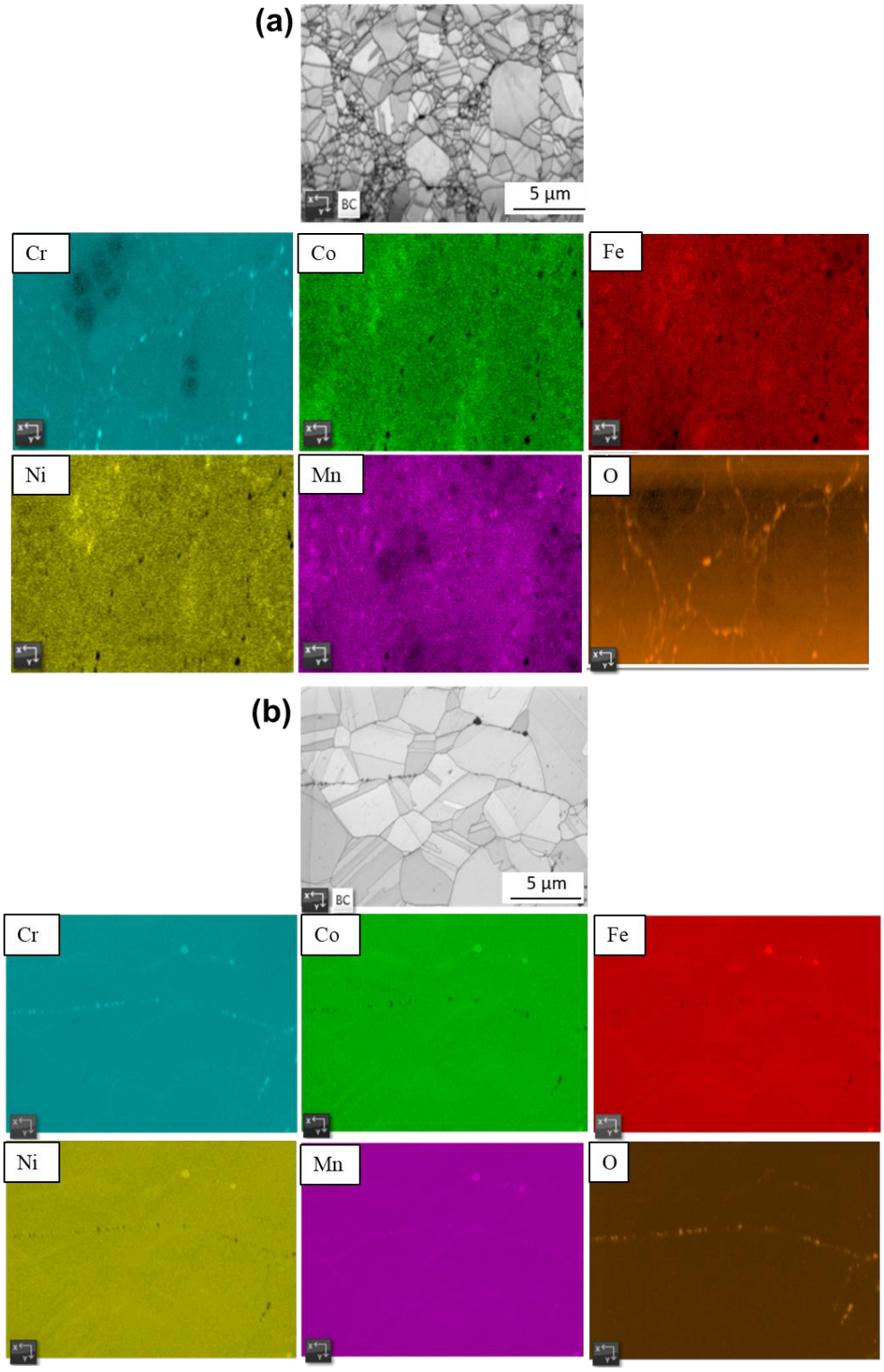

Figure 7.10: EDX mapping of the samples annealed at (a) 800 °C (HT800) and (b) 1000 °C (HT1000). The EDX mapping suggests the oxides to be likely rich in Cr and slightly rich in Mn with the absence of other elements.

7.3.3 EBSD analysis

EBSD technique was employed to characterise the microstructure of the as-sprayed and annealed samples as presented in Figure 7.11. The EBSD band contrast (BC) image is shown in Figure 7.11 (a1-d1), the inverse pole figure (IPF) map is shown in Figure 7.11 (a2-d2) and the corresponding kernel average misorientation (KAM) map is presented in Figure 7.11 (a3-d3). The BC image shows the quality of diffracted signals where the bright colour corresponds to a sharp lattice projection. On the other hand, grain boundaries, dislocations or lattice defects correspond to the dark lines. HAGBs were superimposed and indicated by the black lines to reveal the individual grains. There is a higher density of a network of randomly oriented dark lines in the microstructure of the as-sprayed sample (Figure 7.11 (a1)) when compared to the heat-treated samples (Figure 7.11 (b1, c1 and d1)), suggesting a higher density of the network of dislocations or grain boundaries present in the as-sprayed sample. The high density of grain boundaries can be attributed to grain fragmentation or refinement resulting from thermomechanical phenomena such as adiabatic shear instability (ASI) and dynamic recrystallisation (DRX) during the deformation of the HEA particles via the CSAM process [56,137] as established in Chapter 6. The high density of grain boundaries is prevalent in particle impact regions in the microstructure of the as-sprayed sample, resulting in the low indexation quality (dark areas) due to ultrafine grains in those regions. On the other hand, the heat-treated samples are characterised by a significant reduction in the density of dislocations or grain boundaries associated with static recovery and recrystallisation.

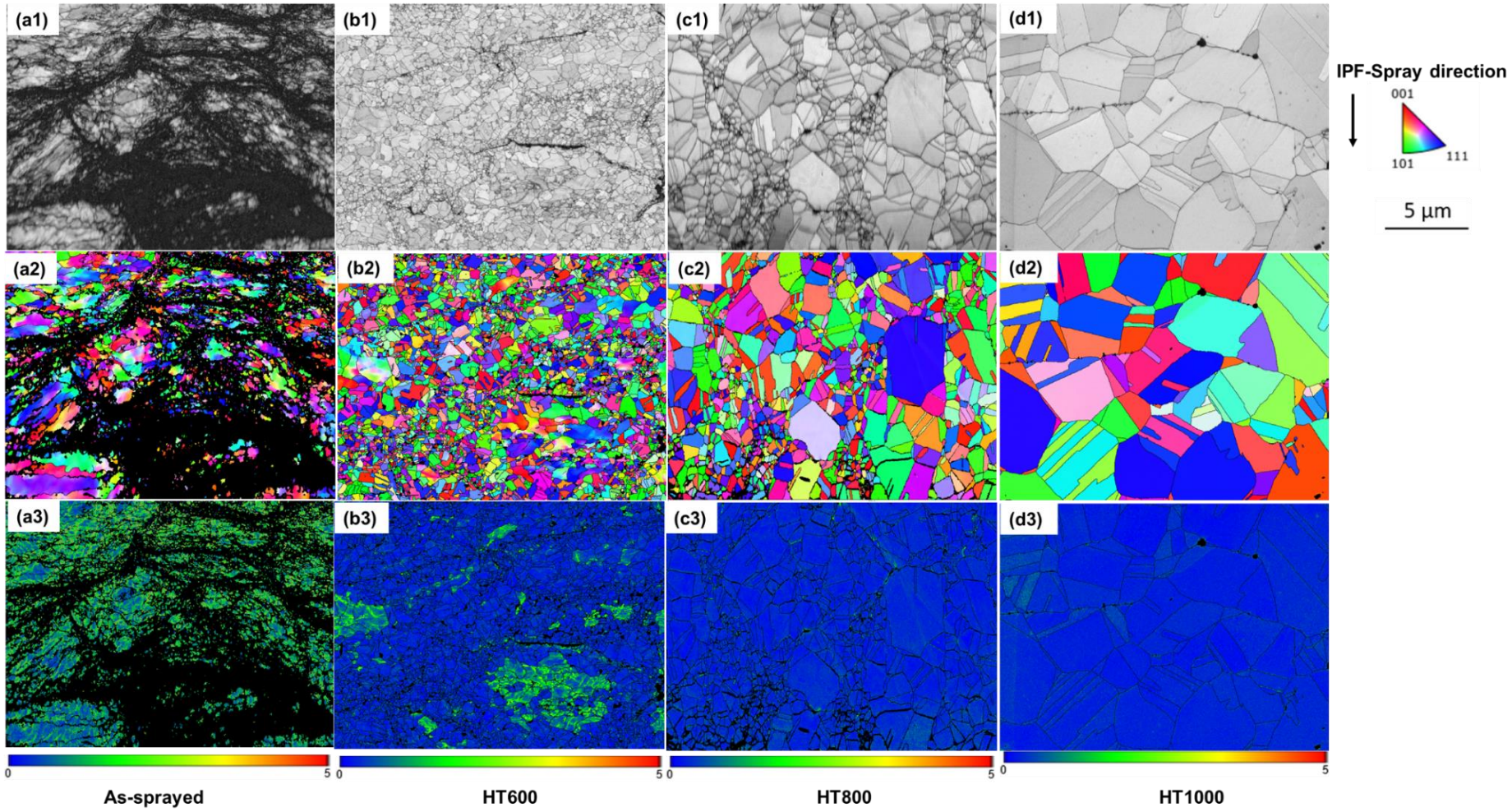

Figure 7.11: Shows the EBSD analysis of the CSAM CoCrFeNiMn HEA deposit: (a) in the as-sprayed state; (b) following heat treatment at 600 ºC, (c) following heat treatment at 800 ºC and (d) following heat-treatment at 1000 ºC.

The IPF map reveals several randomly oriented grains with different shapes and sizes within the as-sprayed (Figure 7.11 (a2)) and annealed samples (Figure 7.11 (b2, c2 and d2)). The microstructure of the as-sprayed sample reveals a heterogeneous microstructure with many ultrafine grains at the bonding regions and elongated and equiaxed coarse grains at particle interiors. The formation of this microstructure can be attributed to the dynamics of the particle deformation during CSAM deposition. On the other hand, the HT600 sample (Figure 7.11 (b2)) shows a slightly reduced heterogeneous microstructure, with highly indexed grains at the bonding regions. This microstructure formed in the HT600 sample can be attributed to static recovery and partial recrystallisation, which is discussed later. The HT800 sample (Figure 7.11(c2)) shows a microstructure with large equiaxed grains surrounded by slightly smaller ones, and growth twins (or annealing twins) can be observed in the interior of larger grains. The larger grains and appearance of the annealing twins in the HT800 sample suggest grain growth and recrystallisation of the deposit subjected to the annealing treatment. Furthermore, the HT1000 sample (Figure 7.11 (d2)) exhibits a more homogeneous distribution of larger equiaxed dislocation-free grains with well-defined grain boundaries, suggesting grain growth and coarsening.

The KAM map, which can provide a quantitative estimate of local misorientation and dislocation density of severely deformed materials and the effect of subsequent annealing treatment, reveals a reasonably uniform high local strain in the microstructure of the as-sprayed sample (Figure 7.11(a3)) compared to the annealed samples (Figure 7.11 (b3), (c3) and (d3)). The green colour in the KAM map represents the highest misorientation or local strain. Thus, the highest strain

can be observed in almost all grains in the as-sprayed sample; however, there is a significant reduction in the average strain value in the annealed samples, decreasing further with the increase in the annealing temperature. The high local strain and ultrafine grains at the bonding regions, and the elongated grains at the interiors of the particles in the as-sprayed microstructure disappeared during the high-temperature annealing resulting in nucleation and growth of strain-free and low dislocation density equiaxed grains. A small fraction of the area in the interiors of the deformed grains in the HT600 sample (Figure 7.11 (b3)) indicates the presence of high local strain or dislocations. This indicates that a significant fraction of grains with local strains or low-misorientation angles were likely retained following the annealing at 600 ºC.

The change in the grain structure during the heat treatment of the CSAM HEA deposit is evident by the grain size evolution from the as-sprayed to the annealed samples, as shown in Figure 7.12a. The figure presents the number or frequency of the grain size distribution of the as-sprayed and heat-treated samples. The average grain size increases as the annealing treatment temperature increases. Most grains in the as-sprayed and HT600 samples are generally below 0.7 μm in size, while those in the HT800 and HT1000 samples are about 1-2.5 μm. Additionally, the distribution (or fraction) of the LAGBs, HAGBs and Σ3 (60°) twinning boundary is shown in Figure 7.12b. Most grains in the as-sprayed sample were of LAGBs and HAGBs. A fraction of deformation twins were likely formed in the as-sprayed deposit, and previous studies have observed deformation twins in the CSAM HEA deposit [63,64,75]. On the other hand, the annealing treatment of the CSAM HEA deposit significantly reduces the number of grains with low-angle misorientation,

specifically for the HT800 and HT1000 samples. There is also a significant difference in the fraction of HAGBs in the samples, which decreased as the annealing temperature increased. Since the as-sprayed sample has undergone large plastic deformation, a higher fraction of HAGBs is expected as established in Chapter 6; nevertheless, the severely deformed grains are now resolved in the HT600 sample because of stress relief and reduced dislocation density within the sample, resulting in the higher fraction of the HAGBs in the HT600 sample (see Figure 7.12b). On the other hand, a higher fraction of annealing twins formed as the annealing treatment temperature increased. Even though similar domain or area sizes were examined under the EBSD microscope for all samples, the larger grain sizes and consequently, fewer grains in the HT1000 sample likely contributed to the lower fraction of annealing twin and HAGBs presented in Figure 7.12b.

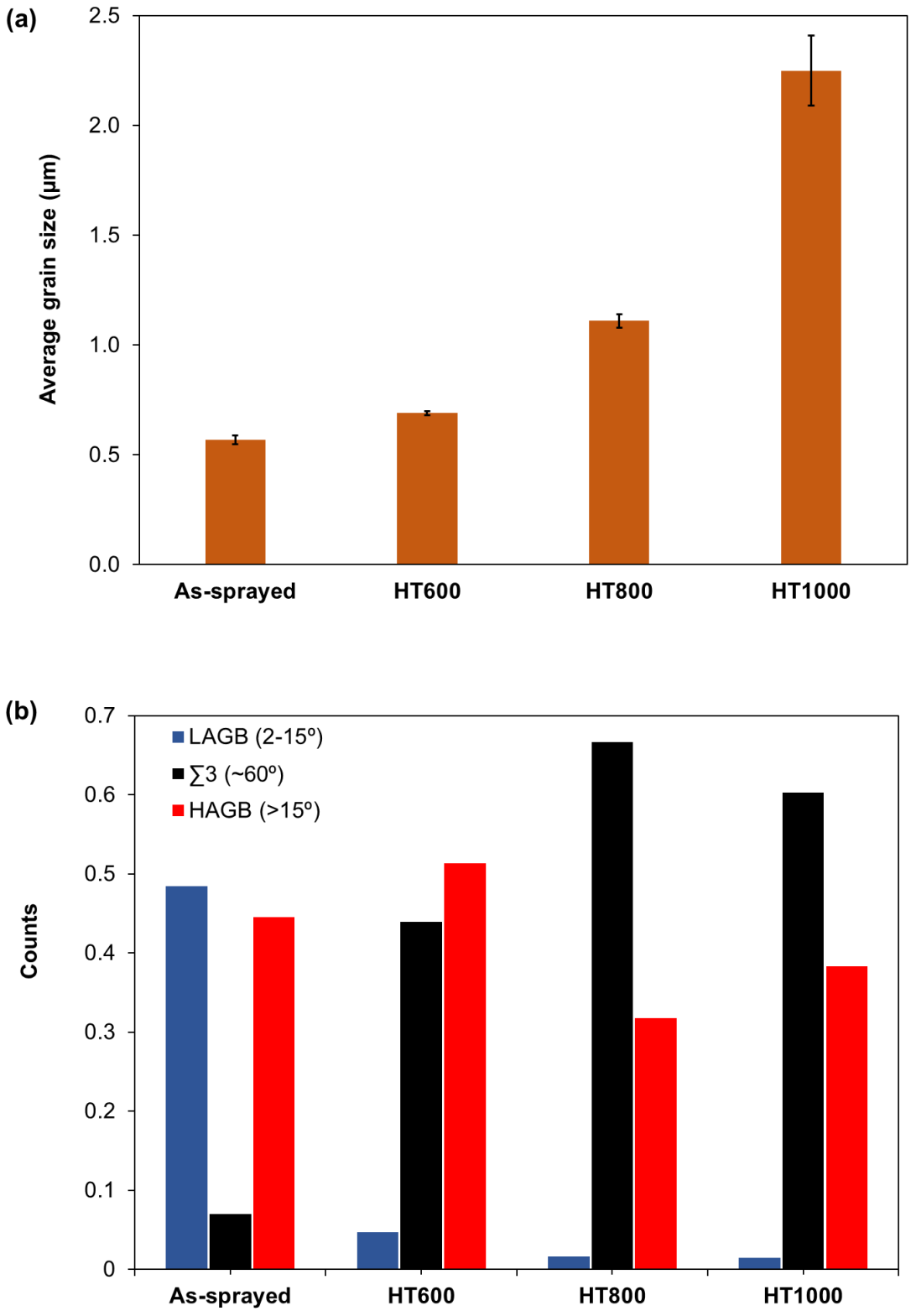

Figure 7.12: The plots of (a) average grain sizes of the as-sprayed (or as-deposited) and heat-treated samples and (b) the average distribution of the misorientation angles—LAGBs, HAGBs and twin boundary for the as-sprayed and annealed samples.

7.3.4 Mechanical properties

The average nanohardness and reduced modulus values, determined from indents performed at the middle part of the cross-sections of the as-sprayed and heat-treated samples are presented in Figure 7.13a. The greater nanohardness of the as-sprayed sample (5.14 ± 0.08 GPa) can be attributed to its microstructure, consisting of ultra-fine grains with a high local strain or dislocation density. The reduced modulus (as described in detail in Chapter 3 Section 3.7.1, on the other hand, increased from (176.82 ± 1.77) GPa in the as-sprayed sample to (188.66 ± 1.72) GPa in the HT1000 sample. A greater reduced modulus of (196.65 ± 1.79) GPa was measured in the HT600 sample, likely due to the presence of the Cr-rich phase particles, discussed later in Section 7.4.4.

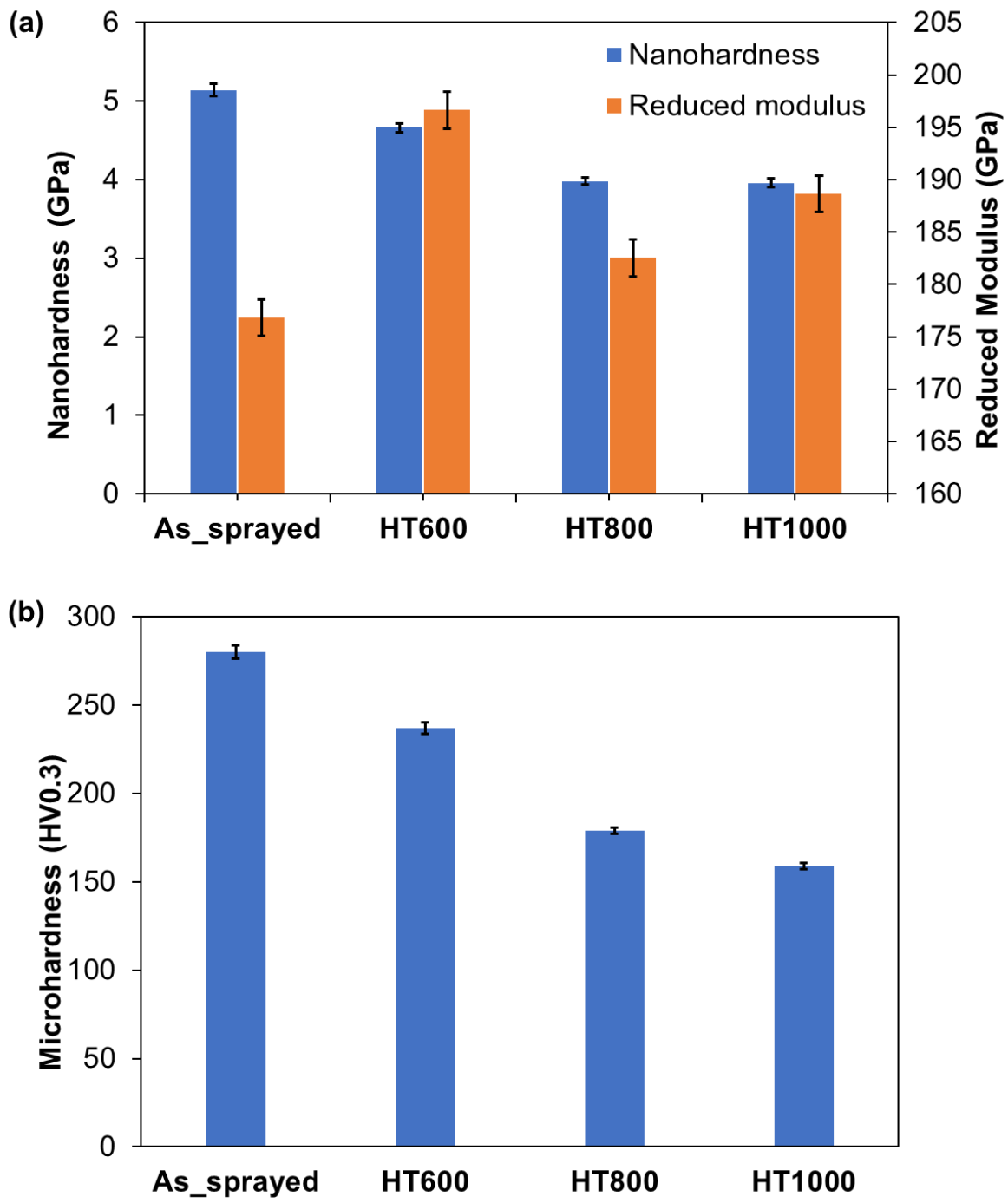

Figure 7.13: The plots of the average values of the measured (a) nanohardness and reduced modulus and (b) microhardness of the as-sprayed and heat-treated samples.

The average measured microhardness of the as-sprayed and annealed samples is presented in Figure 7.13b. Again, the high density of dislocations and ultrafine grain structure resulted in the greater microhardness of (280 ± 3.59) HV0.3 measured in

the as-sprayed sample. By increasing the annealing temperature, the measured microhardness value decreases to (159 ± 1.67) HV0.3 due to recrystallisation and grain growth.

The influence of the annealing treatment was also evidenced by the tensile test performed for the as-sprayed and heat-treated samples. The result of the tensile tests is presented in Figure 7.14. The figure shows the dependence of the tensile strength (UTS) and fracture strain on the annealing temperature. Average tensile strength of 25.9 MPa and fracture strain of 0.3% was obtained in the as-sprayed sample. A significant increase in the tensile strength and fracture strain is displayed by the HT600 sample (51.7 MPa and 1%) but decreased slightly for the HT800 sample (43.5 MPa and 0.3%). The same trend was observed for the reduced modulus of the HT600 and HT800 samples, as provided in Figure 7.13a. For the HT1000 sample, the average tensile strength and fracture strain increased more significantly (152.3 MPa and ~2%), which can be due to the relatively lower porosity, consolidated microstructure, and grain growth due to recrystallisation, as mentioned earlier.

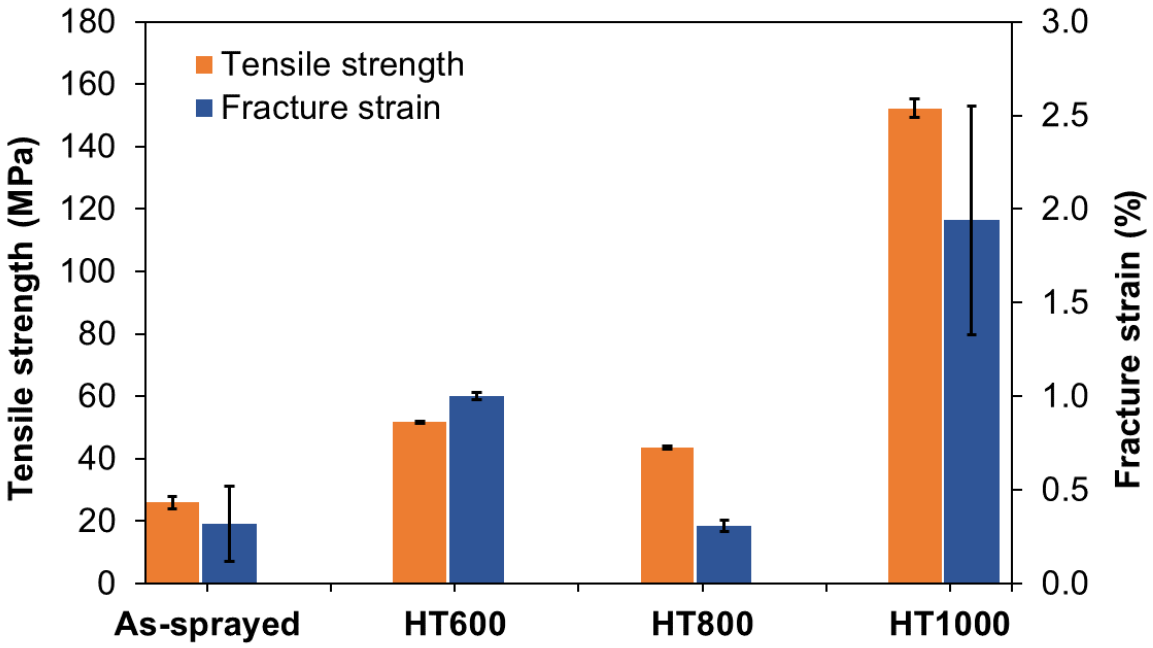

Figure 7.14: Plot of the tensile strength (ultimate tensile strength, UTS) and fracture strain (or strain at failure) of the tested samples; as-sprayed and heat-treated.

The fractured surfaces of the tensile tested samples examined under the FEG SEM in the top view are shown in Figure 7.15 and Figure 7.16. This was performed to gain insight into the micro-mechanism of the deformation behaviours and type of failure of the as-sprayed and heat-treated samples under the tensile loading. The low-magnification SEM image in Figure 7.15a shows the microstructure of the fractured surfaces of the as-sprayed tensile test sample. The figure reveals inter-particle failure, initiated mostly at inter-particle boundaries. In addition, there is a larger area of the fractured surface showing pores, which may have initiated cracks and, subsequently, early failure of the sample. Moreover, the high magnification SEM micrograph in Figure 7.16a further reveals that particle-particle failure occurred for the as-sprayed sample during the tensile testing. A very small area on the fractured surface of the as-sprayed sample reveals a dimple pattern or void coalescence, which indicates some metallic bond (as indicated in Figure 7.16a).

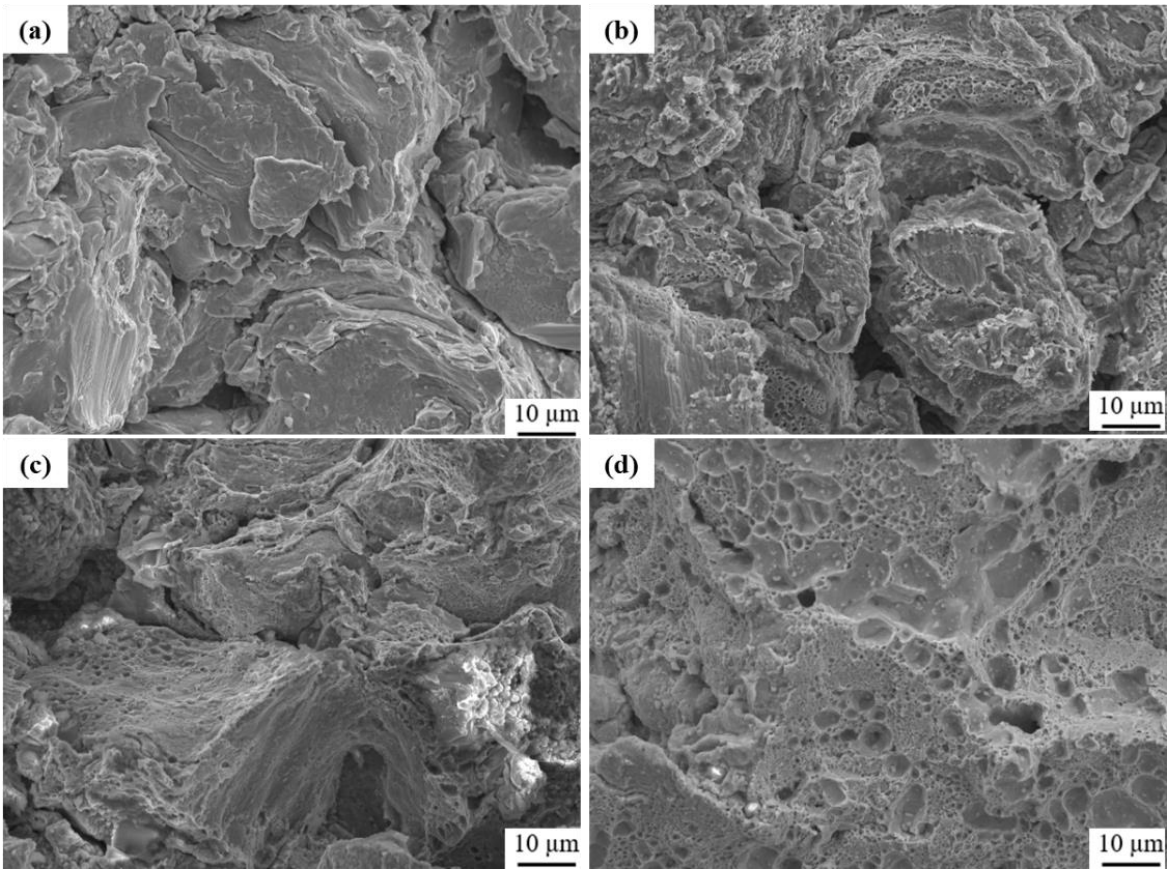

Figure 7.15: Shows the low-magnification SEM images of the fractured surfaces of the CSAM CoCrFeNiMn HEA deposit; (a) as-sprayed, (b) HT600, (c) HT800 and (d) HT1000 samples.

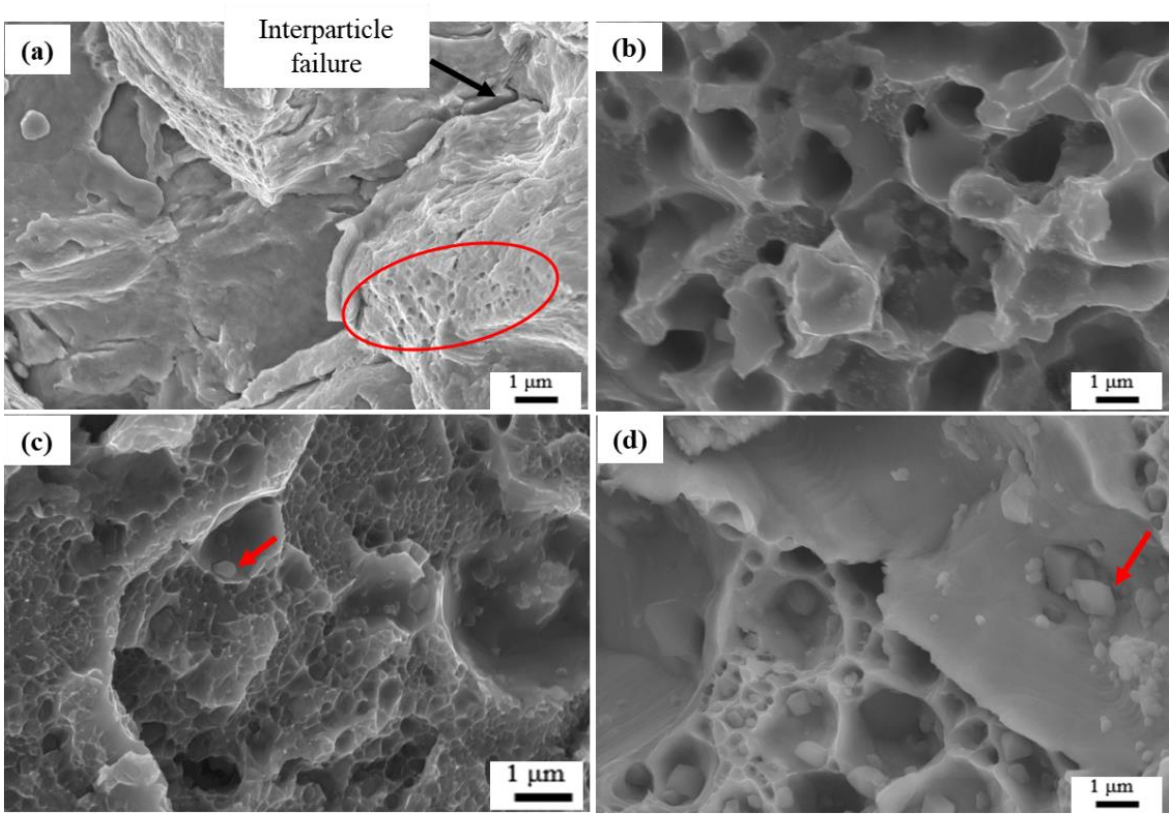

Figure 7.16: Shows the high-magnification SEM images of the fractured surfaces of the CSAM HEA deposit; (a) as-sprayed, (b) HT600, (c) HT800 and (d) HT1000 samples. The red arrows denote particles within the dimple sites, likely oxides. The denoted circular shape indicates a dimple pattern on the fractured surface of the as-sprayed sample indicating a metallic bond. The black arrow shows an area of inter-particle failure.

The HT600 and HT800 samples show fracture morphology with less prominent inter-particle failure, as shown in the low magnification SEM image in Figure 7.15b and c. From the high magnification SEM micrographs in Figure 7.16b and c, most of the fractured surface of the HT600 and HT800 samples shows a dimple pattern or void coalescence relating to ductile failure. The HT800 sample appears to have a wide variety of dimples, with some having sizes larger than those in the HT600 sample. In addition, the fracture surface of the HT800 sample reveals fine particles at the bottom of the dimple or void sites, shown in Figure 7.16c. The particles are likely the Cr-Mn oxides observed in the XRD analysis and BSE micrographs in Section 7.3.2, likely initiating crack propagation. There is also a large area on the

fractured surfaces of the HT600 and HT800 samples shown in Figure 7.16b and c, showing pores and particle-particle failure. The void coalescence and inter-particle failure observed in these samples suggest a mixed failure mode.

The fracture morphology of the HT1000 sample, shown in Figure 7.15d and Figure 7.16d, reveals a more uniform trans-granular dimple pattern, making it difficult to distinguish individual sprayed particles. Unlike the other tested samples, the respective dimple pattern appears to cover most of the observed fractured surface. Regions of large pores are also observed on the fractured surface, which likely initiated cracks, and subsequently failure. A closer view of the fractured surface reveals precipitates at the bottom of the trans-granular dimple sites, likely to be the Cr-Mn oxides (like what was observed in the HT800 fractured surface), initiating crack propagation. Interestingly, a deformation feature was observed at a dimple site of the HT1000 sample, which is believed to have occurred during the tensile loading of the specimen, shown in the high magnification SEM micrograph in Figure 7.16d. This deformation feature requires further characterisation as obtaining detailed information on the feature using the SEM is difficult, which can be a future study.

7.4 Discussion

7.4.1 Effect of annealing on porosity of the HEA deposits

It is widely accepted that the bonding mechanism of metallic powder particles during CSAM is attributed to adiabatic shear instability (ASI) taking place at or above the critical velocity of the given material [56,57,133]. The occurrence of ASI has been

widely measured by the shear localisation strain of various materials. Consequently, materials with high critical strain (i.e., high strain hardening and resistance to strain localisation) for ASI would require high critical velocity. Due to the high strain hardening and resistance to shear localisation of the CoCrFeNiMn HEA [64,301], it may be challenging to produce a pore-free deposit with the CSAM process. A moderate average porosity of ~ 2.4%, as presented in Figure 7.2, was obtained in the as-sprayed sample. The SEM micrograph in Figure 7.1a suggests that the pores were likely formed from the incomplete bonding of particles at the impact interfaces. The annealing treatment performed, however, significantly improved the microstructure of the CSAM HEA deposit. A decrease in porosity to ~ 0.6% was obtained after annealing at 1000 ºC, as shown in Figure 7.1d and Figure 7.2. Although porosity was reduced, the pores observed in the heat-treated samples in Figure 7.1 can be attributed to incomplete metallurgical bonding or “sintering” of the splats at the interfaces.

A schematic illustration of the effect of annealing on the porosity of the deposited sample is presented in Figure 7.17. The figures show that upon impact the sprayed particles are deformed and bond to themselves; however, due to the impact behaviour of the HEA particles, pores are formed and consequently, incomplete metallurgical bonds between particles. During the annealing treatment, the sintering of sprayed particles occurs as the grains of the particles at the interfaces grow, closing the pores. Many pores that were present in the as-sprayed deposit however remain after annealing as the pores were not completely closed. Nevertheless, the annealing treatment significantly reduces the number of pores and closes many tiny pores, therefore reducing the degree of porosity in the deposits. Future investigation

may involve increasing the annealing time under the same temperature conditions, to produce dense deposits via the annealing treatment process.

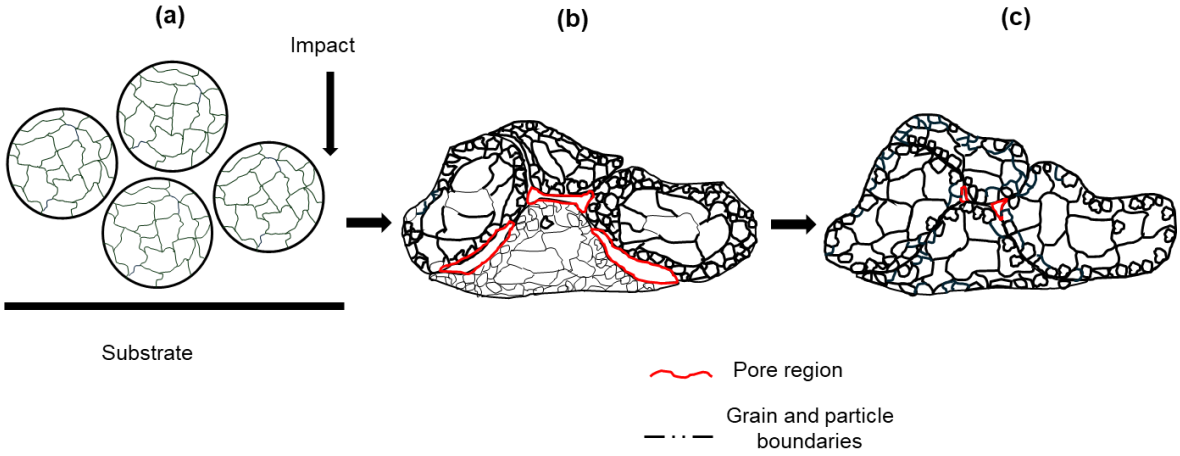

Figure 7.17: Shows a schematic illustration of the effect of annealing treatment on closing the pores in the sprayed HEA deposit: (a) the particles are impacted on the substrate, and (b) upon impact they deform severely and bond to themselves and the substrate; however, pores are formed at the impact interfaces due to insufficient deformation. (c) Under annealing conditions, pores are closed due to diffusion of the grains at the boundaries and grains growth, but some pores remain in the annealed deposit.

7.4.2 Effect of annealing on phase transformation and microstructure changes

The composition of the deposit heat-treated at 600 ºC (i.e., HT600 sample) exhibited two distinct phases: the FCC matrix phase and the Cr-rich phase, as shown in Figure 7.3 and Figure 7.4. The Cr-rich phase was observed to be formed along grain boundaries of the FCC matrix, suggesting that these locations likely serve as both fast routes and preferential sites for the nucleation and growth of the Cr-rich phase [339]. Moreover, a high density of grain boundaries was observed at impact regions associated with the large strain experienced by those regions. The large strain in those regions of the deposited samples likely contributed to the phase

transformation that occurred in the HT600 sample during annealing. This phase transformation mechanism has been reported by previous studies in the severely deformed HEA sample [240,246,262].

After the annealing treatment at 800 and 1000 ºC, the deposit achieved a single-phase FCC (as shown in Figure 7.8 and Figure 7.9). The Cr-rich phase appears to have been dissolved into the HEA FCC matrix, attributed to the high configurational entropy of the solid solution FCC at sufficiently high temperatures [35,36]. In addition, the precipitation and formation mechanism of the NiMn phase observed in the SEM image of the HT800 sample shown in Figure 7.7, requires further investigation as the phase was not detectable within the limit of sensitivity of the XRD analysis employed, likely due to their small volume fraction. Nevertheless, the phase has been reported to be formed during the short-term annealing of severely deformed samples of the HEA at temperatures below or at 450 ºC [240,254]. Oxide particles were formed in the deposits heat-treated at high temperatures (i.e., HT800 and HT1000 samples), as shown in Figure 7.8 and Figure 7.9. The oxide particles formed are due to the oxidation of the samples during the air annealing.

The EBSD analysis provided in Figure 7.11 and Figure 7.12 revealed that the annealing treatment process generates different microstructural features and grain structures in the deposit. In the as-sprayed sample, as shown in Figure 7.11(a), a heterogeneous microstructure was formed because of the high strain, strain rate and temperature gradients experienced by the HEA powder particles during the CSAM process [56,137,138,141]. Highly deformed regions with ultrafine equiaxed grains are observed at the particle-particle interfaces, while more lightly deformed regions with coarse grains are observed at particle interiors as illustrated in Figure

7.17. Because of the severe plastic deformation and associated temperature rise during deposition, the grains of the CSAM deposit are refined via dynamic recrystallisation (DRX) and ASI, as explained in detail in Chapter 6. The annealing treatment at 600 ºC (i.e., HT600 sample) performed for the as-sprayed sample provided an additional driving force for static recovery and partial recrystallisation as shown in Figure 7.11(b), releasing much of the stored energy from the deformed sample. The microstructure in the HT600 sample can be compared against the as-sprayed microstructure. It was observed that grains in the peripheral or interfacial regions that were originally characterised by ultrafine grain structure in the as-sprayed sample (shown in Figure 7.11(a)) are also relatively unaffected by the annealing treatment but appeared to be dislocation-free. Additionally, some of the interiors of the HT600 particles did not significantly change, characterised by high local strain and dislocations, as shown in the EBSD maps in Figure 7.11(b). This retention of the grain structure in the HT600 sample can be attributed to the presence of the Cr-rich phase particles along the grain boundaries, hindering grain boundary migration [59,87]. Moreover, report of previous studies [340,341] shows that second-phase particles can hinder grain growth in the HEA and form fine grain structure. This was attributed to the pinning effect of the second-phase particles on the grain boundaries of the FCC matrix. Another distinct microstructure was formed in the HT1000 sample (shown in Figure 7.11(d)), consisting of dislocation-free large equiaxed grains resulting from grain growth and coarsening, with annealing twins—indicating stress relief. A similar microstructure was observed in the HT800 sample shown in Figure 7.11(c) but with smaller grain sizes, as presented in Figure 7.12.

7.4.3 Influence of deposit microstructures on mechanical performances

The distinct microstructures obtained via the CSAM process, and the subsequent annealing treatment can explain the described differences in the mechanical properties of the samples and the resulting fractured surfaces of the micro-flat tensile specimens. The greater hardness obtained in the as-sprayed sample presented in Figure 7.13, is attributed to the strengthening mechanisms distinguished in the microstructure; grain boundary and dislocation strengthening. The measured hardness decreased as the annealing temperature increased as a general tendency attributed to static recovery, recrystallisation and grain growth. In contrast, the reduced modulus increases as temperature increases, attributable to the mechanisms responsible for the decrease in the hardness. The mechanism responsible for the exceptionally greater reduced modulus obtained in the HT600 sample and its tensile properties compared to the HT800 sample will be discussed later. An increase in the tensile strength and fracture strain was obtained with an increase in the annealing temperature, as provided in Figure 7.14.

As illustrated by the fractured surfaces in Figure 7.15a and Figure 7.16a, the as-sprayed sample is characterised by the brittle rupture between non-bonded particles and regions exhibiting defects such as pores. This explains the low tensile strength and fracture strain of the sample, provided in Figure 7.14. Since all sorts of microstructural defects in the as-sprayed deposit can be reduced by diffusion, annealing treatment improves their tensile properties. There was a slight increase in the tensile strength and fracture strain in the HT600 and HT800 samples, as

shown in Figure 7.14. This can be explained by the fracture morphology of the HT600 and HT800 samples shown in Figure 7.16b and c. Dimple patterns or void coalescence, characteristic of ductile failure, were observed on the fractured surfaces of the tested samples, which is more prominent in the HT800 sample. The change from brittle failure in the as-sprayed sample to ductile failure after annealing treatment can be attributed to the reduced interfaces not being metallurgically bonded, and porosity. Nevertheless, large areas on the fractured surfaces of the HT600 and HT800 samples shown in Figure 7.15b and c, reveal a brittle rupture due to non-bonded areas and pores still present, suggesting a mixed mode failure.

A better tensile performance was obtained with the sample heat-treated at 1000 ºC. Moreover, the fractured surface of the HT1000 sample, shown in Figure 7.15d and Figure 7.16d, indicates a ductile failure with various dimple patterns. This is attributed to the consolidated microstructure and uniform local microstructures, resulting in the increased tensile strength and fracture strain of the tested samples, as presented in Figure 7.14. This can also be due to the increased metallurgically bonded interfaces and recrystallisation at 1000 ºC (as discussed earlier and as shown in the EBSD analysis in Figure 7.11). However, the fracture morphology reveals fine particles at the bottom of the dimple sites that are likely oxide precipitates, as shown in Figure 7.16d, suggesting crack propagation sites. The distance between the oxides is small to allow substantial ductile deformation of the HEA matrix, which likely lowers the tensile properties of the sample. The oxidation of the deposit can be eliminated or minimised if heat-treated in a protective environment. The present study shows that the mechanical properties of the CSAM

HEA deposits can be improved by annealing treatment at 1000 ºC; however, porosity needs to be further reduced for better mechanical performance.

When comparing the tensile properties of the samples obtained in this thesis with the bulk counterpart of the HEA manufactured using other AM techniques and casting or forging methods, the ductility and strength of the samples are very low even after the annealing treatment. For instance, yield strength and elongation of over 500 MPa and 25% [257], and about 350 MPa and over 70% [42] have been reported for the HEA manufactured using AM and casting methods, respectively. The evaluated low tensile properties of the HEA samples in this thesis can be attributed to the porous microstructure of the samples. Another contributing factor is the brittle nature of cold-sprayed deposits due to severe work hardening of the deposited material in the as-sprayed condition, which may not be significantly relieved after the annealing treatment. To improve the structural integrity of repaired parts using the technique described in this chapter, an optimal deposit must be first obtained before annealing. Consequently, the tensile properties of the HEA deposit after annealing can be comparable to or greater than those manufactured using conventional manufacturing techniques.

7.4.4 Mechanistic understanding of the Cr-rich phase strengthening effect on the annealed HEA deposit

What is interesting is the clear difference in the mechanical properties of the HT600 and HT800 samples. The HT800 sample shows a lower hardness, reduced modulus, tensile strength, and fracture strain compared to the HT600 sample, as

shown in Figure 7.13 and Figure 7.14. Moreover, on the corresponding fractured surfaces, the more dimple patterns observed in the HT800 sample in Figure 7.16c, on the one hand, indicate improved tensile properties compared to the as-sprayed sample. On the other hand, the oxides observed at the dimple sites and the porosity might also indicate an increased number of crack nucleation sites, resulting in lower tensile properties. Even though higher porosity and less dimple pattern or void coalescence were observed in the HT600 sample, a plausible explanation for the greater mechanical performance can be attributed to the presence of the Cr-rich precipitates. Figure 7.18 shows a schematic illustration explaining the strengthening mechanism of the Cr-rich phase particles in the microstructure of the HT600 sample. The Cr-rich precipitates are likely to contribute to the increased mechanical properties by partly constraining the deformation of the surrounding FCC matrix under mechanical loading [240]. Additionally, the fine-grained structure formed in the HT600 sample because of the pinning effect of the Cr-rich particles and the partial recrystallisation (as discussed earlier) likely contributed to the improved mechanical properties.

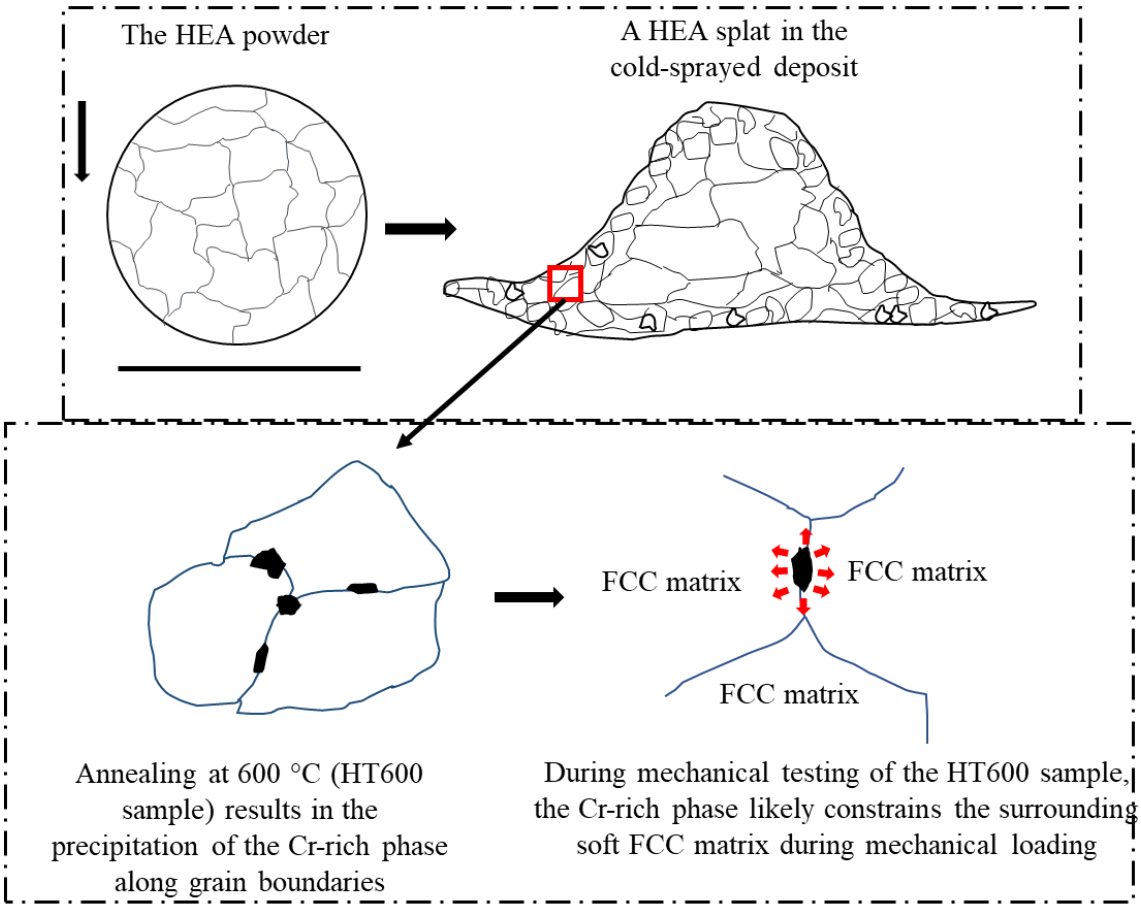

Figure 7.18: Shows a schematic illustration explaining the strengthening effect of the Cr-rich phase particles in the sample annealed at 600 ºC, under mechanical loading.

Although previous studies have reported that the Cr-rich phase, being intermetallic, can result in low ductility [240]—a drawback to the tensile ductility of the CoCrFeNiMn HEA. It is likely that the small volume fraction of the Cr-rich phase (~7.5% as obtained by XRD Rietveld refinement) when compared to what has been obtained by previous studies (20-30% [254,342]) and the CALPHAD data (~35%) likely contributed to the improved fracture strain of the HT600 sample when compared to that of the HT800 sample. In addition, different elemental compositions of the Cr-rich phases have been reported. For instance, previous research has reported between 45-90 at.% of Cr [239,240,254], whereas the SEM-EDX measurement provided in Section 7.3.2 reveals 33 at.% of Cr. The different

chemical compositions can suggest different hardness and degrees of brittleness; unfortunately, no hardness results of the various Cr-rich phases have been reported, probably due to their small size. It is therefore believed that the small volume fraction and at.% of Cr in the Cr-rich precipitate, together with the fine-grained structure and the partially recrystallised microstructure resulted in the improved mechanical properties of the HT600 sample. A similar observation has been reported in previous studies. For example, Bae et al. [263] reported an improved strength-ductility combination of the cold-rolled HEA when annealed at an intermediate temperature (650 ºC for 1 hr), which was attributed to the small volume fraction of the Cr-rich phase and partially recrystallised microstructure. This research is a first step towards a more profound understanding of the microstructure evolution and mechanical properties of the CSAM HEA deposit when subjected to annealing treatment at various temperatures.

7.5 Conclusions

In this chapter, a ~2 mm thick deposit of the CoCrFeNiMn HEA was produced using the CSAM process. The as-sprayed samples were heat-treated at various temperatures to improve the microstructure, leading to distinct microstructural characteristics. The effect of the microstructure on the mechanical performance of the deposits was analysed and discussed. The annealing treatment changes the tensile micro-deformation behaviour of the HEA deposit from a brittle failure to a ductile failure. The main findings of the present study can be summarised as follows:

- The annealing treatment performed for the deposited sample resulted in the consolidation of the deposit, increasing metallurgically bonded areas. Porosity decreases as the annealing temperature increases.

- The mechanical performance of the HEA deposit strongly depends on the microstructure and annealing conditions after CSAM. Although greater hardness was obtained in the as-deposited and heat-treated sample at 600 ºC, better tensile properties were obtained with samples heat-treated at 1000 ºC, due to increased metallurgical bonded areas.

- The heat-treated sample at 600 ºC exhibited a partially recrystallised microstructure composed of dislocation-free fine equiaxed grains at the particles peripheral, grains with high dislocations at the particles' interiors, and with a small fraction of Cr-rich phase particles. At 800 and 1000 ºC annealing temperature, recrystallisation and grain growth occurred with single-phase FCC.

- Against the mechanical performance, the heat-treated sample at 600 ºC was considerably greater than the sample heat-treated at 800 ºC. The better mechanical performance of the heat-treated sample at 600 ºC is attributed to the partially recrystallised microstructure with Cr-rich phase particles.

8 Measurement and numerical modelling of residual stress formed in CSAM CoCrFeNiMn HEA deposit

8.1 Introduction

Previous chapters have revealed and demonstrated that CSAM of the CoCrFeNiMn HEA feedstock material can be employed to repair components made of stainless steels, and other metallic alloys. In addition to the repair capability is the possibility to manufacture components using the HEA and the CSAM process. Subsequently, it is desired that the repaired or manufactured components possess excellent structural integrity or mechanical properties for in-service applications. The structural integrity of the components can be influenced by residual stresses formed in the component likely introduced during the CSAM process. Therefore, is it crucial to understand the formation of residual stress in the components during the repair or manufacturing process. In this chapter, the residual stress of a thicker deposit of the HEA on the stainless steel substrate was measured and numerically analysed. The motivation for the study presented in this chapter resulted from what was observed during the CSAM process of depositing the thick deposit of the HEA on the substrate. Delamination of the deposit from the substrate was observed during the spray process and that prompted the investigation into understanding the stresses that may have been developed using the spraying parameters employed. The investigation informed the possible optimum process conditions, and hence the

spraying parameters for the materials and substrate combinations, for future investigations.

In the open literature, residual stresses induced by CSAM have been investigated by several researchers for various deposit-substrate material combinations and spraying parameters. The outcome of the residual stresses during CSAM, measured using various experimental techniques and numerical or analytical methods, have been based on two main mechanisms: peening dominant and thermal mismatch dominant [159] mechanisms. The evolution of these mechanisms, however, depends on the thermo-mechanical effects induced by the CSAM process. Detailed information and discussion of the residual stress in CSAM deposits relevant to the work in this thesis have been provided in Chapter 2 Section 2.7. Regardless, a brief discussion of some of the studies relevant to the work in this chapter is provided here.

Luzin et al. [219] investigated the residual stress in CSAM Cu and Al deposits on Cu and Al alloy substrates, sprayed using Helium (He) at $\leq$ 200 ºC and 0.62 MPa. It was reported that the compressive residual stresses were largely due to kinetic (peening effect due to plastic deformation of microparticles) and not by thermal effects. Contrarily, Luzin et al. [84] demonstrated in another study that the residual stresses in CSAM Ti deposit on Fe and Al substrates were mainly formed through a thermal mismatch mechanism due to the difference in thermal expansion coefficients of the materials. This thermal effect was ten times larger than the compressive deposition (peening) stress. Similarly, Spencer et al. [220] reported a thermal mismatch dominant mechanism in CSAM pure Al on Mg alloy substrate using nitrogen (N_2) at 550 ºC and 3.85 MPa. Moreover, tensile residual stresses

(quenching stress and thermal mismatch dominant mechanisms) in CSAM deposits have been reported by several other researchers [83,85,202], attributed to the gas temperatures and material combinations employed. Apart from the aforementioned spraying conditions, the nozzle transverse speed and powder feed rate have been reported to significantly influence the sign and magnitude of residual stresses in CSAM deposits. For example, Vargas-Uscategui et al. [211] have reported tensile residual stress formed in a CSAM hollow Ti cylinder, attributed to the slow nozzle transverse speed and high powder feed rate employed in the study. Meanwhile, Brown et al. [212] reported compressive residual stress in a CSAM CuNi deposit when using higher nozzle transverse speed.

Despite these several investigations, there are, however, limited studies on the residual stress of CSAM CoCrFeNiMn HEA [204]. There is a wide gap in knowledge on the through-thickness residual stress formed in CSAM CoCrFeNiMn HEA. Moreover, for even other metallic CSAM deposits, there are limited reports on the residual stresses measured using the contour method of stress measurement, and numerical modelling employed to predict and understand the evolution of stress during CSAM. It is therefore important to understand the nature, evolution, and magnitude of through-thickness residual stress formed in CoCrFeNiMn deposits for possible repair applications and component manufacturing. The residual stress formed will thus influence the fatigue and fracture performance of a repaired part or component [80–82], hence the mechanical integrity of the components.

8.2 CSAM HEA depositions

The CoCrFeNiMn HEA powder was used to produce a thick deposit on the stainless steel 304 (SS304) substrate. The surface morphology, particle size distribution, and chemical composition of the powder are provided in Chapter 5 Section 5.3. The substrates had dimensions of 60 × 25 mm and a thickness of 2 mm. The substrates were roughened by grinding with P240 SiC paper, cleaned with industrial methylated spirit (IMS), and dried with compressed air before spraying. Deposits were manufactured using the CSAM set-up provided in Chapter 3 Section 3.2. Helium was used as the propellant and powder carrier gas with a stagnation temperature of 400 °C and a pressure of 3.3 MPa. The powder feeder was set at 2 rpm, resulting in a powder feed rate of 38 g/min. The scanning speed (or transverse speed) of the CSAM nozzle was 60 mm/s, resulting in a deposit thickness of approximately 4.2 mm, with four passes. Three substrates were clamped side by side on a sample holder that was moved by a robotic arm (ABB robot, UK). The CSAM HEA deposit sample was prepared following the metallographic procedures outlined in Chapter 3 Section 3.3. The microstructure of the deposit was examined using the Philips XL30 scanning electron microscope (SEM), and back-scattered electron (BSE) images were taken to measure the porosity and thickness of the deposit using the ImageJ imaging analysis technique described in Chapter 3 Section 3.6.

8.3 Residual stress measurement

The residual stress of the deposited sample was measured using the contour method. A detailed description of the principle of the contour method is provided in Chapter 3 Section 3.8, along with the experimental procedures and parameters employed in this study. The contour method is a promising technique for residual stress measurement in CSAM-repaired parts or manufactured components for the aerospace sector. The main steps of this technique are sample cutting, surface contour measurement (displacement of the cut surface), data analysis, and finite-element (FE) modelling. There are limited studies that have reported the residual stress of CSAM deposits measured using the contour method [85,211,217]. Through-thickness residual stresses can be obtained using the XRD technique with incremental material removal [81,207,343]; however, the technique can be labour-intensive for thick deposits. Another technique is the neutron diffraction stress measurement, which can measure through-thickness residual stresses of thick deposits; however, it can be significantly affected by sample positioning, neutron beam path in the sample, and texture [83,84,344]. The contour method, on the other hand, is insensitive to the material microstructure [345], making it a powerful technique for measuring the through-thickness residual stress in thick CSAM deposits.

In the present work, the contour method was employed to measure the residual stress in a 4.2-mm thick deposit of CoCrFeNiMn HEA on a 2-mm thick SS304 substrate, as shown in Figure 8.1a. The figure also shows where the sample was cut in half, and the residual stress component of interest was measured normal to

the surface of the cut, which is the longitudinal stress (σ_x) of the sample (shown schematically in Figure 8.1b). Two high-quality cut surfaces were obtained without grinding, and special care was applied during cutting to control and optimise the cutting step and minimise the associated errors in stress. The residual stress measured with the contour method was used to validate the results of the thermo-mechanical finite element analysis (FEA) employed in this thesis.

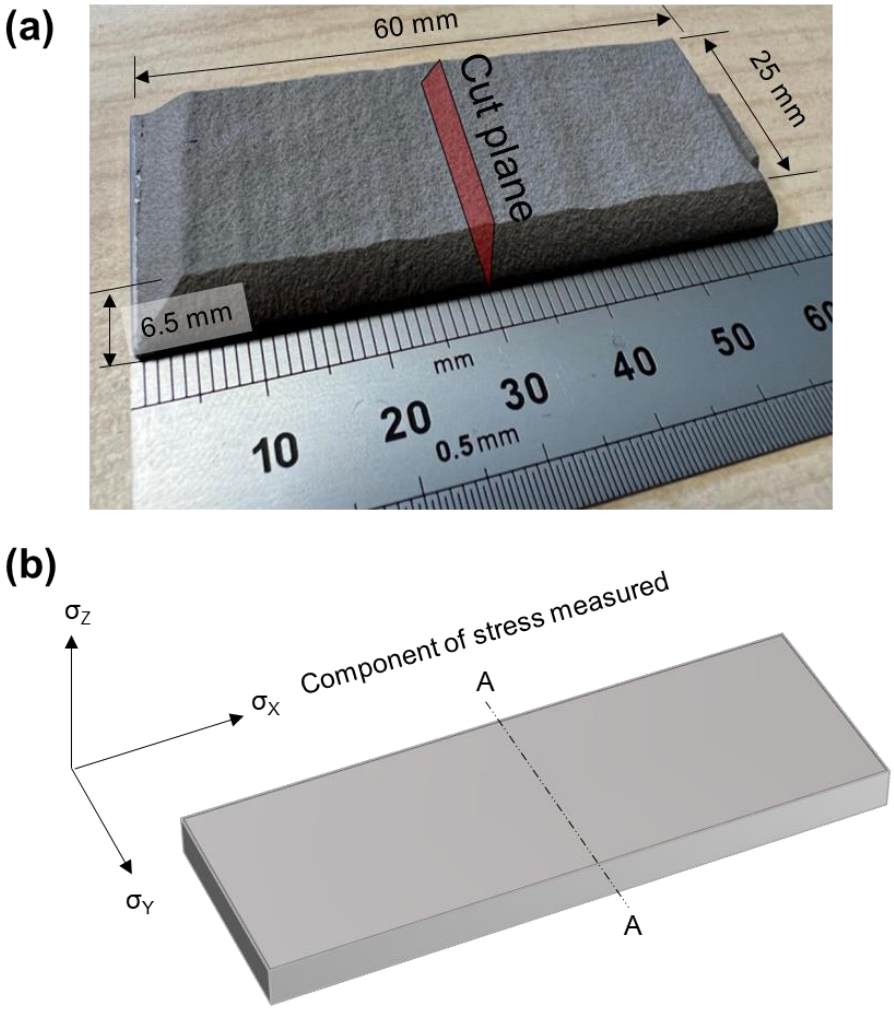

Figure 8.1: (a) The CSAM HEA deposit on the SS304 substrate, showing the cutting plane at the mid-length of the specimen (A—A), (b) schematic showing the stress component of interest, i.e., stress normal to the cut surface, which is the longitudinal stress.

8.4 Numerical modelling of residual stress

A sequentially coupled thermo-mechanical FE model was used to simulate the residual stress evolution in the thick deposit. The model combines the thermal and mechanical effects of the CSAM process. A 2D plane strain FE model with temperature-dependent material properties was employed for residual stress analysis. A detailed description of the thermo-mechanical model is provided in Chapter 4 Section 4.3. The element birth technique was employed for material deposition, where a progressive block of material was activated or added to the model, using the method described in Chapter 4 Section 4.3.2. This technique is simple and efficient because it captures the thermal history and mechanical behaviour of the model as a material is being added [225–227].

A surface heat flux load of 1.3 W/mm^2 was applied to the surface of the material during deposition. The surface heat flux corresponds to the thermal field from the hot gas impinging on the surface of the deposit during the CSAM. This was evaluated using the empirical equations described in Chapter 4 Section 4.3.3, following the experimental spraying conditions employed for the HEA deposition. The thermal and mechanical boundary conditions employed for the model are described in Chapter 4 Section 4.3. Because of the nonlinearity associated with modelling the particle impacts, the contributions from the peening or deposition peening stress were extracted from the explicit dynamic model for the multi-particle impacts described in Chapter 4 Section 4.2.2, with the results provided in Chapter 6. The average of the components of the deposition stress extracted from a region of 165 µm × 400 µm in the explicit multi-particle dynamic model is presented in

Table 8.1. These values are used as the initial stresses in the 2D thermo-mechanical FE model. This technique or scheme of the residual stress analysis—coupled implicit-explicit scheme–has been reported in other studies [225–227]; however, the deposition peening stresses from those studies were extracted from single particle impacts, leaving out the contributions of several particle impacts and different particle sizes, as is typical of the CSAM process. The temperature generated from the plastic deformation of the HEA particles was also extracted from the explicit multi-particle impact model. The temperature of the deposit from the explicit FE model was approximately 823 K, whereas the substrate temperature was approximately 323 K.

Table 8.1: Peening deposition stresses extracted from the multi-particle impact FE model in Chapter 6. The stresses were implemented in the 2D thermo-mechanical finite element model as initial stress values.

Stress (MPa)	$\boldsymbol{\sigma_X}$	$\boldsymbol{\sigma_Y}$	$\boldsymbol{\sigma_z}$	$\boldsymbol{\sigma_{XY}}$
Deposit	-66.6	-30	-203	22.3
Interface	-70.2	-175	-343	-0.2
Substrate	-30.8	-333	-271.2	0.71

8.5 Results

8.5.1 Deposit microstructure

The microstructures of the polished cross-sectional CSAM HEA deposits are shown in Figure 8.2 and Figure 8.3. The average with the standard error mean of the measurement of the thickness and porosity of the deposit was estimated as (4.2± 0.1) mm and (3.5±0.1) % respectively. The cross-sectioned SEM image shown in Figure 8.2(a) reveals a debonded interface at the edge of the deposit, which was also observed after EDM cutting of the deposit for the contour method of residual stress measurement. However, the deposit remained adhered to the substrate at the central region as shown in Figure 8.2b. Also, the SEM images shown in Figure 8.3 revealed a porous top layer of the deposit and denser interfacial layers. A porosity of (4.7±0.5)% was measured for the top layers of the deposit, whereas the middle layers exhibited (3.1±0.2)% and interface layers; the layers between the deposit and substrate interface, exhibited (2.9±0.2)% porosity. The decrease in porosity suggests the effect of peening or tampering of previously deposited layers by subsequent layers during the CSAM deposition process [346].

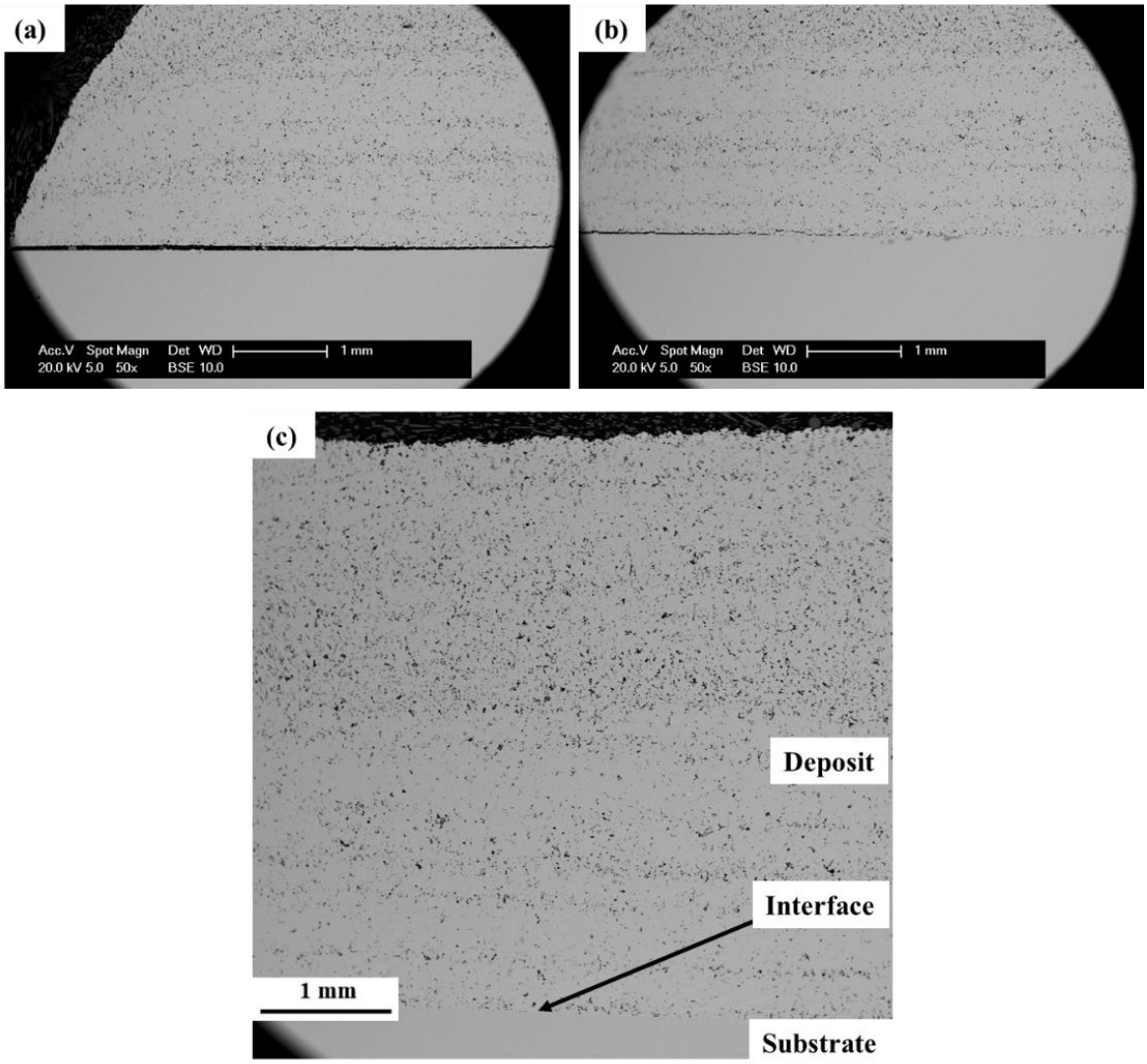

Figure 8.2: SEM micrographs showing CSAM deposit, substrate and the interface: (a) interfacial delamination at the sample edge and (b) good bonding region. The SEM microstructure in (c) also shows the through-thickness image of the deposit on the substrate.

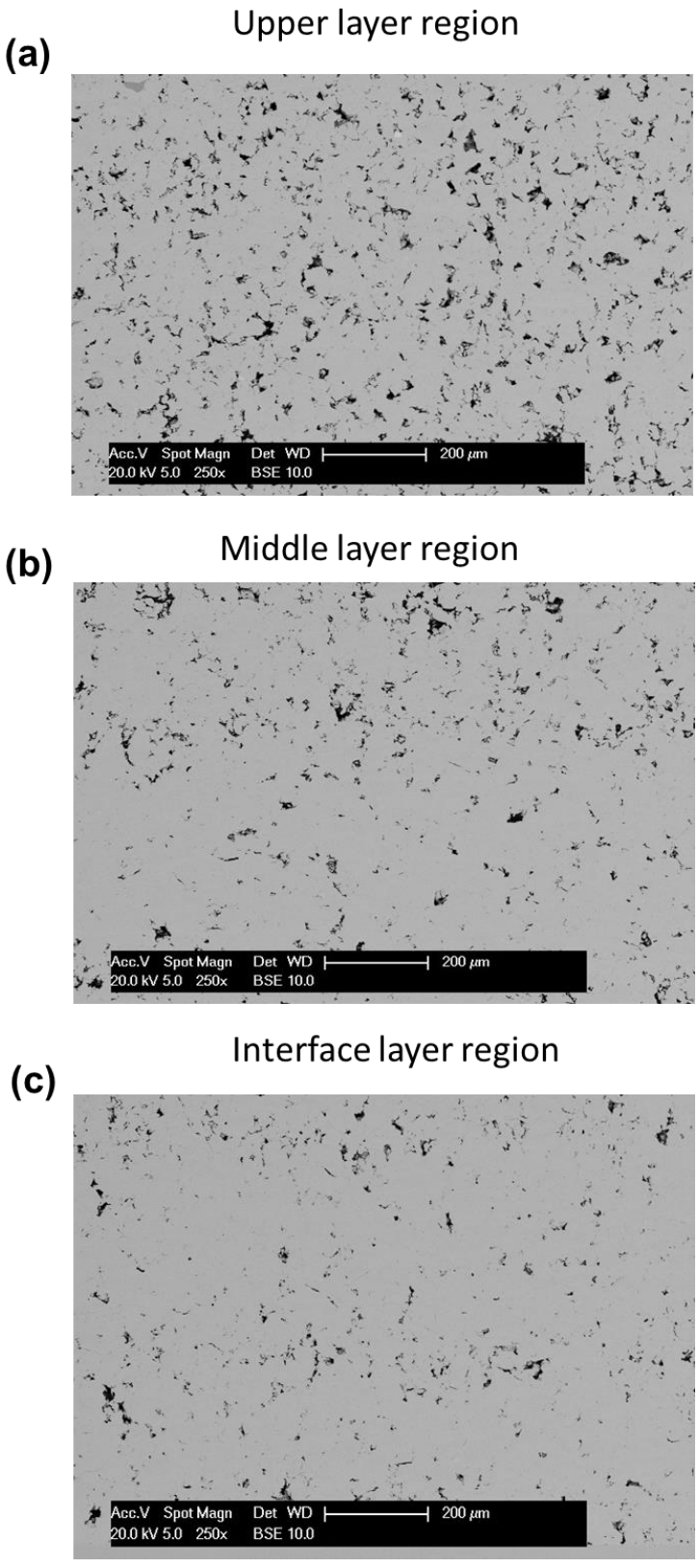

Figure 8.3: SEM images of the thick CSAM HEA deposit, showing region within each layer in the deposit characterised by different degrees of porosity: (a) upper layer exhibits (4.7±0.5)%, (b) middle layer exhibits (3.1±0.2)% and (c) interface layer exhibit (2.9±0.2)%.

8.5.2 Measured residual stress and validation of the numerical analysis

The contour profile of the CSAM HEA deposit on the SS304 substrate sample measured using a Zeiss Eclipse coordinate measuring machine (CMM) with a Micro-epsilon ILD2210 laser triangulation probe is shown in Figure 8.4a. The figure shows the displacement field normal to the cut surface, which results from the stress relief after cutting. Using the colour map, red indicates the relaxed outwards displacement, while blue indicates the inward displacement of the cut sample surface. The gap between the deposit and substrate shown in the figure is a result of the analysis procedure, performed to eliminate the influence of interfacial debonding on the data of the contour method. For stress analysis, the interfacial values were extrapolated to obtain stresses present at the interfaces. Figure 8.4b presents the 2D residual stress map for the CSAM HEA deposit on the SS304 substrate produced using the contour method. The residual stress is the longitudinal stress component of the cut surface. The results showed tensile residual stress formed in the deposit, with the highest tensile stress near the deposit-substrate interface, reaching ~370 MPa. This region was delaminated from the substrate, which likely occurred during the CSAM process. Moreover, complete delamination of the deposit from the substrate was observed during the CSAM process, which is a plausible explanation for the high tensile residual stress at the debonded interfacial region. Peak compressive residual stresses were also observed at the sides of the deposit, with the highest compressive stress formed in this region, reaching ~580 MPa. The compressive residual stresses at the sides of the deposits likely balanced the tensile stresses for the equilibrium of the debonded interfacial

region. The residual stresses measured for the sample thus reach the material yielding point of about 350 MPa [42], which is not desirable for a typical repaired or manufactured part.

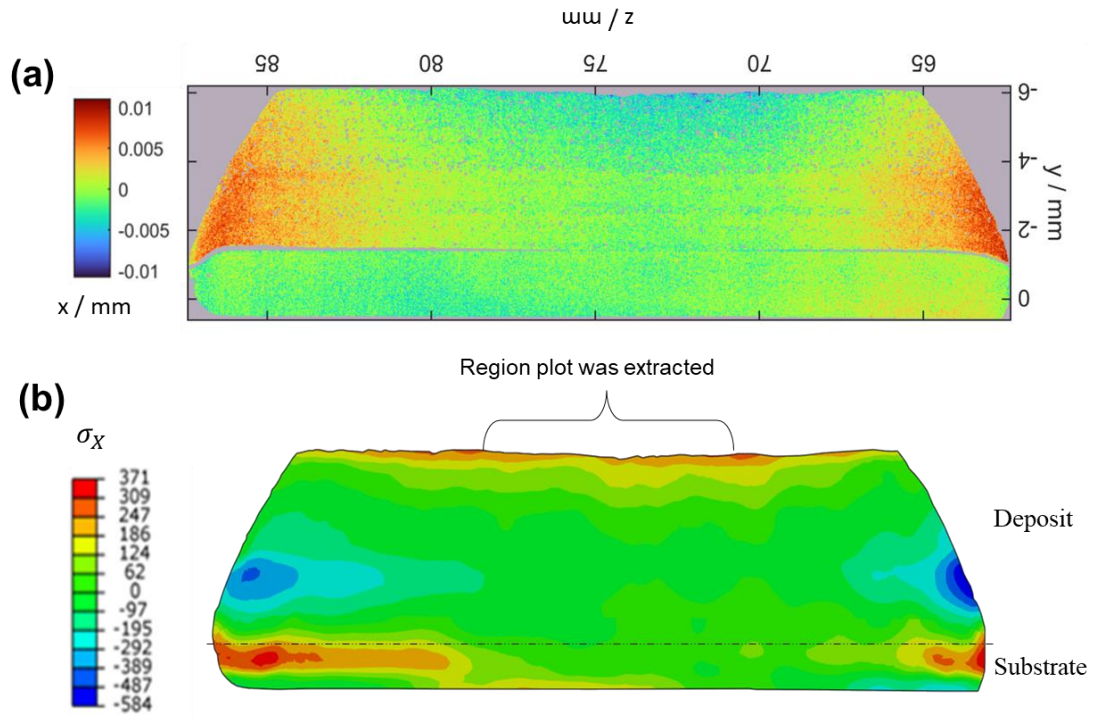

Figure 8.4: (a) shows the averaged surface displacement or contour map of the cut surface over the transverse cut plane of the CSAM deposit. Note that the grey space between the deposit and substrate indicates delamination of the deposit as observed earlier in the SEM image of the deposit. (b) displays the two-dimensional longitudinal residual stress map in the cut plane of the CSAM HEA deposit on the SS304 substrate. The denoted region from which data was extracted is shown in Figure 8.6

The explicit-implicit FEA technique was employed to analyse the residual stress formation mechanism during CSAM. Figure 8.5 shows a map of the residual stress distribution obtained from the FEA of the CSAM HEA deposit on the SS304 substrate. An enlarged view of the central region denoted by the square on the figure is also displayed. The figure shows that the highest compressive stress was obtained in the interface layer of the deposit, reaching ~250 MPa. This high

compressive stress decreased from the interface layer to the top layers, changing to tensile stress at the top surface of the deposit. Comparing the data extracted from approximately the same region in the sample from the contour method and the numerical model (see Figure 8.6), the highest tensile stresses were obtained at the top of the deposit and the bottom of the substrate. Note the periodicity observed in the colour map is because the FE model assumed square blocks of elements are deposited on the substrate as the nozzle moves past the substrate surface. The difference in the magnitude of the residual stress in the sample obtained using the contour method and the FEA can be attributed to the assumptions of the FE model. Moreover, the contour method can be prone to errors at the cut surfaces, owing to outliers that can be created in the displacement profiles induced during the cutting [280]. Although this was minimised by using sacrificial material on all boundaries of the cut plane, the influence of outlier data points in the contour measuring machine can still affect the residual stress magnitude at the cut surfaces.

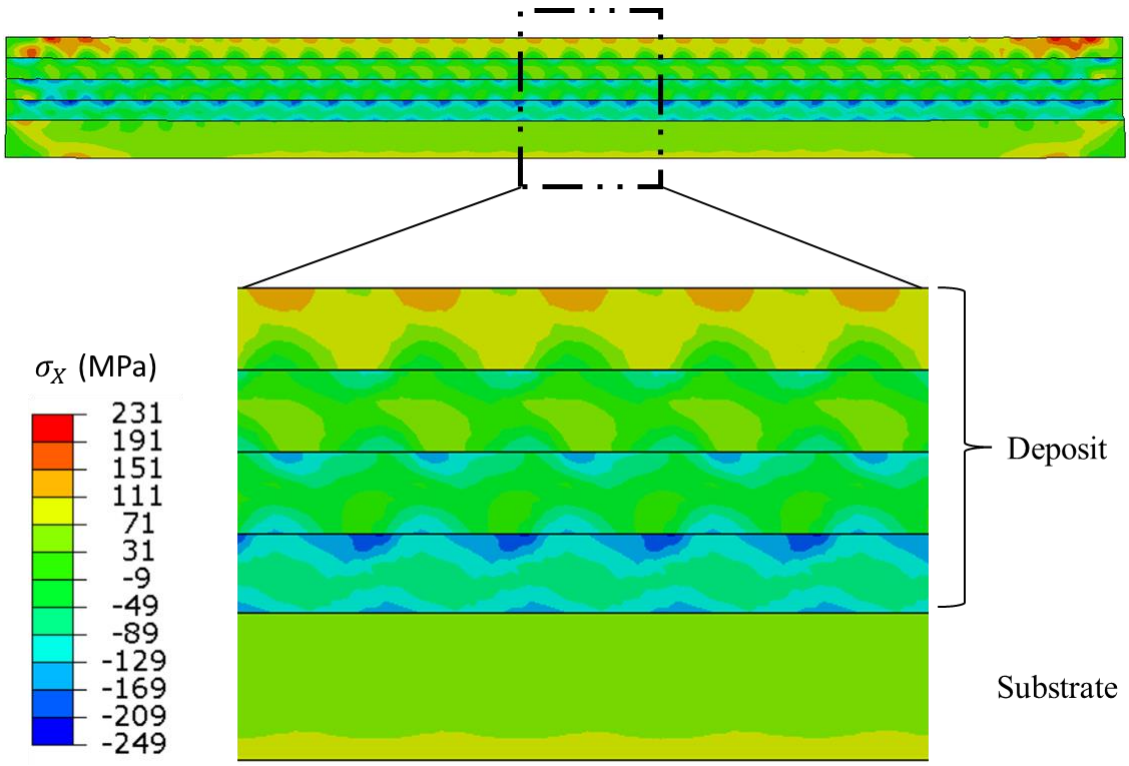

Figure 8.5: Residual stress map from the numerical model: shows the 2D FE model of the HEA deposit on the substrate along the length of the sample, and the enlarged view at the central region where the data in Figure 8.6 was extracted from. The periodicity in the contour maps is attributed to the square block of elements deposited as the nozzle moves past the substrate during spraying; an assumption made in the FE model.

Through-thickness residual stress profile was extracted from the adhered interfacial region of the deposit-substrate presented in Figure 8.6. The data from the measured residual stress using the contour method was employed for the validation of the FEA. A comparison between the results of the contour method and the FEA is presented in Figure 8.6. The figure shows the distributions of the longitudinal residual stresses obtained by both the contour method and the FEA at the mid-section of the HEA deposit-substrate sample. The residual stress presented for the contour method was extracted over the central 10 mm length region of the contour cut surface (as shown in Figure 8.4b), with the average reported, and the error bar represents the standard error of the mean of the measurement. In addition, the

average and standard error of the FEA were extracted over the central 4-mm length region from the 2D plane strain FE model (see Figure 8.5). It is evident from the data presented in Figure 8.6 that tensile residual stresses developed on the top surface of the deposit. These stresses gradually decrease to a region of approximately 2 mm in the deposit, which becomes compressive in the interior of the deposit towards the interfacial region. The compressive stress then changes to tensile stress in the substrate. There is a good agreement between the measured residual stress and FEA but with a slight deviation in the results, such as the magnitude of the residual stresses and the smoother curve of the contour method, which can be attributed to the assumptions made in the FE model. Another likely reason is the effect of residual stress redistribution due to the delamination of the deposit from the substrate at the interface (see Figure 8.2). The effect of delamination or cracking on the residual stress was not included in the FE model. The influence of the delamination can provide more information on the residual stress formed, but this is beyond the scope of this work, which can be a future investigation.

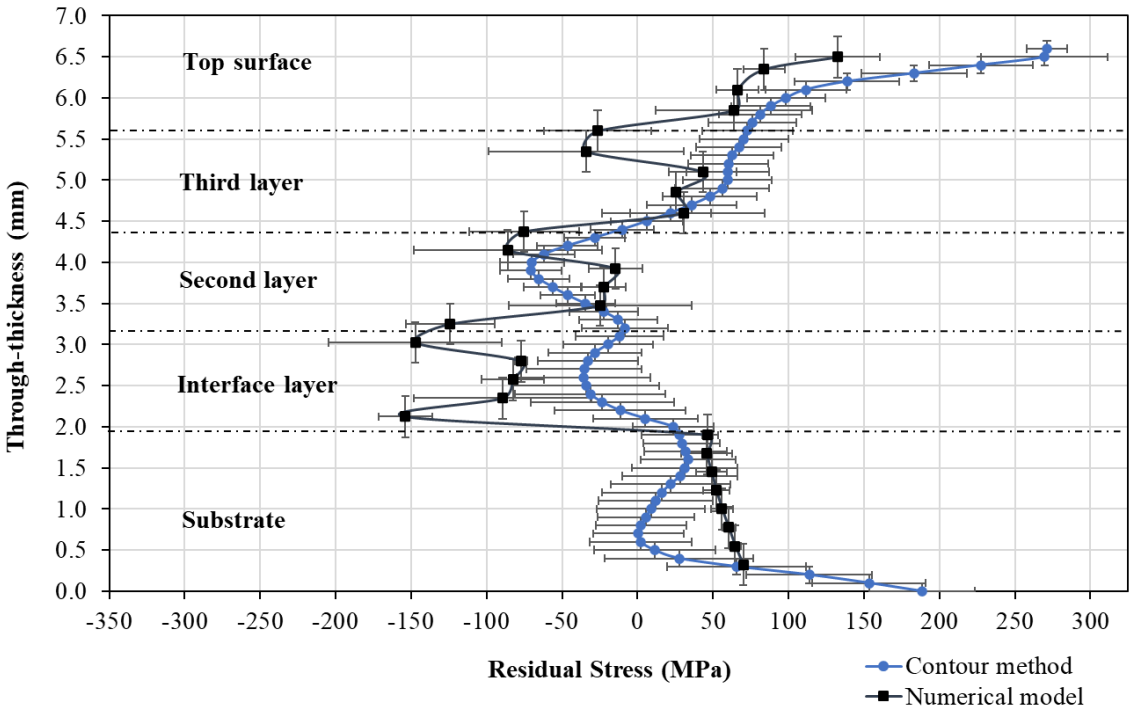

Figure 8.6: Through-thickness residual stress distributions of the HEA deposit on the SS304 substrate, measured using the contour method and numerically analysed using the coupled thermo-mechanical model. An average with the standard error of the mean is presented, extracted from the regions denoted in Figure 8.4 and Figure 8.5

It is noteworthy that the measured residual stress within the substrate shows regions of compressive stress in the middle of the substrate, whereas tensile stresses are formed away from the substrate surface and towards the substrate bottom. A plausible explanation is the effect of the substrate clamping or support during spraying, a manufacturing constraint that is yet to be explored for the CSAM process. Future investigations may involve varying the support or clamping arrangement or constraints of the substrate during CSAM and the subsequent effects on the residual stress formation.

8.5.3 Finite element analysis of the in-situ stress evolutions during the CSAM of the HEA

The explicit-implicit FEA technique was employed to understand the in-situ stress evolution in the sample during the deposition of each layer. This technique is a cost-effective method as compared to experimental techniques. Figure 8.7 shows the evolution of stress and temperature during the deposition of each layer on the substrate. The regions of the selected element were at the mid-length of the substrate surface, at the deposit mid-layer and at the surface of the deposit top layer, as shown schematically in Figure 8.7. Figure 8.7 (A) shows that the deposition of each layer on the substrate surface resulted in deformation-induced compressive stress, which gradually increased with the increasing number of layers being added. At the same time, the temperature of the substrate surface gradually increased as more layers were added. On the other hand, the temperature and stress evolution in the deposit were also analysed to understand the residual stress formation mechanism within the deposits. Figure 8.7 (B) presents the evolution of temperature and stress of the surface of the second layer of the deposit. It was observed that the temperature of the selected element rises to ~850 K; with the initial particle deposition temperature of T = 473 K, the rise in temperature during deposition resulted in ΔT = ~377 K. As more layers were added on the deposited layer, temperature decreases, while the tensile stress state changed to a compressive stress state upon cooling. Similarly, the initial temperature rise to ~850K was observed at the selected element on the surface of the top deposited layer, decreasing as the deposition source passed through the selected element. The same observation can be seen for the stress on the surface of the top layer.

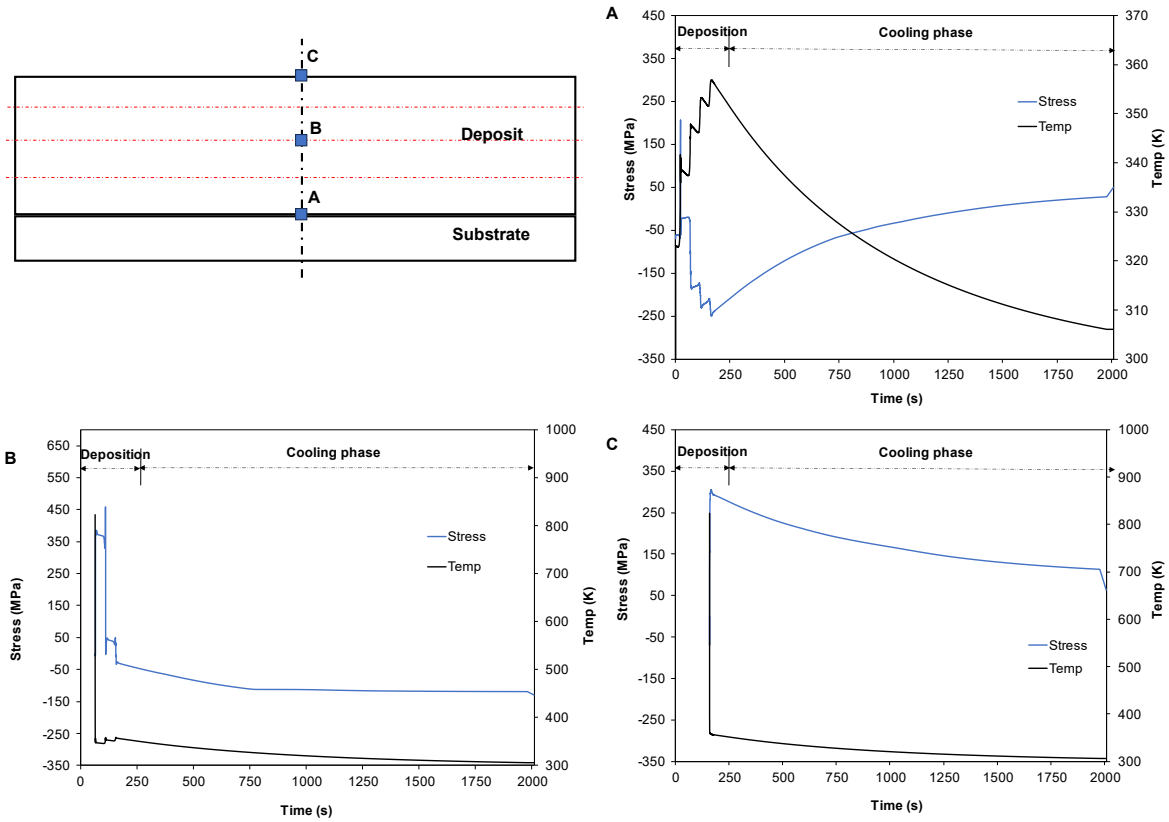

Figure 8.7: Numerical prediction of the stresses and temperature evolutions during the deposition process and cooling of the deposit-substrate altogether: (A) presents the field variables for the substrate, (B) shows that within the deposit and (C) shows that on the surface of the deposit. The element selected was at the mid-length of the substrate and middle layer of the deposit, and the surface of the deposit as presented schematically. Both the deposition and cooling phases are shown in the figure.

The provided field variables presented in Figure 8.7 imply that as the nozzle or spraying gas jet was in the proximity of the selected element of the substrate surface (Figure 8.7 (A)), the compressive stress which existed on the substrate surface owing to the peening effect of the particles, suddenly changed to tensile stress as the nozzle passes over the respective element. This suggests that it is likely that the heat input from the gas jet on the substrate surface induces a steep thermal gradient, resulting in thermally induced tensile stress. While the deposited layer thermally expands, it is also constricted by the underlying colder substrate material,

promoting the development of a compressive stress zone on the substrate surface. The compressive stress gradually increases as more layers are added, reaching as shown in Figure 8.7 (A). Upon cooling, tensile residual stress was, however, formed in the substrate. Similarly, as the nozzle moves through the proximity of the selected element in the deposit (Figure 8.7 (B)), tensile stress was also formed owing to the high thermal gradient of the deposit because of the rapid temperature rise to ~850 K and rapid cooling to ~350 K, as shown in Figure 8.7 (B). The addition of more layers resulted in a decrease in the magnitude of the tensile stress, likely due to heat dissipation before the deposition of subsequent layers. Moreover, the temperature of the deposited layer remained at ~350 K during the deposition of the subsequent layers. Upon cooling, the tensile stress became compressive residual stress. It appears that the peening effect on the last deposited layer (Figure 8.7 (C)) is likely, not prominent, consequently, the effect of the thermal gradient on that layer would be dominant, resulting in a tensile stress state upon cooling.

A schematic of the stress profiles after subsequent deposition of each layer from the FEA is presented in Figure 8.8. As shown in Figure 8.8, tensile stress was formed after the deposition of the first layer, with the substrate in a compressive stress state. The deposition of the second layer led to a decrease in the magnitude of the tensile stress in the first layer, whereas the second layer formed a tensile stress state. As more layers were added, the tensile stress in the first layer further decreased, becoming compressive stress at the end of the deposition. The same trend is observed for the second layer as more layers were added, except for the third and fourth layers which remained in a tensile stress state even after deposition, with the largest magnitude observed for the fourth (or top) layer.

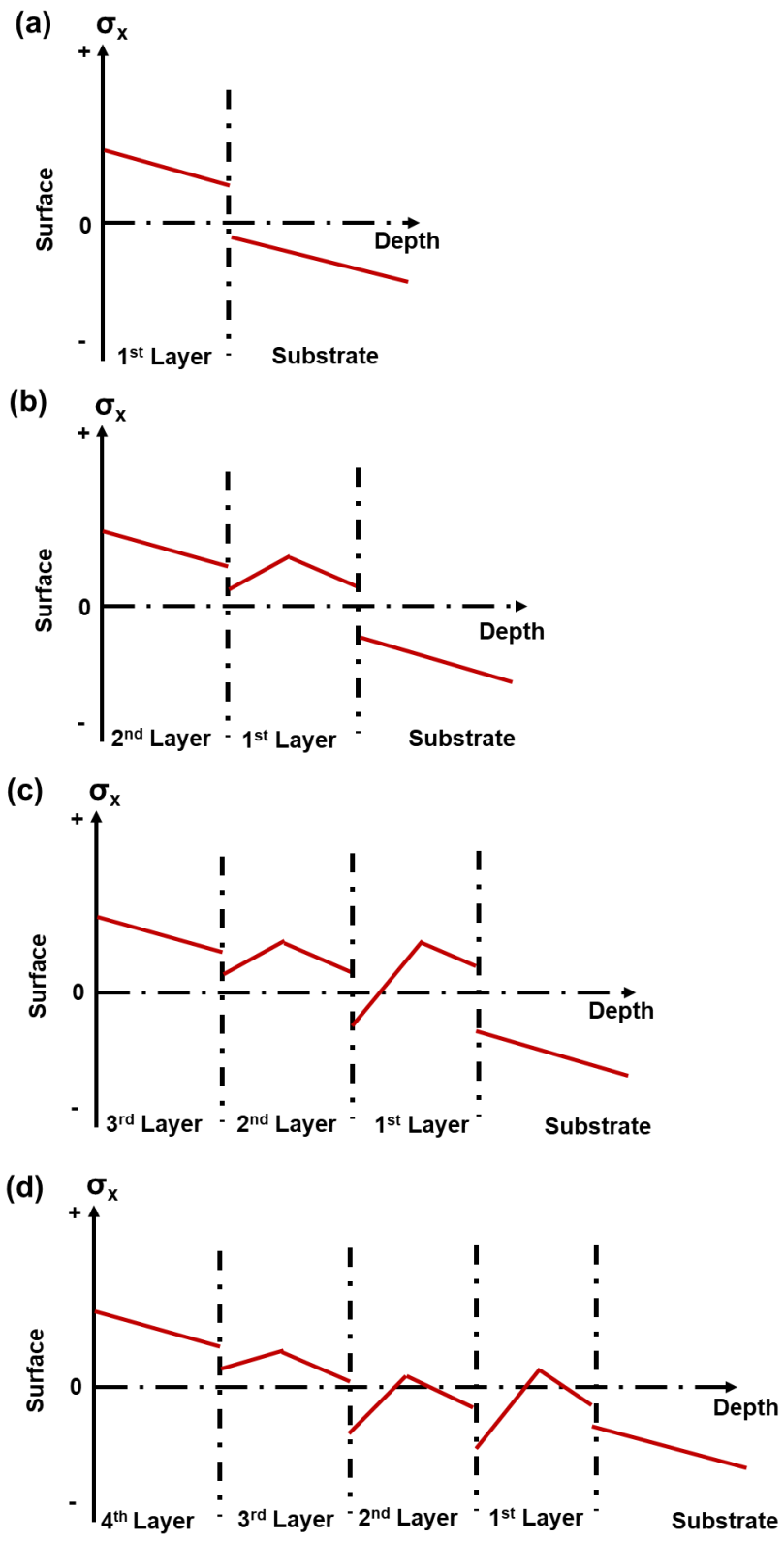

Figure 8.8: Shows the schematic diagram of stress profiles and their evolutions as layers of the deposit were added in the FEM: (a) after the deposition of the first layer on the substrate, (b) second layer, that is, after two layers have been added, (c) third layer and (d) fourth or top surface layer, that is, the end of the CSAM deposition before the cooling phase.

During the deposition of the layers, the substrate remained in a compressive stress state. The subsequent cooling of the deposit-substrate sample, altogether, resulted in tensile residual stresses formed in the substrate and top layers, which were mechanically balanced by compressive stresses formed in the first and second layer—interfacial layers of the deposit, as presented schematically in Figure 8.9. It is noteworthy that the discontinuity in the stress profiles between each layer of deposit layers and substrate is assumed since line profiles were used for the schematics. Moreover, this method of stress profile illustration is generally used in the open cold spray literature [206] to explain stress changes from one layer to another layer or material of deposit and substrate. The experimental residual stress profile provides smoother transitioning or curves as can be seen in Figure 8.6.

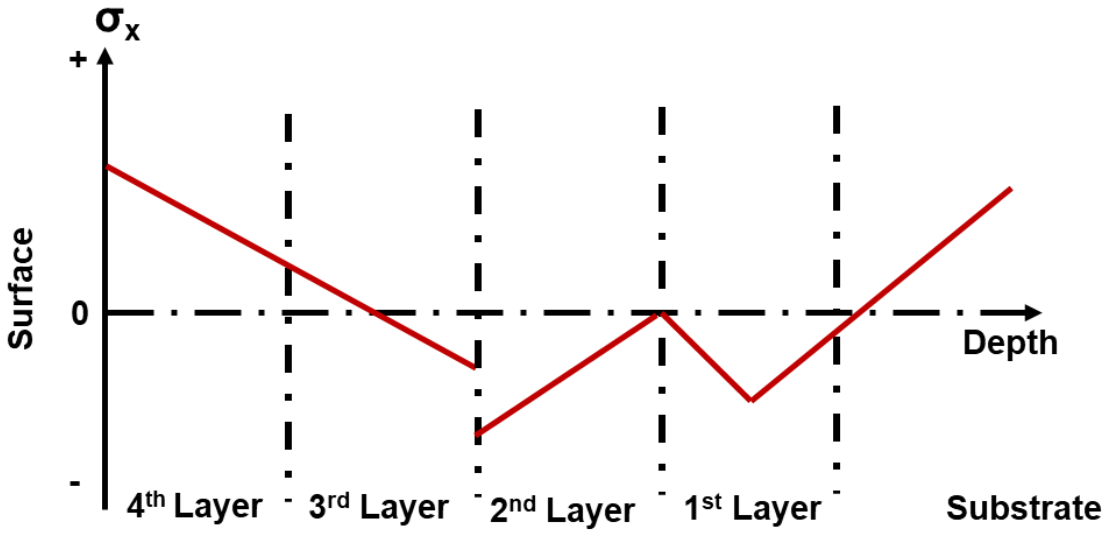

Figure 8.9: Schematic illustration of the final residual stress profile after the cool-down stage of the CSAM HEA deposited layers on the SS304 substrate.

Although the influence of delamination at the deposit-substrate interface was not included in the numerical model, the shear stress (τ_{XZ}) component from the numerical model can describe the interface shearing effect on possible delamination

of the deposit [234]. Figure 8.10 shows that the interfacial region of the deposit-substrate at the edges has more severe stress gradients owing to the stress concentrations. The shear stress was compressive during the deposition but became tensile during the cooling phase, as shown in Figure 8.10b. This is likely because of the difference in the coefficients of thermal expansion (CTEs) between the sprayed HEA and SS304 substrate. Also, the mechanical constraint on the substrate during the deposition may contribute to the delamination. In addition, a high compressive shear stress was observed within the deposit, as shown in Figure 8.10b, to balance the tensile shear stress in the interfacial region. Similar stress states were also observed in the residual stress map from the contour method shown in Figure 8.10, showing confidence in the numerical model devised in this study.

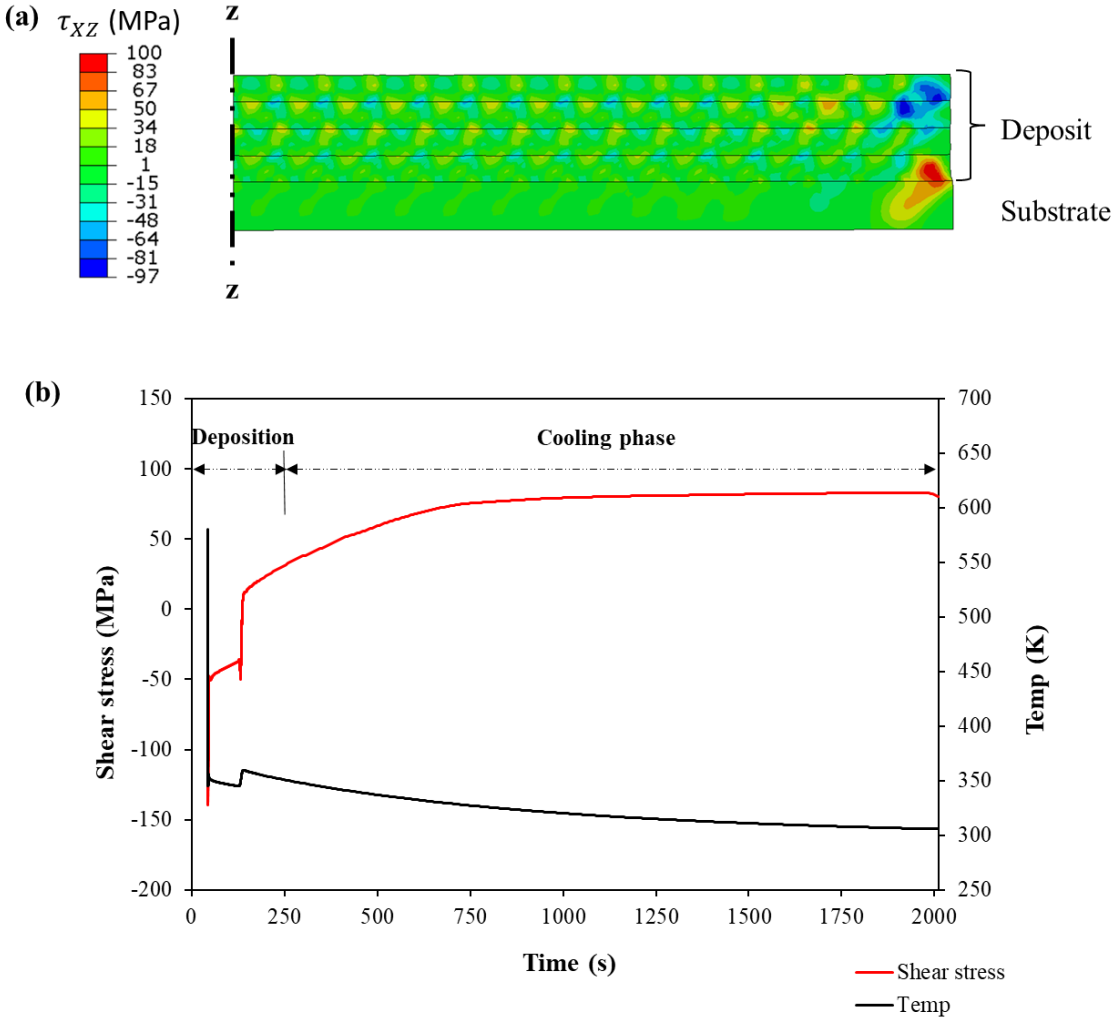

Figure 8.10: The residual shear stress map of the FE model, showing the gradient of shear stress at the edge (a). The map shown is half the model. (b) shows the evolution of the shear stress and temperature of an element at the high tensile shear stress region.

8.6 Discussion

In this chapter, an explicit-implicit FEA strategy was developed, which constitutes the key physics and spraying parameters of the CSAM process. The FEA allows for investigations of the effect of CSAM process conditions on the thermal and residual stress fields; hence reducing the time-consuming and costly experimental tests. The

FEA, through accurate validations, can be employed as a quality control tool during the repair and manufacturing of parts in the aerospace sector.

The through-thickness residual stress of a ~4.2 mm thick CSAM CoCrFeNiMn HEA deposit on an austenitic stainless steel 304 substrate was investigated. The results of the residual stress measured using the contour method and numerically analysed using the thermo-mechanical FEA revealed that tensile stresses were formed on the deposit surface and substrate but mechanically balanced by compressive stresses at the deposit interior. Interestingly, layer-by-layer induced changes in the residual stress distribution were observed in the deposit-substrate system as presented in Figure 8.6 and Figure 8.9

8.6.1 Residual stress formation mechanism during the CSAM of CoCrFeNiMn HEA

In this thesis, the residual stress build-up during the CSAM of the HEA on the SS304 substrate can be established on two main mechanisms: temperature gradient mechanism (quenching stress) and cool-down stage (thermal misfit) [206,347,348]. The first mechanism is related to a large temperature gradient induced by the thermal input from the spraying process (gas jet and plastic deformation of sprayed particles), as revealed by the FEA presented in Figure 8.7. Consequently, thermally induced tensile stresses appear owing to the contraction of the thermally expanding deposited layers as they rapidly cool down to the temperature of the underlying material or substrate. The second stress formation mechanism results when the deposited top layers and the previously deposited layers and substrate cool down

together. The cooling results in the differential thermal contraction/shrinkage of the top layers, restrained by the colder underlying materials, leading to the top layers under tension balanced with compressive under layers of the deposit, and the substrate in tension. Figure 8.11 provides a schematic illustration that explains the residual stress formation mechanism during the CSAM deposition, which is akin to the schematic illustration presented in Figure 8.9

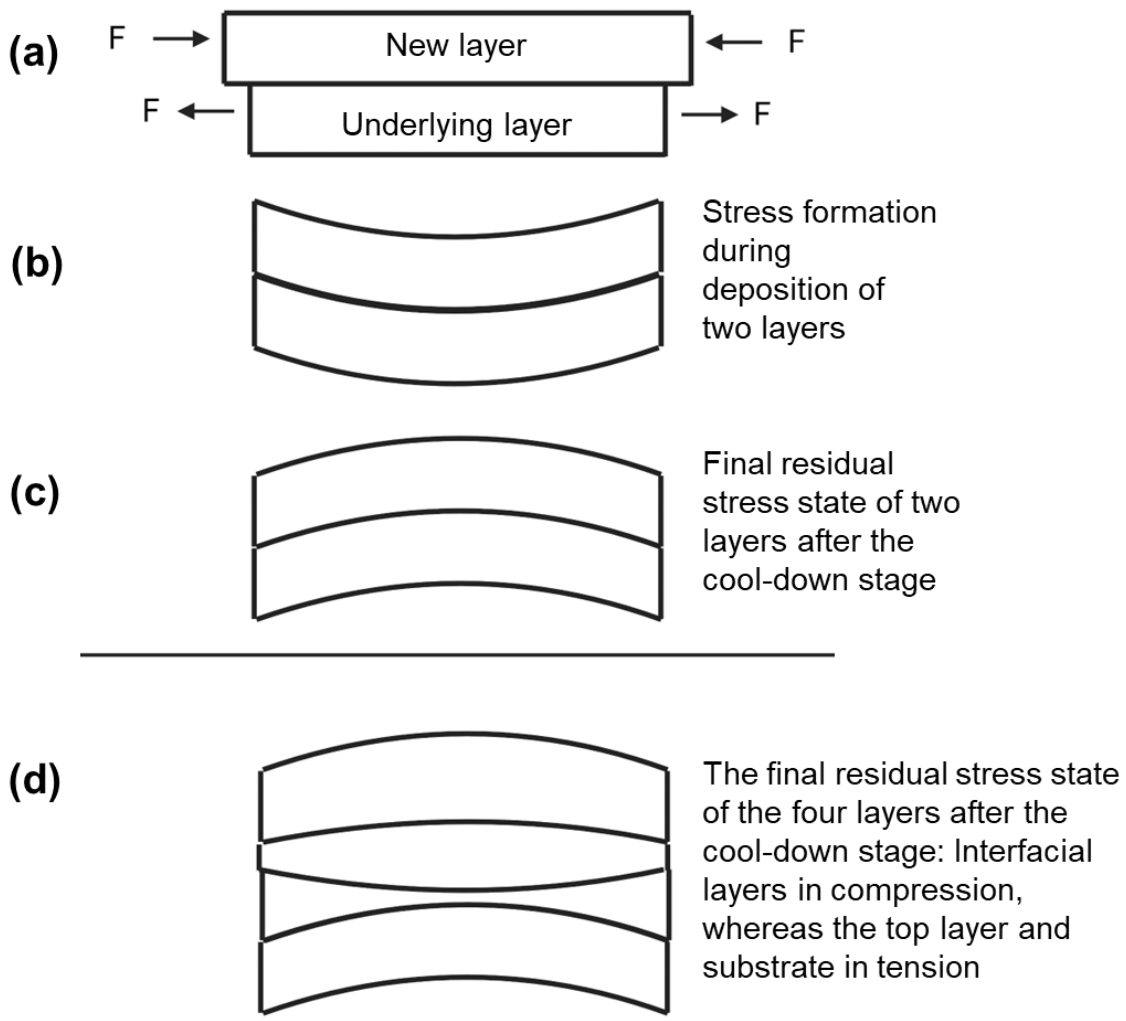

Figure 8.11: Schematic illustration of the curvature of deposited layers and substrates during and after the CSAM deposition process. (a) Unconstrained strains develop when a layer is deposited on the substrate or underlying layer because of temperature differences. (b) As a result of strain compatibility at the interfaces, bending and balance of bending moment occurred leading to deposit and substrate in compression. (c) After the cool-down stage, the tensile residual stress is formed for the deposited layers. This is the case of two layers or a layer on a substrate. The final residual stress state after the cool-down stage is presented with the curvature in (d). The interfacial layers are in compression balanced by others in tension.

The FEA provided information that explains the mechanism responsible for the layer-by-layer induced changes observed in the residual stress distribution in Figure 8.6 and Figure 8.8. Although the initial deposition stress is the same for each layer (as presented in Table 8.1), the magnitude of the through-thickness residual stress distribution appears to fluctuate with the different layers. It is clear from the second

mechanism discussed earlier, that the cooling phase of the deposited-substrate leads to differential thermal contraction/shrinkage generating thermal misfit strain [347,349]. The thermal misfit strain is influenced by the difference in the CTEs (or $\Delta\alpha$) of the materials and the drop in temperature (ΔT). Since the material of the deposited layers is the same, there is no difference in the CTEs; however, if successive deposit layers arrive while the deposited layers have different curvatures (see Figure 8.11), then a misfit strain can be generated between the layers [350,351]. The reason for this may be the deposit temperature and the long exposure time before the arrival of successive layers as a slow nozzle transverse speed was employed for the deposition of each layer. As a result of these factors involved in the spraying process, one can argue that in-situ annealing during the layer depositions (as observed in Figure 8.7) may play a key role in the stress formation mechanism [207], hence the non-uniform thermal misfit strains, resulting in the layer-by-layer induced changes in the magnitude and sign of the residual stress between each layer. A more detailed experimental residual stress measurement on several samples obtained with varying spraying parameters would be required to establish this phenomenon. There are also limitations in the assumption made for the FEA as clearly stated in this study, a more robust model can be developed for future investigations.

8.6.2 The effect of the spraying conditions on the residual stress formed in the CSAM HEA

The two mechanisms established earlier have been developed by Mercelis and Kruth [348] to describe the residual stress distribution in AM processes like laser

powder bed fusion (selective laser melting or sintering). Moreover, the residual stress distribution in the CSAM HEA on SS304 (He at 400 ºC and 3.3 MPa) can be compared to the stress distribution in a selective laser melted/sintered steel [352] and the CoCrFeNiMn [79] on similar substrates. Similarly, the tensile residual stress formed in the CSAM-deposited HEA in this thesis has been reported in other studies. For example, CSAM Ti64 on Ti64 substrate (N_2 at 1100 ºC and 5 MPa) [85], CSAM high-strength duplex stainless steel on SS316L substrate (N_2 at 800 ºC and 3.5 MPa) [83], and tensile stresses formed on Al 7075 on Mg alloy substrate (N_2 at 400 ºC and 1.38 MPa) [353]. Furthermore, tensile residual stress has been reported to be formed when CP Ti was CSAM-deposited on a carbon steel substrate (N_2 at 700 ºC and 3.5 MPa) [202].

It appears that these studies reveal processes where quenching stress and thermal misfit are dominant over peening deposition stress; peening deposition stresses give rise to surface compressive residual stresses usually formed in CSAM deposition [81,202,206,207,213,354]. Several investigations have been performed to understand the evolution of residual stresses in CSAM deposits, with several authors reporting that the sign and magnitude of residual stress depend on the spraying parameters and material combinations. Among the spraying parameters, gas temperature, nozzle transverse speed and powder feed rate have been reported to significantly influence the residual stress formed in CSAM deposits. For instance, Vargas-Uscategui et al. [211] reported that slow nozzle transverse speed and high powder feed rate resulted in tensile residual stress formed in a CSAM-manufactured hollow Ti cylinder. In another study by Brown et al. [212], higher compressive stresses were obtained in CSAM CuNi deposits when using higher

nozzle transverse speed (200-400 mm/s), whereas high carrier gas flow rate (inducing high thermal gradient) resulted in tensile residual stresses. Moreover, Luzin et al. [84] reported that thermal mismatch was the dominant contributing term to the residual stress of a thick deposit of Ti on an Al baseplate. The same dominant mechanism was reported by Spencer et al. [220] when pure Al was deposited on a Mg alloy (N_2 at 550 ºC and 3.85 MPa). Apart from the aforementioned spraying conditions, the tensile residual stresses in CSAM deposits can also be attributed to the high gas temperature ≥ 400 ºC [159] employed for the spraying. In addition to that is the effect of different material combinations, which is due to the differences in their CTEs, giving rise to thermal stresses [202,220]. Since there is a small difference in the CTEs of the HEA (~16.2 $x10^{-6}$ /K) and SS304 (~17.5 $x10^{-6}$ /K) at the spraying gas temperature [291], it is evident therefore that the dominant quenching and thermal misfit strain on the residual stress of the HEA on the SS304 substrate during the CSAM is a consequence of the spraying parameters employed.

It is well-known that the CSAM process introduces beneficial compressive residual stresses in both deposited and substrate materials resulting from the peening effect of sprayed particles [80,81,159,206,207], similar to the shot peening process. These beneficial compressive residual stresses have been reported to significantly increase the fatigue performance of CSAM samples [80,81]. However, the presence of tensile residual stress in the CSAM HEA deposit and substrate can initiate crack and its propagation leading to reduced fatigue life and limiting the structural application of the repaired or manufactured component. Moreover, the presence of the tensile residual stress will increase the tendency of debonding at the deposit-substrate interface, as observed in Figure 8.1a, which limits the maximum deposit

thickness that can be obtained [85,213]. It is therefore recommended that spraying strategies should be developed to minimise the build-up of tensile residual stresses in thick deposits of the HEA for structural applications as this is likely to occur under the spraying conditions employed in this study. More research is thus required in this area (as there is a wide knowledge gap on the residual stress formation during CSAM of HEAs) to understand the influence of spraying parameters and materials combinations on the residual stress of the CSAM HEA deposits.

8.7 Conclusions

In this chapter, the through-thickness distribution of residual stress in a ~4.5 mm thick deposit of CSAM CoCrFeNiMn HEA on SS304 substrate was measured experimentally using the contour method and XRD technique. A sequentially coupled thermo-mechanical FE model was developed to predict and evaluate the thermo-mechanical effects of the CSAM process. A good agreement was attained between the contour method and the FE model, showing confidence in the modelling method developed in this study. The following conclusions can be drawn from the work in this chapter:

- Tensile residual stresses were present at the top surface of the deposit and substrate, which were mechanically balanced by compressive residual stresses at the interfacial layers of the deposit.

- The residual stress formation mechanism in the deposit-substrate was established on two mechanisms: the temperature gradient mechanism and

the thermal mismatch mechanism during the cool-down stage. This was attributed to the thermal effects arising from the gas temperature, slow nozzle speed and powder feed rate employed for the CSAM deposition. These mechanisms dominate the peening effect from the microparticle impacts during deposition.

- The stress profiles show layer-by-layer induced fluctuations in the residual stress distribution within the deposit. This was attributed to the in-situ annealing effect likely a consequence of the deposit temperature and exposure time of deposited layers before the arrival of subsequent layers.

In this chapter, it is clear that deposition at a slow nozzle scanning speed, high gas temperature and powder feed rate would likely result in tensile stresses formed in cold sprayed deposits. The presence of these stresses would compromise the structural integrity of the repaired or manufactured parts. It is recommended that lower powder feed rates, faster nozzle scanning speeds, and lighter gas that can provide higher particle velocity without significant gas heating should be employed for the CSAM deposition of the HEA. The study of this chapter however requires further analysis and experimental investigations, for instance, a wide range of spraying parameters explored, and the residual stresses of the samples measured. The investigations of this study thus indicate that there is a wide gap in knowledge and the limited exploration of CSAM of the HEA for industrial applications and aerospace structures. This cost-effective CSAM process can be further explored for the repair and manufacturing of aerospace components, such as the repair of integrally bladed rotors or turbine blisks, impellers and nozzle guide vanes.

9 General conclusions and contributions to knowledge

9.1 General conclusions

The overall aim of this thesis was to investigate the feasibility of repair and manufacture of aerospace components or parts using the CSAM process with the new metallic alloys, CoCrFeNiMn HEA. The research project focused on experimental and numerical investigations of the HEA during CSAM deposition, the influence of post-deposition annealing on the microstructure and mechanical properties of the deposit, and the residual stress formed in the deposit.

In general, the research demonstrated that aerospace structures can be repaired using the CSAM process with the HEA feedstock material. This is important for parts made of stainless steel, being a similar material to the HEA. This allows for maintaining the strength-weight ratio while improving the structural integrity of the parts because of the mechanical properties of the HEA and the solid-state nature of the CSAM process. In this thesis, the window of deposition that specifies the process conditions for the CSAM deposition of the HEA was established, including the critical velocities of the HEA on several metallic substrates. After deposition under optimum process conditions, the thesis also recommended the post-deposition annealing treatment that can be performed to improve the microstructure as well as the mechanical properties of the HEA deposits. Annealing treatment at 1000 ºC produces the best result in terms of the consolidation of the microstructure

and strength-ductility combination. It was recommended in this thesis based on the results obtained that annealing treatment at 600 ºC would result in a precipitate-hardened deposit, leading to greater strength without loss in ductility but under a controlled annealing temperature and time. It was also found that the process conditions; low nozzle scanning speed during spraying, high gas temperature and powder feed rates can induce detrimental residual stress on the repaired or manufactured parts, and as such it was recommended that lower transverse speed, powder feed rate and gas temperature should be employed to achieve compressive residual stress throughout the repaired or manufactured parts/components.

In this thesis, the Johnson-Cook (J-C) material model of the CoCrFeNiMn HEA was assessed and determined for the ultra-high strain rate deposition modelling typical for the CSAM process. The established material model parameters can be employed for future investigations. The technique employed in assessing the material model provides the researchers with a robust and cost-effective approach to assessing material models for deformation modelling in FEA codes. Furthermore, an explicit-implicit FEA technique developed in this thesis incorporates the peening effects of the random distributions of particles typical of the CSAM feedstock material on the residual stress formation during the deposition process. The technique provides a computationally cost-effective method for quality control of the CSAM process for the repair and manufacture of critical parts in aerospace.

More specifically, the general conclusions drawn from this thesis are as follows:

- The deposition mechanism of the CoCrFeNiMn HEA onto various substrates during CSAM deposition was experimentally and numerically investigated.

The HEA particles during deposition were observed to form metallurgical bonds and mechanical interlocks on four different substrates: Ti6Al4V, SS304, CP Al and Al6082.

- The Johnson-Cook (J-C) material model data for the deposition modelling of the CoCrFeNiMn HEA particles were assessed and determined in this thesis. This was done by selecting a set of material data for the HEA and assessing with single particle impact analysis through flattening ratio as a mechanistic “diagnostic tool”. The most suitable J-C set of material data that best predicted the impact morphology of HEA particles was determined and presented in this thesis. This material model data can be employed for finite element analysis (FEA) of the impact phenomena of the HEA during CSAM deposition. Subsequently, the critical velocities of the 25 µm HEA particles on Ti6Al4V, SS304, CP Al, and Al6082 substrates were determined as 700, 800, 563, and 618 m/s, respectively.

- Following the determination of the critical velocities of the HEA on the substrates, thick HEA deposits were manufactured using a set of spraying parameters that lie in the window of deposition for the HEA. The deposition mechanism of the HEA particles during the deposit build-up was investigated using EBSD and FEA multi-particle deposition methods. A heterogeneous microstructure was observed in the HEA deposit with a distribution of ultrafine and coarse grains at the particle interfaces and interiors, respectively.

- The formation mechanisms of the heterogeneous microstructure were studied using a misorientation profile from the EBSD and FEA. It was found that adiabatic shear instability (ASI) and dynamic recrystallisation (DRX) produced by subgrain rotation (continuous DRX) dominated the particle interfaces during the CSAM deposition of the HEA. The particle interfaces were characterised by severe deformation with highly misoriented equiaxed ultrafine grains, whereas limited deformation and grains of LAGBs were observed in the particle interiors. Hence, the inhomogeneous microstructure formed in the HEA deposit contributed to variations in the measured nanohardness, with greater values measured at the particle interfaces when compared with the particle interiors.

- The HEA deposit manufactured was however characterised by a porous microstructure attributed to the high strain hardening and resistance to shear localisation of the HEA material. Consequently, post-deposition annealing was performed to improve the microstructure of the deposit and, hence its mechanical properties. Annealing was performed at 600, 800, and 1000 °C for 5 hrs. The hardness (nano-and microhardness) and tensile properties (using microflat dogbones) of the as-sprayed and annealed deposits were evaluated.

- The as-sprayed deposit of the HEA was measured at 5.14 GPa and 280 HV0.3, whereas the HEA deposit annealed at 1000 °C was measured at 3.96 GPa and 159 HV0.3. The tensile strength of the as-sprayed HEA deposit was ~26 MPa, whereas that of the HEA deposit annealed at 1000 °C was ~152

MPa. The improved mechanical performance of the annealed deposit was attributed to the increased metallurgically bonded areas and the reduced porosity of the deposit. Moreover, the lower measured hardness values are attributed to recrystallisation and grain growth during annealing.

- Interestingly, in this study, the mechanical performance of the HEA deposit annealed at 600 °C was considerably better than that of the deposit annealed at 800 °C. The deposit annealed at 600 °C exhibited a partially recrystallised microstructure with a small volume fraction of Cr-rich precipitates. The partially recrystallised microstructure was composed of dislocation-free fine equiaxed grains at the particle interfaces and grains of high local strain at the particle interiors. The formation of Cr-rich precipitates was attributed to the large number of grain boundaries in the deposit, which served as preferential sites for the nucleation and growth of the precipitates when the HEA deposit was annealed at intermediate temperatures.

- In this thesis, debonding of the HEA deposit on the SS304 substrate was observed during the CSAM deposition. This motivated the study of residual stress formed in HEA deposits, highlighting the importance of CSAM spraying conditions in the manufacturing and repair of large components with the HEA. With the contour method of stress measurement and the FE explicit-implicit scheme, the through-thickness stress profile in a ~ 4.2 mm thick deposit of the HEA on the SS304 substrate was evaluated. Good agreement was obtained between the experimental data and the FE results, showing confidence in the model employed in this thesis.

- The residual stress formed in the deposit-substrate system is based on two mechanisms: the temperature gradient and thermal mismatch during the cooling process after deposition. These mechanisms were attributed to the thermal impacts that arose from the gas temperature, slow transverse, and high powder rate employed for the CSAM deposition. These mechanisms dominate the peening effect of the particles during deposition. Consequently, tensile residual stress was formed on the top surface of the deposit, which was mechanically balanced by compressive residual stress at the interfacial layers of the deposit.

- Interestingly, the residual stress profiles obtained for the HEA deposit on stainless steel substrate showed layer-by-layer-induced fluctuations rather than a linear profile. This layer-by-layer change in the stress sign was attributed to the in-situ annealing of the deposited layers before the arrival of subsequent layers.

9.2 Contributions to knowledge

The research undertaken in this thesis contributed to and advanced knowledge of CSAM of CoCrFeNiMn HEA. The following are the main contributions to the knowledge in the research area:

- This thesis ultimately shows that CoCrFeNiMn HEA particles exhibit deposition mechanisms like those of other metallic materials, particularly

stainless steels, and nickel, during CSAM; however, a higher critical velocity may be required to obtain dense deposits of the HEA.

- This thesis provided a mechanistic method of determining material model data that can predict more accurately the impact morphology of metals during CSAM. The thesis provided Johnson-Cook material model data for the HEA and determined the critical velocity of the HEA.

- The thesis argues that Cr-rich precipitates formed during the post-deposition annealing treatment of the HEA deposit can be utilised to strengthen the deposit without loss of ductility. However, this can be realised under an optimised annealing treatment to obtain a consolidated microstructure of the deposit.

- The thesis advances knowledge in residual stress measurement and analysis using the contour method and finite elements analysis for CSAM. The thesis contributed by providing a cost- and time-effective quality control method for assessing residual stresses of CSAM deposits, which indicates opportunities for the aerospace & space sector to advance the manufacturing and repair of components with promising end-use performance with CSAM of HEAs.

- Although tensile stress was formed in the thick HEA deposit obtained in this thesis, which can be detrimental to the structural integrity of the components, there is a need for optimisation of the CSAM process to achieve beneficial compressive residual stress for the HEA.

10 Future work

This chapter suggests potential future work relevant to this thesis that can further enhance our understanding of the CSAM of CoCrFeNiMn HEA for the manufacturing and repair of the aerospace sector.

10.1 Development of pore-free deposits of HEA with CSAM

Research on the CSAM of HEAs is in its early stages, and thus, there is a wide knowledge gap that needs to be covered, particularly for obtaining dense deposits of HEAs as these new alloys pose as difficult-to-spray materials for CSAM. While this thesis provides information on the impact phenomena and determines the critical velocity of a 25 µm CoCrFeNiMn HEA on different substrates using experimental impact tests and finite element analysis, further investigation is required to obtain the critical velocities of a wide range of particle sizes. With this information, an optimised particle size distribution that would yield pore-free HEA deposits can be obtained once the particle impact velocities are known. In addition to the particle size distribution, spraying parameters can be varied to obtain pore-free deposits. For example, varying the gas pressure and temperature, nozzle transverse speed, powder feed rate, stand-off distance, and nozzle geometry yields pore-free deposits of the HEA for structural repair and component manufacturing. Moreover, most published articles in the open literature employ Helium (He) gas as the propellant gas for the CSAM of HEAs. The high cost of He and its unavailability makes CSAM of HEAs challenging; hence, low-cost Nitrogen (N_2) gas is required for the deposition of HEAs, but this requires a gas preheater to achieve higher

particle velocities for developing pore-free deposits. In addition, there is very limited work on the laser-assisted CSAM of HEAs, which can provide additional thermal heat for the thermal softening of the feedstock powder and substrate, promoting HEAs particle deformation and hence pore-free deposits.

While this thesis provided Johnson-Cook (J-C) material model data that were used for the finite element analysis of the HEA studied, further investigations are required to develop other material model data that best predict the impact morphology of the HEA. High strain rate (typical of CSAM) material model data for HEA should be determined experimentally.

A coupled Eulerian-Lagrangian (CEL) finite element model for predicting the porosity of HEA deposits during CSAM could not be completed in this study; hence, further work is required to employ the model to predict the porosity of HEA deposits under varying spraying parameters and particle size distributions. A Python script for the CEL model was developed during this research project and can be implemented in future work.

In this thesis, the contour method and explicit-implicit finite element technique for residual stress measurement and analysis of the CSAM HEA deposit were studied, and good agreement was obtained. A set of spraying parameters was studied; however, the residual stress was tensile in nature because of the spraying parameters employed. Therefore, further investigation is required to optimise the spraying process to yield pore-free deposits with beneficial compressive residual stresses. In addition to the contour method, further investigations can employ other

methods, such as neutron diffraction, for residual stress measurements of HEA deposits.

10.2 Deposit characterisation and annealing treatment

In this study, the deposition mechanism of CoCrFeNiMn HEA during CSAM was investigated. Although electron backscattered diffraction (EBSD) was employed to characterise the microstructure of the HEA, other material characterisation techniques such as focused ion beam (FIB) lift-out of the deposit could be performed and analysed using transmission electron microscopy (TEM). These techniques can be employed to understand microstructural evolution, such as deformation twinning and grain refinement of the HEA during CSAM. This would provide useful information about the microstructural features of the bonding regions and insights into the characteristics of the alloy that can result in its extensive particle deformation and pore-free deposit formation. Furthermore, although ex-situ EBSD and nanohardness were employed in this thesis, further investigation can employ in-situ characterisation of the HEA deposit to understand the influence of the deposition mechanism and microstructure of the HEA on the nano-mechanical properties of the deposits.

While this study reported improved microstructure and mechanical properties of HEA deposits following post-deposition annealing treatment, more work needs to be done to investigate the influence of annealing temperature and time on the development of the microstructure, particularly the precipitate formation, volume fraction, and nucleation mechanisms in the sprayed particles. EBSD and energy-

dispersive X-ray spectroscopy (EDX) were employed to investigate the Cr-rich precipitates formed in the deposits. Further investigation is required to elucidate the detailed formation mechanism of the precipitates and any other precipitates that can be formed, depending on the annealing temperature and time. Techniques such as TEM and EDX can be employed for such investigations. In this thesis, a small volume fraction of Cr-rich precipitates was argued to provide excellent strength without loss of ductility. However, an optimised annealing treatment is required for better mechanical performance, whereby consolidated microstructures are obtained with a small volume fraction of the precipitates.

Although tensile tests using microflat dogbone samples were performed in this thesis, further investigation of the tensile properties of as-sprayed and annealed deposits of the CSAM HEA is needed. Few samples could be employed for the tensile test in this study; however, to obtain better statistical data for the tensile values, more tests need to be performed. Larger tensile test samples can be employed for such analyses because of the challenge of testing very small samples. Other micro-mechanical tests can be performed to evaluate the mechanical performance of CSAM HEA deposits suitable for structural repair and component manufacturing in the aerospace sector.

References

[1] Adding value to the economy, Aviat. Benefits Beyond Borders. (2017). https://aviationbenefits.org/economic-growth/adding-value-to-the-economy/ (accessed January 4, 2024).

[2] Global Space Exploration Market Size To Surpass USD 1879 Billion By 2032|CAGR of 16.21%, Spherical Insights. (2023). https://www.globenewswire.com/news-release/2023/05/16/2670325/0/en/Global-Space-Exploration-Market-Size-To-Surpass-USD-1879-Billion-By-2032-CAGR-of-16-21.html (accessed January 4, 2024).

[3] PwC's Global aerospace and defense industry performance and outlook 2023, PwC. (2023). www.pwc.com/us/aerospaceanddefense.

[4] B. Blakey-Milner, P. Gradl, G. Snedden, M. Brooks, J. Pitot, E. Lopez, M. Leary, F. Berto, A. du Plessis, Metal additive manufacturing in aerospace: A review, Mater. Des. 209 (2021) 110008. https://doi.org/10.1016/j.matdes.2021.110008.

[5] D. Herzog, V. Seyda, E. Wycisk, C. Emmelmann, Additive manufacturing of metals, Acta Mater. 117 (2016) 371–392. https://doi.org/10.1016/j.actamat.2016.07.019.

[6] P. Gradl, O.R. Mireles, C. Katsarelis, T.M. Smith, J. Sowards, A. Park, P. Chen, D. Tinker, C. Protz, T. Teasley, D.L. Ellis, C. Kantzos, Advancement of Extreme Environment Additively Manufactured Alloys for Next Generation Space Propulsion Applications, Acta Astronaut. 2011 (2023) 483–497. https://doi.org/https://doi.org/10.1016/j.actaastro.2023.06.035.

[7] M. Hoffmann, A. Elwany, In-Space Additive Manufacturing: A Review, J. Manuf. Sci. Eng. 145 (2023). https://doi.org/10.1115/1.4055603.

[8] H. Richard, T. Chris, S. Chris, The UK Additive Manufacturing Landscape, 2022.

[9] Global Aerospace Additive Manufacturing Market Research Report-Forecast Till 2032, Mark. Res. Futur. (2021) 134. https://www.marketresearchfuture.com/reports/aerospace-additive-manufacturing-market-1551 (accessed January 5, 2024).

[10] Wohlers Associates, Wohlers report: 3D Printing and Additive Manufacturing State of the Industry. Annual Worldwide Progress Report, 2018.

[11] J.C. Najmon, S. Raeisi, T. Andres, Review of additive manufacturing technologies and applications in the aerospace industry., in: Addit. Manuf. Aerosp. Ind., 2019: pp. 7–31. https://doi.org/https://doi.org/10.1016/B978-0-12-814062-8.00002-9.

[12] K. Kanishka, B. Acherjee, A systematic review of additive manufacturing-based remanufacturing techniques for component repair and restoration, J. Manuf. Process. 89 (2023) 220–283.

https://doi.org/10.1016/j.jmapro.2023.01.034.

[13] T. DebRoy, H.L. Wei, J.S. Zuback, T. Mukherjee, J.W. Elmer, J.O. Milewski, A.M. Beese, A. Wilson-Heid, A. De, W. Zhang, Additive manufacturing of metallic components – Process, structure and properties, Prog. Mater. Sci. 92 (2018) 112–224. https://doi.org/10.1016/j.pmatsci.2017.10.001.

[14] L. Parry, I.A. Ashcroft, R.D. Wildman, Understanding the effect of laser scan strategy on residual stress in selective laser melting through thermo-mechanical simulation, Addit. Manuf. 12 (2016) 1–15. https://doi.org/10.1016/j.addma.2016.05.014.

[15] B. Onuike, A. Bandyopadhyay, Additive manufacturing of Inconel 718 – Ti6Al4V bimetallic structures, Addit. Manuf. 22 (2018) 844–851. https://doi.org/10.1016/j.addma.2018.06.025.

[16] C. Li, Z.Y. Liu, X.Y. Fang, Y.B. Guo, Residual Stress in Metal Additive Manufacturing, Procedia CIRP. 71 (2018) 348–353. https://doi.org/10.1016/j.procir.2018.05.039.

[17] T.R. Walker, C.J. Bennett, T.L. Lee, A.T. Clare, A validated analytical-numerical modelling strategy to predict residual stresses in single-track laser deposited IN718, Int. J. Mech. Sci. 151 (2019) 609–621. https://doi.org/10.1016/j.ijmecsci.2018.12.004.

[18] D. Rejeski, F. Zhao, Y. Huang, Research needs and recommendations on environmental implications of additive manufacturing, Addit. Manuf. 19 (2018) 21–28. https://doi.org/10.1016/j.addma.2017.10.019.

[19] Cold Spray Technology Market Size, Share & Trends Analysis Report By Material (Nickel, Copper, Aluminum, Titanium), By Service (Cold Spray Additive Manufacturing), By End-use, By Region, And Segment Forecasts, 2023 - 2030, Res. Mark. - Mark. Res. Reports - Welcome. (2023). https://www.researchandmarkets.com/report/cold-spraying-equipment (accessed January 5, 2024).

[20] P. T.M., Benefit Cost Analysis: ESTCP Funded Cold Spray Technology for DOD Applications. Technical Report, 2015.

[21] R.C. Dykhuizen, M.F. Smith, Gas Dynamic Principles of Cold Spray, J. Therm. Spray Technol. 7 (1998) 205–212. https://doi.org/10.1361/105996398770350945.

[22] T.H.V. Steenkiste, J.R. Smith, R.E. Teets, Aluminum coatings via kinetic spray with relatively large powder particles, Surf. Coatings Technol. 154 (2002) 237–252. https://doi.org/10.1016/S0257-8972(02)00018-X.

[23] A.P. Alkhimov, V.F. Kosarev, S. V. Klinkov, The features of cold spray nozzle design, J. Therm. Spray Technol. 10 (2001) 375–381. https://doi.org/10.1361/105996301770349466.

[24] M. Lewke, H. Wu, A. List, F. Gärtner, T. Klassen, A. Fay, Automated Path and Trajectory Planning for Automated Repair of Damaged Components by Cold Spray, J. Therm. Spray Technol. 84536 (2023) 15. https://doi.org/10.1007/s11666-023-01697-w.

[25] Impact Innovation demonstrates Ti6Al4V Cold Spray Additive

Manufacturing, Met. AM Mag. (2022). https://www.metal-am.com/impact-innovations-demonstrates-ti6al4v-cold-spray-additive-manufacturing/.

[26] M. Guerges, NASA Additively Manufactured Rocket Engine Hardware Passes Cold Spray, Hot Fire Tests, (2021). https://www.nasa.gov/centers-and-facilities/marshall/nasa-additively-manufactured-rocket-engine-hardware-passes-cold-spray-hot-fire-tests/ (accessed November 14, 2023).

[27] Y. Li, C.J. Li, G.J. Yang, L.K. Xing, Thermal fatigue behavior of thermal barrier coatings with the MCrAlY bond coats by cold spraying and low-pressure plasma spraying, Surf. Coatings Technol. 205 (2010) 2225–2233. https://doi.org/10.1016/j.surfcoat.2010.08.144.

[28] A. Vardelle, C. Moreau, J. Akedo, H. Ashrafizadeh, C.C. Berndt, J.O. Berghaus, M. Boulos, J. Brogan, A.C. Bourtsalas, A. Dolatabadi, M. Dorfman, T.J. Eden, P. Fauchais, G. Fisher, F. Gaertner, M. Gindrat, R. Henne, M. Hyland, E. Irissou, E.H. Jordan, K.A. Khor, A. Killinger, Y.C. Lau, C.J. Li, L. Li, J. Longtin, N. Markocsan, P.J. Masset, J. Matejicek, G. Mauer, A. McDonald, J. Mostaghimi, S. Sampath, G. Schiller, K. Shinoda, M.F. Smith, A.A. Syed, N.J. Themelis, F.L. Toma, J.P. Trelles, R. Vassen, P. Vuoristo, The 2016 Thermal Spray Roadmap, J. Therm. Spray Technol. 25 (2016) 1376–1440. https://doi.org/10.1007/s11666-016-0473-x.

[29] J. Tam, W. Li, B. Yu, D. Poirier, J.G. Legoux, P. Lin, G. Palumbo, J.D. Giallonardo, U. Erb, Reducing complex microstructural heterogeneity in electrodeposited and cold sprayed copper coating junctions, Surf. Coatings Technol. 404 (2020) 126479. https://doi.org/10.1016/j.surfcoat.2020.126479.

[30] A. Manap, Y. Ichikawa, K. Ogawa, Computational simulation for cold sprayed deposition, in: Elyt Lab. Work. Sendai, Japan, 2011.

[31] S. Yin, P. Cavaliere, B. Aldwell, R. Jenkins, H. Liao, W. Li, R. Lupoi, Cold spray additive manufacturing and repair: Fundamentals and applications, Addit. Manuf. 21 (2018) 628–650. https://doi.org/10.1016/j.addma.2018.04.017.

[32] V. Champagne, D. Helfritch, Critical Assessment 11: Structural repairs by cold spray, Mater. Sci. Technol. (United Kingdom). 31 (2015) 627–634. https://doi.org/10.1179/1743284714Y.0000000723.

[33] V.K. Champagne, The repair of magnesium rotorcraft components by cold spray, J. Fail. Anal. Prev. 8 (2008) 164–175. https://doi.org/10.1007/s11668-008-9116-y.

[34] P.R. Gradl, C.S. Protz, D.L. Ellis, S.E. Greene, Progress in additively manufactured copper-alloy GRCop-84, GRCop-42, and bimetallic combustion chambers for liquid rocket engines, in: Int. Astronaut. Congr., 2019.

[35] J.W. Yeh, S.K. Chen, S.J. Lin, J.Y. Gan, T.S. Chin, T.T. Shun, C.H. Tsau, S.Y. Chang, Nanostructured high-entropy alloys with multiple principal elements: Novel alloy design concepts and outcomes, Adv. Eng. Mater. 6 (2004) 299–303. https://doi.org/10.1002/adem.200300567.

[36] B. Cantor, I.T.H. Chang, P. Knight, A.J.B. Vincent, Microstructural development in equiatomic multicomponent alloys, Mater. Sci. Eng. A. 375–

377 (2004) 213–218. https://doi.org/10.1016/j.msea.2003.10.257.

[37] Z. Li, S. Zhao, R.O. Ritchie, M.A. Meyers, Mechanical properties of high-entropy alloys with emphasis on face-centered cubic alloys, Prog. Mater. Sci. 102 (2019) 296–345. https://doi.org/10.1016/j.pmatsci.2018.12.003.

[38] M.A. Mahmood, F.G. Alabtah, Y. Al-Hamidi, M. Khraisheh, On the laser additive manufacturing of high-entropy alloys: A critical assessment of in-situ monitoring techniques and their suitability, Mater. Des. 226 (2023) 111658. https://doi.org/10.1016/j.matdes.2023.111658.

[39] A. Anupam, S. Kumar, N.M. Chavan, B.S. Murty, R.S. Kottada, First report on cold-sprayed AlCoCrFeNi high-entropy alloy and its isothermal oxidation, J. Mater. Res. 34 (2019) 796–806. https://doi.org/10.1557/jmr.2019.38.

[40] S. Yin, W. Li, B. Song, X. Yan, M. Kuang, Y. Xu, K. Wen, R. Lupoi, Deposition of FeCoNiCrMn high entropy alloy (HEA) coating via cold spraying, J. Mater. Sci. Technol. 35 (2019) 1003–1007. https://doi.org/10.1016/j.jmst.2018.12.015.

[41] B. Gludovatz, A. Hohenwarter, D. Catoor, E.H. Chang, E.P. George, R.O. Ritchie, A fracture-resistant high-entropy alloy for cryogenic applications, Science (80-.). 345 (2014) 1153–1158. https://doi.org/10.1126/science.1254581.

[42] F. Otto, A. Dlouhý, C. Somsen, H. Bei, G. Eggeler, E.P. George, The influences of temperature and microstructure on the tensile properties of a CoCrFeMnNi high-entropy alloy, Acta Mater. 61 (2013) 5743–5755. https://doi.org/10.1016/j.actamat.2013.06.018.

[43] N. Stepanov, M. Tikhonovsky, N. Yurchenko, D. Zyabkin, M. Klimova, S. Zherebtsov, A. Efimov, G. Salishchev, Effect of cryo-deformation on structure and properties of CoCrFeNiMn high-entropy alloy, Intermetallics. 59 (2015) 8–17. https://doi.org/10.1016/j.intermet.2014.12.004.

[44] F. Otto, N.L. Hanold, E.P. George, Microstructural evolution after thermomechanical processing in an equiatomic, single-phase CoCrFeMnNi high-entropy alloy with special focus on twin boundaries, Intermetallics. 54 (2014) 39–48. https://doi.org/10.1016/J.INTERMET.2014.05.014.

[45] Y.J. Kwon, J.W. Won, S.H. Park, J.H. Lee, K.R. Lim, Y.S. Na, C.S. Lee, Ultrahigh-strength CoCrFeMnNi high-entropy alloy wire rod with excellent resistance to hydrogen embrittlement, Mater. Sci. Eng. A. 732 (2018) 105–111. https://doi.org/10.1016/j.msea.2018.06.086.

[46] Y. Shi, B. Yang, P.K. Liaw, Corrosion-resistant high-entropy alloys: A review, Metals (Basel). 7 (2017) 1–18. https://doi.org/10.3390/met7020043.

[47] G. Wang, Y. Lu, Y. Zhang, S. Xia, C.M. Lousada, H. Mao, A.C. Maier, P.A. Korzhavyi, R. Sandström, Y. Wang, Nonlinear Oxidation Behavior in Pure Ni and Ni-Containing Entropic Alloys, Front. Mater. | Www.Frontiersin.Org. 5 (2018) 53. https://doi.org/10.3389/fmats.2018.00053.

[48] A. Alkhimov, A. Papyrin, V. Kosarev, Gas-dynamic spraying method for applying a coating, US Pat. 5,302,414. (1994) 13. https://patents.google.com/patent/US5302414A/en (accessed September 28, 2020).

[49] A. Papyrin, The development of the cold spray process, in: Cold Spray Mater. Depos. Process Fundam. Appl., Elsevier Ltd., 2007: pp. 11–42. https://doi.org/10.1533/9781845693787.1.11.

[50] E. Irissou, J.G. Legoux, A.N. Ryabinin, B. Jodoin, C. Moreau, Review on cold spray process and technology: Part I - Intellectual property, J. Therm. Spray Technol. 17 (2008) 495–516. https://doi.org/10.1007/s11666-008-9203-3.

[51] ISO/ASTM, Additive Manufacturing - General Principles Termonology (ASTM52900), 2015. http://www.iso.org/standard/69669.html.

[52] J. Yin, W. Zhang, L. Ke, H. Wei, D. Wang, L. Yang, H. Zhu, P. Dong, G. Wang, X. Zeng, Vaporization of alloying elements and explosion behavior during laser powder bed fusion of Cu–10Zn alloy, Int. J. Mach. Tools Manuf. 161 (2021) 103686. https://doi.org/10.1016/j.ijmachtools.2020.103686.

[53] T. Yuan, Z. Yu, S. Chen, M. Xu, X. Jiang, Loss of elemental Mg during wire + arc additive manufacturing of Al-Mg alloy and its effect on mechanical properties, J. Manuf. Process. 49 (2020) 456–462. https://doi.org/10.1016/j.jmapro.2019.10.033.

[54] Q. Sui, Z. Wang, J. Wang, S. Xu, F. Zhao, L. Gong, B. Liu, J. Liu, G. Liu, The microstructure and mechanical properties of the additive manufactured AlCoCrFeNi high entropy alloy, Mater. Sci. Eng. A. 833 (2022) 142507. https://doi.org/10.1016/j.msea.2021.142507.

[55] N.T. Aboulkhair, N.M. Everitt, I. Ashcroft, C. Tuck, Reducing porosity in AlSi10Mg parts processed by selective laser melting, Addit. Manuf. 1 (2014) 77–86. https://doi.org/10.1016/j.addma.2014.08.001.

[56] H. Assadi, F. Gärtner, T. Stoltenhoff, H. Kreye, Bonding mechanism in cold gas spraying, Acta Mater. 51 (2003) 4379–4394. https://doi.org/10.1016/S1359-6454(03)00274-X.

[57] T. Schmidt, F. Gärtner, H. Assadi, H. Kreye, Development of a generalized parameter window for cold spray deposition, Acta Mater. 54 (2006) 729–742. https://doi.org/10.1016/j.actamat.2005.10.005.

[58] M.F. Smith, Comparing cold spray with thermal spray coating technologies, in: Cold Spray Mater. Depos. Process Fundam. Appl., Elsevier Ltd., 2007: pp. 43–61. https://doi.org/10.1533/9781845693787.1.43.

[59] M.R. Rokni, S.R. Nutt, C.A. Widener, V.K. Champagne, R.H. Hrabe, Review of Relationship Between Particle Deformation, Coating Microstructure, and Properties in High-Pressure Cold Spray, J. Therm. Spray Technol. 26 (2017) 1308–1355. https://doi.org/10.1007/s11666-017-0575-0.

[60] S. Bagherifard, S. Monti, M.V. Zuccoli, M. Riccio, J. Kondás, M. Guagliano, Cold spray deposition for additive manufacturing of freeform structural components compared to selective laser melting, Mater. Sci. Eng. A. 721 (2018) 339–350. https://doi.org/10.1016/J.MSEA.2018.02.094.

[61] S. Yoon, G. Bae, Y. Xiong, S. Kumar, K. Kang, J.J. Kim, C. Lee, Strain-enhanced nanocrystallization of a CuNiTiZr bulk metallic glass coating by a kinetic spraying process, Acta Mater. 57 (2009) 6191–6199. https://doi.org/10.1016/j.actamat.2009.08.045.

[62] J. Henao, A. Concustell, S. Dosta, G. Bolelli, I.G. Cano, L. Lusvarghi, J.M. Guilemany, Deposition mechanisms of metallic glass particles by Cold Gas Spraying, Acta Mater. 125 (2017) 327–339. https://doi.org/10.1016/j.actamat.2016.12.007.

[63] R. Nikbakht, M. Saadati, T.-S. Kim, M. Jahazi, H.S. Kim, B. Jodoin, Cold Spray Deposition Characteristic and Bonding of CrMnCoFeNi High Entropy Alloy, Surf. Coatings Technol. 425 (2021) 127748. https://doi.org/10.1016/J.SURFCOAT.2021.127748.

[64] C.J. Akisin, B. Dovgyy, C.J. Bennett, M.S. Pham, F. Venturi, T. Hussain, Microstructural Study of Cold-Sprayed CoCrFeNiMn High Entropy Alloy, J. Therm. Spray Technol. (2023) 1–24. https://doi.org/10.1007/s11666-023-01646-7.

[65] L.S. Wang, H.F. Zhou, K.J. Zhang, Y.Y. Wang, C.X.C.J. Li, X.T. Luo, G.J. Yang, C.X.C.J. Li, Effect of the powder particle structure and substrate hardness during vacuum cold spraying of Al2O3, Ceram. Int. 43 (2017) 4390–4398. https://doi.org/10.1016/j.ceramint.2016.12.085.

[66] L. He, M. Hassani, A Review of the Mechanical and Tribological Behavior of Cold Spray Metal Matrix Composites, J. Therm. Spray Technol. (2020). https://doi.org/10.1007/s11666-020-01091-w.

[67] A. Ganesan, M. Yamada, M. Fukumoto, Cold Spray Coating Deposition Mechanism on the Thermoplastic and Thermosetting Polymer Substrates, Springer. 22 (2013) 1275–1282. https://doi.org/10.1007/s11666-013-9984-x.

[68] Y.T.R. Lee, H. Ashrafizadeh, G. Fisher, A. McDonald, Effect of type of reinforcing particles on the deposition efficiency and wear resistance of low-pressure cold-sprayed metal matrix composite coatings, Surf. Coatings Technol. 324 (2017) 190–200. https://doi.org/10.1016/j.surfcoat.2017.05.057.

[69] C.J. Akisin, · F Venturi, · M Bai, · C J Bennett, · T Hussain, Microstructure, mechanical and wear resistance properties of low-pressure cold-sprayed Al-7 Mg/Al 2 O 3 and Al-10 Mg/Al 2 O 3 composite coatings, Emergent Mater. 4 (2021) 1569–1581. https://doi.org/10.1007/s42247-021-00293-4.

[70] N.M. Melendez, V. V. Narulkar, G.A. Fisher, A.G. McDonald, Effect of reinforcing particles on the wear rate of low-pressure cold-sprayed WC-based MMC coatings, Wear. 306 (2013) 185–195. https://doi.org/10.1016/j.wear.2013.08.006.

[71] K.J. Hodder, H. Izadi, A.G. McDonald, A.P. Gerlich, Fabrication of aluminum-alumina metal matrix composites via cold gas dynamic spraying at low pressure followed by friction stir processing, Mater. Sci. Eng. A. 556 (2012) 114–121. https://doi.org/10.1016/j.msea.2012.06.066.

[72] S.Q. Fan, G.J. Yang, C.J. Li, G.J. Liu, C.X. Li, L.Z. Zhang, Characterization of microstructure of nano-TiO2 coating deposited by vacuum cold spraying, Proc. Int. Therm. Spray Conf. 15 (2006) 513–517. https://doi.org/10.1361/105996306X146901.

[73] D. Hanft, J. Exner, M. Schubert, T. Stöcker, P. Fuierer, R. Moos, An overview of the Aerosol Deposition method: Process fundamentals and new

trends in materials applications, J. Ceram. Sci. Technol. 6 (2015) 147–181. https://doi.org/10.4416/JCST2015-00018.

[74] M. Bray, A. Cockburn, W. O'Neill, The Laser-assisted Cold Spray process and deposit characterisation, Surf. Coatings Technol. 203 (2009) 2851–2857. https://doi.org/10.1016/j.surfcoat.2009.02.135.

[75] R. Nikbakht, C. V. Cojocaru, M. Aghasibeig, É. Irissou, T.-S. Kim, H.S. Kim, B. Jodoin, Cold Spray and Laser-Assisted Cold Spray of CrMnCoFeNi High Entropy Alloy Using Nitrogen as the Propelling Gas, J. Therm. Spray Technol. 31 (2022) 1129–1142. https://doi.org/10.1007/s11666-022-01361-9.

[76] J. Karthikeyan, The advantages and disadvantages of the cold spray coating process, in: Cold Spray Mater. Depos. Process Fundam. Appl., Elsevier Ltd., 2007: pp. 62–71. https://doi.org/10.1533/9781845693787.1.62.

[77] G. Prashar, H. Vasudev, A comprehensive review on sustainable cold spray additive manufacturing: State of the art, challenges and future challenges, J. Clean. Prod. 310 (2021) 127606. https://doi.org/10.1016/j.jclepro.2021.127606.

[78] L. Ajdelsztajn, A. Zúñiga, B. Jodoin, E.J. Lavernia, Cold-spray processing of a nanocrystalline Al-Cu-Mg-Fe-Ni alloy with Sc, J. Therm. Spray Technol. 15 (2006) 184–190. https://doi.org/10.1361/105996306X107995.

[79] Z. Tong, X. Ren, J. Jiao, W. Zhou, Y. Ren, Y. Ye, E.A. Larson, J. Gu, Laser additive manufacturing of FeCrCoMnNi high-entropy alloy: Effect of heat treatment on microstructure, residual stress and mechanical property, J. Alloys Compd. 785 (2019) 1144–1159. https://doi.org/10.1016/j.jallcom.2019.01.213.

[80] C.M. Sample, V.K. Champagne, A.T. Nardi, D.A. Lados, Factors Governing Static Properties and Fatigue, Fatigue Crack Growth, and Fracture Mechanisms in Cold Spray Alloys and Coatings/Repairs: A Review, Addit. Manuf. (2020) 101371. https://doi.org/10.1016/j.addma.2020.101371.

[81] R. Ghelichi, D. MacDonald, S. Bagherifard, H. Jahed, M. Guagliano, B. Jodoin, Microstructure and fatigue behavior of cold spray coated Al5052, Acta Mater. 60 (2012) 6555–6561. https://doi.org/10.1016/j.actamat.2012.08.020.

[82] A. Moridi, S.M. Hassani-Gangaraj, S. Vezzú, L. Trško, M. Guagliano, Fatigue behavior of cold spray coatings: The effect of conventional and severe shot peening as pre-/post-treatment, Surf. Coatings Technol. 283 (2015) 247–254. https://doi.org/10.1016/j.surfcoat.2015.10.063.

[83] V. Luzin, D. Fraser, Neutron Through-thickness Stress Measurements in Two-Phase Coatings with High Spatial Resolution, Mater. Res. Proc. 4 (2018) 111–116.

[84] V. Luzin, O. Kirstein, S.H. Zahiri, D. Fraser, Residual Stress Buildup in Ti Components Produced by Cold Spray Additive Manufacturing (CSAM), J. Therm. Spray Technol. 29 (2020) 1498–1507. https://doi.org/10.1007/s11666-020-01048-z.

[85] D. Boruah, B. Ahmad, T.L. Lee, S. Kabra, A.K. Syed, P. McNutt, M. Doré, X.

Zhang, Evaluation of residual stresses induced by cold spraying of Ti-6Al-4V on Ti-6Al-4V substrates, Surf. Coatings Technol. 374 (2019) 591–602. https://doi.org/10.1016/j.surfcoat.2019.06.028.

[86] A. Sabard, P. McNutt, H. Begg, T. Hussain, Cold spray deposition of solution heat treated, artificially aged and naturally aged Al 7075 powder, Surf. Coatings Technol. 385 (2020) 125367. https://doi.org/10.1016/j.surfcoat.2020.125367.

[87] M.R. Rokni, C.A. Widener, V.K. Champagne, G.A. Crawford, S.R. Nutt, The effects of heat treatment on 7075 Al cold spray deposits, Surf. Coatings Technol. 310 (2017) 278–285. https://doi.org/10.1016/j.surfcoat.2016.10.064.

[88] N. Fan, A. Rafferty, R. Lupoi, W. Li, Y. Xie, S. Yin, Microstructure evolution and mechanical behavior of additively manufactured CoCrFeNi high-entropy alloy fabricated via cold spraying and post-annealing, Mater. Sci. Eng. A. (2023) 144748. https://doi.org/10.1016/j.msea.2023.144748.

[89] A. Sova, S. Grigoriev, A. Okunkova, I. Smurov, Potential of cold gas dynamic spray as additive manufacturing technology, Int. J. Adv. Manuf. Technol. 69 (2013) 2269–2278. https://doi.org/10.1007/s00170-013-5166-8.

[90] A. Sova, S. Klinkov, V. Kosarev, N. Ryashin, I. Smurov, Preliminary study on deposition of aluminium and copper powders by cold spray micronozzle using helium, Surf. Coatings Technol. 220 (2013) 98–101. https://doi.org/10.1016/j.surfcoat.2012.09.036.

[91] T. Schmidt, H. Assadi, F. Gärtner, H. Richter, T. Stoltenhoff, H. Kreye, T. Klassen, From particle acceleration to impact and bonding in cold spraying, J. Therm. Spray Technol. 18 (2009) 794–808. https://doi.org/10.1007/s11666-009-9357-7.

[92] J. Pattison, S. Celotto, A. Khan, W. O'Neill, Standoff distance and bow shock phenomena in the Cold Spray process, Surf. Coatings Technol. 202 (2008) 1443–1454. https://doi.org/10.1016/j.surfcoat.2007.06.065.

[93] W. Wong, P. Vo, E. Irissou, A.N. Ryabinin, J.G. Legoux, S. Yue, Effect of particle morphology and size distribution on cold-sprayed pure titanium coatings, J. Therm. Spray Technol. 22 (2013) 1140–1153. https://doi.org/10.1007/s11666-013-9951-6.

[94] Y. Chang, J. Wang, P. Mohanty, M.T. Khan, L.N.U. Rehman, L. Shan, C. Fu, J. Wang, The Effect of Cr Particle Size on Cr Deposition Efficiency during Cold Spraying, J. Mater. Eng. Perform. 31 (2022) 4060–4067. https://doi.org/10.1007/s11665-021-06486-6.

[95] B. Jodoin, L. Ajdelsztajn, E. Sansoucy, A. Zúñiga, P. Richer, E.J. Lavernia, Effect of particle size, morphology, and hardness on cold gas dynamic sprayed aluminum alloy coatings, Surf. Coatings Technol. 201 (2006) 3422–3429. https://doi.org/10.1016/j.surfcoat.2006.07.232.

[96] C.J. Li, W.Y. Li, H. Liao, Examination of the critical velocity for deposition of particles in cold spraying, J. Therm. Spray Technol. 15 (2006) 212–222. https://doi.org/10.1361/105996306X108093.

[97] K. Kang, S. Yoon, Y. Ji, C. Lee, Oxidation dependency of critical velocity for

aluminum feedstock deposition in kinetic spraying process, Mater. Sci. Eng. A. 486 (2008) 300–307. https://doi.org/10.1016/j.msea.2007.09.010.

[98] C.J. Li, H.T. Wang, Q. Zhang, G.J. Yang, W.Y. Li, H.L. Liao, Influence of spray materials and their surface oxidation on the critical velocity in cold spraying, in: J. Therm. Spray Technol., 2010: pp. 95–101. https://doi.org/10.1007/s11666-009-9427-x.

[99] S. Yin, X. Wang, W. Li, H. Liao, H. Jie, Deformation behavior of the oxide film on the surface of cold sprayed powder particle, Appl. Surf. Sci. 259 (2012) 294–300. https://doi.org/10.1016/j.apsusc.2012.07.036.

[100] O.C. Ozdemir, C.A. Widener, M.J. Carter, K.W. Johnson, Predicting the Effects of Powder Feeding Rates on Particle Impact Conditions and Cold Spray Deposited Coatings, J. Therm. Spray Technol. 26 (2017) 1598–1615. https://doi.org/10.1007/s11666-017-0611-0.

[101] K. Taylor, B. Jodoin, J. Karov, Particle loading effect in cold spray, J. Therm. Spray Technol. 15 (2006) 273–279. https://doi.org/10.1361/105996306X108237.

[102] M. Meyer, S. Yin, R. Lupoi, Particle In-Flight Velocity and Dispersion Measurements at Increasing Particle Feed Rates in Cold Spray, J. Therm. Spray Technol. 26 (2017) 60–70. https://doi.org/10.1007/s11666-016-0496-3.

[103] R.A. Seraj, A. Abdollah-zadeh, S. Dosta, H. Canales, H. Assadi, I.G. Cano, The effect of traverse speed on deposition efficiency of cold sprayed Stellite 21, Surf. Coatings Technol. 366 (2019) 24–34. https://doi.org/10.1016/j.surfcoat.2019.03.012.

[104] A.W.Y. Tan, W. Sun, Y.P. Phang, M. Dai, I. Marinescu, Z. Dong, E. Liu, Effects of Traverse Scanning Speed of Spray Nozzle on the Microstructure and Mechanical Properties of Cold-Sprayed Ti6Al4V Coatings, J. Therm. Spray Technol. 26 (2017) 1484–1497. https://doi.org/10.1007/s11666-017-0619-5.

[105] K. Sakaki, The influence of nozzle design in the cold spray process, in: Cold Spray Mater. Depos. Process Fundam. Appl., Elsevier Ltd., 2007: pp. 117–126. https://doi.org/10.1533/9781845693787.2.117.

[106] M.F. Smith, Introduction to Cold Spray, in: C.. Kay, J. Karthikeyan (Eds.), High Press. Cold Spray-Principles Appl., ASM International, 2016: pp. 1–16. https://doi.org/10.31399/asm.tb.hpcspa.t54460001.

[107] D.L. Gilmore, R.C. Dykhuizen, R.A. Neiser, T.J. Roemer, M.F. Smith, Particle velocity and deposition efficiency in the cold spray process, J. Therm. Spray Technol. 8 (1999) 576–582. https://doi.org/10.1361/105996399770350278.

[108] S. Yin, M. Meyer, W. Li, H. Liao, R. Lupoi, Gas Flow, Particle Acceleration, and Heat Transfer in Cold Spray: A review, J. Therm. Spray Technol. 25 (2016) 874–896. https://doi.org/10.1007/s11666-016-0406-8.

[109] B. Samareh, O. Stier, V. Lüthen, A. Dolatabadi, Assessment of CFD modeling via Flow visualization in cold spray process, J. Therm. Spray Technol. 18 (2009) 934–943. https://doi.org/10.1007/s11666-009-9363-9.

[110] M. Grujicic, C.L. Zhao, C. Tong, W.S. DeRosset, D. Helfritch, Analysis of the impact velocity of powder particles in the cold-gas dynamic-spray process, Mater. Sci. Eng. A. 368 (2004) 222–230. https://doi.org/10.1016/j.msea.2003.10.312.

[111] T. Stoltenhoff, H. Kreye, H.J. Richter, An analysis of the cold spray process and its coatings, J. Therm. Spray Technol. 11 (2002) 542–550. https://doi.org/10.1361/105996302770348682.

[112] K. Versteeg H., M. W., An Introduction to Computational Fluid Dynamics: The finite volume method, Second Edi, Prentice-Hall, Pearson, 2007. https://doi.org/10.1109/mcc.1998.736434.

[113] H. Tabbara, S. Gu, D.G. McCartney, T.S. Price, P.H. Shipway, Study on process optimization of cold gas spraying, J. Therm. Spray Technol. 20 (2011) 608–620. https://doi.org/10.1007/s11666-010-9564-2.

[114] B. Samareh, A. Dolatabadi, A three-dimensional analysis of the cold spray process: The effects of substrate location and shape, J. Therm. Spray Technol. 16 (2007) 634–642. https://doi.org/10.1007/s11666-007-9082-z.

[115] T. Han, Z. Zhao, B.A. Gillispie, J.R. Smith, Effects of spray conditions on coating formation by the kinetic spray process, J. Therm. Spray Technol. 14 (2005) 373–383. https://doi.org/10.1361/105996305X59369.

[116] V.K. Champagne, D.J. Helfritch, S.P.G. Dinavahi, P.F. Leyman, Theoretical and experimental particle velocity in cold spray, J. Therm. Spray Technol. 20 (2011) 425–431. https://doi.org/10.1007/s11666-010-9530-z.

[117] C.T. Crowe, Drag coefficient of particles in a rocket nozzle, AIAA J. 5 (1967) 1021–1022.

[118] C.B. Henderson, Drag coefficients of spheres in continuum and rarefield flows, AIAA J. 14 (1976) 707–708.

[119] R. W.E., M. W.R.J., Evaporation from Drops, Chem. Eng. Prog. 48 (1952) 141–146. https://cir.nii.ac.jp/crid/1570009749314758656 (accessed June 13, 2023).

[120] M.W. Lee, J.J. Park, D.Y. Kim, S.S. Yoon, H.Y. Kim, S.C. James, S. Chandra, T. Coyle, Numerical studies on the effects of stagnation pressure and temperature on supersonic flow characteristics in cold spray applications, J. Therm. Spray Technol. 20 (2011) 1085–1097. https://doi.org/10.1007/s11666-011-9641-1.

[121] S. Yin, M. Zhang, Z. Guo, H. Liao, X. Wang, Numerical investigations on the effect of total pressure and nozzle divergent length on the flow character and particle impact velocity in cold spraying, Surf. Coatings Technol. 232 (2013) 290–297. https://doi.org/10.1016/j.surfcoat.2013.05.017.

[122] X.J. Ning, Q.S. Wang, Z. Ma, H.J. Kim, Numerical study of in-flight particle parameters in low-pressure cold spray process, J. Therm. Spray Technol. 19 (2010) 1211–1217. https://doi.org/10.1007/s11666-010-9548-2.

[123] R. Huang, H. Fukanuma, Study of the influence of particle velocity on adhesive strength of cold spray deposits, J. Therm. Spray Technol. 21 (2012) 541–549. https://doi.org/10.1007/s11666-011-9707-0.

[124] X. Suo, S. Yin, M.P. Planche, T. Liu, H. Liao, Strong effect of carrier gas species on particle velocity during cold spray processes, Surf. Coatings Technol. 268 (2015) 90–93. https://doi.org/10.1016/j.surfcoat.2014.04.039.

[125] H. Assadi, T. Schmidt, H. Richter, J.O. Kliemann, K. Binder, F. Gärtner, T. Klassen, H. Kreye, On parameter selection in cold spraying, J. Therm. Spray Technol. 20 (2011) 1161–1176. https://doi.org/10.1007/s11666-011-9662-9.

[126] W.Y. Li, C. Zhang, X.P. Guo, G. Zhang, H.L. Liao, C.J. Li, C. Coddet, Effect of standoff distance on coating deposition characteristics in cold spraying, Mater. Des. 29 (2008) 297–304. https://doi.org/10.1016/j.matdes.2007.02.005.

[127] H. Koivuluoto, J. Lagerbom, M. Kylmälahti, P. Vuoristo, Microstructure and mechanical properties of low-pressure cold-sprayed (LPCS) coatings, in: J. Therm. Spray Technol., Springer, 2008: pp. 721–727. https://doi.org/10.1007/s11666-008-9245-6.

[128] A. Silvello, P. Cavaliere, S. Yin, R. Lupoi, I. Garcia Cano, S. Dosta, Microstructural, Mechanical and Wear Behavior of HVOF and Cold-Sprayed High-Entropy Alloys (HEAs) Coatings, J. Therm. Spray Technol. 31 (2022) 1184–1206. https://doi.org/10.1007/s11666-021-01293-w.

[129] S. Feng, S. Guan, W.A. Story, J. Ren, S. Zhang, A. Te, M.A. Gleason, J. Heelan, C. Walde, A. Birt, K.L. Tsaknopoulos, D.L. Cote, W. Kapalczynski, A.T. Naardi, V.K. Champagne, M.J. Siopis, W. Chen, Cold Spray Additive Manufacturing of CoCrFeNiMn High-Entropy Alloy: Process Development, Microstructure, and Mechanical Properties, J. Therm. Spray Technol. 31 (2022) 1222–1231. https://doi.org/10.1007/s11666-022-01374-4.

[130] H. Assadi, H. Kreye, F. Gärtner, T. Klassen, Cold spraying – A materials perspective, Acta Mater. 116 (2016) 382–407. https://doi.org/10.1016/j.actamat.2016.06.034.

[131] G. Bae, Y. Xiong, S. Kumar, K. Kang, C. Lee, General aspects of interface bonding in kinetic sprayed coatings, Acta Mater. 56 (2008) 4858–4868. https://doi.org/10.1016/j.actamat.2008.06.003.

[132] R. Nikbakht, S.H. Seyedein, S. Kheirandish, H. Assadi, B. Jodoin, Asymmetrical bonding in cold spraying of dissimilar materials, Appl. Surf. Sci. 444 (2018) 621–632. https://doi.org/10.1016/j.apsusc.2018.03.103.

[133] M. Grujicic, C.L. Zhao, W.S. DeRosset, D. Helfritch, Adiabatic shear instability based mechanism for particles/substrate bonding in the cold-gas dynamic-spray process, Mater. Des. 25 (2004) 681–688. https://doi.org/10.1016/j.matdes.2004.03.008.

[134] W.Y. Li, H. Liao, C.J. Li, H.S. Bang, C. Coddet, Numerical simulation of deformation behavior of Al particles impacting on Al substrate and effect of surface oxide films on interfacial bonding in cold spraying, Appl. Surf. Sci. 253 (2007) 5084–5091. https://doi.org/10.1016/j.apsusc.2006.11.020.

[135] W.Y. Li, C.J. Li, H. Liao, Significant influence of particle surface oxidation on deposition efficiency, interface microstructure and adhesive strength of cold-sprayed copper coatings, Appl. Surf. Sci. 256 (2010) 4953–4958. https://doi.org/10.1016/j.apsusc.2010.03.008.

[136] M. Hassani-Gangaraj, D. Veysset, V.K. Champagne, K.A. Nelson, C.A. Schuh, Adiabatic shear instability is not necessary for adhesion in cold spray, Acta Mater. 158 (2018) 430–439. https://doi.org/10.1016/j.actamat.2018.07.065.

[137] Y. Zou, W. Qin, E. Irissou, J.G. Legoux, S. Yue, J.A. Szpunar, Dynamic recrystallization in the particle/particle interfacial region of cold-sprayed nickel coating: Electron backscatter diffraction characterization, Scr. Mater. 61 (2009) 899–902. https://doi.org/10.1016/j.scriptamat.2009.07.020.

[138] K.H. Kim, M. Watanabe, J. Kawakita, S. Kuroda, Grain refinement in a single titanium powder particle impacted at high velocity, Scr. Mater. 59 (2008) 768–771. https://doi.org/10.1016/j.scriptamat.2008.06.020.

[139] T. Hussain, D.G. McCartney, P.H. Shipway, D. Zhang, Bonding mechanisms in cold spraying: The contributions of metallurgical and mechanical components, J. Therm. Spray Technol. 18 (2009) 364–379. https://doi.org/10.1007/s11666-009-9298-1.

[140] S. Yin, J. Cizek, J. Cupera, M. Hassani, X. Luo, R. Jenkins, Y. Xie, W. Li, R. Lupoi, Formation conditions of vortex-like intermixing interfaces in cold spray, Mater. Des. 200 (2021) 109444. https://doi.org/10.1016/j.matdes.2020.109444.

[141] C.J. Akisin, C.J. Bennett, F. Venturi, H. Assadi, T. Hussain, Numerical and Experimental Analysis of the Deformation Behavior of CoCrFeNiMn High Entropy Alloy Particles onto Various Substrates During Cold Spraying, J. Therm. Spray Technol. 31 (2022) 1085–1111. https://doi.org/10.1007/s11666-022-01377-1.

[142] V.K. Champagne, D. Helfritch, P. Leyman, S. Grendahl, B. Klotz, Interface material mixing formed by the deposition of copper on aluminum by means of the cold spray process, J. Therm. Spray Technol. 14 (2005) 330–334. https://doi.org/10.1361/105996305X59332.

[143] M. Grujicic, J.R. Saylor, D.E. Beasley, W.S. DeRosset, D. Helfritch, Computational analysis of the interfacial bonding between feed-powder particles and the substrate in the cold-gas dynamic-spray process, Appl. Surf. Sci. 219 (2003) 211–227. https://doi.org/10.1016/S0169-4332(03)00643-3.

[144] J. Wu, H. Fang, S. Yoon, H. Kim, C. Lee, The rebound phenomenon in kinetic spraying deposition, Scr. Mater. 54 (2006) 665–669. https://doi.org/10.1016/j.scriptamat.2005.10.028.

[145] K. Huang, R.E. Logé, A review of dynamic recrystallization phenomena in metallic materials, Mater. Des. 111 (2016) 548–574. https://doi.org/10.1016/j.matdes.2016.09.012.

[146] Y. Zou, Cold Spray Additive Manufacturing: Microstructure Evolution and Bonding Features, Accounts Mater. Res. (2021). https://doi.org/10.1021/accountsmr.1c00138.

[147] Z. Liu, H. Wang, M.J.. Haché, X. Chu, E. Irissou, Y. Zou, Prediction of Heterogeneous Microstructural Evolution in Cold-Sprayed Copper Coatings Using Local Zener-Hollomon Parameter and Strain, SSRN Electron. J.

(2020). https://doi.org/10.2139/ssrn.3542971.

[148] P.C. King, S.H. Zahiri, M. Jahedi, Microstructural refinement within a cold-sprayed copper particle, Metall. Mater. Trans. A Phys. Metall. Mater. Sci. 40 (2009) 2115–2123. https://doi.org/10.1007/s11661-009-9882-5.

[149] X.T. Luo, C.X.C.J. Li, F.L. Shang, G.J. Yang, Y.Y. Wang, C.X.C.J. Li, High velocity impact induced microstructure evolution during deposition of cold spray coatings: A review, Surf. Coatings Technol. 254 (2014) 11–20. https://doi.org/10.1016/j.surfcoat.2014.06.006.

[150] M.R. Rokni, C.A. Widener, O.C. Ozdemir, G.A. Crawford, Microstructure and mechanical properties of cold sprayed 6061 Al in As-sprayed and heat treated condition, Surf. Coatings Technol. 309 (2017) 641–650. https://doi.org/10.1016/j.surfcoat.2016.12.035.

[151] M.R. Rokni, C.A. Widener, G.A. Crawford, M.K. West, An investigation into microstructure and mechanical properties of cold sprayed 7075 Al deposition, Mater. Sci. Eng. A. 625 (2015) 19–27. https://doi.org/10.1016/j.msea.2014.11.059.

[152] M.R. Rokni, C.A. Widener, V.R. Champagne, Microstructural evolution of 6061 aluminum gas-atomized powder and high-pressure cold-sprayed deposition, J. Therm. Spray Technol. 23 (2014) 514–524. https://doi.org/10.1007/s11666-013-0049-y.

[153] Y. Zou, D. Goldbaum, J.A. Szpunar, S. Yue, Microstructure and nanohardness of cold-sprayed coatings: Electron backscattered diffraction and nanoindentation studies, Scr. Mater. 62 (2010) 395–398. https://doi.org/10.1016/j.scriptamat.2009.11.034.

[154] G. Bae, K. Kang, J.J. Kim, C. Lee, Nanostructure formation and its effects on the mechanical properties of kinetic sprayed titanium coating, Mater. Sci. Eng. A. 527 (2010) 6313–6319. https://doi.org/10.1016/j.msea.2010.06.037.

[155] M. Hassani-Gangaraj, D. Veysset, K.A. Nelson, C.A. Schuh, In-situ observations of single micro-particle impact bonding, Scr. Mater. 145 (2018) 9–13. https://doi.org/10.1016/j.scriptamat.2017.09.042.

[156] P.C. King, G. Bae, S.H. Zahiri, M. Jahedi, C. Lee, An experimental and finite element study of cold spray copper impact onto two aluminum substrates, in: J. Therm. Spray Technol., 2010: pp. 620–634. https://doi.org/10.1007/s11666-009-9454-7.

[157] S. Suresh, S.W. Lee, M. Aindow, H.D. Brody, V.K. Champagne, A.M. Dongare, Mesoscale modeling of jet initiation behavior and microstructural evolution during cold spray single particle impact, Acta Mater. 182 (2020) 197–206. https://doi.org/10.1016/j.actamat.2019.10.039.

[158] A. Joshi, S. James, Molecular dynamics simulation study of cold spray process, J. Manuf. Process. 33 (2018) 136–143. https://doi.org/10.1016/j.jmapro.2018.05.005.

[159] A. Fardan, C.C. Berndt, R. Ahmed, Numerical modelling of particle impact and residual stresses in cold sprayed coatings: A review, Surf. Coatings Technol. 409 (2021) 126835. https://doi.org/10.1016/j.surfcoat.2021.126835.

[160] W.Y. Li, D.D. Zhang, C.J. Huang, S. Yin, M. Yu, F.F. Wang, H.L. Liao, Modelling of impact behaviour of cold spray particles: Review, Surf. Eng. 30 (2014) 299–308. https://doi.org/10.1179/1743294414Y.0000000268.

[161] J. Xie, D. Nélias, H.W. Le Berre, K. Ogawa, Y. Ichikawa, Simulation of the cold spray particle deposition process, J. Tribol. 137 (2015). https://doi.org/10.1115/1.4030257.

[162] B. Yildirim, S. Muftu, A. Gouldstone, Modeling of high velocity impact of spherical particles, Wear. 270 (2011) 703–713. https://doi.org/10.1016/j.wear.2011.02.003.

[163] W.Y. Li, M. Yu, F.F. Wang, S. Yin, H.L. Liao, A generalized critical velocity window based on material property for cold spraying by eulerian method, J. Therm. Spray Technol. 23 (2014) 557–566. https://doi.org/10.1007/s11666-013-0023-8.

[164] W.Y. Li, K. Yang, S. Yin, X.P. Guo, Numerical Analysis of Cold Spray Particles Impacting Behavior by the Eulerian Method: A Review, J. Therm. Spray Technol. 25 (2016) 1441–1460. https://doi.org/10.1007/s11666-016-0443-3.

[165] G.R. Johnson, W.H. Cook, A Computational Constitutive Model and Data for Metals Subjected to Large Strain, High Strain Rates and High Pressures, Seventh Int. Symp. Ballist. (1983) 541–547.

[166] S. Rahmati, A. Ghaei, The use of particle/substrate material models in simulation of cold-gas dynamic-spray process, J. Therm. Spray Technol. 23 (2014) 530–540. https://doi.org/10.1007/s11666-013-0051-4.

[167] G.R. Johnson, W.H. Cook, Fracture characteristics of three metals subjected to various strains, strain rates, temperatures and pressures, Eng. Fract. Mech. 21 (1985) 31–48. https://doi.org/10.1016/0013-7944(85)90052-9.

[168] F.H. Abed, G.Z. Voyiadjis, A consistent modified Zerilli-Armstrong flow stress model for BCC and FCC metals for elevated temperatures, Acta Mech. 175 (2005) 1–18. https://doi.org/10.1007/s00707-004-0203-1.

[169] G.Z. Voyiadjis, F.H. Abed, Microstructural based models for bcc and fcc metals with temperature and strain rate dependency, in: Mech. Mater., Elsevier, 2005: pp. 355–378. https://doi.org/10.1016/j.mechmat.2004.02.003.

[170] D.L. Preston, D.L. Tonks, D.C. Wallace, Model of plastic deformation for extreme loading conditions, J. Appl. Phys. 93 (2003) 211–220. https://doi.org/10.1063/1.1524706.

[171] H. Huh, H.J. Lee, J.H. Song, Dynamic hardening equation of the auto-body steel sheet with the variation of temperature, Int. J. Automot. Technol. 13 (2012) 43–60. https://doi.org/10.1007/s12239-012-0005-8.

[172] C.Y. Gao, L.C. Zhang, Constitutive modelling of plasticity of fcc metals under extremely high strain rates, Int. J. Plast. 32–33 (2012) 121–133. https://doi.org/10.1016/j.ijplas.2011.12.001.

[173] T. Hussain, D.G. McCartney, P.H. Shipway, Impact phenomena in cold-

spraying of titanium onto various ferrous alloys, Surf. Coatings Technol. 205 (2011) 5021–5027. https://doi.org/10.1016/j.surfcoat.2011.05.003.

[174] H. Assadi, I. Irkhin, H. Gutzmann, F. Gärtner, M. Schulze, M. Villa Vidaller, T. Klassen, Determination of plastic constitutive properties of microparticles through single particle compression, Adv. Powder Technol. 26 (2015) 1544–1554. https://doi.org/10.1016/j.apt.2015.08.013.

[175] J.M. Park, J. Moon, J.W. Bae, M.J. Jang, J. Park, S. Lee, H.S. Kim, Strain rate effects of dynamic compressive deformation on mechanical properties and microstructure of CoCrFeMnNi high-entropy alloy, Mater. Sci. Eng. A. 719 (2018) 155–163. https://doi.org/10.1016/j.msea.2018.02.031.

[176] G.C. Soares, M. Patnamsetty, P. Peura, M. Hokka, Effects of Adiabatic Heating and Strain Rate on the Dynamic Response of a CoCrFeMnNi High-Entropy Alloy, J. Dyn. Behav. Mater. 5 (2019) 320–330. https://doi.org/10.1007/s40870-019-00215-w.

[177] B. Gnanasekaran, G.R. Liu, Y. Fu, G. Wang, W. Niu, T. Lin, A Smoothed Particle Hydrodynamics (SPH) procedure for simulating cold spray process - A study using particles, Surf. Coatings Technol. 377 (2019). https://doi.org/10.1016/j.surfcoat.2019.07.036.

[178] W. Sun, A.W.Y. Tan, A. Bhowmik, I. Marinescu, X. Song, W. Zhai, F. Li, E. Liu, Deposition characteristics of cold sprayed Inconel 718 particles on Inconel 718 substrates with different surface conditions, Mater. Sci. Eng. A. 720 (2018) 75–84. https://doi.org/10.1016/j.msea.2018.02.059.

[179] L.I. Pérez-Andrade, F. Gärtner, M. Villa-Vidaller, T. Klassen, J. Muñoz-Saldaña, J.M. Alvarado-Orozco, Optimization of Inconel 718 thick deposits by cold spray processing and annealing, Surf. Coatings Technol. 378 (2019). https://doi.org/10.1016/j.surfcoat.2019.124997.

[180] L. Perez, J. Colburn, L.N. Brewer, M. Renfro, T. McKechnie, Cold Spray Deposition of Heat-Treated Inconel 718 Powders, in: Therm. Spray 2021 Proc. from Int. Therm. Spray Conf., 2021: pp. 171–176. https://doi.org/10.31399/asm.cp.itsc2021p0171.

[181] M. Villa, S. Dosta, J.M. Guilemany, Optimization of 316L stainless steel coatings on light alloys using Cold Gas Spray, Surf. Coatings Technol. 235 (2013) 220–225. https://doi.org/10.1016/j.surfcoat.2013.07.036.

[182] X. Meng, J. Zhang, J. Zhao, Y. Liang, Y. Zhang, Influence of Gas Temperature on Microstructure and Properties of Cold Spray 304SS Coating, J. Mater. Sci. Technol. 27 (2011) 809–815. https://doi.org/10.1016/S1005-0302(11)60147-3.

[183] S. Yin, X. Wang, X. Suo, H. Liao, Z. Guo, W. Li, C. Coddet, Deposition behavior of thermally softened copper particles in cold spraying, Acta Mater. 61 (2013) 5105–5118. https://doi.org/10.1016/j.actamat.2013.04.041.

[184] H. Assadi, F. Gartner, T. Klassen, Modelling and simulation of cold spray, in: M.K. Charles, J. Karthikeyan (Eds.), High Press. Cold SprayPrinciples Appl., ASM International, 2016: pp. 67–106. https://doi.org/https://doi.org/10.31399/asm.tb.hpcspa.t54460067.

[185] Y. Xie, S. Yin, J. Cizek, J. Cupera, E. Guo, R. Lupoi, Formation mechanism

and microstructure characterization of nickel-aluminum intertwining interface in cold spray, Surf. Coatings Technol. 337 (2018) 447–452. https://doi.org/10.1016/j.surfcoat.2018.01.049.

[186] W.Y. Li, H. Liao, C.J. Li, G. Li, C. Coddet, X. Wang, On high velocity impact of micro-sized metallic particles in cold spraying, Appl. Surf. Sci. 253 (2006) 2852–2862. https://doi.org/10.1016/j.apsusc.2006.05.126.

[187] P.C. King, M. Jahedi, Relationship between particle size and deformation in the cold spray process, Appl. Surf. Sci. 256 (2010) 1735–1738. https://doi.org/10.1016/j.apsusc.2009.09.104.

[188] P.C. King, S.H. Zahiri, M. Jahedi, Focused ion beam micro-dissection of cold-sprayed particles, Acta Mater. 56 (2008) 5617–5626. https://doi.org/10.1016/j.actamat.2008.07.034.

[189] R. Chakrabarty, J. Song, A modified Johnson-Cook material model with strain gradient plasticity consideration for numerical simulation of cold spray process, Surf. Coatings Technol. 397 (2020) 125981. https://doi.org/10.1016/j.surfcoat.2020.125981.

[190] S. Yin, X.F. Wang, W.Y. Li, B.P. Xu, Numerical investigation on effects of interactions between particles on coating formation in cold spraying, J. Therm. Spray Technol. 18 (2009) 686–693. https://doi.org/10.1007/s11666-009-9390-6.

[191] S. Yin, H.L. Liao, X.F. Wang, Euler based finite element analysis on high velocity impact behaviour in cold spraying, Surf. Eng. 30 (2014) 309–315. https://doi.org/10.1179/1743294413Y.0000000240.

[192] G. Bae, S. Kumar, S. Yoon, K. Kang, H. Na, H.J. Kim, C. Lee, Bonding features and associated mechanisms in kinetic sprayed titanium coatings, Acta Mater. 57 (2009) 5654–5666. https://doi.org/10.1016/j.actamat.2009.07.061.

[193] X. Song, K.L. Ng, J.M.K. Chea, W. Sun, A.W.Y. Tan, W. Zhai, F. Li, I. Marinescu, E. Liu, Coupled Eulerian-Lagrangian (CEL) simulation of multiple particle impact during Metal Cold Spray process for coating porosity prediction, Surf. Coatings Technol. 385 (2020). https://doi.org/10.1016/j.surfcoat.2020.125433.

[194] M. Terrone, A. Ardeshiri Lordejani, J. Kondas, S. Bagherifard, A numerical Approach to design and develop freestanding porous structures through cold spray multi-material deposition, Surf. Coatings Technol. 421 (2021) 127423. https://doi.org/10.1016/j.surfcoat.2021.127423.

[195] S. Weiller, F. Delloro, A numerical study of pore formation mechanisms in aluminium cold spray coatings, Addit. Manuf. 60 (2022). https://doi.org/10.1016/j.addma.2022.103193.

[196] S. Yin, X.F. Wang, B.P. Xu, W.Y. Li, Examination on the calculation method for modeling the multi-particle impact process in cold spraying, J. Therm. Spray Technol. 19 (2010) 1032–1041. https://doi.org/10.1007/s11666-010-9489-9.

[197] S. Yin, X.F. Wang, W.Y. Li, H.E. Jie, Effect of substrate hardness on the deformation behavior of subsequently incident particles in cold spraying,

Appl. Surf. Sci. 257 (2011) 7560–7565. https://doi.org/10.1016/j.apsusc.2011.03.126.

[198] X.L. Zhou, X.K. Wu, H.H. Guo, J.G. Wang, J.S. Zhang, Deposition behavior of multi-particle impact in cold spraying process, Int. J. Miner. Metall. Mater. 17 (2010) 635–640. https://doi.org/10.1007/s12613-010-0367-8.

[199] A. Ardeshiri Lordejani, D. Colzani, M. Guagliano, S. Bagherifard, An inclusive numerical framework to assess the role of feedstock features on the quality of cold spray deposits, Mater. Des. 224 (2022) 111374. https://doi.org/10.1016/j.matdes.2022.111374.

[200] K. Spencer, M.X. Zhang, Optimisation of stainless steel cold spray coatings using mixed particle size distributions, Surf. Coatings Technol. 205 (2011) 5135–5140. https://doi.org/10.1016/j.surfcoat.2011.05.020.

[201] L.N. Brewer, J.F. Schiel, E.S.K. Menon, D.J. Woo, The connections between powder variability and coating microstructures for cold spray deposition of austenitic stainless steel, Surf. Coatings Technol. 334 (2018) 50–60. https://doi.org/10.1016/j.surfcoat.2017.10.082.

[202] T. Suhonen, T. Varis, S. Dosta, M. Torrell, J.M. Guilemany, Residual stress development in cold sprayed Al, Cu and Ti coatings, Acta Mater. 61 (2013) 6329–6337. https://doi.org/10.1016/j.actamat.2013.06.033.

[203] W.B. Choi, L. Li, V. Luzin, R. Neiser, T. Gnäupel-Herold, H.J. Prask, S. Sampath, A. Gouldstone, Integrated characterization of cold sprayed aluminum coatings, Acta Mater. 55 (2007) 857–866. https://doi.org/10.1016/j.actamat.2006.09.006.

[204] P. Cavaliere, A. Perrone, A. Silvello, L. A., B. G, I.G. Cano, B. Sadeghi, S. Nagy, Cyclic behavior of FeCoCrNiMn high entropy alloy coatings produced through cold spray, J. Alloys Compd. 931 (2023) 167550. https://doi.org/10.1016/j.jallcom.2005.05.002.

[205] P. Cavaliere, A. Perrone, A. Silvello, A. Laska, G. Blasi, I.G. Cano, Fatigue Bending of V-Notched Cold-Sprayed FeCoCrNiMn Coatings, Metals (Basel). 12 (2022) 1–21. https://doi.org/10.3390/met12050780.

[206] A.S.M. Ang, C.C. Berndt, A review of testing methods for thermal spray coatings, Int. Mater. Rev. 59 (2014) 179–223. https://doi.org/10.1179/1743280414Y.0000000029.

[207] R. Ghelichi, S. Bagherifard, D. Macdonald, I. Fernandez-Pariente, B. Jodoin, M. Guagliano, Experimental and numerical study of residual stress evolution in cold spray coating, Appl. Surf. Sci. 288 (2014) 26–33. https://doi.org/10.1016/j.apsusc.2013.09.074.

[208] A. Moridi, S.M.H. Gangaraj, S. Vezzu, M. Guagliano, Number of Passes and Thickness Effect on Mechanical Characteristics of Cold Spray Coating, Procedia Eng. 74 (2014) 449–459. https://doi.org/10.1016/j.proeng.2014.06.296.

[209] D.J. Barton, V.S. Bhattiprolu, B.C. Hornbuckle, C.M. Batali, K.A. Darling, G.B. Thompson, L.N. Brewer, Residual Stress Generation in Laser-Assisted Cold Spray Deposition of Oxide Dispersion Strengthened Fe91Ni8Zr1, J. Therm. Spray Technol. 29 (2020) 1550–1563.

https://doi.org/10.1007/s11666-020-01079-6.

[210] M.E. Fitzpatrick, A. Fry, P. Holdway, F.A. Kandil, J. Shackleton, L. Suominen, Measurement Good Practice Guide No. 52. Determination of Residual Stresses by X-ray Diffraction, 2005. http://eprintspublications.npl.co.uk/2391/ (accessed April 27, 2023).

[211] A. Vargas-Uscategui, P.C. King, M.J. Styles, M. Saleh, V. Luzin, K. Thorogood, Residual Stresses in Cold Spray Additively Manufactured Hollow Titanium Cylinders, J. Therm. Spray Technol. 29 (2020) 1508–1524. https://doi.org/10.1007/s11666-020-01028-3.

[212] R.F. Brown, G.M. Smith, J. Potter, T.J. Eden, Parameter Development via In Situ Residual Stress Measurement and Post-deposition Analysis of Cold Spray CuNi Coatings, J. Therm. Spray Technol. 29 (2020) 1876–1891. https://doi.org/10.1007/s11666-020-01109-3.

[213] R. Singh, S. Schruefer, S. Wilson, J. Gibmeier, R. Vassen, Influence of coating thickness on residual stress and adhesion-strength of cold-sprayed Inconel 718 coatings, Surf. Coat. Technol. 350 (2018) 64–73. https://doi.org/10.1016/j.surfcoat.2018.06.080.

[214] K. Bobzin, W. Wietheger, M.A. Knoch, A. Schacht, U. Reisgen, R. Sharma, L. Oster, Comparison of Residual Stress Measurements Conducted by X-ray Stress Analysis and Incremental Hole Drilling Method, J. Therm. Spray Technol. 29 (2020) 1218–1228. https://doi.org/10.1007/s11666-020-01056-z.

[215] S. Rech, A. Trentin, S. Vezzu, J. Legoux, E. Irissou, M. Guagliano, Influence of Pre-Heated Al 6061 Substrate Temperature on the Residual Stresses of Multipass Al Coatings Deposited by Cold Spray, J. Therm. Spray Technol. 20 (2011) 243–251. https://doi.org/10.1007/s11666-010-9596-7.

[216] Q. Wang, N. Ma, W. Huang, J. Shi, X. Luo, S. Morooka, M. Watanabe, Key role of temperature on delamination in solid- state additive manufacturing via supersonic impact, Mater. Res. Lett. 11 (2023) 742–748. https://doi.org/10.1080/21663831.2023.2227221.

[217] Q. Wang, X. Luo, S. Tsutsumi, T. Sasaki, C. Li, N. Ma, Measurement and analysis of cold spray residual stress using arbitrary Lagrangian–Eulerian method, Addit. Manuf. 35 (2020) 101296. https://doi.org/10.1016/j.addma.2020.101296.

[218] M.B. Prime, The contour method: Simple 2-D mapping of residual stresses, in: ASME Int. Mech. Eng. Congr. Expo. Proc., 2000: pp. 121–127. https://doi.org/10.1115/IMECE2000-1262.

[219] V. Luzin, K. Spencer, M.X. Zhang, Residual stress and thermo-mechanical properties of cold spray metal coatings, Acta Mater. 59 (2011) 1259–1270. https://doi.org/10.1016/j.actamat.2010.10.058.

[220] K. Spencer, V. Luzin, N. Matthews, M.X. Zhang, Residual stresses in cold spray Al coatings: The effect of alloying and of process parameters, Surf. Coatings Technol. 206 (2012) 4249–4255. https://doi.org/10.1016/j.surfcoat.2012.04.034.

[221] X. Song, J. Everaerts, W. Zhai, H. Zheng, A.W.Y. Tan, W. Sun, F. Li, I.

Marinescu, E. Liu, A.M. Korsunsky, Residual stresses in single particle splat of metal cold spray process – Numerical simulation and direct measurement, Mater. Lett. 230 (2018) 152–156. https://doi.org/10.1016/j.matlet.2018.07.117.

[222] W. Li, K. Yang, D. Zhang, X. Zhou, Residual Stress Analysis of Cold-Sprayed Copper Coatings by Numerical Simulation, J. Therm. Spray Technol. 25 (2016) 131–142. https://doi.org/10.1007/s11666-015-0308-1.

[223] E. Lin, Q. Chen, O.C. Ozdemir, V.K. Champagne, S. Müftü, Effects of Interface Bonding on the Residual Stresses in Cold-Sprayed Al-6061: A Numerical Investigation, J. Therm. Spray Technol. 28 (2019) 472–483. https://doi.org/10.1007/s11666-019-00827-7.

[224] M. Saleh, V. Luzin, K. Spencer, Analysis of the residual stress and bonding mechanism in the cold spray technique using experimental and numerical methods, Surf. Coatings Technol. 252 (2014) 15–28. https://doi.org/10.1016/j.surfcoat.2014.04.059.

[225] P. Bansal, P.H. Shipway, S.B. Leen, A hybrid implicit-explicit finite element methodology for coating formation in the high-velocity oxy-fuel spraying process, Proc. Inst. Mech. Eng. Part L J. Mater. Des. Appl. 221 (2007) 285–297. https://doi.org/10.1243/14644207JMDA159.

[226] P. Bansal, P.H. Shipway, S.B. Leen, Effect of particle impact on residual stress development in HVOF sprayed coatings, in: Proc. Int. Therm. Spray Conf., 2006: pp. 570–575. https://doi.org/10.1361/105996306X146703.

[227] F. Oviedo, A. Valarezo, Residual Stress in High-Velocity Impact Coatings: Parametric Finite Element Analysis Approach, J. Therm. Spray Technol. 29 (2020) 1268–1288. https://doi.org/10.1007/s11666-020-01026-5.

[228] O. Ozdemir, Q. Chen, … S.M.-J. of T.S., undefined 2019, Modeling the continuous heat generation in the cold spray coating process, Springer. 28 (2019) 108–123. https://doi.org/10.1007/s11666-018-0794-z.

[229] A. Mcdonald, A. Ryabinin, A.G. Mcdonald, A.N. Ryabinin, E. Irissou, J.-G. Legoux, Gas-substrate heat exchange during cold-gas dynamic spraying, Springer. 22 (2013) 391–397. https://doi.org/10.1007/s11666-012-9828-0.

[230] A. Nastic, B. Jodoin, Evaluation of Heat Transfer Transport Coefficient for Cold Spray Through Computational Fluid Dynamics and Particle In-Flight Temperature Measurement Using a High-Speed IR Camera, J. Therm. Spray Technol. 27 (2018) 1491–1517. https://doi.org/10.1007/s11666-018-0787-y.

[231] Z. Arabgol, H. Assadi, T. Schmidt, F. Gärtner, T. Klassen, Analysis of thermal history and residual stress in cold-sprayed coatings, in: J. Therm. Spray Technol., Springer, 2014: pp. 84–90. https://doi.org/10.1007/s11666-013-9976-x.

[232] E. Lin, I. Nault, O.C. Ozdemir, V.K. Champagne, A. Nardi, S. Müftü, Thermo-Mechanical Deformation History and the Residual Stress Distribution in Cold Spray, J. Therm. Spray Technol. 29 (2020) 1424–1436. https://doi.org/10.1007/s11666-020-01034-5.

[233] C. Chen, Y. Xie, C. Verdy, R. Huang, H. Liao, Z. Ren, S. Deng, Numerical

investigation of transient coating build-up and heat transfer in cold spray, Surf. Coatings Technol. 326 (2017) 355–365. https://doi.org/10.1016/j.surfcoat.2017.07.069.

[234] E. Lin, I. Nault, V.K. Champagne, A. Nardi, S. Müftü, Analysis of Interface Fracture of Cold-Sprayed Coatings Due to Thermal Cycling, J. Therm. Spray Technol. 29 (2020) 158–172. https://doi.org/10.1007/s11666-019-00942-5.

[235] J.F. Molinari, M. Ortiz, A study of solid-particle erosion of metallic targets, Int. J. Impact Eng. 27 (2002) 347–358. https://doi.org/10.1016/S0734-743X(01)00055-0.

[236] D.B. Miracle, J.D. Miller, O.N. Senkov, C. Woodward, M.D. Uchic, J. Tiley, Exploration and development of high entropy alloys for structural applications, Entropy. 16 (2014) 494–525. https://doi.org/10.3390/e16010494.

[237] D.B. Miracle, O.N. Senkov, A critical review of high entropy alloys and related concepts, Acta Mater. 122 (2017) 448–511. https://doi.org/10.1016/j.actamat.2016.08.081.

[238] J.W. Yeh, Recent progress in high-entropy alloys, Ann. Chim. Sci. Des Mater. 31 (2006) 633–648. https://doi.org/10.3166/acsm.31.633-648.

[239] F. Otto, A. Dlouhý, K.G. Pradeep, M. Kuběnová, D. Raabe, G. Eggeler, E.P. George, Decomposition of the single-phase high-entropy alloy CrMnFeCoNi after prolonged anneals at intermediate temperatures, Acta Mater. 112 (2016) 40–52. https://doi.org/10.1016/j.actamat.2016.04.005.

[240] B. Schuh, F. Mendez-Martin, B. Völker, E.P. George, H. Clemens, R. Pippan, A. Hohenwarter, Mechanical properties, microstructure and thermal stability of a nanocrystalline CoCrFeMnNi high-entropy alloy after severe plastic deformation, Acta Mater. 96 (2015) 258–268. https://doi.org/10.1016/j.actamat.2015.06.025.

[241] M.H. Tsai, J.W. Yeh, High-entropy alloys: A critical review, Mater. Res. Lett. 2 (2014) 107–123. https://doi.org/10.1080/21663831.2014.912690.

[242] E.J. Pickering, N.G. Jones, High-entropy alloys: a critical assessment of their founding principles and future prospects, Int. Mater. Rev. 61 (2016) 183–202. https://doi.org/10.1080/09506608.2016.1180020.

[243] J.W. Yeh, Alloy design strategies and future trends in high-entropy alloys, JOM. 65 (2013) 1759–1771. https://doi.org/10.1007/s11837-013-0761-6.

[244] J. Chen, X. Zhou, W. Wang, B. Liu, Y. Lv, W. Yang, D. Xu, Y. Liu, A review on fundamental of high entropy alloys with promising high–temperature properties, J. Alloys Compd. 760 (2018) 15–30. https://doi.org/10.1016/j.jallcom.2018.05.067.

[245] Y. Zhang, Y.J. Zhou, J.P. Lin, G.L. Chen, P.K. Liaw, Solid-solution phase formation rules for multi-component alloys, Adv. Eng. Mater. 10 (2008) 534–538. https://doi.org/10.1002/adem.200700240.

[246] H. Shahmir, M.S. Mehranpour, S.A. Arsalan Shams, T.G. Langdon, Twenty years of the CoCrFeNiMn high-entropy alloy: achieving exceptional mechanical properties through microstructure engineering, J. Mater. Res.

Technol. 23 (2023) 3362–3423. https://doi.org/10.1016/j.jmrt.2023.01.181.

[247] X. Yang, Y. Zhang, Prediction of high-entropy stabilized solid-solution in multi-component alloys, Mater. Chem. Phys. 132 (2012) 233–238. https://doi.org/10.1016/j.matchemphys.2011.11.021.

[248] S. Guo, C.T. Liu, Phase stability in high entropy alloys: Formation of solid-solution phase or amorphous phase, Prog. Nat. Sci. Mater. Int. 21 (2011) 433–446. https://doi.org/10.1016/S1002-0071(12)60080-X.

[249] S. Guo, C. Ng, J. Lu, C.T. Liu, Effect of valence electron concentration on stability of fcc or bcc phase in high entropy alloys, J. Appl. Phys. 109 (2011). https://doi.org/10.1063/1.3587228.

[250] C. Zhang, F. Zhang, S. Chen, W. Cao, Computational thermodynamics aided high-entropy alloy design, Jom. 64 (2012) 839–845. https://doi.org/10.1007/s11837-012-0365-6.

[251] F. Zhang, C. Zhang, S.L. Chen, J. Zhu, W.S. Cao, U.R. Kattner, An understanding of high entropy alloys from phase diagram calculations, Calphad Comput. Coupling Phase Diagrams Thermochem. 45 (2014) 1–10. https://doi.org/10.1016/j.calphad.2013.10.006.

[252] R. Raghavan, K.C. Hari Kumar, B.S. Murty, Analysis of phase formation in multi-component alloys, J. Alloys Compd. 544 (2012) 152–158. https://doi.org/10.1016/j.jallcom.2012.07.105.

[253] K.-C. Chou, Y. Austin Chang, A Study of Ternary Geometrical Models, Berichte Der Bunsengesellschaft Für Phys. Chemie. 93 (1989) 735–741. https://doi.org/10.1002/bbpc.19890930615.

[254] H. Shahmir, J. He, Z. Lu, M. Kawasaki, T.G. Langdon, Effect of annealing on mechanical properties of a nanocrystalline CoCrFeNiMn high-entropy alloy processed by high-pressure torsion, Mater. Sci. Eng. A. 676 (2016) 294–303. https://doi.org/10.1016/j.msea.2016.08.118.

[255] H. Shahmir, T. Mousavi, J. He, Z. Lu, M. Kawasaki, T.G. Langdon, Microstructure and properties of a CoCrFeNiMn high-entropy alloy processed by equal-channel angular pressing, Mater. Sci. Eng. A. 705 (2017) 411–419. https://doi.org/10.1016/j.msea.2017.08.083.

[256] B. Dovgyy, A. Piglione, P.A. Hooper, M.S. Pham, Comprehensive assessment of the printability of CoNiCrFeMn in Laser Powder Bed Fusion, Mater. Des. 194 (2020) 108845. https://doi.org/10.1016/j.matdes.2020.108845.

[257] M. Jin, A. Piglione, B. Dovgyy, E. Hosseini, P.A. Hooper, S.R. Holdsworth, M.S. Pham, Cyclic plasticity and fatigue damage of CrMnFeCoNi high entropy alloy fabricated by laser powder-bed fusion, Addit. Manuf. 36 (2020) 101584. https://doi.org/10.1016/j.addma.2020.101584.

[258] A. Ostovari Moghaddam, N.A. Shaburova, M.N. Samodurova, A. Abdollahzadeh, E.A. Trofimov, Additive manufacturing of high entropy alloys: A practical review, J. Mater. Sci. Technol. 77 (2021) 131–162. https://doi.org/10.1016/j.jmst.2020.11.029.

[259] H. Shahmir, P. Asghari-Rad, M.S. Mehranpour, F. Forghani, H.S. Kim, M.

Nili-Ahmadabadi, Evidence of FCC to HCP and BCC-martensitic transformations in a CoCrFeNiMn high-entropy alloy by severe plastic deformation, Mater. Sci. Eng. A. 807 (2021) 140875. https://doi.org/10.1016/j.msea.2021.140875.

[260] Z. Li, L. Fu, H. Zheng, R. Yu, L. Lv, Y. Sun, X. Dong, A. Shan, Effect of Annealing Temperature on Microstructure and Mechanical Properties of a Severe Cold-Rolled FeCoCrNiMn High-Entropy Alloy, Metall. Mater. Trans. A Phys. Metall. Mater. Sci. 50 (2019) 3223–3237. https://doi.org/10.1007/s11661-019-05231-y.

[261] E.J. Pickering, R. Muñoz-Moreno, H.J. Stone, N.G. Jones, Precipitation in the equiatomic high-entropy alloy CrMnFeCoNi, Scr. Mater. 113 (2016) 106–109. https://doi.org/10.1016/j.scriptamat.2015.10.025.

[262] G. Laplanche, O. Horst, F. Otto, G. Eggeler, E.P. George, Microstructural evolution of a CoCrFeMnNi high-entropy alloy after swaging and annealing, J. Alloys Compd. 647 (2015) 548–557. https://doi.org/10.1016/j.jallcom.2015.05.129.

[263] J.W. Bae, J. Moon, M.J. Jang, D. Yim, D. Kim, S. Lee, H.S. Kim, Trade-off between tensile property and formability by partial recrystallization of CrMnFeCoNi high-entropy alloy, Mater. Sci. Eng. A. 703 (2017) 324–330. https://doi.org/10.1016/j.msea.2017.07.079.

[264] J. Gu, S. Ni, Y. Liu, M. Song, Regulating the strength and ductility of a cold rolled FeCrCoMnNi high-entropy alloy via annealing treatment, Mater. Sci. Eng. A. 755 (2019) 289–294. https://doi.org/10.1016/j.msea.2019.04.025.

[265] Y. Xu, W. Li, L. Qu, X. Yang, B. Song, R. Lupoi, S. Yin, Solid-state cold spraying of FeCoCrNiMn high-entropy alloy: an insight into microstructure evolution and oxidation behavior at 700-900 °C, J. Mater. Sci. Technol. 68 (2020) 172–183. https://doi.org/10.1016/j.jmst.2020.06.041.

[266] P. Yu, N. Fan, Y. Zhang, Z. Wang, W. Li, Microstructure evolution and composition redistribution of FeCoNiCrMn high entropy alloy under extreme plastic deformation, (2022). https://doi.org/10.1080/21663831.2021.2023678.

[267] M. Laurent-Brocq, A. Akhatova, L. Perrière, S. Chebini, X. Sauvage, E. Leroy, Y. Champion, Insights into the phase diagram of the CrMnFeCoNi high entropy alloy, Acta Mater. 88 (2015) 355–365. https://doi.org/10.1016/j.actamat.2015.01.068.

[268] J.-E. Ahn, Y.-K. Kim, S.-H. Yoon, K.-A. Lee, Tuning the Microstructure and Mechanical Properties of Cold Sprayed Equiatomic CoCrFeMnNi High-Entropy Alloy Coating Layer, Met. Mater. Int. (2020) 1–10. https://doi.org/10.1007/s12540-020-00886-4.

[269] J. Mahaffey, A. Vackel, S. Whetten, M. Melia, A.B. Kustas, Structure Evolution and Corrosion Performance of CoCrFeMnNi High Entropy Alloy Coatings Produced Via Plasma Spray and Cold Spray, J. Therm. Spray Technol. 31 (2022) 1143–1154. https://doi.org/10.1007/s11666-022-01373-5.

[270] C.J. Akisin, C.J. Bennett, F. Venturi, T. Hussain, Effect of Heat-Treatment

on the Microstructure and Mechanical Properties of CoCrFeNiMn High Entropy Alloy Additively Manufactured via Cold Spray, in: ITSC 2023 Proc. from Int. Therm. Spray Conf., ASM International, 2023: pp. 400–407. https://doi.org/10.31399/asm.cp.itsc2023p0400.

[271] HORIBA INSTRUMENTS INCORPORATED, A GUIDEBOOK TO PARTICLE SIZE MEASUREMENT, 2022.

[272] J.. Goldstein, D.. Newbury, J.. Micheal, N.. Ritchie, J.. Scott, D.. Joy, Scanning electron microscopy and X-ray microanalysis, Fourth edi, Springer, 2017. https://doi.org/https://doi.org/10.1007/978-1-4939-6676-9.

[273] W. Pantleon, Resolving the geometrically necessary dislocation content by conventional electron backscattering diffraction, Scr. Mater. 58 (2008) 994–997. https://doi.org/10.1016/J.SCRIPTAMAT.2008.01.050.

[274] W.C. Oliver, G.M. Pharr, Measurement of hardness and elastic modulus by instrumented indentation: Advances in understanding and refinements to methodology, J. Mater. Res. 19 (2004) 3–20. https://doi.org/10.1557/jmr.2004.19.1.3.

[275] T.A. Owoseni, M. Bai, N. Curry, E.H. Lester, D.M. Grant, T. Hussain, Residual Stress Measurement of Suspension HVOF-Sprayed Alumina Coating via a Hole-Drilling Method, J. Therm. Spray Technol. 29 (2020) 1339–1350. https://doi.org/10.1007/s11666-020-01072-z.

[276] ASTM E8, ASTM E8/E8M standard test methods for tension testing of metallic materials 1, Annu. B. ASTM Stand. 4. (2010) 1–27. https://doi.org/10.1520/E0008.

[277] F. Gärtner, T. Stoltenhoff, J. Voyer, H. Kreye, S. Riekehr, M. Koçak, Mechanical properties of cold-sprayed and thermally sprayed copper coatings, Surf. Coatings Technol. 200 (2006) 6770–6782. https://doi.org/10.1016/j.surfcoat.2005.10.007.

[278] N. Hutasoit, M.A. Javed, R.A.R. Rashid, S. Wade, S. Palanisamy, Effects of build orientation and heat treatment on microstructure, mechanical and corrosion properties of Al6061 aluminium parts built by cold spray additive manufacturing process, Int. J. Mech. Sci. 204 (2021) 106526. https://doi.org/10.1016/j.ijmecsci.2021.106526.

[279] G.S. Schajer, Practical Residual Stress Measurement Methods, John Wiley & Sons, Ltd, 2013. https://doi.org/10.1002/9781118402832.

[280] M.B. Prime, A.L. Kastengren, The contour method cutting assumption: Error minimization and correction, in: Conf. Proc. Soc. Exp. Mech. Ser., Springer New York LLC, 2011: pp. 233–250. https://doi.org/10.1007/978-1-4419-9792-0_40.

[281] F. Hosseinzadeh, P. Ledgard, P.J. Bouchard, Controlling the Cut in Contour Residual Stress Measurements of Electron Beam Welded Ti-6Al-4V Alloy Plates, Exp. Mech. 53 (2013) 829–839. https://doi.org/10.1007/s11340-012-9686-1.

[282] A. Haglund, M. Koehler, D. Catoor, E.P. George, V. Keppens, Polycrystalline elastic moduli of a high-entropy alloy at cryogenic temperatures, Intermetallics. 58 (2015) 62–64.

https://doi.org/10.1016/j.intermet.2014.11.005.

[283] L. Davidson, W. Selada, An Introduction to Turbulence Models, 2016.

[284] W.Y. Li, W. Gao, Some aspects on 3D numerical modeling of high velocity impact of particles in cold spraying by explicit finite element analysis, Appl. Surf. Sci. 255 (2009) 7878–7892. https://doi.org/10.1016/j.apsusc.2009.04.135.

[285] A.N. Ryabinin, E. Irissou, A. McDonald, J.G. Legoux, Simulation of gas-substrate heat exchange during cold-gas dynamic spraying, Int. J. Therm. Sci. 56 (2012) 12–18. https://doi.org/10.1016/j.ijthermalsci.2012.01.007.

[286] R.W. Lewis, K. Morgan, H.R. Thomas, K.N. Seetharamu, The finite element method in heat transfer analysis, 1995. https://doi.org/10.1016/s0928-4869(97)84250-4.

[287] D. Deng, H. Murakawa, Numerical simulation of temperature field and residual stress in multi-pass welds in stainless steel pipe and comparison with experimental measurements, Comput. Mater. Sci. 37 (2006) 269–277. https://doi.org/10.1016/j.commatsci.2005.07.007.

[288] K. Choong S., Thermophysical Properties of Stainless Steels, Argonne, Illinois, 1975.

[289] T.R. Walker, Development of a Coupled Numerical-Analytical Modelling Approach for Coaxial Direct Energy Deposition, University of Nottingham, United Kingdom, 2020.

[290] K. Jin, S. Mu, K. An, W.D. Porter, G.D. Samolyuk, G.M. Stocks, H. Bei, Thermophysical properties of Ni-containing single-phase concentrated solid solution alloys, Mater. Des. 117 (2017) 185–192. https://doi.org/10.1016/j.matdes.2016.12.079.

[291] G. Laplanche, P. Gadaud, O. Horst, F. Otto, G. Eggeler, E.P. George, Temperature dependencies of the elastic moduli and thermal expansion coefficient of an equiatomic, single-phase CoCrFeMnNi high-entropy alloy, J. Alloys Compd. 623 (2015) 348–353. https://doi.org/10.1016/j.jallcom.2014.11.061.

[292] J. Xu, J. Chen, Y. Duan, C. Yu, J. Chen, H. Lu, Comparison of residual stress induced by TIG and LBW in girth weld of AISI 304 stainless steel pipes, J. Mater. Process. Technol. 248 (2017) 178–184. https://doi.org/10.1016/j.jmatprotec.2017.05.014.

[293] T.S. Byun, N. Hashimoto, K. Farrell, Temperature dependence of strain hardening and plastic instability behaviors in austenitic stainless steels, Acta Mater. 52 (2004) 3889–3899. https://doi.org/10.1016/j.actamat.2004.05.003.

[294] M. Razavipour, B. Jodoin, Material Model for Predicting Dynamic Response of Copper and Nickel at Very High Strain Rates Under Cold Spray Conditions, J. Therm. Spray Technol. (2021) 1–20. https://doi.org/10.1007/s11666-020-01137-z.

[295] M.V. Vidaller, A. List, F. Gaertner, T. Klassen, S. Dosta, J.M. Guilemany, Single Impact Bonding of Cold Sprayed Ti-6Al-4V Powders on Different Substrates, J. Therm. Spray Technol. 24 (2015) 644–658.

https://doi.org/10.1007/s11666-014-0200-4.

[296] A.A. Tiamiyu, C.A. Schuh, Particle flattening during cold spray: Mechanistic regimes revealed by single particle impact tests, Surf. Coatings Technol. 403 (2020). https://doi.org/10.1016/j.surfcoat.2020.126386.

[297] R. Bobbili, V. Madhu, A modified Johnson-Cook model for FeCoNiCr high entropy alloy over a wide range of strain rates, Mater. Lett. 218 (2018) 103–105. https://doi.org/10.1016/j.matlet.2018.01.163.

[298] T. Özel, Y. Karpat, Identification of constitutive material model parameters for high-strain rate metal cutting conditions using evolutionary computational algorithms, Mater. Manuf. Process. 22 (2007) 659–667. https://doi.org/10.1080/10426910701323631.

[299] A.S. Khan, Y.S. Suh, R. Kazmi, Quasi-static and dynamic loading responses and constitutive modeling of titanium alloys, Int. J. Plast. 20 (2004) 2233–2248. https://doi.org/10.1016/J.IJPLAS.2003.06.005.

[300] H. Fukanuma, N. Ohno, B. Sun, R. Huang, In-flight particle velocity measurements with DPV-2000 in cold spray, Surf. Coatings Technol. 201 (2006) 1935–1941. https://doi.org/10.1016/j.surfcoat.2006.04.035.

[301] Z. Li, S. Zhao, S.M. Alotaibi, Y. Liu, B. Wang, M.A. Meyers, Adiabatic shear localization in the CrMnFeCoNi high-entropy alloy, Acta Mater. 151 (2018) 424–431. https://doi.org/10.1016/j.actamat.2018.03.040.

[302] B. Wang, A. Fu, X. Huang, B. Liu, Y. Liu, Z. Li, X. Zan, Mechanical Properties and Microstructure of the CoCrFeMnNi High Entropy Alloy Under High Strain Rate Compression, J. Mater. Eng. Perform. 25 (2016) 2985–2992. https://doi.org/10.1007/s11665-016-2105-5.

[303] P. Krasauskas, S. Kilikevičius, R.Č.- Mechanics, undefined 2014, Experimental analysis and numerical simulation of the stainless AISI 304 steel friction drilling process, Mechanika.Ktu.Lt. 20 (n.d.) 590–595. https://doi.org/10.5755/j01.mech.20.6.8664.

[304] G. Kay, Failure Modeling of Titanium-6Al-4V and 2024-T3 Aluminum with the Johnson-Cook Material Model, (2002). https://doi.org/10.2172/15006359.

[305] S.P.F.C. Jaspers, J.H. Dautzenberg, Material behaviour in conditions similar to metal cutting: Flow stress in the primary shear zone, J. Mater. Process. Technol. 122 (2002) 322–330. https://doi.org/10.1016/S0924-0136(01)01228-6.

[306] Y. Ichikawa, K. Ogawa, Critical Deposition Condition of CoNiCrAlY Cold Spray Based on Particle Deformation Behavior, J. Therm. Spray Technol. 26 (2017) 340–349. https://doi.org/10.1007/s11666-016-0477-6.

[307] Z. Arabgol, M. Villa Vidaller, H. Assadi, F. Gärtner, T. Klassen, Influence of thermal properties and temperature of substrate on the quality of cold-sprayed deposits, Acta Mater. 127 (2017) 287–301. https://doi.org/10.1016/j.actamat.2017.01.040.

[308] G. Sethi, N.S. Myers, R.M. German, An overview of dynamic compaction in powder metallurgy, Int. Mater. Rev. 53 (2008) 219–234.

https://doi.org/10.1179/174328008X309690.

[309] M. Hassani-Gangaraj, D. Veysset, K.A. Nelson, C.A. Schuh, Melt-driven erosion in microparticle impact, Nat. Commun. 9 (2018). https://doi.org/10.1038/s41467-018-07509-y.

[310] P. Coddet, C. Verdy, C. Coddet, F. Debray, F. Lecouturier, Mechanical properties of thick 304L stainless steel deposits processed by He cold spray, Surf. Coatings Technol. 277 (2015) 74–80. https://doi.org/10.1016/j.surfcoat.2015.07.001.

[311] M. Hassani-Gangaraj, D. Veysset, K.A. Nelson, C.A. Schuh, Melting Can Hinder Impact-Induced Adhesion, Phys. Rev. Lett. 119 (2017). https://doi.org/10.1103/PhysRevLett.119.175701.

[312] R.J. EICHELBERGER, J.W. GEHRING, Effects of Meteoroid Impacts on Space Vehicles, ARS J. 32 (1962) 1583–1591. https://doi.org/10.2514/8.6339.

[313] R. Singh, J. Kondás, C. Bauer, J. Cizek, J. Medricky, S. Csaki, J. Čupera, R. Procházka, D. Melzer, P. Konopík, Bulk-like ductility of cold spray additively manufactured copper in the as-sprayed state, Addit. Manuf. Lett. 3 (2022) 100052. https://doi.org/10.1016/j.addlet.2022.100052.

[314] C. Chen, Y. Xie, S. Yin, W. Li, X. Luo, X. Xie, R. Zhao, C. Deng, J. Wang, H. Liao, M. Liu, Z. Ren, Ductile and high strength Cu fabricated by solid-state cold spray additive manufacturing, J. Mater. Sci. Technol. 134 (2023) 234–243. https://doi.org/10.1016/J.JMST.2022.07.003.

[315] G.K. Williamson, W.H. Hall, X-ray line broadening from filed aluminium and wolfram, Acta Metall. 1 (1953) 22–31. https://doi.org/10.1016/0001-6160(53)90006-6.

[316] H. Jones, Microstructure of rapidly solidified materials, Mater. Sci. Eng. 65 (1984) 145–156. https://doi.org/10.1016/0025-5416(84)90208-8.

[317] V.K. Champagne, D.J. Helfritch, M.D. Trexler, B.M. Gabriel, The effect of cold spray impact velocity on deposit hardness, Model. Simul. Mater. Sci. Eng. 18 (2010) 8. https://doi.org/10.1088/0965-0393/18/6/065011.

[318] R. Chakrabarty, J. Song, Numerical simulations of ceramic deposition and retention in metal-ceramic composite cold spray, Surf. Coatings Technol. 385 (2020). https://doi.org/10.1016/j.surfcoat.2019.125324.

[319] T. Ungár, Á. Révész, A. Borbély, Dislocations and Grain Size in Electrodeposited Nanocrystalline Ni Determined by the Modified Williamson-Hall and Warren-Averbach Procedures, J. Appl. Crystallogr. 31 (1998) 554–558. https://doi.org/10.1107/S0021889897019559.

[320] G. Laplanche, A. Kostka, O.M. Horst, G. Eggeler, E.P. George, Microstructure evolution and critical stress for twinning in the CrMnFeCoNi high-entropy alloy, Acta Mater. 118 (2016) 152–163. https://doi.org/10.1016/j.actamat.2016.07.038.

[321] CHIN GY, HOSFORD WF, MENDORF DR, ACCOMMODATION OF CONSTRAINED DEFORMATION IN F.C.C. METALS BY SLIP AND TWINNING, in: 1969: pp. 433–456. https://doi.org/10.1098/rspa.1969.0051.

[322] M. Naeem, H. He, S. Harjo, T. Kawasaki, F. Zhang, B. Wang, S. Lan, Z. Wu, Y. Wu, Z. Lu, C.T. Liu, X.L. Wang, Extremely high dislocation density and deformation pathway of CrMnFeCoNi high entropy alloy at ultralow temperature, Scr. Mater. 188 (2020) 21–25. https://doi.org/10.1016/j.scriptamat.2020.07.004.

[323] G. Bae, J. Il Jang, C. Lee, Correlation of particle impact conditions with bonding, nanocrystal formation and mechanical properties in kinetic sprayed nickel, Acta Mater. 60 (2012) 3524–3535. https://doi.org/10.1016/j.actamat.2012.03.001.

[324] C. Haase, F. Tang, M.B. Wilms, A. Weisheit, B. Hallstedt, Combining thermodynamic modeling and 3D printing of elemental powder blends for high-throughput investigation of high-entropy alloys – Towards rapid alloy screening and design, Mater. Sci. Eng. A. 688 (2017) 180–189. https://doi.org/10.1016/j.msea.2017.01.099.

[325] M.A. Meyers, Y.B. Xu, Q. Xue, M.T. Pérez-Prado, T.R. McNelley, Microstructural evolution in adiabatic shear localization in stainless steel, Acta Mater. 51 (2003) 1307–1325. https://doi.org/10.1016/S1359-6454(02)00526-8.

[326] B.B. Jung, H.K. Lee, H.C. Park, Effect of grain size on the indentation hardness for polycrystalline materials by the modified strain gradient theory, Int. J. Solids Struct. 50 (2013) 2719–2724. https://doi.org/10.1016/j.ijsolstr.2013.05.002.

[327] W.H. Liu, Y. Wu, J.Y. He, T.G. Nieh, Z.P. Lu, Grain growth and the Hall-Petch relationship in a high-entropy FeCrNiCoMn alloy, Scr. Mater. 68 (2013) 526–529. https://doi.org/10.1016/j.scriptamat.2012.12.002.

[328] G.I. Taylor, Plastic strain in metals, Twenty-Eighth May Lect. to Inst. Met. (1938) 307–325. https://ci.nii.ac.jp/naid/10026664057/ (accessed July 28, 2022).

[329] W.F. Hosford, Mechanical behavior of materials, 2005. https://doi.org/10.1017/CBO9780511810930.

[330] R. Li, P. Niu, T. Yuan, P. Cao, C. Chen, K. Zhou, Selective laser melting of an equiatomic CoCrFeMnNi high-entropy alloy: Processability, non-equilibrium microstructure and mechanical property, J. Alloys Compd. 746 (2018) 125–134. https://doi.org/10.1016/j.jallcom.2018.02.298.

[331] J.R. Cahoon, W.H. Broughton, A.R. Kutzak, The determination of yield strength from hardness measurements, Metall. Trans. 2 (1971) 1979–1983. https://doi.org/10.1007/BF02913433.

[332] S. Yin, J. Cizek, X. Yan, R. Lupoi, Annealing strategies for enhancing mechanical properties of additively manufactured 316L stainless steel deposited by cold spray, Surf. Coatings Technol. 370 (2019) 353–361. https://doi.org/10.1016/j.surfcoat.2019.04.012.

[333] S. Bagherifard, S. Monti, M.V. Zuccoli, M. Riccio, J. Kondás, M. Guagliano, Cold spray deposition for additive manufacturing of freeform structural components compared to selective laser melting, Mater. Sci. Eng. A. 721 (2018) 339–350. https://doi.org/10.1016/j.msea.2018.02.094.

[334] P. Scardi, M. Leoni, Whole powder pattern modelling, Acta Crystallogr. Sect. A Found. Crystallogr. 58 (2002) 190–200. https://doi.org/10.1107/S0108767301021298.

[335] K.A. Christofidou, T.P. McAuliffe, P.M. Mignanelli, H.J. Stone, N.G. Jones, On the prediction and the formation of the sigma phase in CrMnCoFeNix high entropy alloys, J. Alloys Compd. 770 (2019) 285–293. https://doi.org/10.1016/j.jallcom.2018.08.032.

[336] M.E. Bloomfield, K.A. Christofidou, F. Monni, Q. Yang, M. Hang, N.G. Jones, The influence of Fe variations on the phase stability of CrMnFexCoNi alloys following long-duration exposures at intermediate temperatures, Intermetallics. 131 (2021) 107108. https://doi.org/10.1016/j.intermet.2021.107108.

[337] M.E. Bloomfield, K.A. Christofidou, N.G. Jones, Effect of Co on the phase stability of CrMnFeCoxNi high entropy alloys following long-duration exposures at intermediate temperatures, Intermetallics. 114 (2019) 106582. https://doi.org/10.1016/j.intermet.2019.106582.

[338] M. Heczko, V. Mazánová, R. Gröger, T. Záležák, M.S. Hooshmand, E.P. George, M.J. Mills, A. Dlouhý, Elemental segregation to lattice defects in the CrMnFeCoNi high-entropy alloy during high temperature exposures, Acta Mater. 208 (2021) 116719. https://doi.org/10.1016/j.actamat.2021.116719.

[339] J.W. Cahn, The kinetics of grain boundary nucleated reactions, Acta Metall. 4 (1956) 449–459. https://doi.org/10.1016/0001-6160(56)90041-4.

[340] N.D. Stepanov, D.G. Shaysultanov, R.S. Chernichenko, D.M. Ikornikov, V.N. Sanin, S. V. Zherebtsov, Mechanical properties of a new high entropy alloy with a duplex ultra-fine grained structure, Mater. Sci. Eng. A. 728 (2018) 54–62. https://doi.org/10.1016/j.msea.2018.04.118.

[341] M. V. Klimova, D.G. Shaysultanov, S. V. Zherebtsov, N.D. Stepanov, Effect of second phase particles on mechanical properties and grain growth in a CoCrFeMnNi high entropy alloy, Mater. Sci. Eng. A. 748 (2019) 228–235. https://doi.org/10.1016/j.msea.2019.01.112.

[342] T.H. Chou, J.C. Huang, C.H. Yang, S.K. Lin, T.G. Nieh, Consideration of kinetics on intermetallics formation in solid-solution high entropy alloys, Acta Mater. 195 (2020) 71–80. https://doi.org/10.1016/j.actamat.2020.05.015.

[343] K.S. Al-Hamdani, J.W. Murray, T. Hussain, A.T. Clare, Heat-treatment and mechanical properties of cold-sprayed high strength Al alloys from satellited feedstocks, Surf. Coatings Technol. 374 (2019) 21–31. https://doi.org/10.1016/j.surfcoat.2019.05.043.

[344] B. Ahmad, S.O. van der Veen, M.E. Fitzpatrick, H. Guo, Measurement and modelling of residual stress in wire-feed additively manufactured titanium, Mater. Sci. Technol. (United Kingdom). 34 (2018) 2250–2259. https://doi.org/10.1080/02670836.2018.1528747.

[345] B. Ahmad, S.O. van der Veen, M.E. Fitzpatrick, H. Guo, Measurement and modelling of residual stress in wire-feed additively manufactured titanium, Mater. Sci. Technol. (United Kingdom). 34 (2018) 2250–2259. https://doi.org/10.1080/02670836.2018.1528747.

[346] T. Hussain, D.G. McCartney, P.H. Shipway, T. Marrocco, Corrosion behavior of cold sprayed titanium coatings and free standing deposits, J. Therm. Spray Technol. 20 (2011) 260–274. https://doi.org/10.1007/s11666-010-9540-x.

[347] T.W. Clyne, S.C. Gill, Residual stresses in thermal spray coatings and their effect on interfacial adhesion: A review of recent work, J. Therm. Spray Technol. 5 (1996) 401–418. https://doi.org/10.1007/BF02645271.

[348] P. Mercelis, J.P. Kruth, Residual stresses in selective laser sintering and selective laser melting, Rapid Prototyp. J. 12 (2006) 254–265. https://doi.org/10.1108/13552540610707013.

[349] Y.C. Tsui, T.W. Clyne, An analytical model for predicting residual stresses in progressively deposited coatings: Part 1: Planar geometry, Thin Solid Films. 306 (1997) 23–33. https://doi.org/10.1016/S0040-6090(97)00199-5.

[350] T.W. Clyne, Residual stresses in surface coatings and their effects on interfacial debonding, Key Eng. Mater. (1996) 307–330. https://doi.org/10.4028/www.scientific.net/kem.116-117.307.

[351] S. Kuroda, Y. Tashiro, H. Yumoto, S. Taira, H. Fukanuma, S. Tobe, Peening Action and Residual Stresses in High- Velocity Oxygen Fuel Thermal Spraying of 316L Stainless Steel, J. Therm. Spray Technol. 10 (2001) 367–374.

[352] M. Shiomi, K. Osakada, K. Nakamura, T. Yamashita, F. Abe, Residual stress within metallic model made by selective laser melting process, CIRP Ann. - Manuf. Technol. 53 (2004) 195–198. https://doi.org/10.1016/S0007-8506(07)60677-5.

[353] B. Marzbanrad, E. Toyserkani, H. Jahed, Customization of residual stress induced in cold spray printing, J. Mater. Process. Technol. 289 (2021). https://doi.org/10.1016/j.jmatprotec.2020.116928.

[354] R.C. McCune, W.T. Donlon, O.O. Popoola, E.L. Cartwright, Characterization of copper layers produced by cold gas-dynamic spraying, J. Therm. Spray Technol. 9 (2000) 73–82. https://doi.org/10.1361/105996300770350087.